

**NEW ORGANIC AND INORGANIC
FUNCTIONAL MATERIALS FOR
PHOTOVOLTAIC APPLICATIONS:
SYNTHESIS, CHARACTERIZATION,
AND DEVICE PERFORMANCE STUDIES**

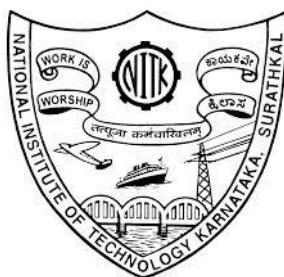
Thesis

Submitted in partial fulfilment of the requirements for the degree of

DOCTOR OF PHILOSOPHY

by

KAVYASHREE SUKAD KEREMANE



DEPARTMENT OF CHEMISTRY

NATIONAL INSTITUTE OF TECHNOLOGY KARNATAKA

SURATHKAL, MANGALORE - 575 025

January, 2022

DECLARATION

By the Ph.D. Research Scholar

I hereby declare that the Research Thesis entitled “**New Organic and Inorganic Functional Materials for Photovoltaic Applications: Synthesis, Characterization, and Device Performance Studies**” which is being submitted to the **National Institute of Technology Karnataka, Surathkal** in partial fulfilment of the requirements for the award of the Degree of **Doctor of Philosophy in Chemistry** is a *bonafide report of the research work carried out by me*. The material contained in this Research Thesis has not been submitted to any University or Institution for the award of any degree.



Kavyashree Sukad Keremane

Reg. No. 165027CY16F03

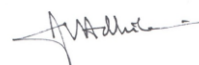
Department of Chemistry

Place: NITK, Surathkal

Date: 28-01-2022

CERTIFICATE

This is to certify that the Research Thesis entitled “**New Organic and Inorganic Functional Materials for Photovoltaic Applications: Synthesis, Characterization, and Device Performance Studies**” submitted by **Ms. Kavyashree Sukad Keremane** (Register Number: **165027CY16F03**) as the record of the research work carried out by her *is accepted as the Research Thesis submission* in partial fulfilment of the requirements for the award of degree of Doctor of Philosophy.



Prof. A. Vasudeva Adhikari

Research Guide

Date: 28-01-2022



Dr. Udaya Kumar D.

Research Guide (Administrative)

Date: 28-01-2022



Chairman - DRPC

Date: 28-01-2022

DEDICATED TO
MY BELOVED
FAMILY

ACKNOWLEDGEMENTS

It has been a great and memorable time in my life to pursue my Ph.D. studies at National Institute of Technology Karnataka. First and foremost, I thank the almighty **GOD** for instilling a curious spirit in me and giving me the wisdom, patience, and strength to successfully complete my thesis. My research would not have been possible without the support and contributions of many people who kindly helped me to make this dissertation possible.

I would like to express my profound sense of gratitude to my research supervisor **Dr. Airody Vasudeva Adhikari**, Retired Professor, Department of Chemistry, NITK for his invaluable guidance, tremendous academic support throughout the course of this investigation. He constantly encouraged and inspired me with his intensive research capability at every stage of my research. The directions he gave and the knowledge he shared in each and every single step of this work made it all possible. It has been a great honor and pleasure to conduct my Ph.D. journey under his supervision. I am extremely thankful to him for all his support during my research work.

Besides my advisor, I would like to express my sincere gratitude to my co-guide **Dr. Udaya Kumar D.**, Department of Chemistry, NITK for all the academic as well as administrative support, and encouragement to complete this endeavor successfully.

I sincerely thank **Prof. K. Umamaheshwar Rao**, Director, NITK, for providing necessary facilities to carry out this research work. I express my earnest thanks to the RPAC members, Dr. Beneesh P. B., Department of Chemistry and Dr. Rathnamala Rao, Department of Electronics and Communication Engineering, NITK for insightful comments and constructive criticism towards the improvement of research quality.

My special thanks to **Prof. Subodh G. Mhaisalkar**, Executive Director, School of Material Science and Engineering, NTU, Singapore for extending the laboratory facility to carry out the studies on carbon-based perovskite solar cells. Also, I am thankful to **Dr. Ahmed El-Shafei**, Department of Textile Engineering, Chemistry and Science at NC State University, USA, and **Dr. Fabrice Odobel**, University of Nantes, France for providing the fabrication facility for *n*-type and *p*-type DSSCs, respectively.

I am also thankful to Prof. A. N. Shetty, Prof. A. C. Hegde, Prof. B. R. Bhat, Prof. D. K. Bhat, Prof. A. M. Isloor, Dr. D. R. Trivedi, Dr. Sib Sankar Mal, Dr. Saikat Dutta, Dr. Debashree Chakraborty, Dr. Vijayendra S. Shetti, and Dr. Lakshmi Vellanki, Department of Chemistry for their constant support and encouragement. I also wish to extend my gratitude to all non-teaching staff in the Department of Chemistry.

I am grateful to Prof. A. S. Achalkumar, Department of Chemistry, IIT Guwahati, for helping with characterization studies. I thank the Indian Institute of Science (IISc), Bangalore, Manipal Institute of Technology (MIT), Manipal and Mangalore University for providing NMR and Mass Spectral facilities.

I also thank my group members Dr. Praveen Naik, Dr. Naveen Chandra P., Dr. Vinayakumara, Dr. Rajalakshmi K., Mr. Madhukara Acharya, Ms. Vishrutha, Ms. Sruthi H., and Mr. S. S. Sudhanva Prasad for their constant support, encouragement, and company.

I am grateful to my dear friends Mr. Gururaj Acharya, Mr. A. Sampath Kumar, Ms. Nurul Ain Nisrina, and Dr. Sateesh Prathapani for their support and help during my research work. I extend my sincere thanks to all the research scholars in the Department of Chemistry for their constant help and support.

Mere words are not enough to express my gratitude to my family, father Mr. Sukad H. N. and mother Mrs. Bhavani B. N. for instilling in me the virtues of perseverance, commitment, love, and prayers. I also thank my brother Mr. Bhargav Keremane for his constant support, and relentless encouragement to strive for excellence. Finally, I thank all my family members and friends for their love and constant support.

KAVYASHREE S. KEREMANE

ABSTRACT

Over the past three decades, the dye-sensitized solar cell (DSSC) and perovskite solar cell (PSC), which belong to the third-generation solar cells have emerged as an attractive, and promising photovoltaic technologies due to their superior performance, lightweight, flexibility, eco-friendly nature, and low manufacturing costs. On this basis, in the present work, the attention has been focused on the three areas of solar cell research, *viz.* new organic *n*-/*p*-type dyes as sensitizers/co-sensitizers for DSSCs, new organic hole-transport materials for PSCs, and solvent selection as well as the development of large-area carbon-based PSCs.

Based on the detailed literature survey, thirty-four new metal-free *n*-type dyes, *viz.* ***n*-K₁₋₃₄**, and eight *p*-type dyes, *viz.* ***p*-K₃₅₋₄₂** were designed as potential sensitizers/co-sensitizers for DSSC applications. Also, two new organic molecules (***h*-K₄₃₋₄₄**) were designed as possible HTMs for PSCs. All of them were successfully synthesized and characterized. Further, they were subjected to in-depth optical, electrochemical, theoretical, and photovoltaic studies. From these studies, it is clear that the synthesized molecules possess all the prerequisites to act as sensitizers/HTMs in the devices. Amongst the *n*-type molecules, the dye ***n*-K₅** displayed the optimum *PCE* of 2.44 % as a sensitizer and ***n*-K₆** dye showcased an improved *PCE* of 8.81 % as co-sensitizer along with Ru-based **HD-2** sensitizer. The photovoltaic results of *p*-type molecules disclose that the ***p*-K₃₆**-based DSSC showed *PCE* of 0.031 %, comparable with that of benchmark reference **P1**. Furthermore, among the newly synthesized HTMs, the ***h*-K₄₃** displayed a better *PCE* of 2.55 % in PSCs. To sum up, by further optimizing the molecular structure of dyes/HTMs it is possible to further ameliorate the photovoltaic performance of devices.

Further, a detailed investigation was carried out on the selection of appropriate solvent for a single-step deposition of mixed-cation perovskite in carbon-based PSCs (C-PSCs) using the Lewis acid-base adduct approach. Strikingly, the device fabricated using DMSO solvent yielded the highest *PCE* of 12.33%. In continuation, the highly efficient and stable large-area C-PSCs have been developed using CsBr modified mp-TiO₂ as a superior electron transport material, with *PCE* 12.59% (active area 0.7 cm²) and 11.55 % (active area 70 cm²). Conclusively, this exploration is expected to provide deeper insights for the further scaling-up of carbon-based PSCs with improved efficiency and stability for their future commercial applications.

Keywords: DSSC; *n*-/*p*-type sensitizers; co-sensitizers; HTM; PSC; DFT; Photovoltaic devices

CONTENTS

CHAPTER 1

INTRODUCTION

PART A: PHOTOVOLTAIC CELLS: AN OVERVIEW

1.1	A BRIEF INTRODUCTION TO PHOTOVOLTAICS	01
1.2	SOLAR CELL TECHNOLOGIES	02
1.3	PRESENT SCENARIO OF PHOTOVOLTAIC TECHNOLOGY	02
1.4	PHOTOVOLTAIC PARAMETERS	03
1.4.1	Short-circuit photocurrent (J_{SC})	03
1.4.2	Open-circuit photovoltage (V_{OC})	04
1.4.3	Fill factor (FF)	04
1.4.4	Power conversion efficiency (η)	04
1.4.5	Incident-photon-current conversion efficiency ($IPCE$)	05
1.5	DYE-SENSITIZED SOLAR CELL (DSSC)	05
1.5.1	Working principle of DSSC	06
1.5.2	<i>n</i> -Type dye-sensitized solar cell (<i>n</i> -type DSSC)	07
1.5.3	<i>p</i> -Type dye sensitized solar cell (<i>p</i> -type DSSC)	10
1.5.4	Components of <i>n</i> -/ <i>p</i> -type DSSC	11
1.5.4.1	Transparent conductive substrate (TCS)	12
1.5.4.2	Mesoporous Semiconductor	12
1.5.4.3	Sensitizer	13
1.5.4.3.1	Dyes for TiO ₂ -based <i>n</i> -type DSSCs	14
1.5.4.3.2	Dyes for NiO-based <i>p</i> -type DSSCs	17
1.5.4.4	Counter electrode	18
1.5.4.5	Electrolyte	18
1.5.5	Advantages and challenges in the field of DSSC	19
1.6	PEROVSKITE SOLAR CELL (PSC)	19
1.6.1	Device architecture of perovskite solar cells	20
1.6.2	Working principle of perovskite solar cells	21
1.6.3	Hole transporting materials (HTMs)	22
1.6.4	Carbon-based perovskite solar cells (C-PSCs)	24
1.6.4.1	Device architecture and working principle	25
1.6.4.2	Scaling up of perovskite solar cells	26
1.7	INSPIRATION FOR PRESENT WORK	27
1.8	CHARACTERIZATION TECHNIQUES	28
1.9	BROAD OBJECTIVES OF PRESENT WORK	29
	PART B: LITERATURE REVIEW, SCOPE, AND OBJECTIVES	30
1.10	LITERATURE REVIEW	30
1.10.1	<i>n</i> -Type organic chromophores for DSSC	31

1.10.1.1	Carbazole-based sensitizers	31
1.10.1.2	Thiophene-based sensitizers	35
1.10.1.3	Phenoxazine-based sensitizers	38
1.10.1.4	Co-sensitizers for Ru(II) based <i>n</i> -type DSSCs	42
1.10.2	<i>p</i> -Type organic chromophores for DSSC	47
1.10.3	Hole-transport materials for PSCs	52
1.10.4	Carbon-based perovskite solar cells	57
1.11	SALIENT FEATURES OF THE LITERATURE REVIEW	59
1.12	RESEARCH GAP	60
1.13	SCOPE AND OBJECTIVES	61
1.14	THESIS STRUCTURE	63

CHAPTER 2

DESIGN, SYNTHESIS AND STRUCTURAL CHARACTERIZATION OF NEW ORGANIC ENTITIES

2.1	INTRODUCTION	65
2.2	MOLECULAR DESIGN OF NEW ORGANIC MATERIALS	66
2.2.1	New <i>n</i> -type organic sensitizers/co-sensitizers for DSSCs	66
2.2.1.1	Design of Series-1 (<i>n</i> - K ₁₋₄)	66
2.2.1.2	Design of Series-2 (<i>n</i> - K ₅₋₁₁)	67
2.2.1.3	Design of Series-3 (<i>n</i> - K ₁₂₋₁₈)	68
2.2.1.4	Design of Series-4 (<i>n</i> - K ₁₉₋₂₁)	68
2.2.1.5	Design of Series-5 (<i>n</i> - K ₂₂₋₂₄)	69
2.2.1.6	Design of Series-6 (<i>n</i> - K ₂₅₋₂₈)	70
2.2.1.7	Design of Series-7 (<i>n</i> - K ₂₉₋₃₁)	70
2.2.1.8	Design of Series-8 (<i>n</i> - K ₃₂₋₃₄)	71
2.2.2	New <i>p</i> -type organic sensitizers for DSSCs	72
2.2.2.1	Design of Series-9 (<i>p</i> - K ₃₅₋₄₀)	72
2.2.2.2	Design of Series-10 (<i>p</i> - K ₄₁₋₄₂)	73
2.2.3	New organic HTMs for perovskite solar cells	74
2.2.3.1	Design of Series-11 (<i>h</i> - K ₄₃₋₄₄)	74
2.3	EXPERIMENTAL	75
2.3.1	Materials and Methods	76
2.3.2	Synthesis	76
2.3.2.1	Synthesis of <i>n</i> -type organic dyes <i>n</i> - K ₁₋₃₄ (Series 1-8)	76
2.3.2.1.1	Synthesis of chromophores <i>n</i> - K ₁₋₄ (Series 1)	76
2.3.2.1.2	Synthesis of chromophores <i>n</i> - K ₅₋₁₁ (Series 2)	82
2.3.2.1.3	Synthesis of chromophores <i>n</i> - K ₁₂₋₁₈ (Series 3)	88
2.3.2.1.4	Synthesis of chromophores <i>n</i> - K ₁₉₋₂₁ (Series 4)	93
2.3.2.1.5	Synthesis of chromophores <i>n</i> - K ₂₂₋₂₄ (Series 5)	97

	2.3.2.1.6 Synthesis of chromophores <i>n</i> - K ₂₅₋₂₈ (Series 6)	100
	2.3.2.1.7 Synthesis of chromophores <i>n</i> - K ₂₉₋₃₁ (Series 7)	105
	2.3.2.1.8 Synthesis of chromophores <i>n</i> - K ₃₂₋₃₄ (Series 8)	110
2.3.2.2	Synthesis of <i>p</i> -type organic dyes <i>p</i> - K ₃₅₋₄₂ (Series 9-10)	113
	2.3.2.2.1 Synthesis of chromophores <i>p</i> - K ₃₅₋₄₀ (Series 9)	113
	2.3.2.2.2 Synthesis of chromophores <i>p</i> - K ₄₁₋₄₂ (Series 10)	121
2.3.2.3	Synthesis of organic HTMs <i>h</i> - K ₄₃₋₄₄ (Series 11)	125
2.3.3	Results and discussion	129
2.3.3.1	<i>n</i> -Type organic dyes <i>n</i> - K ₁₋₃₄ (Series 1-8)	129
2.3.3.2	<i>p</i> -Type organic dyes <i>p</i> - K ₃₅₋₄₂ (Series 9-10)	149
2.3.3.3	Hole-transport materials <i>h</i> - K ₄₃₋₄₄ (Series 11)	154
2.4	CONCLUSIONS	156

CHAPTER 3

PHOTOPHYSICAL, ELECTROCHEMICAL, AND THEORETICAL INVESTIGATIONS

3.1	PHOTOPHYSICAL INVESTIGATION	157
3.1.1	Introduction	157
3.1.2	Materials and methods	158
3.1.3	Experimental	158
3.1.4	Results and discussion	158
3.1.4.1	Photophysical studies of <i>n</i> -type organic chromophores <i>n</i> - K ₁₋₃₄ (Series 1-8)	158
3.1.4.2	Photophysical studies of <i>p</i> -type organic chromophores <i>p</i> - K ₃₅₋₄₂ (Series 9-10)	168
3.1.4.3	Photophysical studies of organic HTMs <i>h</i> - K ₄₃₋₄₄ (Series 11)	170
3.2	ELECTROCHEMICAL INVESTIGATION	173
3.2.1	Materials and methods	174
3.2.2	Experimental	175
3.2.3	Results and discussion	175
3.2.3.1	Electrochemical studies of <i>n</i> -type organic chromophores <i>n</i> - K ₁₋₃₄ (Series 1-8)	175
3.2.3.2	Electrochemical studies of <i>p</i> -type organic chromophores <i>p</i> - K ₃₅₋₄₂ (Series 9-10)	189
3.2.3.3	Electrochemical studies of organic HTMs <i>h</i> - K ₄₃₋₄₄ (Series 11)	191
3.3	THEORETICAL INVESTIGATION	192
3.3.1	Simulations	193
3.3.2	Results and discussion	193
3.3.2.1	Theoretical studies of <i>n</i> -type organic chromophores <i>n</i> - K ₁₋₃₄ (Series 1-8)	193
3.3.2.2	Theoretical studies of <i>p</i> -type organic chromophores <i>p</i> - K ₃₅₋₄₂	199

		(Series 9-10)	
	3.3.2.3	Theoretical studies of organic HTMs <i>h-K</i> ₄₃₋₄₄ (Series 11)	200
	3.3.3	TD-DFT Simulations	202
3.4		CONCLUSIONS	204

CHAPTER 4

PHOTOVOLTAIC INVESTIGATIONS

4.1		PHOTOVOLTAIC STUDIES	205
	4.1.1	Introduction	205
	4.1.2	Materials and methods	206
	4.1.3	Experimental	206
	4.1.3.1	Fabrication of <i>n</i> -type DSSCs sensitized with dyes <i>n-K</i> ₁₋₃₄	207
	4.1.3.2	Fabrication of <i>n</i> -type DSSCs co-sensitized with dyes <i>n-K</i> ₁₋₃₄	208
	4.1.3.3	Fabrication of <i>p</i> -type DSSCs sensitized with dyes <i>p-K</i> ₃₅₋₄₂	209
	4.1.3.4	Fabrication of perovskite solar cells using HTMs <i>h-K</i> ₄₃₋₄₄	210
	4.1.4	Results and discussion	210
	4.1.4.1	Photovoltaic performance of devices sensitized/co-sensitized with <i>n</i> -type dyes (<i>n-K</i> ₁₋₁₈)	210
		4.1.4.1.1 Photovoltaic performance of Series-1 sensitizers/co-sensitizers (<i>n-K</i> ₁₋₄)	210
		4.1.4.1.2 Photovoltaic performance of Series-2 sensitizers/co-sensitizers (<i>n-K</i> ₅₋₁₁)	214
		4.1.4.1.3 Photovoltaic performance of Series-3 sensitizers/co-sensitizers (<i>n-K</i> ₁₂₋₁₈)	217
	4.1.4.2	Photovoltaic performance of devices sensitized with <i>p</i> -type dyes (<i>p-K</i> ₃₅₋₄₂)	221
		4.1.4.2.1 Photovoltaic performance of Series-9 sensitizers (<i>p-K</i> ₃₅₋₄₀)	221
		4.1.4.2.2 Photovoltaic performance of Series-10 sensitizers (<i>p-K</i> ₄₁₋₄₂)	223
	4.1.4.4	Photovoltaic performance of hole-transporting materials (<i>h-K</i> ₄₃₋₄₄)	225
4.2		CONCLUSIONS	227

CHAPTER 5

CARBON-BASED PRINTABLE PEROVSKITE SOLAR CELLS

5.1		MIXED-CATION HYBRID LEAD HALIDE PEROVSKITE SOLAR CELLS: SOLVENT SELECTION VIA ADDUCT APPROACH	229
	5.1.1	INTRODUCTION	229

5.1.2	EXPERIMENTAL SECTION	230
5.1.2.1	Preparation of materials	230
5.1.2.2	Solar cell fabrication	231
5.1.2.3	Characterization	233
5.1.3	RESULTS AND DISCUSSION	233
5.1.3.1	Structural and optical characterization of perovskite films	235
5.1.3.2	Device performance studies	241
5.1.3.3	Stability and reproducibility studies of the devices	244
5.1.3.4	Scaling up	246
5.1.4	CONCLUSIONS	247
5.2	LARGE-AREA MAPbI ₃ PEROVSKITE SOLAR CELLS (70 CM ²): IMPROVING THE PERFORMANCE BY INCORPORATING CESIUM HALIDE IN MESOPOROUS TiO ₂	247
5.2.1	INTRODUCTION	247
5.2.2	RESULTS AND DISCUSSION	248
5.2.2.1	Structural and optical characterization of perovskite films	248
5.2.2.2	Device performance studies	252
5.2.2.3	Scaling up	256
5.2.2.4	Stability and reproducibility studies of the devices	258
5.2.3	CONCLUSIONS	262
CHAPTER 6		
SUMMARY AND CONCLUSIONS		
6.1	SUMMARY	263
6.2	CONCLUSIONS	265
6.3	SCOPE FOR FUTURE WORK	267
	REFERENCES	269
	LIST OF PUBLICATIONS	279
	CURRICULUM VITAE	283

LIST OF FIGURES

Figure 1.1	Schematic representation of <i>n</i> -type DSSC	8
Figure 1.2	Schematic illustrations of <i>n</i> -type DSSC energy levels stating the various competing photophysical pathways	9
Figure 1.3	Schematic representation of working of <i>p</i> -type DSSC	10
Figure 1.4	Schematic illustrations of the key processes in a <i>p</i> -type DSSC	11
Figure 1.5	D- π -A configuration of <i>n</i> -type metal-free organic chromophore	15
Figure 1.6	D- π -A configuration of <i>p</i> -type metal-free organic chromophore	18
Figure 1.7	Schematic representation of device architecture of PSCs. (a) Regular mesoscopic <i>n-i-p</i> , (b) Regular planar <i>n-i-p</i> , (c) Inverted (planar) <i>p-i-n</i> , (d) Electron transport layer-free architecture, (e and f) Hole-transport layer-free architecture. Energy band diagram of typical (g) <i>n-i-p</i> and (h) <i>p-i-n</i> PSCs	21
Figure 1.8	Schematic representation of device architecture of carbon-based PSCs. (a) mesoporous C-PSCs, (b) planar C-PSCs, and (c) energy band diagram of C-PSCs	26
Figure 2.1	Molecular design of new chromophores <i>n</i>-K₁₋₄ (Series-1)	67
Figure 2.2	Molecular design of new chromophores <i>n</i>-K₅₋₁₁ (Series-2)	67
Figure 2.3	Molecular design of new chromophores <i>n</i>-K₁₂₋₁₈ (Series-3)	68
Figure 2.4	Molecular design of new chromophores <i>n</i>-K₁₉₋₂₁ (Series-4)	69
Figure 2.5	Molecular design of new chromophores <i>n</i>-K₂₂₋₂₄ (Series-5)	69
Figure 2.6	Molecular design of new chromophores <i>n</i>-K₂₅₋₂₈ (Series-6)	70
Figure 2.7	Molecular design of new chromophores <i>n</i>-K₂₉₋₃₁ (Series-7)	71
Figure 2.8	Molecular design of new chromophores <i>n</i>-K₃₂₋₃₄ (Series-8)	72
Figure 2.9	Molecular design of new chromophores <i>p</i>-K₃₅₋₄₀ (Series-9)	73
Figure 2.10	Molecular design of new chromophores <i>p</i>-K₄₁₋₄₂ (Series-10)	74
Figure 2.11	Molecular design of new HTMs <i>h</i>-K₄₃₋₄₄ (Series-11)	75
Figure 2.12	¹ H NMR spectrum of dye <i>n</i>-K₁ recorded in DMSO-d ₆	130
Figure 2.13	¹³ C NMR spectrum of dye <i>n</i>-K₁ recorded in DMSO-d ₆	130
Figure 2.14	FTIR spectrum of dye <i>n</i>-K₁	131
Figure 2.15	LCMS spectrum of dye <i>n</i>-K₁	131
Figure 2.16	¹ H-NMR spectrum of dye <i>n</i>-K₅ recorded in DMSO-d ₆	132
Figure 2.17	¹³ C-NMR spectrum of dye <i>n</i>-K₅ recorded in DMSO-d ₆	133
Figure 2.18	FTIR spectrum of dye <i>n</i>-K₅	133
Figure 2.19	LCMS spectrum of dye <i>n</i>-K₅	134
Figure 2.20	¹ H-NMR spectrum of dye <i>n</i>-K₁₃ recorded in DMSO-d ₆	135
Figure 2.21	¹³ C-NMR spectrum of dye <i>n</i>-K₁₃ recorded in DMSO-d ₆	135
Figure 2.22	FTIR spectrum of dye <i>n</i>-K₁₃	136
Figure 2.23	LCMS spectrum of dye <i>n</i>-K₁₃	136
Figure 2.24	¹ H-NMR spectrum of dye <i>n</i>-K₁₉ recorded in DMSO-d ₆	137
Figure 2.25	¹³ C-NMR spectrum of dye <i>n</i>-K₁₉ recorded in DMSO-d ₆	138
Figure 2.26	FTIR spectrum of dye <i>n</i>-K₁₉	138
Figure 2.27	LCMS spectrum of dye <i>n</i>-K₁₉	139

Figure 2.28	$^1\text{H-NMR}$ spectrum of dye <i>n-K</i>₂₂ recorded in DMSO- d_6	140
Figure 2.29	$^{13}\text{C-NMR}$ spectrum of dye <i>n-K</i>₂₂ recorded in DMSO- d_6	140
Figure 2.30	FTIR spectrum of dye <i>n-K</i>₂₂	141
Figure 2.31	LCMS spectrum of dye <i>n-K</i>₂₂	141
Figure 2.32	$^1\text{H-NMR}$ spectrum of dye <i>n-K</i>₂₅ recorded in DMSO- d_6	142
Figure 2.33	$^{13}\text{C-NMR}$ spectrum of dye <i>n-K</i>₂₅ recorded in DMSO- d_6	143
Figure 2.34	FTIR spectrum of dye <i>n-K</i>₂₅	143
Figure 2.35	LCMS spectrum of dye <i>n-K</i>₂₅	144
Figure 2.36	$^1\text{H-NMR}$ spectrum of dye <i>n-K</i>₂₉ recorded in DMSO- d_6	145
Figure 2.37	$^{13}\text{C-NMR}$ spectrum of dye <i>n-K</i>₂₉ recorded in DMSO- d_6	145
Figure 2.38	FTIR spectrum of dye <i>n-K</i>₂₉	146
Figure 2.39	LCMS spectrum of dye <i>n-K</i>₂₉	146
Figure 2.40	$^1\text{H-NMR}$ spectrum of dye <i>n-K</i>₃₂ recorded in DMSO- d_6	147
Figure 2.41	$^{13}\text{C-NMR}$ spectrum of dye <i>n-K</i>₃₂ recorded in DMSO- d_6	148
Figure 2.42	FTIR spectrum of dye <i>n-K</i>₃₂	148
Figure 2.43	LCMS spectrum of dye <i>n-K</i>₃₂	149
Figure 2.44	$^1\text{H-NMR}$ spectrum of dye <i>p-K</i>₃₆ recorded in DMSO- d_6	150
Figure 2.45	$^{13}\text{C-NMR}$ spectrum of dye <i>p-K</i>₃₆ recorded in DMSO- d_6	150
Figure 2.46	FTIR spectrum of dye <i>p-K</i>₃₆	151
Figure 2.47	LCMS spectrum of dye <i>p-K</i>₃₆	151
Figure 2.48	$^1\text{H-NMR}$ spectrum of dye <i>p-K</i>₄₁ recorded in DMSO- d_6	152
Figure 2.49	$^{13}\text{C-NMR}$ spectrum of dye <i>p-K</i>₄₁ recorded in DMSO- d_6	153
Figure 2.50	FTIR spectrum of dye <i>p-K</i>₄₁	153
Figure 2.51	FT-IR spectrum of dye <i>p-K</i>₄₁	154
Figure 2.52	$^1\text{H-NMR}$ spectrum of dye <i>h-K</i>₄₃ recorded in DMSO- d_6	155
Figure 2.53	$^{13}\text{C-NMR}$ spectrum of dye <i>h-K</i>₄₃ recorded in DMSO- d_6	155
Figure 2.54	LCMS spectrum of dye <i>h-K</i>₄₃	155
Figure 2.55	FTIR spectrum of dye <i>h-K</i>₄₃	156
Figure 3.1	(a) Normalized UV-Vis absorption and (b) fluorescence emission spectra of <i>n-K</i>₁₋₄ recorded in 10^{-5} M DMF solution under ambient atmosphere	159
Figure 3.2	(a) Normalized UV-Vis absorption and (b) fluorescence emission spectra of <i>n-K</i>₅₋₁₁ recorded in 10^{-5} M DMF solution	161
Figure 3.3	(a) Normalized UV-Vis absorption and (b) fluorescence emission spectra of <i>n-K</i>₁₂₋₁₈ recorded in 10^{-5} M DMF solution	163
Figure 3.4	(a) Normalized UV-Vis absorption and (b) fluorescence emission spectra of <i>n-K</i>₁₉₋₂₁ recorded in 10^{-5} M DMF solution	164
Figure 3.5	(a) Normalized UV-Vis absorption and (b) fluorescence emission spectra of <i>n-K</i>₂₂₋₂₄ recorded in 10^{-5} M DMF solution	165
Figure 3.6	(a) Normalized UV-Vis absorption and (b) fluorescence emission spectra of <i>n-K</i>₂₅₋₂₈ recorded in 10^{-5} M DMF solution	166
Figure 3.7	(a) Normalized UV-Vis absorption and (b) fluorescence emission spectra of <i>n-K</i>₂₉₋₃₁ recorded in 10^{-5} M CHCl_3 solution	167

Figure 3.8	(a) Normalized UV-Vis absorption and (b) fluorescence emission spectra of <i>n</i>-K₃₂₋₃₄ recorded in 10 ⁻⁵ M CHCl ₃ solution	168
Figure 3.9	(a) Normalized UV-Vis absorption and (b) fluorescence emission spectra of <i>n</i>-K₃₅₋₄₀ recorded in 10 ⁻⁵ M CHCl ₃ solution	169
Figure 3.10	(a) Normalized UV-Vis absorption and (b) fluorescence emission spectra of <i>n</i>-K₄₁₋₄₂ recorded in 10 ⁻⁵ M DMF solution	170
Figure 3.11	Normalized UV-Vis absorption and fluorescence emission spectra of <i>n</i>-K₄₃₋₄₄ recorded in 10 ⁻⁵ M CHCl ₃ solution	171
Figure 3.12	(a) Cyclic Voltammograms of <i>n</i>-K₁₋₄ ; (b) Molecular energy level diagram showing experimental HOMO, LUMO, and bandgap values of <i>n</i>-K₁₋₄	178
Figure 3.13	(a) Cyclic Voltammograms of <i>n</i>-K₅₋₁₁ ; (b) Molecular energy level diagram showing experimental HOMO, LUMO, and bandgap values of <i>n</i>-K₅₋₁₁	180
Figure 3.14	(a) Cyclic Voltammograms of <i>n</i>-K₁₂₋₁₈ ; (b) Molecular energy level diagram showing experimental HOMO, LUMO, and bandgaps of <i>n</i>-K₁₂₋₁₈	181
Figure 3.15	(a) Cyclic Voltammograms of <i>n</i>-K₁₉₋₂₁ ; (b) Molecular energy level diagram showing experimental HOMO, LUMO, and bandgap values of <i>n</i>-K₁₉₋₂₁	182
Figure 3.16	(a) Cyclic Voltammograms of <i>n</i>-K₂₂₋₂₄ ; (b) Molecular energy level diagram showing experimental HOMO, LUMO, and bandgap values of <i>n</i>-K₂₂₋₂₄	183
Figure 3.17	(a) Cyclic Voltammograms of <i>n</i>-K₂₅₋₂₈ ; (b) Molecular energy level diagram showing experimental HOMO, LUMO, and bandgap values of <i>n</i>-K₂₅₋₂₈	185
Figure 3.18	(a) Cyclic Voltammograms of <i>n</i>-K₂₉₋₃₁ ; (b) Molecular energy level diagram showing experimental HOMO, LUMO, and bandgap values of <i>n</i>-K₂₉₋₃₁	186
Figure 3.19	(a) Cyclic Voltammograms of <i>n</i>-K₃₂₋₃₄ ; (b) Molecular energy level diagram showing experimental HOMO, LUMO, and bandgap values of <i>n</i>-K₃₂₋₃₄	187
Figure 3.20	Cyclic Voltammograms of (a) <i>p</i>-K₃₅₋₄₀ and (b) <i>p</i>-K₄₁₋₄₂	190
Figure 3.21	(a) Cyclic Voltammograms of <i>h</i>-K₄₃₋₄₄ ; (b) Molecular energy level diagram showing experimental HOMO, LUMO, and bandgap values of <i>h</i>-K₄₃₋₄₄	192
Figure 3.22	HOMO and LUMO levels of dyes <i>n</i>-K₁₋₄	194
Figure 3.23	HOMO and LUMO levels of dyes (a) <i>n</i>-K₅₋₁₁ and (b) <i>n</i>-K₁₂₋₁₈	196
Figure 3.24	HOMO and LUMO levels of dyes (a) <i>n</i>-K₁₉₋₂₁ and (b) <i>n</i>-K₂₂₋₂₄	197
Figure 3.25	HOMO and LUMO levels of dyes <i>n</i>-K₂₅₋₂₈	198
Figure 3.26	HOMO and LUMO levels of dyes (a) <i>n</i>-K₂₉₋₃₁ and (b) <i>n</i>-K₃₂₋₃₄	199
Figure 3.27	HOMO and LUMO levels of dyes (a) <i>p</i>-K₃₅₋₄₀ and (b) <i>p</i>-K₄₁₋₄₂	200
Figure 3.28	HOMO and LUMO levels of dyes <i>h</i>-K₄₃₋₄₄	202

Figure 3.29	Simulated absorption spectra of (a) <i>n-K</i> ₁₀ , (b) <i>n-K</i> ₂₀ , (c) <i>n-K</i> ₃₀ and (d) <i>p-K</i> ₄₀	203
Figure 3.30	Simulated IR spectra of (a) <i>n-K</i> ₁₀ , (b) <i>n-K</i> ₂₀ , (c) <i>n-K</i> ₃₀ and (d) <i>p-K</i> ₄₀	203
Figure 4.1	(a) Current density-voltage plots; (b) <i>IPCE</i> spectra of DSSCs sensitized with dyes <i>n-K</i> ₁₋₄ under illumination of simulated solar light (AM 1.5G, 100 mW/cm ²)	212
Figure 4.2	(a) Current density-voltage plots; (b) <i>IPCE</i> spectra of DSSCs fabricated using <i>n-K</i> ₅₋₁₁ as co-sensitizers along with a Ruthenium-based dye HD-2 under illumination of simulated solar light (AM 1.5G, 100 mW/cm ²)	214
Figure 4.3	(a) Current density-voltage plots; (b) <i>IPCE</i> spectra of DSSCs sensitized with dyes <i>n-K</i> ₅₋₁₁ under illumination of simulated solar light (AM 1.5G, 100 mW/cm ²)	216
Figure 4.4	(a) Current density-voltage plots; (b) <i>IPCE</i> spectra of DSSCs fabricated using <i>n-K</i> ₅₋₁₁ as co-sensitizers along with a Ruthenium-based dye HD-2 under illumination of simulated solar light (AM 1.5G, 100 mW/cm ²)	217
Figure 4.5	(a) Current density-voltage plots; (b) <i>IPCE</i> spectra of DSSCs sensitized with dyes <i>n-K</i> ₁₂₋₁₈ under illumination of simulated solar light (AM 1.5G, 100 mW/cm ²)	218
Figure 4.6	(a) Current density-voltage plots; (b) <i>IPCE</i> spectra of DSSCs fabricated using <i>n-K</i> ₁₂₋₁₈ dyes as co-sensitizers along with a Ruthenium-based dye HD-2 under illumination of simulated solar light (AM 1.5G, 100 mW/cm ²)	219
Figure 4.7	Current density-voltage plots of DSSCs sensitized with (a) <i>p-K</i> ₃₅ , (b) <i>p-K</i> ₃₆ , (c) <i>p-K</i> ₃₇ , (d) <i>p-K</i> ₃₈ , (e) <i>p-K</i> ₃₉ , (f) <i>p-K</i> ₄₀ , and (g) P1 dyes	222
Figure 4.8	<i>IPCE</i> spectra of DSSCs sensitized with dyes <i>p-K</i> ₃₅₋₄₀ under illumination of simulated solar light (AM 1.5G, 100 mW/cm ²)	223
Figure 4.9	Current density-voltage plots of DSSCs sensitized with (a) <i>p-K</i> ₄₁ , (b) <i>p-K</i> ₄₂ , and (c) P1 dyes	224
Figure 4.10	<i>IPCE</i> spectra of DSSCs sensitized with dyes <i>p-K</i> ₄₁₋₄₂ under illumination of simulated solar light (AM 1.5G, 100 mW/cm ²)	224
Figure 4.11	(a) Schematic representation of device architecture and <i>J-V</i> characteristics of (b) Spiro-OMeTAD, (c) <i>h-K</i> ₄₃ , and (d) <i>h-K</i> ₄₄	226
Figure 4.12	<i>IPCE</i> spectra of <i>h-K</i> ₄₃₋₄₄ along with reference Spiro-OMeTAD under illumination of solar light (AM 1.5G, 100 mW/cm ²)	227
Figure 5.1	(a) Schematic representation of precursor, adduct formation, and the perovskite crystallization process in one of the solvents DMSO; (b) Photographic images of fabricated devices in various solvents <i>via</i> adduct approach	235
Figure 5.2	X-ray diffraction spectra of Cs _{0.1} FA _{0.9} PbI ₃ thin-films fabricated using various solvents	236

Figure 5.3	FTIR spectra of DMSO (solvent), $\text{PbI}_2 \cdot \text{DMSO}$ (powder, adduct), and $\text{FAI} \cdot \text{PbI}_2 \cdot \text{DMSO}$ (powder, adduct)	237
Figure 5.4	a) Device fabrication procedure; b) Schematic representation of the device architecture; c) Cross-section SEM images of the perovskite/carbon solar cells fabricated from 1) DMSO, 2) DMF-DMSO, 3) DMF, and 4) GBL-DMSO	239
Figure 5.5	Electronic impedance spectroscopy characteristics in the form of the Nyquist plot of the device fabricated using DMSO as a solvent under dark	240
Figure 5.6	Photovoltaic properties. a) UV-Vis absorption spectra, b) steady-state PL spectra of $\text{Cs}_{0.1}\text{FA}_{0.9}\text{PbI}_3$ devices fabricated using various solvents	241
Figure 5.7	J - V characteristics of the PSCs fabricated using different solvents under standard AM 1.5 G illumination at 100 mWcm^{-2} and in dark	242
Figure 5.8	Reproducible and efficient $\text{Cs}_{0.1}\text{FA}_{0.9}\text{PbI}_3$ PSCs fabricated using DMSO as a solvent. Histograms of a) short-circuit current density (J_{SC}), b) open-circuit voltage (V_{OC}), c) fill factor (FF), and d) power conversion efficiency (PCE)	243
Figure 5.9	$IPCE$ spectra of the $\text{Cs}_{0.1}\text{FA}_{0.9}\text{PbI}_3$ perovskite solar cells fabricated using various solvents and their integrated currents	244
Figure 5.10	The normalized PCE decay of the devices fabricated using different solvent combinations of solvents under ambient environmental conditions and under standard AM 1.5 sun illuminations	245
Figure 5.11	Reproducibility data of $\text{Cs}_{0.1}\text{FA}_{0.9}\text{PbI}_3$ perovskite in various solvents. The statistical distribution of photovoltaic parameters, a) J_{SC} , b) V_{OC} , c) FF , and d) PCE across 62 devices	246
Figure 5.12	X-ray diffractogram of MAPbI_3 perovskite films deposited on 'FTO/c-TiO ₂ /mp-TiO ₂ (with and without CsX)' substrates annealed at 60 °C for 1 h	249
Figure 5.13	(a) Schematic illustration of the device architecture with a flow chart showing the fabrication procedure, (b) Cross-sectional SEM image of the CsBr modified C-PSCs	250
Figure 5.14	(a) Steady-state photoluminescence (PL) spectra and (b) Normalized time-resolved photoluminescence (TRPL) decay plots of the MAPbI_3 perovskite thin films deposited on glass/c-TiO ₂ /mp-TiO ₂ layer	251
Figure 5.15	J - V curves of MAPbI_3 C-PSCs fabricated with and without CsX modification, recorded under standard AM 1.5 G illumination at $100 \text{ mW} \cdot \text{cm}^{-2}$ irradiance and in the dark	254
Figure 5.16	$IPCE$ spectra of the C-PSCs containing various types of mp-TiO ₂ and their integrated currents	255
Figure 5.17	(a) J - V traces of unmodified and CsX mod. 40NR-D large area (70 cm^2) C-PSCs, recorded under one sun ($100 \text{ mW} \cdot \text{cm}^{-2}$) light	257

	irradiance and in the dark and (b) Photograph of printed CsX mod 40NR-D C-PSC module	
Figure 5.18	Aging analysis with respect to device performance parameters: (a) J_{SC} , (b) V_{OC} , (c) FF , (d) PCE as a function of time	259
Figure 5.19	XRD patterns with Cu $K\alpha$ radiation ($\lambda = 1.54056 \text{ \AA}$) of MAPbI ₃ perovskite film: (a) unmodified m-TiO ₂ after UV ageing for 90 min, (b) CsBr modified m-TiO ₂ after UV aging for 90 min	260
Figure 5.20	Stability studies of C-PSCs with and without CsBr modification, the normalized PCE decay rate at 85 °C under ambient air for unencapsulated C-PSCs	261
Figure 5.21	Reproducibility data of C-PSCs using CsX modified and unmodified mp-TiO ₂ . The statistical distribution of photovoltaic parameters: (a) J_{SC} , (b) V_{OC} , (c) FF , (d) PCE	262

LIST OF TABLES

Table 1.1	Organic sensitizers based on carbazole for n -type DSSCs	33
Table 1.2	Organic sensitizers based on thiophene for n -type DSSCs	37
Table 1.3	Organic sensitizers based on phenoxazine for n -type DSSCs	40
Table 1.4	Ruthenium (II) complex based sensitizers	43
Table 1.5	Reported p -type organic sensitizers	50
Table 1.6	Organic small molecules as hole transport materials	54
Table 3.1	Photophysical properties of synthesized organic dyes, <i>i.e.</i> n -type (n - K ₁₋₃₄), p -type (p - K ₃₅₋₄₂), and HTMs (h - K ₄₃₋₄₄)	172
Table 3.2	Electrochemical properties of n -type organic chromophores n - K ₁₋₃₄	187
Table 3.3	Electrochemical properties of p -type organic chromophores p - K ₃₅₋₄₂	190
Table 3.4	Electrochemical properties of HTMs h - K ₄₃₋₄₄	192
Table 4.1	Photovoltaic performance data of devices sensitized with n -type dyes (n - K ₁₋₁₈)	220
Table 4.2	Photovoltaic performance data of devices co-sensitized with n -type dyes (n - K ₁₋₁₈)	220
Table 4.3	Photovoltaic performance data of devices sensitized with p -type dyes (p - K ₃₅₋₄₂)	224
Table 4.4	Photovoltaic performances of synthesized HTMs (h - K ₄₃₋₄₄) along with reference Spiro-OMeTAD	227
Table 5.1	Photovoltaic parameters of the Cs _{0.1} FA _{0.9} PbI ₃ PSCs fabricated using the different combinations of solvents for a device with an active area of 0.09 cm ²	242
Table 5.2	Fitting parameters for the time-resolved PL measurements	252
Table 5.3	Photovoltaic parameters of modified and unmodified C-PSCs with an active area of 0.7 cm ² in both forward (F) and reverse (R) scan.	254
Table 5.4	Solar cell parameters of the CsX modified and unmodified C-PSCs with an active area of 70 cm ²	257

LIST OF ABBREVIATIONS

AM	Air mass
ACN	Acetonitrile
CB	Conduction band
CE	Counter electrode
CHCl ₃	Chloroform
CV	Cyclic voltammetry
DFT	Density functional theory
D- π -A	Donor- π -acceptor
DMF	<i>N, N</i> -Dimethylformamide
DMSO	Dimethyl sulfoxide
DSSC	Dye-sensitized solar cell
Eq	Equation
ESOP	Excited state oxidation potential
ESP	Electrostatic potential
E ₀₋₀	Optical band gap
E _g	Electrochemical band gap
EIS	Electrochemical Impedance spectroscopy
FTO	Fluorine doped tin oxide
FTIR	Fourier transform infrared spectroscopy
FF	Fill factor
GSOP	Ground state oxidation potential
HOMO	Highest occupied molecular orbital
HTM	Hole-transport material
ICT	Intra molecular charge transfer
IPCE	Incident photon to current conversion efficiency
J _{sc}	Short circuit current
LHE	Light harvesting efficiency
LUMO	Lowest unoccupied molecular orbital
MP	Melting point
MS	Mass spectrometry
NMR	Nuclear magnetic resonance

NiO	Nickel oxide
<i>n</i> -K ₁₋₄	<i>n</i> -Type thiophene-based dyes with D- π -A configuration
<i>n</i> -K ₅₋₁₁	<i>n</i> -Type carbazole-based dyes with double D-A configuration
<i>n</i> -K ₁₂₋₁₈	<i>n</i> -Type carbazole-based dyes with double D-A configuration
<i>n</i> -K ₁₉₋₂₁	<i>n</i> -Type carbazole-based dyes with (D- π -A) ₂ configuration
<i>n</i> -K ₂₂₋₂₄	<i>n</i> -Type carbazole-based dyes with (D- π -A) ₂ configuration
<i>n</i> -K ₂₅₋₂₈	<i>n</i> -Type carbazole-based dyes with A-D- π -D-A configuration
<i>n</i> -K ₂₉₋₃₁	<i>n</i> -Type phenoxazine-based dyes with A- π -D- π -A configuration
<i>n</i> -K ₃₂₋₃₄	<i>n</i> -Type phenoxazine-based dyes with A- π -D- π -A configuration
<i>p</i> -K ₃₅₋₄₀	<i>p</i> -Type phenoxazine-based dyes with D-A configuration
<i>p</i> -K ₄₁₋₄₂	<i>p</i> -Type carbazole-based dyes with D- π -A configuration
<i>h</i> -K ₄₃₋₄₄	Carbazole based hole-transport materials
PV	Photovoltaics
PSC	Perovskite solar cell
PCE	Power conversion efficiency
Pt	Platinum
RT	Room temperature
Ru(II)	Ruthenium (II)
S	Sensitizer
SC	Semiconductor
SCE	Standard calomel electrode
TCO	Transparent conducting oxide
TD-DFT	Time-dependent density functional theory
TiO ₂	Titanium dioxide
THF	Tetrahydrofuran
V _{oc}	Open-circuit voltage
VB	Valence band
WE	Working electrode

CHAPTER-1
INTRODUCTION

INTRODUCTION

Abstract

Chapter 1 deals with a brief introduction to photovoltaics followed by a concise account of dye-sensitized solar cells (DSSCs) and perovskite solar cells (PSCs). It also includes the working principles, various cell components, and photovoltaic parameters of DSSCs and PSCs. Further, it covers detailed reported literature on molecular design, synthesis, and performance of n-type and p-type organic sensitizers/co-sensitizers used in DSSCs along with organic and inorganic hybrid perovskite materials employed in PSCs. Furthermore, the chapter covers the scope and objectives of the present research work, derived from the literature survey carried out.

PART A: PHOTOVOLTAIC CELLS: AN OVERVIEW

1.1 A BRIEF INTRODUCTION TO PHOTOVOLTAICS

Energy is the most important part of human civilization and is essential for its survival. With the development of industrial society, the ever-increasing demand for energy by mankind, and the continuous depletion of non-renewable fossil fuels across the globe have forced us to start searching for an alternative, inexhaustible, abundant, and clean source of energy. The availability of renewable energy not only plays a vital role in the daily life of people but also acts as a major driving force of the global economy. Out of all the renewable sources of energy, solar energy is considered to be the abundant natural resource of almost all the energy on the earth. As the growing demand for alternative sources of energy increases, photovoltaic energy conversion furnishes the best option and the finest way to harvest solar energy is the photovoltaic cell or solar cell. The phenomenon of conversion of photons into electricity is known as the photovoltaic effect and was first time discovered by French physicist Alexandre Edmond Becquerel in 1839. Later, in 1883 Charles Fritts developed the first solar cell from a selenium/gold junction with an efficiency of about 1%, and further in 1941 first silicon solar cell was constructed.

1.2 SOLAR CELL TECHNOLOGIES

Power generation through solar photovoltaics has been considered to be a clean sustainable energy technology. The basic requirement of a solar cell is the light-absorbing material within it, in order to absorb the photons directly from sunlight and to generate electrons *via* the photovoltaic effect. A traditional solar cell is made up of two doped materials, one doped with an *n*-type semiconductor, which injects electrons into the conduction band of the *n*-type semiconductor whereas, the other is doped with *p*-type impurities, which injects electron holes into the valence band of the *p*-type semiconductor.

Typically, the solar cell technologies can be broadly classified into three generations depending on their performances, type of absorbing materials used, type of junction formed as well as the cost to efficiency ratio. Among these, the first-generation solar cells usually mentioned as silicon (Si) solar cells have comparatively higher efficiency and are most widely deployed. Currently, 90 % of the photovoltaic market is dominated by mono and polycrystalline Si-based solar cells due to their advanced photovoltaic technology. But the major difficulty in the field of Si solar technologies is their very high production cost and challenging purification steps to obtain high-quality Si. The second-generation solar cells (thin-film solar cells) are made up of materials such as cadmium telluride (CdTe) or copper indium gallium diselenide (CIGS). Although these display low efficiency compared to that of Si solar cells, the motivation behind the development is the flexibility of the material and lower manufacturing costs. The third-generation solar cells comprise all the cells with a variety of technologies that are not grouped under first- and second-generations. Third-generation solar cells are considered to be promising photovoltaics due to their lightweight, flexibility, low manufacturing cost, and eco-friendly nature. In fact, dye-sensitized solar cells (DSSCs) and perovskite solar cells (PSCs) are promising candidates under third-generation solar cells.

1.3 PRESENT SCENARIO OF PHOTOVOLTAIC TECHNOLOGY

Since 2002, the PV market is considered as the world's fastest-growing technology with a growth rate of 48 % and has attracted worldwide attention. But it

can contribute only 0.1 % towards the world energy demand due to the high production and maintenance costs of commercial Si photovoltaics. Si-based solar modules are robust and have a lifetime of about 25 years, but their cost reduction potential seems to be limited. Thus, in recent years, the main focus of researchers is to develop inexpensive organic material as an alternative to inorganic semiconductors. Accordingly, a vast range of research is undertaken to synthesize and optimize novel materials to use in the fields of DSSCs and PSCs. For a better future, tremendous research activities are going on in order to commercialize these solar cells.

1.4 PHOTOVOLTAIC PARAMETERS

The photovoltaic performance of the solar cell mainly depends on the number of parameters such as incident-photo-current conversion efficiency (*IPCE*), short-circuit photocurrent (J_{SC}), open-circuit photovoltage (V_{OC}), fill factor (*FF*), and the overall power conversion efficiency (*PCE*). These photovoltaic parameters are discussed in detail below.

1.4.1 Short-circuit photocurrent (J_{SC})

The short circuit current is defined as the current obtained from the cell when the load resistance is zero or in other words current from the cell when it is short-circuited. Generally, it is calculated by measuring photocurrent per unit area (mA/cm^2) when the cell under irradiation is short-circuited and the corresponding equation is given below (Eq. 1.1).

$$J_{SC} = \frac{I_{SC}}{A} \quad (1.1)$$

where A is the active area of the solar cell. It is a function of the solar illumination optical properties and charge transfer probability of the cell.

The J_{SC} value can be correlated to *IPCE* spectra to give the Eq. 1.2.

$$J_{SC} = e \int IPCE(\lambda) I_S(\lambda) d\lambda \quad (1.2)$$

where $I_S(\lambda)$ is the photo-flux at wavelength λ under standard AM 1.5 light irradiation. The factors which influence J_{SC} are light absorption, light intensity, injection efficiency, and regeneration of the oxidized molecule.

1.4.2 Open-circuit photovoltage (V_{OC})

The V_{OC} can be defined as the difference in the potential between the two terminals in the cell under the illumination of light when the circuit is open. It can be expressed by Eq. 1.3.

$$V_{OC} = \frac{k_B T}{e} \ln \left(\frac{J_{SC}}{J_0} + 1 \right) \quad (1.3)$$

where e is the elementary charge, k_B is the Boltzmann constant, T is the absolute temperature and J_0 is the constant. In the case of DSSC, Eq. 1.3 slightly modifies and takes the form of Eq. 1.4.

$$V_{OC} = \frac{E_{CB}}{e} + \frac{k_B T}{e} \ln \left(\frac{n}{N_{CB}} \right) - \frac{E_{redox}}{q} \quad (1.4)$$

Here, n is the number of electrons in the semiconductor, N_{CB} is the effective density of the states, and E_{redox} is the redox potential of the redox couple.

1.4.3 Fill factor (FF)

The fill factor is derived from the ratio of maximum power output ($J_{max}V_{max}$) per unit area to the product of J_{SC} and V_{OC} (Eq. 1.5).

$$FF = \frac{J_{max}V_{max}}{J_{SC}V_{OC}} \quad (1.5)$$

where J_{max} and V_{max} are the voltage and current at the maximum power point. Generally, the FF is the measure of the square-ness of the current-voltage (I - V) curve. When the FF value is closer to 1, the solar panel can provide the highest output.

1.4.4 Power conversion efficiency (η)

The power conversion efficiency (PCE) of the solar cell is defined as the maximum output of the cell divided by the energy input from the Sun. Mathematically; it can be calculated by the equation given below (Eq. 1.6).

$$\eta = \left(\frac{J_{SC} \times V_{OC} \times FF}{P_{in}} \right) \quad (1.6)$$

where P_{in} is the power input from the sunlight.

The value of ‘ η ’ is mainly influenced by certain factors, such as the intensity of incident light, *IPCE* as well as operating temperature. Thus, in order to obtain the higher *PCE*, it is very essential to optimize the J_{SC} , V_{OC} , and FF values of the cell.

1.4.5 Incident-Photo-Current Conversion Efficiency (*IPCE*)

The *IPCE* is the quantum-yield term for the entire charge injection and collection processes recorded using a single wavelength source. *IPCE* or Quantum efficiency is defined as the ratio of a total number of photo-electrons moved through the external load to the number of incident photons as a function of excitation wavelength. The *IPCE* is calculated by employing Eq. 1.7.

$$IPCE(\lambda) = 1240 \times \frac{J_{SC}}{\lambda \times \Phi} \quad (1.7)$$

where J_{SC} is the short-circuit current (mA/cm^2), λ is the wavelength (nm), and Φ is the incident radiative light flux (W/m^2).

For DSSC, the *IPCE* can be obtained by the product of light-harvesting efficiency ($\text{LHE} = 1-10^{-10}$) at wavelength λ and quantum yield of electron injection (ϕ_{inj}) from the excited dye into the conduction band of semiconductor and the efficiency of collection of the injected electron (η_{coll}) at the FTO glass. The mathematical representation is given in Eq. 1.8.

$$IPCE(\lambda) = LHE(\lambda) \phi_{inj} \eta_{coll} \quad (1.8)$$

1.5 DYE-SENSITIZED SOLAR CELL (DSSC)

Exploring the non-silicon alternatives and developing photovoltaic technology with highly efficient and affordable materials have always been an admired goal of entire material scientists and the device community. In this regard, DSSC that belongs to organic photovoltaics is a promising low-cost and can be considered to be an alternative to the existing crystalline Si and thin-film photovoltaic techniques. In 1991, Prof. Michael Gratzel and O’ Regan developed the solar cell based on the

successful combination of nanostructured electrodes and efficient charge injection dyes. Of lately, the significant collective efforts of many researchers across the globe over the past 20 years have not only plunged the performance of devices, but also brought out various innovative ways of developing robust and durable DSSC with enhanced efficiency.

1.5.1 Working principle of DSSC

The dye-sensitized solar cells are photoelectrochemical devices, where multiple electron transfer processes occur in parallel and in competition. The basic working principle of DSSC depends on three major processes, *viz.* absorption, separation, and charge collection. In conventional silicon solar cells, Si acts as both source of photoelectrons as well as an electric field generator to separate the generated charge and create a current. Unlike other solar cell technologies, in DSSCs, separate mediums are used for light absorption or carrier generation (sensitizer/dye) and carrier transfer (semiconductor oxide layer). The semiconductor oxide layer is majorly used as a charge transport layer and a photosensitizer is exclusively preferred to provide photoelectrons.

In general, the first step of the operating principle of DSSC includes the excitation of the sensitizer from the ground state to the excited state by absorbing photons from sunlight. In continuation, the charge injection occurs from the valence band of the excited dye molecule to the conduction band of the semiconductor oxide layer which results in the formation of excitons and facilitates subsequent charge separation. Finally, the charge transport occurs from the semiconductor oxide layer to the counter electrode through an external load. In parallel, the oxidized sensitizer combines with an electron from the redox mediator and dye regeneration begins to the ground. In total, this cycle completes in a regenerative and stable photovoltaic energy conversion system as no net reaction occurs. Thus, the overall power conversion efficiency depends on the optimization of charge injection, charge recombination, and dye regeneration. There are certain parameters that should be satisfied for efficient electron injection in order to aim for higher efficiency. First of all, there should be a strong covalent bond between the acceptor units of the dye molecule on the

semiconductor oxide layer. Secondly, an optimized distance must be present between the dye and the acceptor metal oxide. Finally, the dye should not be aggregated. However, due to the unwanted reactions, cell efficiency sometimes will drop. The most important loss mechanisms include direct recombination of the excited dye and the recombination of the injected electrons in the semiconductor oxide layer with the oxidized dye or with the holes in the electrolyte. Thus, an optimized molecular design strategy of the sensitizer is necessary in order to suppress the recombination mechanism which further leads to the dark current. Similarly, fast regeneration of the dye molecule is a prerequisite for an efficient DSSC. Generally, the reduced form of redox mediator in the liquid electrolyte helps to regenerate the dye in the ground state prior to the back electron transfer.

Further, based on the working principle and nature of the sensitizer used, DSSC can be broadly classified into two types. They are:

1. *n*-Type dye-sensitized solar cell
2. *p*-Type dye-sensitized solar cell

1.5.2 *n*-Type dye-sensitized solar cell (*n*-type DSSC)

The overall performance of *n*-type DSSC mainly depends on the energy level difference between excited state/LUMO and the ground state/HOMO of the sensitizer, the Fermi level of the semiconductor used, and the redox potential of the electrolyte. In order to achieve this, the LUMO level of the dye used must have energy higher than that of the conduction band (CB) of the semiconductor, whereas the HOMO should be lower than that of redox potential. Thus, *n*-type DSSC comprises a dye molecule that is coated on a semiconductor generally TiO₂ since its conduction band (CB) is lower than that of the LUMO energy level of the dye molecule in order to facilitate fast electron injection.

A typical *n*-type DSSC system consists of the following features:

- An anode: generally, a glass sheet treated with a transparent conductive oxide layer
- A mesoporous semiconductor oxide layer: generally, TiO₂ layer

- A monolayer of sensitizer/dye
- An electrolyte: usually iodide/triiodide system
- A cathode: generally, a transparent glass sheet on which catalyst (usually platinum) is deposited

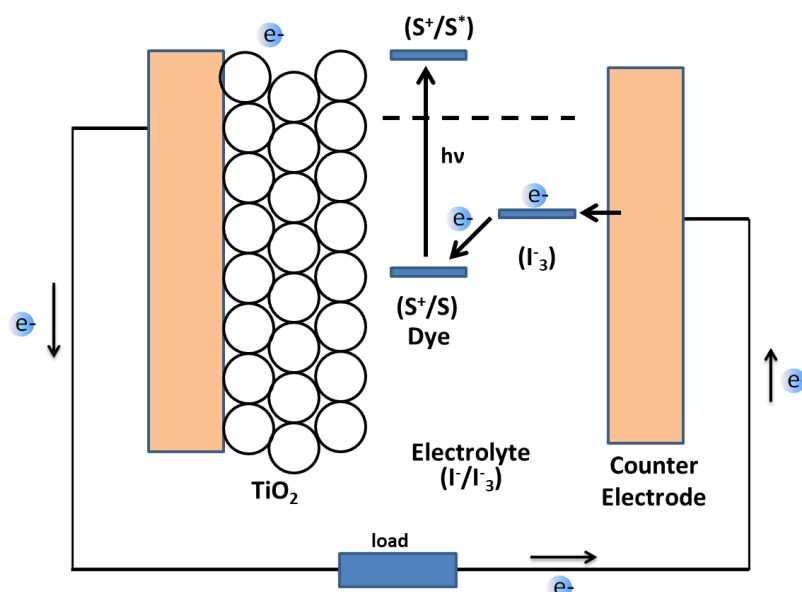
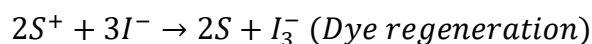
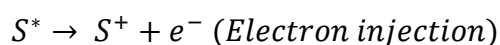
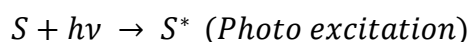


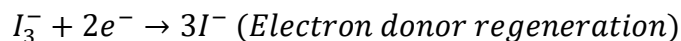
Figure 1.1 Schematic representation of *n*-type DSSC

When exposed to sunlight (**Figure 1.1**), the dye molecule goes to an electronic state change from the ground state (*S*) to an excited state (*S**) from which an electron is injected into the CB of the mesoporous TiO₂ film. The efficient electron injection occurs when the LUMO level of the dye is higher than that of the CB of TiO₂ layer. The circuit will be completed as the movement of electrons occurs through the external load before being collected by the external electrolyte at the cathode surface to complete the cycle. **Figure 1.2** shows the various energy levels present in a typical DSSC and also the electron flow with the solar cell. The operating principle is summarized in the following chemical reactions:

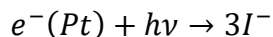
Anode:



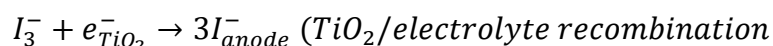
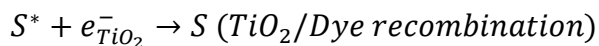
Cathode:



Cell:



The electrons injected should escape from the recombination process to increase charge collection efficiency at the photoelectrode back contact. The two major unwanted processes in a DSSC are due to (i) back electron transfer, at the semiconductor-electrolyte interface, between electrons in the CB of the semiconductor and the oxidized dye molecules also called electron recombination at TiO_2 /Dye interface, and (ii) reduction of I_3^- at the semiconductor surface.



All the operations in the cell are regenerative, so none of the chemical substance undergoes any permanent chemical transformations as shown by the cell reaction.

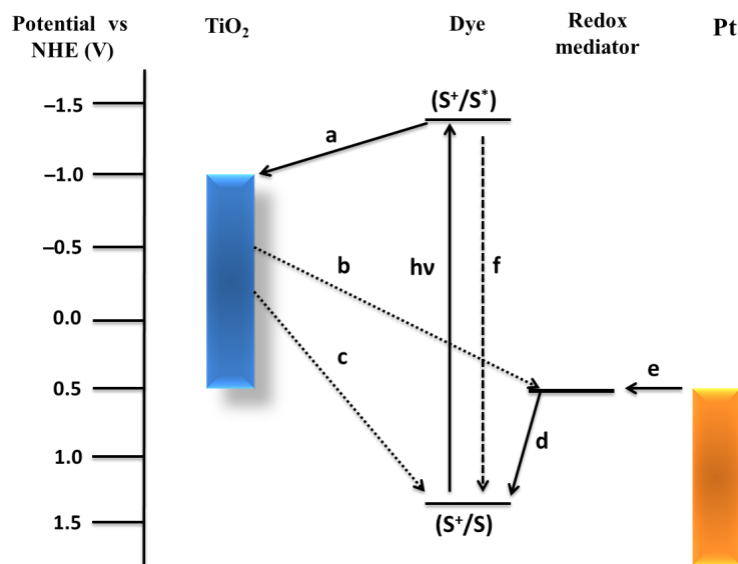


Figure 1.2 Schematic illustrations of *n*-type DSSC energy levels stating the various competing photophysical pathways. They include (a) electron injection, (b) electron recombination with the acceptor species in the electrolyte, and (c) electron recombination with dye cations, (d) regeneration of dye cations by the electrolyte, (e) reduction of the electrolyte at the counter electrode, (f) relaxation of the dye molecule from the excited state

1.5.3 *p*-Type dye sensitized solar cell (*p*-type DSSC)

Typical *p*-type DSSC comprises a photoactive working electrode (cathode), a passive counter electrode (anode), and a redox mediator. Generally, *p*-type DSSC involves a *p*-type semiconductor (usually NiO) which serves as a photoactive cathode. **Figure 1.3** depicts the schematic representation of a *p*-type DSSC. In this case, the adsorbed dye/sensitizer injects holes into the valence band of the semiconductor where they diffuse to the cathode contact, whereas the electrons excited will shift to the electrolyte through which they diffuse to the anode. The basic requirements for the use of this “inverted” type of dye adsorbed on photocathodes are mainly (i) the HOMO level of the dye must be sufficiently below the valence band of the *p*-semiconductor and (ii) the LUMO level must be sufficiently higher in energy than the redox potential of the I_3^-/I^- system.

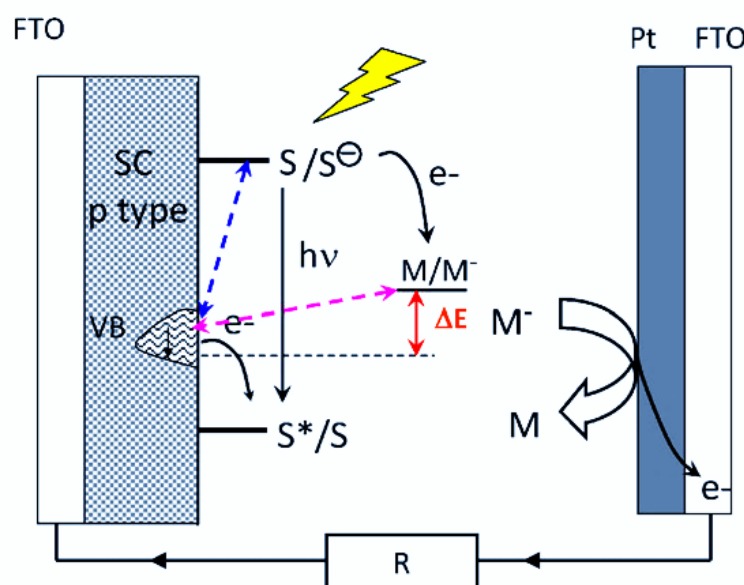


Figure 1.3 Schematic representation of working of *p*-type DSSC (Odobel et al. 2012)

Figure 1.4 illustrates the basic working principle of a *p*-type DSSC under illumination (Qin et al. 2010). As clearly depicted, on excitation, the dye molecule undergoes an electronic state change from the ground state (S) to an excited state (S^*) which decays by hole injection into the VB of the *p*-type semiconductor (*p*-SC) to form the charge-separated state S^-/p -SC. Further, a redox mediator reacts with the reduced dye molecule to restore the ground state of the dye. In continuation, the holes

generated in the semiconductor move to the back collector of the working electrode and the reduced species (I^-) in the electrolyte diffuses to the platinum electrode. This charge collection gives rise to a cathodic photocurrent in the external circuit. Various processes taking place in the cell are summarized below:

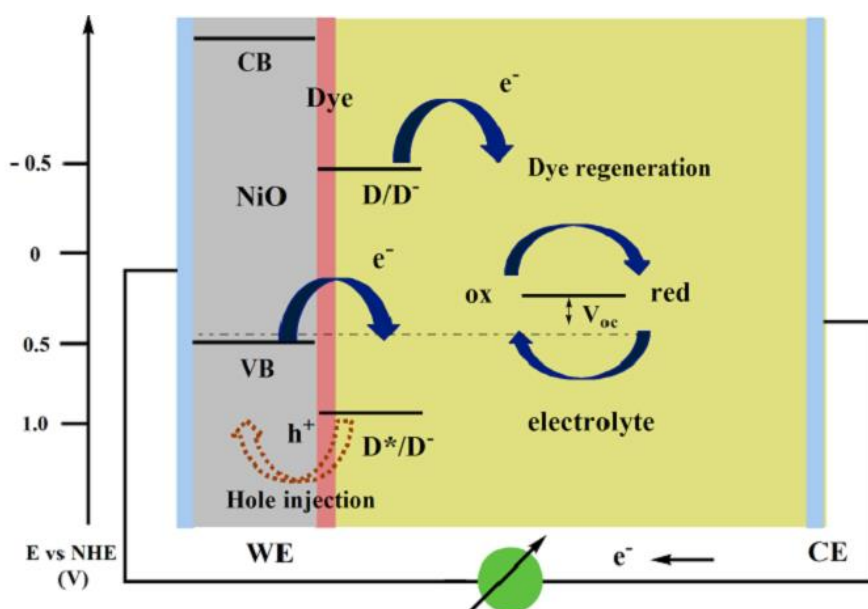
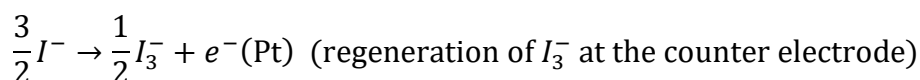
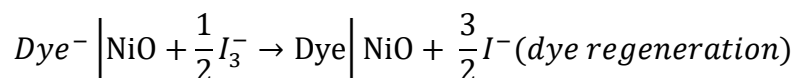
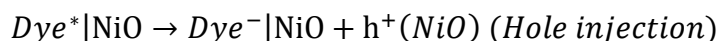
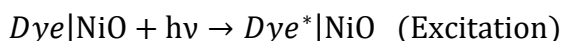


Figure 1.4 Schematic illustrations of the key processes in a *p*-type DSSC (Qin et al. 2010)

1.5.4 Components of *n*-/*p*-type DSSC

Generally, the device architecture of DSSC mainly consists of five major components such as transparent conductive substrate, mesoporous semiconductor, sensitizer, an electrolyte, and a counter electrode.

1.5.4.1 Transparent conductive substrate (TCS)

In DSSCs, the transparent conductive substrate is made up of sheet which provides the space for deposition of the semiconductor as well as a current collector. In order to aim for higher efficiency, the transparency factor must be greater than 80% to allow the passage of maximum sunlight to the active area of the device. In general, FTO (fluorine-doped tin oxide, $\text{SnO}_2: \text{F}$) and ITO (indium tin oxide, $\text{In}_2\text{O}_3: \text{Sn}$) are majorly used as transparent conductive materials. When compared to ITO, FTO substrates are highly recommended in DSSCs since FTO is independent of temperature.

1.5.4.2 Mesoporous Semiconductor

The mesoporous semiconductor is considered to be a very important component used in DSSCs due to their highly desirable properties such as high light-harvesting ability, electron injection, collection, as well as low undesirable recombination capacity. Also, crystallinity, surface area, and morphology are the major characteristic to decide the electron transport nature of the semiconducting material used.

In *n*-type DSSCs, the photoactive electrode or photoanode consists of wide bandgap semiconductors such as titanium oxide (TiO_2), zinc oxide (ZnO), stannic oxide (SnO_2), and chalcogenides, *etc.* Further, from the literature, it is clear that DSSCs based on ZnO/SnO_2 yield a lower performance compared to those based on nanocrystalline TiO_2 . This may be attributed to the vulnerability of the ZnO surface to the acidic environment, the chemical bond with the dye is easily degraded to form dye aggregates that dissipate the energy of absorbed photons. The parameter which affects the mobility of electrons as well as, carrier concentration in semiconductor metal oxides is the type and concentration of cation and anion defects. Among these point defects, the oxygen vacancy has been identified as the one which affects the performance of solar cells. From the literature (Meng et al., 2010) on electron and hole dynamics, it is confirmed that oxygen vacancy on the TiO_2 surface stabilizes the dye adsorption. Further charge injection will be enhanced due to the strong bonding between dye and the semiconductor material.

In *p*-type DSSCs, Nickel oxide (NiO) has been widely used as *p*-type SC for their fabrication. The reason may be due to their resistant nature to photo-corrosion and they can be easily synthesized as nanoparticles so that further transformed into mesoporous films that can have large surface area. NiO also gained much attention due to its utilization in other applications, such as gas sensors, catalysts, magnetic materials, electrochromic devices, and fuel cells. Unlike *n*-type DSSCs, in *p*-type DSSCs the maximum V_{OC} that the cell is based on the position of the valence band potential of the *p*-type SC material. Also, *p*-type metal oxides are known to be much poorer electronic conductors than *n*-type metal oxides.

1.5.4.3 Sensitizer

Among the various components of DSSCs, the sensitizer/dye which harvests the solar energy and helps in electron injection into the mesoporous semiconductor plays a crucial role in achieving the high performance of the cell. These photosensitizers are broadly classified into two major groups. They are (i) metal-based (Ru II) and (ii) metal-free sensitizers. It is well-established that the devices fabricated with dyes based on Ru (II) complexes (Ruthenium-II complexes) showed better conversion efficiency over that of metal-free organic dyes. However, metal-free organic dyes possess several advantages over the former class, such as easy availability, design versatility, high molar extinction coefficients, and cost-effectiveness in their synthesis. An efficient photosensitizer should possess certain requirements such as:

- The photosensitizers should have a broad and intense absorption band in the highest photon-flux region in order to act as a light-harvester.
- It should carry specific anchoring groups such as carboxylate or phosphonate group for strong adsorption onto the semiconductor surface.
- The lowest unoccupied molecular orbital (LUMO) of the *n*-type sensitizer must be higher than that of the conduction band of the semiconductor oxide for efficient electron injection into its conduction band.
- The highest occupied orbital (HOMO) of the *p*-type sensitizer must be sufficiently low to accept electron donation from an electrolyte or a hole conductive material.

- The molar extinction coefficient of the dye must be high in order to obtain a better absorption capacity.
- Stability of the dye.

1.5.4.3.1 Dyes for TiO₂-based *n*-type DSSCs

In recent years, metal-free organic sensitizers as an alternative for metal-based sensitizers have garnered significant attention due to their high molar extinction coefficient, cost-effectiveness, ease of synthesis, flexibility, and eco-friendly nature in tuning the absorbing light spectrum. In order to enhance the photovoltaic performances of the DSSCs, various design strategies have been proposed for designing new organic sensitizers. One such strategy involves a push-pull type structure constituting an electron donor (D), π -conjugated spacer, and electron acceptor (A) moieties. Among these, the most heavily explored configuration is the D- π -A system (**Figure 1.5**). In such a kind of sensitizer, the photoinduced intramolecular charge transfer (ICT) phenomenon can easily be controlled and their photophysical properties can be tuned by varying donor, spacer, and acceptor moieties.

From the literature, it is very clear that certain electron acceptor/anchoring units such as cyanoacrylic acid and rhodanine-3-acetic acid work effectively due to their strong electron-withdrawing ability and effective binding nature on the surface of semiconductor oxide. Recently, rhodanine, barbituric acid, 1,3-dimethylbarbituric acid, 1,3-diethyl-2-thiobarbituric acid, 2,4-thiazolidinedione, oxindole (2-indolone), and 4-nitrophenyl acetonitrile, *etc* are shown to be effective acceptor/anchoring units mainly due to their efficient electron-accepting behavior as well as, effective binding on the surface of TiO₂. Furthermore, thiophene, benzene, and its derivatives have been proven to be good π -bridged conjugated skeletons as well as electron donors because of their small resonance energy, high polarizability, stability, and excellent charge transporting capability. The presence of π -linkers between donor and acceptor moieties not only extends the π -conjugation of the chromophore, but also increases the overall stability.

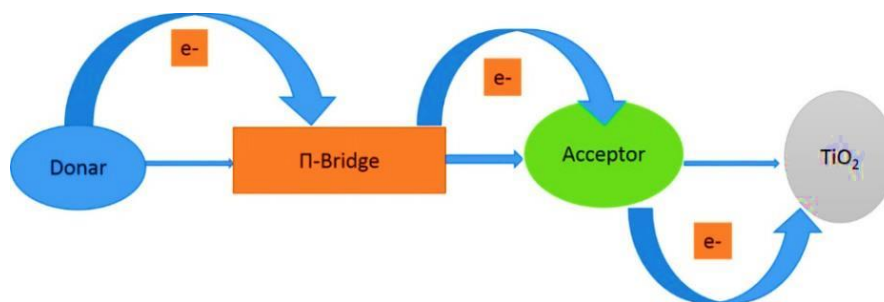


Figure 1.5 D- π -A configuration of *n*-type metal-free organic chromophore (Qin et al. 2008)

Amongst the several heterocyclic electron donor systems, interesting scaffolds, *viz.* carbazole, thiophene, and phenoxazine play a key role in the design of organic chromogens for DSSC applications. Also, the dyes derived from the aforementioned core systems are potential candidates for sensitizing and co-sensitizing DSSCs effectively, as they possess stable configuration and favourable optical as well as electrochemical properties. Consequently, they have been selected as effective donor moieties in our present systematic investigations.

Chemistry of carbazole

The carbazole is a polycyclic aromatic hydrocarbon comprising a pyrrole ring fused between two benzene molecules showing extensive electron delocalization. The presence of a heterocyclic 5-membered nitrogen-containing pyrrole ring in the system enhances the electron-rich nature of carbazole moiety. Further, carbazole is having superior thermal stability and it can be further enhanced by attaching with other moieties. In addition, the carbazole derivatives exhibit higher photoconductivity, a high charge carrying property, and superior chemical stability. The carbazole core moiety can be easily functionalized at the 3rd and 6th positions. Also, the nitrogen atom in the system can be easily substituted with a variety of functional groups favouring a better solubility and fine-tuning of the electronic and optical properties. A detailed literature review reveals that a variety of carbazole-based dyes have been successfully synthesized and employed in devices as efficient sensitizers, this has been elaborated in **Section 1.10.1.1**.

Chemistry of thiophene

Thiophene is a five-membered heterocyclic compound that can undergo extensive substitution reactions. The key parameter of the molecule is that electron pairs present on the sulfur atom are delocalized in the π -electron system and it behaves similar to that of benzene derivative. The thiophene and its derivatives have been proved to be good π -bridged conjugated skeletons as well as electron donors because of their small resonance energy, high polarizability, stability, and excellent charge transporting capability. The introduction of thiophene moieties to heteroaromatic/aromatic systems would lead to facilitate the bathochromic shift of absorption spectra and broaden the spectral region of absorption in the visible region. Also, the incorporation of thiophene linkers enhances the molar absorptivity of the materials and makes the whole molecule to occupy a larger surface area than a molecule with a linear shape, thereby leading to the reduction of loading capacity. The presence of thiophene between donor and acceptor moieties not only extends the π -conjugation of the chromophore but also increases the overall stability. A detailed account of the literature survey pertaining to the dyes based on thiophene core, as effective sensitizers, has been discussed in **Section 1.10.1.2**.

Chemistry of phenoxazine

Phenoxazine is a well-known heterocyclic compound comprising an oxazine ring fused between two benzene molecules showing extensive electron delocalization. Here, the presence of electron-rich heteroatoms, *i.e.* nitrogen and oxygen enhance the electron-donating ability as well as its non-planar butterfly conformation, which will significantly resist the molecular aggregation. Further, the nitrogen atom in the system can be easily substituted with a variety of functional groups which further enhance the charge separation. In addition, the two phenyl rings are arranged at a small torsion angle in order which helps to extend the π -delocalization over the entire chromophore. These structural features of phenoxazine moiety will make it a promising type of sensitizer for DSSC application. A detailed account of the literature survey pertaining to the dyes based on phenoxazine core, as effective sensitizers, has been discussed in **Section 1.10.1.3**.

Organic co-sensitizers for efficient DSSCs

Co-sensitization is one of the most important alternative techniques to fulfil the limitations of a single dye approach. Since an organic dye possesses a characteristic sharp and narrow absorption spectrum, it has poor photon-harvesting ability. In this strategy, a combination of two or more dyes with complementary optical absorption properties is used to improve the overall light-harvesting ability of the cell. Such kind of combinations of dyes collectively affords the panchromatic absorption spectra in the visible region. For example, Ru (II) dye has a lower absorption power with a low molar extinction coefficient at a higher wavelength region, which can be complemented with the high molar extinction coefficient dye, thereby imparting panchromatic behaviour and hence, high *PCE* values to the DSSC. Here, the increased performance is mainly due to their ability to adsorb into pores and voids of TiO₂ semiconductor surface, while the three-dimensional bulky ruthenium-based dye fails to get adsorbed fully. Hence, it is obligatory to understand the importance of simple co-sensitizers and the factors which optimize the interfacial charge transfer in the device. A brief account of the organic co-sensitizers and their performances in the DSSCs sensitized with Ru (II) complex has been discussed in section **1.10.1.4**.

1.5.4.3.2 Dyes for NiO-based *p*-type DSSCs

Unlike *n*-type DSSCs, in *p*-type DSSCs, the excited state of the sensitizer decays by hole injection into the VB edge of the semiconductor NiO. As discussed in the above section, the molecular design strategy for *p*-type dyes is almost similar to that of *n*-type DSSCs, except for the position of the anchoring group (carboxylic acid). In particular, the anchoring group must be present on the donor unit in order to aim for better hole injection. The most common design strategy for *p*-type dyes is the D- π -A approach and is shown in **Figure 1.6**. Generally, the ICT characteristics of a D- π -A type *p*-type dye is strongly dependent on the electron-donating nature of the donor moiety (D), the electron-withdrawing ability of the acceptor units (A), as well as the electronic characteristics of the π -conjugated bridge. Accordingly, the required properties (optical and electrochemical) can be tuned through the chemical modification of each component. Most of the reported *p*-type organic sensitizers are

triphenylamine-based dyes because of their excellent hole transporting ability, but very little literature is available on carbazole and phenoxazine-based chromogens. A detailed account of literature reports on different *p*-type dyes with D- π -A configuration, along with their photovoltaic studies has been explained in **Section 1.10.2**.

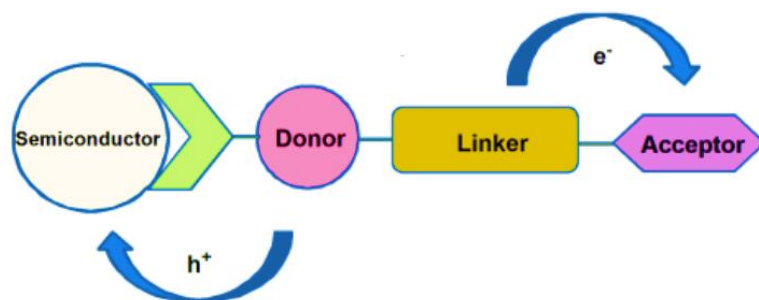


Figure 1.6 D- π -A configuration of *p*-type metal-free organic chromophore (Qin et al. 2008)

1.5.4.4 Counter electrode

Generally, the counter electrode functions as an interface where the oxidized electrolytes get reduced. Low charge transfer resistance and high exchange current densities are the prerequisites of a material to be used as a counter electrode in DSSC. Typically, the electrons moving from the external circuit are transferred back to the redox electrolyte by the counter electrode. Platinum (Pt) is the most preferred catalyst for I_3^- reduction due to its high exchange current density, excellent catalytic activity, and transparency. Recent studies have shown that other materials such as carbon, graphite can be used as an alternative to Pt since it combines sufficient electrical conductivity and heat resistance as well as corrosion resistance and good electrocatalytic activity for the I_3^- reduction.

1.5.4.5 Electrolyte

A final key component of DSSCs is the electrolyte which majorly functions as an electron transporter in the cell. Its key features are as follows:

- The photoexcited dye loses an electron before its contact with the electrolyte.
- The dye molecule which is oxidized has to be reduced further by the electrolyte rather than its recombination with the electrons from the neighbouring dye molecule.

- The reduced electrolyte undergoes a slow reaction with electrons in both TiO₂ and TCO layers.
- The reduction rate of the oxidized ion at the cathode is rapid.

The important constituent of the liquid electrolyte is a redox couple. From the literature, it is evident that most of the electrolyte used in DSSC contains I⁻/I₃⁻ redox system. Redox couple works as a charge carrier collecting electrons at the cathode and transporting electrons back to the dye molecules. The electrolyte is a neutral sink of I⁻ and I₃⁻ maintaining the redox potential in the bulk of the electrolyte *via* the fast redox reaction of the I⁻/I₃⁻ pair. Recently, studies also have been carried out on new cobalt [Co^(II/III)] polypyridyl complexes as a redox couple in combination with ruthenium dyes.

1.5.5 Advantages and challenges in the field of DSSC

Though the performances of 3rd generation of solar cells such as DSSCs are not comparable to Si-solar cells, it has an edge over in some other aspects. The major highlights of these are low-cost and abundantly available eco-friendly raw materials which further makes it cost-effective. Unlike, other generation solar cells, DSSCs do not demand high energy, very high vacuum (costly), and materials involving tedious purification steps. Further, another advantage of DSSCs is that they can even work at low light conditions, which makes them popular over decorative effects when used in indoor applications such as window panels of buildings and constructions.

In the past three decades, researchers in the field of DSSCs have gone on a rocket-up scale. However, some of the factors are able to be tackled to compete with the other photovoltaics. There is much scope for active research on the optimization of various components of DSSCs, mainly the design and selection of sensitizers and electrolyte systems for improving the device parameters (J_{SC} , V_{OC} , FF , and PCE). Among all, the major challenging task is to design an efficient dye with high light-harvesting ability as a sensitizer, which further contributes to the overall performance.

1.6 PEROVSKITE SOLAR CELL (PSC)

Organic-inorganic hybrid lead halide perovskites attracted worldwide researcher's attention due to their potential intriguing properties such as low cost, ease

of fabrication, high absorption coefficients, extremely low exciton binding energy, ambipolar charge transport properties, and low non-radiative carrier recombination rates. Moreover, their ability to capitalize on over 20 years of development of related DSSC and organic photovoltaics is noteworthy. In 2009, Miyasaka et al. developed solar cells based on perovskite as a light-harvester for the first time by incorporating $\text{CH}_3\text{NH}_3\text{PbI}_3$ (MAPbI₃) and $\text{CH}_3\text{NH}_3\text{PbBr}_3$ (MAPbBr₃) as sensitizers into DSSCs; they delivered the *PCE* of 3.8 and 3.1%, respectively. In the past decade, relentless efforts were made to develop the new device architectures for the fabrication of perovskite solar cells (PSCs) with attractive materials, achieving the *PCE* from low (3.8%) to very high (25.2%) values. These PSCs have acquired intense research efforts from both academia as well as industries due to their drastic increment in their *PCE* and excellent stability.

1.6.1 Device architecture of perovskite solar cells

In general, the device architecture of the hybrid organic-inorganic metal halide PSCs is a modified version of the dye-sensitized solar cell (DSSC) architecture wherein the liquid dye/electrolyte has been replaced by perovskite absorber material. One of the main characteristic features of perovskites is their ambipolar nature, where *n*- or *p*-type conduction enables two different types of device architecture. The device architecture of PSCs is mainly composed of a transparent conductive oxide (TCO) as a front electrode, perovskite as a light absorber and is sandwiched between the *n*-type electron transport layer (ETL) and the *p*-type hole transport layer (HTL), and finally, a metal back electrode. The most commonly used ETLs are TiO_2 , SnO_2 , ZnO , or phenyl-C61-butyric acid methyl ester (PCMB), whereas HTLs contains 2,2',7,7'-tetrakis[*N,N*-di-(*p*-methoxyphenyl)amino]-9,9'-spirobifluorene (Spiro-OMeTAD), poly[bis(*p*-phenyl)2,4,6-trimethylphenyl)amine] (PTTA), poly(3,4-ethylenedioxythiophene):poly(styrene-sulfonate) (PEDOT:PSS) or NiO_x . Based on the electrical properties, PSCs can be fabricated in either a regular *n-i-p* or inverted *p-i-n* device configuration. If the solar light is illuminated through ETL, the device structure is called *n-i-p*, on the other hand, if the light illumination occurs through the HTL, the device structure is called *p-i-n* structure. Further, the conventional *n-i-p* devices can be classified into mesoscopic and planar heterojunction structures. In

mesoscopic architecture, the perovskite material is infiltrated into a mesoporous scaffold of a metal oxide (TCO/c-TiO₂/m-TiO₂/perovskite/HTM/metal), whereas in planar heterojunction the perovskite material is sandwiched between electron- and hole-selective contacts. In case of inverted *p-i-n* architecture, the aforementioned stack is inverted (TCO/HTM/perovskite/ETM/metal). Presently, hole transport material (HTM)-free PSCs have been shown to exhibit enhanced performance in both conventional and inverted planar as well as mesoscopic heterojunction structures as shown in **Figure 1.7**.

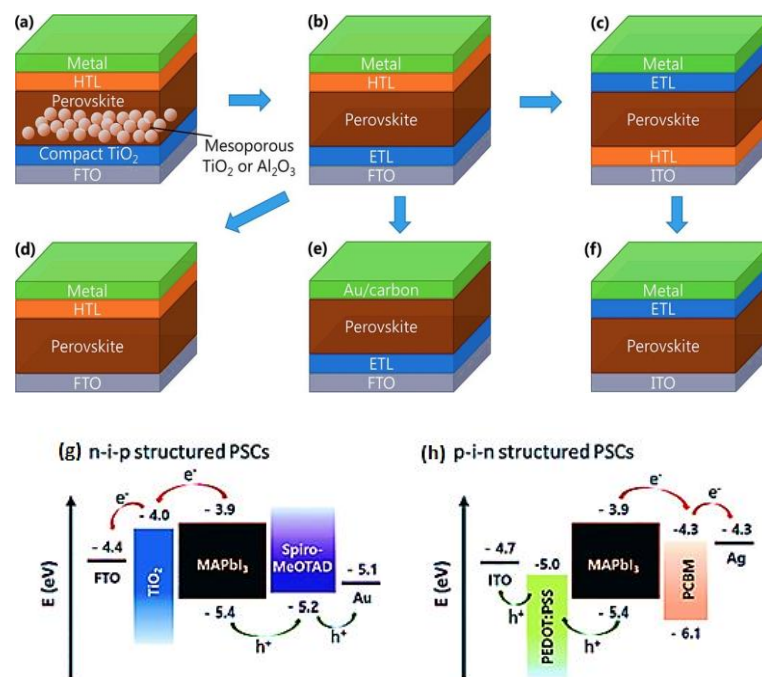


Figure 1.7 Schematic representation of device architecture of PSCs. (a) Regular mesoscopic *n-i-p*, (b) Regular planar *n-i-p*, (c) Inverted (planar) *p-i-n*, (d) Electron transport layer-free architecture, (e and f) Hole transport layer-free architecture. Energy band diagram of typical (g) *n-i-p* and (h) *p-i-n* structured PSCs. (Zhao et al. 2017)

1.6.2 Working principle of perovskite solar cells

A simplified working method for a PSC involves the transmission of the incoming sunlight through a transparent conductive substrate (TCO) and the front interfaces, followed by light absorption by the perovskite material. Generally, in PSCs the photons with enough energy can excite the electrons from the VB to the CB of the semiconductor across the bandgap, followed by carrier extraction of both the electrons

and holes due to the built-in electric fields or diffusion. Hence, a semiconductor with a low bandgap can absorb more amount of light and hence can generate a higher current, whereas a semiconductor with a high bandgap can limit the light absorption as well as the output current. Further, a perovskite material with the appropriate thickness (generally 500 nm), can capture 100% of resonant light due to its low exciton binding energy and the high absorption coefficient of perovskites. The larger carrier diffusion length of perovskite films facilitates the transport of generated carrier to the corresponding interface contacts. In the cell, the generated electrons and holes are collected by the respective electron transport material (ETM) and hole transport material (HTM). At the end, the electrons will transfer from perovskite material to semiconductor oxide (TiO_2) and finally be collected by TCO. At the same time, the holes generated will transfer from HTM to the metal electrodes. Lastly, the TCO and metal electrodes are connected and hence photocurrent will be generated in the outer circuit. During this phenomenon, many undesirable processes such as back charge transfer at the interfaces of semiconductor and the HTM with the perovskite layer, recombination of photogenerated species as well as recombination due to the direct contact between semiconductor and the HTM may happen. By overcoming these extraction barriers at the interfaces, the carrier transport can easily be made to occur through corresponding selective contact interfaces and finally will be extracted to the electrodes.

1.6.3 Hole transporting materials (HTMs)

Hole transporting materials (HTMs) play a pivotal role in determining the overall performance of the PSCs and researchers all over the world are considering different aspects for the development of a new variety of HTMs. In fact, HTM is considered as an important active component in PSCs, which is highly responsible for efficient photogenerated hole extraction mainly at the perovskite/HTM interface and avoiding unwanted charge transfer processes, thereby bringing about enhanced device performance. From the literature, it is evident that a great number of organic HTMs comprised of small molecules or conducting polymers have been incorporated in order to achieve superior photovoltaic properties in PSCs. An ideal HTM must fulfil the following general criteria:

- It must exhibit suitable energy levels, providing the driving force for charge transfer, *i.e.* the HOMO energy level of the HTM must be higher than the valence band edge of the perovskite.
- It must have sufficient hole mobility and high conductivity to facilitate high FF , and V_{OC} which prevents the charge recombination.
- It must have good solubility as well as film-forming property.
- Finally, it should be cost-effective, transparent, eco-friendly, and must exhibit high thermal and photochemical stability in order to resist the external degradation factors.

Consequently, vast research interest has risen for the development of new organic HTMs and also to investigate a better understanding of the correlation between the HTM and the performance of PSCs. A significant number of organic HTMs have been reported so far, to achieve the requirements of an ideal candidate. The most commonly used up-to-date organic HTMs, *viz.* 2,2',7,7'-tetrakis[*N,N*-di-(*p*-methoxyphenyl)amino]-9,9'-spirobifluorene (Spiro-OMeTAD) and even further interesting macromolecule poly[bis(*p*-phenyl)2,4,6-trimethylphenyl]amine (PTTA) were shown to deliver the PCE of $>20\%$ in the device. However, their limitations such as tedious multi-step synthesis, complicated purification steps, instability to humid air, and difficulty in controlling conductivity, stimulate further research to investigate more cost-effective, stable, and dopant-free materials for easy commercialization. In this respect, many efforts have been devoted to exploring better alternatives to the existing materials like spiro-OMeTAD.

Recently, organic small molecules like branched methoxy diphenylamine substituted fluorene derivatives were shown to yield the PCE up to 25.5 %, but their synthetic methods are highly expensive. Moreover, they need dopants like lithium salt of bis(trifluoromethylsulfonyl)imide (LiTFSI) and 4-*tert*-butylpyridine (TBP) for adjusting the conductivity. As an important class of organic HTMs, carbazole and triphenylamine-based compounds have been widely investigated for optoelectronic applications owing to their excellent charge-transporting properties, apart from interesting photoconductive, photo-refractive, and light-emitting behaviour. These small molecules possess many advantages as optoelectronic materials mainly due to

their predictable HOMO-LUMO energy levels, which can be easily tuned through chemical substitution, and high thermal stability, rendering them suitable candidates for thermal evaporation. In addition, being a cheap raw material, it can easily be substituted through simple routes to yield derivatives of high photochemical stability, and also it has the ability to quickly form relatively stable radical cations. However, the organic HTMs are more susceptible to migration of halide ions as well as metal ions and hence cause quick degradation. Although this architecture leads to the highest PCEs, the problem of instability of organic HTM, as well as perovskite in presence of moisture in ambient air challenges the long-term use of the device, creating many hurdles for the commercialization.

Off lately, researchers have proved that perovskite material such as methylammonium lead halide ($\text{CH}_3\text{NH}_3\text{PbI}_3/\text{MAPbI}_3$) could serve as both a light harvester as well as a hole transporter, rendering redundant use of existing HTMs. In general, the HTM-free PSCs mainly include several hole extraction electrodes such as Au, Ni, and carbon. But the expensive Au electrode used in the PSCs requires a high-vacuum evaporation technique, along with the Au migration through HTL into the perovskite layer, thereby restricting the commercial applications. Now, carbon is considered to be the most promising electrode material among all these materials because they are cheap, stable, inherently water-resistant, inert to ion migration, and hence advantageous for high device stability. Benefiting from these advantages of carbon electrodes over other materials, much progress has been made on the development of carbon-based perovskite solar cells.

1.6.4 Carbon-based perovskite solar cells (C-PSCs)

To meet the demand for simple, stable, and low-cost PV techniques, carbon-based hole-transport material-free perovskite devices have gained much interest. As an alternative to the conventional architecture where all the device layers are deposited as compact thin films, a new low-cost PSC device was developed with a high electrically conductive carbon-based whole mesostructured design in order to avoid materials instability and cost challenges. Generally, $>5\ \mu\text{m}$ thick carbon-based electrodes are used in device fabrication to accumulate over excess of perovskite in its porous structure, which makes it more tolerant against the decomposition in the

photo-absorber. In carbon-based mesostructured architecture, an appropriate work function of the carbon materials with perovskite valence band facilitates the effective hole transfer. Further, the use of the carbon layer reduces ion migration and effectively eliminates the use of organic hole-transport material (HTM). In addition to this, the carbon layer acts as a moisture barrier and prevents the hydration of the infiltrated perovskite, thus substantially reduces the degradation kinetics.

1.6.4.1 Device architecture and working principle

Carbon-based PSCs are classified into two subcategories, *viz.* mesoscopic carbon and planar carbon electrode-based cells. The typical whole printable carbon-based mesostructured architecture, which employs a triple-layered architecture of mesoporous TiO₂, ZrO₂, and carbon as a scaffold, is expected to play a pivotal role in the scale-up of low-cost perovskite-based photovoltaic devices. These layers were screen printed on the top of FTO substrate followed by sintering. Further, the perovskite precursor solution is to be infiltrated on top of the mesoscopic scaffold by the traditional drop-casting method from the carbon layer side and finally annealing to obtain the device as shown in **Figure 1.8a**. The schematic representation of planar carbon electrode-based PSC with the FTO/TiO₂/perovskite/carbon device architecture is shown in **Figure 1.8b**. This planar architecture can be made in a similar way as the conventional PSCs based on Au electrode, which involves spin coating technique for deposition of layers.

The energy levels alignment in the C-PSCs is shown in **Figure 1.8c**. The valence band edge (−5.4 eV) is lower than that of the Fermi level (−5.0 eV) of the carbon electrode, whereas the conduction band edge, CBE (−3.9 eV) of typical MAPbI₃ perovskite is found to be higher than that of CBE of TiO₂ semiconductor (−4.0 eV). When the light is illuminated, the perovskite absorber gets excited after absorbing the light resulting in the generation of electrons and holes in the CB and VB of MAPbI₃. Further, the photogenerated electrons will be injected on the CB of TiO₂ whereas the carbon electrode facilitates the extraction of holes. Here, the m-ZrO₂ layer is typically used to separate the TiO₂ and carbon layer contact in order to avoid the short circuit and hence helps in enhancing the overall performance of the device.

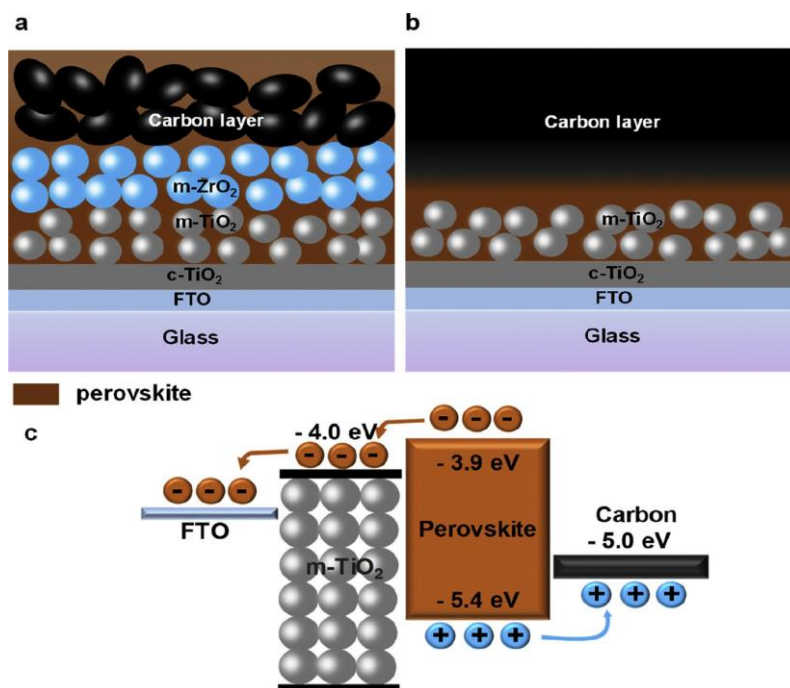


Figure 1.8 Schematic representation of device architecture of carbon-based PSCs. (a) mesoporous C-PSCs, (b) planar C-PSCs, and (c) energy band diagram of C-PSCs. (Duan et al. 2018)

1.6.4.2 Scaling up of perovskite solar cells

Despite significant development of C-PSCs since they were first reported in 2013, their efficiency is still lower than that of HTM-based PSCs. This drawback is not a fundamental issue to C-PSCs, but stems from a lack of optimization, and hence it is very important to address the pending issues in order to increase their commercial competitiveness. Besides, the device architecture as well as, working strategy of C-PSCs is notably different from that of conventional HTM-based PSCs. Hence, there is still scope in enhancing the efficiency and further development of C-PSCs by modifying the device architecture and working principle. Promising research directions were then suggested by addressing a number of factors including materials, structure, interfaces, stability enhancement, and scaling-up of production, to further enhance and promote the commercialization of C-PSCs. From a commercialization point of view, it is very essential to produce bulk-scale, highly stable, and efficient carbon-based perovskite solar modules. By using a conventional spin coating method, it is quite hard to get uniform and high-purity films of perovskite on large substrates in the lab. This scaling-up problem of the deposition method remarkably limits the

PCE of highly stable C-PSC modules. Encouragingly, recent literature on carbon-based PSCs manifests the large-scale production of printable modules using drop-wise infiltration process and slot-die coating technology. Though the scale-up of the perovskite film deposition as well as C-PSCs, in general, has been demonstrated, the challenge remains to be able to consistently form uniform, and high-purity perovskite films. Also, the selection of appropriate solvent is another challenge to obtain a high-quality perovskite layer at a bulk scale. Therefore, the optimization and development of large-scale deposition methods suitable for the fabrication of carbon-based perovskite modules are needed to accelerate the commercialization of C-PSCs.

1.7 INSPIRATION FOR PRESENT WORK

One of the greatest challenges ahead of human society is to harvest the power of the Sun by replacing the existing fossil fuels with clean and cheap alternative sources. In this concern, photovoltaic technology appears to be the only reasonable large-scale answer to the world energy crisis. As the 1st and 2nd generation photovoltaics require high cost as well as high energy consumption for purification and fabrication of raw materials, research on organic photovoltaics especially the DSSC field gains much strength. Here, one of its components, ‘sensitizer’ plays a crucial role in improving its *PCE*. However, developing organic materials with good light-harvesting ability and optimum carrier transport properties is not an easy task. This can be achieved by the use of an appropriate sensitizer, engineered by suitable structural design. Further, carrier transport characteristics can be improved by optimizing the properties of the semiconductor as well as electrolyte. In this regard, it is quite necessary for researchers to design dye molecules with a suitable donor, π -spacer, and an acceptor/anchoring unit to aim for better efficiency. Thus, there is ample scope for the design and development of new sensitizers for DSSC applications.

Later on, the most recent addition to the class of emerging photovoltaic technologies is organic-inorganic perovskite solar cells. When compared to the other solar cell technologies, PSCs have shot up in efficiency from ~3 % to > 25.5 % in less than a decade. Though the achieved PCE is high, PSCs face challenges with perovskite’s stability, reproducibility in device performance and hence, large-scale

production. In order to overcome these challenges, it is very important for researchers to focus on the development of new materials for PSCs and their device engineering. Thus, in the subsequent section, the topics of current research efforts, *i.e.* progress made in the material systems and the challenges in PSCs, will be discussed. In the present work, an attempt has been made to develop efficient metal-free organic sensitizers/co-sensitizers for DSSC applications. Also, investigations have been carried out for the selection of a proper solvent to give high-quality thin films in PSCs, as well as for the development of new organic HTMs for PSC devices. It has also included the development of large-area modules of PSCs with high efficiency.

1.8 CHARACTERIZATION TECHNIQUES

A detailed characterization of materials, and their fabricated devices are necessary to fully understand and optimize the photovoltaic performance as well as their stability. Therefore, several characterizations need to be performed thoroughly. They include mainly structural, photophysical, electrochemical, theoretical, and photoelectrochemical characterizations.

In general, the structures of newly synthesized organic molecules (dyes/HTMs) and their intermediates are well-characterized using spectroscopic techniques like Fourier transform infrared (FTIR) spectroscopy, nuclear magnetic resonance (NMR) spectroscopy, mass spectrometry followed by elemental analysis. The UV-Visible absorption and photoluminescence (PL) studies are employed to investigate the photophysical properties of dyes/HTMs. The optical characterization would yield useful data such as absorption maxima, emission maxima, molar extinction coefficient, Stokes shift, and optical bandgaps, which are needed to understand the light-harvesting ability of the molecules. Further, the cyclic voltammetric (CV) technique is conveniently used to evaluate required electrochemical data along with parameters related to thermodynamic driving forces (E_{ox} , E_{ox}^* , E_g , ΔG_{inj} , ΔG_{rec} , ΔG_{reg} , *etc.*) for the processes involved during energy conversion in the cell. Furthermore, some important data like molecular geometry, electron distributions, energetic properties, and absorption spectra of synthesized dyes/HTMs are obtained by computational studies, *i.e.* with the help of density

functional theory (DFT) and time-dependent density functional theory (TD-DFT) using Turbomole 7.2V software.

Typically, in carbon-based perovskite solar cells, the surface morphology of the carbon composition, as well as microstructural analysis of perovskite films formed, can be conveniently carried out using scanning electron microscope (SEM) studies. Further, the crystal phase composition and light absorption properties of the perovskite film are comprehensively investigated by powdered X-ray diffraction (XRD), UV/Vis absorption spectra, and photoluminescence (PL) spectroscopic techniques. Additionally, time-resolved photoluminescence (TRPL) decay experiments are conducted to reveal the effect of charge extraction and carrier lifetime, respectively.

Finally, the efficiency of a solar cell is determined by its current-voltage (J - V) characteristics under standard illumination conditions. A standard solar spectrum of air mass 1.5 (AM 1.5) with an intensity of 1000 W/m^2 also referred to as 1 sun, is generally used for solar cell characterization. The illumination conditions are provided by a calibrated xenon lamp source. The current-voltage characteristics are monitored under illumination by varying an external load from zero loads (short-circuit condition) to infinite load (open-circuit condition). From the experiments, $IPCE$ characteristic curves are obtained in order to reveal how efficiently light of a specific wavelength is converted to current.

1.9 BROAD OBJECTIVES OF PRESENT WORK

Taking all the above-mentioned points into consideration, in the present work, the attention has been focussed on the three broad areas of solar cell research, *viz.* (A) Organic dyes for DSSCs, (B) Organic HTMs for PSCs, and (C) Studies on carbon-based PSCs.

From the material scientist's point of view, the development of suitable materials for sensitizers, electrodes, semiconductors, and electrolytes plays a very pivotal role in achieving greater performance in DSSCs. So, it has been planned to carry out preliminary investigations on the development of new metal-free organic sensitizers/co-sensitizers for DSSC applications, the study has comprised design,

synthesis, and characterization of new *n*-/*p*-type heterocycle-based chromogens along with their structure-property correlation study.

At the molecular level, the design, geometry, and electronic structure of the HTM contribute effectively to tailor the essential properties in it. Therefore, it has been contemplated to design, synthesize, and characterize new carbazole-based HTMs and to fabricate new PSCs using them, in order to study their structure-property relationship.

With the aim of enhancing the efficiency along with long-term stability, it has been intended to focus on developing the printable carbon-based PSCs by addressing the key requirements in device engineering such as crystal formation, morphology control, and selection of solvents, interface engineering, degradation factor, and reproducibility. All these investigations have been done with the target of developing a novel, cheap, scalable, and large-area perovskite solar module.

PART B: LITERATURE REVIEW, SCOPE, AND OBJECTIVES

1.10 LITERATURE REVIEW

The quest for simple and cost-effective electrical energy generation has led to enhanced attention towards research on third-generation photovoltaics. In this field, dye-sensitized solar cells (DSSCs) and perovskite solar cells (PSCs) have been widely investigated due to their promising performance, eco-friendly, and economically viable nature. Although an enormous number of dyes/HTMs have been reported so far, the quest for finding the suitable highly efficient material is still in progress.

This section covers a brief account of a literature survey on various thiophene, carbazole, and phenoxazine-based metal-free dyes employed as *n*-type sensitizers, carbazole, and phenoxazine-based dyes as *p*-type sensitizers, and carbazole-based organic HTMs. In addition, literature reports on interesting metal-free organic dyes derived from various aromatic systems with different design strategies, as co-sensitizers have been dealt with in the following section. Some of the references on standard Ruthenium complex-based chromophores have been also explained. In the end, the detailed literature on carbon-based perovskite solar cells has been discussed.

1.10.1 *n*-Type organic chromophores for DSSC

In recent years, metal-free organic dyes have received massive interest due to their simplicity in synthesizing, low-cost, high molar extinction coefficients, and reasonable performance when compared to that of standard Ru (II) complexes. As a result, a wide range of organic small molecules as dyes were designed and developed as effective photosensitizers in DSSCs (Mishra et al. 2009; Ooyama and Harima, 2009; Ning et al. 2010). Along with this, the structure-property relationship on device characteristics has been investigated in depth.

A lot of efforts have been made by researchers to improve the performance of new metal-free organic dyes as potential photosensitizers for DSSC applications. In the literature, varieties of design strategies have been reported. Amongst them, D- π -A configured push-pull approach, wherein an electron-rich donor system and electron-deficient or withdrawing scaffolds connected through a π -spacer unit, is being considered to be one of the most promising and successful architectures to improve the photovoltaic performance of DSSCs. So far, several organic dyes are based on electron-rich fused heteroaromatic compounds such as carbazole, indole, triphenylamine, diphenylamine, phenothiazine, and phenoxazine, *etc.* systems have been reported as effective sensitizers with improved efficiency when used in DSSCs. In the present study, thiophene, carbazole, and phenoxazine systems have been used as electron donor systems with different π -spacers and acceptor/anchoring units in the structural design of new sensitizers/co-sensitizers for DSSC fabrication. A brief account of the literature review pertaining to these donor systems is described below.

1.10.1.1 Carbazole-based sensitizers

Carbazole is a tricyclic heteroaromatic compound comprising a pyrrole ring fused in between two benzene moieties. As an important class of heterocyclic moieties, carbazole and its derivatives have been widely investigated in optoelectronic applications owing to their excellent charge-transporting properties apart from interesting photoconductive, photo-refractive, and light-emitting behaviour. Carbazole derivatives possess many advantages as optoelectronic materials mainly due to their predictable HOMO-LUMO energy levels, which can be easily tuned through

chemical substitution, and high thermal stability, rendering them suitable candidates for thermal evaporation. In addition, carbazole, being a cheap raw material can easily be substituted through simple routes to yield derivatives of high photochemical stability and also it has the ability to quickly form relatively stable radical cations. Furthermore, the insertion of bulkier branched alkyl chain at *N*-heteroatom of the ring promotes significant tilting and packing distortion and tends to reduce the aggregation as well as solubility problems causing improved open-circuit voltage (V_{OC}) in the fabricated device (Venkateswararao et al. 2013; Wang et al. 2011). Till date, several new metal-free carbazole-based organic chromophores have been designed and synthesized for DSSC application. Some of the literature reports on carbazole-based sensitizers including their photovoltaic parameters are summarized in **Table 1.1**.

In 2010, Tang et al. reported the design and synthesis of new carbazole-based organic sensitizers bearing triphenylamine as a donor, two units of carbazole as auxiliary donors, and cyanoacetic acid as an electron acceptor/anchoring unit with D-D- π -A architecture (**S 1.1**). In continuation to this, they also investigated the role of co-absorbent CDCA on the photovoltaic performance of DSSCs.

In 2012, Ramkumar and his coworkers demonstrated new D-(π -A)₂ configured carbazole-based dyes bearing cyanovinyl biphenyl unit as a π -linker and cyanoacetic acid as electron acceptor/anchoring unit (**S 1.2**). The experimental results revealed that the dye **S 1.2** displayed overall efficiency of 2.37 %. Later, in 2013, the same group introduced cyanovinyl thiophene unit in dye **S 1.2** as π -spacer to get **S 1.3**, which displayed increased photovoltaic performance of 4.04 % in AM 1.5G illumination.

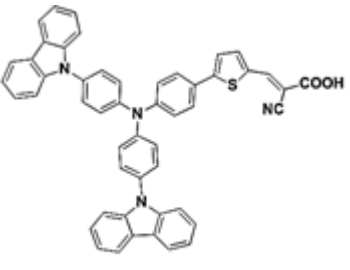
In 2014, Lin et al. synthesized a Y-shaped molecule with D- π -(A)₂ architecture (**S 1.4**) to address the issue of aggregation of dyes on the surface of TiO₂. In the device, the current density drastically increased due to the introduction of two units of cyanoacetic acid as acceptor/anchoring moieties. In the same year, Gupta et al. successfully synthesized new carbazole-based organic dye (**S 1.5**) with A- π -D- π -A architecture, wherein carbazole is connected to two cyanoacetic acid units through π -spacer thiophene ring. The dye molecule displayed an efficiency of 3.8 %.

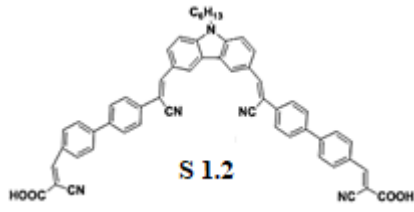
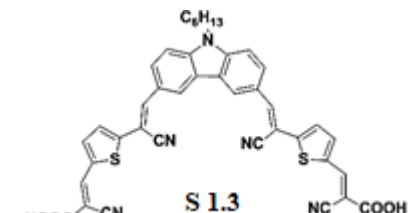
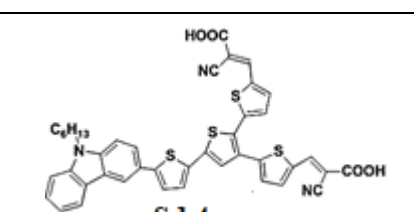
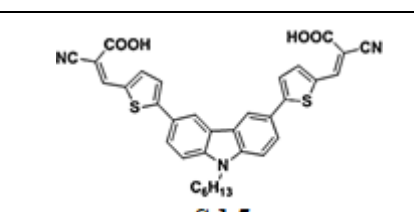
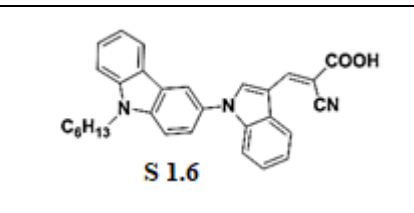
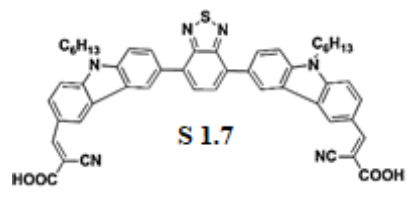
In 2016, Wang et al. demonstrated a detailed investigation on the design and synthesis of a simple D- π -A configured carbazole-based organic chromophore with indole as π -linker and cyanoacetic acid as acceptor units (**S 1.6**). The device fabricated with **S 1.6** showcased exceptional thermal and photochemical stability. Further, in order to address the charge recombination process in DSSCs, Murali et al. designed a bent-shaped carbazole-based dye (**S 1.7**) with A-D- π -D-A architecture. In the design, cyanoacetic acid functions as an electron acceptor/anchoring unit and 2,1,3-benzothiadiazole behaves as a π -spacer. The dye displayed an overall efficiency of 4.35 %.

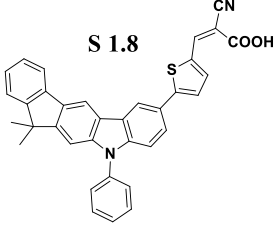
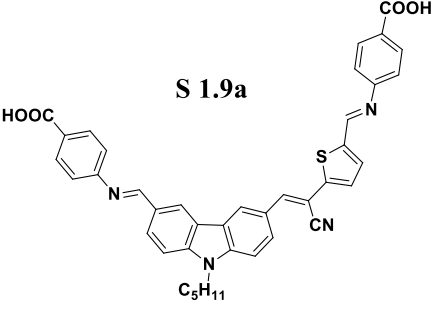
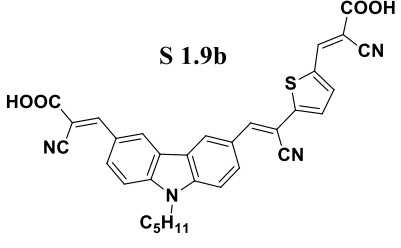
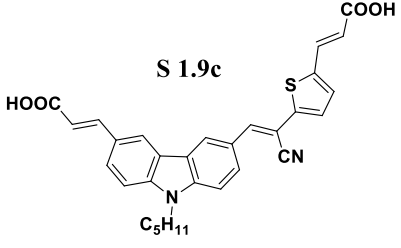
In 2018, Xie et al. reported the synthesis and fabrication of four novel metal-free organic dyes based on indeno[2,1-b]carbazole donors for DSSC application. The difference in a number of spacer units and linking mode led to variations in absorptivity, electron injection, and charge recombination process. Among all the synthesized molecules, dye **S 1.8** with thiophene as π -spacer displayed enhanced efficiency of 5.97 % under standard am 1.5G irradiation.

Recently in 2020, Nesheli et al. reported molecular design, synthesis, and characterization of new unsymmetrical di-anchoring carbazole-based dyes (**S 1.9a-c**) with A- π -D- π -A- π -A architecture. Among the synthesized dyes, the sensitizer **S 1.9a** showcased a better performance of 2.27 %, which may be due to the strong electron-withdrawing nature of the 4-aminobenzoic acid acceptor unit.

Table 1.1 Organic sensitizers based on carbazole for *n*-type DSSCs

Reference	Sensitizer	J_{SC} (mA.cm ⁻²)	V_{OC} (V)	FF	PCE (%)
Tang et al. 2010	 <p style="text-align: center;">S 1.1</p>	8.45	0.75	0.70	4.44

Ramkumar et al. (2012)	 <p style="text-align: center;">S 1.2</p>	5.18	0.76	0.51	2.37
Ramkumar and anandan (2013)	 <p style="text-align: center;">S 1.3</p>	7.64	0.66	0.68	4.04
Lin et al. (2014)	 <p style="text-align: center;">S 1.4</p>	16.98	0.63	0.68	7.28
Gupta et al. (2014)	 <p style="text-align: center;">S 1.5</p>	8.90	0.58	0.74	3.8
Wang et al. 2016	 <p style="text-align: center;">S 1.6</p>	4.18	0.67	0.74	2.09
Murali et al. (2016)	 <p style="text-align: center;">S 1.7</p>	7.51	0.76	0.76	4.35

Xie et al. (2018)	 <p style="text-align: center;">S 1.8</p>	12.34	0.71	0.68	5.97
Nesheli et al. (2020)	 <p style="text-align: center;">S 1.9a</p>	5.95	0.54	0.71	2.27
	 <p style="text-align: center;">S 1.9b</p>	5.66	0.52	0.72	2.14
	 <p style="text-align: center;">S 1.9c</p>	4.99	0.48	0.71	1.69

1.10.1.2 Thiophene-based sensitizers

Thiophene-based π -conjugated systems have attracted much attention in the PV community due to their structural versatility, moderate bandgap, environmental stability, excellent light-harvesting and intrinsic charge transport behaviour. In addition to this, the ring planarity, extended molecular conjugation, and chemical stability have made thiophene and its derivatives promising candidates in solar cells. Numerous novel π -conjugated systems based on thiophene moiety have been designed and synthesized as efficient sensitizers for DSSCs.

In 2015, Matsumura et al. reported two novel thiophene-based D- π -A configured organic photosensitizers (**S 1.10a-b**) with/without the use of a 3,4-ethylenedioxythiophene (EDOT) moiety for *n*-type DSSC application. These new push-pull architected systems consist of triphenylamine as a donor and cyanoacetic acid as a strong acceptor/anchoring unit. Here, the dye **S 1.10a** containing thiophene unit displayed an efficiency of 5 % which is almost similar to that of dye **S 1.10b** with EDOT unit, 4.9 %.

In 2017, Fernandes and his co-workers demonstrated the synthesis and fabrication of two novel heterocyclic dyes **S 1.11a** and **S 1.11b** as active photosensitizers. In this strategy, thiophene, and its derivatives serve as a donor unit, thieno[3,2-*b*]thiophene acts as a spacer and cyanoacetic acid functions as an acceptor/anchoring unit. This multidisciplinary study concerning, optical, electrochemical, and photovoltaic characterization of the dyes reveals that the dye **S 1.11b** containing hexyl-bithiophene donor unit exhibited a superior performance of 2.49 % compared to that of thiophene-based dye **S 1.11a** (0.22 %). This is because of the fact that the introduction of a long alkyl chain into the donor unit drastically suppresses the charge recombination and thus, helps to increase the overall performance of the device.

In 2018, Raposo et al. reported two new heterocyclic push-pull conjugated dyes in which *N,N*-diphenylhydrazones act as electron donor systems, thieno[3,2-*b*]thiophene (**S 1.12a**) or bithiophene (**S 1.12b**) functions as linkers with cyanoacetic acid serving as an electron-withdrawing unit. The dye **S 1.12b** bearing bithiophene spacer exhibits the best *PCE* of 5.10 % compared to **S 1.12a** (3.22 %) when used as a sensitizer for nanocrystalline TiO₂ in DSSCs, which is mainly due to the lower electronic bandgap and longer π -conjugation of the sensitizing dye.

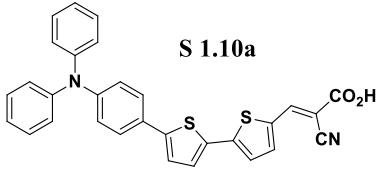
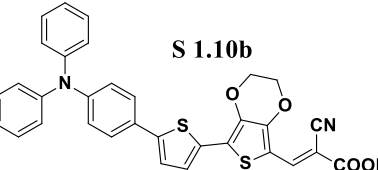
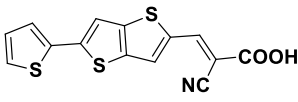
Similarly, in 2019, Lim and his team reported a metal-free organic chromophore featuring an ethynyl-thienothiophene linker with an *n*-hexyl side-chain (**S 1.13**). The results indicate that the presence of *n*-hexyl side chain effectively improves the solubility of the dye molecule, whereas the acetylene linker has been included to promote the planarity between donor and acceptor units and thus enhances

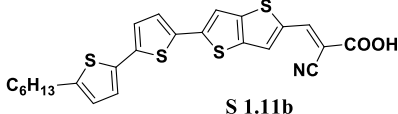
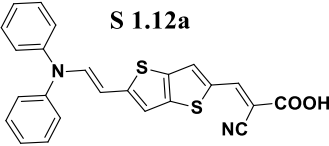
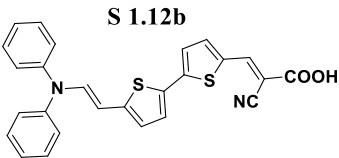
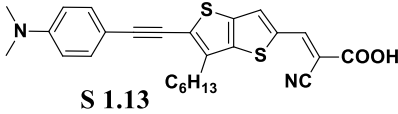
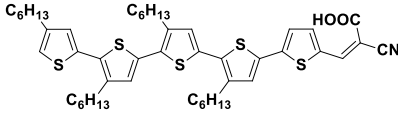
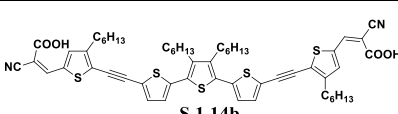
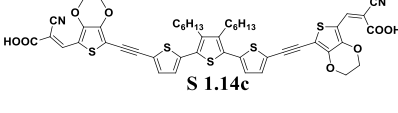
electron delocalization. Interestingly, the dye **S 1.13** displayed an enhanced efficiency of 5.46 % when fabricated without any co-adsorbents.

Recently, Robertson et al. (2021) reported D-A configured thiophene derivatives (**S 1.14a-c**) as active photosensitizers for *n*-type DSSC applications. In this new strategy, the oligothiophene molecule featuring one/two anchoring units, which do not possess strong donor moieties, are easily able to adopt U- or V-shape configuration. The dye **S 1.14a** exhibited a higher performance of 6.24 % compared to that of di-anchoring dyes **S 1.14b-c** (3.7 %), which may be due to the higher current density and lower recombination resistance.

Further, it has been observed that the photovoltaic performance of thiophene-based dyes as sensitizers greatly depends on their molecular geometry. A brief account of literature reports on thiophene-based donors connected to varied electron acceptor/anchoring units has been summarized in **Table 1.2**.

Table 1.2 Organic sensitizers based on thiophene for *n*-type DSSCs

Reference	Sensitizer	J_{SC} (mA.cm ⁻²)	V_{OC} (V)	FF	PCE (%)
Matsumura et al. (2015)	 <p>S 1.10a</p>	12.6	0.71	0.57	5.0
	 <p>S 1.10b</p>	12.9	0.72	0.53	4.9
Fernandes et al. (2017)	 <p>S 1.11a</p>	0.75	0.45	0.62	0.22

	 <p style="text-align: center;">S 1.11b</p>	6.92	0.55	0.65	2.49
Hara et al. (2018)	 <p style="text-align: center;">S 1.12a</p>	6.82	0.62	0.70	3.22
	 <p style="text-align: center;">S 1.12b</p>	10.54	0.64	0.70	5.10
Lim et al. (2019)	 <p style="text-align: center;">S 1.13</p>	12.55	0.62	0.69	5.46
Robertson et al. (2021)	 <p style="text-align: center;">S 1.14a</p>	12.6	0.72	0.69	6.24
	 <p style="text-align: center;">S 1.14b</p>	9.68	0.62	0.62	3.70
	 <p style="text-align: center;">S 1.14c</p>	10.5	0.55	0.64	3.70

1.10.1.3 Phenoxazine-based sensitizers

Among the various electron donor moieties, phenoxazine containing electron-rich nitrogen and oxygen heteroatoms feature unique electronic and optical properties, and hence it can be considered as potential donor candidates in DSSCs. Phenoxazine-based sensitizers have received great attention due to their non-planar configuration, excellent electron-donating ability, which could impede the molecular aggregation and the formation of intermolecular excimers. Recently, a diversity of design

strategies has been reported with the extended electron delocalization to increase the molar absorptivity of the materials. Some of the literature reports on phenoxazines as sensitizers including their photovoltaic parameters are summarized in **Table 1.3**.

In 2011, Karlsson et al. reported two novel organic chromophores (**S 1.15a-b**) based on a phenoxazine donor unit connected to a strong electron acceptor/anchoring cyanoacetic acid forming D-A and D- π -A architectures. From the results, it was concluded that the dye **S 1.15b** shows higher J_{SC} due to the extended conjugation system. However, the photovoltage of dye **S 1.15b** based DSSC is much lower than the dye **S 1.15a**, since the former shows a shorter electron lifetime, which is mainly responsible for the lower V_{OC} . Strikingly, the overall PCE is reached up to 6-6.7 % under the standard AM 1.5 G illuminations at the alight intensity of 100 mWcm^{-2} .

In 2013, Tan and his co-workers demonstrated synthesis, characterization, and fabrication of two new phenoxazine-based molecules (**S 1.16a-b**) as effective photosensitizers. The dye **S 1.16a** involves a D- π -A architecture in which the thiophene unit serves as a spacer and cyanoacetic acid acts as an acceptor unit. The dye **S 1.16b** involves a D-D- π -A configuration in which 10-phenyl-10*H*-phenothiazene serves as an additional donor. The dye **S 1.16b** showcased enhanced overall efficiency of 7.8 % than other **S 1.16a** (6.6 %).

In 2014, Reddy et al. reported two new organic dyes **S 1.17a-b**, comprising electron-rich thiophene derivatives as antennas and cyanoacetic acid as an acceptor unit, bridged by phenoxazine donor. From the results, it is clear that both the dye-based devices afforded the best photovoltaic performance of 6 % under standard AM 1.5 G illumination.

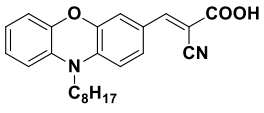
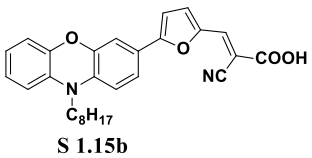
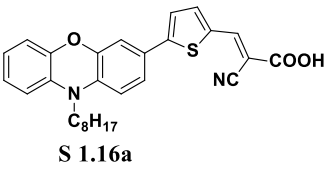
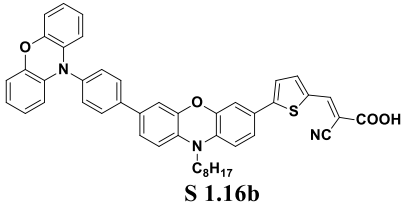
Similarly, in 2015, Li et al. designed and synthesized a series of metal-free organic chromophores composed of phenoxazine unit and indolinum carboxyl acid derivatives. Among these, the dye **S 1.18** bearing squaraine units as linkers between donor and acceptor unit yielded the superior PCE of 5.1 % with J_{SC} of 13.7 mA.cm^{-2} , V_{OC} of 0.50 V, and FF of 0.74 %.

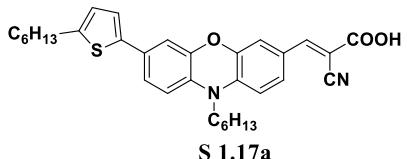
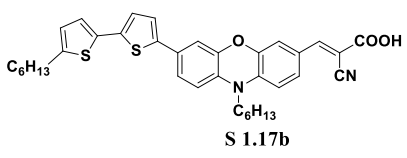
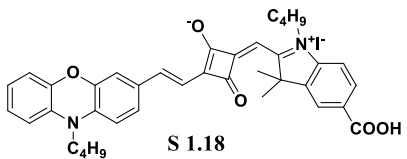
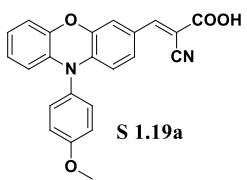
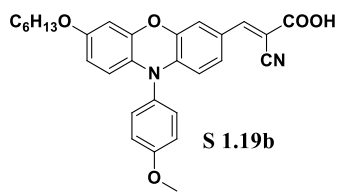
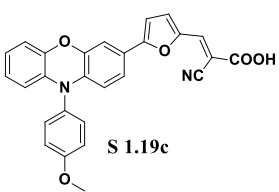
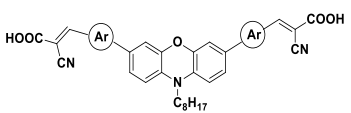
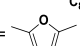
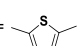
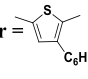
In an attempt to understand the influence of alkyl chains and π -spacers on the efficiency of the phenoxazine-based photosensitizer, Bae et al. (2019) synthesized

three new D-A and D- π -A configured organic dyes **S 1.19a-c** carrying cyanoacetic acid as an acceptor unit. Among the synthesized dyes, the dye **S 1.19c** bearing furan moiety as a spacer showed the best power conversion efficiency of 6.34 %.

Recently, Yen et al. (2021) reported a series of novel double-anchoring phenoxazine-based dyes (**S 1.20a-c**) bearing furan, thiophene, and 3-hexylthiophene as a linker connected to a strong electron acceptor/anchoring cyanoacetic acid forming a D- π -A architecture. The double anchoring strategy exhibits strong electronic coupling with semiconductor surfaces, providing an efficient charge injection rate. Fundamental studies concluded that the *PCE* of dye **S 1.20b** reached up to 3.8 % higher than that of dye **S 1.20a** (1.53 %) and **S 1.20c** (2.92 %) under standard illumination.

Table 1.3 Organic sensitizers based on phenoxazine for *n*-type DSSCs

Reference	Sensitizer	J_{SC} (mA.cm ⁻²)	V_{OC} (V)	<i>FF</i>	<i>PCE</i> (%)
Karlsson et al. (2011)	 S 1.15a	12.25	0.76	0.72	6.70
	 S 1.15b	14.22	0.70	0.60	6.03
Tan et al. (2013)	 S 1.16a	12.58	0.74	0.71	6.6
	 S 1.16b	13.98	0.76	0.73	7.8

Reddy et al. (2014)	 <p>S 1.17a</p>	11.56	0.72	0.71	6.0
	 <p>S 1.17b</p>	12.07	0.72	0.68	6.0
Li et al. (2015)	 <p>S 1.18</p>	13.7	0.50	0.74	5.1
Bae et al. (2019)	 <p>S 1.19a</p>	7.90	0.76	0.75	4.49
	 <p>S 1.19b</p>	9.03	0.80	0.73	5.25
	 <p>S 1.19c</p>	11.16	0.77	0.74	6.34
Yen et al. (2021)	 <p>S 1.20a : Ar = </p>	3.31	0.64	0.72	1.53
	S 1.20b : Ar = 	8.14	0.68	0.69	3.80
	S 1.20c : Ar = 	5.62	0.68	0.76	2.92

1.10.1.4 Co-sensitizers for Ru (II) based n-type DSSCs

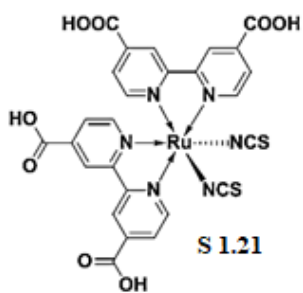
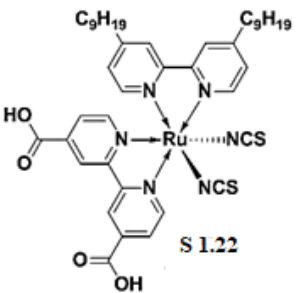
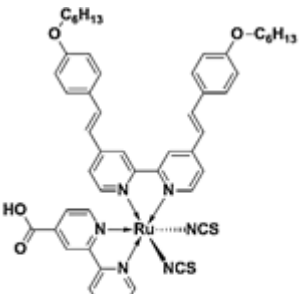
The overall performance of the DSSCs mainly depends on the light-harvesting ability and charge injection kinetics of dye molecules. Even though varieties of metal-free organic sensitizers have been reported so far, their efficiency is found to be lower when compared to that of Ru (II) complexes, mainly due to their relatively narrow absorption profile in the visible region. In order to achieve enhanced photovoltaic performance, the dye should possess a broad and intense absorption characteristic profile in the region of UV-Visible and near IR. In this regard, the co-sensitization approach has emerged as a most effective strategy that affords performance gain in DSSCs *via* nudging efficiencies of devices to reach the highest recorded values.

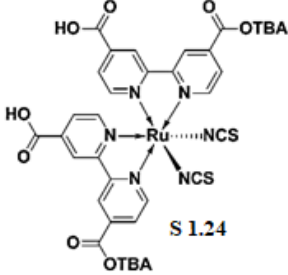
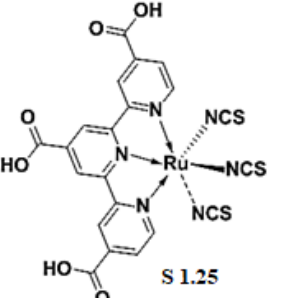
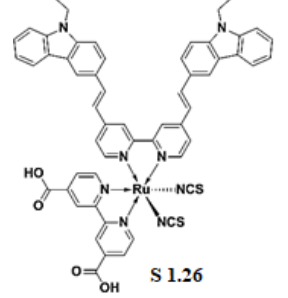
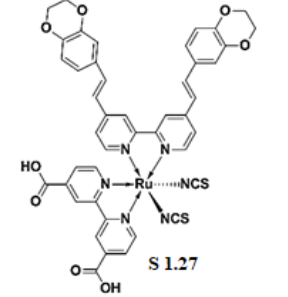
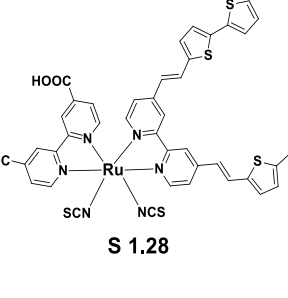
Co-sensitization is one of the effective methods to broaden the absorption region that extends throughout the UV-visible and near IR region. In this technique, the dyes used are a complement each other in their absorption properties and do not interfere with the sensitization properties of the other dye. Generally, the bulky molecules of Ru-based dye inadequately adsorb on the surface of semiconducting metal oxide leaving behind the larger voids between adsorbed molecules. These created voids would now be covered uniformly by the small molecules of co-sensitizer, providing a larger surface area for light-harvesting. Further, the uniform dye adsorption on the TiO₂ surface drastically reduces dye aggregation of Ru-dye as well as back-reaction of the I₃⁻/I⁻ on the TiO₂ surface inside the device. Recently, the small organic dyes carrying a wide range of interesting scaffolds such as carbazole, thiophene, phenoxazine, indole, and phenothiazine, *etc.* have been proven as effective co-sensitizers along with metal-based sensitizers. The reason may be due to the extended π -conjugation in the molecules increases the light-harvesting capacity, and hence the overall performance (Mishra et al. 2010, Hagfeldt et al. 2010, Wu and Zhu 2013).

At present, the DSSCs based on standard Ru(II)-polypyridyl complexes (**S1.21-S1.28**) as active sensitizers have displayed optimum overall efficiency exceeding 10 % under standard 1.5 G solar light illumination (**Table 1.4**). In 1993, Nazeeruddin and his co-workers reported a detailed investigation on luminescence-visible light absorption, electrochemical, and photovoltaic properties of Ru (II)

complexes. The reported dye is popularly known as **N3 (S 1.21)** as a sensitizer exhibited an outstanding performance of 11.03 % in the ambient conditions. Later, a variety of ruthenium-based dyes such as **N719 (S 1.24)**, **NCSU-10 (S 1.26)**, **HD-2 (S 1.27)**, **MH-12 (S 1.28)**, *etc.* have been reported with excellent efficiencies. In the present study, **HD-2**, and **MH-12** sensitized DSSCs were used for co-sensitization studies of newly synthesized thiophene, carbazole, and phenoxazine-based organic chromophores.

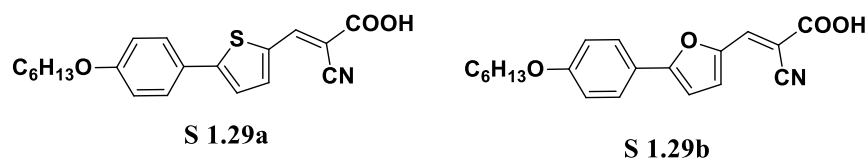
Table 1.4 Ruthenium (II) complex based sensitizers

Reference	Sensitizer	J_{sc} (mA.cm ⁻²)	V_{oc} (V)	FF	PCE (%)
Nazeeruddin et al. (1993)	 <p style="text-align: center;">S 1.21</p>	16.80	0.85	0.77	11.03
Wang et al. (2003)	 <p style="text-align: center;">S 1.22</p>	14.6	0.72	0.69	7.3
Wang et al. (2005)	 <p style="text-align: center;">S 1.23</p>	14.61	0.71	0.67	7.0

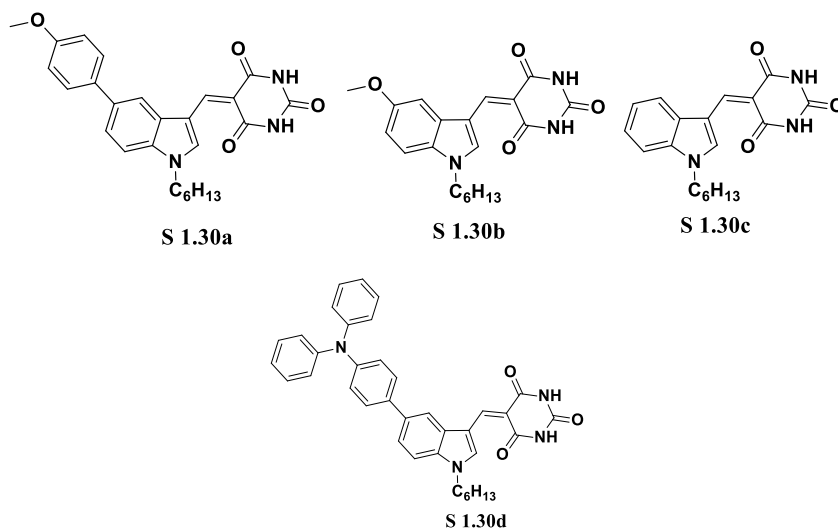
Ito et al. (2005)	 <p style="text-align: center;">S 1.24</p>	18.7	0.79	0.71	10.6
Chilba et al. (2006)	 <p style="text-align: center;">S 1.25</p>	20.90	0.73	0.72	11.0
Cheema et al. (2014)	 <p style="text-align: center;">S 1.26</p>	19.58	0.71	0.73	10.19
Cheema et al. (2014)	 <p style="text-align: center;">S 1.27</p>	19.67	0.69	0.70	9.50
Abdellah et al. (2019)	 <p style="text-align: center;">S 1.28</p>	20.23	0.65	0.56	8.09

In the literature, a wide range of co-sensitizers has been reported for ruthenium-complex sensitized DSSCs. Some of the important works of literatures pertaining to organic co-sensitizers are summarized below.

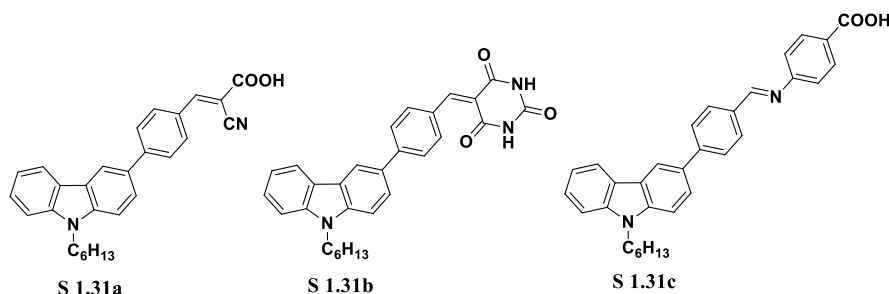
In 2016, Luo et al. reported two new D- π -A configured organic dyes as effective co-sensitizers for **N719**-based DSSCs. The design strategy involves hexyloxy-substituted phenyl ring as an electron donor, cyanoacetic acid as an electron acceptor, and thiophene (**S 1.29a**) or furan (**S 1.29b**) as the π -spacers. The studies indicated that both the co-sensitizers showcased better performance than the cell fabricated with **N719** dye alone.



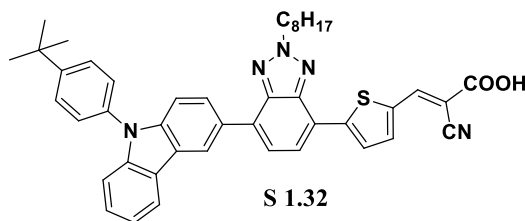
In 2016, Babu et al. reported two new indole-based dyes (**S 1.30a-c**) bearing auxiliary donor groups such as methoxy (**S 1.30b**) and 4-methoxyphenyl (**S 1.30a**) with different anchoring units. For co-sensitization studies, the authors used Ru-based **NCSU-10** as a sensitizer (**S 1.26**). The study showed that **S 1.30c** displayed maximum enhancement with an efficiency of 10.12 %. The reason behind this is efficient suppression of undesirable charge recombination process. Later, the same group reported double donor-based architecture for indole and triphenylamine dye (**S 1.30d**). When this dye (**S 1.30d**) carrying barbituric acid anchor, was subjected to co-sensitization studies along with Ru-based **HD-2** (7.6 %) as a base dye, the performance was enhanced to 8.06 %.



In 2018, Naik et al. reported a series of carbazole-based dyes with D- π -A architecture carrying phenyl spacer with cyanoacetic acid (**S 1.31a**) and barbituric acid (**S 1.31b**) as anchoring units as effective co-sensitizers with the ruthenium-based **NCSU-10** and **N3** sensitizers. The study revealed that **S 1.31a** showed superior performance of 9.19 % along with **NCSU-10**. Further, the same group (2018) reported a detailed investigation on the synthesis of four different D-A type carbazole-based co-sensitizers along with **NCSU-10** as a base dye. Among all, the dye **S 1.31c** bearing carbazole donor and 4-aminobenzoic acid as an acceptor showcased *PCE* of 9.55 %, which is higher than the base dye alone.

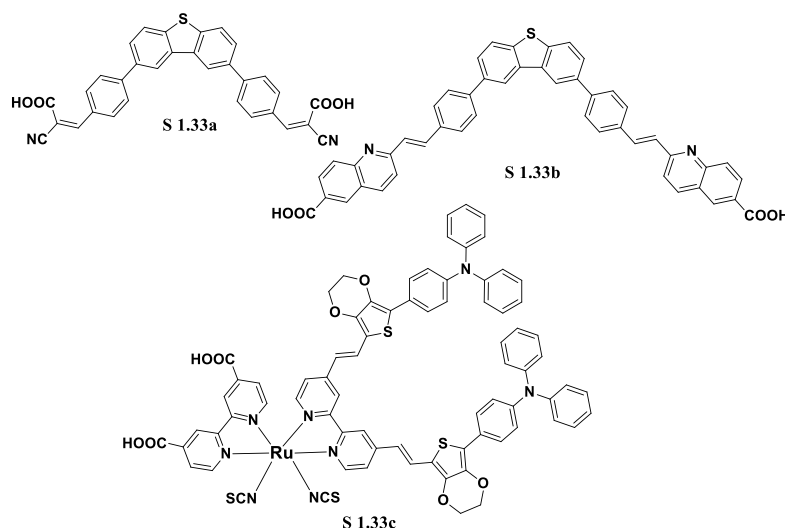


In 2019, Zheng et al. demonstrated *N*-substituted benzotriazole (**S 1.32**) as an interesting co-sensitizer along with two porphyrin-based dyes as base dyes (**XW40** and **XW41**). It was concluded that the rigid benzotriazole-based dye can be act as an effective co-sensitizer with the *PCE* enhancement of 10.6 and 10.2 % when used with the sensitizer **XW40** and **XW41**, respectively.

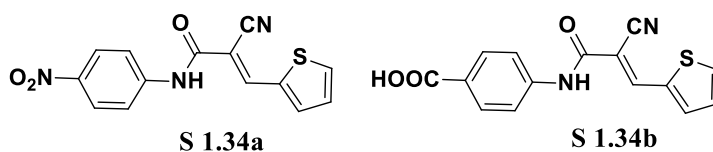


In 2020, Abdellah et al. reported synthesis, and fabrication of two new A- π -D- π -A configured organic dyes (**S 1.33a-b**) as effective co-sensitizers for Ru-based **S 1.33c** DSSCs. This design strategy involves dibenzothiophene as a donor, phenyl units as linkers with different anchoring units such as cyanoacetic acid **S 1.33a** and 2-methylquinoline-6-carboxylic acid (**S 1.33b**). From the results, it is clear that **S 1.33a** and **S 1.33b** displayed enhanced efficiency of 6.25 and 6.19 %, which outperformed the device employing **S 1.33c** alone (5.54 %). This may be due to the new co-

sensitizers effectively occupy the pores and gaps between the Ru-based sensitizer and acts as a physical insulator between TiO₂ semiconductor and redox electrolyte, thus suppresses the charge recombination.



Recently, in 2021, Althagafi et al. reported thiophene-based metal-free organic dyes (**S 1.34a-b**) as active co-sensitizers along with a Ru-based **N719** sensitizer. Interestingly, co-sensitizer **S 1.34a-b** along with **N719** gave superior *PCE* of 7.69 % and 8.09 % respectively, whereas Ru-based **N719** alone gave an efficiency of 7.61 %. The higher *PCE* values of **S 1.34b** compared to **S 1.34a** can be attributed to the presence of a strong anchoring unit (-COOH) which helps in better dye adsorption on the surface of the TiO₂ layer.



1.10.2 *p*-Type organic chromophores for DSSC

Till date, most of the reported literature in the area of DSSCs is centered upon the sensitization by *n*-type organic semiconductors consisting of an active photoanode (TiO₂) and a passive cathode made of a platinum film. The recent literature reveals that *p*-type DSSCs comprising a photoactive cathode (NiO) can also be envisioned for effective solar energy harvesting (Odobel et al., 2010, 2012, 2013). Interestingly, they

provide an access to the development of new sandwiched ‘tandem’ DSSCs consisting of both photoactive anode and cathode (He et al. 1999, 2000; Nakasa et al. 2005; Gibson et al. 2009; Nattestad et al. 2010; Farré et al. 2017). Indeed, such tandem cells make use of both *n*-type as well as *p*-type organic sensitizers in a single device. Thus, *p*-type DSSC is considered as a missing key component for the construction of tandem DSSCs. A thorough literature survey reveals that there are only limited reports available on *p*-type sensitizers and the efficiencies of these are much lesser than that of *n*-type DSSCs (Mishra et al., 2009; Yen et al., 2010). Some of the selected references have been summarized in **Table 1.5**.

In 2008, Qin et al. in their pioneer work reported the detailed investigations on triphenylamine-based *p*-type DSSCs with the A- π -D- π -A architecture for the first time. Here, the thiophene unit serves as π -spacer and cyanoacetic acid acts as electron acceptor moieties. The *p*-type DSSC sensitized with dye **S 1.35** displayed the *PCE* of 0.08 % when fabricated with NiO as a photocathode. Later words, Li et al. (2010) achieved an overall efficiency of 0.15% with the same dye and photocathode.

In 2009, Qin et al. demonstrated triphenylamine-based *p*-type dye (**S 1.36**) with phenylene group as a π -spacer and cyanoacetic acid as electron acceptor moieties. According to the authors, the chromophore **S 1.36** showed an efficiency of 0.09 %. In 2010, the same group reported two new D- π -A architecture organic chromophores derived from **S 1.35** as effective sensitizers for *p*-type DSSC. The design strategy involves triphenylamine bearing the carboxylic acid unit as an effective donor, thiophene unit as a π -spacer, and different electron acceptors such as tri-cyanovinylene (**S 1.37**), and 1, 3-diethyl-2-thiobarbituric acid (**S 1.38**). In addition, they have carried out a detailed investigation on the effect of electron acceptor units on the photophysical, electrochemical as well as photovoltaic performance of the dyes.

In 2011, Yen and his co-workers investigated the synthesis and fabrication studies of new D- π -A arylamine-based sensitizers (**S 1.39**) for *p*-type DSSC. The *PCE* of dye reached 0.1 %, concluding the sensitizers with two anchoring units resulted in enhancing the photovoltaic performance of the device. In the same year, Ji et al. reported the D- π -A structured metal-free sensitizer (**S 1.40**), which contains

triphenylamine core carrying two carboxylic groups as a hole donating donor, and ethoxythiophene as a π -linker with an efficiency of 0.060 %. Similarly, in 2013, Cui et al. reported two new D- π -A configured triphenylamine-based organic chromophores, **S 1.41a** and **S 1.41b** by modifying the structure of **S 1.36** sensitizer. From the results, it is clear that the dye containing 4-phenylpyridine as an anchoring moiety showed an enhanced performance of 0.16 % when compared to that of pyridine anchored dye (0.093 %).

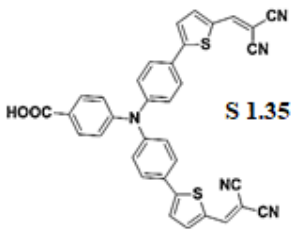
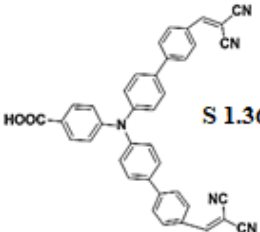
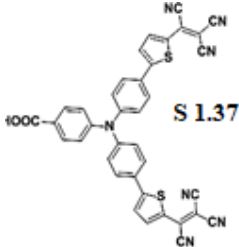
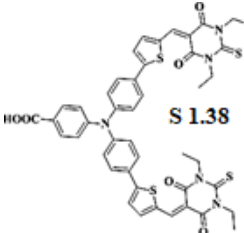
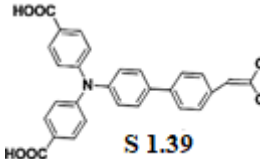
In 2014, Warnan and his co-workers reported the design, synthesis, and device fabrication studies of a thiophene-based p-type DSSC (**S 1.42**). In the new design, hexyl-thiophene serves as a donor moiety, nitrophenyl as an acceptor unit, and acetylacetone as an anchoring group with an efficiency of 0.03 %. Similarly, in 2015, Zhang et al. demonstrated D- π -A configured high performing p-type organic sensitizer (**S 1.43**). This design strategy involves triphenylamine as an effective donor moiety, quinoid thiophene as a π -spacer, and malononitrile as an electron acceptor unit. This new dye **S 1.43** showcased an efficiency of 0.33 % with a superior J_{SC} value (8.2 mA.cm⁻²) under standard light illumination conditions.

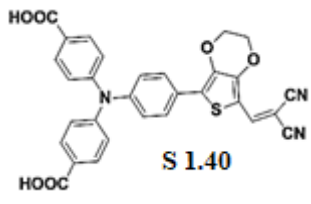
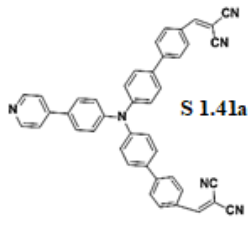
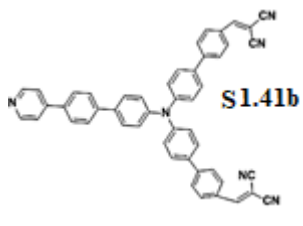
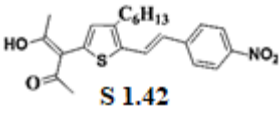
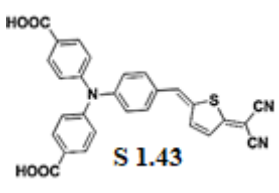
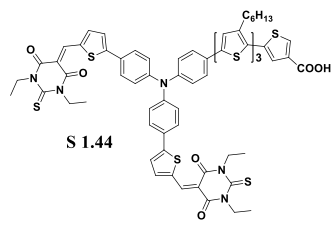
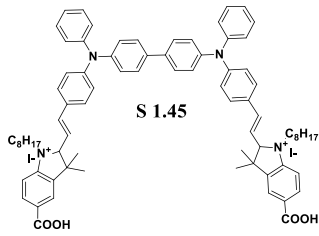
In 2016, Wu et al. reported triphenylamine-based p-type sensitizer (**S 1.44**) carrying 1,3-diethyl-2-thiobarbituric acid as an anchoring unit. In this new strategy, four alkylated thiophene units were inserted between donor and acceptor units in order to shift the LUMO level of the dye molecule away from the semiconductor surface. The dye displayed an efficiency of 0.317 % under AM 1.5G conditions. Further, in 2017, Bao and his co-workers reported synthesis, characterization, and fabrication of a new dibranched hemicyanine organic dye (**S 1.45**) as an active photosensitizer for p-type DSSC. From the results, it is clear that there is an increase in charge transfer and current density, which ultimately gives a *PCE* of 0.05 %.

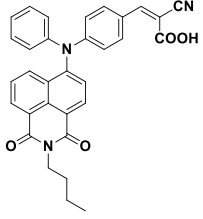
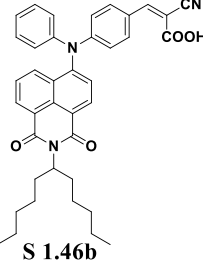
Recently in 2020, Sahiner et al. reported diphenylamine-based p-type sensitizer with naphthalene imide as an electron acceptor. In this design, carboxylic acid units were attached to the dye molecule, so that they can be easily adsorbed on the surface of NiO electrodes. The dye molecule **S 1.46b** displayed an enhanced *PCE* of 0.19 % compared to that of **S 1.46a** (0.12 %). The reason may be due to a high dye-

loading of **S 1.46b** on the NiO surface. Here, the presence of a branched alkyl chain suppresses the dye-aggregation.

Table 1.5 Reported *p*-type organic sensitizers

Reference	Sensitizer	J_{SC} (mA.cm ⁻²)	V_{OC} (V)	FF	PCE (%)
Qin et al. (2008)	 S 1.35	2.51	0.11	0.29	0.08
Qin et al. (2009)	 S 1.36	2.48	0.10	0.36	0.09
Qin et al. (2010)	 S 1.37	1.36	0.055	0.34	0.03
Qin et al. (2010)	 S 1.38	3.37	0.063	0.31	0.07
Yen et al. (2011)	 S 1.39	2.25	0.012	0.33	0.093

Ji et al. (2011)	 <p style="text-align: center;">S 1.40</p>	1.74	0.090	0.38	0.060
Cui et al. (2013)	 <p style="text-align: center;">S 1.41a</p>	2.66	0.098	0.35	0.093
	 <p style="text-align: center;">S 1.41b</p>	4.05	0.12	0.34	0.16
Warnan et al. (2014)	 <p style="text-align: center;">S 1.42</p>	1.29	0.075	0.31	0.030
Zhang et al. (2015)	 <p style="text-align: center;">S 1.43</p>	8.2	0.12	0.34	0.33
Wu et al. (2016)	 <p style="text-align: center;">S 1.44</p>	6.73	0.15	0.31	0.31
Bao et al. (2017)	 <p style="text-align: center;">S 1.45</p>	2.17	0.075	0.30	0.05

Sahiner et al. (2020)	 <p style="text-align: center;">S 1.46a</p>	3.85	0.10	0.31	0.12
	 <p style="text-align: center;">S 1.46b</p>	5.70	0.11	0.31	0.19

1.10.3 Hole-transport materials for PSCs

Hole transport materials (HTMs) play a key role in the extraction of holes from the photo-excited perovskite layer and transfer them into the counter electrode, as well as to further restraining charge recombination at the interfaces between perovskite and HTM layers. Organic small molecules are often selected as effective HTMs due to their advantages like high solution processibility, tuneable optoelectronic properties *via* structural modification. Spiro-OMeTAD is considered one of the widely used organic HTMs for PSC applications. Though Spiro-OMeTAD based HTMs succeeded in achieving high efficiency, yet its multistep synthesis, low-yield, and complicated purification steps are projected to be significant drawbacks. Recently, many organic small molecules based HTMs with high device performance have been investigated from pyrene, thiophene, triphenylamine, carbazole, and phenothiazine derivatives. Among all the heterocyclic molecules, carbazole and its derivatives are considered as one of the most promising candidates in optoelectronic applications owing to their excellent charge-transporting properties apart from interesting photoconductive, photo-refractive, and light-emitting behaviour. In the present study, carbazole systems have been used as electron donor systems for perovskite solar cell fabrication. A brief account of the literature review pertaining to

these donor systems is described below. Some of the selected references have been summarized in **Table 1.6**.

In 2014, Xu et al. designed and synthesized two new carbazole-based hole-transport materials (**S 1.47a-b**) of different hole mobility, oxidation potential, and electrical conductivity. Employing perovskite as a light-harvesting material, the devices made up of HTM **S 1.47b** displayed superior *PCE* of 9.8 %, than that of HTM **S 1.47a** (7.6 %), which is much comparable with that of benchmark reference HTM Spiro-OMeTAD (10.2 %). The reason behind this may be HTM **S 1.47b** showcased higher hole mobility and conductivity than HTM **S 1.47a**, leading to enhanced photovoltaic performance of the devices investigated. Similarly, in 2015, Gratia et al. systematically investigated novel methoxydiphenylamine-substituted carbazole-based HTM **S 1.48** for perovskite solar cells. From the results, it was concluded that the device employed HTM **S 1.48** displayed an efficiency of 16.91 %, which is the second-highest efficiency reported after Spiro-OMeTAD.

In 2016, Wang et al. reported a carbazole-based hole-transporting material (**S 1.49**) with low dopant content for PSC application. The results clearly quantify that the HTM **S 1.49** showed *PCE* of 4.53 %, which is much comparable with that of reference Spiro-OMeTAD (5.10 %), and hence, it can be concluded that carbazole-based materials are a promising class of HTMs for PSCs.

In 2017, Daskeviciene and his team designed and synthesized a simple carbazole-based conjugated enamine **S 1.50**, and incorporated it into perovskite solar cell to study its effect. When the HTM **S 1.50** was used with mixed cation perovskite in device fabrication, it displayed an enhanced efficiency of 17.8 %, which is much comparable to the state-of-the-art material Spiro-OMeTAD (18.6 %) on a like-to-like comparison.

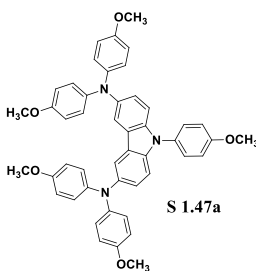
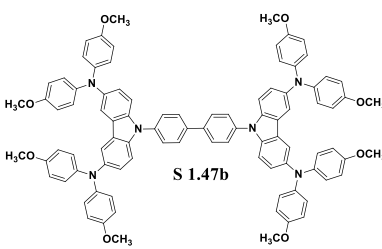
In 2018, Li et al. developed a new class of asymmetric diphenylamine-substituted carbazole-based (DPACZ) compounds (**S 1.51a-d**) as effective HTMs for PSCs. The design strategy of DPACZ-based HTMs involves different substituted *S,N*-heterocyclic units such as phenothiazine and dithieno[3,2-b:2',3'-d]pyrrole units, which endowed the HTMs with different photophysical and electrochemical properties. Among all the synthesized HTMs, the device made up of HTM **S 1.51d**

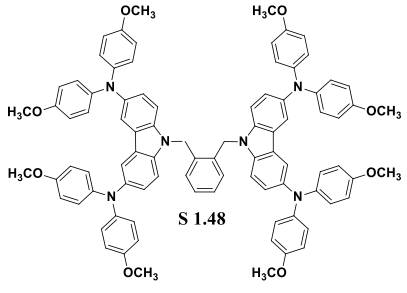
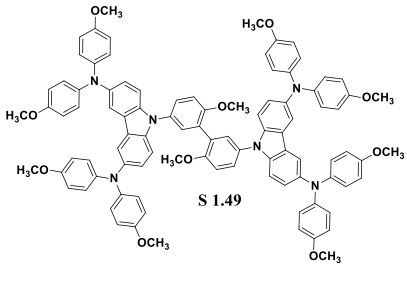
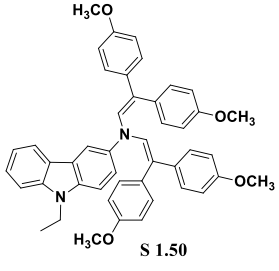
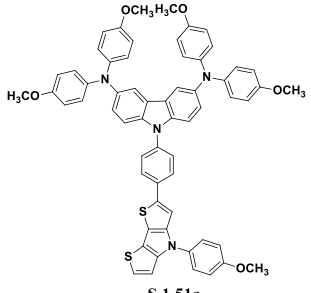
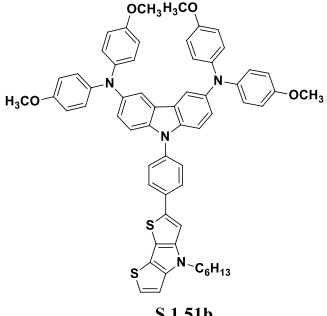
displayed a higher *PCE* of 17.17 %, which may be due to the superior hole mobility, film quality, and hole-extracting nature at the interface.

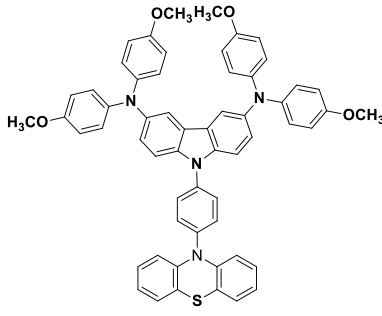
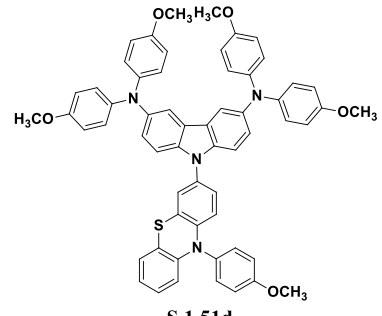
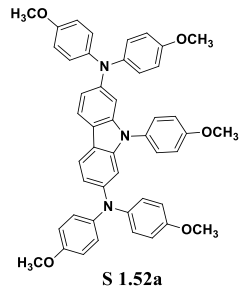
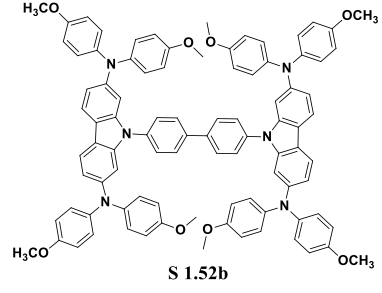
In 2019, Wang and his co-workers reported carbazole-based HTMs **S 1.52a-b**, with 2,7-substitution at the carbazole core for PSC application. The effects of linking topology on the photophysical, electrochemical properties of HTMs **S 1.52a-b** were compared with that of earlier reported 3,6-substituted carbazole-based HTMs **S 1.47a-b**. In this study, the results clearly demonstrated that the HTM **S 1.52b** showed a better performance of 19.2% than that of **S 1.52a** (18.3%), which may be due to the high hole mobility, conductivity, and film-forming nature.

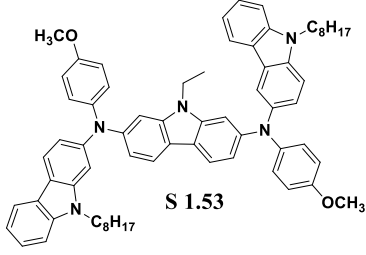
In 2020, Gao et al. investigated carbazole-based HTM **S 1.53** with branched alkyl substituents together with radical triarylamine salts as dopants. The results speculate that the introduction of more ethylhexyl chains at the periphery position showcased improved hydrophobicity, which further helps in suppressing moisture diffusion into the water-sensitive active precursor layer. The perovskite solar cell devices based on this optimized HTM **S 1.53** displayed enhanced *PCE* of 17.75 % with high stability.

Table 1.6 Organic small molecules as hole transport materials

Reference	Sensitizer	J_{SC} (mA.cm ⁻²)	V_{OC} (V)	<i>FF</i>	<i>PCE</i> (%)
Xu et al. 2014	 <p style="text-align: center;">S 1.47a</p>	17.14	0.76	0.58	7.60
	 <p style="text-align: center;">S 1.47b</p>	16.79	0.88	0.66	9.80

Gratia et al. 2015	 <p style="text-align: center;">S 1.48</p>	21.38	1.08	0.73	16.91
Wang et al. 2016	 <p style="text-align: center;">S 1.49</p>	8.47	1.03	0.52	4.53
Daskeviciene et al. 2017	 <p style="text-align: center;">S 1.50</p>	22.5	1.07	0.74	17.8
Li et al. 2018	 <p style="text-align: center;">S 1.51a</p>	21.56	1.02	0.72	15.88
	 <p style="text-align: center;">S 1.51b</p>	21.56	1.02	0.66	14.72

	 <p style="text-align: center;">S 1.51c</p>	21.97	1.01	0.66	14.86
	 <p style="text-align: center;">S 1.51d</p>	22.24	1.05	0.73	17.27
Wang et al. 2019	 <p style="text-align: center;">S 1.52a</p>	21.6	1.13	0.75	18.3
	 <p style="text-align: center;">S 1.52b</p>	22.5	1.14	0.74	19.2

Gao et al. 2020	 <p style="text-align: center;">S 1.53</p>	22.19	1.08	0.74	17.75
--------------------	---	-------	------	------	-------

1.10.4 Carbon-based perovskite solar cells

Most of the reported high-efficiency perovskite solar cells involving organic HTMs are expensive and operationally unstable. Many systematic investigations have been carried out by researchers to address the perovskite degradation *via* moisture, oxygen, UV light, heat, and electrical bias. To resolve this ambiguity, several strategies have been proposed to investigate the stability challenges in perovskite solar cells. However, it is still a major challenge for the PV community to combine both highly efficient light absorption as well as charge extraction with stable performance in the perovskite device. In order to sort out the issues of instability, perovskite degradation, high-cost, and manufacturing complexity, the carbon-based perovskite solar cell (C-PSC) concept has been introduced. During the past few years, much progress has been made in C-PSCs. As expected, significantly high stability along with good efficiency has been reported for the C-PSCs, making it the most promising solar cell technology for commercialization. A brief account of the literature review on C-PSCs has been described below.

In 2014, Yang et al. developed a new concept of clamping solar cells by judiciously interfacing perovskite photoanode with MAPbI₃ films for the first time using cost-effective, abundant, and environmentally stable candle soot as an efficient hole-extractor. Further, the device fabricated achieved a certified efficiency of 11.02 % (J_{SC} : 16.50 mA.cm⁻², V_{OC} : 0.88 V, and FF : 67 %) with superior stability, making an excellent step towards roll-to-roll production of perovskite solar cells.

In the same year, Mei et al. (2014) investigated the fabrication of hole-conductor free perovskite solar cell that uses a simple mesoscopic TiO₂/ZrO₂/C triple-layer as a scaffold to host the perovskite absorber. The resulting device achieved a certified PCE of 12.8 % with excellent stability for >1000 hours under ambient

atmosphere. Similarly, in 2015, Li and his co-workers demonstrated the fabrication of hole-conductor-free carbon-based PSCs with triple-layered architecture and performed extensive stability tests under outdoor conditions to prove the durability of the devices. The devices with active area 0.283 cm^2 showed an excellent *PCE* of 12.9 % (J_{SC} : $22.7 \text{ mA}\cdot\text{cm}^{-2}$, V_{OC} : 0.85 V, and *FF*: 66 %).

In 2016, Mhaisalkar's group in collaboration with Dyesol reported a facile and cost-effective approach for the fabrication of large-area (31 cm^2 and 70 cm^2) monolithic carbon-based perovskite solar modules. Strikingly, the perovskite modules which were fabricated using scalable screen-printing technique displayed an impressive *PCE* of 10.46 % and 10.74 % for an active area of 31 cm^2 and 70 cm^2 , respectively with excellent stability of more than 2000 hours in an ambient atmosphere.

In 2017, Kapoor et al. did a systematic study on the incorporation of excess amounts of lead iodide on the performance of fully printable carbon-based PSCs. From the results, it can be concluded that the device with 5 % excess PbI_2 in its stoichiometric MAPbI_3 solution gives the highest efficiency of 11.4 % (J_{SC} : $23.3 \text{ mA}\cdot\text{cm}^{-2}$, V_{OC} : 0.92 V, and *FF*: 53.8 %) with an active area of 0.8 cm^2 .

In 2018, Bashir et al. reported the use of cobalt oxide, Co_3O_4 for enhancing the hole transport nature at fully printable carbon-based PSCs. The study revealed that improved performance of 13.27% (J_{SC} : $23.43 \text{ mA}\cdot\text{cm}^{-2}$, V_{OC} : 0.88 V, and *FF*: 64 %) was achieved for the device with an active area of 0.09 cm^2 made up of inorganic spinel Co_3O_4 in carbon compared to that of standard carbon-based devices (*PCE*: 11.25%, J_{SC} : $21.64 \text{ mA}\cdot\text{cm}^{-2}$, V_{OC} : 0.86 V, and *FF*: 60 %).

In 2019, He and his co-workers reported the studies on low-cost carbon-based electrodes for PSCs by using cheaper small-molecule semiconductor copper phthalocyanine (CuPc) as an interface modifier as well as a dopant. The resultant device with planar architecture displayed an enhanced efficiency of 14.8%, which may be due to the superior hole-extraction and higher work function ability of the CuPc-modified carbon electrodes. In continuation, they also reported the fabrication of large-area (22.4 cm^2) C-PSCs with a *PCE* of ~7 %, demonstrating their capability of upscaling and flexibility.

Recently in 2020, Wang et al. reported a detailed investigation on mesoporous carbon-based fully printable monoclinic CsPbBr₃ perovskite solar cells with superior stability under high temperature and high humidity. The screen-printing technique was used to construct a triple-layered mesoscopic scaffold of m-TiO₂, ZrO₂, and carbon layer in which the pure-phase monoclinic CsPbBr₃ was formed. The device displayed a high efficiency of 7.52% and underwent a 1000 h damp heat test along with the 200 cycle's thermal cycling test to prove the superior stability of devices.

1.11 SALIENT FEATURES OF THE LITERATURE REVIEW

Based on the detailed literature review, the following observations can be drawn.

A) Organic dyes for DSSC

- The push-pull (D-A and D- π -A) architecture is a widely used design strategy for organic chromophores.
- The dyes should exhibit a broad absorption band and a superior molar extinction coefficient for efficient light-harvesting.
- The dye molecule must contain at least one anchoring group for efficient adsorption on the semiconductor surface.
- The HOMO-LUMO energy levels of the dyes should match with the respective semiconductor.
- Carbazole and phenoxazine derivatives are considered to be most promising donor systems in DSSCs.
- Thiophene and phenylene units are active conjugated spacers due to their ability of efficient charge separation.
- Widely used anchoring/accepting groups so far for a sensitizer is cyanoacetic acid, rhodanine-3-acetic acid, and barbituric acid.
- Co-sensitization of metal-free dyes with Ru(II)-based sensitizer is an emerging technique to enhance the performance of *n*-type DSSCs.
- There is a good scope for variation of donor moiety, π -spacer, and electron acceptor/anchoring group in organic chromophore-based sensitizer to improve the efficiency of DSSCs.

B) Organic HTMs for PSCs

- The HTM must possess high hole mobility for efficient hole extraction and transport.
- It should exhibit matching energy alignment with perovskite absorber.
- Low-cost of production and good solubility in common solvents are preferred for the facile synthesis of HTMs.
- The HTM should exhibit high optical, thermal, chemical, and environmental (air and water) stability.
- Carbazole and its derivatives are widely investigated donor systems in HTMs.

C) Studies on carbon-based PSCs

- Carbon-based PSCs are comparatively low-cost both in material and the required equipment.
- In hole-transport-layer-free devices, perovskite material can simultaneously act as a light harvester as well as hole-transporter.
- MAPbI₃ is the most commonly used perovskite material.
- C-PSCs are arguably the most promising for commercialization applications because of their excellent stability, low cost, high performance, and simple manufacturing process.
- Their efficiency and stability can be further tuned by conducting detailed investigations on crystal formation, precise control over morphology, selection of solvents, additives, theoretical modelling, and interface engineering for their future commercial applications.

1.12 RESEARCH GAP

From the detailed literature review, it is worth noticing that dyes/HTMs play a pivotal role in enhancing the performance of DSSCs/PSCs. Even though major breakthroughs have been made, there is still ample scope to continue research studies on investigations of new sensitizers/HTMs which can enhance the efficiency of the solar cell to a larger extent. Moreover, there is a good scope to establish structure-performance correlation studies so that it sets to establish new guidelines which can be applied to ensure better results. Further, it is required to introduce cost-effective method for the synthesis of new organic dyes/HTMs by using a simple synthetic

strategy. Also, it is very important to address the effect of multiple donor/anchoring groups, tuning the bandgap, dye aggregation, molecular interactions, carrier mobility, and recombination kinetics on device performance.

Most of the reported carbon-based PSCs research is based on $\text{CH}_3\text{NH}_3\text{PbI}_3$ (MAPbI₃) as a light-harvester. But the challenge with MAPbI₃ composition is its low crystallization energy which makes it unstable towards light and heat. In order to aim for higher efficiency, the two-cation (Cs, FA) perovskite was chosen as the state-of-the-art perovskite, which has been less explored in terms of efficiency and stability. In addition, the major issue for the development of C-PSCs in the industry is not just to enhance the device efficiency, but also to improve the photovoltaic stability and to understand the underlying mechanism that could lead to degradation. Hence, there is lots of scope for the further development of C-PSCs with improved efficiency and stability for their future commercial applications.

1.13 SCOPE AND OBJECTIVES

Till date, several organic chromophores with different structural configurations have been explored as effective sensitizers/co-sensitizers for DSSC application. Indeed, there are still great challenges to design and synthesize suitable organic molecules for DSSCs and identifying the parameters limiting the performance of solar cells. By modifying the design strategy of the molecule, one can easily alter the optical as well as electrochemical properties, which affect majorly the light-harvesting ability and different charge-transfer processes in the cell.

The development of highly efficient dopant-free HTMs for PSCs is still one of the most thrilling research areas in the growth of this emerging photovoltaic technology. So, there is a lot of scope for developing suitable low-cost and eco-friendly hole-transport materials for emerging perovskite solar cells application and to correlate the structure with performance parameters of the new HTMs.

Further, to develop commercialized perovskite solar modules with the required characteristics, the PV community must need to concentrate on developing new materials and fabrication processes that balance both high efficiency as well as long-term stability. Though the achieved *PCE* of PSCs is high, the challenges such as

perovskites stability and reproducibility in device performance limit their large-scale production.

Based on the above facts and the detailed literature survey, the following main objectives have been intended in the present research work involving studies on both DSSCs and PSCs.

A) Organic dyes for DSSCs

- (i) To design, synthesize and characterize new *n*-type organic dyes containing thiophene, carbazole, and phenoxazine core as a donor with various design strategies, *viz.* D- π -A (**Series-1**), double D-A (**Series-2** and **Series-3**), double D- π -A (**Series-4** and **Series-5**), A-D- π -D-A (**Series-6**), and A- π -D- π -A (**Series-7** and **Series-8**) as sensitizers/co-sensitizers and *p*-type organic dyes carrying phenoxazine (**Series-9**) and carbazole (**Series-10**) with different accepting/anchoring groups, as effective sensitizers
- (ii) To carry out photophysical, electrochemical, and theoretical studies of newly synthesized *n*-/*p*-type dyes
- (iii) To fabricate *n*-/*p*-type DSSCs employing new dyes and quantify the performance of the newly synthesized sensitizers in terms of the parameters such as incident photon to current efficiency (*IPCE*), short circuit photocurrent (J_{sc}), open-circuit photovoltage (V_{oc}), and the overall efficiency of the photovoltaic cell (η_{cell}) for correlating the structure-property relationships

B) Organic HTMs for PSCs

- (i) To design, synthesize and characterize new organic HTMs carrying carbazole as a donor (**Series-11**) with different pendent groups for perovskite solar cell applications
- (ii) To fabricate the newly developed PSCs and measure the performance of the newly synthesized HTMs in terms of their various photovoltaic parameters for studying structure-property relationships

C) Studies on carbon-based PSCs

- (i) To synthesize and characterize cesium-formamidinium lead iodide ($\text{Cs}_{0.1}\text{FA}_{0.9}\text{PbI}_3$)/methyl ammonium lead halide ($\text{CH}_3\text{NH}_3\text{PbI}_3/\text{MAPbI}_3$)

perovskite materials and to investigate their solvent selection/ETL modification for fully printable mesoporous carbon-based perovskite solar cells

- (ii) To fabricate the new carbon-based PSCs and their scaling up

Conclusively, from the detailed literature survey, it is clear that metal-free organic dyes with varieties of design strategies were used for developing new sensitizers as well as co-sensitizers for DSSC application. Among the various heterocyclic donor units reported in the literature, carbazole, thiophene, and phenoxazine derivatives are anticipated to be the most promising candidates to act as sensitizers for DSSC application. In addition, carbazole-based compounds have been widely investigated in optoelectronic applications owing to their excellent charge-transporting properties apart from interesting photoconductive, photo-refractive, and light-emitting behaviour. Thus, these molecules may act as excellent hole-transport materials for perovskite solar cell application.

Further, the major problem identified in carbon-based mixed cation PSCs is the selection of a suitable solvent for single-step solution-processed perovskite deposition in order to promote their scalable production. By keeping this in mind, detailed investigations on solvent selection need to be carried out to address the infiltration challenges in mixed-cation lead halide perovskite. Also, in order to overcome perovskite's stability challenges, detailed studies need to be performed by addressing the key parameters in the device engineering such as selection of TiO₂ particle size, and modification of ETL layer to aim for the fabrication of large-area perovskite solar modules. Convincingly, the detailed investigation on solvent selection as well as m-TiO₂ modification will provide a methodological base to further enhance the commercialization prospect of the carbon-based perovskite solar cells.

1.14 THESIS STRUCTURE

The entire thesis has been divided into six chapters. **Chapter 1** outlines a brief introduction to photovoltaics, followed by a brief account of dye-sensitized solar cells and perovskite solar cells. Further, the chapter incorporates a review of the literature reported on various types of dyes as well as PSCs. Furthermore, it includes the scope

and objectives of the present research work, arrived at on the basis of a detailed literature survey.

The structural design as well as the experimental protocols leading to the synthesis of new organic molecules as sensitizers/co-sensitizers for DSSCs and HTMs for PSCs has been elaborated in **Chapter 2**. In addition, their structural characterization by spectral techniques has been discussed in detail. **Chapter 3** describes a detailed account of the investigation of optical and electrochemical properties of synthesized dyes/HTMs. It also includes their theoretical investigations. **Chapter 4** covers a detailed study on photovoltaic performances of the selected molecules as sensitizers/HTMs in DSSCs/PSCs. It also comprises the co-sensitization studies of selected *n*-type dyes along with Ru-based sensitizers in DSSCs.

Chapter 5 encompasses the work related to carbon-based perovskite solar cells. The chapter includes a detailed investigation on the selection of appropriate solvent for a single-step deposition of mixed-cation perovskite for highly reproducible carbon-based PSCs using the Lewis acid-base adducts approach. It also covers a detailed study on ETL (m-TiO₂) modification by using CsX as an active interface modifier in the fabrication of MAPbI₃ carbon-based PSCs and their scaling up. Further, it includes a discussion on the structural as well as optical characterization and photovoltaic properties of carbon-based PSCs. Finally, **Chapter 6** summarizes the important conclusions and outcomes of the research work.

The detailed description of the design, synthesis and structural characterization of eleven new series of organic materials (dyes/HTMs) has been discussed in **Chapter 3**.

CHAPTER-2

**DESIGN, SYNTHESIS AND STRUCTURAL
CHARACTERIZATION OF NEW ORGANIC
ENTITIES**

DESIGN, SYNTHESIS AND STRUCTURAL CHARACTERIZATION OF NEW ORGANIC ENTITIES

Abstract

*This chapter includes the structural design of eight series of n-type, two series of p-type organic dyes, and one series of organic hole-transport materials. Further, it covers detailed synthetic pathways and purification techniques used for newly designed dyes **n-K₁₋₃₄**, **p-K₃₅₋₄₂**, and HTMs **h-K₄₃₋₄₄**. Furthermore, it comprises structural characterization of new intermediates as well as target molecules, using FTIR, ¹H NMR, ¹³C NMR, Mass spectral studies, and elemental analysis. Also, a detailed discussion has been included in it.*

2.1 INTRODUCTION

In the previous chapter, a detailed literature survey on metal-free organic dyes (*n*-type and *p*-type) for dye-sensitized solar cells as well as hole-transport materials for perovskite solar cells has been given. Most often, the development of new materials for solar cell applications starts with the design of new target molecules with the strong support of a thorough literature survey. This is an important step before going for their actual synthesis. Accordingly, in this chapter, the design of eight new series comprehending thirty-four metal-free organic dyes (**n-K₁₋₃₄**) as effective *n*-type sensitizers/co-sensitizers, two new series containing eight organic dyes (**p-K₃₅₋₄₂**) as potential *p*-type sensitizers, and two new organic molecules (**h-K₄₃₋₄₄**) as potential HTMs have been discussed in detail (**Figures 2.1-2.11**). For the design, the push-pull approach has been successfully employed and their properties were tuned by incorporating appropriate donors, π -spacers, and linking scaffolds. Finally, different synthetic strategies have been followed to obtain the products in good yield through multi-step sequences. **Schemes 2.1-2.11** summarize the synthesis of newly designed molecules following the standard synthetic routes for all the series. Different design strategies used for altogether eleven new series of organic molecules have been described in the following section.

2.2 MOLECULAR DESIGN OF NEW ORGANIC MATERIALS

2.2.1 New *n*-type organic sensitizers/co-sensitizers for dye-sensitized solar cells

A survey of the pertinent literature reveals that metal-free organic dyes with varieties of design strategies such as D-A, D- π -A, D- π -A- π -A, D-D- π -A, and A- π -D- π -A were used for developing new sensitizers as well as co-sensitizers for DSSC applications. Further, it is important to observe that several organic chromophores have been used as effective donors with different anchoring/accepting units using the aforementioned strategies. Among the various heterocyclic donor units reported in the literature, carbazole, thiophene, and phenoxazine scaffolds were shown to possess good thermal, electrochemical, and photochemical stabilities. Keeping in view of their several merits, the present research work has been aimed at the design of new organic photosensitizers/co-sensitizers carrying thiophene (**Series-1**), carbazole (**Series-2** to **Series-6**), and phenoxazine (**Series-7** and **Series-8**) as donor systems and different electron-withdrawing moieties as acceptor/anchoring systems.

2.2.1.1 Design of Series-1 (*n*-**K**₁₋₄)

In **Series-1**, four new D- π -A configured organic sensitizers/co-sensitizers, *n*-**K**₁₋₄ consisting of *O*-alkyl substituted phenyl groups (dodecyloxyphenyl and bisdodecyloxyphenyl) as the electron donor, cyanovinylene together with thiophene units as the π -spacer, and cyanoacetic acid and barbituric acid groups as the electron acceptor/anchoring units were designed. From the literature, it is clear that the incorporation of long alkoxy chains on the donor part significantly reduces the extent of hydration of the TiO₂ surface, and enhances the electron-donating strength. Due to their favorable size, and simpler design strategy, these molecules are expected to perform better in the device when employed as co-sensitizers. **Figure 2.1** depicts the design strategy involved in **Series-1** chromophores (*n*-**K**₁₋₄).

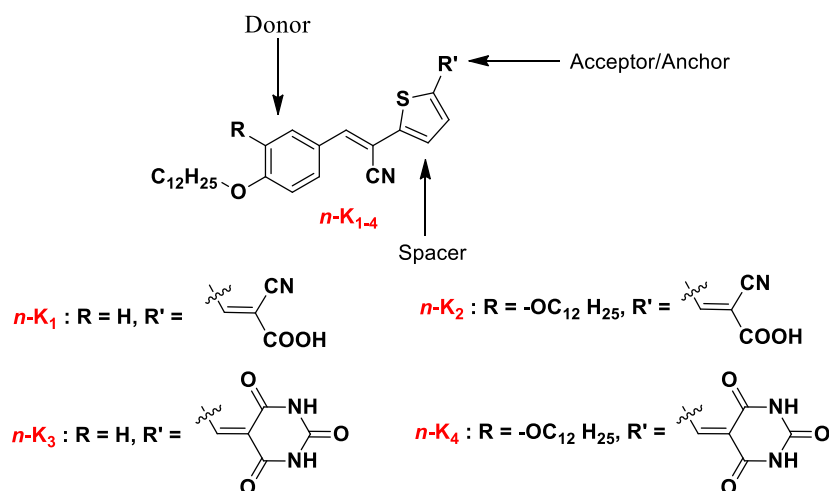


Figure 2.1 Molecular design of new chromophores $n\text{-K}_{1-4}$ (Series-1)

2.2.1.2 Design of Series-2 ($n\text{-K}_{5-11}$)

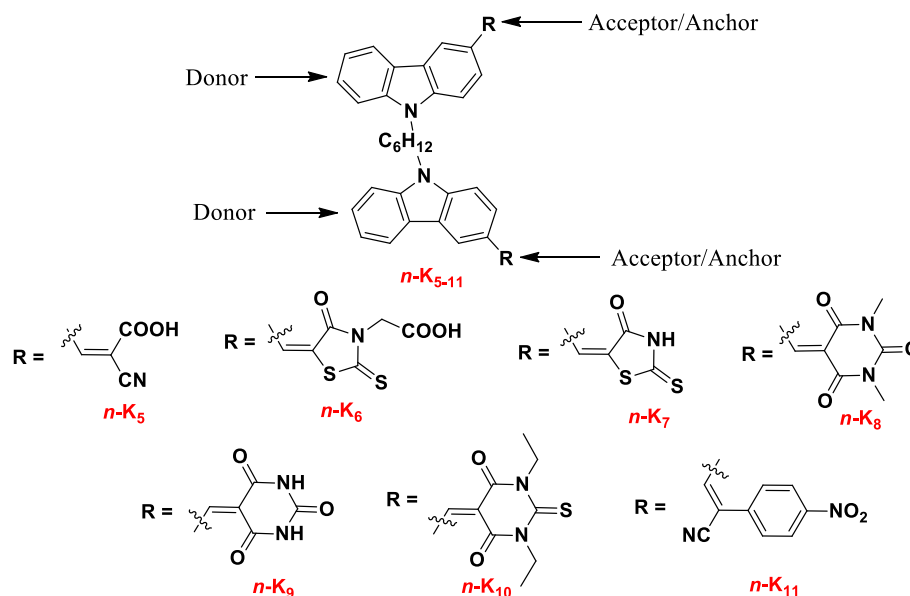


Figure 2.2 Molecular design of new chromophores $n\text{-K}_{5-11}$ (Series-2)

In **Series-2**, seven new double D-A type organic sensitizers/co-sensitizers ($n\text{-K}_{5-11}$) comprising carbazole-based twin molecules as electron donors, non-conjugated n -hexyl chain as an extended linker with multiple acceptor units, *viz.* cyanoacetic acid, rhodanine-3-acetic acid, rhodanine, 1,3-dimethylbarbituric acid, barbituric acid, 1,3-diethyl-2-thiobarbituric acid, and 4-nitrophenylacetonitrile, were designed. The presence of two symmetric D-A chains in this strategy could enhance the overall efficiency of DSSCs compared to that of a single D-A configured dye due to its

extended light-harvesting nature. **Figure 2.2** summarizes the design strategy involved in **Series-2** chromophores ($n\text{-K}_{5-11}$).

2.2.1.3 Design of Series-3 ($n\text{-K}_{12-18}$)

Seven new double D-A configured sensitizers/co-sensitizers ($n\text{-K}_{12-18}$) consisting of carbazole twin cores as an effective donor, linked by an n -pentyl chain with different acceptor/anchoring units, *viz.* cyanoacetic acid, rhodanine-3-acetic acid, barbituric acid, and thiobarbituric acid, were designed. **Figure 2.3** summarizes the design strategy involved in **Series-3** chromophores ($n\text{-K}_{12-18}$). It is hoped that these organic chromogens would show a broader and more intense absorption band in the UV and visible region, which could produce higher J_{SC} and $IPCE$ in the DSSCs.

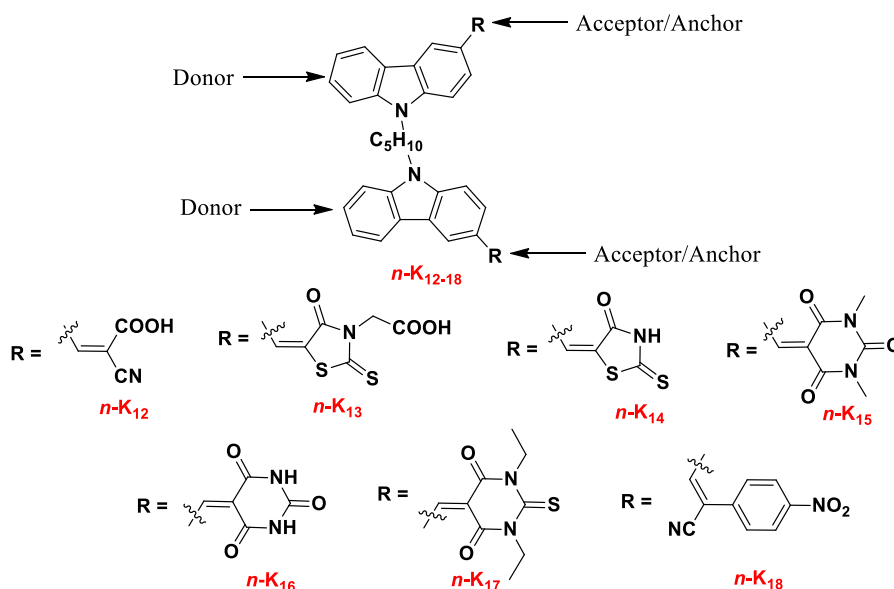


Figure 2.3 Molecular design of new chromophores $n\text{-K}_{12-18}$ (**Series-3**)

2.2.1.4 Design of Series-4 ($n\text{-K}_{19-21}$)

Figure 2.4 displays the design approach used for three new double D- π -A configured organic sensitizers/co-sensitizers of **Series-4** chromophores, *i.e.* $n\text{-K}_{19-21}$. The newly designed dyes comprise twin carbazole rings linked by a linear pentyl chain as an effective electron donor, cyano vinylene and phenyl groups as π -spacers, while cyanoacetic acid, rhodanine-3-acetic acid, and barbituric acid as electron acceptor/anchoring units. Owing to the two different light-harvesting units in a single dye molecule, $n\text{-K}_{19-21}$ has been expected to exhibit a stronger as well as broader

absorption range, resulting in superior device performance when employed as sensitizers/co-sensitizers for DSSC application.

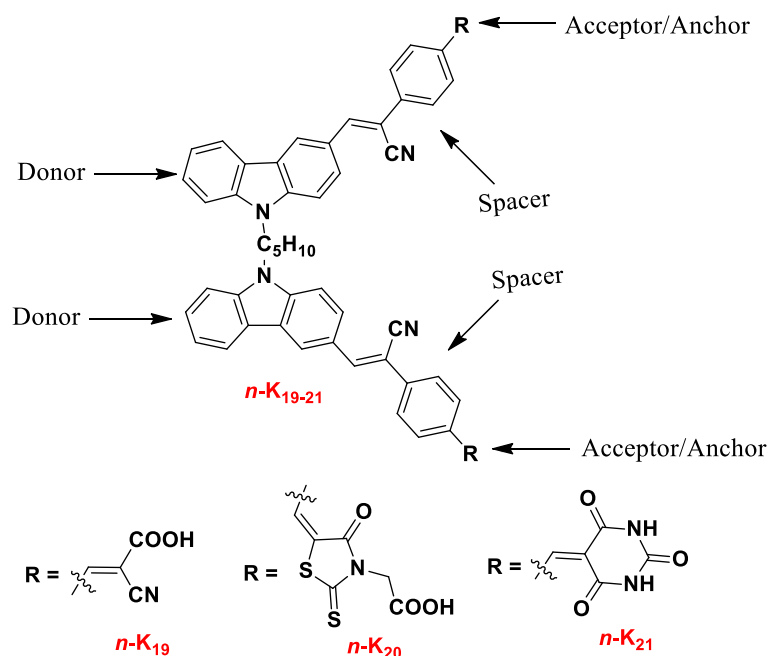


Figure 2.4 Molecular design of new chromophores $n\text{-K}_{19-21}$ (Series-4)

2.2.1.5 Design of Series-5 ($n\text{-K}_{22-24}$)

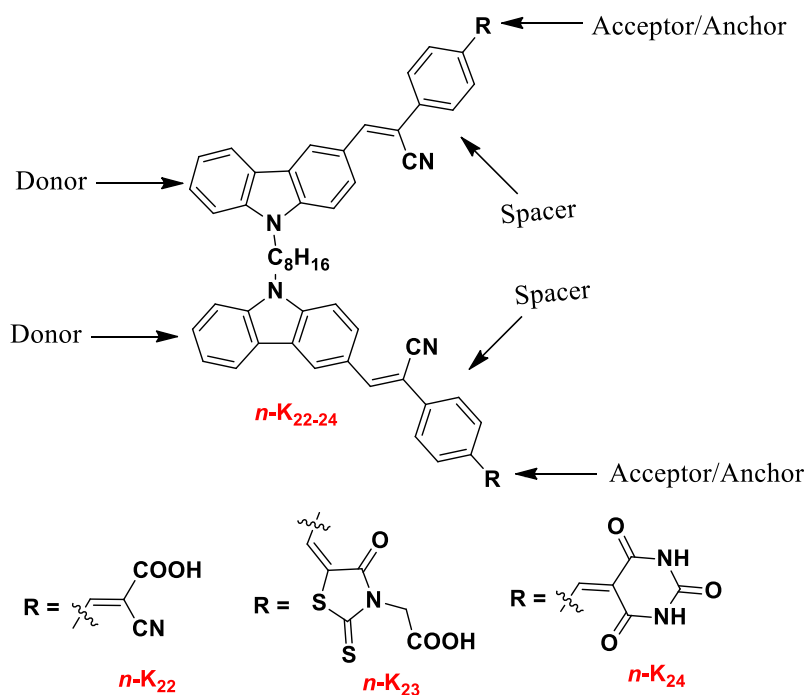


Figure 2.5 Molecular design of new chromophores $n\text{-K}_{22-24}$ (Series-5)

In **Series-5**, three new organic sensitizers/co-sensitizers ($n\text{-K}_{22-24}$) with (D- π -A)₂ architecture were designed as shown in **Figure 2.5**. In the new design strategy, two carbazole units linked by an *n*-octyl chain acts as a double donor scaffold, cyano vinylene, and phenyl groups as π -spacers, while cyanoacetic acid, rhodanine-3-acetic acid, and barbituric acid as electron acceptor/anchoring units. These chromophores with required structural features are predicted to possess all the advantages of ideal sensitizers as well as co-sensitizers.

2.2.1.6 Design of Series-6 ($n\text{-K}_{25-28}$)

Four conceptually new symmetric bi-anchored organic dyes with A-D- π -D-A configuration ($n\text{-K}_{25-28}$) were designed as shown in **Figure 2.6**. In this new design strategy, *N*-substituted carbazole moiety acts as an electron donor unit, (1,4-phenylene)diacetonitrile group acts as a spacer, while cyanoacetic acid, barbituric acid, rhodanine-3-acetic acid, and rhodanine were chosen as electron acceptor/anchoring units. These molecules are anticipated to act as ideal sensitizers as they fulfil all the prerequisites.

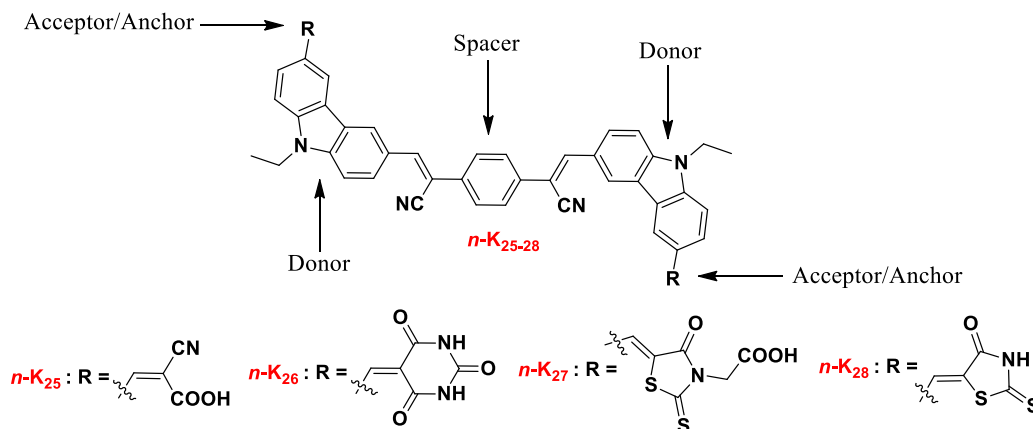


Figure 2.6 Molecular design of new chromophores $n\text{-K}_{25-28}$ (**Series-6**)

2.2.1.7 Design of Series-7 ($n\text{-K}_{29-31}$)

In **Series-7**, three new A- π -D- π -A type chromogens, viz. $n\text{-K}_{29-31}$ were designed. In this strategy, we have chosen phenoxazine as an electron-donating system, cyano vinylene, and thiophene groups as π -spacers, while cyanoacetic acid, rhodanine-3-acetic acid, and barbituric acid as electron acceptor/anchoring units. As per the literature reports, phenoxazine core is considered as a potential donor candidate in

push-pull type sensitizers for DSSC application. The presence of thiophene spacer provides good conjugation, superior thermal stability, high polarizability, and excellent charge transporting capability. Further, the di-anchoring molecules have many advantages over mono-anchored dyes, such as excellent stability, extended conjugation, multi-binding ability on the semiconductor surface, and a good electron extraction channel. Consequently, bi-anchored dyes $n\text{-K}_{29-31}$ is anticipated to show superior device performance. The design strategy of **Series-7** chromophores is summarized in **Figure 2.7**.

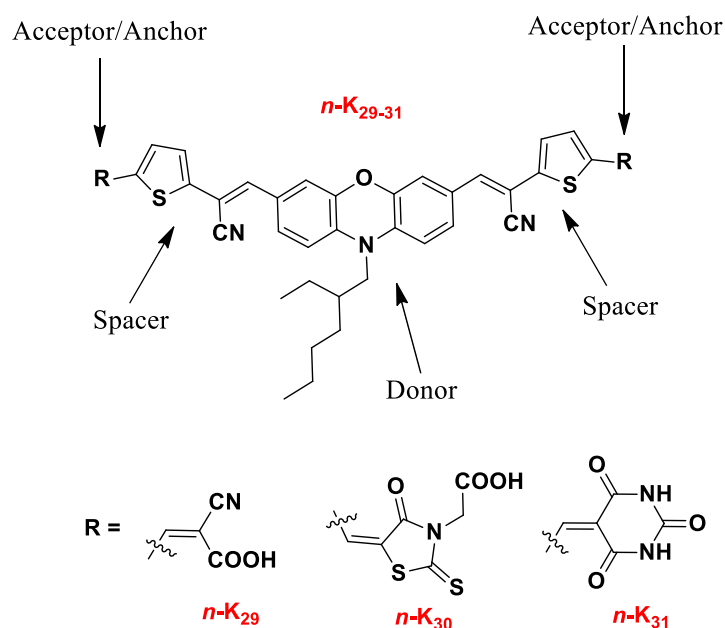


Figure 2.7 Molecular design of new chromophores $n\text{-K}_{29-31}$ (**Series-7**)

2.2.1.8 Design of Series-8 ($n\text{-K}_{32-34}$)

Four new symmetrical bi-anchored organic dyes, *i.e.* $n\text{-K}_{32-34}$ with A- π -D- π -A configuration were designed in **Series-8** (**Figure 2.8**). The new design with phenoxazine central core consists of vinylene and phenylene groups as π -spacers, while cyanoacetic acid, rhodanine-3-acetic acid, and barbituric acid as electron acceptor/anchoring units. Here, the length of branched alkyl chains significantly affects charge delocalization property, structural planarity, and further helps to suppress the dye aggregation. Here, different anchoring groups were incorporated in order to study the effect of binding nature of dye on the TiO_2 surface. These new

chromophores can act as efficient sensitizers as well as co-sensitizers due to their favorable structural features.

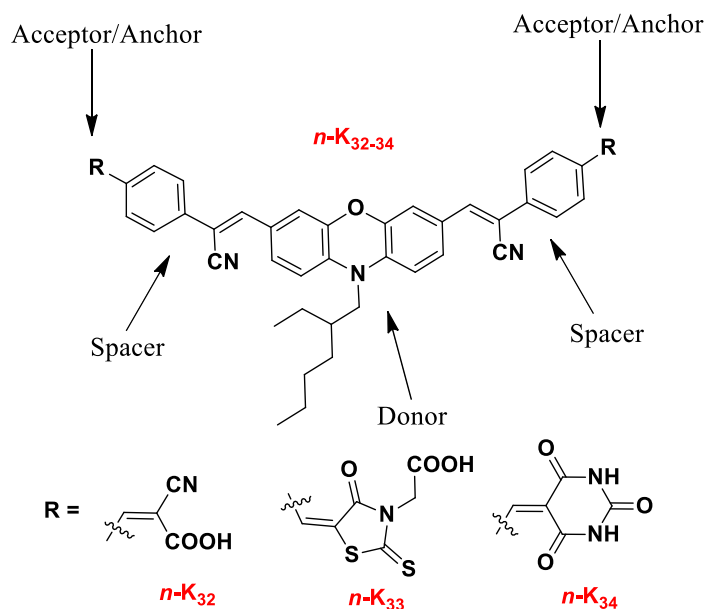


Figure 2.8 Molecular design of new chromophores $n\text{-K}_{32-34}$ (Series-8)

2.2.2 New p -type organic sensitizers for dye-sensitized solar cells

In the literature, several aromatic/heteroaromatic metal-free dyes with various design strategies were designed and investigated as potential p -type sensitizers for DSSCs. Further, it is important to observe that among the various heterocyclic donor units reported in the literature, carbazole, and phenoxazine are noteworthy, as they possess good thermal and photochemical stability with attractive optical properties. Accordingly, the present research work has been aimed at design of new organic photosensitizers carrying phenoxazine (Series-9), and carbazole (Series-10) as donor systems and different electron-withdrawing moieties as acceptor/anchoring systems.

2.2.2.1 Design of Series-9 ($p\text{-K}_{35-40}$)

The structural design of six new D-A configured p -type chromophores, *i.e.* $p\text{-K}_{35-40}$ is shown in **Figure 2.9**. In the new design, phenoxazine core functions as a donor, carboxylic acid serves as an anchoring group, while electron-withdrawing N,N -dimethyl barbituric acid, N,N -diethyl thiobarbituric acid, malononitrile, 3-ethylrhodanine, (3,5,5-trimethylcyclohex-2-enylidene)malononitrile, and 2-oxindole

work as electron acceptor units. While designing these new *p*-type dyes, certain important parameters have been considered, they include appropriate theoretical HOMO-LUMO levels, thermodynamic feasibility of dye regeneration and hole injection, selection of anchoring and acceptor groups that decide the overall efficiency of the devices. Hence, it is anticipated that the new molecules *p*-**K**₃₅₋₄₀ when employed as photosensitizers in DSSC would show superior performance in the devices.

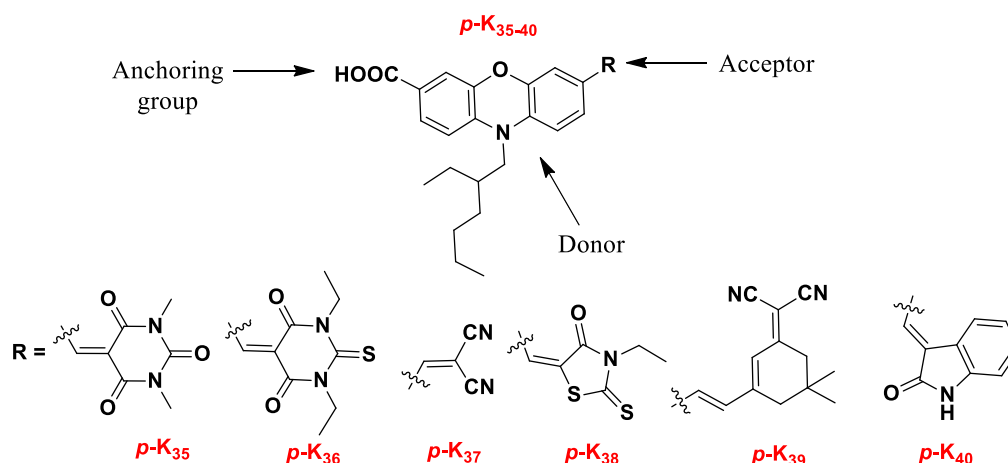


Figure 2.9 Molecular design of new chromophores *p*-**K**₃₅₋₄₀ (Series-9)

2.2.2.2 Design of Series-10 (*p*-**K**₄₁₋₄₂)

Figure 2.10 depicts the structural design strategy of two new D- π -A configured *p*-type metal-free chromophores (*p*-**K**₄₁₋₄₂). The molecular design involves electron-rich carboxy substituted carbazole unit along with a thiophene acetonitrile spacer attached to two different electron-withdrawing species, *viz.* malononitrile, and barbituric acid. Here, the insertion of bulkier branched alkyl chain at *N*-heteroatom of the ring promotes significant tilting and packing distortion and tends to reduce the dye aggregation as well as solubility problems causing improved open-circuit voltage (V_{oc}) in the fabricated devices. Thus, these molecules could bring about effective sensitization due to their favourable structural features.

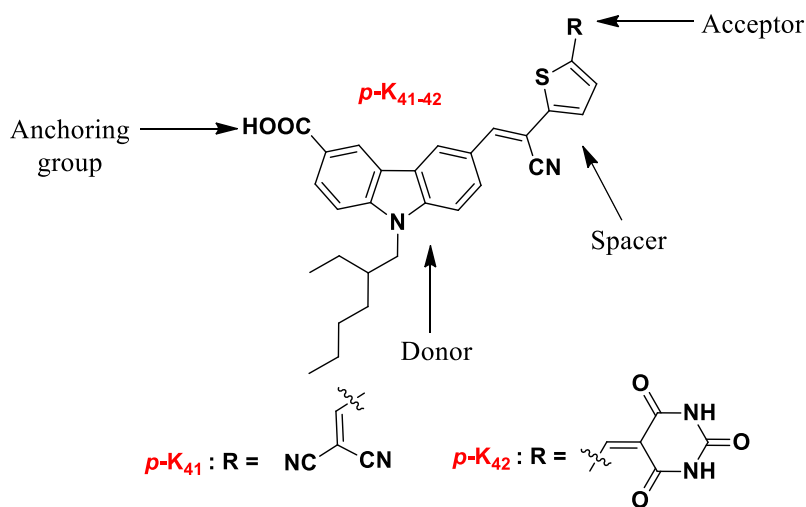


Figure 2.10 Molecular design of new chromophores *p-K*₄₁₋₄₂ (**Series-10**)

2.2.3 New organic HTMs for perovskite solar cells

From the detailed literature survey, it is crystal clear that among the various organic small molecule-based HTMs, carbazole and its derivatives are considered as one of the most promising candidates for optoelectronic applications. Accordingly, in the present study, carbazole-based small molecules have been selected as electron donor systems for the design of new HTMs in perovskite solar cell fabrication.

2.2.3.1 Design of Series-11 (*h-K*₄₃₋₄₄)

Figure 2.11 portrays the design of two novel carbazole-based small molecules, *h-K*₄₃₋₄₄ comprising mono/dimethoxyphenyl and carbazole units as the electron-donating moieties, cyanovinylene groups as the electron-accepting systems with extended π -conjugation. In this design strategy, carbazole has been selected as a central core due to its advantages such as cheap raw material can easily be substituted through simple routes to yield derivatives of high photochemical stability, and also it has the ability to quickly form relatively stable radical cations. Also, it was reported that the length of alkyl chains with significant branching influences the HTM solubility in common organic solvents, and thereby influences the film quality. Because of their easy synthesis as well as facile availability of starting materials, these newly designed molecules are expected to be cost-effective HTMs and hence, they are attractive for commercial prospects of PSCs as HTMs.

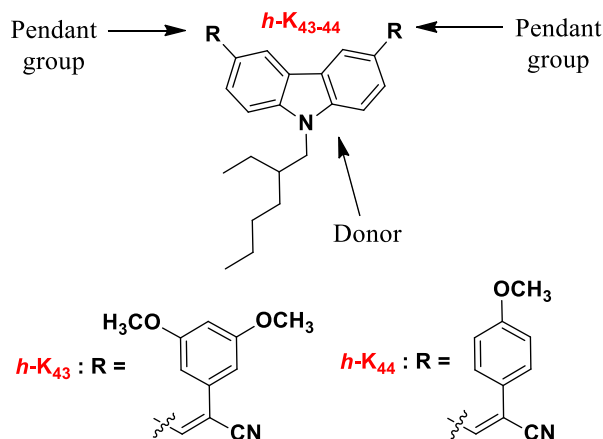


Figure 2.11 Molecular design of new HTMs $h\text{-K}_{43-44}$ (Series-11)

Thus, based on the detailed literature survey, thirty-four new metal-free organic dyes ($n\text{-K}_{1-34}$) as effective n -type sensitizers, eight new organic dyes ($p\text{-K}_{35-42}$) as potential p -type sensitizers, and two new organic molecules ($h\text{-K}_{43-44}$) as potential HTMs have been successfully designed for DSSC/PSC applications. The newly designed molecules were synthesized by adopting well-established synthetic protocols to aim for maximum yield (Schemes 2.1 to 2.11). For all the synthesized molecules, appropriate purification methods have been developed and further, the purified compounds have been characterized by various spectral techniques such as FTIR, NMR spectroscopy, and mass spectrometry followed by elemental analysis. The photophysical properties were evaluated by UV-Visible absorption, and photoluminescence (PL) studies. Further, their electrochemical properties were determined by cyclic voltammetric (CV) studies. Additionally, theoretical studies have been performed to measure molecular geometry, electron distributions, and energetic properties of the synthesized molecules. Finally, performance studies have been carried out by evaluating the parameters such as J_{SC} , V_{OC} , FF , PCE , and $IPCE$.

2.3 EXPERIMENTAL

The materials used, experimental protocols, and purification techniques used for newly designed molecules are given in this section. In addition, their structural characterization data are also included.

2.3.1 Materials and methods

All the starting materials and reagents used for synthesis were procured from Sigma Aldrich, Alfa Aesar and Spectrochem companies. All the solvents used in the reactions were synthetic grade and used without further purification. The reactions were carried out under an inert atmosphere and their progress was monitored using the thin-layer chromatography (TLC) technique. The synthesized intermediates and final compounds were purified using recrystallization or column chromatography techniques. ^1H and ^{13}C NMR spectra of all the molecules were recorded in $\text{CDCl}_3/\text{DMSO-d}_6$ solvent on a Bruker Avance 400/500 MHz spectrophotometer. The chemical shift (δ) was expressed in ppm with tetramethylsilane (TMS) as an internal standard. ATR-FTIR spectra were recorded using Bruker Alpha FTIR spectrometer equipped with silicon carbide as IR source. Mass and elemental analysis of the synthesized dyes were measured using LC-MS6410Q (Agilent Technologies), Waters HPLC-TOF mass analyzer, and Flash EA1112 CHNS elemental analyzer (Thermo Scientific), respectively.

2.3.2 Synthesis

The detailed synthetic strategy used for all the target molecules and respective purification techniques along with their characterization data are elaborated in the following section.

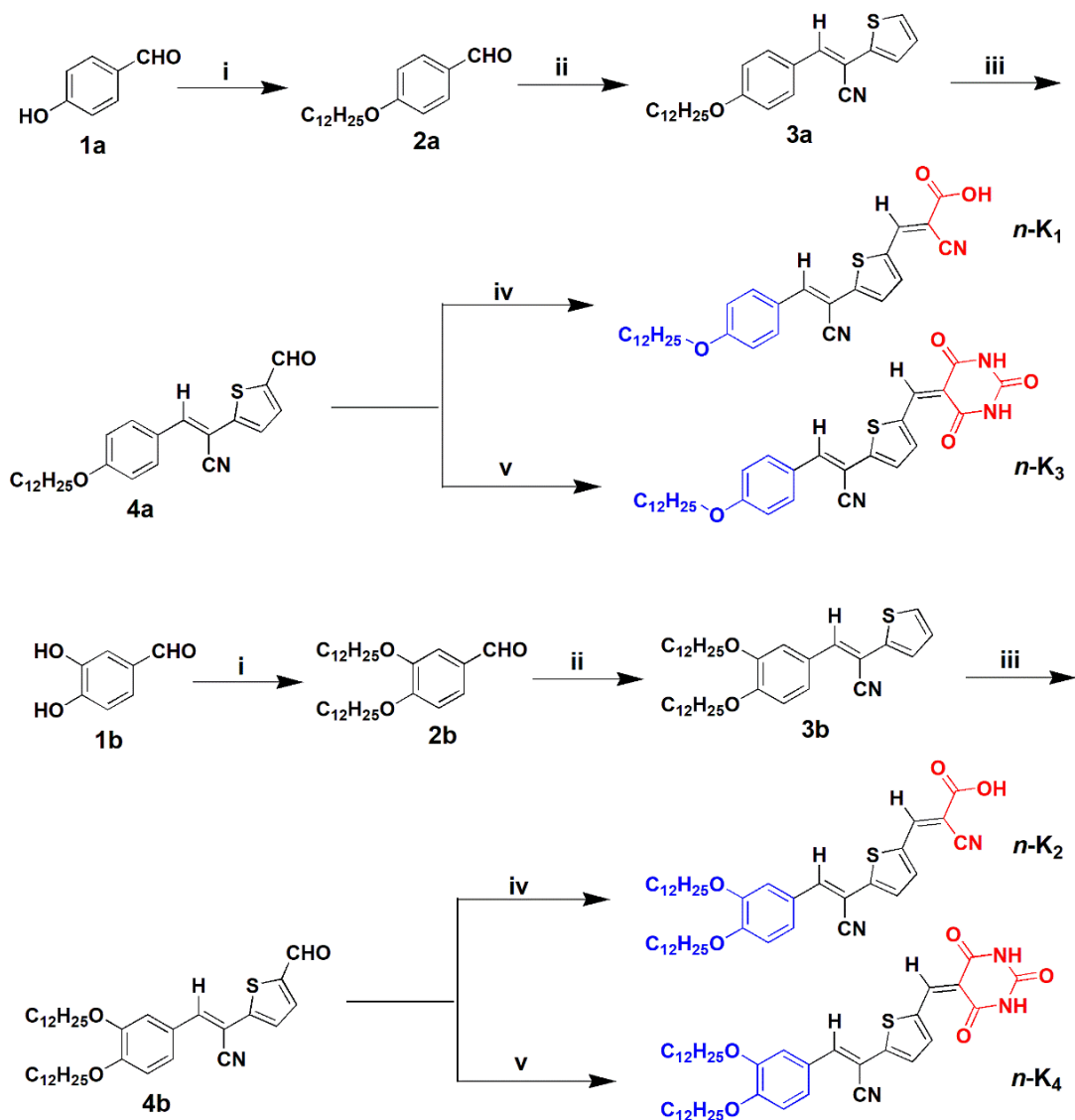
2.3.2.1 Synthesis of *n*-type organic dyes *n-K*₁₋₃₄ (Series 1-8)

The synthetic protocols employed for the preparation of dyes *n-K*₁₋₃₄ from simple starting materials thiophene, carbazole, and phenoxazine are given here.

2.3.2.1.1 Synthesis of chromophores *n-K*_{1,4} (Series-1)

The synthetic pathways of four new metal-free organic dyes *n-K*_{1,4} are shown in **Scheme 2.1**. The required intermediates alkoxy benzaldehydes **2a-b** were synthesized from 4-hydroxybenzaldehyde (**1a**) or 3,4-dihydroxybenzaldehyde (**1b**) by reacting it with 1-bromododecane in presence of potassium carbonate. Subsequently, the aldehydes **2a-b** were condensed with thiophene-2-acetonitrile by the Knoevenagel protocol to obtain the substituted thiophenyl acrylonitriles **3a** and **3b** as intermediates. Further, these intermediates were formylated using the standard Vilsmeier-Hack

reaction protocol to yield precursors **4a** and **4b**. In the final step, the target molecules *n-K*₁₋₄ were obtained by following the Knoevenagel condensation protocol, wherein the key precursor **4a** or **4b** was condensed with an active methylene compound, *viz.* cyanoacetic acid and barbituric acid. The synthetic procedures for the intermediates and the final dyes *n-K*₁₋₄ are given in the following section.



Scheme 2.1 Synthetic routes for the dyes *n-K*₁₋₄: (i) 1-Bromododecane, potassium carbonate, DMF, RT, 10 h (ii) Thiophene-2-acetonitrile, sodium methoxide, methanol, RT, 6 h (iii) POCl₃, DMF, RT, 12 h (iv) Cyanoacetic acid, ammonium acetate, glacial CH₃COOH, 110 °C, 10 h (v) Barbituric acid, methanol, 60 °C, 10 h.

General method for the synthesis of intermediates 2a-b

A mixture of 4-hydroxybenzaldehyde or 3,4-dihydroxybenzaldehyde (**1**, 1 eq) was dissolved in a minimum amount of DMF and stirred for 0.5 h under an argon atmosphere at room temperature. Later potassium carbonate (3 eq) is added to the above mixture. Further, 1-bromododecane (1.2 eq) was added to the above reaction mixture and was heated with stirring at 80 °C for 12 h. The reaction progress was monitored using the thin-layer chromatography (TLC). After completion of the reaction, the reaction mixture was cooled, poured into ice-cold water, and extracted with dichloromethane (3 x 30 mL). The combined organic layer was dried using sodium sulphate and the solvent was removed under reduced pressure. Finally, the crude product was purified by the column chromatography method using 100-200 silica mesh (pet ether:ethyl acetate, 3:1, as eluent) to obtain the pure product as a colorless liquid. Yield: 89-91%.

General method for the synthesis of intermediates 3a-b

Intermediate **2a** or **2b** (1 eq) and thiophene-2-acetonitrile (1.2 eq) were slowly added to the round-bottomed flask containing freshly prepared sodium methoxide (1.8 eq, 50 mL) solution. The reaction mass was stirred at room temperature under an argon atmosphere for 8 h. The bright yellow precipitate formed was filtered off, washed with cold methanol and finally, it was recrystallized from chloroform to give a fine yellow solid of **3a-b**.

(E)-3-(4-(Dodecyloxy)phenyl)-2-(thiophen-2-yl)acrylonitrile (3a)

¹H NMR (400 MHz, DMSO-d₆, δ ppm): 7.84-7.82 (d, 1H), 7.33-7.26 (m, 4H), 7.06 (s, 1H), 6.96-6.94 (d, 2H), 4.03-4.00 (t, 2H), 1.82-1.27 (m, 20H), 0.88-0.87 (t, 3H). **FT-IR (ATR)**, ν cm⁻¹: 2850 (C-H stretch), 2218 (C≡N stretch), 1510 (C=C). Melting point: 176 °C. Yield: 83%.

(E)-3-(3, 4-Bis (dodecyloxy)phenyl)-2-(thiophen-2-yl)acrylonitrile (3b)

¹H NMR (400 MHz, DMSO-d₆, δ ppm): 7.58 (s, 1H), 7.33-7.31 (m, 4H), 7.06 (s, 1H), 6.91-6.89(d, 1H), 4.09-4.06 (t, 4H), 2.17-2.15 (d, 2H), 1.86-1.83 (d, 2H), 1.54-1.26(m, 36H), 0.89-0.86 (t, 6H). **FT-IR (ATR)**, ν cm⁻¹: 2851 (C-H stretch), 2208 (C≡N stretch), 1599 (C=C). Melting point: 189 °C. Yield: 81%.

General method for the synthesis of intermediates 4a-b

DMF (5 eq) and phosphorous oxychloride (5 eq) were mixed under an argon atmosphere and stirred at -3 to 4 °C for 30 minutes in order to get white-colored Vielsmeier salt. To this salt, the intermediate **3a** or **3b** (1 eq) in dichloroethane (2-3 mL) was added and stirring was continued at room temperature for 12 h. After completion of the reaction, the reaction mass was poured into ice-cold water and subsequently basified by using a 5M NaOH solution. The precipitated solid was filtered and collected. The crude product was further purified by column chromatography (100-200 mesh and hexane:EtOAc, 3:1 eluent) and finally, it was recrystallized from ethanol to get the pure dark orange-colored solid **4a-b**.

(E)-3-(4-(Dodecyloxy)phenyl)-2-(5-formylthiophen-2-yl)acrylonitrile (4a)

¹H NMR (400 MHz, DMSO-d₆, δ ppm): 9.86 (s, 1H), 7.84-7.82 (d, 1H), 7.69 (s, 1H), 7.33-7.26 (m, 2H), 7.37-7.36 (d, 2H), 6.96-6.94 (d, 1H), 4.03-4.00 (t, 2H), 1.82-1.27 (m, 20H), 0.88-0.87 (t, 3H). **FT-IR (ATR)**, ν cm⁻¹: 3057-2712 (C-H stretch), 2212 (C≡N stretch), 1669 (C=O), 1589 (C=C). Melting point: 196 °C. Yield: 83%.

(E)-3-(3, 4-Bis (dodecyloxy)phenyl)-2-(5-formylthiophen-2-yl)acrylonitrile (4b)

¹H NMR (400 MHz, DMSO-d₆, δ ppm): 9.86 (s, 1H), 7.70-7.69 (d, 1H), 7.69-7.63 (d, 1H), 7.45 (s, 1H), 7.40-7.39 (d, 1H), 7.37-7.36 (d, 1H), 6.91-6.89(d, 1H), 4.08-4.04 (t, 4H), 1.85-1.81 (m, 6H), 1.49-1.45 (m, 6H), 1.35-1.25 (m, 28H), 0.86-0.85 (t, 6H). **FT-IR (ATR)**, ν cm⁻¹: 3042 (C-H stretch), 2208 (C≡N stretch), 1665 (C=O), 1595 (C=C). Melting point: 208 °C. Yield: 79%.

General method for the synthesis of dyes n-K_{1,2}

A mixture of intermediate **4a**, 3-(4-(dodecyloxy)phenyl)-2-(5-formylthiophen-2-yl)acrylonitrile or **4b**, 3-(3,4-bis(dodecyloxy)phenyl)-2-(5-formylthiophen-2-yl)acrylonitrile (1 eq), cyanoacetic acid (1.2 eq), ammonium acetate (10 eq), and glacial acetic acid (10-15 mL) was taken in an RB flask and refluxed for 12 h under an argon atmosphere. The progress of the reaction was monitored using the TLC technique. After its completion, the reaction mixture was cooled to room temperature

and was poured into ice-cold water. The solid obtained was filtered, washed with cold water, and finally, dried. The crude product was recrystallized from absolute methanol to get the pure product **n-K₁₋₂**.

(E)-2-Cyano-3-(5-((E)-1-cyano-2-(4-(dodecyloxy)phenyl)vinyl)thiophen-2-yl)acrylic acid (n-K₁)

Bright red solid, Yield: 73%. Melting point: 244-246 °C. ¹H NMR (400 MHz, DMSO-d₆, δ ppm): 11.33 (s, 1H), 8.48 (s, 1H), 8.18-8.17 (d, 1H), 8.07 (s, 1H), 8.02-8.00 (d, 2H), 7.65-7.64 (d, 1H), 7.13-7.11 (d, 2H), 4.08-4.00 (t, 2H), 1.75-1.24 (m, 20H), 0.86-0.83 (t, 3H). ¹³C NMR (400 MHz, DMSO-d₆, δ ppm): 166.50, 161.27, 159.04, 156.95, 144.29, 144.02, 143.26, 139.36, 137.32, 136.52, 135.41, 126.70, 126.45, 125.62, 119.94, 116.09, 114.35, 114.08, 113.48, 112.96, 47.42, 43.91, 43.41, 36.55, 30.14, 28.44, 23.71, 22.98, 14.27, 12.68, 12.63, 11.19. Anal. Calcd. for C₂₉H₃₄N₂O₃S: C, 70.99; H, 6.91; N, 5.71 and found C, 71.02; H, 6.87; N, 5.74. **FT-IR (ATR)**, ν cm⁻¹: 2923, 2850 (C-H stretch), 2208 (C≡N stretch), 1664 (C=O stretch), 1599, 1510 (C=C stretch). **Mass (m/z)**: Calculated: 490.23; Obtained (M-H): 489.10.

(E)-3-(5-((E)-2-(3,4-Bis(dodecyloxy)phenyl)-1-cyanovinyl)thiophen-2-yl)-2-cyanoacrylic acid (n-K₂)

Dark red solid, Yield: 69%. Melting point: 296-298 °C. ¹H NMR (400 MHz, DMSO-d₆, δ ppm): 8.31 (s, 1H), 8.16 (s, 1H), 7.70 (s, 1H), 7.60-7.49 (d, 2H), 7.32-7.12 (d, 2H), 4.25-4.00 (t, 4H), 1.75-1.25 (m, 40H), 0.85-0.65 (t, 6H). ¹³C NMR (400 MHz, DMSO-d₆, δ ppm): 164.10, 162.37, 158.04, 155.15, 143.29, 143.02, 142.26, 139.26, 138.12, 137.52, 135.41, 125.70, 125.45, 124.62, 118.64, 116.39, 114.55, 114.08, 113.48, 111.96, 47.62, 42.45, 37.65, 30.44, 28.14, 23.71, 22.98, 14.67, 12.18. Anal. Calcd. for C₄₁H₅₈N₂O₄S: C, 72.96; H, 8.66; N, 4.15; and found C, 73.00; H, 8.63; N, 4.16. **FT-IR (ATR)**, ν cm⁻¹: 2925, 2851 (C-H stretch), 2208 (C≡N stretch), 1664 (C=O stretch), 1599, 1510 (C=C stretch). **Mass (m/z)**: Calculated: 674.41; Obtained (M-H): 673.

General method for the synthesis of dyes n-K₃₋₄

A mixture of intermediate **4a**, 3-(4-(dodecyloxy)phenyl)-2-(5-formylthiophen-2-yl)acrylonitrile or intermediate **4b**, 3-(3,4-bis(dodecyloxy)phenyl)-2-(5-

formylthiophen-2-yl)acrylonitrile (1 eq) was dissolved in 10-15 mL of absolute methanol and to this mixture 1.2 eq of an active methylene compound like cyanoacetic acid or barbituric acid (anchor) was added under argon atmosphere and heated at 60 °C with stirring for 10 h. After completion of the reaction, the content was cooled to room temperature, and the precipitated solid was filtered, washed with cold methanol and collected. It was further recrystallized from the CHCl₃-hexane mixture to get a pure product.

(E)-3-(4-(Dodecyloxy)phenyl)-2-(5-((2,4,6-trioxotetrahydropyrimidin-5(2H)-ylidene)methyl)thiophen-2-yl) acrylonitrile (n-K₃)

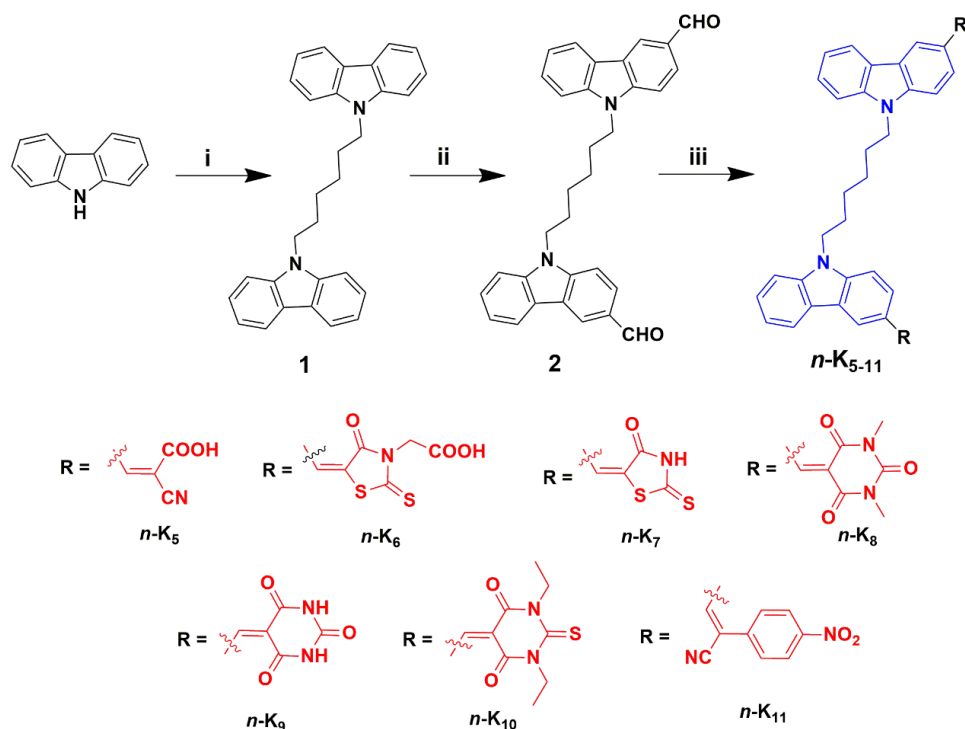
Bright red solid, Yield: 74%. Melting point: 340-342°C. ¹H NMR (400 MHz, DMSO-d₆, δ ppm): 11.34 (s, 2H), 8.48 (s, 1H), 8.18-8.17 (d, 1H), 8.07 (s, 1H), 8.02-8.00 (d, 2H), 7.65-7.64 (d, 1H), 7.13-7.11 (d, 2H), 4.09-4.06 (t, 2H), 1.76-1.75 (m, 2H), 1.73-1.69 (m, 2H), 1.41-1.39 (m, 16H), 0.86-0.83 (t, 3H). ¹³C NMR (400 MHz, DMSO-d₆, ppm): 167.24, 164.71, 157.35, 143.01, 141.14, 135.69, 127.49, 119.70, 118.12, 110.22, 109.45, 40.60, 40.40, 40.29, 40.14, 39.79, 39.51, 39.31, 31.40, 28.92, 26.59, 22.40, 14.39. Anal. Calcd. for C₃₀H₃₅N₃O₄S: C, 67.52; H, 6.61; N, 7.87; and found C, 67.55; H, 6.63; N, 7.85. **FT-IR (ATR)**, ν cm⁻¹: 3203 (N-H stretch), 2944, 2835 (C-H stretch), 2320 (C≡N stretch), 1595, 1522, 1494 (C=C stretch). **Mass (m/z)**: Calculated: 533.23; Obtained (M-H): 532.10.

(E)-3-(3,4-Bis(dodecyloxy)phenyl)-2-(5-((2,4,6-trioxotetrahydropyrimidin-5(2H)-ylidene) methyl) thiophen-2-yl)acrylonitrile (n-K₄)

Blackish brown colored solid, Yield: 71%; Melting point: 338-340°C. ¹H NMR (400 MHz, DMSO-d₆, δ ppm): 11.34 (s, 2H), 8.47 (s, 1H), 8.00-7.98 (d, 3H), 7.61-7.60 (d, 1H), 7.13-7.11 (d, 2H), 4.09-4.06 (t, 4H), 1.74-1.71 (m, 4H), 1.41-1.24 (m, 36H), 0.86-0.84 (t, 6H). ¹³C NMR (400 MHz, DMSO-d₆, δ ppm): 162.99, 161.60, 156.87, 152.41, 146.19, 143.23, 139.42, 136.22, 135.79, 126.45, 126.40, 125.22, 119.82, 116.32, 114.63, 113.79, 112.80, 47.32, 36.49, 31.15, 30.57, 29.07, 28.45, 24.46, 11.96. Anal. Calcd. for C₄₂H₅₉N₃O₅S: C, 70.26; H, 8.28; N, 5.85; and found C, 70.28; H, 8.30; N, 5.81. **FT-IR (ATR)**, ν cm⁻¹: 3192 (N-H stretch), 2840 (C-H stretch), 2322 (C≡N stretch), 1529, 1495 (C=C stretch). **Mass (m/z)**: Calculated: 718; Obtained (M-H): 717.

2.3.2.1.2 Synthesis of chromophores *n-K*₅₋₁₁ (Series-2)

The synthetic pathways of seven new metal-free dyes *n-K*₅₋₁₁ are shown in **Scheme 2.2**. The requisite intermediate 1,6-di(9*H*-carbazole-9-yl)hexane (**1**) was obtained from 9*H*-carbazole by treating it with 1,6-dibromohexane in presence of a strong base, *i.e.* sodium hydride. This was converted to the key precursor 9,9'-(hexane-1,6-diyl)bis(9*H*-carbazole-3-carbaldehyde) (**2**) through the Vilsmeier-Hack reaction protocol with good yield. In the final step, the target molecules *n-K*₅₋₁₁ were obtained by following the Knoevenagel condensation protocol, wherein the precursor **2** was condensed with various active methylene compounds, *viz.* cyanoacetic acid, rhodanine-3-acetic acid, rhodanine, barbituric acid, 1,3-dimethylbarbituric acid, 1,3-diethyl-2-thiobarbituric acid, and 4-nitrophenyl acetonitrile. The synthetic procedures for the intermediates and the final dyes *n-K*₅₋₁₁ are given in the following section.



Scheme 2.2 Synthetic routes for the dyes *n-K*₅₋₁₁: (i) 1,6-Dibromohexane, NaH, DMF, RT, 12 h (ii) POCl₃, DMF, 110 °C, 2 h (iii) *n-K*₅₋₇: Cyanoacetic acid/rhodanine-3-acetic acid/ rhodanine, ammonium acetate, glacial CH₃COOH, 110 °C, 12 h; *n-K*₈₋₁₀: 1,3-dimethylbarbituric acid/barbituric acid/1,3-diethyl-2-thiobarbituric acid, methanol, 60 °C, 10 h; *n-K*₁₁: 4-nitrophenyl acetonitrile, potassium *tert*-butoxide, methanol, 60 °C, 6 h.

Synthesis of 1,6-di(9H-carbazole-9-yl)hexane (1)

A mixture of carbazole (12 g, 71.70 mmol), NaH (3.5 g, 143.35 mmol) was dissolved in 30 mL of DMF and stirred at 0 °C for half an hour under an argon atmosphere. Further, 1,6-dibromohexane (7 g, 28.69 mmol) was added into the reaction mixture and continued stirring at room temperature for 12 h. After completion of the reaction, the reaction mixture was cooled and poured into crushed ice (250 mL) and neutralization was done using a saturated solution of ammonium chloride. The precipitate formed was filtered, washed with ice-cold water, and finally it was recrystallized using ethanol to get off-white solid as a product. Yield: 92 %. Melting point: 108-110 °C.

¹H NMR (400 MHz, CDCl₃, δ ppm): 8.10-8.08 (d, 4H), 7.44-7.41 (m, 4H), 7.33-7.23 (t, 4H), 7.21-7.20 (d, 4H), 4.25-4.22 (t, 4H), 1.83-1.81 (t, 3H), 1.57-1.26 (m, 5H). Anal. Calcd. for C₃₀H₂₈N₂: C, 86.50; H, 6.78; N, 6.72; and found C, 86.13; H, 6.49; N, 6.13. **FT-IR (ATR)**, ν cm⁻¹: 3063, 2956 (C-H), 1589, 1533, 1482 (C=C).

Synthesis of 9,9'-(hexane-1,6-diyl)bis(9H-carbazole-3-carbaldehyde) (2)

In a cleaned two neck round-bottom flask, freshly distilled DMF (18.58 mL, 240.06 mmol) was taken and cooled at -3 to 4 °C. Then, phosphorous oxychloride, POCl₃ (22.4 mL, 240.06 mmol) was added drop-wise with constant stirring at the same temperature under an argon atmosphere to obtain a glassy white salt. To this mixture, 1,6-di(9H-carbazole-9-yl)hexane (**1**, 5 g, 12 mmol) dissolved in dichloroethane (10-12 mL) was added. The reaction mixture was refluxed at 110 °C for 2 h. After completion of the reaction, the reaction mass was poured into 200 mL crushed ice and subsequently basified by using a 5 M NaOH solution. The product formed was extracted with dichloromethane (50 mL x 4) and the organic layer was dried over sodium sulphate and evaporated under reduced pressure. The impure residue was later purified by column chromatography on silica gel (100-200 mesh and hexane: EtOAc, 3:1 eluent) to yield pale brown solid (**2**). Yield: 69%. Melting point: 148-150 °C.

¹H NMR (400 MHz, CDCl₃, δ ppm): 10.07 (s, 2H), 8.58-8.58 (d, 2H), 7.95-7.93 (t, 2h), 7.49-7.48 (t, 2H), 7.47-7.46 (d, 2H), 7.36-7.28 (m, 6H), 4.27-4.25 (t, 4H),

1.84-1.81 (t, 4H), 1.58-1.34 (m, 4H). Anal. Calcd. for C₃₂H₂₈N₂O₂: C, 81.33; H, 5.97; N, 5.93; and found C, 81.46; H, 5.89; N, 5.13. **FT-IR (ATR)**, ν cm⁻¹: 2956, 2927 (C-H), 1681 (C=O), 1587, 1482 (C=C).

Synthesis of (2E,2'E)-3,3'-(9,9'-(hexane-1,6-diyl)bis(9H-carbazole-9,3-diyl))bis(2-cyano acrylic acid) (n-K₅)

A mixture of intermediate 9,9'-(hexane-1,6-diyl)bis(9H-carbazole-3-carbaldehyde) (**2**, 0.5 g, 1.058 mmol), cyanoacetic acid (0.17 g, 2.11 mmol), ammonium acetate (0.89 g, 11.6 mmol), and glacial acetic acid (5 mL) were taken in a RB flask and refluxed for 12 h under an argon atmosphere. After its completion, the reaction mixture was quenched in ice-cold water. The solid obtained was filtered, washed with cold water, and finally, dried. The crude product was recrystallized from absolute methanol to get the pure product **n-K₅** as bright yellow solid. Yield: 89%. Melting point: 280-282 °C.

¹H NMR (400 MHz, DMSO-d₆, δ ppm): 10.05 (s, 1H), 8.85 (s, 1H), 8.75 (s, 1H), 8.45 (s, 1H), 8.29-8.26 (t, 2H), 8.15-8.14 (d, 1H), 7.96-7.95 (d, 1H), 7.77-7.76 (d, 1H), 7.72-7.71 (d, 1H), 7.64-7.63 (m, 2H), 7.52-7.51 (m, 3H), 7.32-7.29 (dd, 2H), 4.42-4.39 (t, 4H), 1.72-1.31 (m, 8H). **¹³C NMR** (400 MHz, DMSO-d₆, δ ppm): 192.27, 164.63, 155.66, 143.94, 143.11, 141.19, 141.12, 128.67, 128.12, 127.33, 127.15, 127.03, 126.06, 124.42, 122.92, 122.77, 122.69, 122.64, 122.41, 121.28, 120.99, 120.79, 120.56, 117.79, 110.67, 110.45, 110.15, 98.85, 31.15, 28.69, 26.42. Anal. Calcd. for C₃₈H₃₀N₄O₄: C, 75.23; H, 4.98; N, 9.24 and found C, 75.39; H, 4.12; N, 9.21. **FT-IR (ATR)**, ν cm⁻¹: 2942, 2860 (C-H stretch), 2226 (C≡N stretch), 1687 (C=O stretch), 1581, 1495 (C=C stretch). **Mass (m/z)**: Calculated: 606.67; Obtained (M-H): 605.25.

Synthesis of 2-((E)-5-((9-(6-(3-((Z)-(3-(carboxymethyl)-4-oxo-2-thioxothiazolidin-5-ylidene) methyl)-9H-carbazole-9-yl)hexyl)-9H-carbazole-3-yl)methylene)-4-oxo-2-thioxo thiazolidin-3-yl)acetic acid (n-K₆)

A mixture of intermediate 9,9'-(hexane-1,6-diyl)bis(9H-carbazole-3-carbaldehyde) (**2**, 0.5 g, 1.058 mmol), rhodanine-3-acetic acid (0.4 g, 2.11 mmol), ammonium acetate (0.89 g, 11.6 mmol), and glacial acetic acid (5 mL) was taken in

an RB flask and refluxed for 12 h under an argon atmosphere. The completion of the reaction was monitored using the TLC technique. After its completion, the reaction mixture was cooled to room temperature and was poured into ice-cold water. The solid obtained was filtered, washed with cold water, and finally, dried. The crude product was recrystallized from absolute methanol to get the pure product **n-K₆** as pale yellow solid. Yield: 86%. Melting point: 330-332 °C.

¹H NMR (400 MHz, DMSO-d₆, δ ppm): 10.05 (s, 1H), 8.74 (s, 1H), 8.49-8.48 (d, 1H), 8.29-8.27 (d, 2H), 8.06-8.05 (d, 1H), 7.96-7.94 (d, 1H), 7.74-7.71 (t, 4H), 7.64-7.62 (m, 2H), 7.53-7.51 (t, 2H), 7.31-7.28 (t, 2H), 4.75 (m, 3H), 4.40 (m, 5H), 1.72-1.31 (m, 8H). **¹³C NMR** (400 MHz, DMSO-d₆, δ ppm): 193.66, 192.29, 166.99, 143.95, 141.90, 141.20, 141.13, 129.03, 128.67, 127.30, 127.17, 127.04, 124.93, 124.46, 124.08, 123.45, 122.69, 122.64, 122.32, 121.38, 121.29, 120.57, 117.77, 110.99, 110.47, 110.18, 28.69, 26.43. Anal. Calcd. for C₄₂H₃₄N₄O₆S₄: C, 61.59; H, 4.18; N, 6.84 and found C, 61.32; H, 4.12; N, 6.82. **FT-IR (ATR)**, ν cm⁻¹: 2936 (C-H stretch), 2360 (C≡N stretch), 1678 (C=O stretch), 1577, 1494 (C=C stretch). **Mass (m/z)**: Calculated: 818.14; Obtained (M-H): 817.25.

Synthesis of (5Z,5'E)-5,5'-(9,9'-(hexane-1,6-diyl)bis(9H-carbazole-9,3-diyl))bis(methanylylidene))bis(2-thioxothiazolidin-4-one) (n-K₇)

A mixture of intermediate 9,9'-(hexane-1,6-diyl)bis(9H-carbazole-3-carbaldehyde) (**2**, 0.5 g, 1.058 mmol), rhodanine (0.28 g, 2.11 mmol), and ammonium acetate (0.89 g, 11.6 mmol) and glacial acetic acid (5 mL) were taken in a RB flask and refluxed for 12 h under an argon atmosphere. After the reaction completion, the reaction mixture was cooled to room temperature and was poured into ice-cold water. The solid obtained was filtered, washed with cold water, dried, and recrystallized using absolute methanol to get the pure product **n-K₇** as a pale yellowish-orange solid. Yield: 83%. Melting point: 294-296 °C.

¹H NMR (400 MHz, DMSO-d₆, δ ppm): 10.05 (s, 1H), 8.75 (s, 1H), 8.41-8.40 (t, 1H), 8.33-8.25 (m, 3H), 7.96-7.94 (dd, 1H), 7.83-7.82 (d, 1H), 7.71-7.70 (t, 2H), 7.64-7.63 (m, 4H), 7.51-7.49 (m, 2H), 7.31-7.27 (m, 2H), 4.40-4.38 (t, 4H), 1.71-1.30 (m, 8H). **¹³C NMR** (400 MHz, DMSO-d₆, δ ppm): 196.16, 192.28, 170.05, 141.19, 141.08, 128.67, 127.15, 124.17, 123.36, 122.69, 122.64, 122.30, 121.28, 120.55,

120.39, 110.82, 110.44, 110.13, 28.67, 26.42. Anal. Calcd. for $C_{38}H_{30}N_4O_2S_4$: C, 64.93; H, 4.30; N, 7.97 and found C, 64.90; H, 4.29; N, 7.96. **FT-IR (ATR)**, ν cm^{-1} : 3033, 2845 (C-H stretch), 2360 (C \equiv N stretch), 1678 (C=O stretch), 1572 (C=C stretch). **Mass (m/z)**: Calculated: 702.13; Obtained (M-H): 701.10.

Synthesis of 5,5'-((9,9'-(hexane-1,6-diyl)bis(9H-carbazole-9,3-diyl))bis(methanylylidene))bis(1,3-dimethylpyrimidine-2,4,6(1H,3H,5H)-trione) (n-K₈)

9,9'-(Hexane-1,6-diyl)bis(9H-carbazole-3-carbaldehyde) (**2**, 0.5 g, 1.058 mmol), was dissolved in 10 mL of absolute methanol and to this mixture 1.2 eq of an active methylene compound like 1,3-dimethylbarbituric acid (0.33 g, 2.11 mmol) was added under an argon atmosphere and heated at 60 °C with stirring for 10 h. After completion of the reaction, the content was cooled to room temperature and the precipitated solid was filtered, washed with cold methanol, and collected. It was further recrystallized from the CHCl₃-hexane mixture to get the pure product **n-K₈** as a pale orange solid. Yield: 89%. Melting point: 202-204 °C.

¹H NMR (400 MHz, DMSO-d₆, δ ppm): 9.27 (s, 2H), 8.75 (s, 1H), 8.61 (s, 1H), 8.33-8.28 (t, 2H), 7.96-7.95 (d, 2H), 7.73-7.64 (m, 3H), 7.52-7.50 (t, 3H), 7.31-7.30 (m, 2H), 4.41-4.37 (m, 12H), 4.05-4.01 (m, 4H), 1.99-0.83 (m, 8H). **¹³C NMR** (400 MHz, DMSO-d₆, δ ppm): 160.06, 142.28, 141.09, 127.61, 127.13, 127.08, 125.89, 123.06, 122.55, 119.14, 114.43, 109.82, 107.84, 77.36, 77.24, 77.04, 76.72, 55.46, 47.80, 39.51, 31.01, 28.82, 24.42, 23.02, 14.03, 10.09. Anal. Calcd. for $C_{44}H_{40}N_6O_6$: C, 70.57; H, 5.38; N, 11.22 and found C, 70.50; H, 5.39; N, 11.21. **FT-IR (ATR)**, ν cm^{-1} : 2944 (C-H stretch), 2360 (C \equiv N stretch), 1661 (C=O stretch), 1595, 1544, 1491 (C=C stretch). **Mass (m/z)**: Calculated: 748.30; Obtained (M-H): 747.25.

Synthesis of 5,5'-((9,9'-(hexane-1,6-diyl)bis(9H-carbazole-9,3-diyl))bis(methanylylidene)) bis(pyrimidine-2,4,6(1H,3H,5H)-trione) (n-K₉)

The intermediate 9,9'-(hexane-1,6-diyl)bis(9H-carbazole-3-carbaldehyde) (**2**, 0.5 g, 1.058 mmol), was dissolved in 10 mL of absolute methanol and to this mixture 1.2 eq of an active methylene compound like barbituric acid (0.27 g, 2.11 mmol) was added under an argon atmosphere and heated at 60 °C with stirring for 10 h. After completion of the reaction, the content was cooled to room temperature, and the

precipitated solid was filtered, washed with cold methanol, and collected. It was further recrystallized from the CHCl_3 -hexane mixture to get the pure product **n-K₉** as a red solid. Yield: 91%. Melting point: 214-216 °C.

¹H NMR (400 MHz, DMSO-d₆, δ ppm): 11.31 (s, 2H), 11.19 (s, 2H), 9.29 (s, 2H), 8.75 (s, 1H), 8.62-8.60 (d, 1H), 8.52 (s, 1H), 8.33 (s, 1H), 8.18-8.17 (d, 2H), 7.72-7.64 (m, 5H), 7.52-7.50 (t, 2H), 7.32-7.28 (m, 2H), 4.42-4.40 (t, 4H), 1.73-1.33 (m, 8H). **¹³C NMR** (400 MHz, DMSO-d₆, δ ppm): 164.70, 162.89, 157.33, 150.76, 143.53, 141.16, 133.76, 129.98, 127.17, 123.91, 122.84, 122.63, 120.98, 120.91, 114.55, 110.64, 109.66, 28.73, 26.44. Anal. Calcd. for $\text{C}_{40}\text{H}_{32}\text{N}_6\text{O}_6$: C, 69.35; H, 4.66; N, 12.13 and found C, 69.28; H, 4.60; N, 12.11. **FT-IR (ATR)**, ν cm^{-1} : 3192 (N-H stretch), 3047, 2840 (C-H stretch), 2333 (C \equiv N stretch), 1664 (C=O stretch), 1529, 1495 (C=C stretch). **Mass (m/z)**: Calculated: 692.24; Obtained (M-H): 691.30.

Synthesis of 5,5'-((9,9'-(hexane-1,6-diyl)bis(9H-carbazole-9,3-diyl))bis(methanylylidene)) bis(1,3-diethyl-2-thioxodihydropyrimidine-4,6(1H,5H)-dione) (n-K₁₀)

9,9'-(Hexane-1,6-diyl)bis(9H-carbazole-3-carbaldehyde) (**2**, 0.5 g, 1.058 mmol), was dissolved in 10 mL of absolute methanol and to this mixture 1.2 eq of 1,3-diethyl-2-thiobarbituric acid (0.42 g, 2.11 mmol) was added under an argon atmosphere and heated at 60 °C with stirring for 10 h. After completion of the reaction, the content was cooled to room temperature and the precipitated solid was filtered, washed with cold methanol, and collected. It was further recrystallized from the CHCl_3 -hexane mixture to get the pure product **n-K₁₀** as bright orange solid. Yield: 86%. Melting point: 290-292 °C.

¹H NMR (400 MHz, DMSO-d₆, δ ppm): 8.75 (s, 2H), 8.32-8.28 (d, 4H), 7.96-7.95 (m, 2H), 7.73-7.71 (m, 2H), 7.66-7.63 (m, 2H), 7.52-7.49 (t, 2H), 7.31-7.28 (t, 2H), 4.49-4.30 (m, 12H), 1.72 (m, 4H), 1.31-1.05 (m, 16H). **¹³C NMR** (400 MHz, DMSO-d₆, δ ppm): 162.89, 157.33, 150.76, 143.53, 141.16, 133.76, 129.98, 127.17, 123.91, 122.84, 122.63, 120.98, 120.91, 114.55, 110.64, 109.66, 28.73, 26.44. Anal. Calcd. for $\text{C}_{48}\text{H}_{48}\text{N}_6\text{O}_4\text{S}_2$: C, 68.87; H, 5.78; N, 10.04 and found C, 68.91; H, 5.72; N, 10.01. **FT-IR (ATR)**, ν cm^{-1} : 3109 (N-H stretch), 2979, 2931 (C-H stretch), 2361 (C \equiv N stretch), 1691 (C=O stretch), 1531, 1497 (C=C stretch). **Mass (m/z)**: Calculated: 836.32; Obtained (M-H): 835.20.

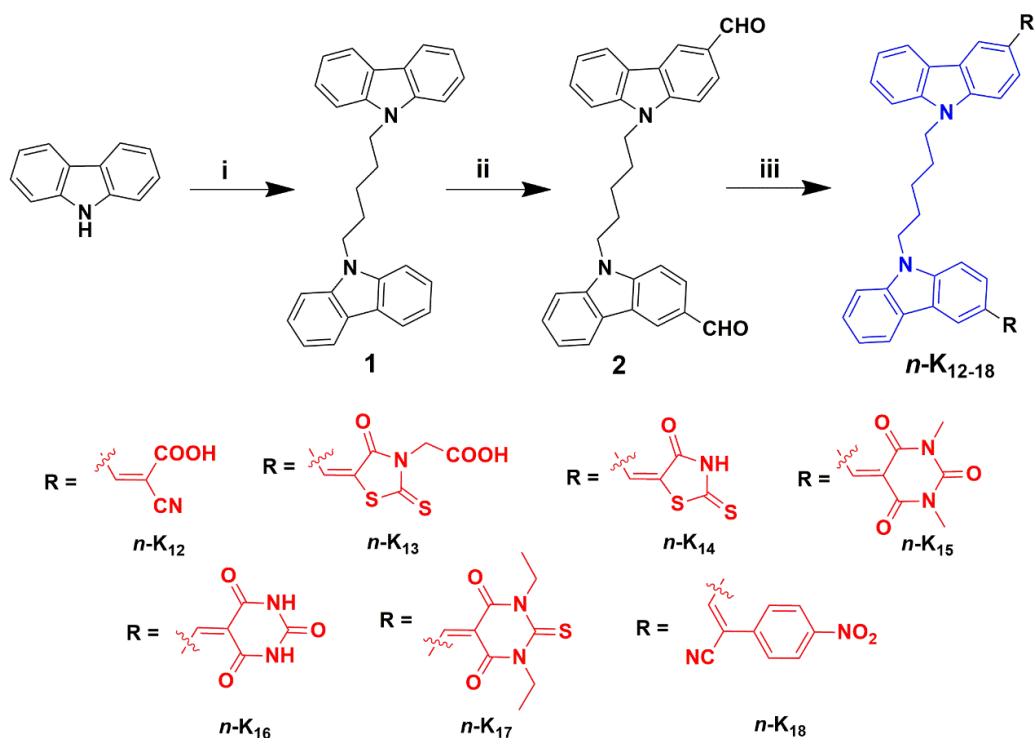
Synthesis of (2Z,2'Z)-3,3'-(9,9'-(hexane-1,6-diyl)bis(9H-carbazole-9,3-diyl))bis(2-(4-nitrophenyl)acrylonitrile) (n-K₁₁)

A mixture of 9,9'-(hexane-1,6-diyl)bis(9H-carbazole-3-carbaldehyde) (**2**, 0.5 g, 1.058 mmol), and potassium *tert*-butoxide (0.58 g, 5.25 mmol) was dissolved in dry methanol (15 mL) and stirred at room temperature under an argon atmosphere for 15 min. Later, 4-nitrophenyl acetonitrile (0.34 g, 2.11 mmol) was added while stirring and the reaction mixture was refluxed for 6 h. The precipitate formed was filtered, washed with absolute methanol and finally, it was recrystallized from chloroform to obtain a brown solid. Yield: 89%. Melting point: 192-194 °C.

¹H NMR (400 MHz, DMSO-d₆, δ ppm): 8.75 (s, 2H), 8.32-8.27 (m, 9H), 7.96-7.94 (dd, 2H), 7.72-7.62 (d, 5H), 7.52-7.49 (t, 3H), 7.31-7.28 (t, 3H), 4.41-4.38 (t, 4H), 1.71 (m, 4H), 1.38 (m, 4H). ¹³C NMR (400 MHz, DMSO-d₆, δ ppm): 192.31, 143.94, 141.19, 128.66, 127.17, 122.63, 121.30, 120.57, 110.48, 110.19, 79.64, 42.84, 40.37, 40.23, 40.10, 39.96, 39.82, 39.68, 39.54, 28.70, 26.43. Anal. Calcd. for C₄₈H₃₆N₆O₄: C, 75.77; H, 4.77; N, 11.05 and found C, 75.70; H, 4.75; N, 11.03. FT-IR (ATR), ν cm⁻¹: 2942, 2826 (C-H stretch), 2207 (C≡N stretch), 1680 (C=O stretch), 1580, 1517 (C=C stretch). Mass (m/z): Calculated: 760.84; Obtained (M): 760.31.

2.3.2.1.3 Synthesis of chromophores n-K₁₂₋₁₈ (Series-3)

The synthetic pathways of seven new metal-free organic dyes n-K₁₂₋₁₈ are shown in **Scheme 2.3**. The necessary intermediates and final compounds were synthesized using the same procedures followed in **Series 2** by incorporating slight modification in the alkyl chain length. Unlike 1,6-dibromhexane in **Series 2**, here we have used 1,5-dibrompentane as a linker between carbazole twin molecules in order to study the effect of alkyl chain length on the performance of devices. The procedures, as well as characterization data, for the intermediates and the final dyes n-K₁₂₋₁₈ are given in the following section.



Scheme 2.3 Synthetic routes for the dyes ***n-K*₁₂₋₁₈**: (i) 1,5-Dibromopentane, NaH, DMF, RT, 12 h (ii) POCl₃, DMF, 110 °C, 2 h (iii) ***n-K*₁₂₋₁₄**: Cyanoacetic acid/rhodanine-3-acetic acid/rhodanine, ammonium acetate, glacial CH₃COOH, 110 °C, 12 h; ***n-K*₁₅₋₁₇**: 1,3-dimethylbarbituric acid/barbituric acid/ 1,3-diethyl-2-thiobarbituric acid, methanol, 60 °C, 10 h; ***n-K*₁₈**: 4-nitrophenyl acetonitrile, potassium *tert*-butoxide, methanol, 60 °C, 6 h.

1,5-Di(9H-carbazole-9-yl)pentane (**1**)

Off-white solid. Yield: 89%. Melting point: 103-104 °C. ¹H NMR (400 MHz, CDCl₃, δ ppm): 8.11-8.09 (d, 3H), 7.46-7.43 (m, 4H), 7.33-7.31 (d, 4H), 7.23-7.22 (t, 5H), 4.25-4.22 (t, 4H), 1.92-1.86 (m, 2H), 1.55 (m, 1H), 1.47-1.44 (m, 2H), 1.26 (m, 1H). Anal. Calcd. for C₂₉H₂₆N₂: C, 86.53; H, 6.51; N, 6.96; and found C, 86.59; H, 6.54; N, 6.92.

9,9'-(Pentane-1,5-diyl)bis(9H-carbazole-3-carbaldehyde) (**2**)

Light brown solid. Yield: 72 %. Melting point: 140-142 °C. ¹H NMR (400 MHz, CDCl₃, δ ppm): 10.07 (s, 2H), 8.58-8.58 (d, 2H), 7.95-7.93 (t, 2H), 7.49-7.48 (t, 2H), 7.47-7.46 (d, 2H), 7.36-7.28 (m, 6H), 4.27-4.25 (t, 4H), 1.84-1.81 (t, 3H), 1.58 (m, 1H), 1.37-1.34 (m, 2H). Anal. Calcd. for C₃₁H₂₆N₂O₂: C, 81.20; H, 5.72; N, 6.11;

and found C, 81.14; H, 5.76; N, 6.10. **FT-IR (ATR)**, ν cm^{-1} : 2956, 2927 (C-H), 1681 (C=O), 1587, 1482 (C=C).

(2Z,2'Z)-3,3'-(9,9'-(Pentane-1,5-diyl)bis(9H-carbazole-9,3-diyl))bis(2-cyano acrylic acid) (n-K₁₂)

Bright yellow solid, Yield: 90%. Melting point: 290-292 °C. **¹H NMR** (400 MHz, DMSO-d₆, δ ppm): 10.05 (s, 1H), 8.81 (s, 2H), 8.45 (s, 2H), 8.25-8.24 (d, 2H), 8.15-8.13 (d, 2H), 7.73-7.71 (d, 2H), 7.63-7.61 (d, 2H), 7.52-7.49 (t, 2H), 7.32-7.30 (t, 2H), 4.42-4.40 (t, 4H), 1.91-1.80 (m, 4H), 1.36 (m, 2H). **¹³C NMR** (400 MHz, DMSO-d₆, δ ppm): 192.24, 164.65, 155.60, 143.95, 143.11, 141.12, 128.64, 128.11, 127.32, 127.14, 125.97, 122.90, 122.78, 122.40, 120.94, 120.77, 120.53, 119.05, 117.84, 110.67, 110.15, 109.61, 98.92, 28.62, 24.67. Anal. Calcd. for C₃₇H₂₈N₄O₄: C, 74.99; H, 4.76; N, 9.45 and found C, 74.21; H, 4.12; N, 9.41. **FT-IR (ATR)**, ν cm^{-1} : 2942, 2860 (C-H stretch), 2226 (C≡N stretch), 1687 (C=O stretch), 1581, 1495 (C=C stretch). **Mass (m/z)**: Calculated: 592.21; Obtained (M-H): 591.25.

2-((E)-5-((9-(5-(3-((Z)-(3-(Carboxymethyl)-4-oxo-2-thioxothiazolidin-5-ylidene)methyl)-9H-carbazole-9-yl)pentyl)-9H-carbazole-3-yl)methylene)-4-oxo-2-thioxothiazolidin-3-yl)acetic acid (n-K₁₃)

Pale yellow solid, Yield: 83%. Melting point: 352-354 °C. **¹H NMR** (400 MHz, DMSO-d₆, δ ppm): 10.05 (s, 1H), 8.73 (s, 1H), 8.47-8.45 (m, 2H), 8.28-8.26 (m, 2H), 8.06-8.04 (m, 2H), 7.93-7.91 (d, 1H), 7.66-7.59 (m, 4H), 7.50-7.48 (t, 2H), 7.30-7.28 (t, 2H), 4.77-4.76 (s, 4H), 4.41-4.37 (m, 4H), 1.80-1.79 (m, 4H), 1.35-1.34 (m, 2H). **¹³C NMR** (400 MHz, DMSO-d₆, δ ppm): 193.66, 192.30, 166.99, 143.95, 141.90, 141.20, 141.13, 129.03, 128.67, 127.17, 124.94, 123.45, 122.69, 122.32, 121.29, 120.57, 117.77, 110.99, 110.47, 110.18, 28.69, 26.43. Anal. Calcd. for C₄₁H₃₂N₄O₆S₄: C, 61.17; H, 4.01; N, 6.96 and found C, 61.32; H, 4.12; N, 6.92. **FT-IR (ATR)**, ν cm^{-1} : 3049, 2936 (C-H stretch), 2361 (C≡N stretch), 1700 (C=O stretch), 1577, 1494 (C=C stretch). **Mass (m/z)**: Calculated: 804.12; Obtained (M-H): 803.15.

(5Z,5'E)-5,5'-((9,9'-(Pentane-1,5-diyl)bis(9H-carbazole-9,3-diyl))bis(methanylylidene))bis(2-thioxothiazolidin-4-one) (n-K₁₄)

Yellowish orange solid, Yield: 83%. Melting point: 334-336 °C. ¹H NMR (400 MHz, DMSO-d₆, δ ppm): 8.73 (s, 1H), 8.39-8.24 (m, 4H), 7.92-7.82 (m, 2H), 7.67-7.59 (m, 6H), 7.58-7.48 (m, 2H), 7.29-7.27 (t, 2H), 4.41-4.32 (m, 4H), 1.80 (m, 4H), 1.36-1.34 (m, 2H). ¹³C NMR (400 MHz, DMSO-d₆, δ ppm): 196.00, 192.22, 170.04, 143.95, 141.64, 141.19, 141.06, 134.00, 128.70, 128.65, 127.17, 126.07, 124.30, 124.16, 123.31, 122.69, 122.61, 122.30, 121.60, 121.23, 120.67, 120.54, 120.37, 119.06, 110.80, 110.41, 110.15, 109.61, 42.90, 28.82, 24.70. Anal. Calcd. for C₃₇H₂₈N₄O₂S₄: C, 64.51; H, 4.10; N, 8.13 and found C, 64.62; H, 4.12; N, 8.10. **FT-IR (ATR)**, ν cm⁻¹: 3137, 3045, 2850 (C-H stretch), 2371 (C≡N stretch), 1681 (C=O stretch), 1571 (C=C). **Mass (m/z)**: Calculated: 688.11; Obtained (M-H): 687.15.

5,5'-((9,9'-(Pentane-1,5-diyl)bis(9H-carbazole-9,3-diyl))bis(methanylylidene))bis(1,3-dimethylpyrimidine-2,4,6(1H,3H,5H)-trione) (n-K₁₅)

Orange solid, Yield: 84%. Melting point: 296-298 °C. ¹H NMR (400 MHz, DMSO-d₆, δ ppm): 9.27 (s, 1H), 8.75 (s, 1H), 8.61 (s, 1H), 8.33-8.28 (t, 2H), 7.96-7.95 (d, 2H), 7.73-7.64 (m, 3H), 7.52-7.50 (t, 3H), 7.31-7.30 (m, 2H), 4.41 (m, 12H), 4.05-4.01 (m, 4H), 1.99 (m, 2H), 1.72 (m, 2H), 1.19-1.17 (m, 2H). ¹³C NMR (400 MHz, DMSO-d₆, δ ppm): 164.70, 162.89, 157.33, 150.76, 143.53, 141.16, 133.76, 129.98, 127.17, 123.91, 122.84, 122.63, 120.98, 120.91, 114.55, 110.64, 109.66, 28.73, 26.44. Anal. Calcd. for C₄₃H₃₈N₆O₆: C, 70.29; H, 5.21; N, 11.44 and found C, 70.32; H, 5.26; N, 11.41. **FT-IR (ATR)**, ν cm⁻¹: 3051, 2952, 2927 (C-H stretch), 2360 (C≡N stretch), 1650 (C=O stretch), 1541, 1465 (C=C stretch). **Mass (m/z)**: Calculated: 734.29; Obtained (M): 734.25.

5,5'-((9,9'-(Pentane-1,5-diyl)bis(9H-carbazole-9,3-diyl))bis(methanylylidene))bis(pyrimidine-2,4,6(1H,3H,5H)-trione) (n-K₁₆)

Bright red solid, Yield: 89%. Melting point: 216-218 °C. ¹H NMR (400 MHz, DMSO-d₆, δ ppm): 11.32 (s, 2H), 11.20 (s, 2H), 10.05 (s, 1H), 9.28-9.27 (m, 1H), 8.73 (s, 1H), 8.60-8.59 (m, 3H), 8.28-8.27 (d, 1H), 8.17-8.12 (m, 1H), 7.92-7.91 (m, 2H), 7.67-7.61 (m, 3H), 7.50-7.49 (m, 2H), 7.32-7.28 (m, 2H), 4.41-4.40 (t, 4H),

1.81-1.78 (m, 4H), 1.39-1.35 (m, 2H). ^{13}C NMR (400 MHz, DMSO-d₆, δ ppm): 164.72, 162.90, 157.36, 150.76, 143.97, 143.56, 141.17, 133.79, 129.94, 128.66, 127.17, 123.92, 122.85, 122.69, 122.63, 121.24, 120.90, 120.55, 114.53, 110.69, 110.51, 110.19, 109.71, 43.03, 28.82, 24.69. Anal. Calcd. for C₃₉H₃₀N₆O₆: C, 69.02; H, 4.46; N, 12.38 and found C, 69.12; H, 4.40; N, 12.32. **FT-IR (ATR)**, ν cm⁻¹: 3203 (N-H stretch), 3050, 2944, 2835 (C-H stretch), 2320 (C \equiv N stretch), 1664 (C=O stretch), 1594, 1522, 1494 (C=C stretch). **Mass (m/z)**: Calculated: 678.22; Obtained (M-H): 677.30.

5,5'-((9,9'-(Pentane-1,5-diyl)bis(9H-carbazole-9,3-diyl))bis(methanylylidene))bis(1,3-diethyl-2-thioxodihydropyrimidine-4,6(1H,5H)-dione) (n-K₁₇)

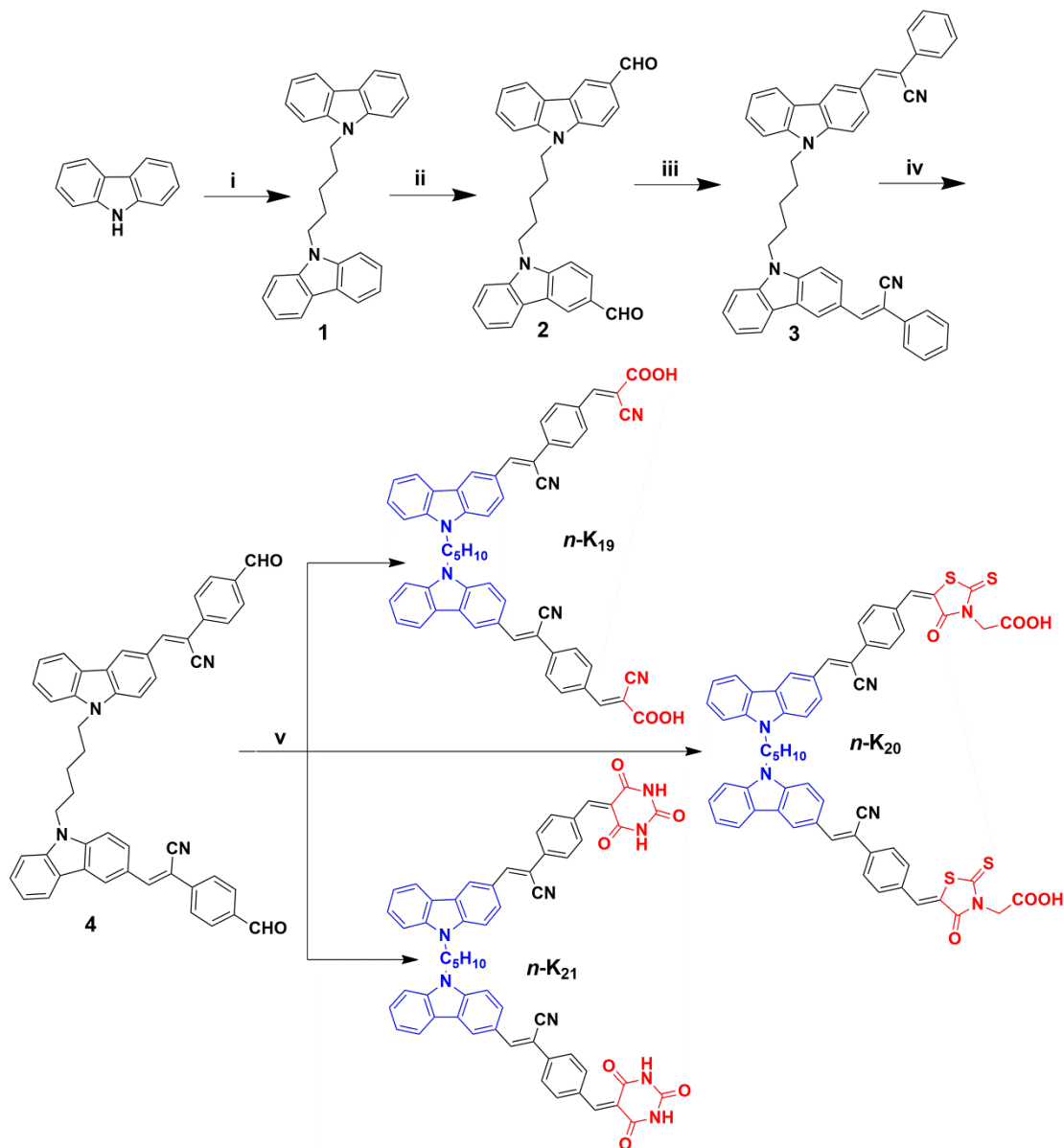
Bright orange solid, Yield: 82%. Melting point: 258-260 °C. ^1H NMR (400 MHz, DMSO-d₆, δ ppm): 8.74 (s, 2H), 8.28-8.27 (d, 1H), 8.14-8.12 (d, 1H), 7.95-7.91 (m, 2H), 7.70-7.61 (m, 4H), 7.51-7.50 (m, 2H), 7.41-7.39 (t, 1H), 7.31-7.28 (t, 2H), 7.19-7.17 (t, 1H), 4.48-4.32 (m, 12H), 1.81-1.80 (m, 6H), 1.24-1.16 (m, 12H). ^{13}C NMR (400 MHz, DMSO-d₆, δ ppm): 164.73, 150.77, 127.18, 122.61, 121.25, 120.51, 42.95, 40.49, 40.37, 40.23, 40.09, 39.95, 39.81, 39.67, 39.53, 28.83, 24.69. Anal. Calcd. for C₄₇H₄₆N₆O₄S₂: C, 68.59; H, 5.63; N, 10.21 and found C, 68.62; H, 5.59; N, 10.20. **FT-IR (ATR)**, ν cm⁻¹: 2982, 2926, 2857 (C-H stretch), 2360 (C \equiv N stretch), 1663 (C=O stretch), 1519, 1493 (C=C stretch). **Mass (m/z)**: Calculated: 822.30; Obtained (M-H): 821.34.

(2Z,2'Z)-3,3'-((9,9'-(Pentane-1,5-diyl)bis(9H-carbazole-9,3-diyl))bis(2-(4-nitrophenyl)acrylonitrile) (n-K₁₈)

Brown solid, Yield: 83%. Melting point: 192-194 °C. ^1H NMR (400 MHz, DMSO-d₆, δ ppm): 8.74-8.73 (m, 4H), 8.28-8.27 (m, 3H), 7.93-7.91 (m, 4H), 7.78-7.58 (m, 7H), 7.51-7.48 (t, 3H), 7.31-7.28 (t, 3H), 4.42-4.39 (t, 4H), 1.82-1.80 (m, 4H), 1.39-1.34 (m, 2H). ^{13}C NMR (400 MHz, DMSO-d₆, δ ppm): 148.66, 148.29, 141.32, 140.28, 126.92, 126.27, 124.80, 122.06, 121.49, 118.12, 117.77, 110.31, 108.83, 107.56, 107.01, 76.32, 76.00, 75.68, 55.08, 55.03, 46.79, 38.49, 29.98, 27.78, 23.39, 21.99, 12.99. Anal. Calcd. for C₄₇H₃₄N₆O₄: C, 75.59; H, 4.59; N, 11.25 and found C, 75.52; H, 4.51; N, 11.23. **FT-IR (ATR)**, ν cm⁻¹: 3050 (C-H stretch), 2314

($C\equiv N$ stretch), 1590, 1515, 1497 ($C=C$ stretch). **Mass (m/z):** Calculated: 746.26; Obtained (M-H): 745.12.

2.3.2.1.4 Synthesis of chromophores *n-K*₁₉₋₂₁ (Series-4)



Scheme 2.4 Synthetic routes for the dyes *n-K*₁₉₋₂₁: (i) 1,5-Dibromopentane, NaH, DMF, RT, 12 h (ii) POCl₃, DMF, 110 °C, 2 h (iii) Phenylacetonitrile, potassium *tert*-butoxide, methanol, 70 °C, 12 h; (iv) POCl₃, DMF, 110 °C, 12 h; (v) *n-K*₁₉₋₂₀: Cyanoacetic acid/ rhodanine-3-acetic acid, ammonium acetate, glacial CH₃COOH, 110 °C, 12 h; *n-K*₂₁: Barbituric acid, methanol, 60 °C, 10 h

The synthetic pathways of four new metal-free organic dyes **n-K₁₉₋₂₁** are shown in **Scheme 2.4**. The intermediates **1** and **2** were synthesized according to the procedures documented under the synthesis of **Series 3**. Here, intermediate **2** was condensed with phenylacetonitrile by the Knoevenagel condensation to obtain intermediate **3**. Furthermore, intermediate **3** was subjected to the Vilsmeier-Hack reaction to form the key precursor **4**. In the final step, the target molecules **n-K₁₉₋₂₁** were obtained in good yield by following the Knoevenagel condensation of precursor **4** with cyanoacetic acid, rhodanine-3-acetic acid, and barbituric acid, respectively. The synthetic procedures for the intermediates and the final dyes **n-K₁₉₋₂₁** are given in the following section.

Synthesis of (2Z,2'Z)-3,3'-(9,9'-(pentane-1,5-diyl)bis(9H-carbazole-9,3-diyl))bis(2-phenylacrylonitrile) (3)

Initially, the starting material 9,9'-(pentane-1,5-diyl)bis(9H-carbazole-3-carbaldehyde) (**2**, 1 g, 2.18 mmol) was dissolved in methanol (15 mL) and stirred at room temperature. To this mixture, potassium *tert*-butoxide (1.22 g, 10.90 mmol) was added with constant stirring. Finally, phenylacetonitrile (0.5 mL, 4.36 mmol) was added to the same reaction mixture and the reaction mixture was refluxed at 70 °C for 12 h. After the completion of the reaction, the reaction mixture was cooled down, the bright yellow precipitate formed was filtered off, washed with cold methanol thoroughly, and finally, it was recrystallized from chloroform-hexane to give a fine yellow solid of **3**. Yield: 83 %. Melting point: 170-172 °C.

¹H NMR (400 MHz, CDCl₃, δ ppm): 8.58-8.58 (d, 2H), 8.15-8.15 (d, 2H), 8.13-8.13 (d, 2H), 7.94-7.94 (d, 2H), 7.93-7.70 (m, 3H), 7.48-7.44 (m, 5H), 7.36-7.30 (m, 10H), 4.27-4.25 (t, 4H), 1.92-1.86 (m, 2H), 1.59-1.39 (m, 4H). Anal. Calcd. for C₄₇H₃₆N₄: C, 85.95; H, 5.52; N, 8.53; and found C, 84.64; H, 5.48; N, 8.10.

Synthesis of (2Z,2'Z)-3,3'-(9,9'-(pentane-1,5-diyl)bis(9H-carbazole-9,3-diyl))bis(2-(4-formylphenyl)acrylonitrile) (4)

In a dry and cleaned two-neck round bottom flask, freshly distilled DMF (2.54 mL, 3.2 mmol) was taken and POCl₃ (3.48 mL, 3.7 mmol) was added drop-wise with constant stirring at 0 °C under an argon atmosphere to obtain a glassy white salt. To

this mixture, compound **3** (1 g, 1.49 mmol) dissolved in dichloroethane (5 mL) was added slowly. The reaction mixture was refluxed at 110 °C for 12 h under inert conditions only. The reaction was monitored carefully by the TLC technique. After completion of the reaction, the obtained reaction mass was cooled to room temperature and poured into ice-cold water, and basified by using a 5 M NaOH solution. Further, the product formed was extracted with dichloromethane (50 mL x 4). The organic layer was dried using anhydrous sodium sulphate. The solvent obtained was evaporated under reduced pressure to get a crude oily product. The impure residue was later purified by column chromatography on silica gel (100-200 mesh) to brown solid (**4**). Yield: 76 %. Melting point: 194-196 °C.

¹H NMR (400 MHz, CDCl₃, δ ppm): 10.08 (s, 2H), 8.58 (s, 2H), 8.15-8.13 (d, 3H), 7.94-7.94 (d, 2H), 7.93-7.72 (m, 3H), 7.48-7.44 (m, 5H), 7.36-7.30 (m, 9H), 4.27-4.25 (t, 4H), 1.92-1.86 (m, 2H), 1.59-1.39 (m, 4H). Anal. Calcd. for C₄₉H₃₆N₄O₂: C, 82.56; H, 5.09; N, 7.86; and found C, 82.50; H, 5.00; N, 7.81.

General method for the synthesis of dyes n-K₁₉₋₂₀

A mixture of intermediate **4** (1 eq), ammonium acetate (11 eq), and glacial acetic acid (10-15 mL) was taken in an RB flask and stirred constantly. To this reaction mixture, an active methylene compound such as cyanoacetic acid or rhodanine-3-acetic acid (2 eq) was added and then refluxed for 12 h under an argon atmosphere. The completion of the reaction was monitored using the TLC technique. After its completion, the reaction mixture was cooled to room temperature and was poured into ice-cold water. The solid obtained was filtered, washed with cold water, and finally, dried. The crude product was recrystallized from absolute methanol to get the pure product **n-K₁₉₋₂₀**.

(2E,2'E)-3,3'-(((1Z,1'Z)-(9,9'-(Pentane-1,5-diyl)bis(9H-carbazole-9,3-diyl))bis(1-cyanoethene-2,1-diyl))bis(4,1-phenylene))bis(2-cyanoacrylic acid) (n-K₁₉)

Bright yellow solid, Yield: 88 %. Melting point: 312-314 °C. ¹H NMR (400 MHz, DMSO-d₆, δ ppm): 8.79-8.68 (m, 2H), 8.31-8.15 (m, 8H), 7.79 (s, 6H), 7.52-7.43 (m, 10H), 4.42 (t, 4H), 1.76 (m, 2H), 1.22 (m, 4H). ¹³C NMR (400 MHz, DMSO-d₆, δ ppm): 162.92, 150.55 143.94, 143.83, 141.19, 141.12, 128.41, 128.12,

127.33, 127.15, 127.03, 126.06, 124.42, 122.92, 122.85, 122.69, 122.64, 122.41, 121.28, 120.99, 120.79, 120.56, 117.79, 110.67, 110.45, 110.15, 98.77, 90.42, 42.89, 42.83, 31.15, 28.69, 26.42. Anal. Calcd. for $C_{55}H_{38}N_6O_4$: C, 78.00; H, 4.52; N, 9.92 and found C, 77.18; H, 4.12; N, 9.59. **FT-IR (ATR)**, ν cm^{-1} : 3414.24 (O-H stretch), 2925, 2863 (C-H stretch), 2210 (C \equiv N stretch), 1667 (C=O stretch), 1584, 1439 (C=C stretch). **Mass (m/z)**: Calculated: 846.93; Obtained (M-H): 845.28.

2-((E)-5-(4-((Z)-2-(9-(5-(3-((Z)-2-(4-((Z)-3-(Carboxymethyl)-4-oxo-2-thioxothiazolidin-5-ylidene)methyl)phenyl)-2-cyanovinyl)-9H-carbazol-9-yl)pentyl)-9H-carbazol-3-yl)-1-cyanovinyl)benzylidene)-4-oxo-2-thioxothiazolidin-3-yl)acetic acid (n-K₂₀)

Pale orange solid, Yield: 93%. Melting point: 382-384 °C. **¹H NMR** (400 MHz, DMSO-d₆, δ ppm): 8.72 (s, 2H), 8.66 (s, 2H), 8.10-8.02 (m, 8H), 7.70 (m, 3H), 7.59-7.57 (m, 3H), 7.49-7.47 (m, 3H), 7.38 (s, 2H), 7.29-7.27 (m, 3H), 4.66 (t, 4H), 4.34 (t, 4H), 1.91-1.79 (m, 4H), 1.23 (m, 2H). **¹³C NMR** (400 MHz, DMSO-d₆, δ ppm): 174.29, 166.99, 143.95, 141.90, 141.20, 141.13, 129.03, 128.67, 127.30, 127.17, 127.04, 124.93, 124.46, 124.08, 123.45, 122.69, 122.64, 122.32, 121.38, 121.29, 120.57, 117.77, 110.99, 110.69, 110.47, 42.85, 28.49, 26.41. Anal. Calcd. for $C_{59}H_{42}N_6O_6S_4$: C, 66.90; H, 4.00; N, 7.93 and found C, 65.42; H, 3.92; N, 7.90. **FT-IR (ATR)**, ν cm^{-1} : 3403 (O-H stretch), 2925, 2863 (C-H stretch), 2209 (C \equiv N stretch), 1709 (C=O stretch), 1580, 1484 (C=C stretch). **Mass (m/z)**: Calculated: 1059.26; Obtained (M-H): 1058.10.

Synthesis of (2Z,2'Z)-3,3'-(9,9'-(pentane-1,5-diyl)bis(9H-carbazole-9,3-diyl))bis(2-(4-((2,4,6-trioxotetrahydropyrimidin-5(2H)-ylidene)methyl)phenyl)acrylonitrile) (n-K₂₁)

The intermediate **4** (0.5 g, 0.70 mmol), was dissolved in 10 mL of absolute methanol and to this mixture 2 eq of an active methylene compound like barbituric acid (0.17 g, 1.40 mmol) was added under an argon atmosphere and heated at 60 °C with stirring for 10 h. After completion of the reaction, the content was cooled to room temperature, and the precipitated solid was filtered, washed with cold methanol, and collected. It was further recrystallized from the CHCl₃-hexane mixture to get the pure product **n-K₂₁** as a brownish-red solid. Yield: 91%. Melting point: 256-258 °C.

¹H NMR (400 MHz, DMSO-d₆, δ ppm): 11.21 (s, 2H), 10.78 (s, 2H), 9.90 (s, 1H), 8.71-8.53 (m, 4H), 8.12 (s, 5H), 7.97-7.44 (m, 16 H), 4.04-4.02 (t, 4H), 1.99-1.82 (m, 3H), 1.37-1.06 (m, 3H). **¹³C NMR** (400 MHz, DMSO-d₆, δ ppm): 164.76, 162.84, 157.33, 150.76, 143.53, 143.16, 133.70, 129.98, 127.17, 123.91, 122.89, 122.66, 120.98, 120.91, 114.55, 110.44, 109.63, 44.03, 28.73, 26.64. Anal. Calcd. for C₅₇H₄₀N₈O₆: C, 73.38; H, 4.32; N, 12.01 and found C, 71.92; H, 4.30; N, 12.06. **FT-IR (ATR)**, ν cm⁻¹: 3205 (N-H stretch), 3050, 2944, (C-H stretch), 2318 (C≡N stretch), 1669 (C=O stretch), 1584, 1532 (C=C stretch). **Mass (m/z)**: Calculated: 932.98; Obtained (M-H): 931.20.

2.3.2.1.5 Synthesis of chromophores *n*-**K**₂₂₋₂₄ (**Series-5**)

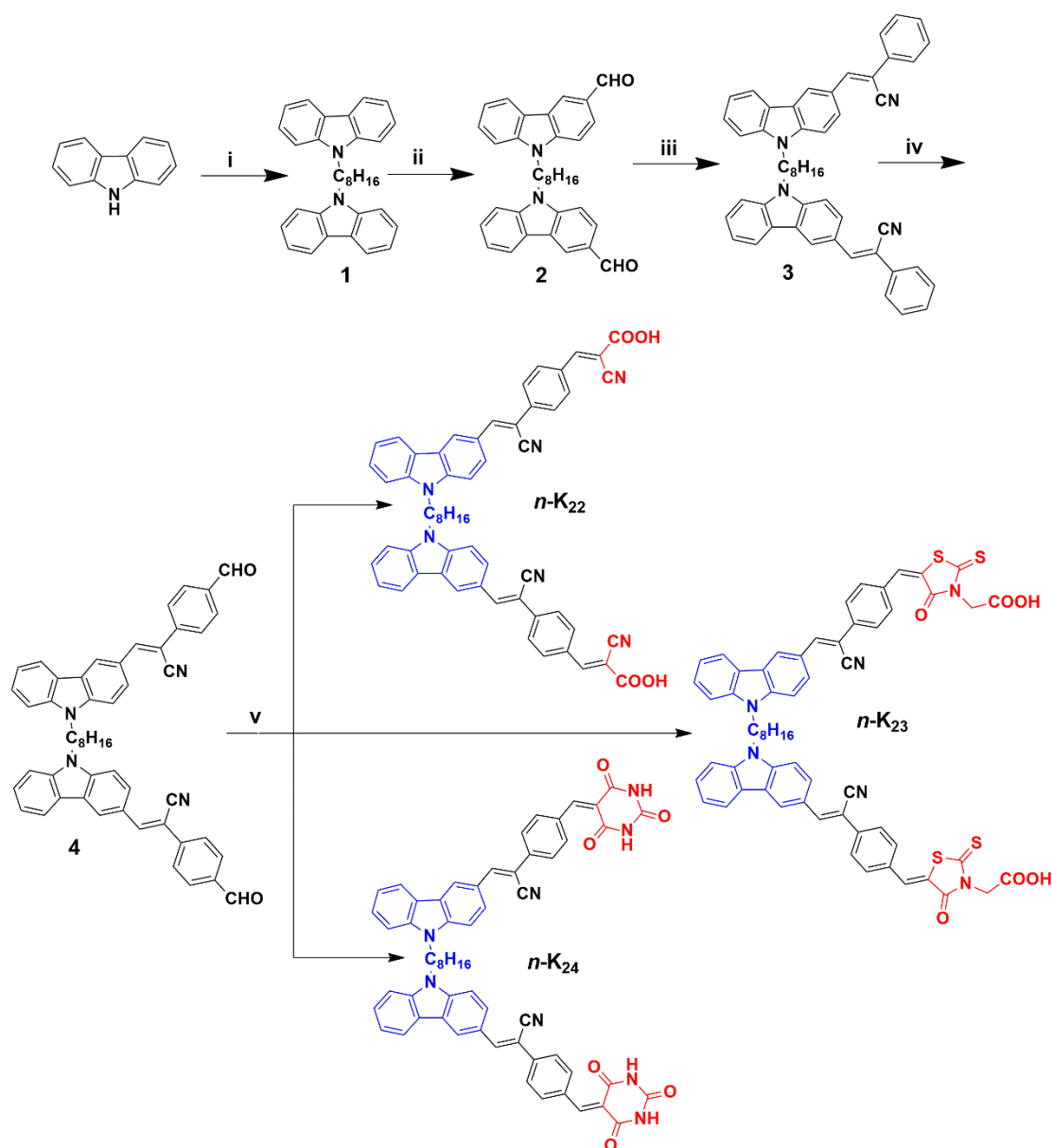
The synthetic pathways of four new metal-free organic dyes *n*-**K**₂₂₋₂₄ are shown in **Scheme 2.5**. All the required intermediates and target molecules were synthesized from the similar well-documented procedure as shown in **Series 4** by making a slight modification in the alkyl chain length. Unlike 1,5-dibromopentane in **Series 4**, here, 1,8-dibromooctane was used as a linker between carbazole twin molecules in order to study the effect of alkyl chain length on the performance of the devices. The characterization data for the intermediates and the final dyes *n*-**K**₂₂₋₂₄ are given in the following section.

1,8-Di(9H-carbazol-9-yl)octane (1)

Off-white solid, Yield: 86%. Melting point: 96-98 °C. **¹H NMR** (400 MHz, CDCl₃, δ ppm): 8.10-8.08 (d, 4H), 7.44-7.41 (m, 4H), 7.33-7.31 (d, 4H), 7.23-7.20 (m, 4H), 4.25-4.22 (t, 4H), 1.83-1.81 (m, 4H), 1.57 (m, 1H), 1.39-1.36 (m, 5H), 1.26-0.87 (m, 2H). Anal. Calcd. for C₃₂H₃₂N₂: C, 86.44; H, 7.25; N, 6.30; and found C, 86.19; H, 7.09; N, 6.02.

9,9'-(Octane-1,8-diyl)bis(9H-carbazole-3-carbaldehyde) (2)

Pale yellowish-brown solid, Yield: 76 %. Melting point: 118-120 °C. **¹H NMR** (400 MHz, CDCl₃, δ ppm): 10.07 (s, 2H), 8.58-8.57 (d, 2H), 7.99-7.97 (d, 3H), 7.52-7.48 (m, 3H), 7.42-7.39 (m, 4H), 7.31-7.28 (m, 2H), 4.29-4.26 (t, 4H), 1.85-1.79 (m, 4H), 1.30-1.25 (m, 8H). Anal. Calcd. for C₃₄H₃₂N₂O₂: C, 81.57; H, 6.44; N, 5.60; and found C, 81.14; H, 6.46; N, 5.10.



Scheme 2.5 Synthetic routes for the dyes *n*-K₂₂₋₂₄: (i) 1,8-Dibromooctane, NaH, DMF, RT, 12 h (ii) POCl₃, DMF, 110 °C, 2 h (iii) Phenylacetonitrile, sodium methoxide, methanol, RT, 6 h; (iv) POCl₃, DMF, 110 °C, 12 h; (v) *n*-K₂₂₋₂₃: Cyanoacetic acid/ rhodanine-3-acetic acid, ammonium acetate, glacial CH₃COOH, 110 °C, 12 h; *n*-K₂₄: Barbituric acid, methanol, 60 °C, 10 h

(2*Z*,2'*Z*)-3,3'-(9,9'-(Octane-1,8-diyl)bis(9*H*-carbazole-9,3-diyl))bis(2-phenylacrylonitrile) (**3**)

Fine yellow solid, Yield: 85 %. Melting point: 130-132 °C. ¹H NMR (400 MHz, CDCl₃, δ ppm): 8.58-8.58 (d, 2H), 8.15-8.15 (d, 2H), 8.13-8.13 (d, 2H), 7.94-

7.94 (d, 2H), 7.93-7.70 (m, 3H), 7.48-7.44 (m, 5H), 7.36-7.30 (m, 10H), 4.27-4.25 (t, 4H), 1.92-1.86 (m, 4H), 1.59-1.39 (m, 8H). Anal. Calcd. for C₅₉H₄₂N₄: C, 85.93; H, 6.06; N, 8.02; and found C, 84.54; H, 5.96; N, 8.10.

(2Z,2'Z)-3,3'-(9,9'-(Octane-1,8-diyl)bis(9H-carbazole-9,3-diyl))bis(2-(4-formylphenyl)acrylonitrile) (4)

Brown solid, Yield: 71 %. Melting point: 152-154 °C. ¹H NMR (400 MHz, CDCl₃, δ ppm): 10.08 (s, 2H), 8.58 (s, 2H), 8.15-8.13 (d, 3H), 7.94-7.94 (d, 2H), 7.93-7.72 (m, 3H), 7.48-7.44 (m, 5H), 7.36-7.30 (m, 9H), 4.27-4.25 (t, 4H), 1.92-1.86 (m, 4H), 1.59-1.39 (m, 8H). Anal. Calcd. for C₅₂H₄₂N₄O₂: C, 82.73; H, 5.61; N, 7.42; and found C, 82.14; H, 5.16; N, 7.21.

(2E,2'E)-3,3'-(((1Z,1'Z)-(9,9'-(Octane-1,8-diyl)bis(9H-carbazole-9,3-diyl))bis(1-cyanoethene-2,1-diyl))bis(4,1-phenylene))bis(2-cyanoacrylic acid) (n-K₂₂)

Bright brown-yellow solid, Yield: 83 %. Melting point: 286-288 °C. ¹H NMR (400 MHz, DMSO-d₆, δ ppm): 8.79-8.68 (m, 3H), 8.31-8.15 (m, 7H), 7.79 (s, 6H), 7.52-7.43 (m, 10H), 4.42 (t, 4H), 1.76 (m, 4H), 1.22 (m, 8H). ¹³C NMR (400 MHz, DMSO-d₆, δ ppm): 164.70, 162.89, 157.33, 150.76, 143.53, 141.16, 133.76, 129.98, 127.17, 123.91, 122.84, 122.63, 122.63, 120.98, 120.91, 114.55, 110.64, 109.66, 28.73, 26.44. Anal. Calcd. for C₅₈H₄₄N₆O₄: C, 78.36; H, 4.99; N, 9.45 and found C, 78.21; H, 4.32; N, 9.40. **FT-IR (ATR)**, ν cm⁻¹: 2942, 2860 (C-H stretch), 2226 (C≡N stretch), 1687 (C=O stretch), 1581, 1495 (C=C stretch). **Mass (m/z)**: Calculated: 889.01; Obtained (M-H): 888.31.

2-((E)-5-(4-((Z)-2-(9-(8-(3-((Z)-2-(4-((Z)-3-(Carboxymethyl)-4-oxo-2-thioxothiazolidin-5-ylidene)methyl)phenyl)-2-cyanovinyl)-9H-carbazol-9-yl)octyl)-9H-carbazol-3-yl)-1-cyanovinyl)benzylidene)-4-oxo-2-thioxothiazolidin-3-yl)acetic acid (n-K₂₃)

Pale greenish-yellow solid, Yield: 89 %. Melting point: 348-350 °C. ¹H NMR (400 MHz, DMSO-d₆, δ ppm): 8.72 (s, 2H), 8.66 (s, 2H), 8.10-8.02 (m, 8H), 7.70 (m, 3H), 7.59-7.57 (m, 3H), 7.49-7.47 (m, 3H), 7.38 (s, 2H), 7.29.27 (m, 3H), 4.66 (t, 4H), 4.34 (t, 4H), 1.91-79 (m, 8H), 1.23 (m, 4H). ¹³C NMR (400 MHz, DMSO-d₆, δ ppm): 191.85, 168.99, 146.15, 142.90, 141.20, 141.13, 129.03, 128.67, 127.17,

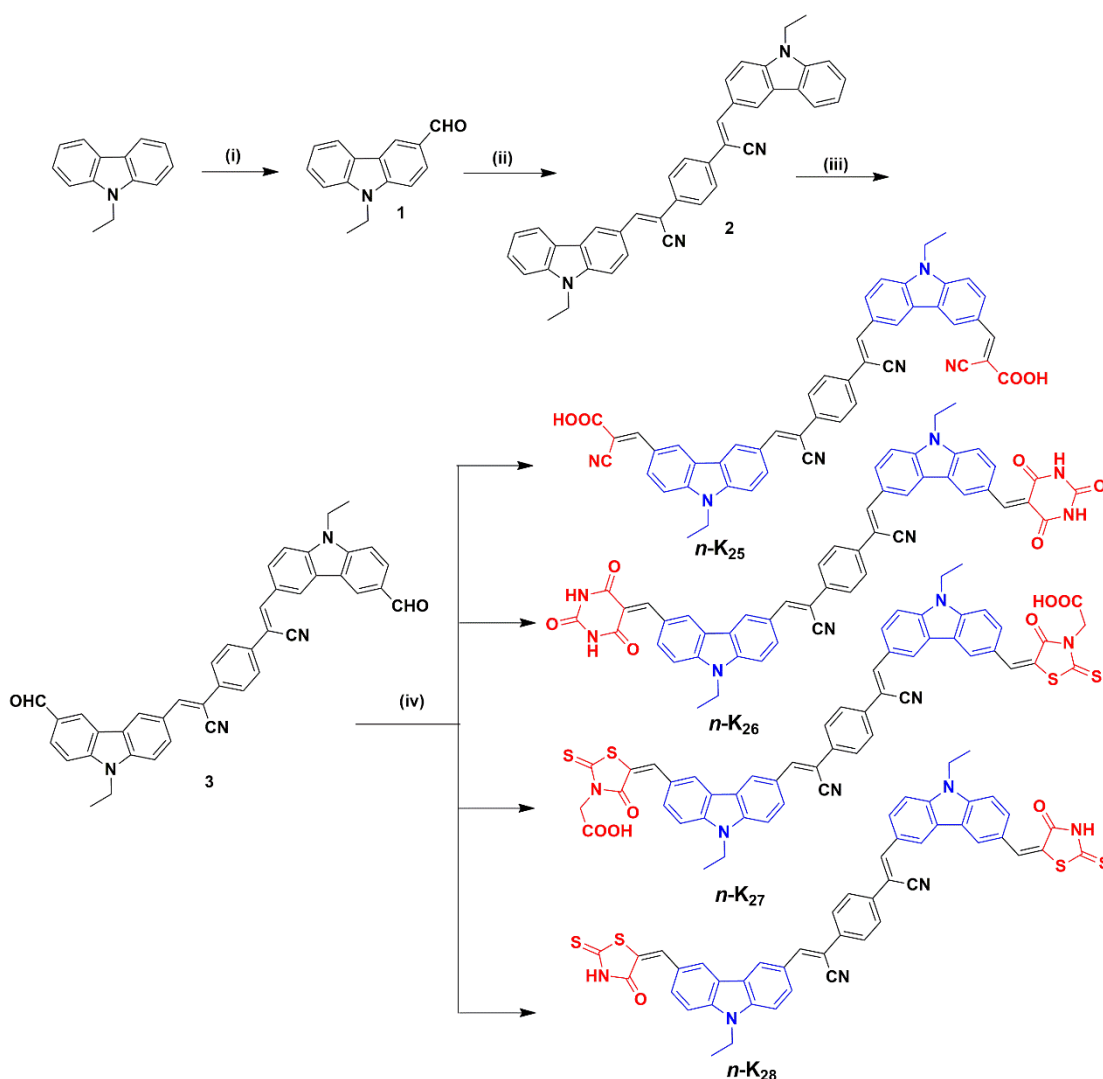
124.94, 123.45, 122.29, 121.57, 118.77, 110.19, 28.19, 24.43. Anal. Calcd. for $C_{62}H_{48}N_6O_6S_4$: C, 67.61; H, 4.39; N, 7.63 and found C, 66.35; H, 4.19; N, 7.61. **FT-IR (ATR)**, ν cm^{-1} : 2936 (C-H stretch), 2360 (C \equiv N stretch), 1700 (C=O stretch), 1577, 1494 (C=C stretch). **Mass (m/z)**: Calculated: 1101.34; Obtained (M-H): 1100.15.

(2Z,2'Z)-3,3'-(9,9'-(Octane-1,8-diyl)bis(9H-carbazole-9,3-diyl))bis(2-(4-((2,4,6-trioxotetrahydropyrimidin-5(2H)-ylidene)methyl)phenyl)acrylonitrile) (**n-K₂₄**)

Bright red solid, Yield: 87%. Melting point: 230-232 °C. **¹H NMR** (400 MHz, DMSO-d₆, δ ppm): 10.00 (s, 4H), 8.74 (m, 2H), 8.19 (s, 6H), 7.79-7.52 (m, 10), 7.44-1.24 (m, 8H), 4.44-4.33 (t, 4H), 1.75 (m, 3H), 1.22 (m, 9H). **¹³C NMR** (400 MHz, DMSO-d₆, δ ppm): 164.15, 155.20, 143.95, 143.41, 142.12, 128.94, 128.11, 127.84, 125.97, 122.78, 122.40, 121.94, 120.77, 120.53, 119.05, 118.84, 110.67, 109.61, 28.12, 24.67. Anal. Calcd. for $C_{60}H_{46}N_8O_6$: C, 73.91; H, 4.76; N, 11.49 and found C, 73.89; H, 4.70; N, 11.32. **FT-IR (ATR)**, ν cm^{-1} : 3192 (N-H stretch), 3047, 2840 (C-H stretch), 2333 (C \equiv N stretch), 1664 (C=O stretch), 1529, 1495 (C=C stretch). **Mass (m/z)**: Calculated: 975.06; Obtained (M-H): 974.30.

2.3.2.1.6 Synthesis of chromophores **n-K₂₅₋₂₈** (**Series-6**)

The synthetic pathways of four new metal-free organic dyes **n-K₂₅₋₂₈** are shown in **Scheme 2.6**. The requisite intermediate 9-ethyl-9H-carbazole-3-carbaldehyde (**1**) was obtained from 9-ethylcarbazole using the standard Vilsmeier-Hack reaction protocol. The intermediate **1** was treated with (1,4-phenylene)diacetonitrile in the presence of sodium methoxide to yield (2Z,2'Z)-2,2'-(1,4-Phenylene)bis(3-(9-ethyl-9H-carbazol-3-yl)acrylonitrile) (**2**). The intermediate **2** was further subjected to the Vilsmeier-Haack formylation reaction to yield corresponding dialdehyde compound **3** with an excellent yield. This penultimate compound **3** was finally condensed with cyanoacetic acid, barbituric acid, rhodanine-3-acetic acid, and rhodanine in the presence of ammonium acetate to get the target dyes, **n-K₂₅₋₂₈**. The detailed synthetic methods for the intermediates and the final dyes **n-K₂₅₋₂₈** are given in the following section.



Scheme 2.6 Synthetic routes for the dyes *n-K*₂₅₋₂₈ : (i) POCl₃, DMF, RT, 24 h (ii) (1,4-Phenylene)diacetonitrile, sodium methoxide, methanol, RT, 6 h; (iii) POCl₃, DMF, 110 °C, 12 h; (iv) *n-K*₂₅, *n-K*₂₇, *n-K*₂₈: Cyanoacetic acid/rhodanine-3-acetic acid/rhodanine, ammonium acetate, glacial CH₃COOH, 110 °C, 12 h; *n-K*₂₆: Barbituric acid, methanol, 60 °C, 10 h.

Synthesis of 9-ethyl-9H-carbazole-3-carbaldehyde (1)

In a cleaned two-neck round bottom flask, freshly distilled DMF (9.95 mL, 128.03 mmol) was taken and cooled at -3 to 4 °C. Then, phosphorous oxychloride, POCl₃ (11.97 mL, 128.03 mmol) was added drop-wise with constant stirring at the same temperature under an argon atmosphere to obtain a glassy white salt. To this mixture, the starting material 9-ethylcarbazole (5 g, 25.60 mmol) dissolved in dichloroethane (10-12 mL) was added. The reaction mixture was refluxed at 110 °C

for 2 h. After completion of the reaction, the reaction mass was cooled to room temperature and poured into 200 mL crushed ice, and subsequently basified by using a 5 M NaOH solution. The product formed was extracted with dichloromethane (50 mL x 4) and the organic layer was dried over sodium sulphate and evaporated under reduced pressure. The impure residue was later purified by column chromatography on silica gel (100-200 mesh, hexane: EtOAc eluent) to yield a fine brown solid (**1**). Yield: 89%. Melting point: 86-88 °C.

Synthesis of (2Z,2'Z)-2,2'-(1,4-phenylene)bis(3-(9-ethyl-9H-carbazol-3-yl)acrylonitrile) (2)

To a freshly prepared solution of sodium methoxide (0.12 g, 5.3 mmol of sodium in 10 mL of methanol), the 9-ethyl-9H-carbazole-3-carbaldehyde (**1**, 0.1 g, 0.44 mmol) was added uniformly with constant stirring at room temperature. Further, (1,4-phenylene)diacetonitrile (0.035 g, 0.22 mmol) was added to the same reaction mixture, and the reaction was continued for 6 h at room temperature. After the completion of the reaction, the bright yellow precipitate formed was filtered off, washed with cold methanol thoroughly, and finally, it was recrystallized from chloroform-hexane to give a fine yellow solid of **2**. Yield: 88 %. Melting point: 110-112 °C.

¹H NMR (400 MHz, CDCl₃, δ ppm): 8.67 (s, 2H), 8.20-8.16 (t, 4H), 7.78-7.77 (d, 6H), 7.57-7.53 (m, 2H), 7.49-7.45 (m, 4H), 7.35-7.31 (m, 2H), 4.42-4.37 (q, 4H), 1.51-1.47 (t, 6H). ¹³C NMR (400 MHz, CDCl₃, δ ppm): 143.58, 143.58, 140.54, 140.54, 127.28, 127.28, 126.50, 126.50, 126.09, 126.09, 124.67, 124.67, 123.37, 123.37, 122.88, 122.87, 122.82, 122.82, 120.83, 120.83, 119.91, 119.90, 108.97, 108.97, 108.89, 106.36, 106.36, 37.84, 13.89, 13.89. Anal. Calcd. for C₄₀H₃₀N₄: C, 84.78; H, 5.34; N, 9.89; and found C, 84.44; H, 5.16; N, 9.10.

Synthesis of (2Z,2'Z)-2,2'-(1,4-phenylene)bis(3-(9-ethyl-6-formyl-9H-carbazol-3-yl)acrylonitrile) (3)

In a dry and cleaned two-neck round bottom flask, freshly distilled DMF (0.29 mL, 3.87 mmol) was taken and POCl₃ (0.4 mL, 4.41 mmol) was added drop-wise with constant stirring at 0 °C under argon atmosphere to obtain a glassy white salt. To

this mixture, compound **2** (0.1 g, 0.17 mmol) dissolved in dichloroethane (2 mL) was added slowly. The reaction mixture was refluxed at 110 °C for 12 h under inert conditions only. The reaction was monitored carefully by the TLC technique. After completion of the reaction, the obtained reaction mass was cooled to room temperature and poured into ice-cold water, and basified by using 5 M NaOH solution. Further, the product formed was extracted with dichloromethane (50 mL x 4). The organic layer was dried using anhydrous sodium sulphate. The solvent obtained was evaporated under reduced pressure to get a crude oily product. The impure residue was later purified by column chromatography on silica gel (100-200 mesh and hexane: DCM, 3:1 eluent) to yield a pale greenish-brown solid (**3**). Yield: 80 %. Melting point: 138-140 °C.

¹H NMR (400 MHz, CDCl₃, δ ppm): 10.07 (s, 2H), 8.67 (s, 2H), 8.20-8.16 (t, 4H), 7.78-7.77 (d, 6H), 7.57-7.53 (m, 2H), 7.49-7.45 (m, 4H), 7.35-7.31 (m, 2H), 4.42-4.37 (q, 4H), 1.51-1.47 (t, 6H). Anal. Calcd. for C₄₂H₃₀N₄O₂: C, 81.01; H, 4.86; N, 9.00; and found C, 80.96; H, 4.82; N, 9.12.

General method for the synthesis of dyes n-K₂₅, n-K₂₇, and n-K₂₈

A mixture of intermediate **3** (1 eq), ammonium acetate (11 eq) and glacial acetic acid (10-15 mL) was taken in an RB flask and stirred constantly. To this reaction mixture, one of the active methylene compounds such as cyanoacetic acid, rhodanine-3-acetic acid, or rhodanine (2 eq) was added and then refluxed for 12 h under an argon atmosphere. The completion of the reaction was monitored using the TLC technique. After its completion, the reaction mixture was cooled to room temperature and was poured into ice-cold water. The solid obtained was filtered, washed with cold water, and finally, dried. The crude product was recrystallized from absolute methanol to get the pure product **n-K₂₅**, **n-K₂₇**, and **n-K₂₈**

(2E,2'E)-3,3'-(6,6'-((1Z,1'Z)-1,4-Phenylenebis(2-cyanoethene-2,1-diyl))bis(9-ethyl-9H-carbazole-6,3-diyl))bis(2-cyanoacrylic acid) (n-K₂₅)

Bright greenish-yellow solid, Yield: 90 %. Melting point: 240-242 °C. ¹H NMR (400 MHz, DMSO-d₆, δ ppm): 10.10 (s, 2H), 8.67 (s, 2H), 8.20-8.16 (t, 4H), 7.78-7.77 (d, 6H), 7.57-7.53 (m, 2H), 7.49-7.45 (m, 4H), 7.35-7.31 (m, 2H), 4.42-4.37

(q, 4H), 1.51-1.47 (t, 6H). ^{13}C NMR (400 MHz, DMSO- d_6 , δ ppm): 164.70, 162.89, 157.33, 143.58, 143.58, 141.25, 141.25, 140.54, 140.54, 135.18, 135.18, 127.28, 126.09, 126.09, 119.91, 119.90, 108.97, 108.97, 108.89, 106.36, 106.36, 37.84, 13.89, 13.89. Anal. Calcd. for $\text{C}_{48}\text{H}_{32}\text{N}_6\text{O}_4$: C, 76.18; H, 4.26; N, 11.10 and found C, 76.26; H, 4.16; N, 11.01. **FT-IR (ATR)**, ν cm^{-1} : 2958, 2928 (C-H stretch), 2211 ($\text{C}\equiv\text{N}$ stretch), 1672 (C=O stretch), 1492 (C=C) stretch). **Mass (m/z)**: Calculated: 756.81; Obtained (M): 756.25.

2,2'-((5E,5'E)-5,5'-((6,6'-((1Z,1'Z)-1,4-Phenylenebis(2-cyanoethene-2,1-diyl))bis(9-ethyl-9H-carbazole-6,3-diyl))bis(methanylylidene))bis(4-oxo-2-thioxothiazolidin-3-yl-5-ylidene))diacetic acid (n-K₂₇)

Pale greenish-yellow solid, Yield: 93%. Melting point: 280-282 °C. ^1H NMR (400 MHz, DMSO- d_6 , δ ppm): 10.07 (s, 2H), 8.65 (s, 2H), 8.20-8.16 (t, 4H), 7.78-7.77 (d, 6H), 7.57-7.53 (m, 2H), 7.49-7.44 (m, 4H), 7.35-7.29 (m, 2H), 4.42-4.37 (q, 4H), 4.26 (s, 4H), 1.51-1.47 (t, 6H). ^{13}C NMR (400 MHz, DMSO- d_6 , δ ppm): 193.66, 192.29, 166.99, 164.10, 162.89, 157.33, 143.58, 143.58, 141.25, 141.25, 140.54, 140.54, 135.18, 135.18, 128.67, 127.28, 126.09, 126.09, 119.91, 119.90, 108.97, 108.97, 108.89, 106.36, 106.36, 37.84, 13.99, 13.89. Anal. Calcd. for $\text{C}_{52}\text{H}_{36}\text{N}_6\text{O}_6\text{S}_4$: C, 64.44; H, 3.74; N, 8.67 and found C, 64.32; H, 3.12; N, 8.16. **FT-IR (ATR)**, ν cm^{-1} : 3019, 2956 (C-H stretch), 2341 ($\text{C}\equiv\text{N}$ stretch), 1697 (C=O stretch), 1587, 1498 (C=C stretch). **Mass (m/z)**: Calculated: 969.14; Obtained (M-H): 968.21.

(2Z,2'Z)-2,2'-(1,4-Phenylene)bis(3-(9-ethyl-6-(E)-(4-oxo-2-thioxothiazolidin-5-ylidene)methyl)-9H-carbazol-3-yl)acrylonitrile (n-K₂₈)

Pale yellow solid, Yield: 93%. Melting point: 272-274 °C. ^1H NMR (400 MHz, DMSO- d_6 , δ ppm): 8.62 (s, 2H), 8.20-8.16 (t, 4H), 7.78-7.77 (d, 6H), 7.57 (s, 2H), 7.49-7.44 (m, 4H), 7.35-7.27 (m, 4H), 4.42-4.37 (q, 4H), 1.51-1.47 (t, 6H). ^{13}C NMR (400 MHz, DMSO- d_6 , δ ppm): 192.26, 172.66, 162.88, 157.43, 143.68, 143.58, 141.25, 141.25, 140.54, 140.54, 135.18, 135.18, 128.67, 127.28, 126.09, 126.09, 119.91, 119.90, 108.97, 108.97, 108.89, 106.36, 106.36, 37.74, 13.89, 13.89. Anal. Calcd. for $\text{C}_{48}\text{H}_{32}\text{N}_6\text{O}_2\text{S}_4$: C, 67.58; H, 3.78; N, 9.85 and found C, 66.83; H, 3.12; N, 9.76. **FT-IR (ATR)**, ν cm^{-1} : 3049, 2936 (C-H stretch), 2331 ($\text{C}\equiv\text{N}$ stretch), 1700

(C=O stretch), 1567, 1494 (C=C stretch). **Mass (m/z)**: Calculated: 853.07; Obtained (M-H): 853.19.

Synthesis of (2Z,2'Z)-2,2'-(1,4-Phenylene)bis(3-(9-ethyl-6-((2,4,6-trioxotetrahydro pyrimidin-5(2H)-ylidene)methyl)-9H-carbazol-3-yl)acrylonitrile) (n-K₂₆)

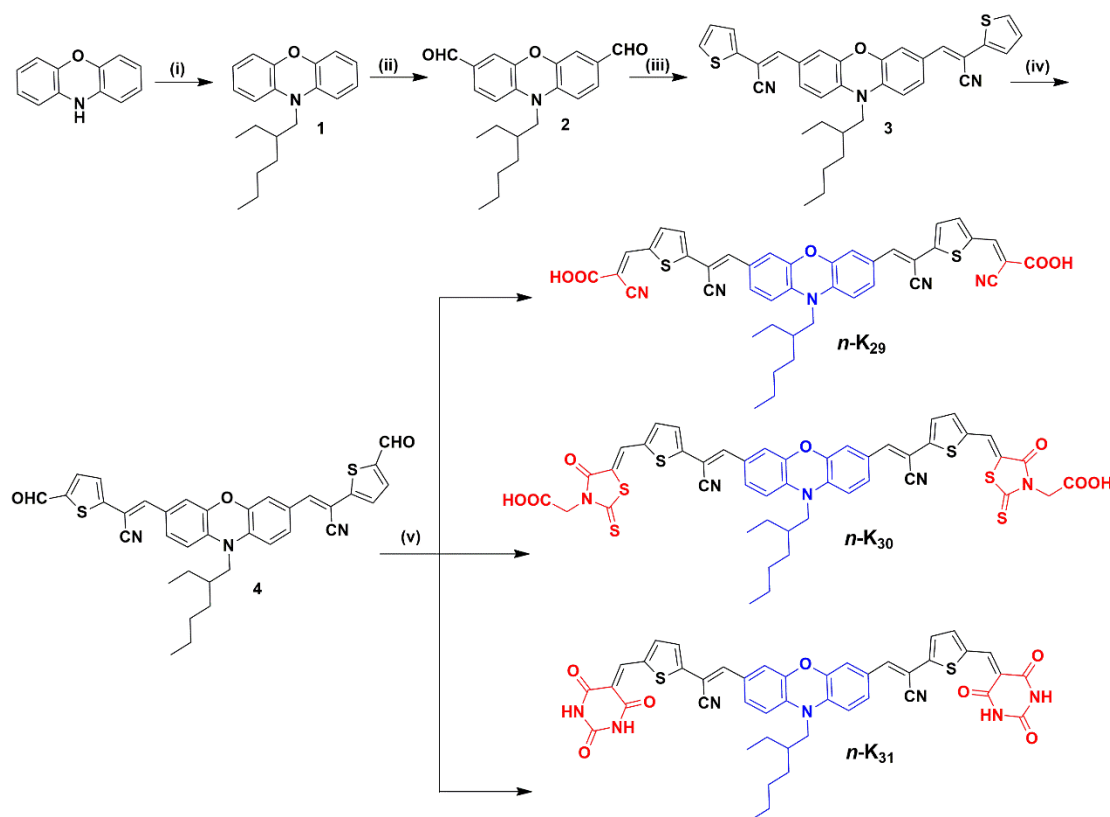
The intermediate **3** (0.5 g, 0.80 mmol), was dissolved in 10 mL of absolute methanol and to this mixture, 1.2 eq of an active methylene compound like barbituric acid (0.2 g, 1.60 mmol) was added under an argon atmosphere and heated at 60 °C with stirring for 10 h. After completion of the reaction, the reaction mixture was cooled, and the precipitated solid was filtered, washed with cold methanol, and collected. It was further recrystallized from the CHCl₃-hexane mixture to get the pure product **n-K₂₆** as greenish-red solid. Yield: 90%. Melting point: 216-218 °C.

¹H NMR (400 MHz, DMSO-d₆, δ ppm): 10.12 (s, 2H), 10.03 (s, 2H), 8.90-8.73 (m, 3H), 8.54-8.48 (m, 2H), 8.37-8.06 (m, 4H), 7.95-7.48 (m, 10H), 7.45-7.23 (m, 1H), 4.58-4.56 (t, 4H), 1.40-1.34 (m, 6H). **¹³C NMR** (400 MHz, DMSO-d₆, δ ppm): 162.89, 157.58, 143.33, 143.28, 141.25, 140.54, 140.54, 135.18, 135.18, 127.28, 126.09, 126.09, 119.91, 119.90, 108.97, 108.89, 106.36, 106.36, 37.89, 13.84, 13.84. Anal. Calcd. for C₅₀H₃₄N₈O₆: C, 71.25; H, 4.07; N, 13.29 and found C, 71.20; H, 4.03; N, 13.21. **FT-IR (ATR)**, ν cm⁻¹: 3196 (N-H stretch), 3030, 2954, (C-H stretch), 2318 (C≡N stretch), 1669 (C=O stretch), 1574, 1552, 1494 (C=C stretch). **Mass (m/z)**: Calculated: 842.85; Obtained (M-H): 841.30.

2.3.2.1.7 Synthesis of chromophores **n-K₂₉₋₃₁** (**Series-7**)

The target compounds of **Series 7** were synthesized according to **Scheme 2.7**. The requisite intermediate 10-(2-Ethylhexyl)-10H-phenoxazine (**1**) was obtained from starting material phenoxazine by treating it with 2-ethylhexyl bromide in the presence of sodium hydride. This was converted to the key precursor intermediate 10-(2-ethylhexyl)-10H-phenoxazine-3,7-dicarbaldehyde (**2**) through the Vilsmeier-Hack reaction protocol. The intermediate **2** was further condensed with thiophene-2-acetonitrile by the Knoevenagel condensation to obtain intermediate **3**. Furthermore, intermediate **3** was subjected to the Vilsmeier-Hack reaction to form the precursor **4**. In the final step, the target molecules **n-K₂₉₋₃₁** were obtained in good yield by

following the Knoevenagel condensation of precursor **4** with cyanoacetic acid, rhodanine-3-acetic acid, and barbituric acid, respectively. The detailed synthetic methods for the intermediates and the final dyes *n*-**K**₂₉₋₃₁ are given in the following section.



Scheme 2.7 Synthetic routes for the dyes *n*-**K**₂₉₋₃₁: (i) 2-Ethylhexyl bromide, NaH, DMF, RT, 12 h; (ii) POCl₃, DMF, RT, 12 h; (iii) Thiophene-2-acetonitrile, potassium *tert*-butoxide, methanol, 70 °C, 12 h; (iv) POCl₃, DMF, 110 °C, 12 h; (v) *n*-**K**₂₉₋₃₀: Cyanoacetic acid/ rhodanine-3-acetic acid, ammonium acetate, glacial CH₃COOH, 110 °C, 12 h; *n*-**K**₃₁: Barbituric acid, methanol, 60 °C, 10 h.

Synthesis of 10-(2-ethylhexyl)-10H-phenoxazine (**1**)

A mixture of phenoxazine (0.5 g, 2.72 mmol), NaH (1.9 g, 8.16 mmol) was dissolved in a minimum amount of DMF (8 mL) and stirred at room temperature for half an hour under an inert atmosphere. Later, 2-ethylhexyl bromide (0.58 mL, 3.27 mmol) was added into the reaction mixture and continued stirring at room temperature for 12 h. The reaction progress was monitored using TLC. After completion of the reaction, the reaction mixture was cooled and poured into crushed ice (100 mL) and

neutralization was done using a saturated solution of ammonium chloride. The residue formed was extracted with ethyl acetate (50 mL x 4) and the organic layer was dried over sodium sulphate and evaporated under reduced pressure. The impure residue was later purified by column chromatography on silica gel (100-200 mesh and hexane: EtOAc eluent) to yield a colorless liquid as a product. Yield: 98%.

¹H NMR (400 MHz, CDCl₃, δ ppm): 6.77-6.73 (m, 2H), 6.61-6.60 (d, 4H), 6.51-6.49 (m, 2H), 3.39-3.37 (d, 2H), 1.88-1.85 (m, 1H), 1.36-1.29 (m, 8H), 0.90-0.87 (t, 6H). Anal. Calcd. for C₂₀H₂₅NO: C, 81.31; H, 8.53; N, 4.74; and found C, 80.89; H, 8.29; N, 4.06.

Synthesis of 10-(2-ethylhexyl)-10H-phenoxazine-3,7-dicarbaldehyde (2)

In a cleaned two-neck round bottom flask, freshly distilled DMF (0.13 mL, 1.69 mmol) was taken and cooled at -3 to 4 °C. Then, phosphorous oxychloride, POCl₃ (0.09 mL, 1.01 mmol) was added drop-wise with constant stirring at the same temperature under argon atmosphere to obtain a glassy white salt. To this mixture, 10-(2-ethylhexyl)-10H-phenoxazine (**1**, 0.1 g, 0.33 mmol) dissolved in dichloroethane (2 mL) was added. The reaction mixture was refluxed at 95 °C for 12 h. After completion of the reaction, the reaction mass was quenched in cold water and subsequently basified by using a 5 M NaOH solution. The product formed was extracted with ethyl acetate (50 mL x 3) and the organic layer was dried over Na₂SO₄ and finally evaporated under reduced pressure. The impure residue was later purified by column chromatography on silica gel (100-200 mesh and hexane: EtOAc, 3:1 eluent) to yield a light brown solid (**2**). Yield: 75 %. Melting point: 128-130 °C.

¹H NMR (400 MHz, CDCl₃, δ ppm): 9.73 (s, 2H), 7.37-7.36 (d, 1H), 7.35-7.34 (d, 1H), 7.15-7.14 (d, 2H), 6.70-6.68 (d, 2H), 3.57-3.55 (d, 2H), 1.42-1.40 (m, 1H), 1.36-1.31 (m, 8H), 0.99-0.95 (t, 3H), 0.93-0.89 (t, 3H). Anal. Calcd. for C₂₂H₂₅NO₃: C, 75.19; H, 7.17; N, 3.99; and found C, 75.08; H, 7.10; N, 3.84.

Synthesis of (2E,2'E)-3,3'-(10-(2-ethylhexyl)-10H-phenoxazine-3,7-diyl)bis(2-thiophen-2-yl)acrylonitrile (3)

In a cleaned RB flask, the starting material 10-(2-ethylhexyl)-10H-phenoxazine-3,7-dicarbaldehyde (**2**, 0.2 g, 0.56 mmol) and potassium *tert*-butoxide

(0.31 g, 2.84 mmol) were taken and dissolved in dry methanol. To this reaction mixture thiophene-2-acetonitrile (0.2 mL, 1.70 mmol) was added and the reaction mixture was refluxed for 12 h under an inert atmosphere. After the completion of the reaction, the bright yellow precipitate formed was filtered off, washed with cold methanol thoroughly, and finally, it was recrystallized from chloroform-hexane to give a fine yellow solid of **3**. Yield: 80 %. Melting point: 142-144 °C.

¹H NMR (400 MHz, CDCl₃, δ ppm): 7.37-7.34 (m, 2H), 7.32-7.31 (d, 1H), 7.31-7.30 (d, 1H), 7.27-7.26 (d, 1H), 7.25-7.24 (d, 1H), 7.16-7.15 (d, 2H), 7.10 (s, 2H), 7.04-7.03 (d, 1H), 6.58 (s, 1H), 6.56 (s, 1H), 3.49-3.47 (d, 2H), 1.58-1.57 (m, 2H), 1.38-1.24 (m, 7H), 0.96-0.92 (t, 6H). Anal. Calcd. for C₃₄H₃₁N₃OS₂: C, 72.69; H, 5.56; N, 7.48; and found C, 72.38; H, 5.16; N, 7.84.

Synthesis of (2E,2'E)-3,3'-(10-(2-ethylhexyl)-10H-phenoxazine-3,7-diyl)bis(2-(5-formylthiophen-2-yl)acrylonitrile) (4)

In a dry and cleaned two-neck round bottom flask, freshly distilled DMF (0.3 mL, 3.91 mmol) was taken and POCl₃ (0.4 mL, 4.45 mmol) was added drop-wise with constant stirring at 0 °C under argon atmosphere to obtain a glassy white salt. To this mixture, compound **3** (0.1 g, 0.17 mmol) dissolved in dichloroethane (5 mL) was added slowly. The reaction mixture was refluxed at 110 °C for 12 h under inert conditions only. The reaction was monitored carefully by the TLC technique. After completion of the reaction, the obtained reaction mass was cooled to room temperature and poured into ice-cold water, and basified by using 5 M NaOH solution. Further, the product formed was extracted with dichloromethane (50 mL x 4). The organic layer was dried using anhydrous sodium sulphate. The solvent was evaporated under reduced pressure to get a crude oily product. The impure residue was later purified by column chromatography on silica gel (100-200 mesh and hexane: EtOAc, 3:1 eluent) to yield a pale brown solid (**4**). Yield: 75 %. Melting point: 160-162 °C.

¹H NMR (400 MHz, CDCl₃, δ ppm): 9.87 (s, 2H), 7.71-7.69 (d, 2H), 7.41-7.14 (m, 8H), 6.61-6.63 (d, 2H), 3.51-3.50 (d, 2H), 2.17-2.16 (m, 2H), 1.69-1.25 (m,

7H), 0.97-0.94 (t, 3H), 0.91-0.87 (t, 3H). Anal. Calcd. for C₃₆H₃₁N₃O₃S₂: C, 69.99; H, 5.06; N, 6.80; and found C, 69.90; H, 5.02; N, 6.18.

General method for the synthesis of dyes n-K₂₉₋₃₀

A mixture of intermediate **4** (1 eq), ammonium acetate (10 eq), and glacial acetic acid (10-15 mL) was taken in an RB flask and stirred constantly. To this reaction mixture, an active methylene compound such as cyanoacetic acid or rhodanine-3-acetic acid (1.2 eq) was added and then refluxed for 12 h under an argon atmosphere. After its completion, the reaction mixture was cooled to room temperature and was poured into ice-cold water. The solid obtained was filtered, washed with cold water, and finally, dried. The crude product was recrystallized from absolute methanol to get the pure product **n-K₂₉₋₃₀**.

(2E,2'E)-3,3'-(5,5'-((1E,1'E)-(10-(2-Ethylhexyl)-10H-phenoxazine-3,7-diyl)bis(1-cyanoethene-2,1-diyl))bis(thiophene-5,2-diyl))bis(2-cyanoacrylic acid) (n-K₂₉)

Crimson red color solid, Yield: 86 %. Melting point: 292-294 °C. ¹H NMR (400 MHz, CDCl₃, δ ppm): 10.05 (s, 2H), 7.37-7.34 (m, 2H), 7.32-7.31 (d, 1H), 7.31-7.30 (d, 1H), 7.27-7.26 (d, 1H), 7.25-7.24 (d, 1H), 7.16-7.15 (d, 2H), 7.10 (s, 2H), 7.04-7.03 (d, 2H), 6.58 (s, 1H), 6.56 (s, 1H), 3.49-3.47 (d, 2H), 1.58-1.57 (m, 1H), 1.38-1.24 (m, 8H), 0.96-0.92 (t, 6H). ¹³C NMR (400 MHz, CDCl₃, δ ppm): 189.60, 189.55, 146.86, 145.18, 144.01, 134.47, 134.25, 131.24, 125.45, 123.83, 123.46, 123.31, 121.20, 120.74, 117.31, 115.67, 115.46, 115.36, 113.37, 112.31, 112.04, 48.06, 47.78, 36.68, 30.79, 28.85, 28.80, 24.19, 23.18, 14.12, 11.10, 11.03, 10.94. Anal. Calcd. for C₄₂H₃₃N₅O₅S₂: C, 67.09; H, 4.42; N, 9.31 and found C, 67.01; H, 4.12; N, 9.30. **FT-IR (ATR)**, ν cm⁻¹: 2958, 2928 (C-H stretch), 2211 (C≡N stretch), 1591, 1492 (C=C stretch). **Mass (m/z)**: Calculated: 751.87; Obtained (M-H): 750.08.

2,2'-((5Z,5'Z)-5,5'-((5,5'-((1E,1'E)-(10-(2-Ethylhexyl)-10H-phenoxazine-3,7-diyl)bis(1-cyanoethene-2,1-diyl))bis(thiophene-5,2-diyl))bis(methanylylidene))bis(4-oxo-2-thioxothiazolidin-3-yl-5-ylidene))diacetic acid (n-K₃₀)

Bright red solid, Yield: 91%. Melting point: 312-314 °C. ¹H NMR (400 MHz, CDCl₃, δ ppm): 10.09 (s, 2H), 7.39-7.35 (m, 2H), 7.33-7.32 (d, 1H), 7.31-7.30 (d, 1H), 7.28-7.27 (d, 1H), 7.25-7.24 (d, 1H), 7.16-7.15 (d, 2H), 7.10 (s, 2H), 7.04-7.03

(d, 2H), 6.58 (s, 1H), 6.56 (s, 1H), 3.49-3.47 (d, 2H), 3.45-3.43 (d, 2H), 1.58-1.57 (m, 1H), 1.38-1.24 (m, 8H), 0.96-0.92 (t, 6H). ^{13}C NMR (400 MHz, CDCl_3 , δ ppm): 190.60, 189.90, 145.02, 138.14, 131.21, 128.02, 115.02, 112.35, 48.10, 36.67, 30.64, 29.70, 28.72, 24.09, 23.03, 14.14, 14.00, 10.95. Anal. Calcd. for $\text{C}_{46}\text{H}_{37}\text{N}_5\text{O}_7\text{S}_6$: C, 57.30; H, 3.87; N, 7.26 and found C, 56.90; H, 3.81; N, 7.21. **FT-IR (ATR)**, ν cm^{-1} : 2959 (C-H stretch), 2361 ($\text{C}\equiv\text{N}$ stretch), 1710 (C=O stretch), 1537, 1492 (C=C stretch). **Mass (m/z)**: Calculated: 964.21; Obtained (M-H): 963.16.

Synthesis of (2E,2'E)-3,3'-(10-(2-Ethylhexyl)-10H-phenoxazine-3,7-diyl)bis(2-(5-((2,4,6-trioxotetrahydropyrimidin-5(2H)-ylidene)methyl)thiophen-2-yl)acrylonitrile) (n-K₃₁)

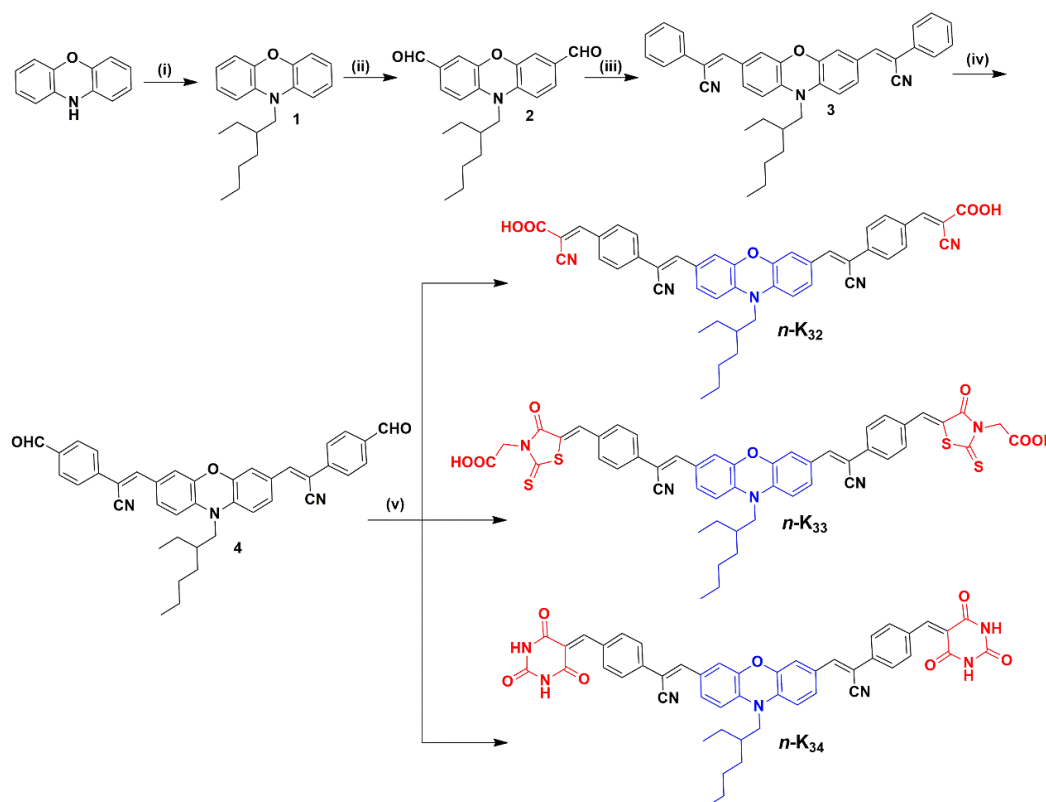
The intermediate **4** (0.5 g, 0.80 mmol), was dissolved in 10 mL of absolute methanol and to this mixture 1.2 eq of an active methylene compound like barbituric acid (0.21 g, 1.61 mmol) was added under argon atmosphere and heated at 60 °C with stirring for 10 h. After completion of the reaction, the content was cooled to room temperature and the precipitated solid was filtered, washed with cold methanol, and collected. It was further recrystallized from the CHCl_3 -hexane mixture to get the pure product **n-K₃₁** as a red solid. Yield: 93%. Melting point: 222-224 °C.

^1H NMR (400 MHz, CDCl_3 , δ ppm): 11.32 (s, 2H), 11.20 (s, 2H), 9.85 (s, 2H), 7.71-7.69 (d, 2H), 7.41-7.14 (m, 8H), 6.61-6.63 (d, 2H), 3.57-3.55 (d, 2H), 1.42-1.40 (m, 1H), 1.36-1.31 (m, 8H), 0.99-0.95 (t, 3H), 0.93-0.89 (t, 3H). ^{13}C NMR (400 MHz, CDCl_3 , δ ppm): 164.62, 162.70, 157.36, 150.76, 143.97, 141.17, 133.79, 129.94, 128.66, 127.17, 125.45, 123.83, 123.31, 121.20, 120.74, 117.31, 115.67, 115.46, 115.36, 113.37, 112.31, 112.04, 48.06, 47.78, 36.68, 30.99, 28.95, 28.60, 24.39, 23.28, 14.32, 11.10. Anal. Calcd. for $\text{C}_{44}\text{H}_{35}\text{N}_7\text{O}_7\text{S}_2$: C, 63.07; H, 4.21; N, 11.70 and found C, 63.12; H, 4.10; N, 11.32. **FT-IR (ATR)**, ν cm^{-1} : 3211 (N-H stretch), 2960 (C-H stretch), 2320 ($\text{C}\equiv\text{N}$ stretch), 1671 (C=O stretch), 1543, 1488 (C=C stretch). **Mass (m/z)**: Calculated: 837.92; Obtained (M-H): 836.11.

2.3.2.1.8 Synthesis of chromophores **n-K₃₂₋₃₄** (Series-8)

The target compounds of **Series-8** were synthesized according to **Scheme 2.8**. The necessary intermediates and target molecules were synthesized using the similar

well-documented procedure as indicated in **Series-7** with a slight modification. The detailed characterization data of the intermediates and the final dyes **n-K**₃₂₋₃₄ are given in the following section.



Scheme 2.8 Synthetic routes for the dyes **n-K**₃₂₋₃₄: (i) 2-Ethylhexyl bromide, NaH, DMF, RT, 12 h; (ii) POCl₃, DMF, RT, 12 h; (iii) Phenylacetonitrile, sodium methoxide, methanol, RT, 6 h; (iv) POCl₃, DMF, 110 °C, 12 h; (v) **n-K**₃₂₋₃₃: Cyanoacetic acid/rhodanine-3-acetic acid, ammonium acetate, glacial CH₃COOH, 110 °C, 12 h; **n-K**₃₄: Barbituric acid, methanol, 60 °C, 10 h.

(2*Z*,2'*Z*)-3,3'-(10-(2-Ethylhexyl)-10*H*-phenoxazine-3,7-diyl)bis(2-phenylacrylonitrile)
(**3**)

Yellow solid, Yield: 89 %. Melting point: 146-148 °C. ¹H NMR (400 MHz, CDCl₃, δ ppm): 7.95-7.91 (m, 4H), 7.37-7.34 (m, 4H), 7.32-7.31 (d, 1H), 7.31-7.30 (d, 1H), 7.25-7.24 (d, 2H), 7.17-7.16 (d, 2H), 7.12 (s, 2H), 6.59 (s, 2H), 3.48-3.46 (d, 2H), 1.56-1.52 (m, 1H), 1.37-1.24 (m, 8H), 0.96-0.92 (t, 6H). Anal. Calcd. for C₃₈H₃₅N₃O: C, 83.03; H, 6.42; N, 7.64; and found C, 82.84; H, 6.40; N, 7.61.

(2Z,2'Z)-3,3'-(10-(2-Ethylhexyl)-10H-phenoxazine-3,7-diyl)bis(2-(4-formylphenyl)acrylonitrile) (**4**)

Pale brown solid, Yield: 75 %. Melting point: 170-172 °C. ¹H NMR (400 MHz, CDCl₃, δ ppm): 9.88 (s, 2H), 7.71-7.69 (m, 2H), 7.37-7.34 (m, 4H), 7.31-7.30 (d, 1H), 7.27-7.26 (d, 1H), 7.25-7.24 (d, 2H), 7.17-7.16 (d, 2H), 7.12 (s, 2H), 7.04-7.03 (d, 2H), 3.48-3.46 (d, 2H), 1.56-1.52 (m, 1H), 1.37-1.24 (m, 8H), 0.96-0.92 (t, 6H). Anal. Calcd. for C₄₀H₃₅N₃O₃: C, 79.31; H, 5.82; N, 6.94; and found C, 79.30; H, 5.69; N, 6.84.

(2E,2'E)-3,3'-(((1Z,1'Z)-(10-(2-Ethylhexyl)-10H-phenoxazine-3,7-diyl)bis(1-cyanoethene-2,1-diyl))bis(4,1-phenylene))bis(2-cyanoacrylic acid) (**n-K₃₂**)

Bright red solid, Yield: 87 %. Melting point: 268-270 °C. ¹H NMR (400 MHz, DMSO-d₆, δ ppm): 10.10 (s, 2H), 8.74 (s, 2H), 8.48-8.46 (d, 2H), 8.27-8.16 (m, 5H), 7.99-7.77 (m, 6H), 7.63 (s, 2H), 4.36 (s, 2H), 2.01-1.91 (m, 1H), 1.33-1.23 (m, 8H), 0.86-0.78 (t, 6H). ¹³C NMR (400 MHz, DMSO-d₆, δ ppm): 164.47, 162.88, 162.74, 156.69, 150.76, 145.08, 144.47, 144.44, 134.76, 134.21, 129.85, 129.53, 128.71, 127.81, 125.20, 125.05, 124.20, 123.04, 122.95, 122.77, 122.58, 122.51, 120.71, 115.80, 111.34, 110.60, 110.53, 47.55, 30.49, 28.36, 24.02, 22.91, 14.22, 14.21, 11.06. Anal. Calcd. for C₄₆H₃₇N₅O₅: C, 74.68; H, 5.04; N, 9.47 and found C, 74.61; H, 5.01; N, 9.46. **FT-IR (ATR)**, ν cm⁻¹: 3394 (O-H stretch), 2957, 2871 (C-H stretch), 2211 (C≡N stretch), 1581, 1498 (C=C). **Mass (m/z)**: Calculated: 739.82; Obtained (M-H): 738.10.

2,2'-((5Z,5'Z)-5,5'-(((1Z,1'Z)-(10-(2-Ethylhexyl)-10H-phenoxazine-3,7-diyl)bis(1-cyanoethene-2,1-diyl))bis(4,1-phenylene))bis(methanylylidene))bis(4-oxo-2-thioxothiazolidin-3-yl-5-ylidene))diacetic acid (**n-K₃₃**)

Orange red solid, Yield: 86 %. Melting point: 322-324 °C. ¹H NMR (400 MHz, DMSO-d₆, δ ppm): 10.05 (s, 2H), 8.72 (s, 2H), 8.48-8.46 (d, 2H), 8.28-8.16 (m, 5H), 7.99-7.75 (m, 6H), 7.63 (s, 2H), 4.77-4.76 (s, 4H), 4.41-4.37 (m, 4H), 2.01-1.91 (m, 1H), 1.33-1.23 (m, 8H), 0.86-0.83 (t, 6H). ¹³C NMR (400 MHz, DMSO-d₆, δ ppm): 193.66, 192.30, 166.99, 156.19, 150.16, 145.08, 144.27, 134.21, 129.85, 129.73, 128.91, 127.89, 125.50, 124.20, 123.04, 122.95, 122.71, 122.58, 122.61,

120.71, 115.80, 111.34, 110.60, 110.53, 47.55, 30.19, 28.56, 24.02, 22.91, 14.32, 14.21, 11.16. Anal. Calcd. for C₅₀H₄₁N₅O₇S₄: C, 63.07; H, 4.34; N, 7.36 and found C, 63.01; H, 4.32; N, 7.31. **FT-IR (ATR)**, ν cm⁻¹: 3642 (O-H stretch), 2957, 2874 (C-H stretch), 2305 (C≡N stretch), 1693 (C=O stretch), 1582, 1497 (C=C). **Mass (m/z)**: Calculated: 952.15; Obtained (M-H): 951.25.

(2*Z*,2'*Z*)-3,3'-(10-(2-Ethylhexyl)-10*H*-phenoxazine-3,7-diyl)bis(2-(4-((2,4,6-trioxotetrahydropyrimidin-5(2*H*)-ylidene)methyl)phenyl)acrylonitrile) (**n-K₃₄**)

Red solid, Yield: 82 %. Melting point: 302-304 °C. **¹H NMR** (400 MHz, DMSO-d₆, δ ppm): 11.28 (s, 2H), 11.20 (s, 2H), 9.82 (s, 2H), 8.82 (s, 2H), 8.48-8.46 (d, 2H), 8.26-8.16 (m, 5H), 7.99-7.75 (m, 5H), 7.63 (s, 2H), 4.27-4.26 (s, 2H), 2.01-1.91 (m, 1H), 1.33-1.25 (m, 8H), 0.89-0.86 (t, 6H). **¹³C NMR** (400 MHz, DMSO-d₆, δ ppm): 162.90, 157.36, 150.76, 143.97, 143.56, 141.17, 133.79, 129.94, 128.66, 127.17, 123.92, 122.85, 122.69, 122.63, 121.24, 120.90, 120.55, 114.53, 110.69, 110.51, 110.19, 109.71, 43.03, 28.82, 24.69, 22.91, 14.56, 14.31, 11.36. Anal. Calcd. for C₄₈H₃₉N₇O₇: C, 69.81; H, 4.76; N, 11.87 and found C, 69.72; H, 4.72; N, 11.32. **FT-IR (ATR)**, ν cm⁻¹: 3203 (N-H stretch), 2959 (C-H stretch), 2304 (C≡N stretch), 1598, 1490 (C=C stretch). **Mass (m/z)**: Calculated: 825.87; Obtained (M-H): 824.40.

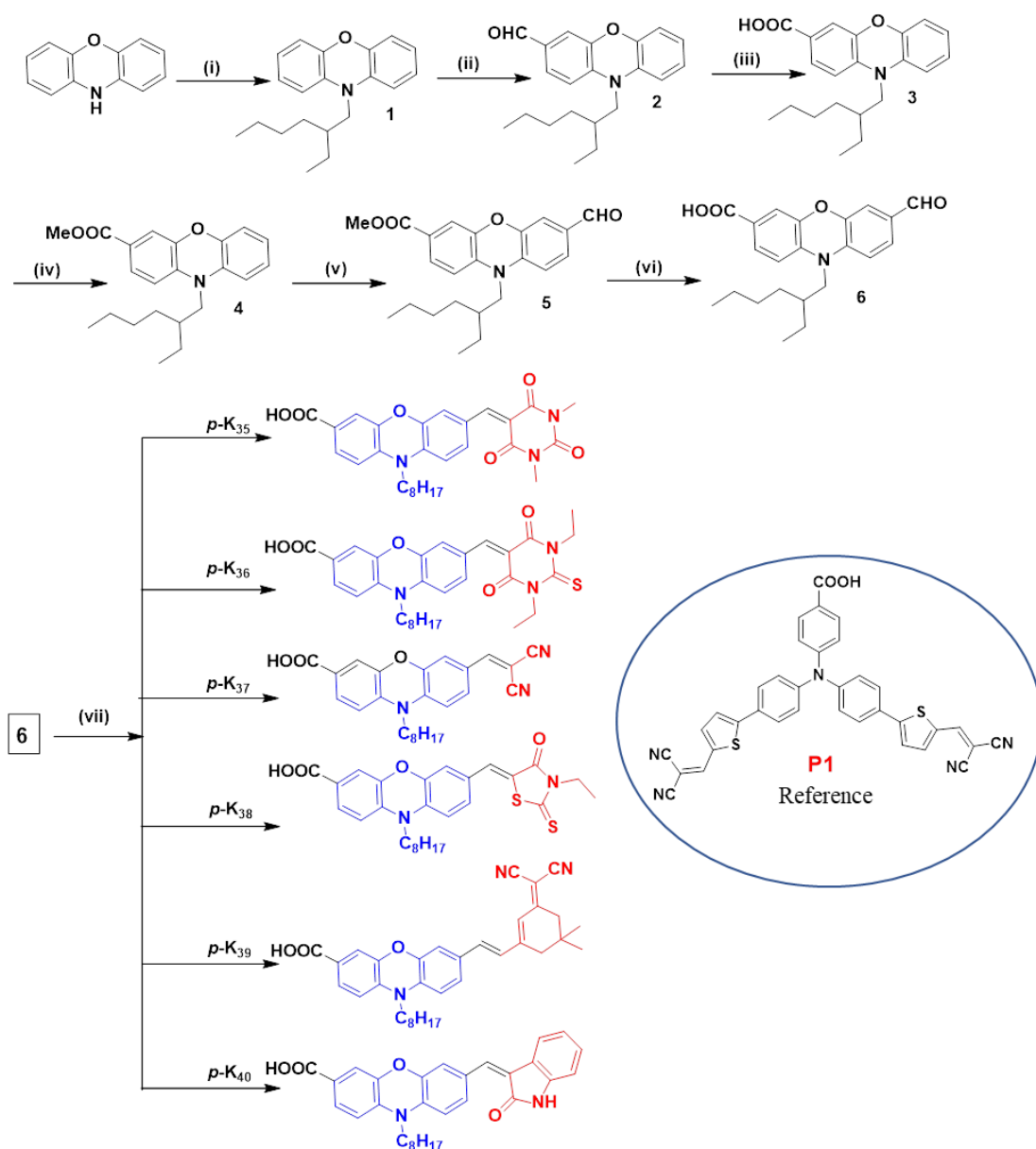
2.3.2.2 Synthesis of *p*-type organic dyes **p-K₃₅₋₄₂** (Series 9-10)

The synthetic protocols employed for the preparation of dyes **n-K₃₅₋₄₂** from simple starting materials, *viz.* carbazole, and phenoxazine are given here.

2.3.2.2.1 Synthesis of chromophores **p-K₃₅₋₄₀** (Series-9)

The synthetic pathways of phenoxazine-based six new organic sensitizers (**p-K₃₅₋₄₀**) with D-A configuration, carrying six different electron acceptor/anchoring units in their structures are depicted in **Scheme 2.9**. The intermediate **1** was synthesized according to the procedure discussed in **Series-7**. This was converted to the key precursor intermediate **2** through the Vilsmeier-Hack reaction protocol. The intermediate **2** was oxidized to get 10-(2-ethylhexyl)-10*H*-phenoxazine-3-carboxylic acid (**3**) with the help of Ag₂O. Then, the carboxylic group of compound **3** was protected by esterifying (Fisher ester synthesis) to give the intermediate **4**. Further, the ester **4** was formylated using the Vilsmeier-Hack reaction protocol and the crude

formylated product was hydrolyzed with lithium hydroxide to get the intermediate **6**. In the final step, the target molecules *p*-**K**₃₅₋₄₀ were obtained in good yield by following the Knoevenagel condensation of 10-(2-ethylhexyl)-7-formyl-10*H*-phenoxazine-3-carboxylic acid (**6**) with *N,N*-dimethyl barbituric acid, *N,N*-diethyl thiobarbituric acid, malononitrile, 3-ethylrhodanine, (3,5,5-trimethylcyclohex-2-enylidene)malononitrile and 2-oxindole, respectively.



Scheme 2.9 Synthetic routes for the dyes *p*-**K**₃₅₋₄₀: (i) 2-Ethylhexyl bromide, NaH, DMF, RT, 12 h; (ii) POCl₃, DMF, RT, 12 h; (iii) Ag₂O, NaOH, EtOH, RT, 12 h; (iv) MeOH, H₂SO₄, reflux; (v) DMF, POCl₃, 90 °C, 12h; (vi) LiOH.H₂O, 80 °C, 12 h; (vii) *p*-**K**₃₅₋₃₆: *N,N*-dimethyl barbituric acid/*N,N*-diethyl thiobarbituric acid,

methanol, 65 °C, 12 h; **p-K₃₇**: malononitrile, DMF, 90 °C, 12 h; **p-K₃₈**: *N*-ethyl rhodanine, glacial acetic acid, 110 °C, 12 h; **p-K₃₉**: (3,5,5-trimethylcyclohex-2-enylidene) malononitrile, piperidine, acetonitrile, 80-85 °C, 12 h; **p-K₄₀**: 2-oxindole, piperidine, ethanol, 80 °C, 12 h.

Synthesis of 10-(2-ethylhexyl)-10H-phenoxazine-3-carbaldehyde (2)

In a cleaned RB flask, freshly distilled DMF (0.13 mL, 1.69 mmol) was taken and cooled at -3 to 4 °C. Then, phosphorous oxychloride, POCl₃ (0.09 mL, 1.01 mmol) was added drop-wise with constant stirring at the same temperature under argon atmosphere to obtain a glassy white salt. To this mixture, 10-(2-ethylhexyl)-10H-phenoxazine (**1**, 0.1 g, 0.33 mmol) dissolved in dichloroethane (2 mL) was added. The reaction mixture was refluxed at 95 °C for 12 h. After completion of the reaction, the reaction mass was cooled to room temperature and poured into 100 mL crushed ice, and subsequently basified by using a 5 M NaOH solution. The product formed was extracted with ethyl acetate (50 mL x 3) and the organic layer was dried over sodium sulphate and evaporated under reduced pressure. The impure residue was later purified by column chromatography on silica gel (100-200 mesh) to yield a light brown solid (**2**). Yield: 79 %. Melting point: 112-114 °C.

¹H NMR (400 MHz, CDCl₃, δ ppm): 9.68 (s, 1H), 7.32-7.30 (m, 1H), 7.10-7.09 (d, 1H), 6.83-6.80 (m, 1H), 6.75-6.74 (d, 1H), 6.68-6.66 (d, 1H), 6.61-6.58 (t, 1H), 3.50-3.48 (d, 2H), 1.92-1.89 (m, 1H), 1.50-1.31 (m, 8H), 0.97-0.94 (t, 3H), 0.92-0.89 (t, 3H). ¹³C NMR (400 MHz, CDCl₃, δ ppm): 189.63, 145.18, 144.77, 140.16, 132.09, 129.80, 128.43, 123.70, 122.55, 115.84, 114.41, 112.82, 111.23, 47.77, 36.64, 30.68, 28.75, 24.10, 23.07, 14.03, 10.97. Anal. Calcd. for C₂₁H₂₅NO₂: C, 77.98; H, 7.79; N, 4.33; and found C, 77.90; H, 7.71; N, 4.23.

Synthesis of 10-(2-ethylhexyl)-10H-phenoxazine-3-carboxylic acid (3)

In a cleaned RB flask, sodium hydroxide (0.67 g, 17 mmol) was taken and slowly dissolved in 100 mL of ethanol by stirring under an ice bath. Further, the silver oxide (0.35 g, 1.54 mmol) was suspended in this solution and to this mixture 10-(2-ethylhexyl)-10H-phenoxazine-3-carbaldehyde (**2**, 0.1 g, 0.309 mmol) dissolved in 10 mL of toluene solution was slowly added with constant stirring at RT. The stirring was continued for 16-18 h under an argon atmosphere. After completion of the

reaction, the reaction mixture was filtered through a celite bed. Further, the solvent of the filtrate was removed under vacuum and the obtained residue was washed with distilled water. The product was extracted with ethyl acetate (4×100 mL) and the organic phase was washed with 10% sodium bicarbonate solution. Pre-cooled 10 % HCl was added to the collected aqueous layer and the pH of the solution was brought to slightly acidic. The precipitated solid was filtered and dried. The residue was purified using column chromatography on 200-400 mesh silica using 2:1 hexane/ethyl acetate mixture as the mobile phase to get a pale-yellow solid. Yield: 79 %. Melting point: 138-140 °C.

^1H NMR (400 MHz, CDCl_3 , δ ppm): 9.72 (s, 1H), 7.61-7.59 (m, 1H), 7.36-7.28 (m, 3H), 7.13-7.12 (d, 1H), 6.67-6.61 (m, 2H), 3.55-3.54 (d, 2H), 1.91-1.89 (m, 1H), 1.51-1.33 (m, 8H), 0.99-0.95 (t, 3H), 0.93-0.89 (t, 3H). **^{13}C NMR** (400 MHz, CDCl_3 , δ ppm): 189.70, 170.09, 145.17, 144.30, 138.59, 137.35, 130.93, 128.11, 127.08, 123.00, 117.02, 114.90, 112.14, 47.99, 36.64, 30.65, 28.72, 24.09, 23.03, 14.01, 10.95. Anal. Calcd. for $\text{C}_{21}\text{H}_{25}\text{NO}_3$: C, 74.31; H, 7.42; N, 4.13; and found C, 74.29; H, 7.41; N, 4.03.

Synthesis of methyl 10-(2-ethylhexyl)-10H-phenoxazine-3-carboxylate (4)

In a dry RB flask, 10-(2-ethylhexyl)-10H-phenoxazine-3-carboxylic acid (**3**, 1 g, 3.39 mmol) was dissolved in 15 mL of dry methanol and 2 drops of conc. H_2SO_4 was added. The reaction mixture was further refluxed for 3 h. After completion of the reaction, the product was cooled to RT and the solvent methanol was removed under vacuum using a rota evaporator. The residue was extracted with ethyl acetate (3×30 mL) and the organic layer was washed with a 10 % sodium carbonate solution, followed by water. Then, it was dried using sodium sulfate and the solvent was removed under vacuum to get a pale-yellow liquid. Yield: 90 %.

^1H NMR (400 MHz, CDCl_3 , δ ppm): 7.51-7.49 (m, 1H), 7.24-7.24 (d, 1H), 6.82-6.78 (m, 1H), 6.71-6.69 (m, 1H), 6.65-6.64 (d, 1H), 6.57-6.55 (d, 1H), 6.51-6.49 (d, 1H), 3.86 (s, 3H), 3.45-3.43 (d, 2H), 1.90-1.87 (m, 1H), 1.38-1.32 (m, 8H), 0.96-0.89 (t, 6H). **^{13}C NMR** (400 MHz, CDCl_3 , δ ppm): 166.35, 144.93, 144.43, 138.58, 132.72, 126.19, 123.58, 122.09, 121.94, 116.13, 115.66, 112.51, 111.08, 51.79, 47.63,

36.60, 30.70, 29.73, 28.76, 24.11, 23.08, 14.15, 14.04, 10.97. Anal. Calcd. for $C_{22}H_{27}NO_3$: C, 74.76; H, 7.70; N, 3.96; and found C, 74.25; H, 7.67; N, 3.88.

Synthesis of 10-(2-ethylhexyl)-7-formyl-10H-phenoxazine-3-carboxylic acid (6)

In a cleaned dry RB flask, freshly distilled DMF (4.8 mL, 62.2 mmol), $POCl_3$ (5.8 mL, 62.2 mmol) was added slowly with constant stirring maintained at 0 °C under an argon atmosphere. Then, a solution of methyl 10-(2-ethylhexyl)-10H-phenoxazine-3-carboxylate (**4**, 0.5 g, 1.41 mmol) dissolved in 5 mL of dichloroethane was added to the above reaction mixture with constant stirring. The reaction flask was allowed to attain room temperature and then heated at 90 °C for 12 h. The reaction mass was quenched in ice-cold water. Its pH was adjusted to 1.0 by adding a 5 M sodium hydroxide solution. The solution was extracted with ethyl acetate (4 x 50 mL) and dried over anhydrous sodium sulfate. The solvent was removed under a vacuum. The obtained product (**5**) was dissolved in 10 mL of methanol. To this solution, 0.25 g of $LiOH \cdot H_2O$ dissolved in 10 mL of water was added and stirred at 80 °C for 8 h. Then, the methanol was removed and the solution was diluted with 100 mL of water. Further, the pH of the solution was made to just be acidic by adding pre-cooled 10 % HCl. The precipitated solid was filtered off and purified using column chromatography technique on 200-400 mesh silica using 2:1 hexane/ethyl acetate mixture. Brown color solid, yield 52%. Melting point: 198-200 °C.

1H NMR (400 MHz, $CDCl_3$, δ ppm): 12.69 (s, 1H), 9.68 (s, 1H), 7.46-7.42 (m, 2H), 7.10-7.08 (d, 2H), 7.06-7.04 (d, 1H), 6.98-6.90 (m, 1H), 3.66-3.64 (d, 2H), 1.80-1.79 (m, 1H), 1.42-1.20 (m, 8H), 0.89-0.80 (t, 6H). ^{13}C NMR (400 MHz, $CDCl_3$, δ ppm): 190.54, 166.83, 166.67, 166.60, 144.77, 144.41, 144.11, 144.02, 138.78, 138.44, 137.12, 136.51, 130.78, 128.85, 126.70, 124.82, 124.28, 116.06, 115.79, 114.28, 113.59, 113.46, 113.19, 36.27, 30.24, 30.14, 28.42, 23.70, 22.96, 14.24, 11.16. Anal. Calcd. for $C_{22}H_{25}NO_4$: C, 71.91; H, 6.86; N, 3.81; and found C, 71.90; H, 6.82; N, 3.79.

General synthetic procedure for dyes p-K₃₅₋₃₆

The starting material 10-(2-ethylhexyl)-7-formyl-10H-phenoxazine-3-carboxylic acid (**6**, 0.2 g, 0.54 mmol) was dissolved in 10 mL of absolute methanol

and stirred at room temperature for 0.5 h. Then, respective clear solution of *N,N*-dimethyl barbituric acid (0.1 g, 0.65 mmol, 1.2 eq) or *N,N*-diethyl thiobarbituric acid (0.13 g, 0.65 mmol, 1.2 eq) dissolved in 5 mL of methanol was added to it slowly with constant stirring. Further, the reaction mass was stirred at 65 °C for 10 h. The precipitated solid was filtered and washed with pre-cooled methanol. The obtained dyes were purified by column chromatography with a 2:1 hexane:ethyl acetate solvent system.

7-((1,3-Dimethyl-2,4,6-trioxotetrahydropyrimidin-5(2H)-ylidene)methyl)-10-(2-ethylhexyl)-10H-phenoxazine-3-carboxylic acid (p-K₃₅)

Pinkish red solid, Yield 87 %. Melting point: 228-230 °C. ¹H NMR (400 MHz, DMSO-d₆, δ ppm): 12.74 (s, 1H), 8.10-8.08 (d, 2H), 7.71-7.69 (d, 1H), 7.46-7.44 (d, 1H), 7.12 (s, 1H), 6.94-6.89 (m, 2H), 3.68-3.67 (d, 2H), 3.22 (s, 6H), 1.36-1.23 (m, 9H), 0.89-0.81 (t, 6H). ¹³C NMR (400 MHz, DMSO-d₆, δ ppm): 166.54, 162.99, 161.30, 154.87, 151.41, 144.23, 143.23, 138.42, 136.22, 135.79, 126.45, 126.40, 125.22, 119.82, 116.00, 114.42, 113.79, 112.80, 47.32, 36.49, 31.15, 30.16, 29.07, 28.45, 23.73. Anal. Calcd. for C₂₈H₃₁N₃O₆: C, 66.52; H, 6.18; N, 8.31 and found C, 66.50; H, 6.11; N, 8.26. **FT-IR (ATR)**, ν cm⁻¹: 2961 (C-H stretch), 1670 (C=O stretch), 1558, 1494 (C=C). **Mass (m/z)**: Calculated: 505.56; Obtained (M-H): 504.25.

7-((1,3-Diethyl-4,6-dioxo-2-thioxotetrahydropyrimidin-5(2H)-ylidene)methyl)-10-(2-ethylhexyl)-10H-phenoxazine-3-carboxylic acid (p-K₃₆)

Purple solid, Yield 87%. Melting point: 228-230 °C. ¹H NMR (400 MHz, DMSO-d₆, δ ppm): 12.72 (s, 1H), 8.17-8.13 (m, 2H), 7.80-7.78 (d, 1H), 7.48-7.45 (m, 1H), 7.16 (s, 1H), 6.99-6.95 (m, 2H), 4.45-4.41 (q, 4H), 3.73-3.71 (d, 2H), 1.37-1.34 (m, 1H), 1.24-1.20 (m, 6H), 1.19-0.91 (m, 8H), 0.89-0.81 (t, 6H). ¹³C NMR (400 MHz, DMSO-d₆, δ ppm): 178.89, 166.50, 161.27, 159.04, 156.95, 144.29, 144.02, 143.26, 139.36, 137.32, 136.52, 135.41, 126.70, 126.45, 125.62, 119.94, 116.09, 114.35, 114.08, 113.48, 112.96, 47.42, 43.91, 43.41, 36.55, 30.14, 28.44, 23.71, 22.98, 14.27, 12.68, 12.63, 11.19. Anal. Calcd. for C₃₀H₃₅N₃O₅S: C, 65.55; H, 6.42; N, 7.64 and found C, 65.51; H, 6.39; N, 7.26. **FT-IR (ATR)**, ν cm⁻¹: 2961 (C-H

stretch), 1685 (C=O stretch), 1540, 1490 (C=C). **Mass (m/z):** Calculated: 549.68; Obtained (M+H): 550.25.

Synthesis of 7-(2,2-dicyanovinyl)-10-(2-ethylhexyl)-10H-phenoxazine-3-carboxylic acid (p-K₃₇)

The starting material 10-(2-ethylhexyl)-7-formyl-10H-phenoxazine-3-carboxylic acid (**6**, 0.2 g, 0.54 mmol) was dissolved in 5 mL of DMF and stirred at room temperature for 0.5 h. Then, malononitrile (0.16 mL, 2.72 mmol, 5 eq.) was added to it slowly with constant stirring. Further, the reaction mass was stirred at 90 °C for 12 h. After completion of the reaction, the solvent was removed under vacuum and the crude product was directly purified using column chromatography technique on 200-400 mesh silica using 2:1 hexane/ethyl acetate mixture to get an orange color fine powder as product, yield 78 %, melting point: 260-262 °C.

¹H NMR (400 MHz, DMSO-d₆, δ ppm): 12.63 (s, 1H), 8.18-8.13 (m, 2H), 7.80-7.78 (d, 1H), 7.47-7.45 (m, 1H), 7.15 (s, 1H), 6.98-6.94 (m, 2H), 3.72-3.71 (d, 2H), 1.38-1.34 (m, 1H), 1.19-0.91 (m, 8H), 0.89-0.83 (t, 6H). ¹³C NMR (400 MHz, DMSO-d₆, δ ppm): 166.84, 166.50, 162.77, 158.80, 144.43, 144.22, 144.12, 144.02, 139.29, 138.46, 137.08, 135.59, 131.27, 126.70, 126.16, 122.88, 115.80, 114.27, 113.28, 112.32, 75.59, 62.51, 47.05, 36.39, 36.27, 30.24, 30.08, 29.47, 28.49, 28.39, 23.77, 23.65, 22.97, 14.26, 11.18, 11.15. Anal. Calcd. for C₂₅H₂₅N₃O₃: C, 72.27; H, 6.06; N, 10.11 and found C, 72.09; H, 6.01; N, 10.06. **FT-IR (ATR)**, ν cm⁻¹: 2959, 2926 (C-H stretch), 2222 (C≡N stretch), 1680 (C=O stretch), 1570, 1499 (C=C), 1156 (C-N stretch). **Mass (m/z):** Calculated: 415.48; Obtained (M-H): 414-20.

Synthesis of (Z)-7-((3-ethyl-4-oxo-2-thioxothiazolidin-5-ylidene)methyl)-10-(2-ethylhexyl)-10H-phenoxazine-3-carboxylic acid (p-K₃₈)

A mixture of 10-(2-ethylhexyl)-7-formyl-10H-phenoxazine-3-carboxylic acid (**6**, 0.3 g, 0.81 mmol) 3-ethylrhodanine (0.15 g, 0.97 mmol), and NH₄OAc (0.69 g, 8.98 mmol) was taken in a dry RB flask and dissolved in 10 mL of glacial acetic acid and further stirred at 110 °C for 12 h under an argon atmosphere. The reaction completion was monitored by the TLC method. After completion of the reaction, the content was cooled to room temperature and then it was poured into 100 g of crushed

ice. The obtained red solid was filtered and dried. The product was purified by column chromatography using silica gel (200-400 mesh) and $\text{CHCl}_3:\text{CH}_3\text{OH}$ (10:1) as the mobile phase to get a red color fine powder as product, yield 84 %, melting point: 230-232 °C.

$^1\text{H NMR}$ (400 MHz, DMSO- d_6 , δ ppm): 12.57 (s, 1H), 7.55 (s, 1H), 7.44-7.42 (m, 1H), 7.11-7.04 (m, 2H), 6.89-6.71 (m, 3H), 4.05-4.03 (d, 2H), 3.59-3.33 (m, 2H), 1.31 (m, 1H), 1.22-0.16 (m, 11H), 0.89-0.81 (t, 6H). $^{13}\text{C NMR}$ (400 MHz, DMSO- d_6 , δ ppm): 192.75, 192.40, 167.09, 166.68, 166.60, 158.78, 144.65, 144.31, 144.14, 143.91, 140.47, 137.14, 136.41, 135.73, 135.50, 132.51, 126.88, 126.70, 126.57, 124.69, 124.35, 119.84, 119.25, 117.26, 116.77, 116.01, 114.13, 113.22, 47.30, 35.44, 30.20, 28.45, 23.75, 22.98, 14.26, 12.38, 11.20. Anal. Calcd. for $\text{C}_{27}\text{H}_{30}\text{N}_2\text{O}_4\text{S}_2$: C, 63.50; H, 5.92; N, 5.49 and found C, 63.48; H, 5.91; N, 5.48. **FT-IR (ATR)**, ν cm^{-1} : 2960 (C-H stretch), 1682 (C=O stretch), 1582, 1501 (C=C). **Mass (m/z)**: Calculated: 510.67; Obtained (M-H): 509.20

Synthesis of (E)-7-(2-(3-(dicyanomethylene)-5,5-dimethylcyclohex-1-en-1-yl)vinyl)-10-(2-ethylhexyl)-10H-phenoxazine-3-carboxylic acid (p-K₃₉)

A mixture of 10-(2-ethylhexyl)-7-formyl-10H-phenoxazine-3-carboxylic acid (**6**, 0.2 g, 0.54 mmol), (3,5,5-trimethylcyclohex-2-enylidene) malononitrile (0.4 g, 2.17 mmol), and piperidine (0.5 mL) was taken in a dry RB flask and dissolved in 10 mL of acetonitrile and further stirred at 80-85 °C for 12 h under an argon atmosphere. The reaction completion was monitored by the TLC method. After completion of the reaction, the content was cooled to room temperature, and then it was poured into 100 g of crushed ice. Further, the product was extracted with ethyl acetate (3 × 30 mL). The crude product was purified by column chromatography using silica gel (200-400 mesh) and $\text{CHCl}_3:\text{CH}_3\text{OH}$ (10:1) as the mobile phase to get pink color fine powder as product, yield 78%, melting point: 280-282 °C.

$^1\text{H NMR}$ (400 MHz, DMSO- d_6 , δ ppm): 12.74 (s, 1H), 7.40-7.38 (m, 1H), 7.28 (s, 1H), 7.24 (s, 1H), 7.13 (s, 2H), 7.08 (s, 1H), 6.83 (s, 1H), 6.80-6.76 (m, 2H), 4.90-3.88 (d, 2H), 1.52 (s, 4H), 1.40-1.16 (m, 8H), 1.01 (s, 6H), 0.89-0.80 (t, 6H). $^{13}\text{C NMR}$ (400 MHz, DMSO- d_6 , δ ppm): 168.09, 166.60, 161.27, 159.04, 156.95, 144.29, 144.02, 143.26, 139.36, 137.32, 136.52, 135.41, 126.70, 126.45, 125.69, 124.35,

119.84, 119.25, 117.26, 116.77, 112.22, 48.30, 36.44, 31.20, 28.45, 23.75, 22.98, 14.16, 12.48. Anal. Calcd. for $C_{34}H_{37}N_3O_3$: C, 76.23; H, 6.96; N, 7.84 and found C, 76.18; H, 6.91; N, 7.78. **FT-IR (ATR)**, ν cm^{-1} : 3341 (-O-H stretching), 2956, 2868 (C-H stretch), 2216 ($C\equiv N$ stretch), 1552, 1500 (C=C stretch). **Mass (m/z)**: Calculated: 535.68; Obtained (M-H): 534.20.

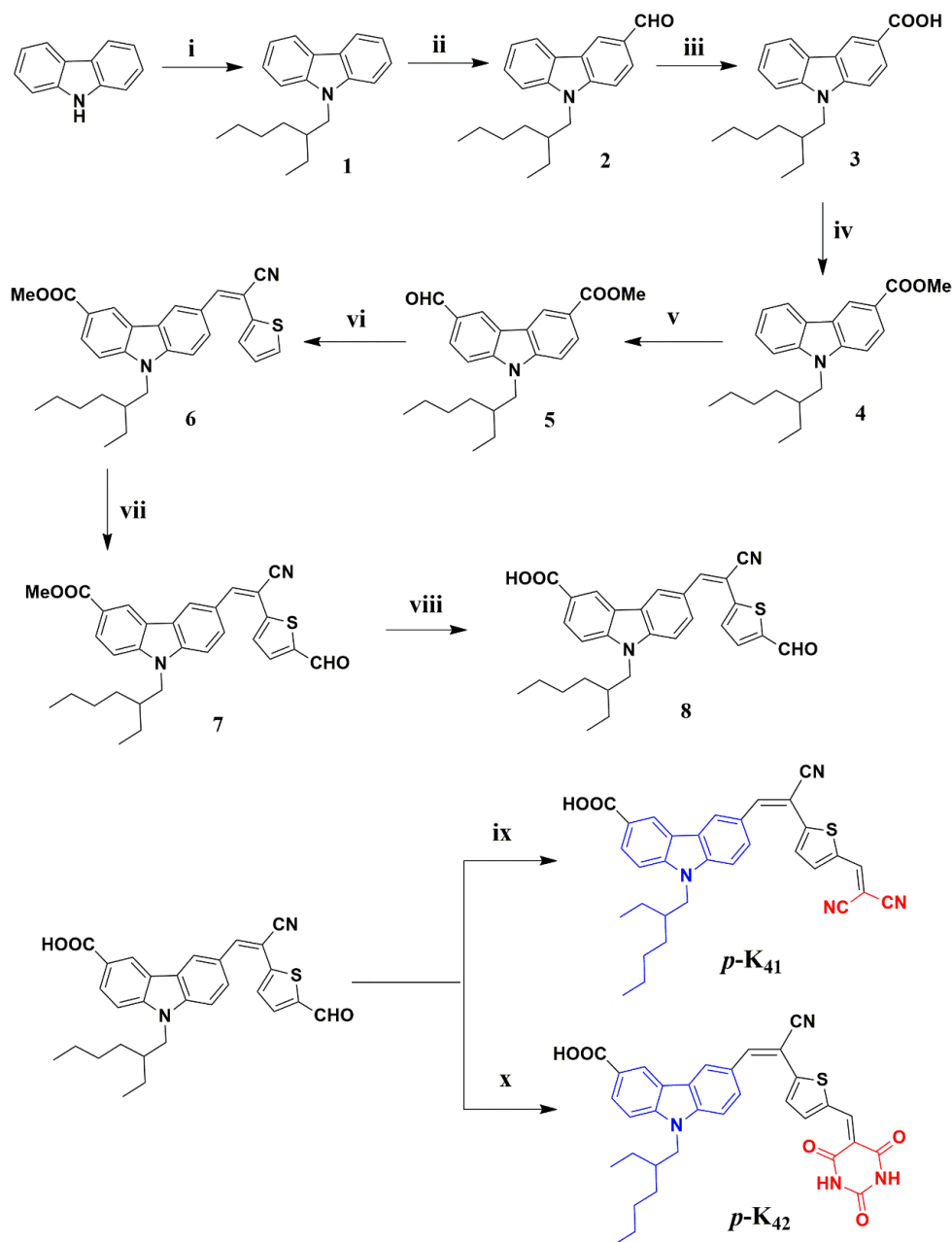
Synthesis of (Z)-10-(2-ethylhexyl)-7-((2-oxindolin-3-ylidene)methyl)-10H-phenoxazine-3-carboxylic acid (p-K₄₀)

A mixture of 10-(2-ethylhexyl)-7-formyl-10H-phenoxazine-3-carboxylic acid (**6**, 0.3 g, 0.81 mmol), 2-oxindole (0.09 g, 0.81 mmol), and piperidine (0.5 mL) was taken in a dry RB flask and dissolved in 8-10 mL of ethanol and further stirred at 80 °C for 12 h under an argon atmosphere. After completion of the reaction, the content was cooled to room temperature. The precipitated solid was filtered and washed with pre-cooled ethanol. The obtained dyes were purified by column chromatography with a 2:1 hexane:ethyl acetate solvent system to get yellowish color fine powder as product, yield 76%, melting point: 266-268 °C.

¹H NMR (400 MHz, DMSO-d₆, δ ppm): 12.52 (s, 1H), 9.26 (s, 1H), 8.27-8.23 (m, 4H), 7.80-7.78 (d, 2H), 7.48-7.45 (m, 2H), 7.15 (s, 1H), 6.98-6.95 (m, 2H), 3.75-3.73 (d, 2H), 1.37-1.34 (m, 1H), 1.18-0.91 (m, 8H), 0.89-0.81 (t, 6H). **¹³C NMR** (400 MHz, DMSO-d₆, δ ppm): 166.38, 164.60, 154.78, 143.65, 140.47, 136.75, 136.41, 135.50, 132.51, 128.88, 126.70, 126.97, 124.69, 124.85, 118.25, 117.26, 116.77, 116.01, 114.13, 112.22, 34.44, 32.20, 28.56, 23.15, 22.88, 14.16, 12.18, 11.40. Anal. Calcd. for $C_{30}H_{30}N_2O_4$: C, 74.67; H, 6.27; N, 5.81 and found C, 74.60; H, 6.18; N, 5.78. **FT-IR (ATR)**, ν cm^{-1} : 2959, 2869 (C-H stretch), 1694 (C=O stretch), 1585, 1502 (C=C). **Mass (m/z)**: Calculated: 482.57; Obtained (M-H): 481.25.

2.3.2.2.2 Synthesis of chromophores **p-K₄₁₋₄₂** (**Series-10**)

The target compounds of **Series 10** were synthesized according to **Scheme 2.10**. The necessary intermediates and target molecules were synthesized using similar well-documented procedures as described in **Series-9** with slight modifications. The detailed characterization data of the intermediates and the final dyes **p-K₄₁₋₄₂** are given in the following section.



Scheme 2.10 Synthetic routes for the dyes *p-K*₄₁₋₄₂: (i) 2-Ethylhexyl bromide, NaH, DMF, RT, 12 h; (ii) POCl₃, DMF, RT, 12 h; (iii) Ag₂O, NaOH, EtOH, RT, 12 h; (iv) MeOH, H₂SO₄, reflux; (v) DMF, POCl₃, 90 °C, 12h; (vi) Thiophene-2-acetonitrile, Na metal, MeOH, RT, 24 h; (vii) DMF, POCl₃, 90 °C, 12h; (viii) LiOH.H₂O, 80 °C, 12 h; (ix) *p-K*₄₁: malononitrile, DMF, 90 °C, 12 h; *p-K*₄₂: barbituric acid, methanol, 65 °C, 12 h.

9-(2-Ethylhexyl)-9H-carbazole (1)

Colorless liquid, Yield: 92%. ¹H NMR (400 MHz, DMSO-d₆, δ ppm): 8.47 (s, 1H), 8.00-7.98 (t, 3H), 7.61 (s, 1H), 7.13-7.11 (d, 3H), 4.07-4.05 (d, 2H), 1.73 (s,

1H), 1.24-1.11 (m, 8H), 0.86-0.84 (t, 6H). Anal. Calcd. for C₂₀H₂₅N: C, 85.97; H, 9.02; N, 5.01; and found C, 85.89; H, 8.99; N, 5.06. **FT-IR (ATR)**, ν cm⁻¹: 3063, 2956 (C-H), 1589, 1533, 1482 (C=C).

9-(2-Ethylhexyl)-9H-carbazole-3-carbaldehyde (2)

Brown solid, Yield: 69%. Melting point: 104-106 °C. **¹H NMR** (400 MHz, DMSO-d₆, δ ppm): 10.09 (s, 1H), 8.89-8.88 (d, 2H), 8.06-8.04 (q, 2H), 7.82-7.81 (d, 2H), 4.39-4.37 (d, 2H), 1.32-1.29 (d, 1H), 1.14-1.11 (m, 9H), 0.85-0.82 (t, 3H), 0.75-0.72 (t, 3H). Anal. Calcd. for C₂₁H₂₅NO: C, 78.77; H, 7.51; N, 4.18; and found C, 78.02; H, 7.49; N, 4.13. **FT-IR (ATR)**, ν cm⁻¹: 3051, 2956 (C-H), 1681 (C=O), 1587, 1482 (C=C).

9-(2-Ethylhexyl)-9H-carbazole-3-carboxylic acid (3)

Pale yellow solid, 75%, Melting point: 138-140 °C. **¹H NMR** (400 MHz, DMSO-d₆, ppm): 12.80 (s, 1H), 8.86-8.84 (d, 1H), 8.32 (s, 1H), 8.11 (s, 1H), 7.72 (s, 1H), 7.59-7.56 (d, 2H), 7.322 (s, 1H), 4.07-4.05 (d, 2H), 1.73 (s, 1H), 1.24-1.11 (m, 8H), 0.86-0.84 (t, 6H). Anal. Calcd. for C₂₁H₂₅NO₂: C, 77.30; H, 7.15; N, 4.72; found; C, 77.26; H, 7.17; N, 4.74.

Methyl 9-(2-ethylhexyl)-9H-carbazole-3-carboxylate (4)

Yellow liquid, Yield: 88 %. **¹H NMR** (400 MHz CDCl₃, ppm): 8.81 (s, 1H), 8.16-8.11 (t, J=7.2 Hz, 2H), 7.50-7.23 (m, 4H), 4.07-4.05 (d, 2H), 3.87 (s, 3H), 1.73 (s, 1H), 1.24-1.11 (m, 8H), 0.86-0.84 (t, 6H). **¹³C NMR** (400 MHz CDCl₃, ppm): 167.97, 143.13, 141.03, 127.26, 126.33, 123.02, 122.90, 122.60, 120.66, 120.62, 119.83, 109.14, 108.19, 51.93, 43.30, 31.55, 28.90, 26.94, 22.55, 14.23, 14.18, 14.02. Anal. Calcd. for C₂₂H₂₇NO₂: C, 77.66; H, 7.44; N, 4.53; found; C, 77.64; H, 7.49; N, 4.53.

Methyl 9-(2-ethylhexyl)-6-formyl-9H-carbazole-3-carboxylate (5)

Brown solid. Yield 52%. Melting point: 196-198 °C. **¹H NMR** (400 MHz CDCl₃, ppm): 10.31 (s, 1H), 8.98 (s, 1H), 8.68 (s, 1H), 8.33-8.31 (d, J=7.6 Hz, 1H), 8.10-8.08 (d, J=8.8Hz, 1H) 7.54-7.30 (m, 2H), 4.07-4.05 (d, 2H), 3.89 (s, 3H), 1.73 (s, 1H), 1.24-1.11 (m, 8H), 0.86-0.84 (t, 6H). **¹³C NMR** (400 MHz, DMSO-d₆, ppm):

193.52, 167.24, 164.71, 157.35, 143.01, 141.14, 135.69, 127.49, 119.70, 118.12, 110.22, 109.45, 40.60, 40.40, 40.29, 40.14, 39.79, 39.51, 39.31, 31.40, 28.92, 26.59, 22.40, 14.39. Anal. Calcd. for $C_{23}H_{27}NO_3$: C, 74.30; H, 6.50; N, 4.33; found; C, 74.28; H, 6.55; N, 4.33.

(Z)-Methyl 6-(2-cyano-2-(thiophen-2-yl)vinyl)-9-(2-ethylhexyl)-9H-carbazole-3-carboxylate (**6**)

Pale yellow solid. Yield 74%. Melting point: 210-212 °C. $^1\text{H NMR}$ (400 MHz CDCl_3 , ppm): 8.97 (s, 1H), 8.66-8.64 (d, 2H), 8.33-8.31 (d, 2H), 8.10-8.06 (m, 2H) 7.54-7.30 (m, 3H), 4.38 (d, 2H), 3.89 (s, 3H), 1.76-1.71 (m, 1H), 1.28-1.13 (m, 8H), 0.85-0.81 (t, 6H). $^{13}\text{C NMR}$ (400 MHz, DMSO-d_6 , ppm): 166.97, 144.13, 141.03, 128.26, 126.33, 124.02, 122.90, 122.60, 120.66, 120.62, 119.83, 109.14, 108.19, 51.93, 43.30, 31.55, 28.90, 26.94, 22.55, 14.53, 14.38, 14.12. Anal. Calcd. for $C_{29}H_{30}N_2O_2S$: C, 74.01; H, 6.43; N, 5.95; found; C, 74.18; H, 6.38; N, 5.91.

(Z)-6-(2-Cyano-2-(5-formylthiophen-2-yl)vinyl)-9-(2-ethylhexyl)-9H-carbazole-3-carboxylic acid (**8**)

Pale brown solid. Yield 52%. Melting point: 230-232 °C. $^1\text{H NMR}$ (400 MHz CDCl_3 , ppm): 10.13 (s, 1H), 9.63 (s, 1H), 8.97 (s, 1H), 8.68-8.66 (d, 2H), 8.33-8.31 (d, 2H), 8.10-8.06 (m, 2H) 7.54-7.30 (m, 2H), 4.38 (d, 2H), 1.72 (s, 1H), 1.26-1.11 (m, 8H), 0.84-0.80 (t, 6H). $^{13}\text{C NMR}$ (400 MHz, DMSO-d_6 , ppm): 192.52, 166.24, 162.71, 158.35, 142.01, 141.14, 135.69, 128.49, 118.70, 118.12, 110.22, 109.45, 40.60, 40.60, 40.69, 40.24, 39.89, 39.61, 39.31, 31.60, 28.82, 22.60, 14.19. Anal. Calcd. for $C_{29}H_{28}N_2O_3S$: C, 71.87; H, 5.82; N, 5.78; found; C, 71.28; H, 5.80; N, 5.72.

(Z)-6-(2-Cyano-2-(5-(2,2-dicyanovinyl)thiophen-2-yl)vinyl)-9-(2-ethylhexyl)-9H-carbazole-3-carboxylic acid (**p-K₄₁**)

Orange solid, Yield 82%. Melting point: 240-242 °C. $^1\text{H NMR}$ (400 MHz, DMSO-d_6 , δ ppm): 12.57 (s, 1H), 7.67-7.55 (m, 1H), 7.44-7.42 (d, 2H), 6.89-6.87 (d, 3H), 6.85-6.57 (m, 4H), 4.05-4.03 (d, 2H), 1.35-1.31 (m, 1H), 1.24-1.16 (m, 8H), 0.89-0.81 (t, 6H). $^{13}\text{C NMR}$ (400 MHz, DMSO-d_6 , δ ppm): 166.84, 166.50, 162.77, 158.80, 144.43, 144.22, 144.12, 144.02, 139.29, 138.46, 137.08, 135.59, 131.27,

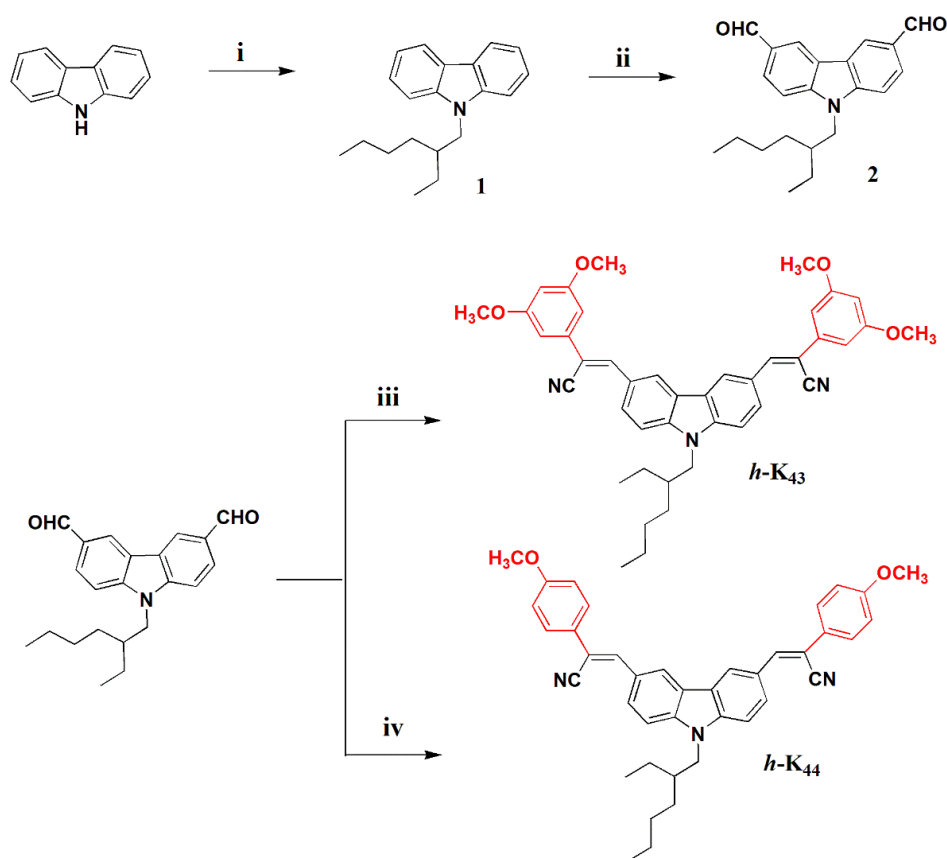
126.70, 126.16, 122.88, 115.80, 114.27, 113.28, 112.32, 75.59, 62.51, 47.05, 36.39, 36.27, 30.24, 30.08, 29.47, 28.49, 28.39, 23.77, 23.65, 22.97, 14.26, 11.18, 11.15. Anal. Calcd. for C₃₂H₂₈N₄O₂: C, 72.16; H, 5.30; N, 10.52 and found C, 72.12; H, 5.16; N, 10.50. **FT-IR (ATR)**, ν cm⁻¹: 2959, 2926 (C-H stretch), 2222 (C≡N stretch), 1680 (C=O stretch), 1570, 1499 (C=C stretch). **Mass (m/z)**: Calculated: 532.66; Obtained: 532.25.

(Z)-6-(2-Cyano-2-(5-((2,4,6-trioxotetrahydropyrimidin-5(2H)-ylidene)methyl)thiophen-2-yl)vinyl)-9-(2-ethylhexyl)-9H-carbazole-3-carboxylic acid (**p-K₄₂**)

Brown solid, Yield 79%. Melting point: 284-286 °C. **¹H NMR** (400 MHz, DMSO-d₆, δ ppm): 12.74 (s, 1H), 9.87 (s, 2H), 8.10-8.08 (d, 2H), 7.71-7.69 (d, 1H), 7.46-7.44 (d, 1H), 7.12 (s, 2H), 6.94-6.89 (m, 4H), 3.68-3.67 (d, 2H), 3.22 (s, 6H), 1.36-1.23 (m, 9H), 0.89-0.81 (t, 6H). **¹³C NMR** (400 MHz, DMSO-d₆, δ ppm): 164.54, 162.99, 161.30, 154.87, 151.41, 144.23, 143.23, 138.42, 136.22, 135.79, 126.45, 126.40, 125.22, 119.82, 116.00, 114.42, 113.79, 112.80, 47.32, 36.49, 31.15, 30.16, 29.07, 28.45, 22.73, 11.18. Anal. Calcd. for C₃₃H₃₀N₄O₅S: C, 66.65; H, 5.08; N, 9.42 and found C, 66.62; H, 5.18; N, 9.40. **FT-IR (ATR)**, ν cm⁻¹: 2961 (C-H stretch), 1670 (C=O stretch), 1558, 1494 (C=C stretch). **Mass (m/z)**: Calculated: 594.68; Obtained (M+H): 595.30.

2.3.2.3 Synthesis of organic HTMs **h-K₄₃₋₄₄** (Series-11)

The synthetic protocols employed for the preparation of dyes **p-K₄₃₋₄₄** from simple starting material carbazole is given here. The target compounds of **Series-11** were synthesized according to **Scheme 2.11**. The requisite intermediate 9-(2-ethylhexyl)-9H-carbazole (**1**) was obtained from 9H-carbazole by treating it with 2-ethylhexyl bromide in presence of a strong base, *i.e.* sodium hydride. This was converted to the key precursor 9-(2-ethylhexyl)-9H-carbazole-3,6-dicarbaldehyde (**2**) through the Vilsmeier-Hack reaction in good yield. Finally, compound **2** on reaction with (3,5-dimethoxyphenyl)acetonitrile and (4-methoxyphenyl) acetonitrile yielded **p-K₄₃₋₄₄** by following the Knoevenagel condensation protocol.



Scheme 2.11 Synthetic routes for the HTMs *h-K*₄₃₋₄₄: (i) 2-Ethylhexyl bromide, NaH, DMF, RT, 12 hours (ii) POCl₃, DMF, 95 °C, 12 hours (iii) (3,5-Dimethoxyphenyl) acetonitrile, potassium *tert*-butoxide, methanol, 60 °C, 6 hours (iv) (4-Methoxyphenyl) acetonitrile, potassium *tert*-butoxide, methanol, 60 °C, 6 hours

Synthesis of 9-(2-ethylhexyl)-9H-carbazole (*I*)

A mixture of carbazole (0.1 g, 0.598 mmol), NaH (0.07 g, 2.99 mmol) was dissolved in a minimum amount of DMF (5 mL) and stirred at room temperature for half an hour under an inert atmosphere. Later, 2-ethylhexyl bromide (0.34 g, 1.79 mmol) was added into the reaction mixture and continued stirring at room temperature for 12 h. The reaction progress was monitored using the thin-layer chromatography (TLC). After completion of the reaction, the reaction mixture was cooled and poured into crushed ice (100 mL) and neutralization was done using a saturated solution of ammonium chloride. The precipitate formed was filtered, washed with ice-cold water and finally, it was recrystallized using ethanol to get colorless liquid as a product. Yield: 92%.

¹H NMR (400 MHz, DMSO-d₆, δ ppm): 8.47 (s, 1H), 8.00-7.98 (t, 3H), 7.61 (s, 1H), 7.13-7.11 (d, 3H), 4.07-4.05 (d, 2H), 1.73 (s, 1H), 1.24-1.11 (m, 8H), 0.86-0.84 (t, 6H). Anal. Calcd. for C₂₀H₂₅N: C, 85.97; H, 9.02; N, 5.01; and found C, 85.89; H, 8.99; N, 5.06. **FT-IR (ATR)**, ν cm⁻¹: 3063, 2956 (C-H), 1589, 1533, 1482 (C=C), 1191 (C-N).

Synthesis of 9-(2-ethylhexyl)-9H-carbazole-3,6-dicarbaldehyde (2)

In a cleaned two-neck round bottom flask, freshly distilled DMF (1.22 mL, 15.75 mmol) was taken and cooled at -3 to 4 °C. Then, phosphorous oxychloride, POCl₃ (1.67 mL, 17.90 mmol) was added drop-wise with constant stirring at the same temperature under an argon atmosphere to obtain a glassy white salt. To this mixture, 9-(2-ethylhexyl)-9H-carbazole (**1**, 0.2 g, 0.71 mmol) dissolved in dichloroethane (2 mL) was added. The reaction mixture was refluxed at 95 °C for 12 h. After completion of the reaction, the reaction mass was cooled to room temperature and poured into 100 mL crushed ice, and subsequently basified by using a 5 M NaOH solution. The product formed was extracted with ethyl acetate (50 mL x 3) and the organic layer was dried over sodium sulphate and evaporated under reduced pressure. The impure residue was later purified by column chromatography on silica gel (100-200 mesh and hexane: EtOAc, 4:1 eluent) to yield a light brown solid (**2**). Yield: 69%. Melting point: 104-106 °C.

¹H NMR (400 MHz, DMSO-d₆, δ ppm): 10.09 (s, 2H), 8.89-8.88 (d, 2H), 8.06-8.04 (q, 2H), 7.82-7.81 (d, 2H), 4.39-4.37 (d, 2H), 1.32-1.29 (d, 1H), 1.14-1.11 (m, 8H), 0.85-0.82 (t, 3H), 0.75-0.72 (t, 3H). Anal. Calcd. for C₂₂H₂₅NO₂: C, 78.77; H, 7.51; N, 4.18; and found C, 78.02; H, 7.49; N, 4.13. **FT-IR (ATR)**, ν cm⁻¹: 3051, 2956 (C-H), 1681 (C=O), 1587, 1482 (C=C).

Synthesis of (2Z, 2'Z)-3, 3'-(9-(2-ethylhexyl)-9H-carbazole-3,6-diyl)bis(2-(3,5-dimethoxy phenyl)acrylonitrile) (h-K₄₃)

A mixture of 9-(2-ethylhexyl)-9H-carbazole-3,6-dicarbaldehyde (**2**, 0.05 g, 0.14 mmol) and potassium *tert*-butoxide (0.27 g, 2.47 mmol) was dissolved in dry methanol (10 mL) and stirred at room temperature under an argon atmosphere for 15 min. Later, (3,5-dimethoxy phenyl) acetonitrile (0.1 g, 0.62 mmol) was added while

stirring and the reaction mixture was refluxed for 6 h. The precipitate formed was filtered, washed with absolute methanol and finally, it was recrystallized from chloroform to obtain bright yellow color solid. Yield: 84%. Melting point: 192-194 °C.

¹H NMR (400 MHz, DMSO-d₆, δ ppm): 8.72 (s, 2H), 8.18-8.15 (t, 4H), 7.80-7.78 (d, 2H), 7.39 (s, 2H), 7.31-7.28 (d, 2H), 7.10-7.08 (d, 2H), 4.37-4.36 (d, 2H), 3.89 (s, 12H), 1.40-1.31 (m, 9H), 1.30-1.26 (t, 6H). **¹³C NMR** (400 MHz, DMSO-d₆, δ ppm): 148.66, 148.29, 141.32, 140.28, 126.92, 126.27, 124.80, 122.06, 121.49, 118.11, 117.76, 110.31, 108.83, 107.55, 107.01, 76.32, 76.20, 76.00, 75.68, 55.08, 55.03, 46.79, 38.49, 29.98, 28.68, 27.78, 23.39, 21.99, 12.99, 9.87. Anal. Calcd. for C₄₂H₄₃N₃O₄: C, 77.16; H, 6.63; N, 6.43; and found C, 77.54; H, 6.89; N, 6.41. **FT-IR (ATR)**, ν cm⁻¹: 2921 (C-H), 2207 (C≡N), 1592, 1513, 1472 (C=C). **Mass (m/z)**: 653.81; Obtained (M+Na)⁺: 676.31.

Synthesis of (2Z, 2'Z)-3, 3'-(9-(2-ethylhexyl)-9H-carbazole-3,6-diyl)bis(2-(4-methoxyphenyl) acrylonitrile) (h-K₄₄)

A mixture of 9-(2-ethylhexyl)-9H-carbazole-3,6-dicarbaldehyde (**2**, 0.05 g, 0.14 mmol), and potassium *tert*-butoxide (0.27 g, 2.47 mmol) was dissolved in dry methanol (10 mL) and stirred at room temperature under an argon atmosphere for 15 min. Later, (4-methoxyphenyl) acetonitrile (0.09 g, 0.62 mmol) was added while stirring and the reaction mixture was refluxed for 6 h. The precipitate formed was filtered, washed with absolute methanol and finally, it was recrystallized using chloroform to obtain pale orange-yellow color solid. Yield: 79%. Melting point: 178-180 °C.

¹H NMR (400 MHz, DMSO-d₆, δ ppm): 8.72 (s, 2H), 8.19-8.15 (m, 5H), 7.81-7.79 (d, 3H), 7.39 (s, 2H), 7.31-7.28 (d, 2H), 7.11-7.09 (d, 2H), 4.38-4.36 (d, 2H), 3.89 (s, 3H), 3.82 (s, 3H), 2.04-2.03 (d, 1H), 1.18-1.31 (m, 8H), 0.90-0.86 (t, 3H), 0.80-0.77 (t, 3H). **¹³C NMR** (400 MHz, DMSO-d₆, δ ppm): 160.06, 142.27, 141.08, 127.61, 127.13, 127.08, 125.89, 123.06, 122.55, 119.14, 114.43, 109.81, 107.84, 77.35, 77.24, 77.04, 76.72, 55.46, 47.80, 39.51, 31.01, 28.82, 24.42, 23.02, 14.03, 10.90. Anal. Calcd. for C₄₀H₃₉N₃O₂: C, 80.91; H, 6.62; N, 7.08; and found C,

80.76; H, 6.70; N, 7.10. **FT-IR (ATR), ν cm⁻¹**: 3018 (C-H), 2209 (C≡N), 1605, 1510, 1488 (C=C). **Mass (m/z)**: 593.30; Obtained: 593.

2.3.3 Results and discussion

All the designed molecules were synthesized following standard synthetic protocols. The reaction parameters such as temperature, solvent, reaction rate, the concentration of reaction, and catalyst were optimized in order to get a good yield. The chemical structures of newly synthesized target molecules (dyes/HTMs) and their intermediates were confirmed by various spectroscopic techniques including elemental analysis. In the following section, the structural characterization of few selected representative molecules has been discussed.

2.3.3.1 *n*-Type organic dyes *n*-**K**₁₋₃₄ (Series 1-8)

Chromophores *n*-**K**₁₋₄ (Series-1)

Structures of all final compounds as well, as their intermediates were confirmed by ¹H NMR, ¹³C NMR, FTIR, and mass spectral analysis followed by elemental analysis. In this particular series, *n*-**K**₁ was chosen as the representative dye for the discussion. The ¹H NMR spectrum of *n*-**K**₁ is depicted in **Figure 2.12**. The spectrum showed the appearance of a unique peak for a proton of carboxylic acid at δ 11.33 ppm. The eight aromatic protons were observed in the region of δ 8.48-7.11 ppm. The ¹³C NMR spectrum of dye *n*-**K**₁ (**Figure 2.13**) showed the characteristic signals obtained at a higher frequency (downfield region). The carbonyl carbon of *n*-**C**₂ resonated at δ 166.50 and 161.27 ppm, whereas the signals of remaining carbons appearing in the region of δ 159.04-112.96 ppm are due to other aromatic carbons. In addition, the aliphatic carbons appeared around 36.55-11.19 ppm. Further, its FTIR spectrum (**Figure 2.14**), showed a sharp peak at 2208 cm⁻¹ indicating the presence of the cyano group. Finally, the structure of dye *n*-**K**₁ was confirmed by mass spectrophotometric analysis (**Figure 2.15**). The mass spectrum displayed the [M-H] peak at 489.10, which is in agreement with the calculated molecular weight for the formula of C₂₉H₃₄N₂O₃S (490.23). In a similar way, the structures of all other intermediates, as well as final compounds of the **Series-1**, have been confirmed using NMR, FTIR, and mass spectral data.

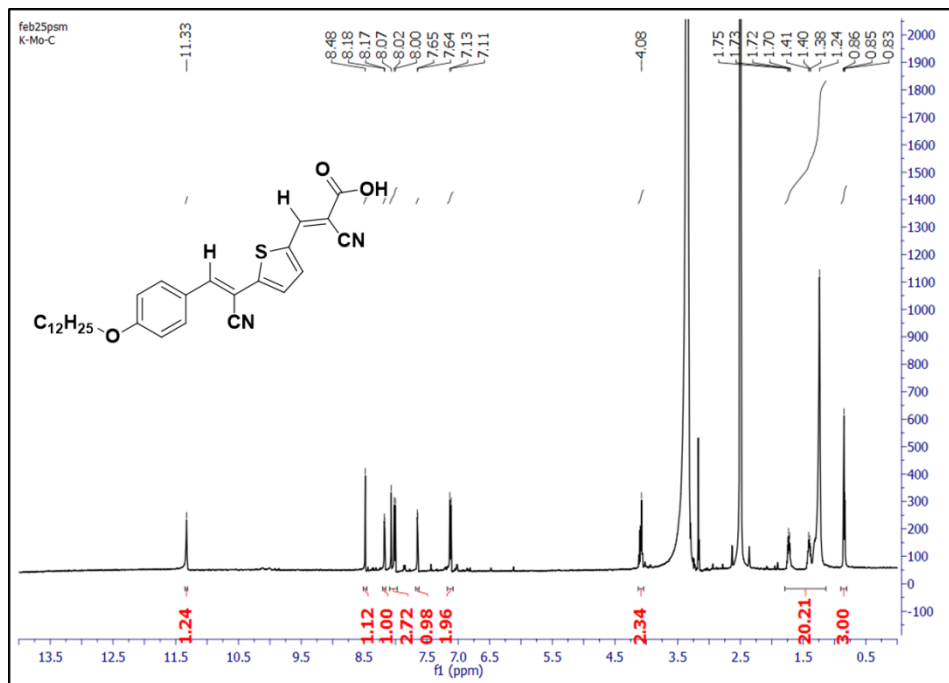


Figure 2.12 ^1H NMR spectrum of dye $n\text{-K}_1$ recorded in DMSO-d_6

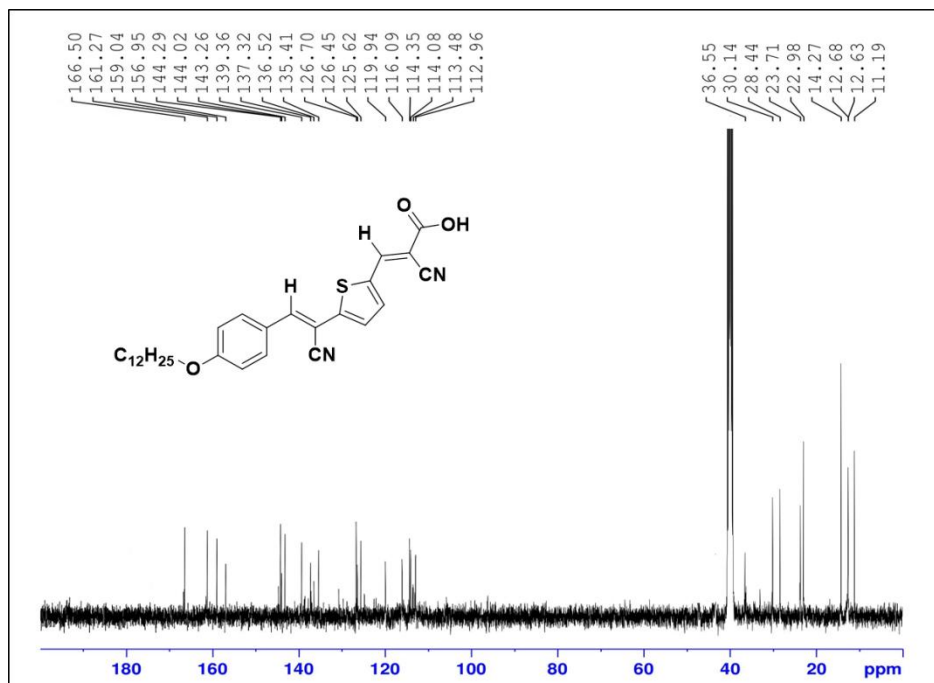


Figure 2.13 ^{13}C NMR spectrum of dye $n\text{-K}_1$ recorded in DMSO-d_6

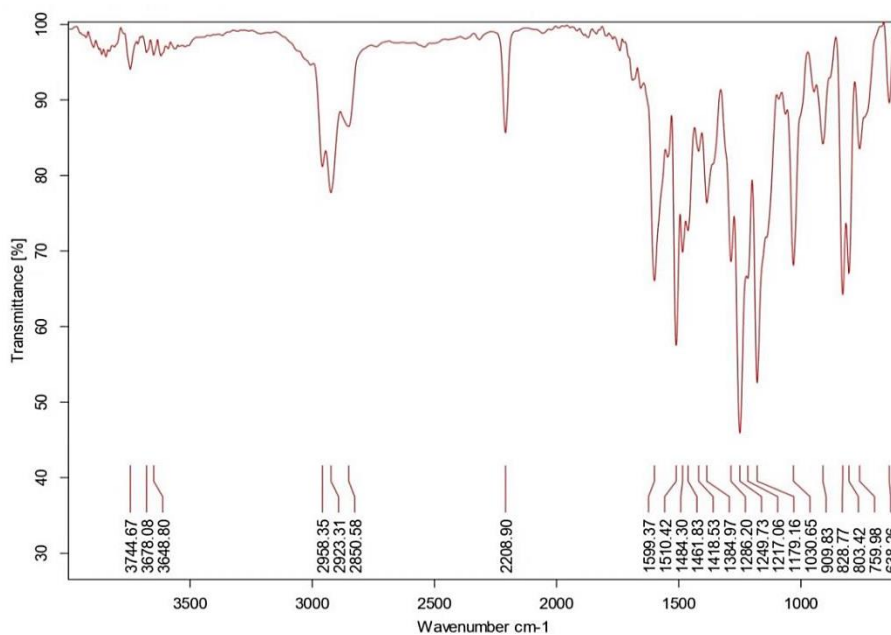


Figure 2.14 FTIR spectrum of dye $n\text{-K}_1$

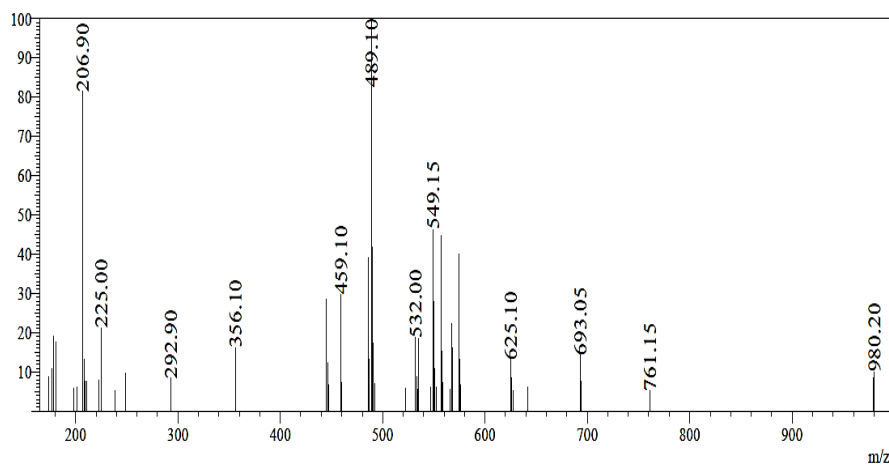


Figure 2.15 LCMS spectrum of dye $n\text{-K}_1$

Chromophores $n\text{-K}_{5-11}$ (Series-2)

The chemical structures of all the target molecules and their respective intermediates of this series were well-characterized by ^1H NMR, ^{13}C NMR, Mass spectrometry/scopy, and elemental analysis. **Figure 2.16** shows the ^1H NMR spectrum of compound $n\text{-K}_5$. The molecule showed one unique resonance peak for the acid proton of cyanoacetic acid, *i.e.* at δ 10.05 ppm. The appearance of a sharp singlet at δ 8.85 and δ 8.75 ppm can be ascribed to the protons of the vinylene group

linked to the aromatic carbazole ring at the 3rd position. All the other aromatic protons of the twin carbazole rings resonated in between δ 8.45 to 7.29 ppm. Further, the appearance of a triplet in between δ 4.42 to 4.39 ppm can be assigned to four protons of methylene (-CH₂) attached to the *N* of the hexyl chain. Also, the primary and secondary protons of the hexyl chain have appeared as peaks in the region of 1.72 to 1.31 ppm as a multiplet. The ¹³C NMR spectrum of *n-K*₅ displayed the characteristic signals at the downfield region (**Figure 2.17**). The two carbonyl carbons of cyanoacetic acid resonated at δ 164.63, 155.66 ppm. The signal that appeared at δ 117.79 ppm is due to the cyano group of cyanoacetic acid. All the other signals in the region of δ 143.94 to 98.85 ppm are due to other aromatic carbons, whereas the aliphatic carbons appeared between 31.15 to 26.42 ppm. Further, the FTIR spectrum (**Figure 2.18**), showed a sharp peak at 2226 cm⁻¹. This indicates the presence of the cyano group, whereas carbonyl vibration has appeared at 1687 cm⁻¹. **Figure 2.19** represents the mass spectrum of *n-K*₅. The spectrum displayed the [M-H] peak at 605.25, which is in good agreement with the calculated molecular weight (606.67), which confirms the chemical structure of the synthesized dye *n-K*₅.

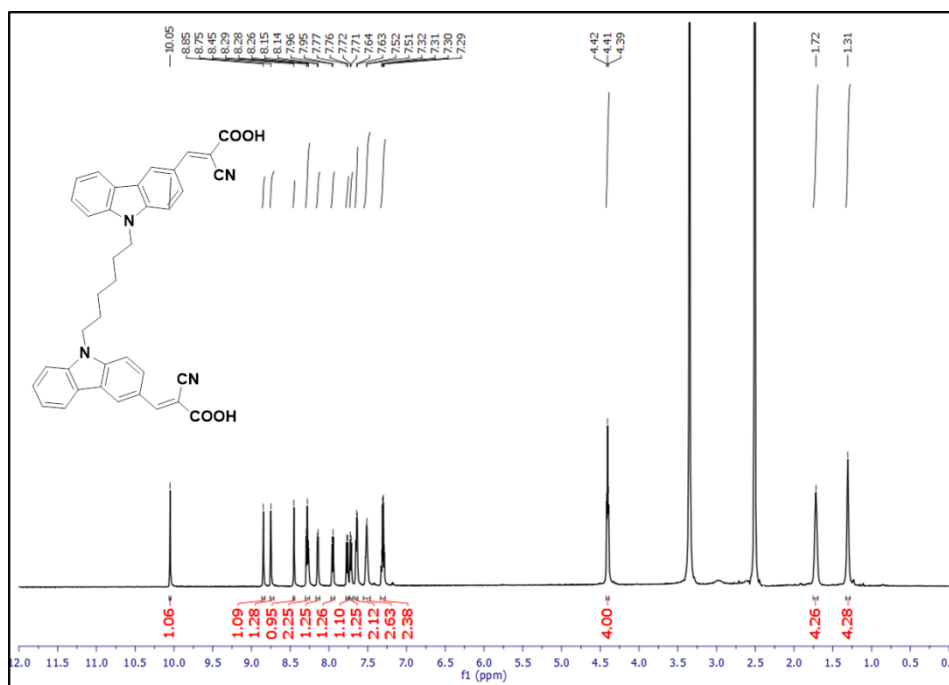


Figure 2.16 ¹H-NMR spectrum of dye *n-K*₅ recorded in DMSO-d₆

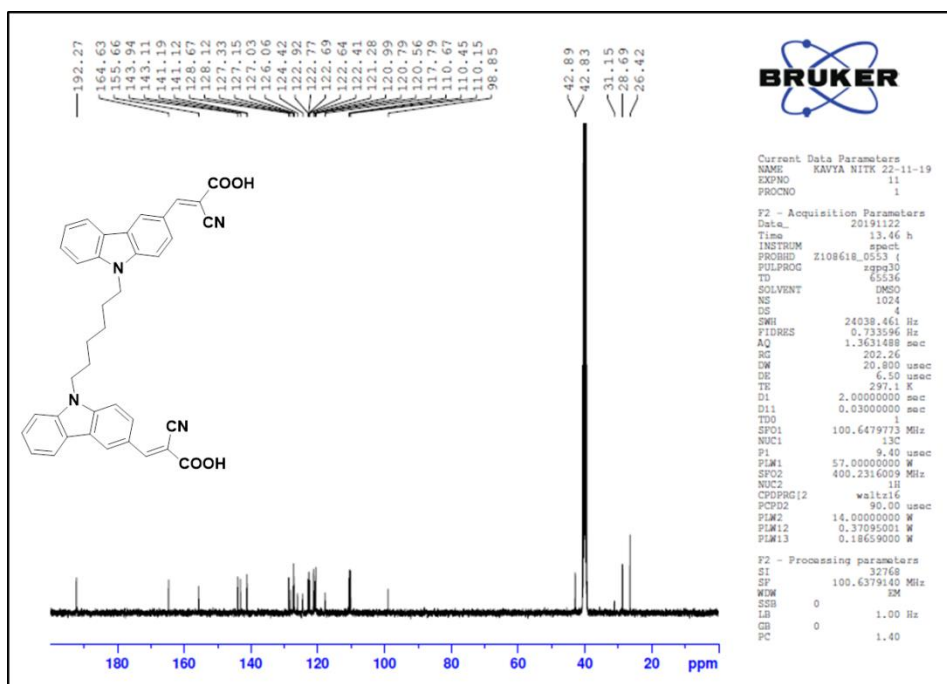


Figure 2.17 ^{13}C -NMR spectrum of dye $n\text{-K}_5$ recorded in DMSO-d_6

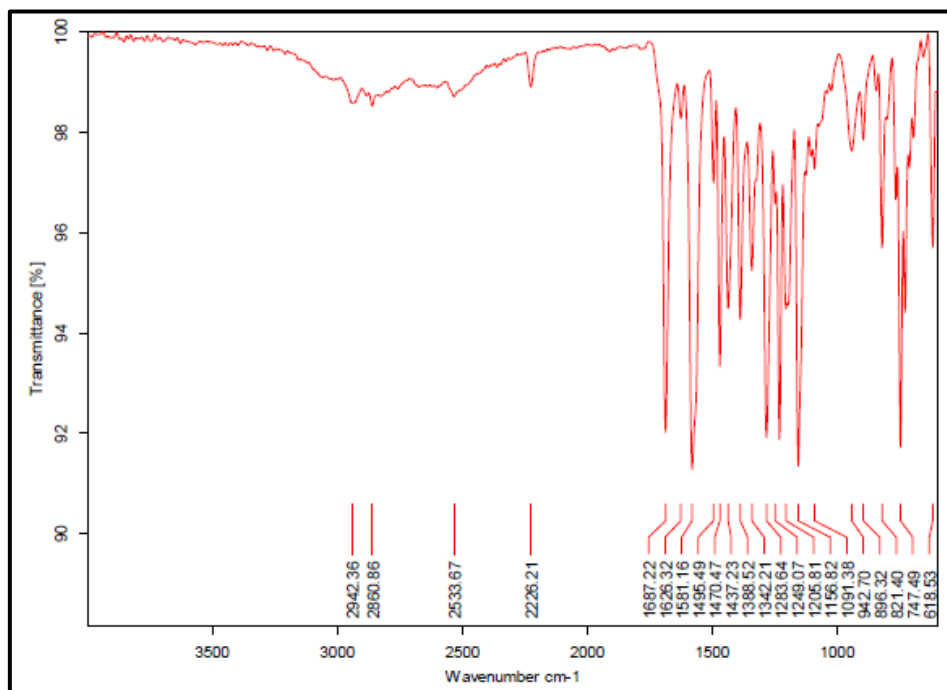


Figure 2.18 FTIR spectrum of dye $n\text{-K}_5$

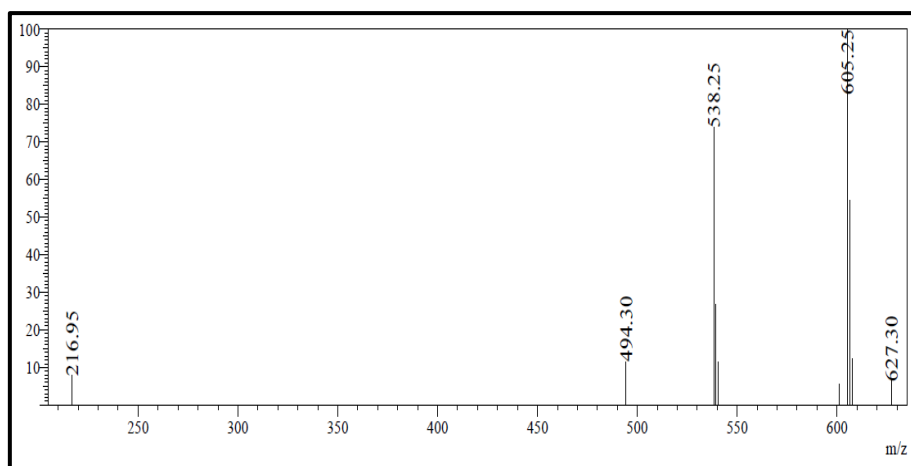


Figure 2.19 LCMS spectrum of dye *n-K*₅

Chromophores *n-K*₁₂₋₁₈ (Series-3)

The molecular structures of all the target molecules and their respective intermediates of this series were well characterized by ¹H NMR, ¹³C NMR, Mass spectrometry/scopy, and elemental analysis. The ¹H NMR, ¹³C NMR, FTIR, and mass spectra of the selected dye *n-K*₁₃ are depicted in **Figures 2.20, 2.21, 2.22, and 2.23**, respectively. In its ¹H NMR spectrum, the molecule showed one unique resonance peak for the acid proton of cyanoacetic acid, *i.e.* one at δ 10.05 ppm. All the other aromatic protons of twin carbazole units appeared in between δ 8.73 to 7.29 ppm. Further, the peaks in the region of 4.77 to 1.34 ppm correspond to primary and secondary protons of the pentyl chain as well as protons of rhodanine-3-acetic acid. The ¹³C NMR spectrum of *n-K*₁₃ displayed the characteristic signals at the downfield region. The two carbons of the thione group in rhodanine-3-acetic acid appeared at δ 193.66 ppm, δ 192.30 ppm, whereas the carbonyl carbons of cyanoacetic acid resonated at δ 166.99 ppm. The signal that appeared at δ 117.77 ppm is due to the cyano group of cyanoacetic acid. All the other signals in the region of δ 143.95 to 110.18 ppm are due to the aromatic carbons, whereas the aliphatic carbons appeared between 28.69 to 26.43 ppm. Further, the FTIR spectrum showed a characteristic sharp peak at 2361 cm⁻¹ demonstrating the presence of the C \equiv N functional group, whereas C=O vibration of carbonyl carbon in cyanoacetic acid appeared at 1700 cm⁻¹. The mass spectrum displayed the [M-H] peak at 803.15, which is matched with the calculated molecular weight.

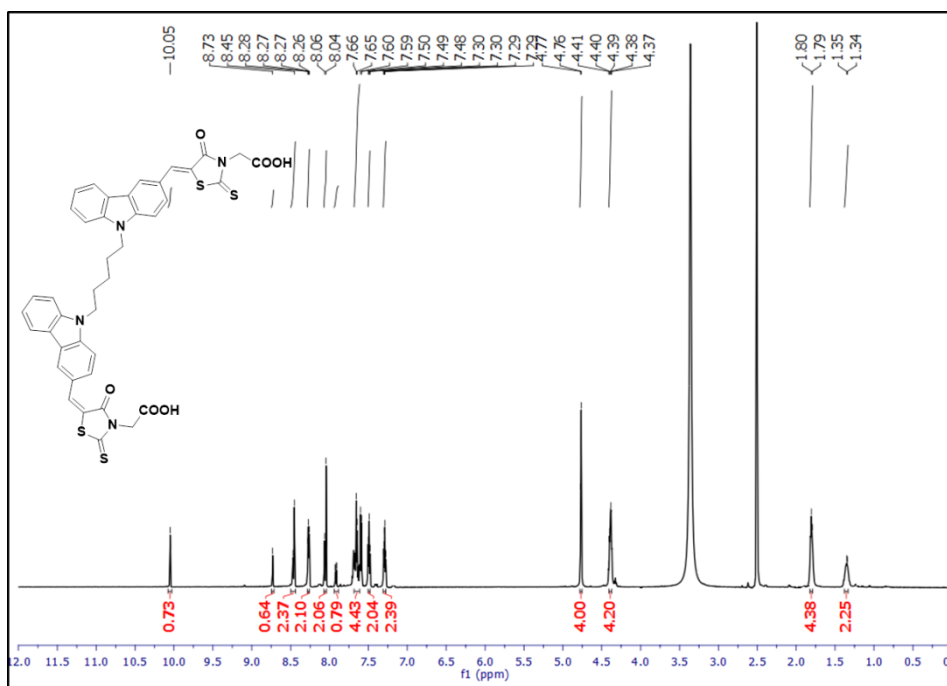


Figure 2.20 $^1\text{H-NMR}$ spectrum of dye *n-K*₁₃ recorded in DMSO-d_6

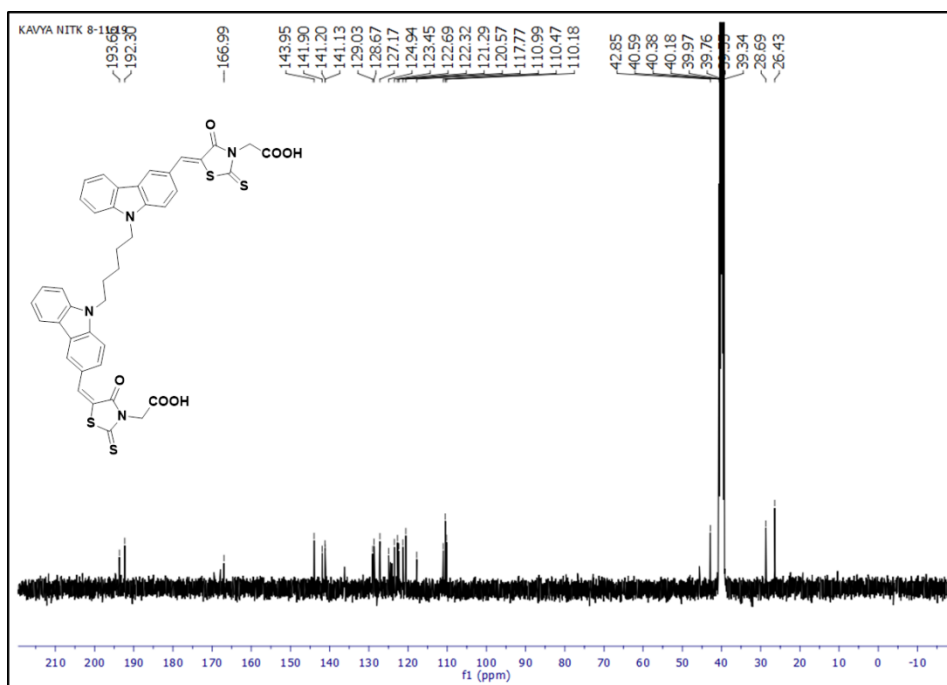


Figure 2.21 $^{13}\text{C-NMR}$ spectrum of dye *n-K*₁₃ recorded in DMSO-d_6

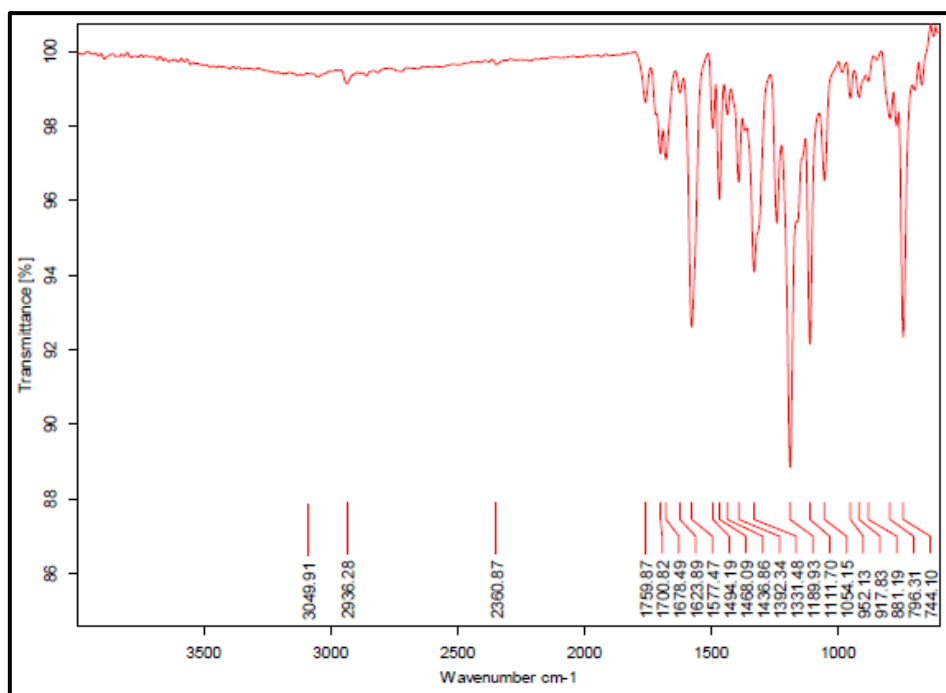


Figure 2.22 FTIR spectrum of dye *n-K*₁₃

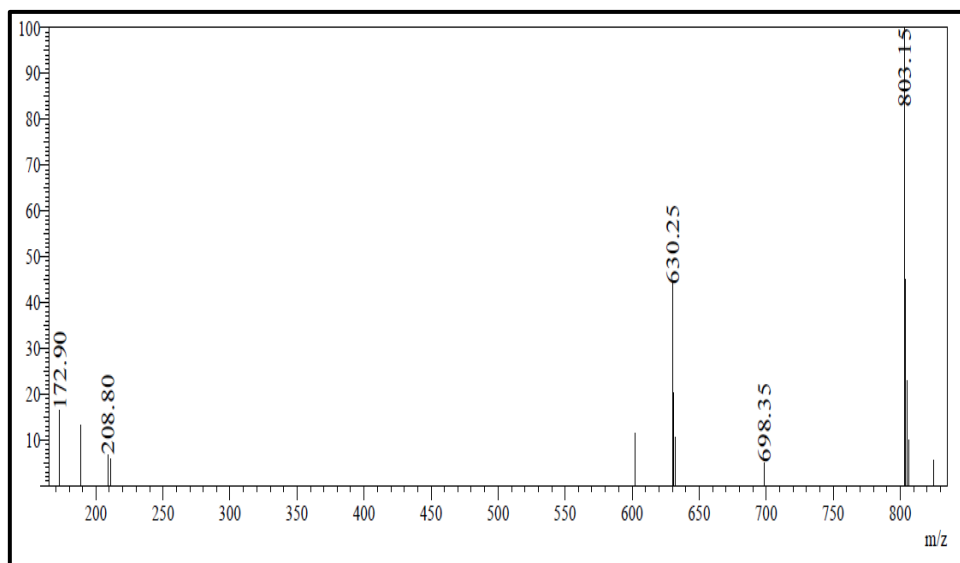


Figure 2.23 LCMS spectrum of dye *n-K*₁₃

Chromophores *n-K*₁₉₋₂₁ (Series-4)

The structures of all the final compounds and their intermediates are well characterized by ¹H NMR, ¹³C NMR, Mass spectrometry/scopy and elemental analysis. In ¹H NMR spectrum (Figure 2.24) of *n-K*₁₉, all the aromatic protons of two carbazole core and phenylene ring resonated in between δ 8.79 to 7.43 ppm. Also, the

peaks in the region of δ 4.42 to 1.22 ppm are due to the primary and secondary protons of the pentyl chain. The ^{13}C NMR spectrum of *n-K*₁₉ (Figure 2.25) displayed the characteristic signals of carbonyl carbons of cyanoacetic acid resonated at δ 162.92 ppm and δ 150.55 ppm. The signal that appeared at δ 117.79 ppm is due to the cyano group of cyanoacetic acid. All the other signals in the region of δ 143.94 to 90.42 ppm are due to other aromatic carbons, whereas the aliphatic carbons appeared between 42.89 to 26.42 ppm. Further, the FTIR spectrum (Figure 2.26) showed a characteristic broad peak at 3414 cm^{-1} , which corresponds to a hydroxyl group (-OH), whereas the sharp peaks at 2210 cm^{-1} and 1667 cm^{-1} represent the presence of $\text{C}\equiv\text{N}$ functional group, carbonyl carbon in cyanoacetic acid, respectively. Finally, its mass spectrum (Figure 2.27) exhibited the [M-H] peak at 845.28, which is in good agreement with the calculated molecular weight (846.93), which confirms the chemical structure of the synthesized molecule *n-K*₁₉.

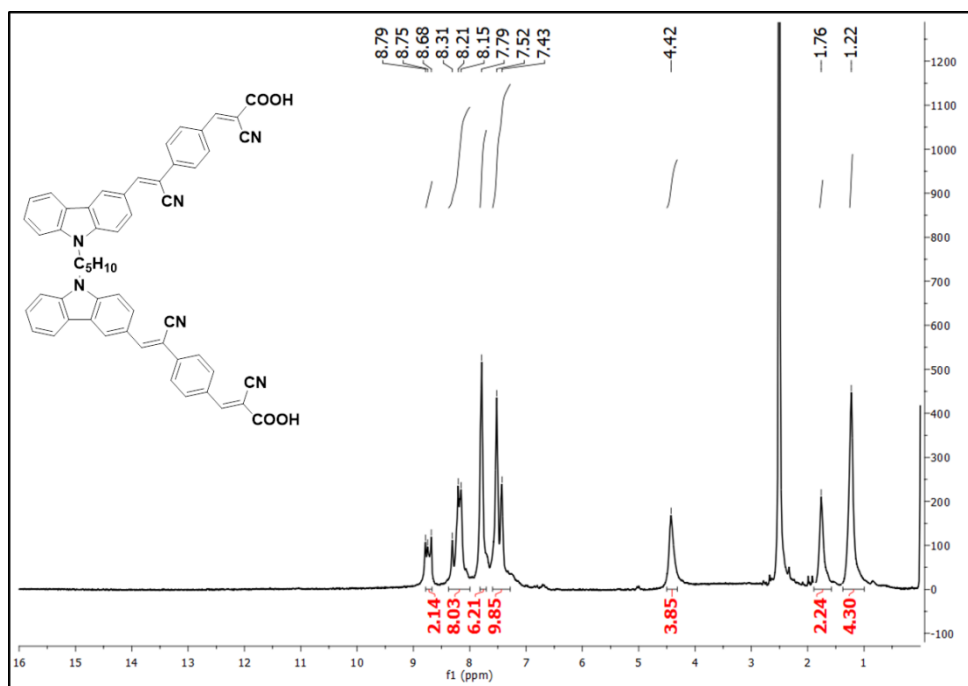


Figure 2.24 ^1H -NMR spectrum of dye *n-K*₁₉ recorded in DMSO-d_6

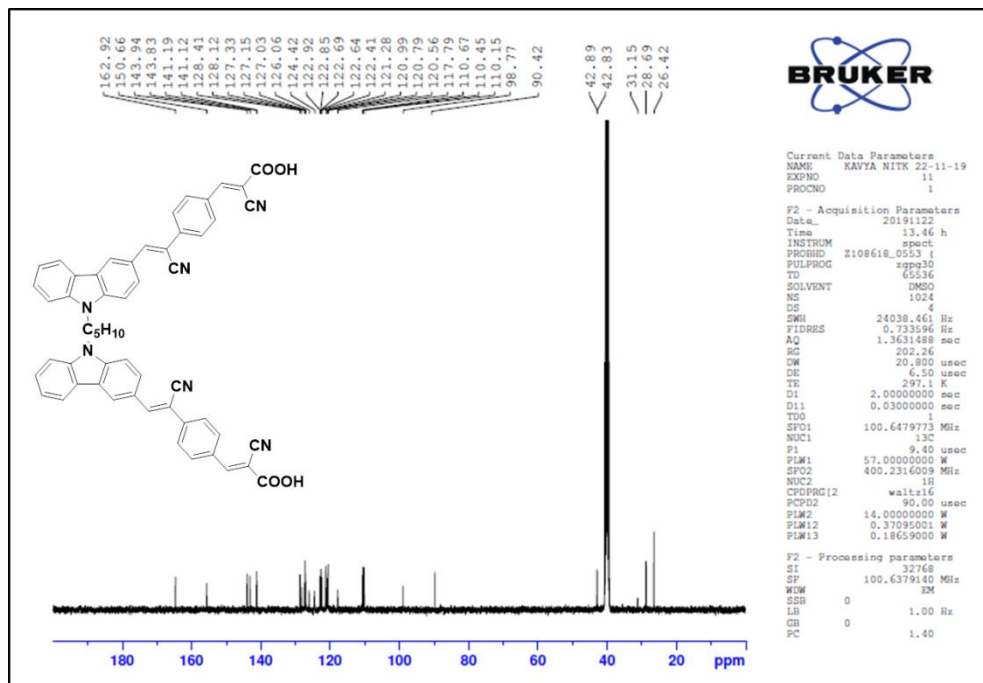


Figure 2.25 ^{13}C -NMR spectrum of dye *n*-**K**₁₉ recorded in DMSO-*d*₆

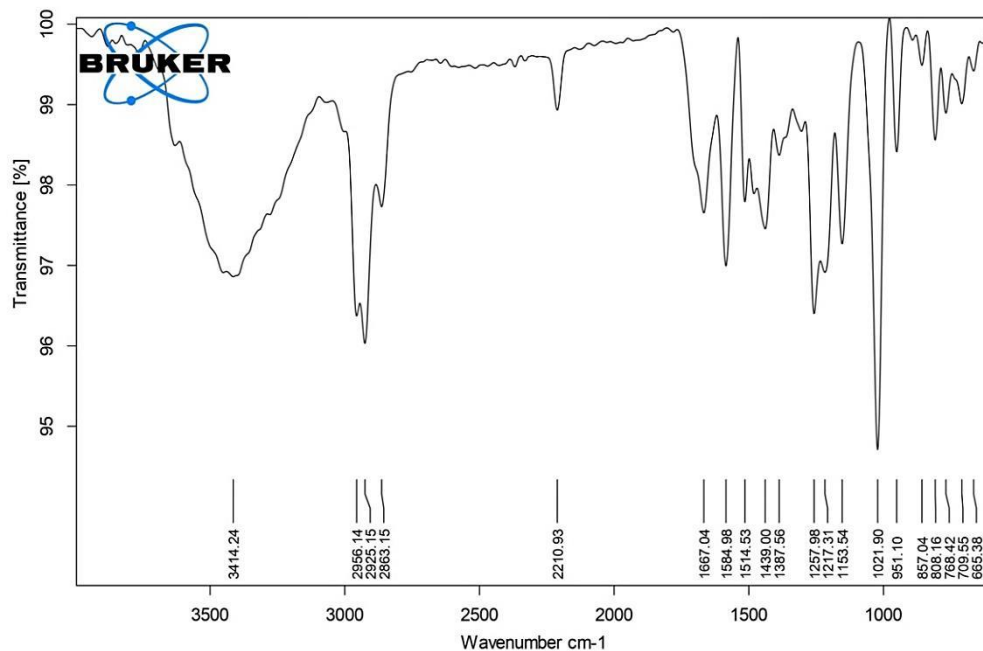


Figure 2.26 FTIR spectrum of dye *n*-**K**₁₉

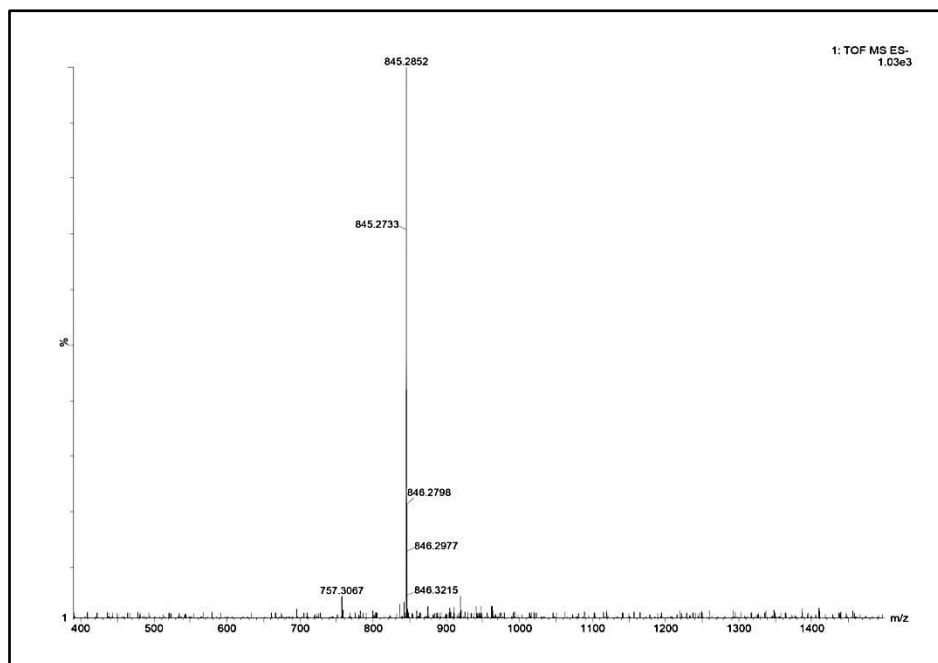


Figure 2.27 LCMS spectrum of dye *n-K*₁₉

Chromophores *n-K*₂₂₋₂₄ (Series-5)

The chemical structures of all the intermediates and final compounds of this series are well-elucidated by ¹H NMR, ¹³C NMR spectroscopy, Mass spectrometry, and elemental analysis. The ¹H NMR spectrum of *n-K*₂₂ is shown in **Figure 2.28**. All the aromatic protons of twin carbazole units and the phenylene ring resonated in between δ 8.79 and 7.43 ppm. Further, the appearance of a singlet in δ 4.42 ppm can be assigned to four protons of methylene (-CH₂) attached to the *N* of the octyl chain. Also, the primary and secondary protons of the octyl chain have appeared as peaks in the region of 1.76 to 1.22 ppm as a multiplet. The ¹³C NMR spectrum of *n-K*₂₂ molecule is shown in **Figure 2.29**. The spectrum showed the characteristic signals of carbonyl carbons of cyanoacetic acid resonated at δ 164.70 ppm and δ 162.89 ppm. The signal that appeared at δ 117.79 ppm is due to the cyano group of cyanoacetic acid. Further, all the other aromatic carbons signals have appeared in the region of δ 157.33 to 109.66 ppm. In addition, the aliphatic carbons resonated between 28.73 to 26.44 ppm. The FTIR spectrum displayed in **Figure 2.30** showed characteristic sharp peaks at 2226 cm⁻¹ and 1687 cm⁻¹ signifying the presence of cyano group, and carbonyl group of cyanoacetic acid, respectively. Finally, its mass spectrum (**Figure**

2.31) exhibited the [M-H] peak at 888.31, which is in good agreement with the calculated molecular mass, confirming the chemical structure of the synthesized molecule *n-K*₂₂.

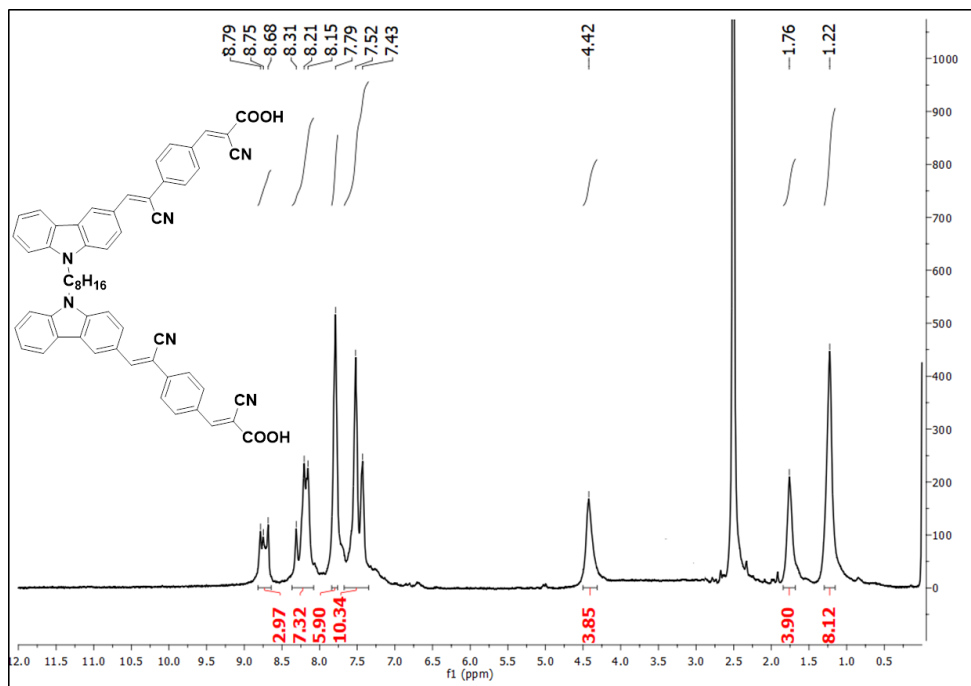


Figure 2.28 ¹H-NMR spectrum of dye *n-K*₂₂ recorded in DMSO-d₆

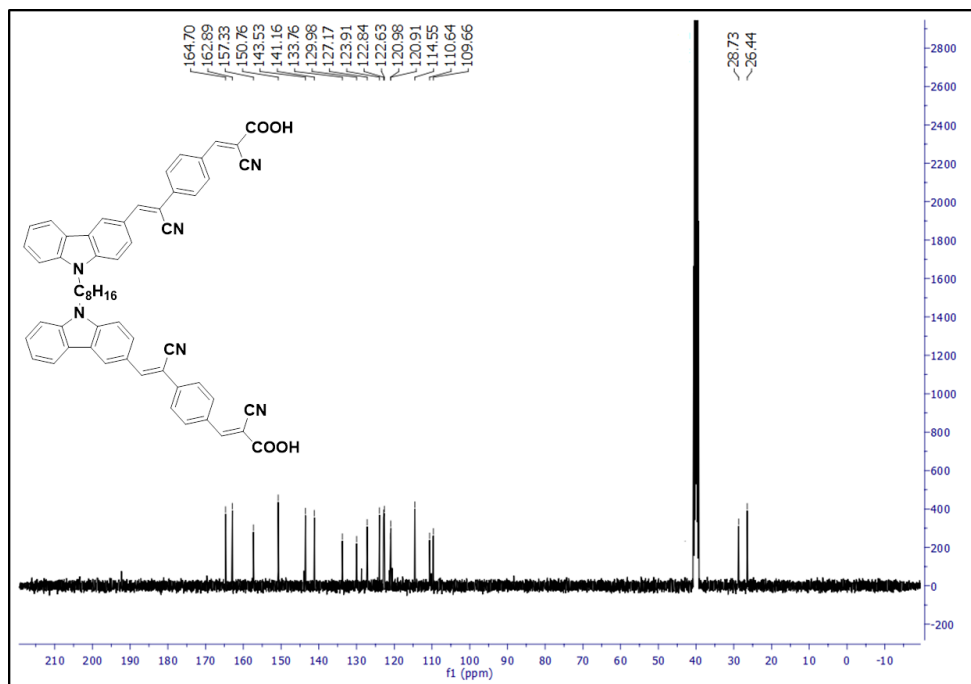


Figure 2.29 ¹³C-NMR spectrum of dye *n-K*₂₂ recorded in DMSO-d₆

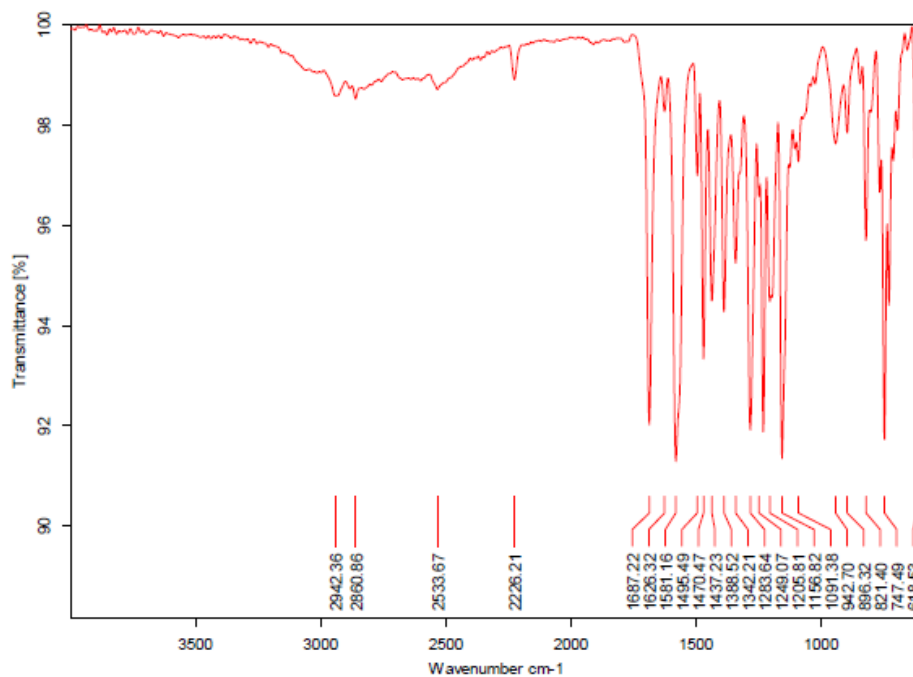


Figure 2.30 FTIR spectrum of dye *n-K*₂₂

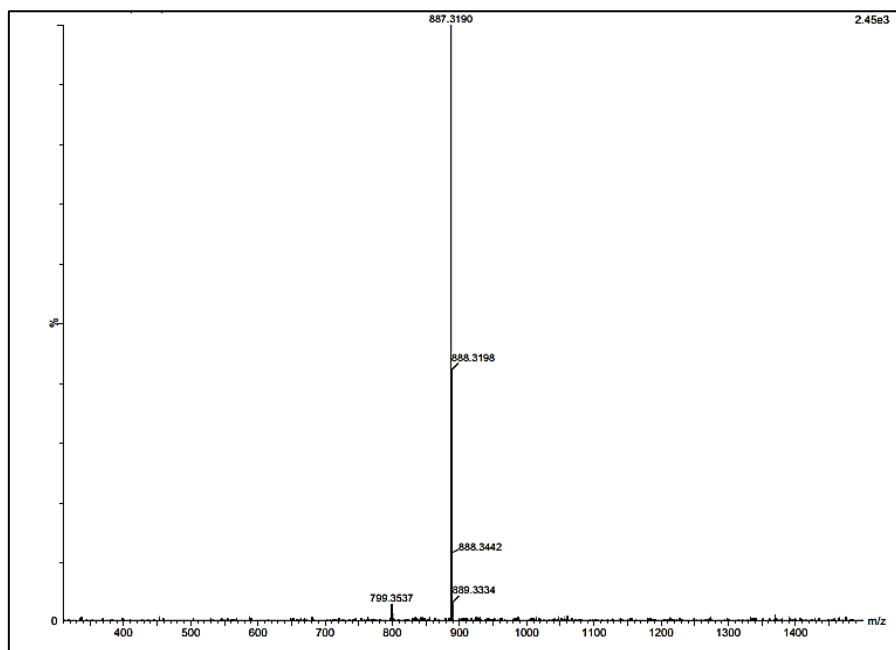


Figure 2.31 LCMS spectrum of dye *n-K*₂₂

Chromophores *n-K*₂₅₋₂₈ (Series-6)

The chemical structures of all the molecules of the series were confirmed by different spectroscopic tools. The ¹H NMR spectrum of *n-K*₂₅ is depicted in **Figure 2.32**. In this spectrum, the molecule showed a sharp singlet at δ 10.10 ppm, which

represents two protons of cyanoacetic acid. The appearance of a sharp singlet at δ 8.67 ppm indicates the presence of two $-\text{CH}$ groups on either side of (1,4-phenylene)diacetonitrile unit. All the aromatic protons of carbazole units and the phenylene ring resonated in between δ 8.20 to 7.31 ppm. Further, the appearance of a quartet in δ 4.42-4.37 ppm can be assigned to four protons of methylene ($-\text{CH}_2$) attached to the *N* of the carbazole core. The ^{13}C NMR spectrum of *n-K*₂₅ is shown in **Figure 2.33**. The spectrum showed the peaks owing to the carbonyl carbons of cyanoacetic acid resonated at δ 164.70 ppm and δ 162.89 ppm. The signal appeared at δ 119.91 and 119.90 ppm is due to the cyano group of cyanoacetic acid. Further, all the other aromatic carbons signals have appeared in the region of δ 157.33 to 106.36 ppm. In addition, the aliphatic carbons appeared between 37.84 to 13.89 ppm. The FTIR spectrum (**Figure 2.34**) displayed sharp peaks at 2211 cm^{-1} and 1672 cm^{-1} indicating the presence of cyano, and carbonyl groups of cyanoacetic acid, respectively. Finally, its mass spectrum (**Figure 2.35**) exhibited the $[\text{M}]$ peak at 756.25, which is in good agreement with the calculated molecular mass (756.81), confirming the chemical structure of the synthesized molecule *n-K*₂₅.

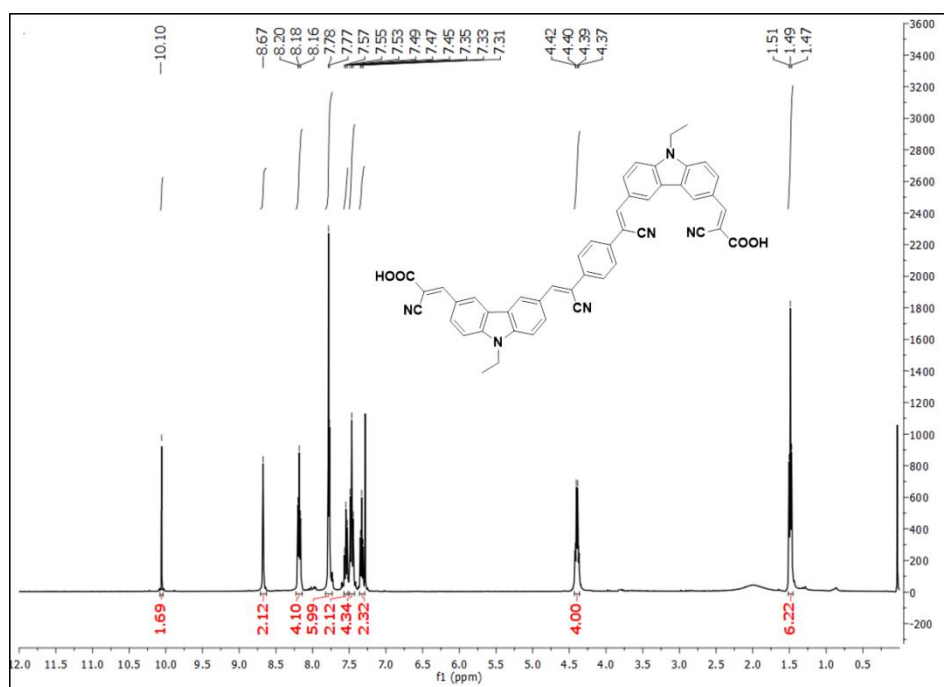


Figure 2.32 ^1H -NMR spectrum of dye *n-K*₂₅ recorded in DMSO-d_6

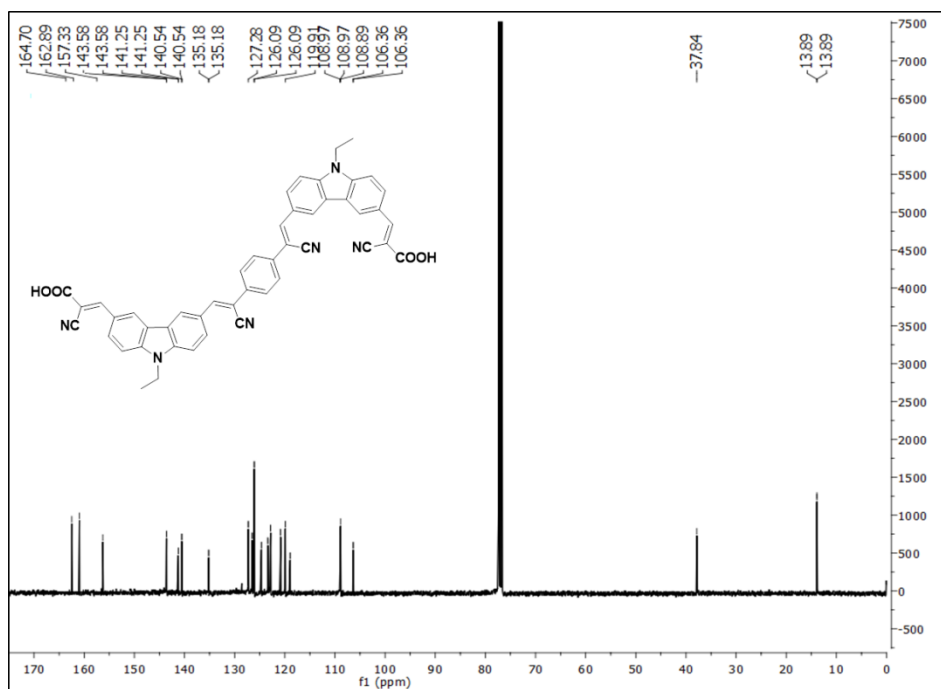


Figure 2.33 ¹³C-NMR spectrum of dye *n-K*₂₅ recorded in DMSO-d₆

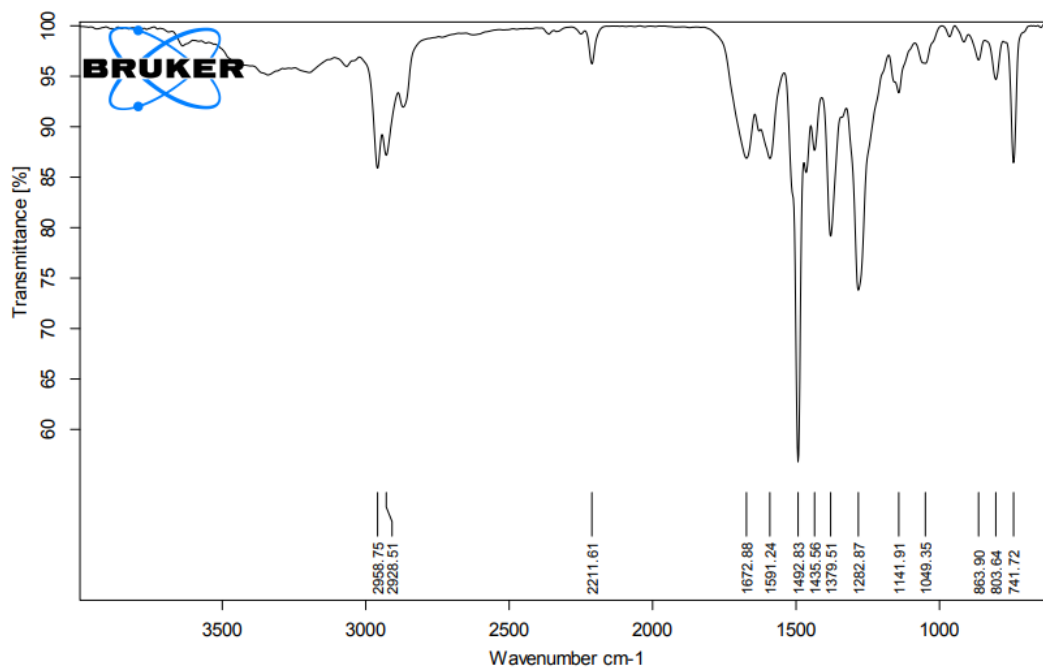


Figure 2.34 FTIR spectrum of dye *n-K*₂₅

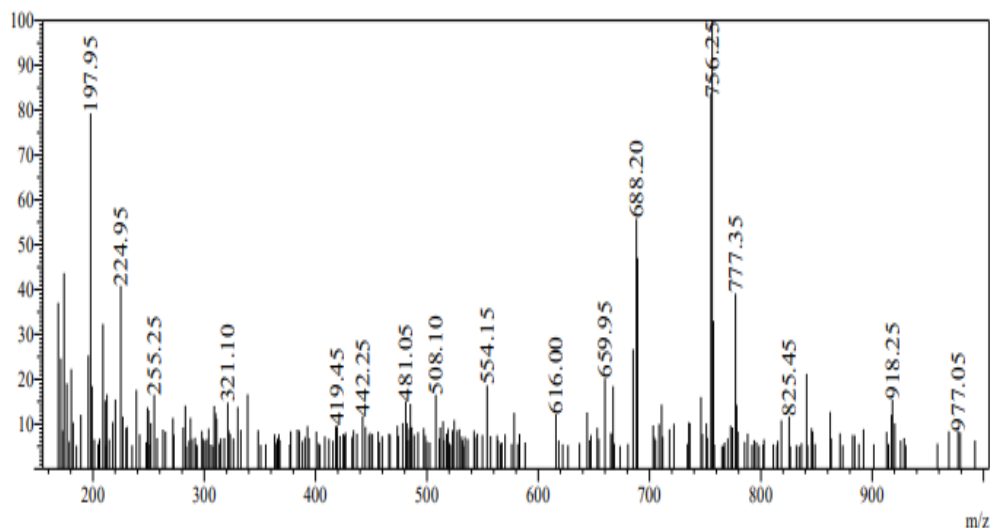


Figure 2.35 LCMS spectrum of dye *n-K*₂₅

Chromophores *n-K*₂₉₋₃₁ (Series-7)

Figures 2.36, 2.37, 2.38, and 2.39 depict the ¹H NMR, ¹³C NMR, FTIR, and mass spectra of molecule *n-K*₂₉. In the ¹H NMR spectrum, the characteristic singlet at δ 10.05 ppm corresponds to two protons of carboxylic acid. All the other aromatic protons of phenoxazine core and thiophene linker resonated in between δ 7.37 to 6.56 ppm. Further, the appearance of a doublet in δ 3.49-3.47 ppm can be assigned to two protons of methylene (-CH₂) in ethylhexyl chain attached to the *N* of the phenoxazine core. In the ¹³C NMR spectrum of *n-K*₂₉, the characteristic peaks of carbonyl carbons resonated at δ 189.60 ppm and δ 189.55 ppm. The signal that appeared at δ 117.31 ppm is due to the cyano group of cyanoacetic acid. All the other aromatic carbons signals are resonated in the region of δ 146.86 to 112.04 ppm, whereas aliphatic carbons appeared between 48.06 to 10.94 ppm. The FTIR spectrum displayed a sharp peak at 2211 cm⁻¹ indicating the presence of a cyano group of cyanoacetic acid. Finally, its mass spectrum displayed the [M-H] peak at 750.08, which is matching with the calculated molecular mass, confirming the chemical structure of the synthesized molecule *n-K*₂₉.

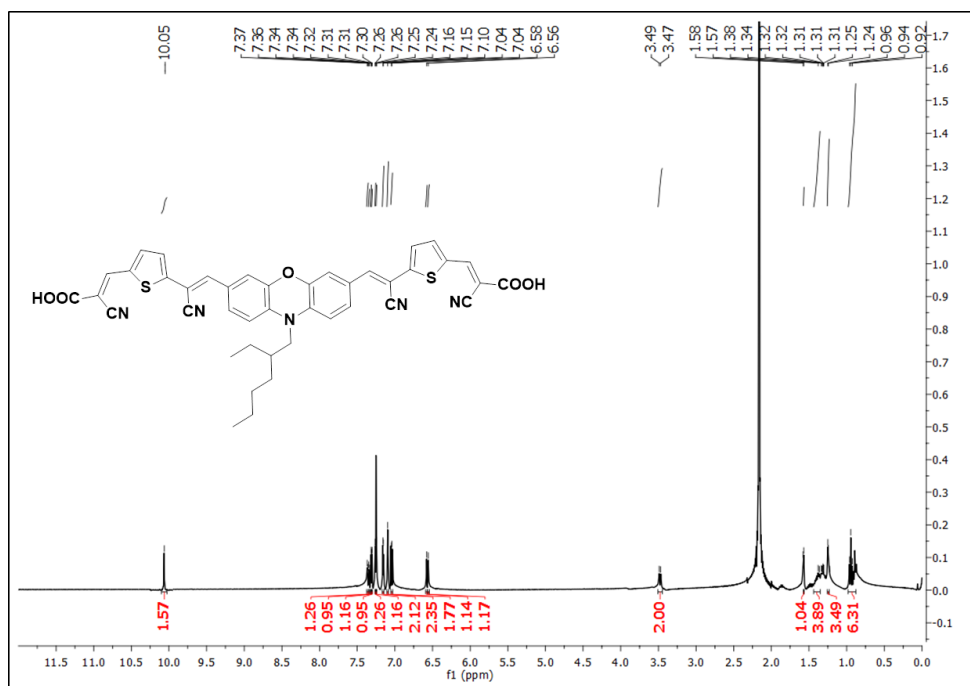


Figure 2.36 $^1\text{H-NMR}$ spectrum of dye *n-K*₂₉ recorded in DMSO-d_6

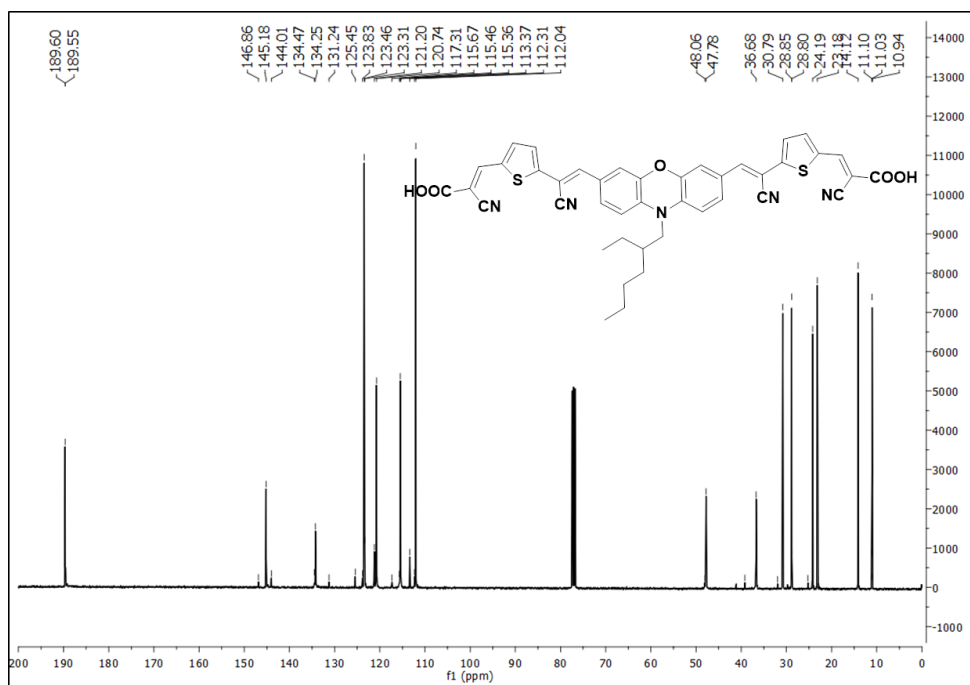


Figure 2.37 $^{13}\text{C-NMR}$ spectrum of dye *n-K*₂₉ recorded in DMSO-d_6

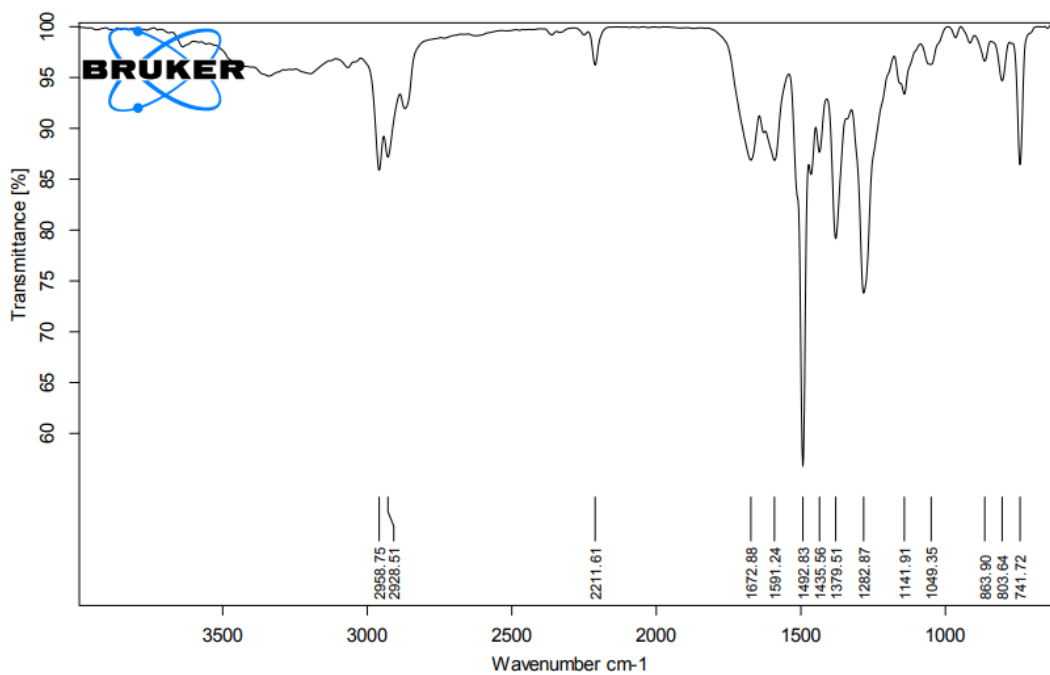


Figure 2.38 FTIR spectrum of dye *n-K*₂₉

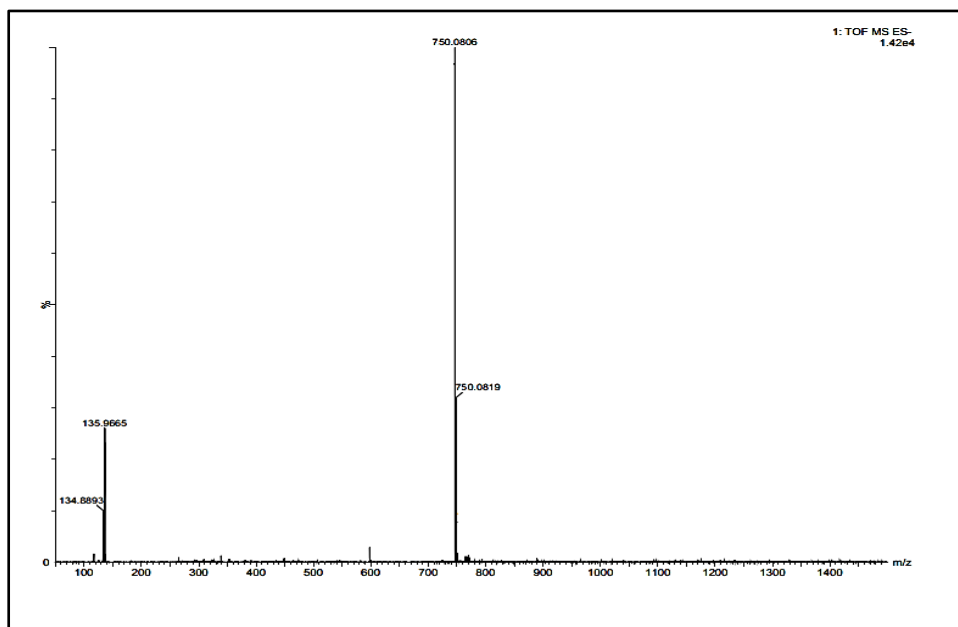


Figure 2.39 LCMS spectrum of dye *n-K*₂₉

Chromophores *n-K*₃₂₋₃₄ (Series-8)

Structures of all final compounds, as well as their intermediates, were confirmed by ¹H NMR, ¹³C NMR, FTIR and mass spectral analysis. In this particular series, *n-K*₃₂ was chosen as the representative dye for the discussion. In the ¹H NMR

spectrum (**Figure 2.40**), the characteristic peak at δ 10.10 ppm represents the presence of two protons of carboxylic acid. The vinylic protons have resonated as a singlet in δ 8.74 ppm. All the aromatic protons of phenoxazine core and phenylene linker resonated in between δ 8.48 to 7.63 ppm, whereas the aliphatic protons appeared in the range of δ 4.36-0.78 ppm. In the ^{13}C NMR spectrum (**Figure 2.41**), the characteristic peaks of carbonyl carbons resonated at δ 164.47 ppm and δ 162.88 ppm. The signals that appeared in the region of δ 156.69 to 110.53 ppm correspond to aromatic carbons, whereas aliphatic carbons appeared between 47.55 and 11.06 ppm. The FTIR spectrum (**Figure 2.42**) displayed a broad peak at 3394 cm^{-1} and a sharp peak at 2211 cm^{-1} indicating the presence of hydroxyl group (O-H) and cyano group ($\text{C}\equiv\text{N}$) of cyanoacetic acid, respectively. Finally, its mass spectrum (**Figure 2.43**) displayed the $[\text{M}-\text{H}]$ peak at 738.10, which is well in agreement with the calculated molecular mass for $\text{C}_{46}\text{H}_{37}\text{N}_5\text{O}_5$, confirming the chemical structure of the synthesized molecule ***n-K*₃₂**.

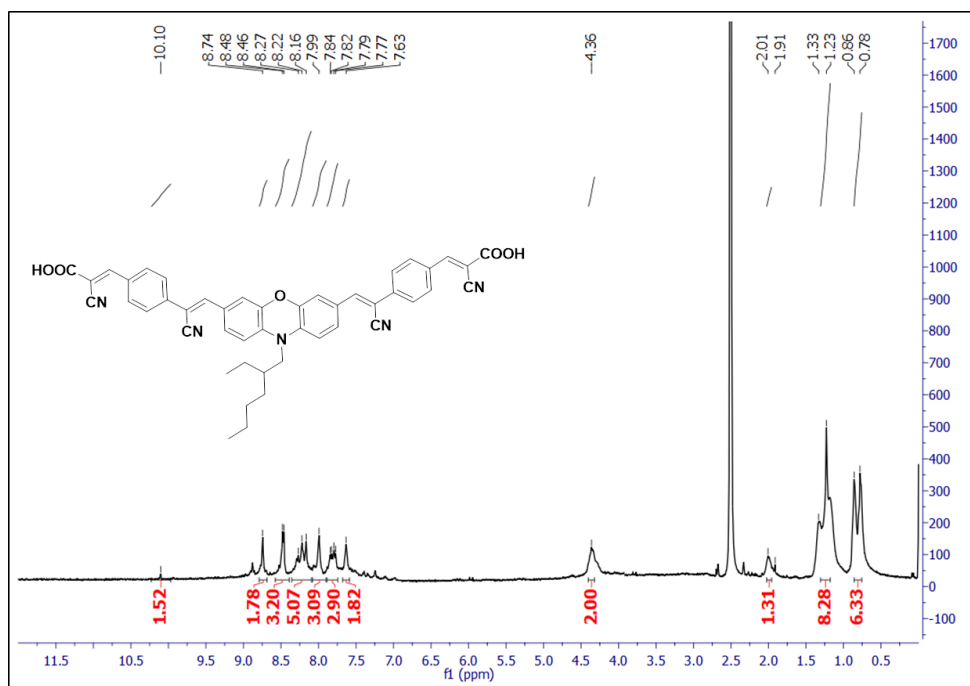


Figure 2.40 ^1H -NMR spectrum of dye ***n-K*₃₂** recorded in $\text{DMSO}-d_6$

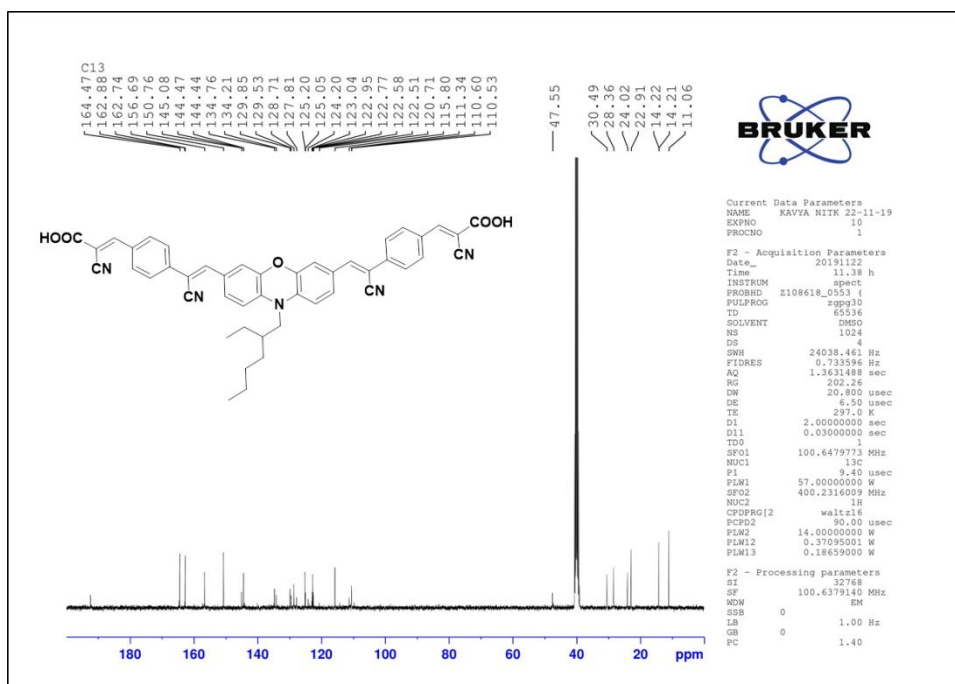


Figure 2.41 ¹³C-NMR spectrum of dye *n-K*₃₂ recorded in DMSO-d₆

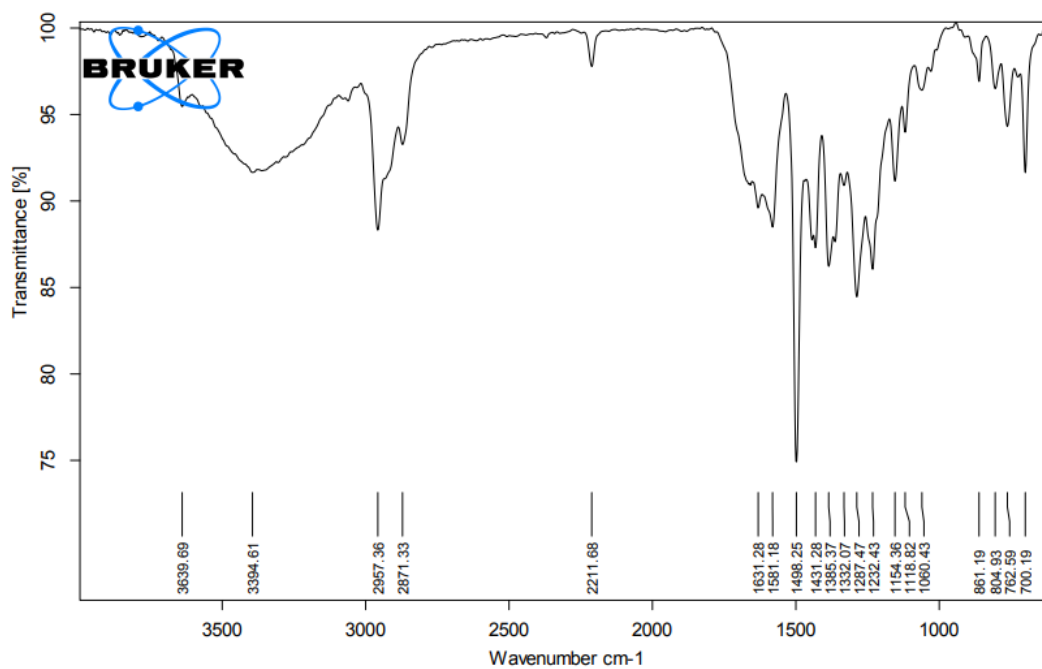


Figure 2.42 FTIR spectrum of dye *n-K*₃₂

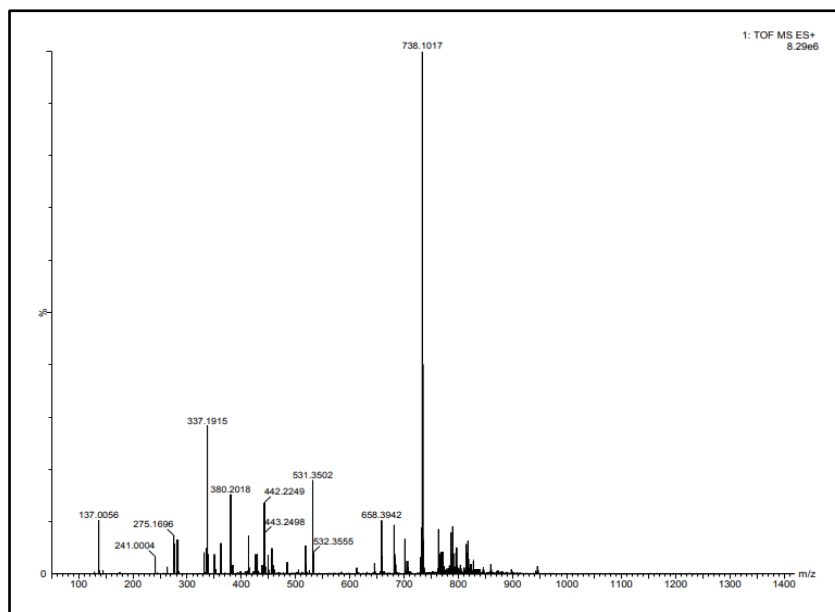


Figure 2.43 LCMS spectrum of dye *n-K*₃₂

2.3.3.2 *p*-Type organic dyes *p-K*₃₅₋₄₂ (Series 9-10)

Chromophores *p-K*₃₅₋₄₀ (Series-9)

The molecular structures belonging to the **Series-9** along with their intermediates were confirmed using different spectral techniques and elemental analysis. ¹H NMR, ¹³C NMR, FTIR, and mass spectra of the dye *p-K*₃₆ are depicted in **Figures 2.44-2.47**, respectively. ¹H NMR spectrum of *p-K*₃₆ accounts for all the protons present in the assigned structure. The appearance of a unique resonance peak at δ 12.72 ppm accounts for the presence of proton of carboxylic acid. All the other aromatic protons of the phenoxazine core resonated in between δ 8.17 to 6.95 ppm. Further, the appearance of a doublet in δ 3.73-3.71 ppm can be ascribed to the presence of two protons of methylene (-CH₂) in the ethylhexyl chain attached to the *N* of the phenoxazine core. The presence of two triplets in between δ 0.91 to 0.87 ppm and δ 0.85 to 0.81 ppm correspond to the 6 protons of two methyl groups (-CH₃) of the ethylhexyl chain. All the other aliphatic protons appeared in the region δ 1.37-1.19 ppm. In the ¹³C NMR spectrum, the peaks correspond to C=S, and two C=O carbons of *N,N*-diethyl thiobarbituric acid, and carbonyl carbon of carboxylic acid were seen at δ 178.89, 161.27, 159.04, and 166.50 ppm, respectively. The signals that appeared in the region of δ 156.95 to 112.96 ppm correspond to aromatic carbons, whereas

aliphatic carbons appeared between 47.42 to 11.19 ppm. The FTIR spectrum displayed a sharp peak at 1685 cm^{-1} indicating the presence of the carbonyl group. Finally, its mass spectrum displayed the $[M+H]$ peak at 550.25, which is well in agreement with the calculated molecular mass for $C_{30}H_{35}N_3O_5S$ (549.68). This confirms the chemical structure of the synthesized molecule *p-K*₃₆.

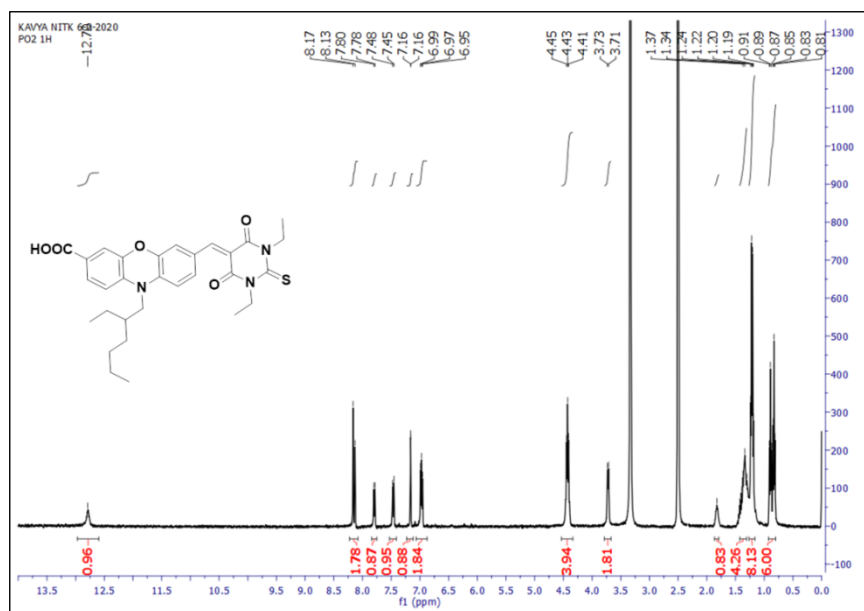


Figure 2.44 $^1\text{H-NMR}$ spectrum of dye *p-K*₃₆ recorded in DMSO-d_6

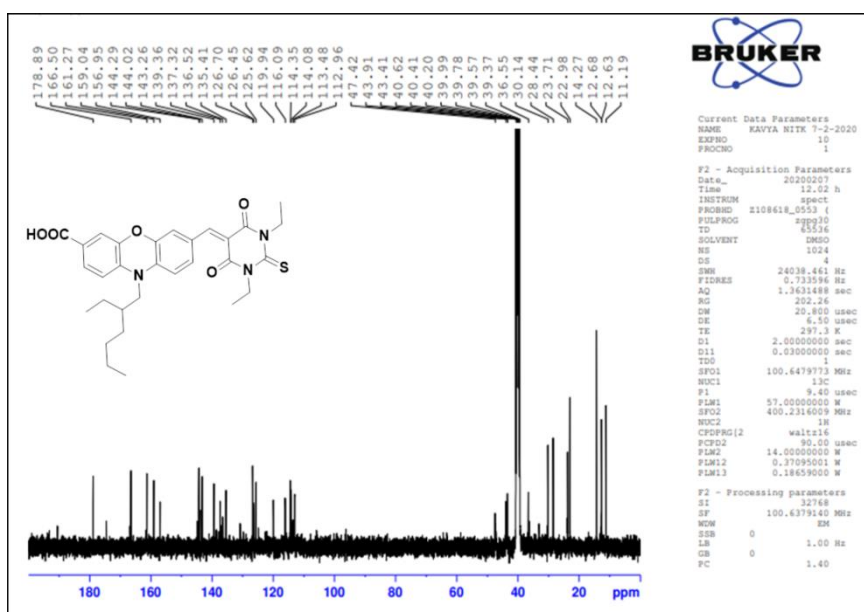


Figure 2.45 $^{13}\text{C-NMR}$ spectrum of dye *p-K*₃₆ recorded in DMSO-d_6

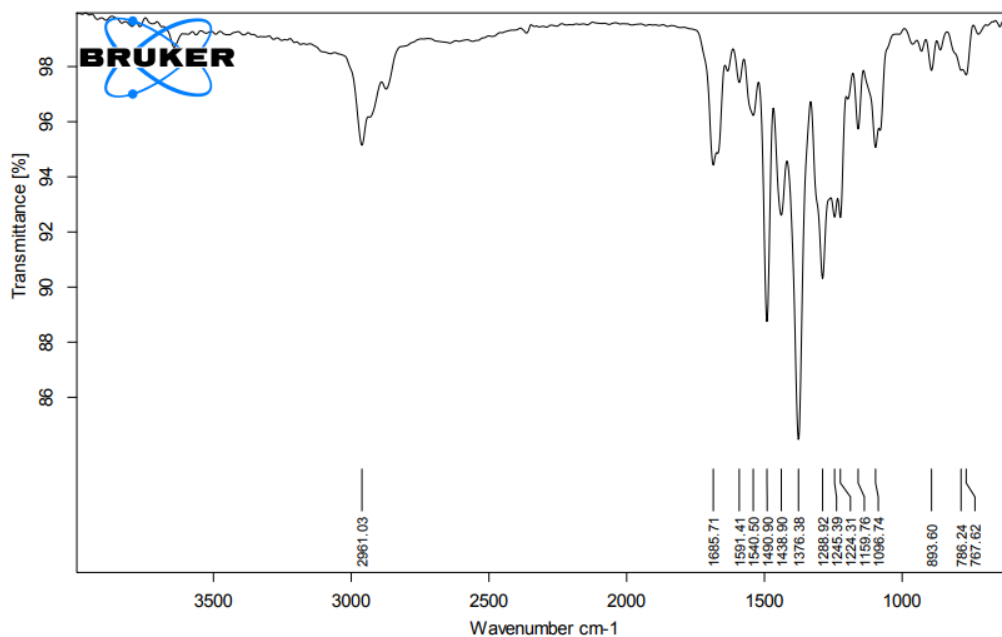


Figure 2.46 FTIR spectrum of dye *p-K*₃₆

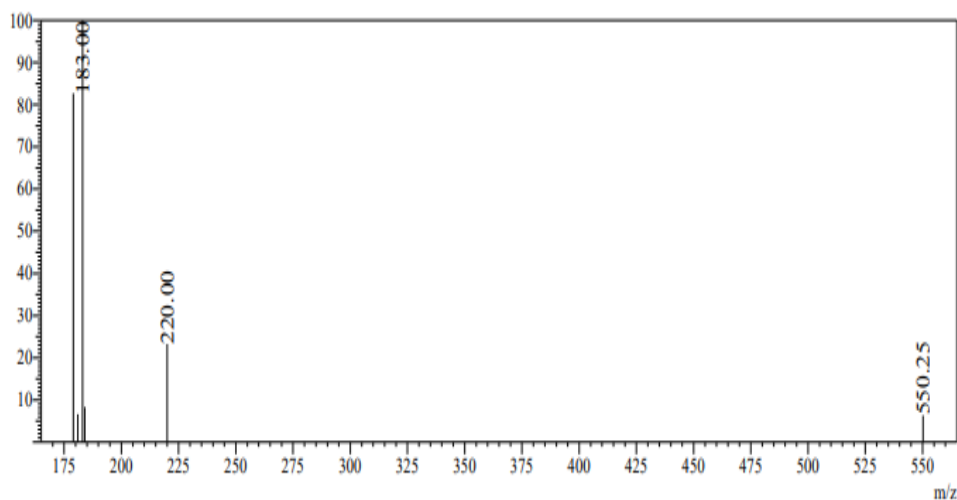


Figure 2.47 LCMS spectrum of dye *p-K*₃₆

Chromophores *p-K*₄₁₋₄₂ (Series-10)

The structural interpretation of all the synthesized molecules and their respective intermediates were carried out using various spectral techniques such as ¹H NMR, ¹³C NMR, FTIR, and Mass spectroscopy/metry followed by elemental analysis. Here, *p-K*₄₁ was chosen for the discussion. In its ¹H NMR spectrum (Figure 2.48), a unique resonance peak for carboxylic acid proton was observed at δ 12.57 ppm as a singlet. All the other aromatic protons of the carbazole core and thiophene unit were

observed in between δ 7.67 to 6.57 ppm. Further, the appearance of a doublet signal in between δ 4.05 and 4.03 ppm can be attributed to two protons of N-CH₂. Also, six protons of two methyl groups of the ethylhexyl chain resonated as triplet peaks at δ 0.89-0.86 ppm and δ 0.84-0.81 ppm, respectively. In addition, the primary and secondary protons of the branched hexyl group appeared as a multiplet in the region of δ 1.35 to 1.16 ppm. The ¹³C NMR spectrum (**Figure 2.49**) of dye *p-K*₄₁ exhibited the characteristic signals which appeared at the high frequency (downfield) region. The carbonyl carbon atom in the acid group resonated at δ 166.84 ppm, while the vinylic carbon signals appeared at δ 166.50 and 162.77 ppm. The signals in the region of δ 158.80 to 112.32 ppm are due to other aromatic carbons. Likewise, all the aliphatic carbons of the ethylhexyl chain of the assigned structure have appeared in between δ 47.05 and 11.15 ppm. The FTIR spectrum (**Figure 2.50**) displayed sharp peaks at 2222 and 1680 cm⁻¹ indicating the presence of cyano and carbonyl groups, respectively. Finally, the observed molecular ion peak at 532.25 in its mass spectrum (**Figure 2.51**) is consistent with the calculated molecular weight of *p-K*₄₁ with chemical formula C₃₂H₂₈N₄O₂.

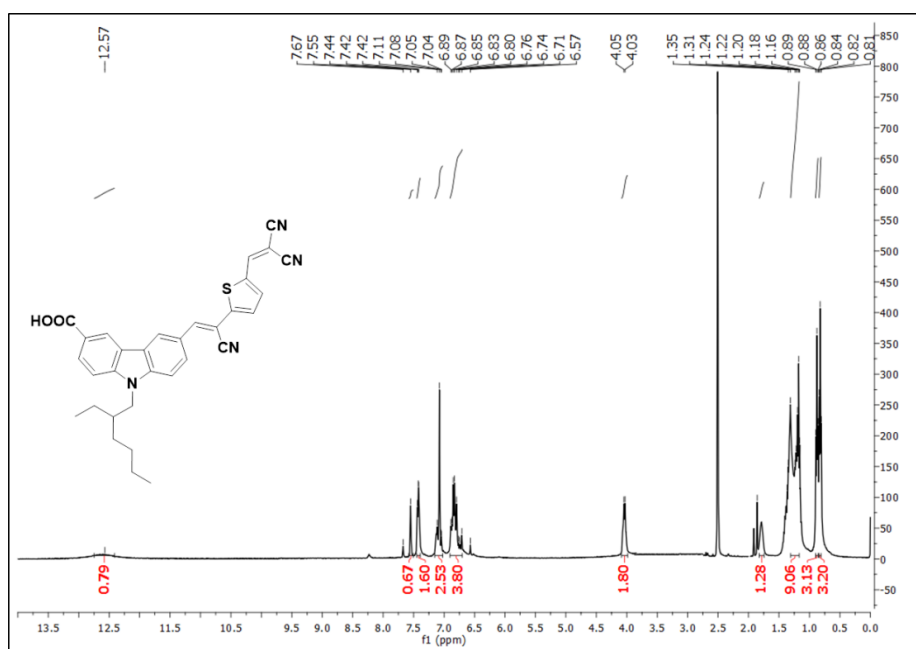


Figure 2.48 ¹H-NMR spectrum of dye *p-K*₄₁ recorded in DMSO-d₆

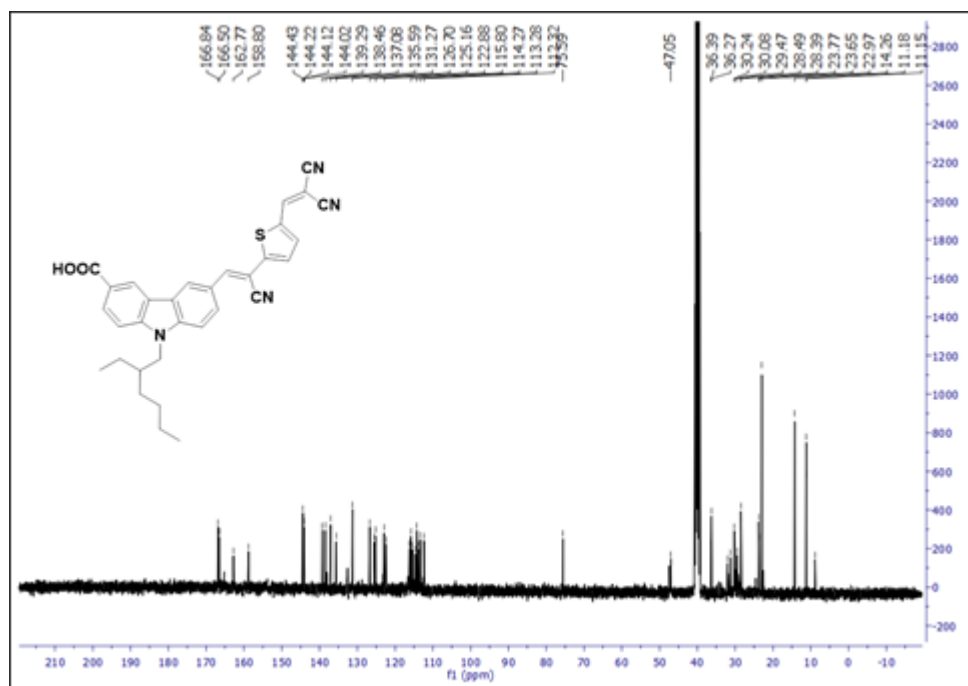


Figure 2.49 ¹³C-NMR spectrum of dye *p-K*₄₁ recorded in DMSO-d₆

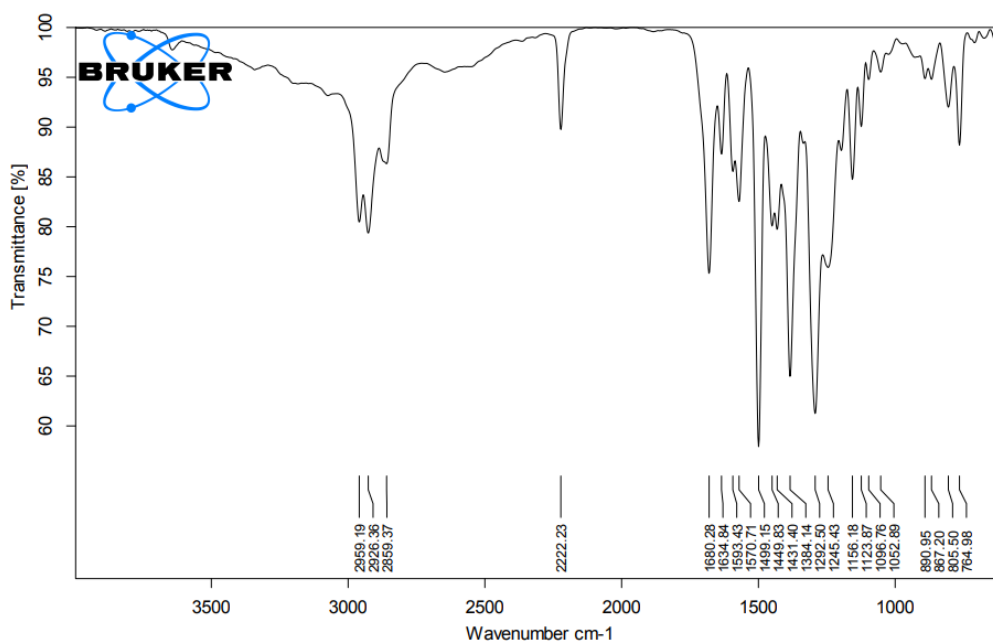


Figure 2.50 FTIR spectrum of dye *p-K*₄₁

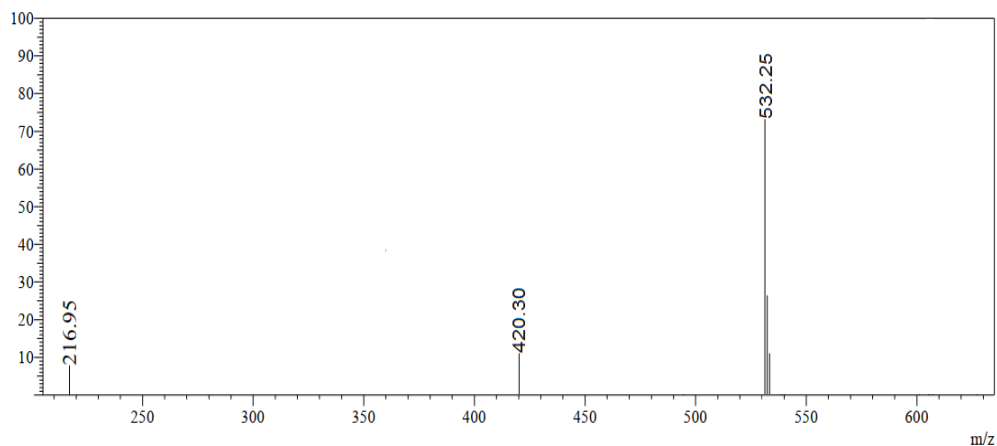
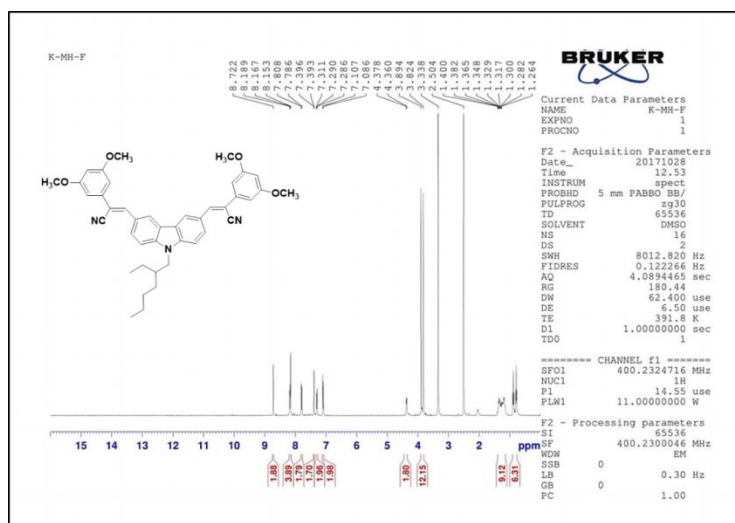
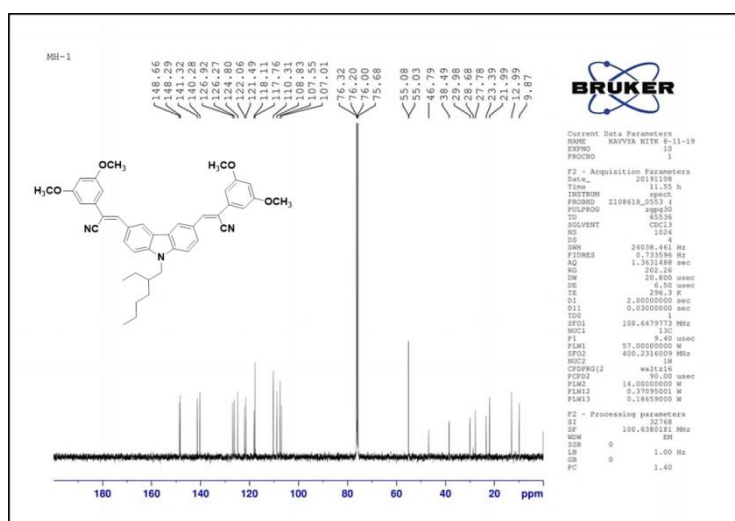
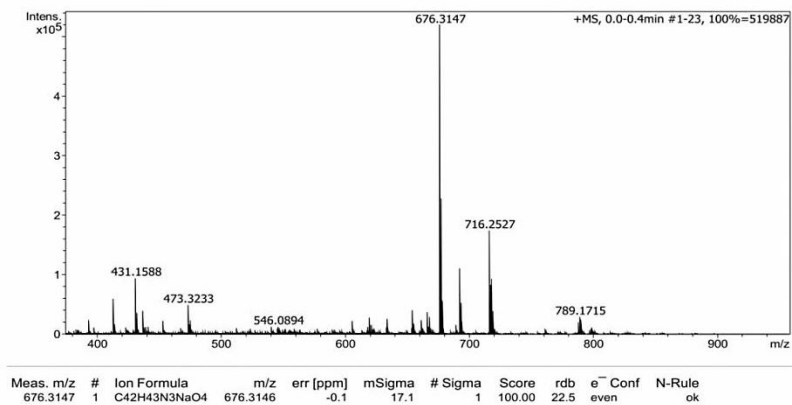


Figure 2.51 LCMS spectrum of dye *p-K*₄₁

2.3.3.3 Hole-transport materials *h-K*₄₃₋₄₄ (Series 11)

The chemical structures of all the target molecules and their intermediates of **Series-11** were confirmed by well-known spectral methods including elemental analysis. In the ¹H NMR spectrum of *h-K*₄₃, a singlet peak resonated at δ 8.72 can be assigned to vinylene proton present in the structure, while all the other aromatic protons of carbazole and phenylene units were observed in the region of δ 8.18 to 7.08 ppm. Further, the appearance of doublet signal in between δ 4.37 to 4.36 ppm can be attributed to two protons of *N*-CH₂, whereas twelve protons of four methoxy groups (-OCH₃) of dimethoxy phenylacetonitrile unit appeared as a singlet at δ 3.89 ppm. Also, the peaks in the region of δ 1.40 to 1.26 ppm correspond to primary and secondary protons of the ethylhexyl chain. The ¹³C NMR spectrum of the molecule showed the four-carbon atoms attached to the methoxy group as peaks at δ 148.66, 148.29, 141.32, and 140.28 ppm. The carbon signals in the region of δ 126.92 to 107.01 ppm are due to other aromatic carbons of carbazole ring, whereas the aliphatic carbons of the ethylhexyl chain appeared in between δ 55.08 to 9.87 ppm. The FTIR spectrum displayed a sharp peak at 2207 indicating the presence of the cyano group. Furthermore, its mass spectrum exhibited the [M+Na]⁺ peak at 676.31, which is in good agreement with the calculated molecular weight. This confirms the chemical structure of the synthesized molecule. **Figures 2.52-2.55** show the ¹H NMR, ¹³C NMR, FTIR, and mass spectra of the *h-K*₄₃, respectively.

Figure 2.52 ^1H -NMR spectrum of dye *h-K*₄₃ recorded in DMSO-*d*₆Figure 2.53 ^{13}C -NMR spectrum of dye *h-K*₄₃ recorded in DMSO-*d*₆Figure 2.54 LCMS spectrum of dye *h-K*₄₃

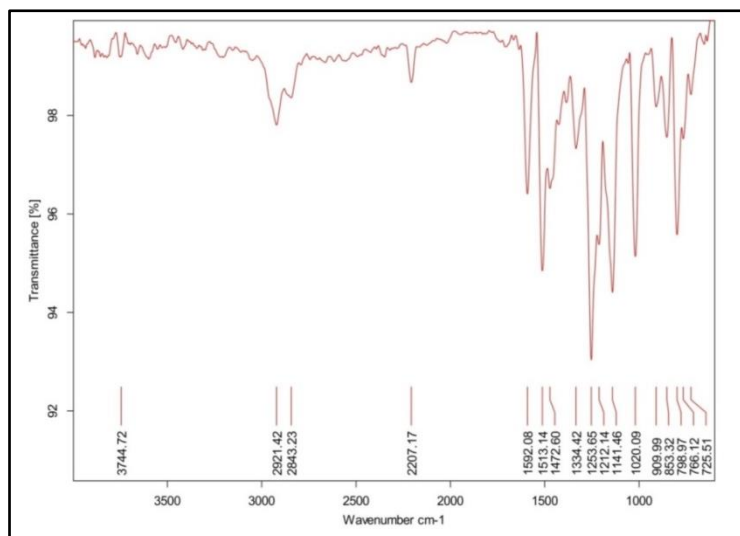


Figure 2.55 FTIR spectrum of dye *h-K*₄₃

2.4 CONCLUSIONS

In conclusion, eight new series having thirty-four metal-free organic dyes (*n-K*₁₋₃₄) as effective *n*-type sensitizers/co-sensitizers, two new series containing eight organic dyes (*p-K*₃₅₋₄₂) as possible *p*-type sensitizers, and two new organic molecules (*h-K*₄₃₋₄₄) as potential HTMs were successfully synthesized, following appropriate synthetic routes, as per **Schemes 2.1-2.11**. The optimized synthetic routes were well established with respect to yield, solvent temperature, reaction rate, concentration, and the other reaction conditions. Also, their purification techniques (column chromatography and recrystallization) have been developed. The chemical structures of all the final molecules and their intermediates were confirmed by various spectroscopic techniques such as ¹H NMR, ¹³C NMR, FTIR spectroscopy, Mass spectrometry and elemental analysis. In the next chapter, detailed photophysical, electrochemical, and theoretical studies of newly synthesized dyes/HTMs have been discussed.

CHAPTER-3
PHOTOPHYSICAL, ELECTROCHEMICAL
AND THEORETICAL INVESTIGATIONS

PHOTOPHYSICAL, ELECTROCHEMICAL AND THEORETICAL INVESTIGATIONS

Abstract

This chapter comprises in-depth photophysical as well as electrochemical studies of thirty-four n-type (n-K₁₋₃₄), eight p-type (p-K₃₅₋₄₂) organic chromophores, and two organic HTMs (h-K₄₃₋₄₄). Further, it involves the theoretical investigation of new dyes/HTMs along with their spectral behavior using DFT and TD-DFT simulations. Also, their structure-property correlation studies have been included.

3.1 PHOTOPHYSICAL INVESTIGATION

Photophysical investigation of newly synthesized organic molecules mainly includes their UV-Vis absorption and emission spectral studies. The obtained photophysical data are quite useful to examine their suitability for DSSC/PSC applications as sensitizers/HTMs.

3.1.1 Introduction

The optical characterization techniques are widely used for the detailed investigation of photophysical characteristics of materials. Among the various techniques, UV-Vis absorption and fluorescence spectroscopy play a significant role in providing valuable information regarding material properties. Generally, UV-Vis absorption spectroscopy involves the measurement of the absorbance of light by a compound as a function of wavelength in the UV-visible range. Here, the dye molecule absorbs the photon from incident light, and then electronic transitions happen from the ground state (HOMO) to an excited state (LUMO). Fluorescence is a complementary technique to UV-Vis absorption, in which emitting of photons occurs when the transitions take place from the higher energy level to the lower energy state. The optical characterization is very essential in evaluating the important photophysical parameters such as the wavelength of maximum absorption and emission, optical band gap, molar extinction coefficient (ϵ), and Stokes shifts of organic dyes/HTMs. This data is necessary

to select the appropriate optical material for photovoltaic applications. Therefore, all the synthesized molecules are subjected to UV-Vis and fluorescence spectral studies in order to evaluate their suitability for their applications in DSSCs/PSCs as sensitizers/HTMs.

3.1.2 Materials and methods

The UV-Vis absorption spectra and fluorescence emission spectra of all the synthesized dyes/HTMs were recorded at room temperature using Analytik Jena SPECORD S 600 spectrophotometer and Jasco FP 6200 spectrophotometer, respectively.

3.1.3 Experimental

The UV-Vis absorption spectra of synthesized target molecules, *i.e.* *n*-type (***n*-K₁₋₃₄**), *p*-type (***p*-K₃₅₋₄₂**) organic chromophores and organic HTMs (***h*-K₄₃₋₄₄**) were measured at the concentration of 10^{-5} M in chloroform/DMF solutions. Further, their emission spectra were obtained by irradiative excitation at the wavelength of their λ_{abs} , using the above-said concentration. Their optical bandgap and Stokes shift values were calculated using the spectral data.

3.1.4 Results and discussion

Results of photochemical studies of new dyes/HTMs have been discussed series-wise in the following section.

3.1.4.1 Photophysical studies of *n*-type organic chromophores ***n*-K₁₋₃₄** (Series 1-8)

Optical properties of dyes ***n*-K₁₋₄** (Series-1)

The UV-vis absorption spectra of synthesized dyes (***n*-K₁₋₄**) were recorded in 10^{-5} M *N,N*-dimethyl formamide (DMF) solution at room temperature. Their spectra are shown in **Figure 3.1a** and the corresponding spectral data are summarized in **Table 3.1**. The observed spectra exhibit two distinct absorption peaks, in which the lower maximum represents π - π^* electronic excitation in the range of 280-370 nm, whereas the higher maximum (400-470 nm) corresponds to the electronic transition from HOMO to LUMO and HOMO-1 to LUMO. As shown in **Figure 3.1a**, the organic sensitizers ***n*-K₁** and ***n*-K₂** exhibit similar types of absorption profiles in the range of 400-410 nm, whereas ***n*-K₃** and

$n\text{-K}_4$ show in the order of 450-460 nm. The observed major λ_{max} at 402 nm ($n\text{-K}_1$), 408 nm ($n\text{-K}_2$), 453 nm ($n\text{-K}_3$), and 461 nm ($n\text{-K}_4$) are attributed to mixed intramolecular charge-transfer (ICT)/ $\pi\text{-}\pi^*$ transition of the chromophores. From the results, we emphasize that dyes $n\text{-K}_3$ and $n\text{-K}_4$ show a bathochromic shift when compared to the data of $n\text{-K}_1$ and $n\text{-K}_2$. This redshift is probably due to the presence of strong electron-withdrawing ability of barbituric acid and increased alkoxy chain numbers which further extend the conjugation of $n\text{-K}_3$ and $n\text{-K}_4$. So, they show an improved light-harvesting ability in the devices.

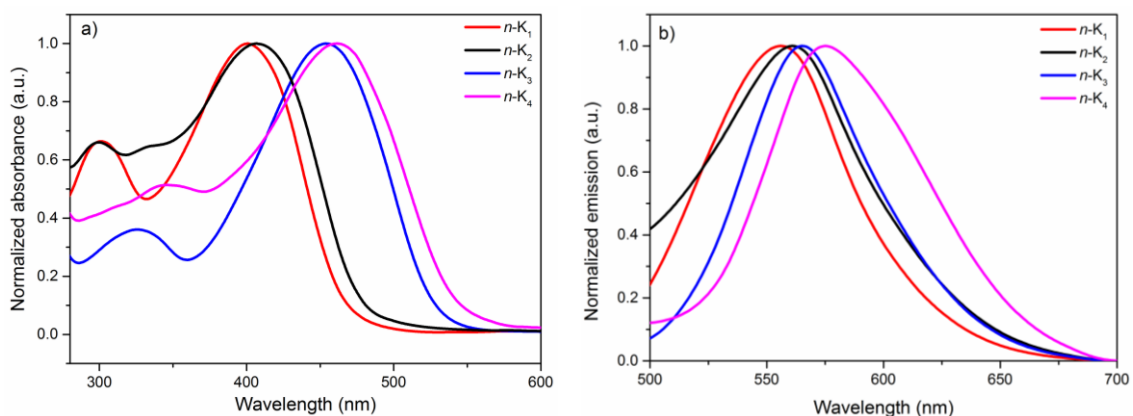


Figure 3.1 (a) Normalized UV-Vis absorption and (b) fluorescence emission spectra of $n\text{-K}_{1-4}$ recorded in 10^{-5} M DMF solution under ambient atmosphere

The fluorescence emission spectra of the dyes $n\text{-K}_{1-4}$ are measured in 10^{-5} M DMF solution by exciting at their respective absorption maxima. **Figure 3.1b** portrays the normalized emission spectra of $n\text{-K}_{1-4}$ and their resultant spectral data are tabulated in **Table 3.1**. All the dyes exhibit a characteristic single emission band in the region of 550-580 nm. The molecule $n\text{-K}_4$ displays λ_{emi} of 575 nm, which is slightly more red-shifted than that of $n\text{-K}_1$ (556 nm), $n\text{-K}_2$ (568 nm), and $n\text{-K}_3$ (569 nm), which may be due to the presence of strong electron-withdrawing barbituric acid. Further, we calculated Stokes shift values as well as the optical bandgap from the obtained absorption and emission spectral data. The acquired bandgaps of $n\text{-K}_{1-4}$ are decreasing in the order, 2.58 eV ($n\text{-K}_2$) > 2.51 eV ($n\text{-K}_1$) > 2.37 eV ($n\text{-K}_3$) > 2.31 eV ($n\text{-K}_4$), whereas Stokes shifts are in the increasing order, $n\text{-K}_4$ (4300 cm^{-1}) < $n\text{-K}_3$ (4500 cm^{-1}) < $n\text{-K}_1$ (6890 cm^{-1}) < $n\text{-K}_2$

(6904 cm^{-1}). It is noted that the Stokes shift values of barbituric acid-bearing molecules (**n-K_{3,4}**) are smaller than that of cyanoacetic acid-based dyes (**n-K_{1,2}**), which could result from their higher planarity, and also illustrating smaller conformational changes in the excited state. Amongst **n-K_{1,4}**, **n-K₂** has the highest Stokes shift with appropriate bandgap and thus, it plays a pivotal role in the light-harvesting phenomenon of solar cells.

Optical properties of dyes **n-K₅₋₁₁** (**Series-2**)

Figure 3.2a displays the UV-vis absorption spectra of double D-A dyes (**n-K₅₋₁₁**) and the corresponding spectral parameters are tabulated in **Table 3.1**. All the dyes showed two distinct strong and broad absorption spectra in the ultraviolet as well as the visible region. The lower absorption band in the region of 280-370 nm is ascribed to π - π^* electronic excitation of conjugated molecules, whereas the higher absorption band (400-470 nm) has been assigned to the intramolecular charge-transfer (ICT) between donor and acceptor units. The observed major λ_{max} at 402 nm (**n-K₅**), 422 nm (**n-K₆**), 421 nm (**n-K₇**), 450 nm (**n-K₈**), 445 nm (**n-K₉**), 468 nm (**n-K₁₀**), and 440 nm (**n-K₁₁**) are attributed to mixed intramolecular charge-transfer (ICT)/ π - π^* transition of the chromophores, which was further confirmed by TD-DFT calculations. From the results, we emphasize that the λ_{abs} of organic sensitizer's **n-K₈₋₁₀** show a bathochromic shift when compared to the other dyes. Especially, the dye **n-K₁₀** possesses relatively broader and more intense absorption compared to all other dyes, which may be due to the elongation of conjugation and superior light-harvesting ability in the presence of strong electron-withdrawing 1,3-diethyl-2-thiobarbituric acid. The aforesaid shift is quite desirable as it shows an improved light-harvesting ability in the devices.

The fluorescence emission spectra of the dyes **n-K₅₋₁₁** are recorded in DMF solution at 10^{-5} M concentration by exciting at their respective absorption maxima. **Figure 3.2b** represents the normalized emission spectra of synthesized dyes **n-K₅₋₁₁** and their resultant spectral parameters are tabulated in **Table 3.1**. All the dye molecules exhibit a characteristic single emission band in the region of 500-570 nm. The molecule **n-K₁₀** displays λ_{emi} of 562 nm, which is slightly more redshifted than that of **n-K₅** (510 nm), **n-K₆** (530 nm), and **n-K₇** (516 nm), **n-K₈** (553 nm), **n-K₉** (535 nm), and **n-K₁₁** (524

nm), which may be due to the presence of strong electron-withdrawing 1,3-diethyl-2-thiobarbituric acid. The observed shift is desirable as it escalates the light-harvesting nature of the sensitizer in the visible region. Further, Stokes shift values were calculated for the dyes and are in an increasing order of $n\text{-K}_{10}$ (3577 cm^{-1}) < $n\text{-K}_9$ (3582 cm^{-1}) < $n\text{-K}_{11}$ < (4080 cm^{-1}) < $n\text{-K}_8$ (3577 cm^{-1}) < $n\text{-K}_7$ (4260 cm^{-1}) < $n\text{-K}_6$ (4896 cm^{-1}) < $n\text{-K}_5$ (5275 cm^{-1}). It is noted that the Stokes shift values of barbituric acid derivatives are smaller than that of cyanoacetic acid and rhodanine derivatives, which could result from higher planarity, also illustrating smaller conformational changes in the excited state. Also, the dye $n\text{-K}_5$ displayed the highest value of stokes shift, which may be caused by large changes in the dipole moment in the excited state, as a result of charge transfer from donor to acceptor moiety. Additionally, the optical bandgaps of synthesized dyes were calculated from the obtained absorption and emission spectral data. The acquired bandgaps of $n\text{-K}_{5-11}$ are decreasing in the order, 2.74 eV ($n\text{-K}_5$) > 2.70 eV ($n\text{-K}_6$) > 2.65 eV ($n\text{-K}_7$) > 2.64 eV ($n\text{-K}_8$) > 2.61 eV ($n\text{-K}_{11}$) > 2.56 eV ($n\text{-K}_9$) > 2.46 eV ($n\text{-K}_{10}$). Furthermore, the molar absorption coefficients (ϵ) of the ICT bands were calculated and are in the range of $14720\text{ M}^{-1}\text{cm}^{-1}$ to $25396\text{ M}^{-1}\text{cm}^{-1}$. Among all, the dye $n\text{-K}_{5-6}$ showed the highest Stokes shift value indicating the enhanced light-harvesting ability of strong electron-withdrawing cyanoacetic acid/rhodanine-3-acetic acid units in the visible region, which could produce greater short-circuit current and thus improved device performance.

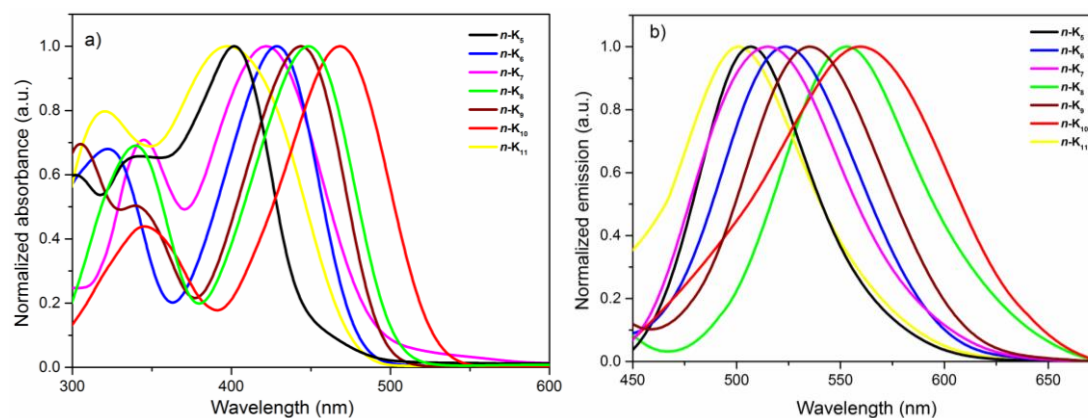


Figure 3.2 (a) Normalized UV-Vis absorption and (b) fluorescence emission spectra of $n\text{-K}_{5-11}$ recorded in 10^{-5} M DMF solution

Optical properties of dyes *n-K*₁₂₋₁₈ (Series-3)

The UV-vis absorption spectra of dyes *n-K*₁₂₋₁₈ were shown in **Figure 3.3a** and the corresponding spectral parameters are summarized in **Table 3.1**. Here, the lower absorption band in the region of 290-360 nm is ascribed to π - π^* electronic excitation of conjugated systems, whereas the higher maximum (400-470 nm) is assigned to the intramolecular charge-transfer (ICT) from HOMO to LUMO and from HOMO-1 to LUMO. Further, the observed major λ_{max} at 408 nm (*n-K*₁₂), 429 nm (*n-K*₁₃), 404 nm (*n-K*₁₄), 448 nm (*n-K*₁₅), 435 nm (*n-K*₁₆), 465 nm (*n-K*₁₇), and 418 nm (*n-K*₁₈) are attributed to mixed intramolecular charge-transfer (ICT)/ π - π^* transition of the chromophores, which was further confirmed by TD-DFT calculations. From the results, we emphasize that the λ_{abs} of organic sensitizers *n-K*₁₅₋₁₇ show a bathochromic shift when compared to the other dyes. Especially, the dye *n-K*₁₇ possesses relatively broader and more intense absorption compared to all other dyes, due to the elongation of conjugation and the presence of strong electron-withdrawing ability of 1,3-diethyl-2-thiobarbituric acid. The aforesaid shift is quite desirable as it shows an improved light-harvesting ability in the devices.

The fluorescence emission spectra of the dyes *n-K*₁₂₋₁₈ are recorded in DMF solution at 10^{-5} M concentration by exciting at their respective absorption maxima. The spectra are showed in **Figure 3.3b**. From the figure, it is clear that all the dye molecules exhibit a characteristic single emission band in the region of 500-560 nm. The molecule *n-K*₁₇ displays λ_{emi} of 556 nm, that is slightly more red-shifted than that of *n-K*₁₂ (515 nm), *n-K*₁₃ (542 nm), *n-K*₁₄ (503 nm), *n-K*₁₅ (549 nm), *n-K*₁₆ (538 nm), *n-K*₁₈ (523 nm), which may be due to the presence of a strong electron-withdrawing 1,3-diethyl-2-thiobarbituric acid. Further, Stokes shift values of the dyes were calculated and are in an increasing order of *n-K*₁₇ (3525 cm^{-1}) < *n-K*₁₅ (4121 cm^{-1}) < *n-K*₁₆ < (4408 cm^{-1}) < *n-K*₁₈ (4803 cm^{-1}) < *n-K*₁₄ (4891 cm^{-1}) < *n-K*₁₃ (4964 cm^{-1}) < *n-K*₁₂ (5109 cm^{-1}). Additionally, the optical bandgaps of synthesized dyes were calculated from the obtained absorption and emission spectral data. The acquired bandgaps of *n-K*₁₂₋₁₈ are decreasing in the order, 2.70 eV (*n-K*₁₂) > 2.68 eV (*n-K*₁₃) > 2.60 eV (*n-K*₁₄) > 2.59 eV (*n-K*₁₅) > 2.58 eV (*n-*

\mathbf{K}_{16}) > 2.55 eV ($n\text{-}\mathbf{K}_{18}$) > 2.44 eV ($n\text{-}\mathbf{K}_{17}$). Furthermore, the molar absorption coefficients (ϵ) of the ICT bands were calculated and are in the range of 16800 $\text{M}^{-1}\text{cm}^{-1}$ to 23717 $\text{M}^{-1}\text{cm}^{-1}$. Among all, the dyes $n\text{-}\mathbf{K}_{12-13}$ show the highest Stokes shift values indicating the enhanced light-harvesting ability of strong electron-withdrawing cyanoacetic acid/rhodanine-3-acetic acid unit in the visible region, which could produce greater, short-circuit current and thus improved performance.

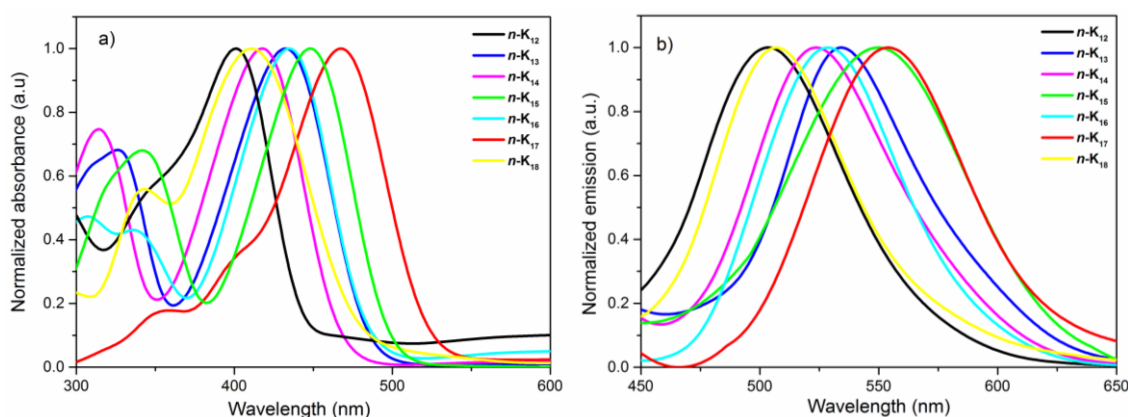


Figure 3.3 (a) Normalized UV-Vis absorption and (b) fluorescence emission spectra of $n\text{-}\mathbf{K}_{12-18}$ recorded in 10^{-5} M DMF solution

Optical properties of dyes $n\text{-}\mathbf{K}_{19-21}$ (Series-4)

The recorded UV-Vis absorption spectra for dyes $n\text{-}\mathbf{K}_{19-21}$ are shown in **Figure 3.4a** and the corresponding data is given in **Table 3.1**. From the figure, it is clear that the observed absorbance values are in the order $n\text{-}\mathbf{K}_{20}$ (437 nm) > $n\text{-}\mathbf{K}_{21}$ (360 nm) > $n\text{-}\mathbf{K}_{19}$ (350 nm). The dye $n\text{-}\mathbf{K}_{20}$ displayed the highest redshift compared to the other two dyes, which may be due to the presence of a strong electron-withdrawing rhodanine-3-acetic acid as an anchoring unit which helps in better extraction of electrons from the donor unit through the spacer. Thus, it results in the broadening of absorption spectra in higher wavelength regions. In addition, the relatively poor performance of $n\text{-}\mathbf{K}_{19}$ and $n\text{-}\mathbf{K}_{21}$ can be a result of dye-aggregation.

Figure 3.4b depicts the emission spectra of dyes $n\text{-}\mathbf{K}_{19-21}$. The obtained λ_{emi} values are in the decreasing order as $n\text{-}\mathbf{K}_{20}$ (535 nm) > $n\text{-}\mathbf{K}_{21}$ (507 nm) > $n\text{-}\mathbf{K}_{19}$ (503 nm),

i.e. the values of λ_{abs} and λ_{emi} are in the same order. Further, the Stokes shifts calculated are in the ascending order, $n\text{-K}_{20}$ (4191 cm^{-1}) < $n\text{-K}_{21}$ (8053 cm^{-1}) < $n\text{-K}_{19}$ (8690 cm^{-1}). It is interesting to note that the order of Stokes shift is opposite to that of the order of absorbance and emissive values. Thus, the highest Stokes shift value of $n\text{-K}_{19}$ may be owing to its proper ICT transfer of electrons. Furthermore, the expansion of the π conjugation has also altered the HOMO and LUMO levels of the dyes, and hence tuning the bandgap of the sensitizers. The calculated bandgaps of the dyes $n\text{-K}_{19-21}$ are 2.81, 2.50, and 2.85 eV, respectively. The lower bandgap of dye $n\text{-K}_{20}$ is attributed to the lowering of LUMO levels. Among all the synthesized molecules, the dye $n\text{-K}_{19}$ carrying cyanoacetic acid shows the highest Stokes shift indicating the greater light-harvesting ability and hence can expect superior photovoltaic performance.

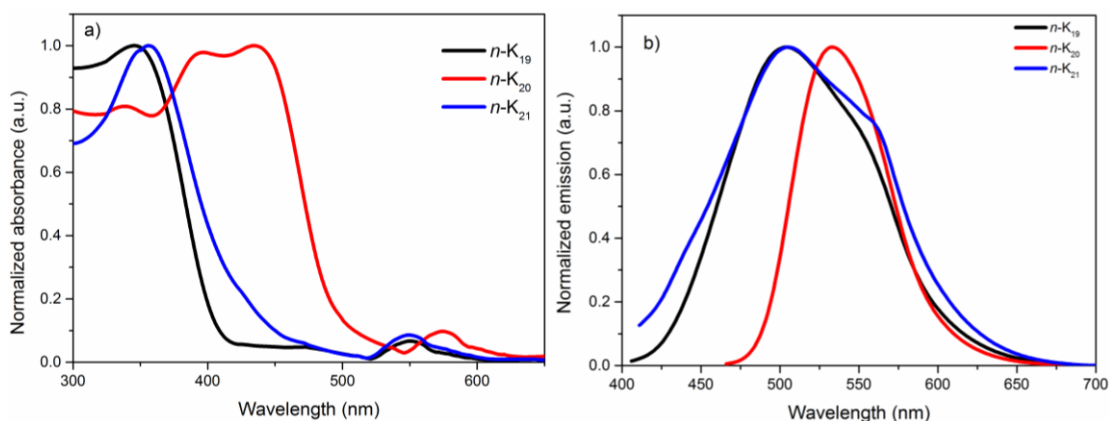


Figure 3.4 (a) Normalized UV-Vis absorption and (b) fluorescence emission spectra of $n\text{-K}_{19-21}$ recorded in 10^{-5} M DMF solution

Optical properties of dyes $n\text{-K}_{22-24}$ (Series-5)

Figures 3.5a and **3.5b** show the UV-Vis absorption and photoluminescence emission spectra of $n\text{-K}_{22-24}$, respectively. The relevant spectral results are presented in **Table 3.1**. From the absorption spectra, it is clear that the dyes $n\text{-K}_{22-24}$ exhibit two major absorption bands in the range of 300-350 nm and 380-410 nm, respectively. Here, the dyes $n\text{-K}_{22-24}$ show absorption bands in the shorter wavelength corresponding to $\pi\text{-}\pi^*$ electronic excitations localized within the carbazole group, whereas the intense band in the longer wavelength region can be attributed to an intermolecular charge-transfer (ICT)

from the donor to the acceptor segment, *i.e.* from twin carbazole units to the corresponding anchor, *viz.* cyanoacetic acid, rhodanine-3-acetic acid, or barbituric acid.

The fluorescence emission spectral data of the dyes $n\text{-K}_{22-24}$ recorded at their excitation wavelength are summarized in **Table 3.1**. All the dyes have exhibit a single band in the range of 490 to 540 nm. The dye $n\text{-K}_{23}$ shows a maximum redshift as compared with other dyes in the series. Further from the results, it is observed that the dye $n\text{-K}_{22}$ showed maximum Stokes shift (6033 cm^{-1}) compared to the other two dyes. This may be due to the strong electron-withdrawing ability of the cyanoacetic acid. Finally, the optical bandgaps of $n\text{-K}_{22-24}$ were determined from the intersection point of normalized absorption and emission spectra, and their calculated values are tabulated in **Table 3.1**.

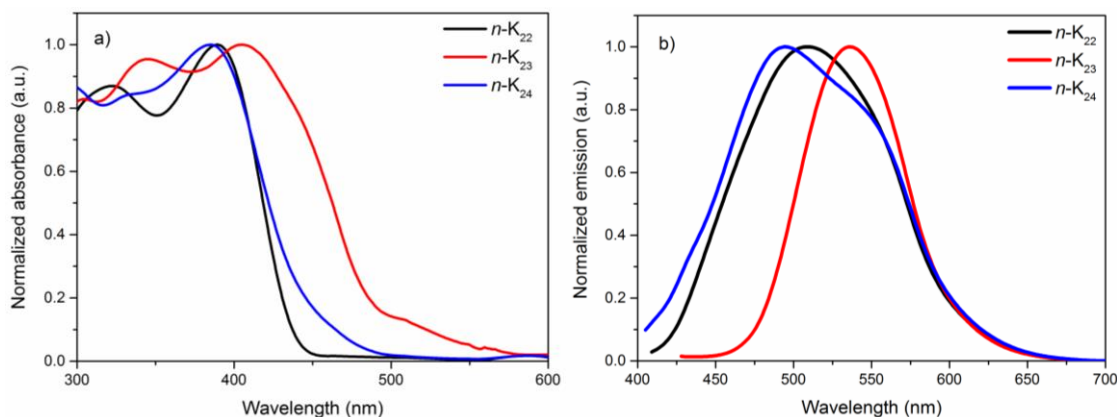


Figure 3.5 (a) Normalized UV-Vis absorption and (b) fluorescence emission spectra of $n\text{-K}_{22-24}$ recorded in 10^{-5} M DMF solution

Optical properties of dyes $n\text{-K}_{25-28}$ (Series-6)

The UV-visible absorption spectra of the new organic dyes, $n\text{-K}_{25-28}$, recorded in 10^{-5} M DMF solution are depicted in **Figure 3.6a** and their corresponding characteristic spectral data are summarized in **Table 3.1**. From **Fig 3.6a**, it is worth noting that the obtained absorption values are in the ascending order: $n\text{-K}_{25}$ (410 nm) < $n\text{-K}_{26}$ (412 nm) < $n\text{-K}_{28}$ (425 nm) < $n\text{-K}_{27}$ (442 nm). From the spectra, it is noteworthy that dyes $n\text{-K}_{27}$ and $n\text{-K}_{28}$ show two distinct absorption peaks, whereas the other two dyes display a

single absorption band. The increased electron extraction in the structures of $n\text{-K}_{27-28}$ reflected in its quite red-shifted absorption values, which may be due to the presence of electron-withdrawing rhodanine derivatives as anchoring units.

The fluorescence emission spectra of dyes $n\text{-K}_{25-28}$ were recorded upon their excitation wavelengths in 10^{-5} M DMF solutions. **Figure 3.6b** depicts the normalized emission spectra of the $n\text{-K}_{25-28}$ and their pertaining spectral data are tabulated in **Table 3.1**. The fluorescence spectra of dyes display a single emission band in the range of 500 to 550 nm. The obtained emission values of the sensitizers $n\text{-K}_{25-28}$ are in the order of $n\text{-K}_{25}$ (504 nm) < $n\text{-K}_{26}$ (508 nm) < $n\text{-K}_{28}$ (523 nm) < $n\text{-K}_{27}$ (546 nm). Further, Stokes shift values ($4309\text{-}4586\text{ cm}^{-1}$) of target molecules were calculated from their normalized UV-Vis absorption and fluorescence emission spectral data. In addition, optical bandgaps of $n\text{-K}_{25-28}$ (2.50-2.66 eV) were determined from the intersection point of normalized absorption and emission spectra, and their calculated values are tabulated in **Table 3.1**.

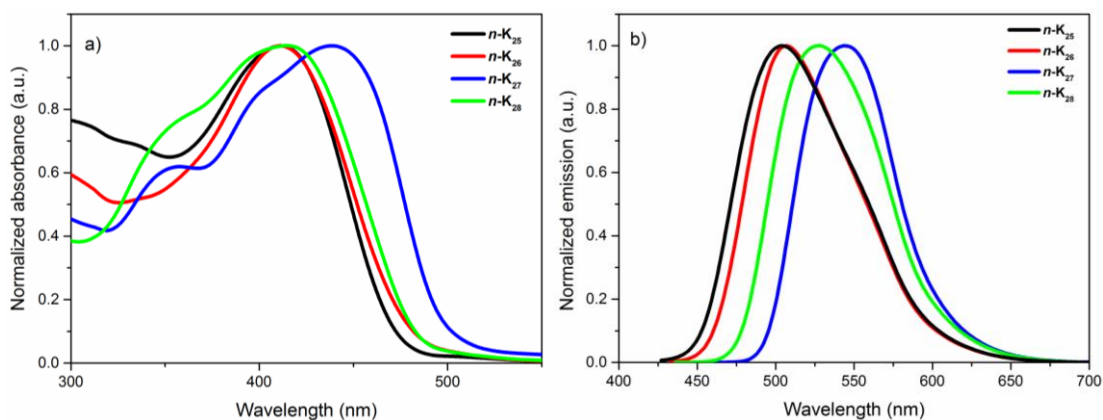


Figure 3.6 (a) Normalized UV-Vis absorption and (b) fluorescence emission spectra of $n\text{-K}_{25-28}$ recorded in 10^{-5} M DMF solution

Optical properties of dyes $n\text{-K}_{29-31}$ (Series-7)

The UV-Vis absorption and fluorescence emission spectra of synthesized chromogens $n\text{-K}_{29-31}$ were recorded in chloroform (10^{-5} M) as a solvent. The UV-Vis absorption spectra (**Figure 3.7a**) of dyes $n\text{-K}_{29-31}$ show two distinctive absorption maxima in the region of 350-450 and 500-600 nm. The former region peaks are

corresponding to π - π^* electronic excitations localized within the phenoxazine and thiophene units, whereas the later region peaks are attributed to intramolecular charge-transfer (ICT) from phenoxazine donor to the acceptor/anchoring units. It is interesting to note that the ICT peak endorsed for the ***n-K*₃₁** dye is redshifted (580 nm) when compared to the other two dyes, *i.e.* ***n-K*₂₉** (517 nm) and ***n-K*₃₀** (546 nm). The reason behind this may be due to the heavy aggregation of dye in solution *via* strong hydrogen bonding between the solvent and NH groups of barbituric acid causing a reorganization of the molecule (Shen et al. 2011; Yen et al. 2013).

From their emission spectra (**Figure 3.7b**), it is crystal clear that all the target molecules depict a strong luminescence maximum in the region of 590-660 nm. The emission values are in a similar trend as that of absorption values. The molecule ***n-K*₃₁** displays λ_{emi} of 660 nm, that is more red-shifted than that of ***n-K*₂₉** (591 nm), and ***n-K*₃₀** (631 nm), which may be due to the presence of strong electron-withdrawing barbituric acid as an anchoring unit. Further, the calculated optical bandgap and Stokes shift values were in the range of 2.03-2.32 eV and 2089-2467 cm^{-1} respectively. It is important to observe that the dye ***n-K*₃₀** bearing rhodanine-3-acetic acid as an anchoring unit shows maximum Stokes shift when compared to the other two dyes, suggesting a significant charge transfer from phenoxazine donor moiety to the respective acceptor/anchoring groups.

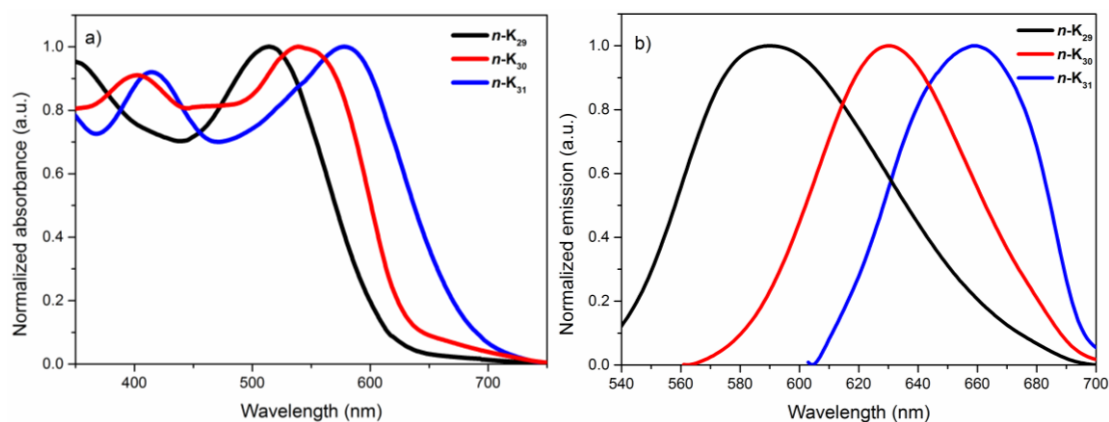


Figure 3.7 (a) Normalized UV-Vis absorption and (b) fluorescence emission spectra of ***n-K*₂₉₋₃₁** recorded in 10^{-5} M CHCl_3 solution

Optical properties of dyes $n\text{-K}_{32-34}$ (Series-8)

The UV-Vis absorption and fluorescence emission spectra of synthesized dyes $n\text{-K}_{32-34}$ were recorded in 10^{-5} M CHCl_3 solution (Figures 3.8a and 3.8b, respectively) and their pertaining results are summarized in Table 3.1. The absorption maxima of dyes are found to be in the decreasing order, $n\text{-K}_{34}$ (515 nm) > $n\text{-K}_{33}$ (494 nm) > $n\text{-K}_{32}$ (432 nm). The dye $n\text{-K}_{34}$ carrying barbituric acid as an acceptor/anchoring unit brings about a bathochromic shift while the other two dyes show a hypsochromic shift. From their fluorescence emission spectra, it is clear that they show strong emission in the decreasing order of $n\text{-K}_{34}$ (573 nm) > $n\text{-K}_{33}$ (564 nm) > $n\text{-K}_{32}$ (534 nm). Further, their optical bandgaps were also calculated from the intersection between normalized absorption and emission spectra, which is found to be in the range of 2.33-2.73 eV. Furthermore, the calculated Stokes shift values of $n\text{-K}_{32-34}$ are found to be 4421, 2512, and 1965 cm^{-1} , respectively. It is important to note that the $n\text{-K}_{32}$ shows the maximum Stokes shift value suggesting the superior light-harvesting capacity of the dye molecule.

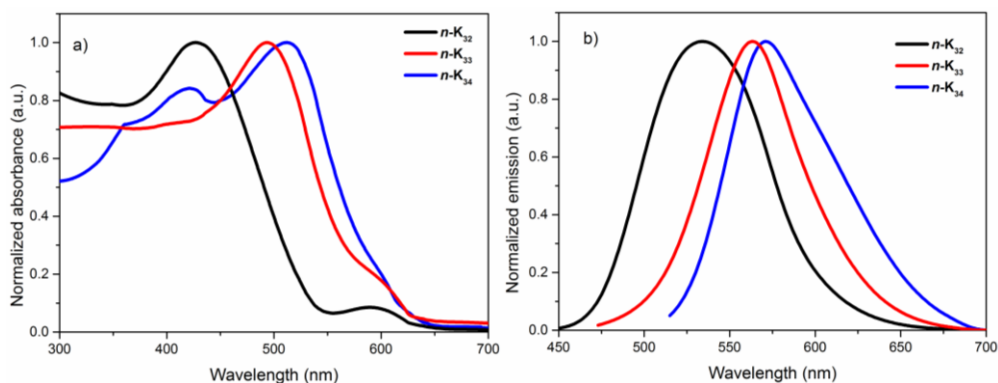


Figure 3.8 (a) Normalized UV-Vis absorption and (b) fluorescence emission spectra of $n\text{-K}_{32-34}$ recorded in 10^{-5} M CHCl_3 solution

3.1.4.2 Photophysical studies of p -type organic chromophores $p\text{-K}_{35-42}$ (Series 9-10)

Optical properties of dyes $p\text{-K}_{35-40}$ (Series-9)

The UV-Vis absorption spectra of the new p -type organic chromophores $p\text{-K}_{35-40}$ obtained in 10^{-5} M CHCl_3 solutions are depicted in Figure 3.9a and the consequential spectral data are summarized in Table 3.1. The absorption spectra of $p\text{-K}_{35-40}$ display two

distinctive absorption bands. The absorption band in the region of 330-430 nm can be assigned to the π - π^* electronic excitations localized within the phenoxazine donor, whereas the peak corresponding to the longer wavelength, *i.e.* 470-570 nm can be attributed to the ICT from the donor to the electron acceptor unit. The major λ_{\max} values are observed at 519 nm (**p-K₃₅**), 549 nm (**p-K₃₆**), 501 nm (**p-K₃₇**), 506 nm (**p-K₃₈**), 521 nm (**p-K₃₉**), and 479 nm (**p-K₄₀**). From the results, it is observed that the λ_{abs} of **p-K₃₆** possesses a relatively broader and more intense absorption band and shows a bathochromic shift when compared to the other dyes. The reason may be due to the elongation of conjugation and superior light-harvesting ability in the presence of strong electron-withdrawing 1,3-diethyl-2-thiobarbituric acid. The aforesaid shift is quite desirable as it shows an improved light-harvesting ability in the devices.

Further, the fluorescence emission spectra of dyes **p-K₃₅₋₄₀** were recorded upon their excitation wavelengths in 10^{-5} M chloroform solution. The normalized emission spectra of the dyes **p-K₃₅₋₄₀** are portrayed in **Figure 3.9b** and their pertaining spectral data are tabulated in **Table 3.1**. The fluorescence emission spectra of all the dyes display a single emission band in the range of 560-640 nm. In addition, Stokes shift and optical bandgap values of dyes calculated from their normalized absorption and emission spectra are found to be in the range of 2386-3394 cm^{-1} and 2.09-2.40 eV, respectively.

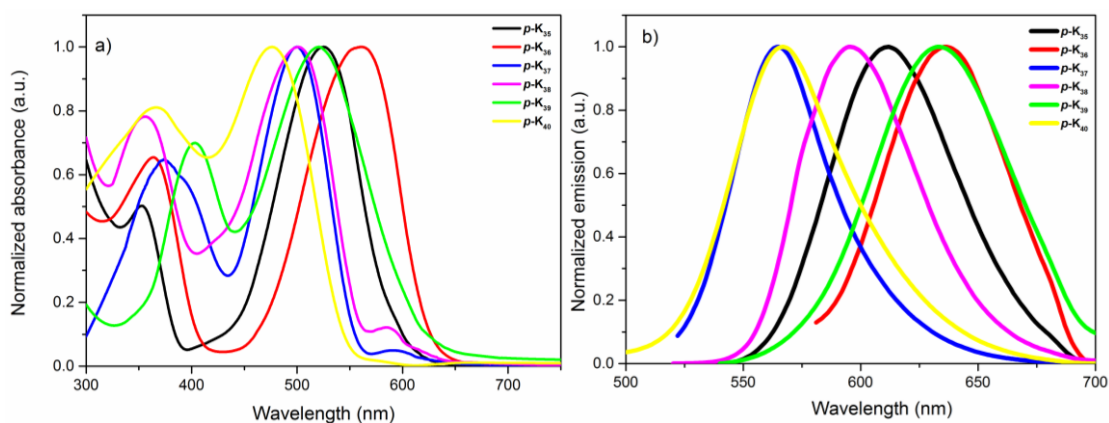


Figure 3.9 (a) Normalized UV-Vis absorption and (b) fluorescence emission spectra of **n-K₃₅₋₄₀** recorded in 10^{-5} M CHCl_3 solution

Optical properties of dyes *p-K*₄₁₋₄₂ (Series-10)

The UV-Vis absorption and fluorescence emission spectra of *p*-type chromogens (*p-K*₄₁₋₄₂) were obtained over the range of wavelength (λ) using DMF as solvent at 10^{-5} M concentration as depicted in **Figures 3.10a** and **3.10b** and their spectral data are summarized in **Table 3.1**. The newly synthesized dyes *p-K*₄₁₋₄₂ show two distinctive absorption bands at 401 nm (*p-K*₄₁) and 521 nm (*p-K*₄₂). The fluorescence emission spectra display a single emission band at 457 nm (*p-K*₄₁) and 598 nm (*p-K*₄₂). Further, Stokes shift value of *p-K*₄₁ (3055 cm^{-1}) is found to be higher than that of *p-K*₄₂ (2471 cm^{-1}), indicating the higher light-harvesting capacity of *p-K*₄₁, which may be due to the presence of better electron-withdrawing malononitrile moiety. The calculated optical bandgaps are found to be 2.90 and 2.32 eV, respectively (**Table 3.1**).

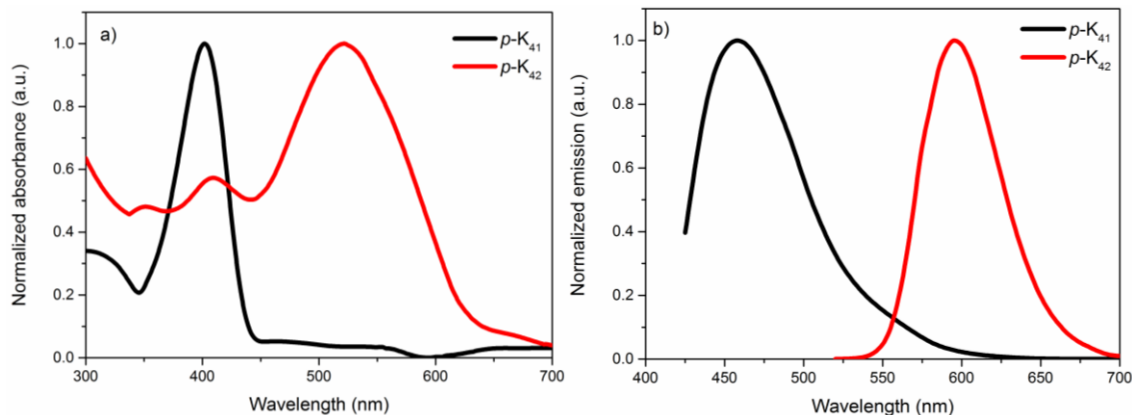


Figure 3.10 (a) Normalized UV-Vis absorption and (b) fluorescence emission spectra of *n-K*₄₁₋₄₂ recorded in 10^{-5} M DMF solution

3.1.4.3 Photophysical studies of organic HTMs *h-K*₄₃₋₄₄ (Series-11)

The optical behaviour (UV-Visible absorption spectra and fluorescence emission spectra) of the newly synthesized HTMs *h-K*₄₃₋₄₄ were recorded in 10^{-5} M CHCl_3 solution. Their spectra are displayed in **Figure 3.11** and their corresponding data are tabulated in **Table 3.1**. From their spectra, we can conclude that both *h-K*₄₃₋₄₄ exhibit similar types of absorption profiles and the observed major λ_{max} of *h-K*₄₃ is 428 nm and that of *h-K*₄₄ is 417 nm. This is mainly due to the intramolecular charge-transfer (ICT)/ π -

π^* transition of the chromophores between the donor and acceptor. From the results, it is clear that the observed bathochromic shift of ***h-K*₄₃** when compared to that of ***h-K*₄₄** is mainly due to intermolecular π - π stacking among dimethoxy-based molecules in the solid-state and the presence of extra electron-donating methoxy group. It is also well-known that the number and position of the methoxy groups make a significant influence on the geometrical structure and subsequently on the electronic properties of the molecules, which means that the presence of more pendant methoxy groups augments the electron-donating ability of the molecule, and thus providing superior device performance.

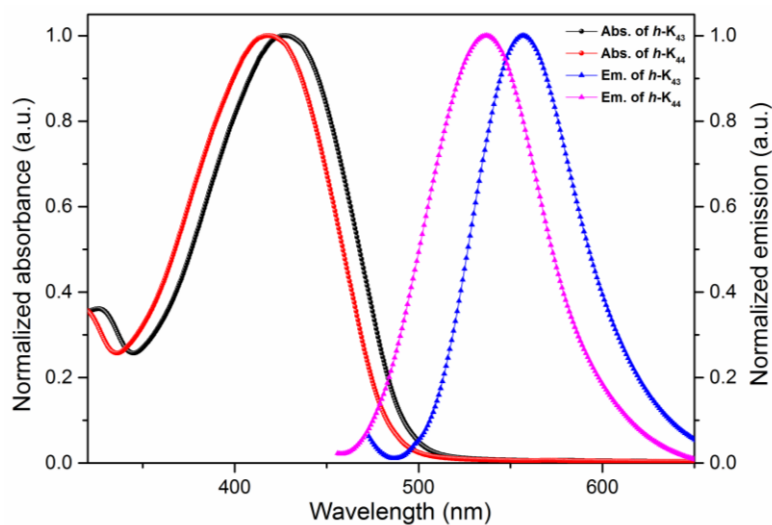


Figure 3.11 Normalized UV-Vis absorption and fluorescence emission spectra of ***h-K*₄₃** recorded in 10^{-5} M CHCl_3 solution

Further, from the PL spectral results, it is clear that both the molecules exhibit solid luminescence maxima in the region of 530-560 nm. The molecule ***h-K*₄₃** displays λ_{emi} of 557 nm, that is slightly more red-shifted compared to that of ***h-K*₄₄** (536 nm), which may be because of the enhanced electron-donating nature of ***h-K*₄₃** in the presence of dimethoxyphenyl group. In continuation, the optical bandgap and Stoke shifts were estimated from the intersection between normalized absorption and emission spectra. Indeed, the Stokes shift plays a key role in deciding whether the synthesized HTMs would undergo any geometrical change on excitation. The calculated bandgaps are 2.52

eV (***h-K*₄₃**), and 2.58 eV (***h-K*₄₄**), whereas Stoke shifts are in the order ***h-K*₄₄** (5323 cm⁻¹) < ***h-K*₄₃** (5410 cm⁻¹). Here, the molecule ***h-K*₄₃** results in a higher Stoke shift value with appropriate bandgap, which ultimately results in the superior molar extinction coefficient for the molecule and thus, it is capable of functioning as a better hole-transporting material.

Table 3.1 Photophysical properties of synthesized organic dyes, *i.e.* *n*-type (***n-K*₁₋₃₄**), *p*-type (***p-K*₃₅₋₄₂**), and HTMs (***h-K*₄₃₋₄₄**)

Series	Compound	λ_{abs} (nm)	λ_{emi} (nm)	Stokes shift (cm ⁻¹)	$E_{0-0 \text{ opt}}$ (eV)
1	<i>n-K</i>₁	402	556	6890	2.51
	<i>n-K</i>₂	408	568	6904	2.58
	<i>n-K</i>₃	453	569	4500	2.37
	<i>n-K</i>₄	461	575	4300	2.31
2	<i>n-K</i>₅	402	510	5275	2.74
	<i>n-K</i>₆	422	530	4896	2.70
	<i>n-K</i>₇	421	516	4260	2.65
	<i>n-K</i>₈	450	553	4242	2.64
	<i>n-K</i>₉	445	535	3782	2.56
	<i>n-K</i>₁₀	468	562	3577	2.46
	<i>n-K</i>₁₁	440	524	4080	2.61
3	<i>n-K</i>₁₂	408	515	5109	2.70
	<i>n-K</i>₁₃	429	542	4964	2.68
	<i>n-K</i>₁₄	404	503	4891	2.60
	<i>n-K</i>₁₅	448	549	4121	2.59
	<i>n-K</i>₁₆	435	538	4408	2.58
	<i>n-K</i>₁₇	465	556	3525	2.44
	<i>n-K</i>₁₈	418	523	4803	2.55
4	<i>n-K</i>₁₉	350	503	8690	2.81
	<i>n-K</i>₂₀	437	535	4191	2.50
	<i>n-K</i>₂₁	360	507	8053	2.85
5	<i>n-K</i>₂₂	390	510	6033	2.85
	<i>n-K</i>₂₃	407	537	5948	2.54
	<i>n-K</i>₂₄	385	495	5772	2.86
	<i>n-K</i>₂₅	410	504	4548	2.64

6	<i>n</i> -K ₂₆	412	508	4586	2.66
	<i>n</i> -K ₂₇	442	546	4309	2.50
	<i>n</i> -K ₂₈	425	523	4408	2.57
7	<i>n</i> -K ₂₉	517	591	2421	2.32
	<i>n</i> -K ₃₀	546	631	2467	2.06
	<i>n</i> -K ₃₁	580	660	2089	2.03
8	<i>n</i> -K ₃₂	432	534	4421	2.73
	<i>n</i> -K ₃₃	494	564	2512	2.39
	<i>n</i> -K ₃₄	515	573	1965	2.33
9	<i>p</i> -K ₃₅	519	615	3007	2.19
	<i>p</i> -K ₃₆	549	639	2565	2.09
	<i>p</i> -K ₃₇	501	569	2386	2.38
	<i>p</i> -K ₃₈	506	597	3012	2.31
	<i>p</i> -K ₃₉	521	627	3244	2.29
	<i>p</i> -K ₄₀	479	568	3394	2.40
10	<i>p</i> -K ₄₁	401	457	3055	2.90
	<i>p</i> -K ₄₂	521	598	2471	2.32
11	<i>h</i> -K ₄₃	428	557	5410	2.52
	<i>h</i> -K ₄₄	417	536	5323	2.58

Conclusively, the detailed studies on photophysical properties revealed that the presence of different electron donors and acceptor/anchoring units in the conjugated electron-bridge structure have led to varied absorption maxima (λ_{abs}) as well as the emission maxima (λ_{em}) of the organic molecules. The results showcase that all the synthesized dyes/HTMs display good absorption as well as emission of photons with higher Stokes shift values, which is desirable for better light-harvesting. It has been well-documented that for better photovoltaic performance, the molecules should possess favourable optical properties. On the basis of the photophysical data, all the synthesized molecules satisfy the basic requirements of a potential sensitizer/HTM for DSSC/PSC device fabrication.

3.2 ELECTROCHEMICAL INVESTIGATION

Electrochemical studies play a pivotal role in understanding the basic electronic structures and redox properties of the materials. It describes their oxidation and reduction

potentials, which are highly useful in determining their HOMO-LUMO energy levels and charge carrying properties of the materials. Generally, the cyclic voltammetry (CV) method is largely employed for electrochemical studies of organic dyes/HTMs. In the present work, CV studies were performed for all the dyes and HTMs in order to evaluate their excited state oxidation potential/lowest unoccupied molecular orbital (ESOP/LUMO) and ground state oxidation potential/highest occupied molecular orbital (GSOP/HOMO) energy levels. Here, the measured ESOP and GSOP of the sensitizers gauge the prospects of effective charge injection as well as regeneration of dyes. In addition, to investigate the thermodynamic feasibility of dye injection, recombination, and regeneration processes, the free energies (ΔG_{inj} , ΔG_{rec} , and ΔG_{reg}) were estimated.

One of the major prerequisites for an ideal *n*-type sensitizers is that the ESOP/LUMO level of the dye should be more electronegative than the CB edge of TiO₂ to ensure effective charge injection, while the GSOP/HOMO level of the sensitizer should be more positive than the redox potential of the electrolyte to ensure effective dye regeneration. However, in case of ideal *p*-type sensitizers, the LUMO level of the dye must be sufficiently higher in energy than the redox potential of the electrolyte, while the HOMO level must be sufficiently below the VB edge of the semiconductor in order to exhibit thermodynamically allowed charge transfer processes. So, all the dyes must satisfy the above mentioned conditions for employing them as suitable candidates for *n*-/*p*-type sensitizers in DSSCs. In case of hole-transport materials, the GSOP/HOMO values of molecules must be more positive than that of the conduction band of the perovskite used for better hole extraction, whereas their ESOPs must be greater than the conduction band edge of the perovskite used, and hence they can block electron transport from perovskite to the Au counter electrode easily. Thus, all the synthesized molecules must satisfy the stringent requirement which is mandatory for the affirmative transition of charges throughout the photo-electronic conversion cycle.

3.2.1 Materials and methods

The supporting electrolyte tetrabutylammonium hexafluorophosphate [TBA] [PF₆] was procured from Sigma Aldrich Company, whereas acetonitrile was purchased

from Merck. The electrochemical characterization was performed on an IVIUM VERTOSTAT electrochemical workstation.

3.2.2 Experimental

The CV measurements for all the synthesized *n*-type chromophores (*n*-**K**₁₋₃₄), *p*-type chromophores (*p*-**K**₃₅₋₄₂), and HTMs (*h*-**K**₄₃₋₄₄) were performed in acetonitrile by using 0.1M tetrabutylammonium hexafluorophosphate [TBA] [PF₆] as a supporting electrolyte. The system was initially calibrated with ferrocene/ferrocenium (Fe/Fe⁺). The CV experiments were conducted by using the three-electrode system, consisting of glassy carbon as the working electrode, platinum as counter and Ag/AgCl as a reference electrode, and data were recorded at a scan rate of 50-100 mV/s.

3.2.3 Results and discussion

Results of electrochemical studies of new dyes/HTMs have been discussed elaborately series-wise in the following section.

3.2.3.1 Electrochemical studies of *n*-type organic chromophores *n*-**K**₁₋₃₄ (Series 1-8)

The feasibility of thermodynamically allowed transfer of electrons from the excited state of the dye molecule to the conduction band (CB) of TiO₂ and its easy regeneration by avoiding the charge recombination between photo-injected electrons in CB of TiO₂ and oxidized dye molecules can be effectively studied using cyclic voltammetry (CV). Using the experimental CV data, the GSOP/HOMO energy levels were calculated from the onset oxidation potential of the oxidation peak using equation (3.1).

$$HOMO = -[E_{onset}^{oxd} + 4.7 \text{ eV}] \quad (3.1)$$

Further, the excited state oxidation potential (ESOP) values were calculated from their ground state oxidation potential (GSOP) values and optical bandgaps E_{0-0} , and respective values in volts (V) against NHE were converted into electron volt (eV) using equation (3.2).

$$LUMO = E_{0-0} + HOMO \quad (3.2)$$

To investigate the thermodynamic feasibility of dye injection, recombination, and regeneration processes of ***n*-K₁₋₃₄**, the free energies (ΔG_{inj} , ΔG_{rec} , and ΔG_{reg}) were estimated using equations (3.3) to (3.5).

$$\Delta G_{inj} = E_{OX}^* - E_{CB} \quad (3.3)$$

$$\Delta G_{rec} = E_{CB} - E_{OX} \quad (3.4)$$

$$\Delta G_{reg} = E_{I_3^-/I^-} - E_{OX} \quad (3.5)$$

The voltammograms obtained for all the *n*-type organic chromophores (***n*-K₁₋₃₄**) are portrayed in **Figures 3.12-3.19**. Also, the schematic representation of their HOMO and LUMO energy levels along with electrochemical bandgaps are included in the same figures. Their calculated electrochemical parameters, viz. E_{ox} , E_{ox}^* , ΔG_{inj} , ΔG_{rec} , and ΔG_{reg} values are tabulated in **Table 3.2**.

Electrochemical studies of dyes ***n*-K₁₋₄** (Series-1)

The generated voltammograms of ***n*-K₁₋₄** are depicted in **Figure 3.12a**. Using the experimental CV data, we have calculated GSOP/HOMO energy levels using equation (3.1) and the values obtained for all the dyes ***n*-K₁₋₄** are summarized in **Table 3.2**. Accordingly, they are found to be -5.43 eV (***n*-K₁**), -5.45 eV (***n*-K₂**), -5.44 eV (***n*-K₃**), and -5.41 eV (***n*-K₄**). The experimental GSOP/HOMO values are found to be lower than that of the redox potential of the I_3^-/I^- electrolyte system (-5.2 eV), suggesting that all the dyes can provide a driving force for their quick ground state regeneration. Further, their excited state oxidation potential (ESOP) values were calculated using equation (3.2). **Figure 3.12b** shows the pictorial representation of their energy level diagram. Their ESOPs are found to be -2.92 eV (***n*-K₁**), -2.87 eV (***n*-K₂**), -3.07 eV (***n*-K₃**), and -3.10 eV (***n*-K₄**), which are greater than the potential of CB of TiO_2 (-4.2 eV) indicating good electron injection from the excited state of the dye molecule to the CB of the TiO_2 . Further, it is observed that the ESOP value of the dye ***n*-K₂** is more electronegative than the other dyes, providing an adequate thermodynamic driving force for the electron injection as well as dye regeneration. This may be attributed to the strong electron-withdrawing nature of cyanoacetic acid along with the increased alkoxy chain strength of

***n-K*₂**. Further, its D-A strength thermodynamically drags electrons from LUMO energy level, and injects to CB edge of the TiO₂ and HOMO energy level towards the redox electrolyte. Conclusively, all the molecules satisfy the basic requirements which facilitate the affirmative transition of charges throughout the photo-electronic conversion cycle.

The thermodynamic data for dye injection, recombination, and regeneration processes of ***n-K*₁₋₄** were estimated using equations (3.3) to (3.5) and the corresponding values are given in **Table 3.2**. The free energy values for electron injection into the CB of TiO₂ of the dyes ***n-K*₁₋₄** were calculated from the difference between the LUMO level of the dyes, and CB of TiO₂ and are in the order, ***n-K*₂** (−1.33 eV) > ***n-K*₁** (−1.28 eV) > ***n-K*₃** (−1.13 eV) > ***n-K*₄** (−1.10 eV). From these results, one can predict that the dye ***n-K*₂** can inject electrons into the CB of TiO₂ more efficiently than the other dyes. The calculated ΔG_{rec} values of dyes ***n-K*₁₋₄** are −1.23 eV (***n-K*₁**), −1.25 eV (***n-K*₂**), −1.24 eV (***n-K*₃**), and −1.21 eV (***n-K*₄**). Similarly, ΔG_{reg} values of dyes ***n-K*₁₋₄** are in the order, ***n-K*₂** (−0.35 eV) > ***n-K*₃** (−0.34 eV) > ***n-K*₁** (−0.33 eV) > ***n-K*₄** (−0.31 eV). From the results, it is clear that the dye ***n-K*₂** comprising two alkoxy chains shows the highest negative free energy for the electron regeneration process to resist its recombination between injected electrons and photo-oxidized dye molecules, indicating the thermodynamic spontaneity of this step. As reported earlier, the presence of two alkoxy chains in its structure would form a hydrophobic layer over the dye in order to protect it against water ingress from the electrolyte. Thus, increased alkoxy chain strength may function as an electrically insulating barrier, thereby minimizing interfacial charge recombination in the DSSCs. Conclusively, all the dyes show nearly the same negative values of free energy changes demonstrating a good balance in thermodynamic properties of various electronic processes.

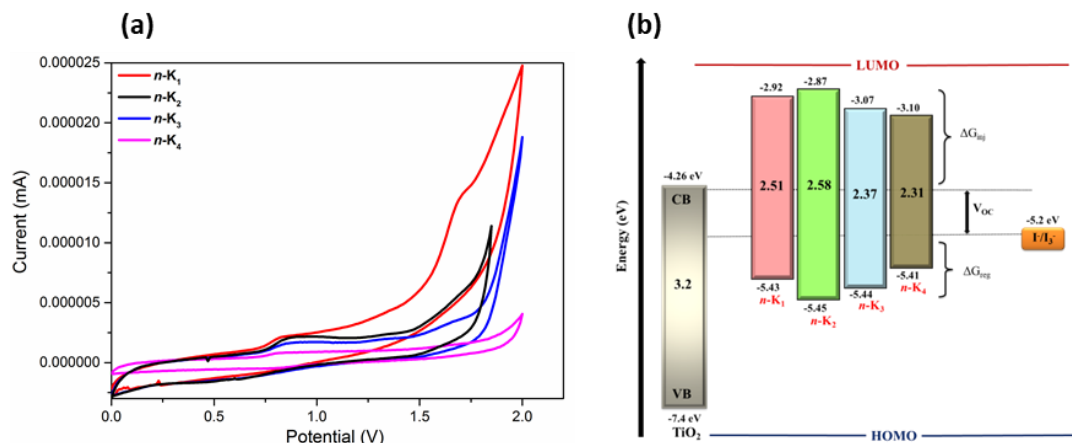


Figure 3.12 (a) Cyclic Voltammograms of $n\text{-K}_{1-4}$; (b) Molecular energy level diagram showing experimental HOMO, LUMO, and bandgap values of $n\text{-K}_{1-4}$

Electrochemical studies of dyes $n\text{-K}_{5-11}$ (Series-2)

The dyes $n\text{-K}_{5-11}$ of **Series-2** is subjected to CV studies and the generated voltammograms along with their schematic representation of HOMO-LUMO levels are depicted in **Figure 3.13**. The corresponding electrochemical data are tabulated in **Table 3.2**. The experimental GSOP/HOMO values of the dyes $n\text{-K}_{5-11}$ are found to be -5.21 eV ($n\text{-K}_5$), -5.23 eV ($n\text{-K}_6$), -5.27 eV ($n\text{-K}_7$), -5.28 eV ($n\text{-K}_8$), -5.46 eV ($n\text{-K}_9$), -5.47 eV ($n\text{-K}_{10}$), and -5.22 eV ($n\text{-K}_{11}$), which are much lower than that of the redox potential of the I_3^-/I^- electrolyte system (-5.2 eV), favoring quick ground state regeneration process. Further, the experimental ESOP/LUMO values of the dyes $n\text{-K}_{5-11}$ are found to be -2.47 eV ($n\text{-K}_5$), -2.53 eV ($n\text{-K}_6$), -2.62 eV ($n\text{-K}_7$), -2.64 eV ($n\text{-K}_8$), -2.90 eV ($n\text{-K}_9$), -3.01 eV ($n\text{-K}_{10}$), and -2.49 eV ($n\text{-K}_{11}$), which are greater than the potential of CB of TiO_2 semiconductor (-4.2 eV) facilitating the enhanced electron injection phenomenon. Among all the dyes, $n\text{-K}_5$ has ideal HOMO and LUMO levels, facilitating an adequate thermodynamic driving force which is mandatory for the affirmative transition of changes throughout the energy cycle. The reason may be due to the presence of superior electron-donating carbazole twin moieties along with a strong electron-withdrawing cyanoacetic acid as an anchoring unit.

The thermodynamic parameters for dye injection, recombination, and regeneration processes of $n\text{-K}_{5-11}$ were estimated by recording free energies (ΔG_{inj} , ΔG_{rec} , and ΔG_{reg}) using equations (3.3) to (3.5) and the corresponding data are summarized in **Table 3.2**. From the calculated data, it is clear that all the free energy values are found to be negative describing the thermodynamical feasibility of aforesaid processes. The ΔG_{inj} (free energy for electron injection from LUMO to the conduction band of TiO_2) values were calculated from the difference between the LUMO level of dyes and semiconductor and are in the order, $n\text{-K}_5$ (−1.73 eV) > $n\text{-K}_{11}$ (−1.70 eV) > $n\text{-K}_6$ (−1.67 eV) > $n\text{-K}_7$ (−1.58 eV) > $n\text{-K}_8$ (−1.56 eV) > $n\text{-K}_9$ (−1.30 eV) > $n\text{-K}_{10}$ (−1.19 eV). It is worth noticing that the dye $n\text{-K}_5$ has the highest value of ΔG_{inj} indicating efficient electron injection to CB of TiO_2 . The reason may be due to the presence of strong electron-withdrawing nature of cyanoacetic acid along with increased carbazole donor strength. Its D-A strength thermodynamically drags electrons from LUMO energy level, and injects to the CB edge of the TiO_2 and HOMO energy level towards the redox electrolyte. The calculated ΔG_{rec} values of dyes $n\text{-K}_{5-11}$ are −1.01 eV ($n\text{-K}_5$), −1.03 eV ($n\text{-K}_6$), −1.07 eV ($n\text{-K}_7$), −1.08 eV ($n\text{-K}_8$), −1.26 eV ($n\text{-K}_9$), −1.27 eV ($n\text{-K}_{10}$), and −1.02 eV ($n\text{-K}_{11}$). Similarly, ΔG_{reg} values of dyes $n\text{-K}_{5-11}$ are found to be −0.11 eV ($n\text{-K}_5$), −0.13 eV ($n\text{-K}_6$), −0.17 eV ($n\text{-K}_7$), −0.18 eV ($n\text{-K}_8$), −0.36 eV ($n\text{-K}_9$), −0.37 eV ($n\text{-K}_{10}$), and −0.12 eV ($n\text{-K}_{11}$). From the results, it is clear that the dye $n\text{-K}_5$ comprising two carbazole donor moieties along with a strong electron acceptor cyanoacetic acid shows the highest negative free energy for the electron regeneration process to resist its recombination between electron injection and photo-oxidized dye molecules, making ΔG_{rec} and ΔG_{reg} processes energetically favorable. The presence of a long linear alkyl chain functions as an insulating barrier, thereby minimizing interfacial charge recombination in the DSSCs. Conclusively, all the dyes fulfil basic requirements by providing nearly the same negative values of free energy changes demonstrating a good balance in thermodynamic properties of various photo-electronic processes.

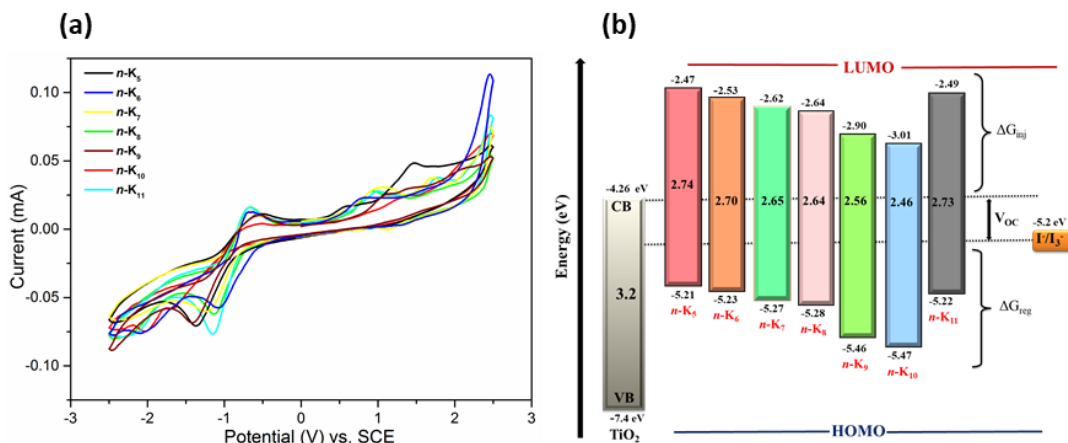


Figure 3.13 (a) Cyclic Voltammograms of $n\text{-K}_{5-11}$; (b) Molecular energy level diagram showing experimental HOMO, LUMO, and bandgap values of $n\text{-K}_{5-11}$

Electrochemical studies of dyes $n\text{-K}_{12-18}$ (Series-3)

The generated voltammograms along with a schematic representation of HOMO and LUMO energy levels of $n\text{-K}_{12-18}$ are depicted in **Figure 3.14** and the corresponding data are summarized in **Table 3.2**. The experimental GSOP/HOMO values of the dyes $n\text{-K}_{12-18}$ are found to be -5.205 eV ($n\text{-K}_{12}$), -5.210 eV ($n\text{-K}_{13}$), -5.23 eV ($n\text{-K}_{14}$), -5.45 eV ($n\text{-K}_{15}$), -5.29 eV ($n\text{-K}_{16}$), -5.41 eV ($n\text{-K}_{17}$), -5.24 eV ($n\text{-K}_{18}$), which are much lower than that of the redox potential of the I_3^-/I^- electrolyte system (-5.2 eV), favoring quick ground state regeneration process. Further, the experimental ESOP/LUMO values of the dyes $n\text{-K}_{12-18}$ are found to be -2.50 eV ($n\text{-K}_{12}$), -2.53 eV ($n\text{-K}_{13}$), -2.63 eV ($n\text{-K}_{14}$), -2.86 eV ($n\text{-K}_{15}$), -2.72 eV ($n\text{-K}_{16}$), -2.97 eV ($n\text{-K}_{17}$), and -2.69 eV ($n\text{-K}_{18}$), which are greater than the potential of CB of TiO_2 semiconductor (-4.2 eV) facilitating enhanced electron injection phenomenon. Among all the dyes, $n\text{-K}_{12}$ has ideal HOMO and LUMO levels, facilitating an adequate thermodynamic driving force which is mandatory for the affirmative transition of changes throughout the energy cycle.

The three different thermodynamic driving forces (ΔG_{inj} , ΔG_{rec} , and ΔG_{reg}) were obtained from equations 3.3-3.5. From the calculated data, it is clear that all the free energy values are found to be negative describing the thermodynamical feasibility of aforesaid processes. The ΔG_{inj} values were calculated from the difference between

LUMO level of dyes and CB of semiconductor and are in the order, $n\text{-K}_{12}$ (-1.69 eV) > $n\text{-K}_{13}$ (-1.67 eV) > $n\text{-K}_{14}$ (-1.57 eV) > $n\text{-K}_{18}$ (-1.51 eV) > $n\text{-K}_{16}$ (-1.48 eV) > $n\text{-K}_{15}$ (-1.34 eV) > $n\text{-K}_{17}$ (-1.23 eV). It is worth noticing that, the dye $n\text{-K}_{12}$ has the highest value of ΔG_{inj} indicating efficient electron injection to CB of TiO_2 . The reason may be due to the presence of a strong electron-withdrawing nature of cyanoacetic acid along with increased carbazole donor strength. The calculated ΔG_{rec} values of dyes $n\text{-K}_{12-18}$ are -1.00 eV ($n\text{-K}_{12}$), -1.01 eV ($n\text{-K}_{13}$), -1.03 eV ($n\text{-K}_{14}$), -1.25 eV ($n\text{-K}_{15}$), -1.09 eV ($n\text{-K}_{16}$), -1.21 eV ($n\text{-K}_{17}$), and -1.04 eV ($n\text{-K}_{18}$). Similarly, ΔG_{reg} values of dyes $n\text{-K}_{12-18}$ are found to be, -0.10 eV ($n\text{-K}_{12}$), -0.11 eV ($n\text{-K}_{13}$), -0.13 eV ($n\text{-K}_{14}$), -0.36 eV ($n\text{-K}_{15}$), -0.19 eV ($n\text{-K}_{16}$), -0.31 eV ($n\text{-K}_{17}$), and -0.14 eV ($n\text{-K}_{18}$). From the results, it is clear that the dye $n\text{-K}_{12}$ comprising two carbazole donor moieties along with a strong electron acceptor cyanoacetic acid shows the highest negative free energy for the electron regeneration process to resist its recombination between electron injection and photo-oxidized dye molecules, making ΔG_{rec} and ΔG_{reg} process energetically favorable. The presence of a long linear alkyl chain functions as an insulating barrier, thereby minimizing interfacial charge recombination in the DSSCs. Conclusively, all the dyes fulfil basic requirements by providing nearly the same negative values of free energy changes demonstrating a good balance in thermodynamic properties of various photo-electronic processes.

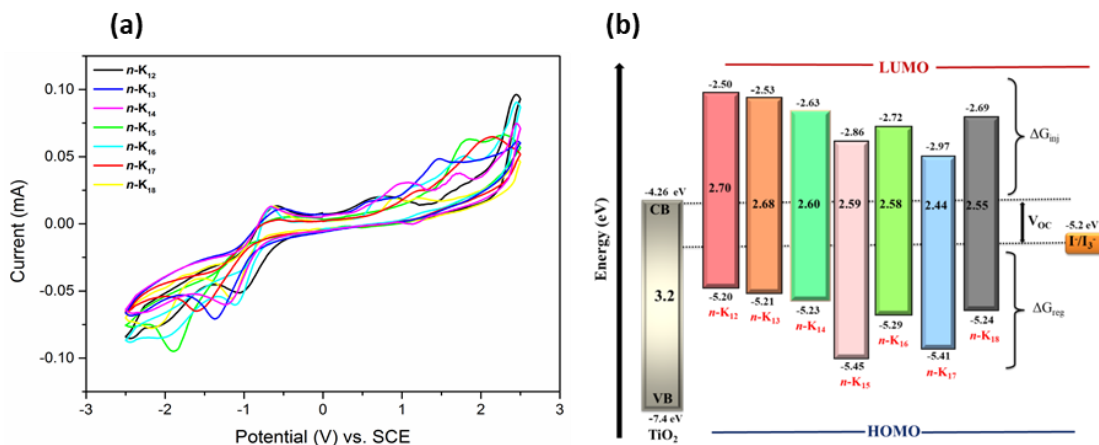


Figure 3.14 (a) Cyclic Voltammograms of $n\text{-K}_{12-18}$; (b) Molecular energy level diagram showing experimental HOMO, LUMO, and bandgaps of $n\text{-K}_{12-18}$

Electrochemical studies of dyes *n-K*₁₉₋₂₁ (Series-4)

Figure 3.15 depicts the voltammograms and schematic representation of HOMO-LUMO energy levels along with calculated bandgaps of *n-K*₁₉₋₂₁ and their data are tabulated in **Table 3.2**. The experimental GSOP/HOMO values of the dyes *n-K*₁₉₋₂₁ are found to be -5.77 eV (*n-K*₁₉), -5.75 eV (*n-K*₂₀), and -5.69 eV (*n-K*₂₁), whereas the ESOP/LUMO values of the dyes are seen to be -2.96 eV (*n-K*₁₉), -3.25 eV (*n-K*₂₀), and -2.84 eV (*n-K*₂₁). All the dyes display ideal HOMO and LUMO levels which are almost matching with the standard sensitizers, facilitating adequate thermodynamic driving forces required throughout the energy cycle.

The thermodynamic parameters (ΔG_{inj} , ΔG_{rec} , and ΔG_{reg}) were estimated from equations 3.3-3.5 and the results have been given in **Table 3.2**. The ΔG_{inj} obtained for *n-K*₁₉₋₂₁ are, *n-K*₁₉ (-1.24 eV), *n-K*₂₀ (-0.95 eV), and *n-K*₂₁ (-1.36 eV). It is important to observe that the dye *n-K*₂₁ has the highest value of ΔG_{inj} demonstrating higher feasibility of electron injection to the CB of semiconductor layer. The calculated ΔG_{rec} values of dyes *n-K*₁₉₋₂₁ are -1.57 eV (*n-K*₁₉), -1.55 eV (*n-K*₂₀), and -1.49 eV (*n-K*₂₁), whereas ΔG_{reg} values of dyes are found to be, -0.67 eV (*n-K*₁₉), -0.65 eV (*n-K*₂₀), and -0.59 eV (*n-K*₂₁). The results indicate that all the dyes of **Series-4** possess superior driving forces for electron injection as well as the dye regeneration process.

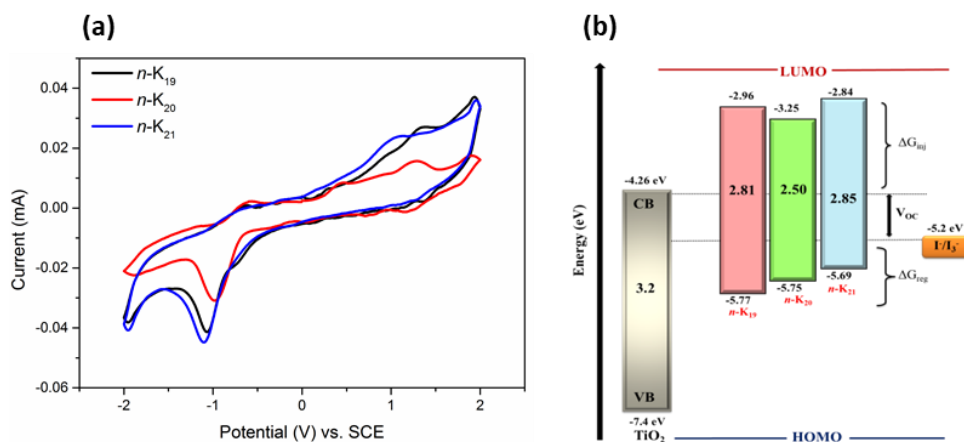


Figure 3.15 (a) Cyclic Voltammograms of *n-K*₁₉₋₂₁; (b) Molecular energy level diagram showing experimental HOMO, LUMO, and bandgap values of *n-K*₁₉₋₂₁

Electrochemical studies of dyes $n\text{-K}_{22-24}$ (Series-5)

Figure 3.16 displays the cyclic voltammetry plots and molecular energy level diagram showing HOMO-LUMO energy levels of organic chromophores $n\text{-K}_{22-24}$. The corresponding electrochemical data are given in **Table 3.2**. The GSOP/HOMO values obtained for the dyes $n\text{-K}_{22-24}$ are found to be -5.49 eV ($n\text{-K}_{22}$), -5.59 eV ($n\text{-K}_{23}$), and -5.63 eV ($n\text{-K}_{24}$), whereas the ESOP/LUMO values of the dyes are found to be -2.64 eV ($n\text{-K}_{22}$), -3.05 eV ($n\text{-K}_{23}$), and -2.77 eV ($n\text{-K}_{24}$). The redox potentials obtained are in agreement with that of standard sensitizers. Thus, from the results it is clear that all the dyes display suitable HOMO and LUMO energy levels, facilitating an adequate thermodynamic driving forces which are mandatory for the affirmative transition of charges throughout the energy cycle.

Table 3.2 depicts thermodynamic parameters ΔG_{inj} , ΔG_{rec} , and ΔG_{reg} as calculated from equations 3.3-3.5. The ΔG_{inj} data obtained for $n\text{-K}_{22-24}$ are, $n\text{-K}_{22}$ (-1.56 eV), $n\text{-K}_{23}$ (-1.15 eV), and $n\text{-K}_{24}$ (-1.43 eV). The calculated ΔG_{rec} values of dyes $n\text{-K}_{22-24}$ are -1.29 eV ($n\text{-K}_{22}$), -1.39 eV ($n\text{-K}_{23}$), and -1.43 eV ($n\text{-K}_{24}$), whereas ΔG_{reg} values of dyes are found to be, -0.39 eV ($n\text{-K}_{22}$), -0.49 eV ($n\text{-K}_{23}$), and -0.53 eV ($n\text{-K}_{24}$). From the results, it is clear that all the dyes possess a stringent requirement which is mandatory for the affirmative transition of charges throughout the photo-electronic conversion cycle.

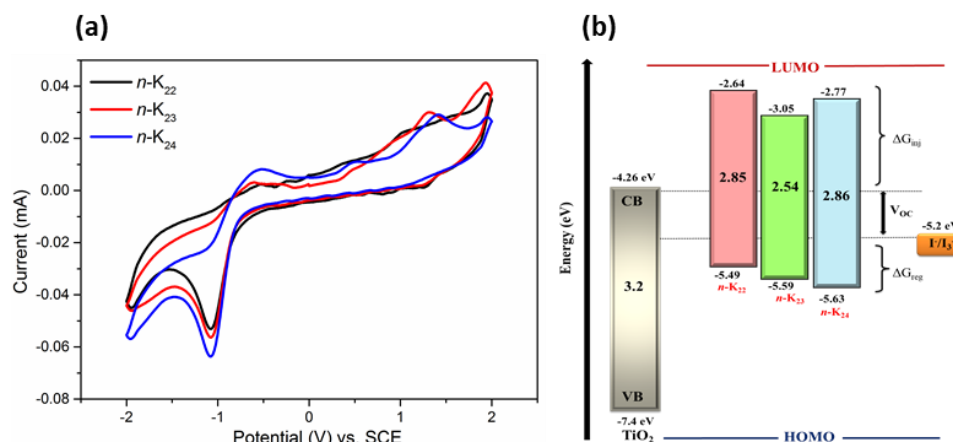


Figure 3.16 (a) Cyclic Voltammograms of $n\text{-K}_{22-24}$; (b) Molecular energy level diagram showing experimental HOMO, LUMO, and bandgap values of $n\text{-K}_{22-24}$

Electrochemical studies of dyes *n-K*₂₅₋₂₈ (Series-6)

The dyes *n-K*₂₅₋₂₈ of Series-6 are subjected to CV studies and the generated voltammograms along with their schematic representation of HOMO-LUMO levels are depicted in **Figure 3.17**. From the CV results, the experimental HOMO values of the dyes *n-K*₂₅₋₂₈ are found to be -5.74 eV (*n-K*₂₅), -5.75 eV (*n-K*₂₆), -5.65 eV (*n-K*₂₇), and -5.67 eV (*n-K*₂₈), which are much lower than that of the redox potential of the I_3^-/I^- electrolyte system (-5.2 eV), favoring quick ground state regeneration process. Further, the experimental LUMO values of the dyes *n-K*₂₅₋₂₈ are found to be -3.10 eV (*n-K*₂₅), -3.09 eV (*n-K*₂₆), -3.15 eV (*n-K*₂₇), and -3.10 eV (*n-K*₂₈), which are greater than the potential of the CB of TiO₂ semiconductor (-4.2 eV) facilitating enhanced electron injection phenomenon.

The thermodynamic processes such as dye injection, recombination, and regeneration processes of *n-K*₂₅₋₂₈ were estimated and the corresponding data are given in **Table 3.2**. From the calculated data, the ΔG_{inj} values were found to be *n-K*₂₅ (-1.10 eV), *n-K*₂₆ (-1.11 eV), *n-K*₂₇ (-1.05 eV), and *n-K*₂₈ (-1.10 eV). It is worth noticing that the dye *n-K*₂₆ has the highest value of ΔG_{inj} indicating efficient electron injection to CB of TiO₂. The reason may be due to the superior anchoring ability of barbituric acid. The calculated ΔG_{rec} values of dyes *n-K*₂₅₋₂₈ are -1.54 eV (*n-K*₂₅), -1.55 eV (*n-K*₂₆), -1.45 eV (*n-K*₂₇), and -1.47 eV (*n-K*₂₈). Similarly, ΔG_{reg} values of dyes *n-K*₂₅₋₂₈ are found to be, -0.64 eV (*n-K*₂₅), -0.65 eV (*n-K*₂₆), -0.55 eV (*n-K*₂₇), and -0.57 eV (*n-K*₂₈). From the results, it is clear that the dye *n-K*₂₆ comprising two carbazole donor moieties along with a strong electron anchoring barbituric acid shows the highest negative free energy for the electron regeneration process to resist its recombination between electron injection and photo-oxidized dye molecules, making ΔG_{rec} and ΔG_{reg} processes energetically favorable. Conclusively, all the dyes fulfil basic requirements by providing nearly the same negative values of free energy changes demonstrating a good balance in thermodynamic properties of various photo-electronic processes.

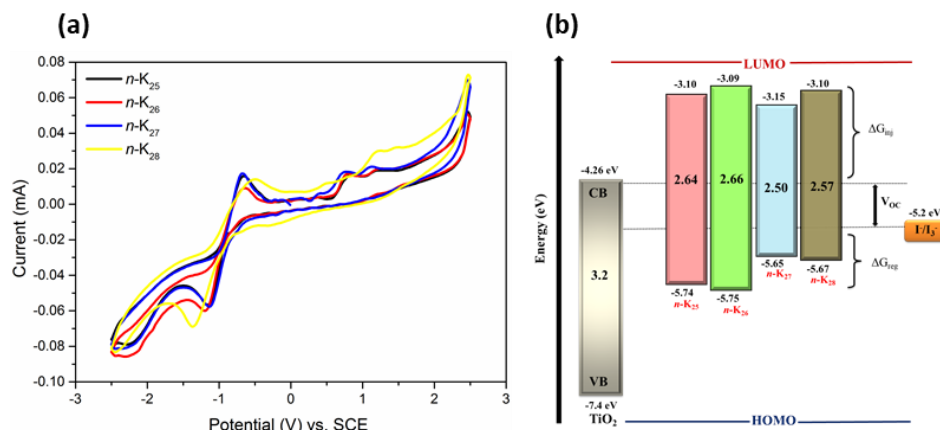


Figure 3.17 (a) Cyclic Voltammograms of $n\text{-K}_{25-28}$; (b) Molecular energy level diagram showing experimental HOMO, LUMO, and bandgap values of $n\text{-K}_{25-28}$

Electrochemical studies of dyes $n\text{-K}_{29-31}$ (Series-7)

Figure 3.18a represents the generated voltammograms of dyes $n\text{-K}_{29-31}$, whereas **Figure 3.18b** shows the pictorial representation of their energy level diagram. From the CV traces of dyes, the experimental GSOP/HOMO values obtained are -5.54 eV ($n\text{-K}_{29}$), -5.56 eV ($n\text{-K}_{30}$), and -5.76 eV ($n\text{-K}_{31}$), whereas ESOP/LUMO values are found to be -3.22 eV ($n\text{-K}_{29}$), -3.50 eV ($n\text{-K}_{30}$), and -3.73 eV ($n\text{-K}_{31}$). From the results, we can conclude that the HOMO values are much lower than the redox potential of the I_3^-/I^- electrolyte system (-5.2 eV), favoring quick ground state regeneration process and LUMO values are greater than the potential of CB of TiO_2 semiconductor (-4.2 eV) facilitating the increased electron injection phenomenon.

Additionally, the parameters leading to driving forces like ΔG_{inj} , ΔG_{rec} , and ΔG_{reg} were calculated from equations 3.3-3.5 (given under **Series-1**). **Table 3.2** shows the calculated electrochemical data of all the dyes. As seen, the ΔG_{inj} values obtained are in the order, $n\text{-K}_{29}$ (-0.98 eV) $>$ $n\text{-K}_{30}$ (-0.70 eV) $>$ $n\text{-K}_{31}$ (-0.47 eV), indicating the dye $n\text{-K}_{29}$ can exhibit superior electron injection to the CB of TiO_2 . The reason may be due to the presence of strong electron anchoring nature of cyanoacetic acid along with increased phenoxazine donor strength *via* thiophene spacer. The calculated ΔG_{rec} values of dyes $n\text{-K}_{29-31}$ are -1.34 eV ($n\text{-K}_{29}$), -1.36 eV ($n\text{-K}_{30}$), and -1.56 eV ($n\text{-K}_{31}$), whereas ΔG_{reg}

values are found to be -0.44 eV ($n\text{-K}_{29}$), -0.46 eV ($n\text{-K}_{30}$), and -0.66 eV ($n\text{-K}_{31}$). From the results, it is clear that all the dyes display efficient electron injection and regeneration by suppressing electron recombination, thus can act as ideal sensitizers for DSSC application.

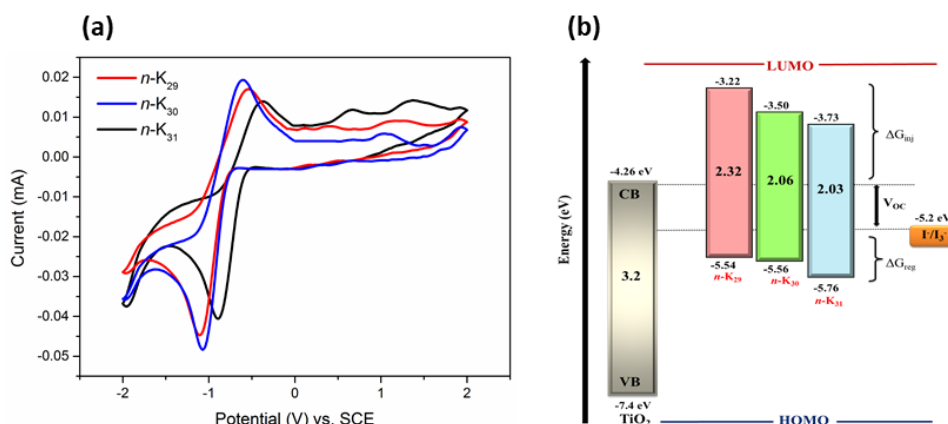


Figure 3.18 (a) Cyclic Voltammograms of $n\text{-K}_{29-31}$; (b) Molecular energy level diagram showing experimental HOMO, LUMO, and bandgap values of $n\text{-K}_{29-31}$

Electrochemical studies of dyes $n\text{-K}_{32-34}$ (Series-8)

Figure 3.19 represents the cyclic voltammograms and schematic representation of HOMO-LUMO energy levels along with calculated bandgaps of $n\text{-K}_{32-34}$ and their data are given in **Table 3.2**. The experimental GSOP/HOMO values of the dyes $n\text{-K}_{32-34}$ calculated from equation 3.1 (given under **Series-1**) are found to be -5.77 eV ($n\text{-K}_{32}$), -5.78 eV ($n\text{-K}_{33}$), and -5.75 eV ($n\text{-K}_{34}$), whereas the ESOP/LUMO values of the dyes calculated from equation 3.2 are found to be -3.04 eV ($n\text{-K}_{32}$), -3.39 eV ($n\text{-K}_{33}$), and -3.42 eV ($n\text{-K}_{34}$). From the results, it is worth noticing that all the dyes display appropriate HOMO and LUMO levels which are almost matching with the standard sensitizers.

The three different thermodynamic parameters (ΔG_{inj} , ΔG_{rec} , and ΔG_{reg}) were estimated from equations 3.3-3.5. The ΔG_{inj} obtained for $n\text{-K}_{32-34}$ are found to be in the decreasing order of $n\text{-K}_{32}$ (-1.16 eV) $>$ $n\text{-K}_{33}$ (-0.81 eV) $>$ $n\text{-K}_{34}$ (-0.78 eV). It is interesting to notice that the dye $n\text{-K}_{32}$ bearing phenoxazine donor and cyanoacetic acid as an anchoring unit displays the highest value of ΔG_{inj} demonstrating superior feasibility

of electron injection to CB of the semiconductor layer. The calculated ΔG_{rec} values of dyes $n\text{-K}_{32-34}$ are -1.57 eV ($n\text{-K}_{32}$), -1.58 eV ($n\text{-K}_{33}$), and -1.55 eV ($n\text{-K}_{34}$), whereas ΔG_{reg} values of dyes are found to be, -0.67 eV ($n\text{-K}_{32}$), -0.68 eV ($n\text{-K}_{33}$), and -0.65 eV ($n\text{-K}_{34}$), respectively. The results indicate that all the dyes in **Series-8** possess superior driving forces for electron injection as well as the dye regeneration process.

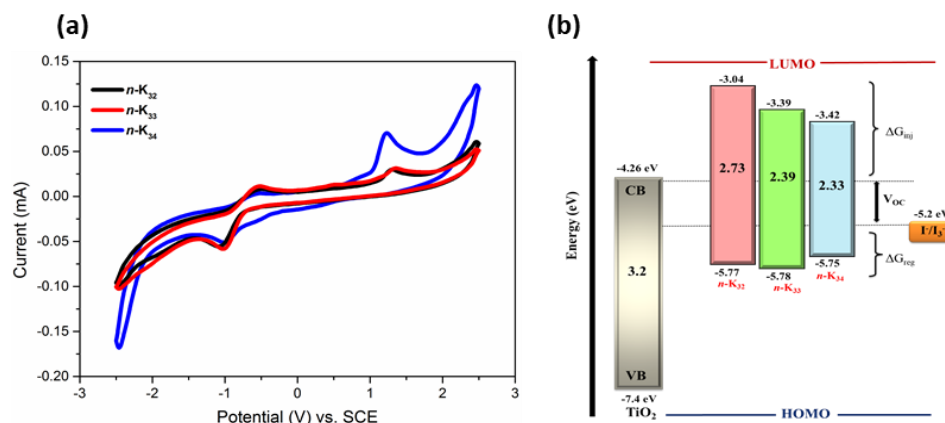


Figure 3.19 (a) Cyclic Voltammograms of $n\text{-K}_{32-34}$; (b) Molecular energy level diagram showing experimental HOMO, LUMO, and bandgap values of $n\text{-K}_{32-34}$

Conclusively, all the synthesized n -type organic chromophores ($n\text{-K}_{1-34}$) fulfilled the essential prerequisites for effective electron injection and dye regeneration processes in the DSSC devices (Koops et al. 2009). Evidently, the presence of various electron donors and acceptors in conjugated structures of these different series has resulted in distinct HOMO and LUMO energy levels. The experimental results clearly indicate the presence of ample thermodynamic driving forces for effective dye regeneration and efficient electron injection in the fabricated cell.

Table 3.2 Electrochemical properties of n -type organic chromophores $n\text{-K}_{1-34}$

Series	Compound	E_{ox} (V) ^d	E_{ox}^* (V) ^d	HOMO (eV) ^d	LUMO (eV) ^d	ΔG_{inj} (eV)	ΔG_{rec} (eV)	ΔG_{reg} (eV)
1	$n\text{-K}_1$	0.73	-1.78	-5.43	-2.92	-1.28	-1.23	-0.33
	$n\text{-K}_2$	0.75	-1.83	-5.45	-2.87	-1.33	-1.25	-0.35
	$n\text{-K}_3$	0.74	-1.63	-5.44	-3.07	-1.13	-1.24	-0.34

	<i>n</i>-K₄	0.71	-1.60	-5.41	-3.10	-1.10	-1.21	-0.31
2	<i>n</i>-K₅	0.51	-2.23	-5.21	-2.47	-1.73	-1.01	-0.11
	<i>n</i>-K₆	0.53	-2.17	-5.23	-2.53	-1.67	-1.03	-0.13
	<i>n</i>-K₇	0.57	-2.08	-5.27	-2.62	-1.58	-1.07	-0.17
	<i>n</i>-K₈	0.58	-2.06	-5.28	-2.64	-1.56	-1.08	-0.18
	<i>n</i>-K₉	0.76	-1.80	-5.46	-2.90	-1.30	-1.26	-0.36
	<i>n</i>-K₁₀	0.77	-1.68	-5.47	-3.01	-1.19	-1.27	-0.37
	<i>n</i>-K₁₁	0.52	-2.20	-5.22	-2.49	-1.70	-1.02	-0.12
3	<i>n</i>-K₁₂	0.50	-2.19	-5.20	-2.50	-1.69	-1.00	-0.10
	<i>n</i>-K₁₃	0.51	-2.17	-5.21	-2.53	-1.67	-1.01	-0.11
	<i>n</i>-K₁₄	0.53	-2.07	-5.23	-2.63	-1.57	-1.03	-0.13
	<i>n</i>-K₁₅	0.75	-1.83	-5.45	-2.86	-1.34	-1.25	-0.36
	<i>n</i>-K₁₆	0.59	-1.98	-5.29	-2.72	-1.48	-1.09	-0.19
	<i>n</i>-K₁₇	0.71	-1.73	-5.41	-2.97	-1.23	-1.21	-0.31
4	<i>n</i>-K₁₈	0.54	-2.01	-5.24	-2.69	-1.51	-1.04	-0.14
	<i>n</i>-K₁₉	1.07	-1.74	-5.77	-2.96	-1.24	-1.57	-0.67
	<i>n</i>-K₂₀	1.05	-1.45	-5.75	-3.25	-0.95	-1.55	-0.65
5	<i>n</i>-K₂₁	0.99	-1.86	-5.69	-2.84	-1.36	-1.49	-0.59
	<i>n</i>-K₂₂	0.79	-2.06	-5.49	-2.64	-1.56	-1.29	-0.39
	<i>n</i>-K₂₃	0.89	-1.65	-5.59	-3.05	-1.15	-1.39	-0.49
6	<i>n</i>-K₂₄	0.93	-1.93	-5.63	-2.77	-1.43	-1.43	-0.53
	<i>n</i>-K₂₅	1.04	-1.60	-5.74	-3.10	-1.10	-1.54	-0.64
	<i>n</i>-K₂₆	1.05	-1.61	-5.75	-3.09	-1.11	-1.55	-0.65
7	<i>n</i>-K₂₇	0.95	-1.55	-5.65	-3.15	-1.05	-1.45	-0.55
	<i>n</i>-K₂₈	0.97	-1.60	-5.67	-3.10	-1.10	-1.47	-0.57
7	<i>n</i>-K₂₉	0.84	-1.48	-5.54	-3.22	-0.98	-1.34	-0.44
	<i>n</i>-K₃₀	0.86	-1.20	-5.56	-3.50	-0.70	-1.36	-0.46
	<i>n</i>-K₃₁	1.06	-0.97	-5.76	-3.73	-0.47	-1.56	-0.66

8	<i>n</i> - K ₃₂	1.07	-1.66	-5.77	-3.04	-1.16	-1.57	-0.67
	<i>n</i> - K ₃₃	1.08	-1.31	-5.78	-3.39	-0.81	-1.58	-0.68
	<i>n</i> - K ₃₄	1.05	-1.28	-5.75	-3.42	-0.78	-1.55	-0.65

The E^* values were formulated by, $E_{ox}^* = E_{ox} - E_{0-0}$.^d All the potentials were obtained during cyclic voltammetric investigations in 0.1 M Bu_4NPF_6 in DMF, and platinum electrode diameter: 1 mm, sweep rate: 100 mVs^{-1}

3.2.3.2 Electrochemical studies of *p*-type organic chromophores *p*-**K**₃₅₋₄₂ (Series 9-10)

The CV study of *p*-**K**₃₅₋₄₂ was performed in acetonitrile solution in order to evaluate their electrochemical processes as well as charge carrying behavior. In the CV experiments, the cyclic voltammograms were recorded at the applied voltage of +2 to -2 V and resultant plots are presented in **Figure 3.20**. All the dyes exhibit ideal HOMO and LUMO levels, facilitating adequate thermodynamic driving forces which are mandatory for the affirmative transition of changes throughout the energy cycle.

Further, the Gibbs free energy to inject charge from the HOMO level of the dye to the VB edge of the NiO was estimated from equation 3.6.

$$\Delta G_{inj} = E_{VB}(NiO) - E_{Red}^* \quad (3.6)$$

$$\Delta G_{reg} = E_{Red} - E_{I_3^-/I_2^-} \quad (3.7)$$

Here, ΔG_{inj} is the Gibbs free energy for injection, E_{Red}^* is the reduction potential of the dye and $E_{VB}(NiO)$ is the Nernst potential of the VB of NiO, *i.e.* 0.30 V vs SCE.

Furthermore, Gibbs free energy for dye regeneration from electrolyte (ΔG_{reg}) was estimated from the difference between reduction potential of the dye and Nernst potential of I_3^-/I_2^- electrolyte system (-0.32 V) and it can be expressed as equation 3.7 and the corresponding calculated ΔG_{inj} and ΔG_{reg} data are given in **Table 3.3**. The calculated Gibbs free energies of both the photoinduced hole injection into the VB of NiO as well as the dye regeneration reaction with redox electrolyte clearly indicates that all the dyes of **Series-9** (*p*-**K**₃₅₋₄₀) and **Series-10** (*p*-**K**₄₁₋₄₂) exhibit sufficient exergonicity of these processes to spontaneously occur.

Conclusively, the electrochemical studies revealed that all the *p*-type organic chromophores (*p*-**K**₃₅₋₄₂) fulfilled the prerequisites for effective electron injection and dye regeneration processes in the fabricated devices.

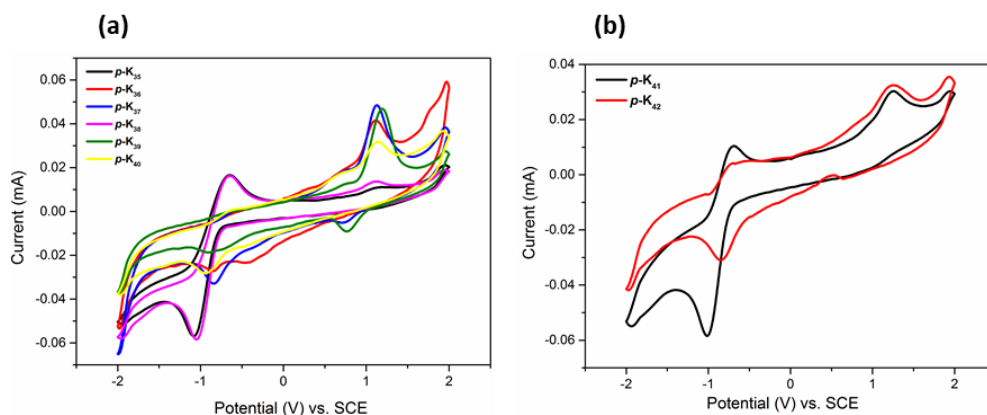


Figure 3.20 Cyclic Voltammograms of (a) *p*-**K**₃₅₋₄₀ and (b) *p*-**K**₄₁₋₄₂

Table 3.3 Electrochemical properties of *p*-type organic chromophores *p*-**K**₃₅₋₄₂

Series	Compound	E_{ox} (V)	E_{Red} (V)	E_{Red}^* (V)	ΔG_{inj} (eV)	ΔG_{reg} (eV)
9	<i>p</i> - K ₃₅	0.69	-0.80	1.39	-1.09	-0.48
	<i>p</i> - K ₃₆	0.87	-0.71	1.38	-1.08	-0.39
	<i>p</i> - K ₃₇	0.85	-0.62	1.76	-1.46	-0.30
	<i>p</i> - K ₃₈	0.83	-0.78	1.53	-1.23	-0.46
	<i>p</i> - K ₃₉	0.93	-0.66	1.63	-1.33	-0.34
	<i>p</i> - K ₄₀	0.82	-0.68	1.72	-1.42	-0.36
10	<i>p</i> - K ₄₁	0.85	-0.75	2.15	-1.85	-0.43
	<i>p</i> - K ₄₂	0.79	-0.60	1.72	-1.42	-0.28

The E^* values were formulated by, $E_{Red}^* = E_{Red} + E_{0-0}$. $\Delta G_{inj} = E_{VB}(\text{NiO}) - E_{Red}^*$ (dye*/dye⁻) with $E_{VB}(\text{NiO}) = 0.30$ V vs SCE. $\Delta G_{reg} = E_{Red}(\text{dye}/\text{dye}^-) - E(I_3^-/I_2^{\bullet-})$ with $E(I_3^-/I_2^{\bullet-}) = -0.32$ V vs SCE (Boschloo et al., 2011; Farré et al., 2016; Black et al., 2017).

3.2.3.3 Electrochemical studies of organic HTMs *h-K*₄₃₋₄₄ (Series-11)

The generated voltammograms of *h-K*₄₃₋₄₄ are depicted in **Figure 3.21a**. From the experimental CV data, we have calculated ground state oxidation potential (GSOP)/HOMO energy levels from the onset oxidation potential of the oxidation peak using equation (3.1) and the values obtained for both the molecules are summarized in **Table 3.4**. Accordingly, they were found to be -5.37 eV (*h-K*₄₃), and -5.39 eV (*h-K*₄₄).

The experimental GSOP/HOMO values of *h-K*₄₃₋₄₄ are in between that of CH₃NH₃PbI₃ perovskite (-5.43 eV) and Au counter electrode (-5.1 eV), suggesting that both the molecules can provide a driving force for their quick ground state regeneration. Further, the excited state oxidation potential (ESOP)/LUMO values were calculated from their GSOP values, and optical bandgaps E_{0-0} and respective values in volts (V) against NHE were converted into electron volt (eV) using equation (3.2). **Table 3.4** depicts the estimated ESOP values of *h-K*₄₃₋₄₄ and **Figure 3.21b** shows the pictorial representation of their energy level diagram. As seen from the table, their ESOPs are -2.85 eV (*h-K*₄₃), and -2.81 eV (*h-K*₄₄), which are greater than the conduction band edge of CH₃NH₃PbI₃ (-3.93 eV), and hence they can block electron transport from perovskite to the Au counter electrode easily. Thus, both the molecules satisfy the stringent requirement which is mandatory for the affirmative transition of charges throughout the photo-electronic conversion cycle. The generated radical cation of the carbazole moiety is stabilized due to the di-substitution in the 3,6-positions of the molecule which ultimately leads to the first quasi-reversible system. Based on these results, we can conclude that both *h-K*₄₃₋₄₄ are potential hole-transporting candidates in CH₃NH₃PbI₃-based solar cells. Here, *h-K*₄₃ has more appropriate energy levels than that of *h-K*₄₄, which mediates holes from CH₃NH₃PbI₃ perovskite to Au counter electrode due to the higher donating capacity of dimethoxy groups on *h-K*₄₃. Also, the introduction of pendant groups improves the oxidation potential of the compounds due to the inductive effect caused by the terminal methoxy groups. Conclusively, both the synthesized molecules (*h-K*₄₃₋₄₄) satisfy the basic requirements of a potential HTM, which further facilitate the affirmative transition of charges throughout the photo-electronic conversion cycle.

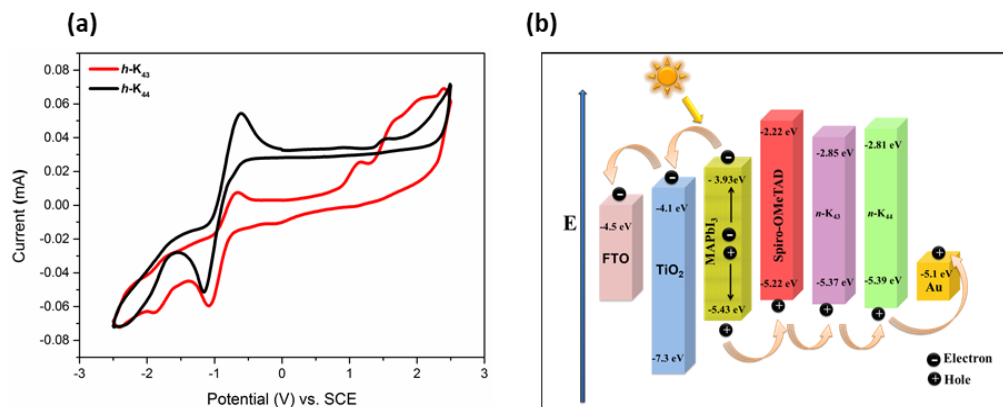


Figure 3.21 (a) Cyclic Voltammograms of *h-K*₄₃₋₄₄; (b) Molecular energy level diagram showing experimental HOMO, LUMO, and bandgap values of *h-K*₄₃₋₄₄

Table 3.4 Electrochemical properties of HTMs *h-K*₄₃₋₄₄

Series	Compound	E_{ox} (V vs. NHE) ^d	$E_{\text{ox}}^{\#}$ (V vs. NHE) ^d	HOMO (eV) ^d	LUMO (eV) ^d
11	<i>h-K</i> ₄₃	0.67	-1.85	-5.37	-2.85
	<i>h-K</i> ₄₄	0.69	-1.89	-5.39	-2.81

The E^* values were formulated by: $E_{\text{ox}}^* = E_{\text{ox}} - E_{0-0}$.^d All the potentials were generated during CV investigations in 0.1 M Bu₄NPF₆ in DMF, with platinum electrode diameter: 1 mm, sweep rate: 100 mVs⁻¹

3.3 THEORETICAL INVESTIGATION

The development of DSSCs/PSCs has been accompanied by computational studies that help to rationalize the relationship between the molecular structure and device performance (Martsinovich and Troisi 2011). In particular, the geometrical configurations, frontier molecular orbitals, and the optical absorption properties of molecules, both isolated as well as adsorbed on the semiconductor surfaces, have been extensively studied using density-functional theory (DFT) and time-dependent DFT studies. The HOMO-LUMO energy levels, bandgaps, spectral data of unknown compounds can be generated using computational studies. Moreover, theoretical investigation of the physical properties of sensitizers/HTMs is very important to disclose

the relationship between the molecular geometry and photovoltaic performance. In addition, computational studies play a significant role in designing new molecules as effective photosensitizers/HTMs for achieving enhanced photovoltaic performance.

The adiabatic quantum calculations with hybrid functional are considered to be one of the reliable computational methodologies in the field of organic photovoltaics, especially in DSSCs/PSCs to estimate the frontier molecular orbital (FMO) levels of potential *n*-/*p*-type sensitizers as well as organic HTMs.

3.3.1 Simulations

In the present study, the DFT simulations were carried out for isolated organic dyes/HTMs in order to evaluate their ground state properties in gas phase. However, the vertical excitation and their response in the excited state of the molecules were computed using TD-DFT simulations. Turbomole 7.2 software package was used to execute the theoretical calculations. Using a semiempirical AM1 basis with MOPAC in Tmolex, we have optimized the ground state geometries of the molecules. Aforesaid geometries were further optimized using C_1 point group symmetry *via* the Becke's three-parameter hybrid functional and Lee-Yang-Parr's gradient-corrected correlation functional (B3LYP) program and basic set def-TZVPP was used for all the calculations (Becke, 1988; Peach et al., 2008). Also, TD-DFT calculations were performed for all the dyes at B3LYP using def TZVP level to generate optical absorption spectra.

3.3.2 Results and discussion

Results of theoretical studies of new dyes/HTMs have been discussed series-wise in the following section.

3.3.2.1 Theoretical studies of *n*-type organic chromophores *n*-**K**₁₋₃₄ (Series 1-8)

Molecular modeling of *n*-**K**₁₋₄ (Series-1)

To gain a much deeper understanding of the geometrical configurations and frontier molecular orbitals of *n*-**K**₁₋₄, the molecular orbital calculations were carried out using the DFT simulations as depicted in **Figure 3.22**. As seen from the figure, in case of

HOMO levels, electron densities of $n\text{-K}_{1-4}$ are primarily distributed along with the donor unit, which clearly indicates the electron-donating capacity of dodecyloxyphenyl/bisdodecyloxyphenyl group along with the thiophene unit. Nevertheless, the electron density distribution in LUMOs is found at the acceptor part, *i.e.* cyanoacetic acid/barbituric acid and π conjugated spacer containing cyanovinylene group.

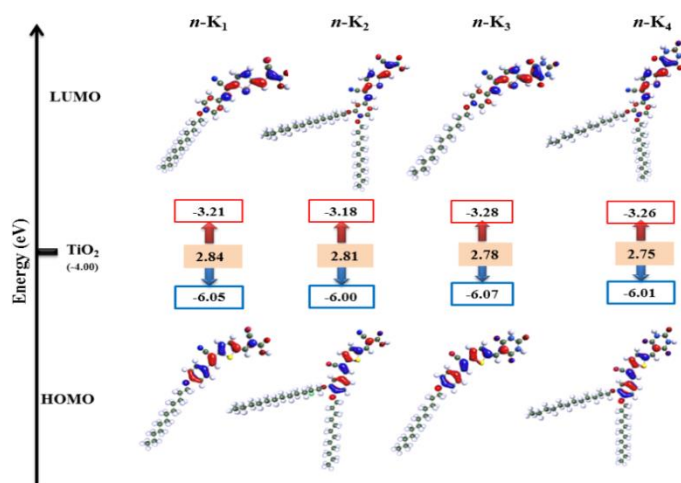


Figure 3.22 The electronic cloud distributions in the FMO levels of dyes $n\text{-K}_{1-4}$

The theoretical HOMO energy levels obtained for dyes $n\text{-K}_{1-4}$ are -6.05 eV ($n\text{-K}_1$), -6.00 eV ($n\text{-K}_2$), -6.07 eV ($n\text{-K}_3$), and -6.01 eV ($n\text{-K}_4$), which are significantly lower than that of the redox potential of I_3^-/I^- electrolyte system (-5.2 eV) confirming the synthesized dyes can undergo a quick ground state regeneration process. The theoretical LUMO energy levels obtained for dyes $n\text{-K}_{1-4}$ are -3.21 eV ($n\text{-K}_1$), -3.18 eV ($n\text{-K}_2$), -3.28 eV ($n\text{-K}_3$), and -3.26 eV ($n\text{-K}_4$), which are significantly higher than the conduction band (CB) of TiO_2 (-4.2 eV) indicating their fast electron injection. The theoretical bandgaps obtained for $n\text{-K}_1$ and $n\text{-K}_2$ are almost the same, *i.e.* 2.84 eV ($n\text{-K}_1$) and 2.81 eV ($n\text{-K}_2$), whereas bandgaps of $n\text{-K}_3$ and $n\text{-K}_4$ are 2.78 eV and 2.75 eV, respectively, which may be due to the different anchoring ability of the molecules. Conclusively, the well-overlapped HOMO and LUMO orbitals of the dyes $n\text{-K}_1$ can guarantee a fast charge transfer between donor and acceptor units and the efficient interfacial injection of

electrons from the excited state of the dye molecule into the conduction band of the TiO₂ semiconductor.

Molecular modeling of *n*-**K**₅₋₁₁ (Series-2) and *n*-**K**₁₂₋₁₈ (Series-3)

The optimized geometries of carbazole-based dyes *n*-**K**₅₋₁₈ are given in **Figure 3.23**. The geometry of the twin carbazole unit in each dye was not precisely planar, rather slightly tilted in the middle with a butterfly shape. Therefore, the non-planar geometry of the carbazole ring can help to suppress the dye aggregation on the TiO₂ surface. The electronic density distributions in the HOMO and LUMO levels of the fourteen different D-A type dyes *n*-**K**₅₋₁₁ and *n*-**K**₁₂₋₁₈ are given in **Figures 3.23a** and **3.23b**, respectively. From the figure, it is clear that the electrons at the HOMO levels are majorly populated on the carbazole donor unit, whereas, the electron density distribution in LUMO has sizably delocalized through different acceptor units of *n*-**K**₅₋₁₈. It is worth noting that the HOMO and LUMO electron density of *n*-**K**₁₀ and *n*-**K**₁₇ is not fully localized on anchoring group, indicating poor anchoring ability of 1,3-diethyl-2-thiobarbituric acid. For all the other molecules there is a clear electron cloud movement from the donor scaffold towards anchoring unit, facilitating an efficient photoinduced interfacial electron transfer from the LUMO to the semiconductor electrode through the effective intramolecular charge separation under the light irradiation.

The theoretical HOMO energy levels obtained for dyes *n*-**K**₅₋₁₁ are -6.23 eV (*n*-**K**₅), -5.76 eV (*n*-**K**₆), -5.76 eV (*n*-**K**₇), -5.98 eV (*n*-**K**₈), -6.07 eV (*n*-**K**₉), -5.89 eV (*n*-**K**₁₀), and -6.02 eV (*n*-**K**₁₁), whereas HOMO values for dyes *n*-**K**₁₂₋₁₈ are -6.14 eV (*n*-**K**₁₂), -5.77 eV (*n*-**K**₁₃), -5.65 eV (*n*-**K**₁₄), -5.91 eV (*n*-**K**₁₅), -5.98 eV (*n*-**K**₁₆), -5.77 eV (*n*-**K**₁₇), and -5.95 eV (*n*-**K**₁₈). All the values are significantly lower than that of the redox potential of the I₃⁻/I⁻ electrolyte system (-5.2 eV) confirming the synthesized dyes can undergo a quick ground state regeneration process. The theoretical LUMO energy levels obtained for dyes *n*-**K**₅₋₁₁ are -2.70 eV (*n*-**K**₅), -2.65 eV (*n*-**K**₆), -2.62 eV (*n*-**K**₇), -2.53 eV (*n*-**K**₈), -2.73 eV (*n*-**K**₉), -2.74 eV (*n*-**K**₁₀), and -2.88 eV (*n*-**K**₁₁), whereas LUMO values for dyes *n*-**K**₁₂₋₁₈ are -2.60 eV (*n*-**K**₁₂), -2.64 eV (*n*-**K**₁₃), -2.47 eV (*n*-**K**₁₄), -2.46 eV (*n*-**K**₁₅), -2.55 eV (*n*-**K**₁₆), -2.66 eV (*n*-**K**₁₇), and -2.81 eV (*n*-**K**₁₈),

indicating their fast electron injection into the TiO₂ layer. The calculated theoretical bandgaps for dyes ***n-K***₅₋₁₁ are in between 3.11-3.52 eV, whereas for dyes ***n-K***₁₂₋₁₈ are in between 3.11-3.54 eV, respectively, which may be due to the different anchoring ability of the molecules. Conclusively, all the molecules display adequate HOMO and LUMO orbitals guarantying favorable charge separation.

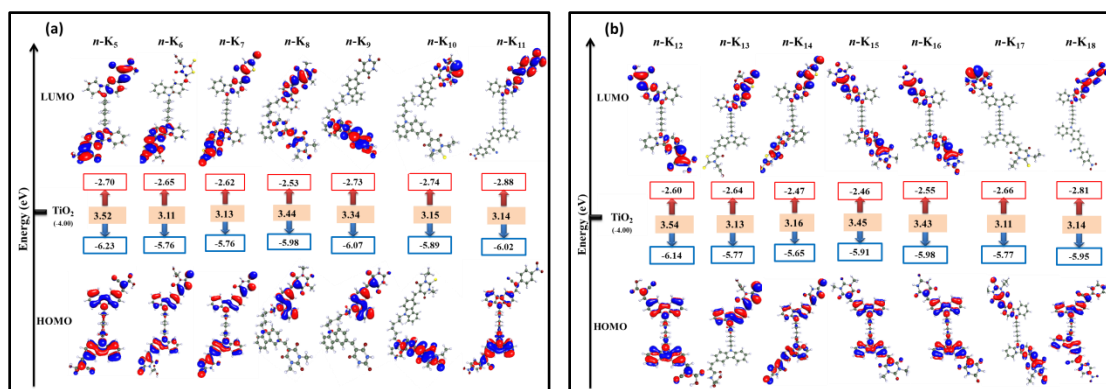


Figure 3.23 HOMO and LUMO levels of dyes (a) ***n-K***₅₋₁₁ and (b) ***n-K***₁₂₋₁₈

Molecular modeling of ***n-K***₁₉₋₂₁ (Series-4) and ***n-K***₂₂₋₂₄ (Series-5)

The electron density distributions in HOMO and LUMO energy levels of ***n-K***₁₉₋₂₁ and ***n-K***₂₂₋₂₄ were visualized using a T-mole visualizer as displayed in **Figure 3.24**. The 3-D structures indicate the effective charge separation in the ground state as well as excited states of the molecules ***n-K***₁₉₋₂₄. From the figure, it is evident that the electron density in HOMO energy levels is predominantly localized on carbazole and phenyl ring in case of all the dyes irrespective of their length of alkyl chain linker. However, there is a clear shift of electron cloud that can be observed in LUMO levels from the electron donor carbazole moiety to the electron acceptor units such as cyanoacetic acid, rhodanine-3-acetic acid, and barbituric acid to a different extent due to their varied electron accepting nature. Interestingly, the LUMO electron density of ***n-K***₁₉ and ***n-K***₂₂ is fully localized on the anchoring cyanoacetic acid (CAA) group, facilitating the electronic coupling between the electron density at its LUMO level and the *d* orbitals of the TiO₂ and hence the overlapped HOMO and LUMO levels on carbazole core guarantees a fast photo-induced electron transfer from donor to acceptor group. Analogously, the electron

density on LUMO levels of $n\text{-K}_{20-21}$ and $n\text{-K}_{23-24}$ is not fully found in the vicinity of –COOH and –NH groups of rhodanine-3-acetic acid and barbituric acid, respectively. The reason may be due to the poor electron-withdrawing capacity of acceptor units compared to that of CAA, and hence it can reduce the flow of electrons to the semiconductor surface. Further, the theoretical HOMO and LUMO energy levels along with their bandgaps for all the molecules of **Series-4** and **Series-5** are portrayed in **Figure 3.24**. From the observed data it can be concluded that all the dyes ($n\text{-K}_{19-24}$) have required HOMO and LUMO energy levels guarantying favorable charge separation.

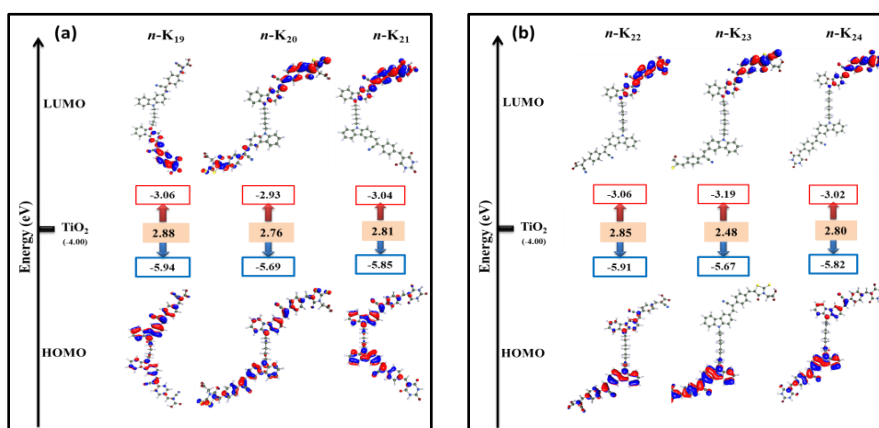


Figure 3.24 HOMO and LUMO levels of dyes (a) $n\text{-K}_{19-21}$ and (b) $n\text{-K}_{22-24}$

Molecular modeling of $n\text{-K}_{25-28}$ (**Series-6**)

The electronic cloud delocalization in FMO levels of the dyes ($n\text{-K}_{25-28}$) along with their HOMO, LUMO, and bandgap values are portrayed in **Figure 3.25**. The 3-D vision in these new A-D- π -D-A dyes represents the effectiveness of intramolecular charge separation, *i.e.* from their ground state to excited states of the molecules. As evidenced from their HOMO energy levels, the systematic electron cloud distributions occurred on donor carbazole units as well as a spacer (1,4-phenylenediacetonitrile). While in LUMO energy levels, the electron cloud has shifted more towards anchoring groups. In addition, the electron cloud was also seen on the electronegative vinylene groups linked to the spacer units.

Interestingly, the LUMO electron density in dyes $n\text{-K}_{25}$ and $n\text{-K}_{28}$ has completely localized on anchoring groups (cyanoacetic acid and rhodanine), facilitating faster photo-induced electron-transfer from donor to acceptor units. However, in dye $n\text{-K}_{26}$, the electron cloud distribution in LUMO level has predominantly concentrated on rhodanine scaffold, especially on the carbonyl as well as thiocarbonyl group resulting in the isolation of LUMO from the anchoring $-\text{COOH}$ group and hence preventing proper injection of electrons in CB of TiO_2 (Tian et al. 2008, 2007). In the case of $n\text{-K}_{27}$, the LUMO level is largely localized on the carbonyl groups of barbituric acid (Beni et al. 2015).

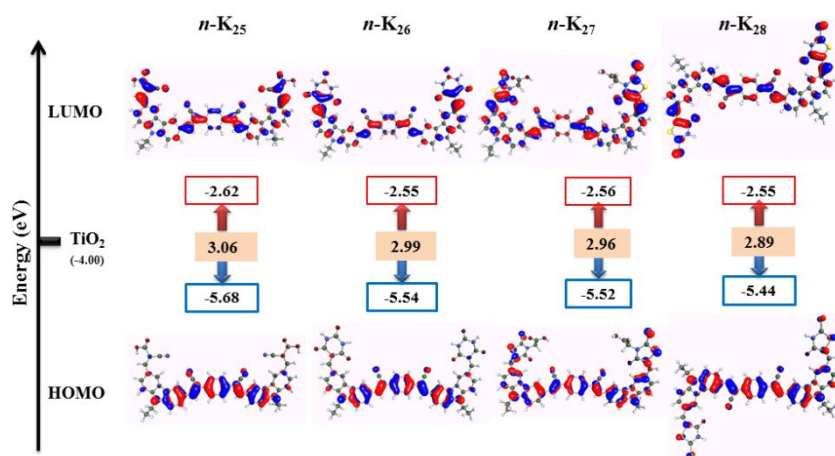


Figure 3.25 HOMO and LUMO levels of dyes $n\text{-K}_{25-28}$

Molecular modeling of $n\text{-K}_{29-31}$ (Series-7) and $n\text{-K}_{32-34}$ (Series-8)

The HOMO and LUMO energy levels of the dyes $n\text{-K}_{29-31}$ and $n\text{-K}_{32-34}$ as obtained from a T-mole visualizer are shown in **Figure 3.26a** and **3.26b**, respectively. As seen from the figure, all the molecules display effective charge separation in HOMO-LUMO energy levels. As expected, the electron cloud distribution in HOMO energy levels of dyes $n\text{-K}_{29-34}$ is predominantly localized on electron donating phenoxazine core. However, in case of LUMO levels of $n\text{-K}_{29-31}$ and $n\text{-K}_{32-34}$, the electron cloud is shifted evidently from the donor phenoxazine molecule to the spacer thiophene acetonitrile/phenylacetonitrile and the respective electron acceptor units in different extents due to their varied electron accepting nature.

As discussed earlier, the LUMO electron density of $n\text{-K}_{29}$ and $n\text{-K}_{32}$ is fully localized on anchoring CAA, facilitating the electronic coupling between the electron density at its LUMO level and the d orbitals of the TiO_2 . While in case of $n\text{-K}_{30-31}$ and $n\text{-K}_{33-34}$, the electron density distribution in LUMO level is predominantly concentrated on the rhodanine units and carbonyl groups rather than $-\text{COOH}$ and $-\text{NH}$ groups of rhodanine-3-acetic acid and barbituric acid scaffold (Beni et al. 2015). Conclusively, the effectively overlapped HOMO and LUMO levels of $n\text{-K}_{29}$ and $n\text{-K}_{32}$ guarantee a fast photo-induced electron transfer from donor phenoxazine to cyanoacetic acid unit via different spacer units. This phenomenon leads to favorable charge separation and hence, impending electron-hole recombination.

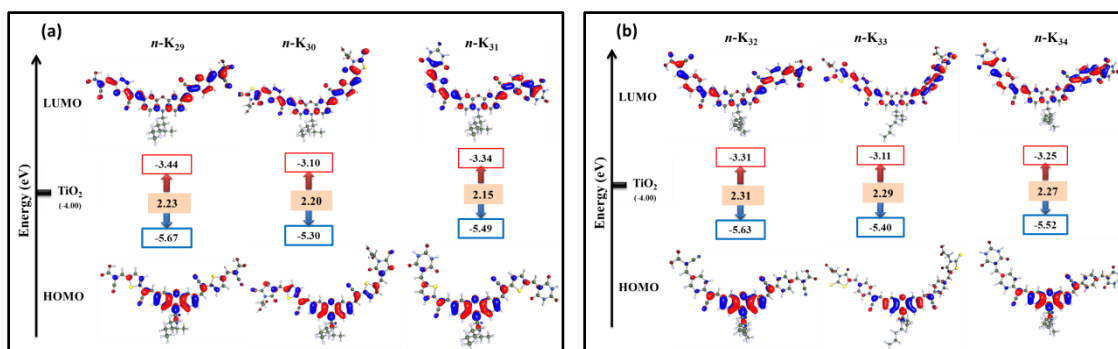


Figure 3.26 HOMO and LUMO levels of dyes (a) $n\text{-K}_{29-31}$ and (b) $n\text{-K}_{32-34}$

3.3.2.2 Theoretical studies of *p*-type organic chromophores $p\text{-K}_{35-42}$ (Series 9-10)

Figure 3.27a-b depicts the distribution of electron density in HOMO and LUMO levels of dyes $p\text{-K}_{35-40}$ (Series-9) and $p\text{-K}_{41-42}$ (Series-10), respectively. The clear charge separation from the ground state of the dye molecule to the excited state can be pictured from 3-D visualization using a T-mole visualizer. It has been well-documented that the electron-donating ability of donor moiety has a greater impact on energy levels and spatial charge distribution of the HOMOs, which further influences the interfacial charge transport. In addition, FMOs are the most widely used to demonstrate the charge transport behaviour of the molecules, as more delocalized FMOs can undergo a quicker charge transport by increasing the electron coupling between adjoining molecules and

reducing nuclear reorganization energy. As evidenced from **Figure 3.27**, the HOMO levels of dyes $p\text{-K}_{35-40}$ are delocalized mainly on donor phenoxazine core, whereas in case of dyes $p\text{-K}_{41-42}$, the electron cloud is delocalized throughout the molecule starting from carbazole to thiophene spacer unit. While in LUMO levels of both the series, the electron density has shifted more towards electron-withdrawing moieties to a different extent based on their electron-accepting nature. The obtained results clearly reveal that the LUMO electron density of all the molecules fully localized on electron-withdrawing moieties, consequently, the holes generated in the donor unit (phenoxazine/carbazole) can be efficiently injected into the VB of the NiO through anchoring carboxylic acid group. Although it is difficult to obtain accurate FMO energies by DFT studies, the changing tendencies between theoretical and experimentally obtained energy values are consistent. Conclusively, all the molecules display adequate HOMO and LUMO orbitals ensuring favorable charge separation.

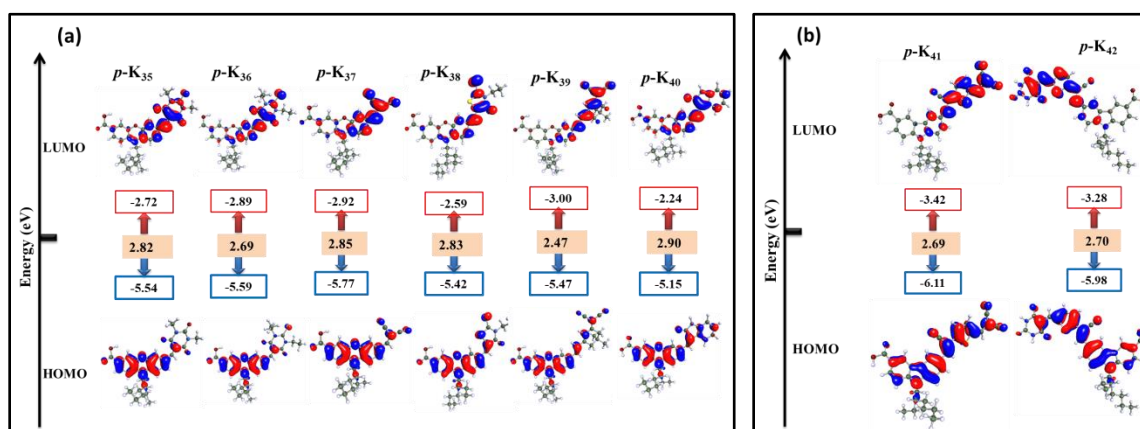


Figure 3.27 HOMO and LUMO levels of dyes (a) $p\text{-K}_{35-40}$ and (b) $p\text{-K}_{41-42}$

3.3.2.3 Theoretical studies of organic HTMs $h\text{-K}_{43-44}$ (Series-11)

The obtained electronic cloud distributions in the frontier molecular orbitals (FMOs) levels of $h\text{-K}_{43-44}$ are shown in **Figure 3.28**. As seen in the figure, in case of HOMO levels, the total electron densities of $h\text{-K}_{43-44}$ are primarily distributed with the donor skeleton, which clearly indicates the electron-donating ability of 9-(2-ethylhexyl)-9*H*-carbazole. In addition to this, the electron density is also slightly distributed over

pendant groups, *i.e.* methoxyphenyl groups. Nevertheless, the electron density distribution in LUMO is mainly localized over electron-withdrawing cyanovinylene moiety. Interestingly, the complete shift of electron density towards the electron-withdrawing cyanovinylene group has been observed in the LUMO level. The major difference between ***h-K*₄₃** and ***h-K*₄₄** lies in their substituent groups, as the former one has an additional methoxy group suggesting a stronger electron-donating capability. Besides, ***h-K*₄₃** has higher HOMO energy as compare to ***h-K*₄₄** due to the existence of additional electron-pushing methoxy functionality. In PSCs, the occurrence of appropriate energy levels between the perovskite and the HTM is absolutely necessary for facilitating effective interfacial charge separation and thereby maximizing the open-circuit voltage (V_{OC}) of the devices. A deeper HOMO level of the molecules usually indicates the larger V_{OC} , since the voltage value is dependent on the difference between HOMO levels of the HTM and the quasi-Fermi level of the TiO₂ semiconductor. The theoretical HOMO energy levels obtained for ***h-K*₄₃₋₄₄** are -5.48 and -5.33 eV, respectively confirming these compounds can undergo a quick ground state regeneration process.

Generally, for promising HTMs, the value of the LUMO levels must be greater than the conduction band of the perovskite (-3.93 eV for CH₃NH₃PbI₃) in order to block the recombination of electrons and holes between the perovskite absorber and the metal electrode (Becke et al. 1993). The theoretical LUMO energy levels obtained for ***h-K*₄₃₋₄₄** are -2.01 and -1.92 eV, respectively, demonstrating their fast electron injection ability. When compared to the conduction edge of the most commonly used perovskite CH₃NH₃PbI₃, the LUMOs of ***h-K*₄₃₋₄₄** give rise to a large energy barrier of 1.92 - 2.01 eV, indicating that the unwanted electron-hole recombination process could be effectively prohibited. From the results, it is clear that both the molecules possess a capability of photo-induced electron transfer from the HOMO-LUMO excitations. The theoretical bandgaps obtained for ***h-K*₄₃₋₄₄** are 3.464 and 3.408 eV, respectively, which may be accredited to the different donating abilities in the molecules.

From the energy level alignments and the frontier orbital distribution, it can be emphasize that the carbazole donor with a branched alkyl chain has been thoughtfully

tailored as the side arms of the molecules. Conclusively, the FMO levels of the $h\text{-K}_{43-44}$ can promise a faster charge-transport between the electron-donor and acceptor units and the well-organized interfacial injection of electrons from the excited level of the HTM into the conduction band (CB) of the semiconductor. Further, the electron distribution pattern in the FMO levels clearly indicates that the molecules $h\text{-K}_{43-44}$ possess good hole-transporting properties, and hence they may turn out to be promising candidates of HTMs.

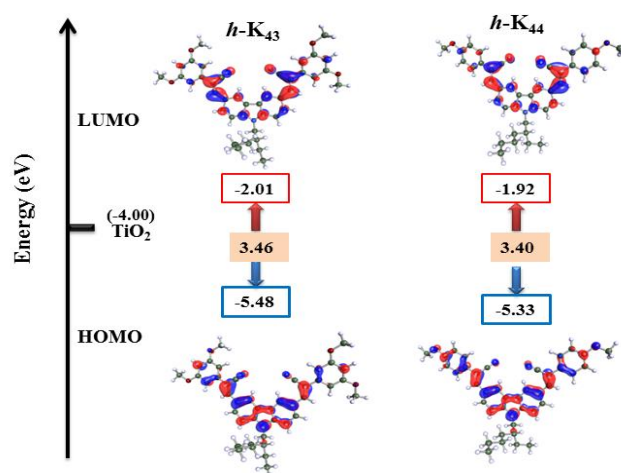


Figure 3.28 HOMO and LUMO levels of dyes $h\text{-K}_{43-44}$

3.3.3 TD-DFT simulations

In order to gain insights into the excitation properties as well as electronic transition, the light absorption properties of n -type chromophores ($n\text{-K}_{1-34}$), p -type chromophores ($p\text{-K}_{35-42}$), and HTMs ($h\text{-K}_{43-44}$) were explored using Time-Dependent Density Functional Theory (TD-DFT) in the presence of time-dependent perturbations. According to adiabatic approximation, TD-DFT temporal nonlocality is neglected, which postulates at any point of time, the exchange-correlation (xc) factor depends exclusively on instantaneous density. Consequently, it can be utilized to the xc functional derived for ground-state DFT, *i.e.* BP (Beck-Perdew) and hybrid functional (B3LYP). In TD-DFT calculations, the basis set used for the calculations generally decides the accuracy of

assimilated results. However, the results of four selected molecules, *n-K*₁₀, *n-K*₂₀, *n-K*₃₀, and *p-K*₄₀ have been discussed as below.

Figure 3.29 depicts the simulated absorption spectrum of dyes *n-K*₁₀, *n-K*₂₀, *n-K*₃₀, and *p-K*₄₀. The simulated data are well in accordance with the experimentally obtained spectra of all the dyes. Further, **Figure 3.30** displays the simulated IR spectrum of *n-K*₁₀, *n-K*₂₀, *n-K*₃₀, and *p-K*₄₀ estimated using TD-DFT calculations with the same conditions as above. The obtained simulated IR spectra are in accordance with the experimentally obtained results. These precise and reliable predictions made by TD-DFT studies indicate that the functional and basis set chosen for TD-DFT calculations are quite appropriate.

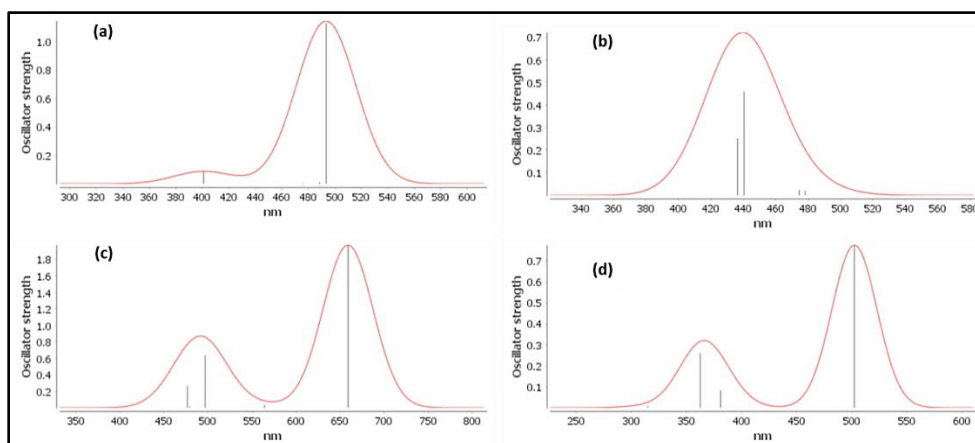


Figure 3.29 Simulated absorption spectra of (a) *n-K*₁₀, (b) *n-K*₂₀, (c) *n-K*₃₀ and (d) *p-K*₄₀

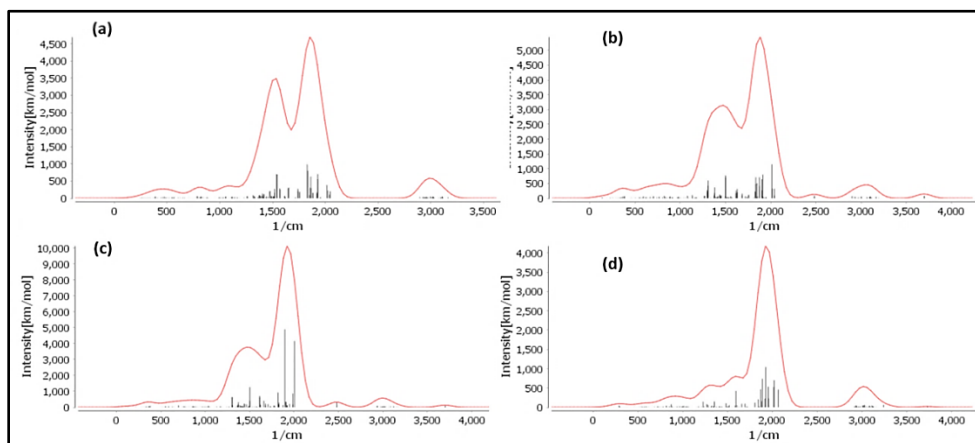


Figure 3.30 Simulated IR spectra of (a) *n-K*₁₀, (b) *n-K*₂₀, (c) *n-K*₃₀ and (d) *p-K*₄₀

3.4 CONCLUSIONS

In summary, all the synthesized target molecules, *i.e.* *n*-type (***n*-K₁₋₃₄**), *p*-type (***p*-K₃₅₋₄₂**) organic chromophores, and organic HTMs (***h*-K₄₃₋₄₄**) were subjected to photophysical, electrochemical, and theoretical studies. Their photophysical characterization reveals that all the molecules display strong absorption in the range of 350-580 nm and emission in the range of 457-660 nm. In addition, the calculated bandgaps are within the range 2.03-2.90 eV, whereas Stoke shifts are in the range of 1965-8690 cm⁻¹. Further, their CV study confirms that the synthesized molecules facilitate the affirmative transition of charges throughout the photo-electronic conversion cycle and thus, they can be used as possible *n*-/*p*-type sensitizers for DSSCs and HTMs for PSCs. Furthermore, from DFT simulations studies, it is evident that all the molecules possess proper charge separation in their FMO levels which is essential for proper charge injection. Finally, electronic excitation data simulated using TD-DFT, were in good agreement with the experimentally obtained results of the molecules, indicating that the exchange-correlation functional and basis set utilized for predicting the spectra of the sensitizers as well as HTMs are quite appropriate for the calculations.

Based on the results of photophysical, electrochemical, and theoretical studies, the devices of selected three series (***n*-K₁₋₄**, ***n*-K₅₋₁₁**, and ***n*-K₁₂₋₁₈**) were fabricated employing them as *n*-type sensitizers. In continuation, the co-sensitization behaviour of ***n*-K₁₋₁₈** carrying thiophene, and carbazole scaffolds was studied using DSSCs sensitized with Ru-based **MH-12/HD-2** dyes in presence of chenodeoxycholic acid (CDCA) as a co-adsorbent. Further, the DSSCs sensitized with *p*-type dyes (***p*-K₃₅₋₄₂**) were fabricated and the PSCs employing ***h*-K₄₃₋₄₄** as HTMs were constructed to generate photoelectrochemical data. In the next chapter, a detailed device fabrication has been discussed.

CHAPTER-4
PHOTOVOLTAIC INVESTIGATIONS

PHOTOVOLTAIC INVESTIGATIONS

Abstract

*This chapter deals with the device fabrication studies of selected three series of newly synthesized n -type dyes (n -**K**₁₋₁₈), p -type dyes (p -**K**₃₅₋₄₂), and h -**K**₄₃₋₄₄ as sensitizers/HTMs for DSSC/PSC applications. Also, it covers a detailed investigation of eighteen n -type dyes n -**K**₁₋₁₈ as co-sensitizers in Ru (II) sensitized DSSCs. Further, it includes an in-depth discussion on structure-device performance relationship of the tested dyes/HTMs.*

4.1 PHOTOVOLTAIC STUDIES

The strategic photovoltaic investigations include the fabrication of n -/ p -type dye-sensitized solar cells as well as perovskite solar cells using newly synthesized sensitizers/co-sensitizers/HTMs and determination of photovoltaic parameters of the new devices. Further, it also deals with the correlation studies between their structure and device performance parameters.

4.1.1 Introduction

A photovoltaic (PV) cell is an electrical device, which converts incident photons to electrical energy. Generation of electrical power under illumination is achieved by the capability of the photovoltaic device to produce voltage over an external load and current through the load at the same time. This is characterized by the current-voltage (J - V) curve of the cell at certain illumination and temperature. When the cell is short-circuited under illumination, the maximum current, the short-circuit current (J_{SC}) is generated, while under open-circuit conditions no current can flow and the voltage is at its maximum, called the open-circuit voltage (V_{OC}). Another important parameter that determines the performance of the device is the fill factor (FF).

In the present work, the selected three series of n -type dyes (n -**K**_{1,4}, n -**K**₅₋₁₁, n -**K**₁₂₋₁₈) were employed as sensitizers in DSSCs, also they were used as co-sensitizers in DSSCs sensitized with standard Ru-based **MH-12/HD-2** dyes in presence of

chenodeoxycholic acid (CDCA) as a co-adsorbent. Further, all the synthesized *p*-type dyes (***p*-K₃₅₋₄₂**) were used as sensitizers in DSSCs and the molecules ***h*-K₄₃₋₄₄** were employed as hole-transport materials in perovskite solar cells. A detailed procedure for DSSC/PSC fabrication as well as a discussion on obtained results is described in the following sections.

4.1.2 Material and methods

The *J-V* (Current-Voltage) characteristics of fabricated *n*-type devices were measured using Oriel SOL3A solar simulator connected to Keithley 2400 source meter. Further, *IPCE* (Incident photon conversion efficiency) spectra of all the fabricated DSSCs were recorded using the QEX10 PV measurement system. Calibration of incident light was performed before measurements using a silicon photodiode (IF035, PV Measurements). All the measurements were carried out without the use of anti-reflecting film.

For *p*-type device fabrication studies, conductive glass substrates (F-doped SnO₂) were purchased from Solaronix (TEC15, sheet resistance 15 Ω/square). A set-up comprising Oriel solar simulator (AM 1.5G, 100 mW/cm²) calibrated with a silicon cell covered with a KG5 filter and attached to Keithley 2400 digital source meter was used for measuring photovoltaic parameters. *IPCE* experiments were carried out for the fabricated devices using ZAHNER's CIMPS-QE/IPCE system.

The photocurrent density- voltage curves (*J-V* characteristics) of the fabricated devices of PSCs were obtained using a Keithley 2400 digital source meter controlled by a computer and a standard AM 1.5 solar simulator. The intensity of the light was calibrated using Oriel reference solar cell. To prevent the inflated photocurrents receiving from stray lights, a black metal mask (active area 0.045 cm²) was placed on the fabricated cell during all the measurements. Further, *IPCE* experiments were performed using the QEX10 PV measurement system.

4.1.3 Experimental

As per the procedure described in the reported literature (El-Shafei et al. 2012 Cheema et al. 2014), DSSCs were fabricated using synthesized *n*-type dyes ***n*-K₁₋₁₈** as sensitizers as well as co-sensitizers. Further, the DSSCs sensitized with *p*-type dyes

(*p-K*₃₅₋₄₂) and the PSCs with the HTMs (*h-K*₄₃₋₄₄) were fabricated according to the standard procedure reported (Ameline et al. 2015, Warnan et al. 2014 and Yin et al. 2017).

4.1.3.1 Fabrication of *n*-type DSSCs sensitized with dyes *n-K*₁₋₁₈

The device fabrication procedure followed for fabrication of *n*-type DSSCs is as follows: The etched fluorine-doped tin oxide (FTO) coated glasses (thickness of 2.2 mm, sheet resistance 8 Ω/cm^2 , TEC, Pilkington) substrates were cleaned with detergent, distilled water, acetone, and ethanol, sequentially. Further, the washed substrates were immersed in a 40 mM aqueous TiCl_4 solution (Wako pure chemical industries, Ltd.) at 70 °C for 30 minutes, flowed by rinsing with water and ethanol. Using a screen-printer, a thin layer with a thickness of around 8-10 μm TiO_2 paste (Solaronix, Ti-Nanoxide D/SP) was coated using a squeegee printing setup. The active area of the substrates is 0.18 cm^2 . The printed substrates were dried at 350 °C for 10 min followed by annealing at 500 °C for 30 minutes, which generally serves as a seed layer. Further, after drying the electrodes, scattering layer (5 μm thick) TiO_2 particles were reprinted onto the already deposited TiO_2 layer and annealed at 350 °C for 10 min followed by heating at 500 °C for 30 minutes. After cooling it to room temperature, TiO_2 electrodes were immersed in 40 mM aqueous TiCl_4 solution at 70 °C for 30 minutes and rinsed with water and ethanol in order to fill up the defective “pin-holes” present in the TiO_2 layer. The electrodes were preheated at 500 °C for 30 minutes and left to cool to 80 °C before dipping into the dye solution. The required dye solutions (0.2 mM) were prepared in 10 mL by dissolving dyes in a mixture of 1:1:1 acetonitrile, *tert*-butanol, and dimethyl sulfoxide (DMSO) solvents. Chenodeoxycholic acid (CDCA) was added to a concentration of 20 mM. The hot electrodes were immersed in dye solutions and kept at room temperature for 20 hours for better adsorption onto the TiO_2 surface.

To prepare the counter electrode, pre-cut transparent conductive oxide (TCO) glasses were taken, washed with distilled water followed by 0.1 M HCl solution in ethanol, subsequently sonication in an acetone bath for 10-15 minutes. The cleaned TCO were then dried at 400 °C for 15 minutes. A thin layer of Pt-paste (Solaronix, Plastisol T/SP) on TCO was printed uniformly and then electrodes were annealed at

450 °C for 10 minutes. The dye-sensitized TiO₂ electrodes were sandwiched with Pt counter electrodes and liquid electrolyte (Solaronix, Iodolyte HI-30) was then injected into the cell, while the two electrodes were held together with the clips. The *J-V* measurements were performed by using a black metal mask with an aperture active area of 0.18 cm² to avoid current overestimation due to its multiple irradiations.

4.1.3.2 Fabrication of *n*-type DSSCs co-sensitized with dyes *n-K₁₋₁₈*

The procedure for fabrication of DSSCs co-sensitized with *n-K₁₋₁₈* is as follows: Fluorine-doped tin oxide (FTO) coated glasses (thickness 2.2 mm, sheet resistance 8 Ω/cm², TEC, Pilkington) were washed gently using detergent, distilled water, acetone, and ethanol, respectively. After that, the cleaned FTO glasses were immersed into a 40 mM aqueous TiCl₄ solution (Wako pure chemical industries, Ltd.) at 70 °C for 30 minutes, followed by rinsing with water and ethanol. Using a screen-printer, a thin layer with a thickness of around 8-10 μm TiO₂ paste (Solaronix, Ti-Nanoxide D/SP) was coated on substrates. The substrates were further annealed at 350 °C for 10 minutes and 500 °C for 30 minutes in order to form a seed layer. On top of this layer, the TiO₂ layer (5 μm thick) was reprinted and annealed at 350 °C for 10 minutes followed by 500 °C for 30 minutes. Further, cooled TiO₂ electrodes were treated with 40 mM aqueous TiCl₄ solution at 70 °C for 30 minutes followed by rinsing with water and ethanol, which fills the defective “pin-holes” present in the TiO₂ layer. Later, the electrodes were preheated at 500 °C for 30 min. The dye solutions (0.2 mM) were prepared in 10 mL by dissolving a combination of dyes (Ru-based and metal-free chromophores) in a mixture of 1:1:1 acetonitrile, *tert*-butanol, and dimethyl sulfoxide (DMSO) solvents. To this mixture, 20 mM chenodeoxycholic acid (CDCA) was added. The hot electrodes were immersed in dye solutions and kept at room temperature for 20 hours in dark for better adsorption of dye onto the TiO₂ surface.

To prepare the counter electrode, the pre-cut TCO glasses were washed with detergents, distilled water, and 0.1 M HCl solution in ethanol, followed by sonication in acetone for 15-20 minutes. These cleaned TCO substrates were dried by annealing at 400 °C for 15 minutes. Further, a thin layer of Pt-paste (Solaronix, Plastisol T/SP) on TCO was printed uniformly on the substrates and annealed at 450 °C for 10 minutes. The dye-sensitized TiO₂ electrodes were sandwiched with Pt counter

electrodes and liquid electrolyte (Solaronix, Iodolyte HI-30) was then injected into the cell, while the two electrodes were held together with the clips. The J - V measurements were performed by using a black metal mask with an aperture active area of 0.18 cm^2 to avoid current overestimation due to its multiple irradiations.

4.1.3.3 Fabrication of p -type DSSCs sensitized with dyes p -K₃₅₋₄₂

The procedure used for fabrication of NiO-based p -type DSSCs is as follows. The FTO coated glass substrates were successively cleaned by sonication in detergent and acidified ethanol for 10 min before annealing at $450 \text{ }^\circ\text{C}$ for 30 min. A NiO dense layer was prepared by spin-coating onto the clean substrates of a 0.5 M nickel acetate solution containing 0.5 M ethanolamine in methoxyethanol at 3000 rpm for 30 s followed by thermal treatment at $500 \text{ }^\circ\text{C}$ for 0.5 hr . Then, NiO paste was screen printed on top of FTO substrates containing NiO dense layer ($30 \pm 5 \text{ nm}$). Here, the NiO screen-printing paste was produced by preparing a slurry of 3 g of NiO nanopowder (Inframat) suspended in 10 mL of freshly distilled ethanol and ball-milled (500 rpm) for 24 h . Further, the slurry was mixed with 10 mL of $10 \text{ wt } \%$ ethanolic ethyl cellulose (Sigma Aldrich) solution and 20 mL terpineol. The solvent was removed using a rotary evaporator. The NiO films were annealed at 450°C for 30 min and thickness was found to be $3.5 \mu\text{m} \pm 50 \text{ nm}$. In continuation, the NiO electrodes were soaked in a solution of nickel acetate in ethanol (20 mM) with 1% ethanolamine for 30 min at $60 \text{ }^\circ\text{C}$ followed by ethanol rinsing and drying in air. The electrodes NiO were finally annealed at $120 \text{ }^\circ\text{C}$ for 60 min , then were dipped in a solution of the dye (0.3 mmol L^{-1} in CH_3CN) and stored at room temperature overnight.

Platinum counter electrodes were prepared by depositing a few drops of an isopropanol solution of hexachloroplatinic acid in distilled isopropanol (2 mg per mL) on FTO plates (TEC7, Solaronix). Substrates were then fired at $375 \text{ }^\circ\text{C}$ for 30 min . The photocathode and the counter electrode were placed on top of each other and sealed using a thin transparent film of Surlyn polymer (DuPont, $25 \mu\text{m}$) as a spacer. A drop of the electrolyte was introduced through a predrilled hole in the counter electrode by vacuum backfilling, the hole was then sealed by a glass stopper with Surlyn. The cell had an active area of 0.25 cm^2 . The electrolyte used is composed of 0.1 M I_2 and 1 M lithium iodide in acetonitrile.

4.1.3.4 Fabrication of perovskite solar cells using HTMs *h-K*₄₃₋₄₄

To begin with, FTO glasses were cleaned thoroughly in a solution of soap, deionized water, acetone, and ethanol, sequentially. After completion of the cleaning process, FTO substrates were sonicated in a water bath for 30 minutes and UV-ozone treatment was done in a UVO cleaner for 30 minutes. About 40-50 nm thickness compact TiO₂ layer on substrates was obtained by the spin-coating process, which was subsequently sintered at 500 °C for 30 minutes. The mesoporous TiO₂ films were spin-coated (4000 rpm) on the top of the compact TiO₂ layer and sintered at 450 °C for 30 minutes. The CH₃NH₃PbI₃ (MAPbI₃) perovskite solution was obtained in one step by dissolving 0.1 mmol of CH₃NH₃I and 0.1 mmol of PbI₂ in 2.8 mL of DMF and the solution was heated at 70 °C for 6 h under N₂ atmosphere. The prepared MAPbI₃ precursor solution was deposited on a substrate film by spin-coating at 3000 rpm for 30 s, and dried on a hot plate at 100 °C for 15 min. Further, the solution of HTMs (48 mM in chlorobenzene) was spin-coated on top of MAPbI₃/TiO₂/FTO substrates at 2000 rpm. Finally, Au coating was made by thermally evaporating Au under vacuum. The *J-V* measurements of PSCs were performed with a black metal mask with an active area of 0.045 cm² to resist current overestimation due to the multiple irradiations.

4.1.4 Results and discussion

The photovoltaic performance data of DSSCs/PSCs are summarized in **Tables 4.1-4.4** and pertaining discussion are elaborated in the following section.

4.1.4.1 Photovoltaic performance of devices sensitized/co-sensitized with *n*-type dyes (*n-K*₁₋₁₈)

The results of photoelectrochemical experiments with regard to both sensitization and co-sensitization studies of the new dyes have been deliberated series-wise as follows.

4.1.4.1.1 Photovoltaic performance of **Series-1** sensitizers/co-sensitizers (*n-K*₁₋₄)

*DSSCs sensitized with n-K*₁₋₄

The photocurrent density-voltage (*J-V*) characteristics curves of the DSSCs fabricated with *n-K*₁₋₄ sensitizers and a liquid electrolyte in acetonitrile under AM 1.5 light illumination (100 mW·cm⁻²) are manifested in **Figure 4.1a** and the relevant

device performance data are tabulated in **Table 4.1**. All the devices were fabricated and characterized under similar conditions in order to get accurate and reliable comparisons. The overall *PCE* of the sensitizer's **n-K₁₋₄** was derived by means of equation (4.1).

$$PCE (\eta) = \frac{J_{SC} \times V_{OC} \times FF}{P_{in}} \quad (4.1)$$

where P_{in} is the power of incident light, J_{SC} is short-circuit current density, V_{OC} is the open-circuit voltage and FF is the fill factor. It is apparent that the device fabricated using dye **n-K₂** as photosensitizer displays the uppermost *PCE* of 1.19 % ($J_{SC} = 3.64$ mA·cm⁻², $V_{OC} = 0.51$ V, and $FF = 64.49\%$) among the other devices based on **n-K₁** ($J_{SC} = 2.25$ mA·cm⁻², $V_{OC} = 0.47$ V, $FF = 50.09$ % and $\eta = 0.54$ %), **n-K₃** ($J_{SC} = 0.64$ mA·cm⁻², $V_{OC} = 0.45$ V, $FF = 74.33$ % and $\eta = 0.22$ %), and **n-K₄** ($J_{SC} = 0.66$ mA·cm⁻², $V_{OC} = 0.47$ V, $FF = 74.63$ % and $\eta = 0.24$ %). The higher *PCE* of **n-K₂**-based device can be assigned to significant electron extraction from electron-rich donor moiety followed by electron injection into CB of TiO₂ by a strong cyanoacetic acid anchoring group of the sensitizer. Besides, the presence of long alkoxy chains significantly reduces the extent of hydration on the TiO₂ surface. Remarkably, **n-K₂** shows the highest J_{SC} among all, which can be attributed to the enhanced charge collection at the adjacent contacts and the favorable negative free energy of electron injection (ΔG_{inj}) from the sensitizers to the CB edge of TiO₂ as explained earlier (**Table 3.2**). The lower J_{SC} of **n-K₁**, **n-K₃**, and **n-K₄** may be ascribed to poor adsorption of dyes on the TiO₂ surface, causing the low light-harvesting capacity of the cell. Indeed, the presence of long alkoxy chains in the structure can retard the recombination dynamics, resulting in a significant increase in the V_{OC} value and overall device performance. The enhanced V_{OC} of **n-K₂** is mostly due to the relative minimization of interfacial electron recombination losses. From the results, it is evident that all the dyes exhibit FF in the range of 50-75 %. The substantial reduction of FF in the case of **n-K₁₋₂** could be attributed to the minor interfacial charge recombination, which may be resulted from the relatively higher series and lower shunt resistance.

In general, the various above-said photovoltaic parameters significantly depend on the interfacial charge recombination, and carrier transport processes,

electron lifetime in the CB of semiconductor TiO_2 (τ_{eff}), and *IPCE* of the fabricated DSSCs. The origin of the change in photocurrent density was investigated by measuring the *IPCE* spectra of the fabricated devices using a QEX10 spectral response measurement system. **Figure 4.1b** displays the *IPCE* spectra of DSSCs fabricated using $n\text{-K}_{1-4}$ dyes. The *IPCE* values are calculated using equation (4.2).

$$IPCE = LHE \times \phi_{inj} \times \phi_{reg} \times \eta_{cc} \quad (4.2)$$

where LHE corresponds to light-harvesting efficiency of the DSSC and is given by $LHE = 1 - 10^{-A}$, A is the absorbance of photoanode which is same as oscillator strength, Φ_{inj} , Φ_{reg} , and η_{cc} are the electron injection, regeneration, and charge collection efficiencies, respectively. From **Figure 4.1b**, it can be noted that the *IPCE* maxima of dye $n\text{-K}_1$ was found to be 41 % (310-471 nm), $n\text{-K}_2$ was 34 % (300-450 nm), $n\text{-K}_3$ was 47 % (300-405 nm), and $n\text{-K}_4$ was 37 % (300-410 nm). Among all the dyes, the dye $n\text{-K}_2$ exhibits the higher *IPCE*, which may be due to the good adsorption capacity of the dye onto the TiO_2 surface through a strong cyanoacetic acid acceptor, which in turn directly influences the electron injection. Also, the increased *IPCE* nature of $n\text{-K}_2$ in a longer wavelength region can be correlated to its better current density value. Nevertheless, $n\text{-K}_{3,4}$ exhibit relatively lower *IPCE* values compared to $n\text{-K}_{1,2}$, which can be attributed to the insufficient adsorption of the dye on the TiO_2 surface due to its weak anchoring nature of barbituric acid. Further, we infer that the hydrophobic bisdodecyloxy chains of $n\text{-K}_2$ are capable of furnishing enhanced spatial separation between electrons and holes, resulting in retardation of electron recombination kinetics and thereby increasing the device performance.

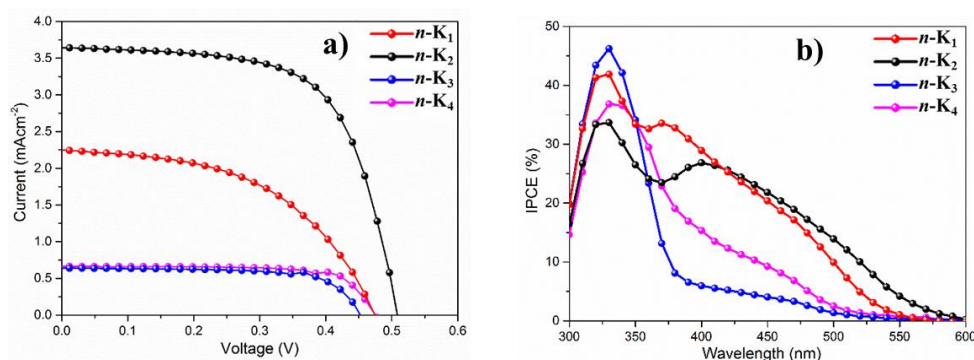


Figure 4.1 (a) Current density-voltage plots; (b) *IPCE* spectra of DSSCs sensitized with dyes $n\text{-K}_{1-4}$ under illumination of simulated solar light (AM 1.5G, 100 mW/cm^2)

DSSCs co-sensitized using $n\text{-K}_{1-4}$ along with Ru-based MH-12 dye

The photocurrent-voltage curves of DSSCs fabricated using $n\text{-K}_{1-4}$ dyes as co-sensitizers along with a Ruthenium-based dye **MH-12** are manifested in **Figure 4.2a** and the corresponding photovoltaic parameters are listed in **Table 4.2**. Interestingly, the co-sensitizer $n\text{-K}_3$ (*i.e.* $n\text{-K}_3+\text{MH-12}$) shows a higher *PCE* of 8.79% ($J_{SC} = 21.69 \text{ mA}\cdot\text{cm}^{-2}$, $V_{OC} = 0.632 \text{ V}$, and $FF = 64.27 \%$) than **MH-12** dye alone ($\eta = 8.18 \%$, $J_{SC} = 20.26 \text{ mA}\cdot\text{cm}^{-2}$, $V_{OC} = 0.644 \text{ V}$, and $FF = 59.10 \%$). Nevertheless, the dye $n\text{-K}_1$ (*i.e.* $n\text{-K}_1+\text{MH-12}$) exhibits *PCE* of 8.01 % ($J_{SC} = 20.64 \text{ mA}\cdot\text{cm}^{-2}$, $V_{OC} = 0.613 \text{ V}$, and $FF = 63.21 \%$), $n\text{-K}_2$ (*i.e.* $n\text{-K}_2+\text{MH-12}$) shows *PCE* of 6.80 % ($J_{SC} = 16.67 \text{ mA}\cdot\text{cm}^{-2}$, $V_{OC} = 0.616 \text{ V}$, and $FF = 66.21 \%$), and $n\text{-K}_4$ (*i.e.* $n\text{-K}_4+\text{MH-12}$) displays *PCE* of 8.17 % ($J_{SC} = 20.07 \text{ mA}\cdot\text{cm}^{-2}$, $V_{OC} = 0.629 \text{ V}$, and $FF = 64.25 \%$). It is worth to note that the device co-sensitized using $n\text{-K}_3$ shows an excellent performance with more than ~7% increment than that of **MH-12** sensitized device (8.18%). This may be attributed to the fact that the recombination of photo injected electrons is significantly hindered by the hydrophilic dodecyloxy alkyl chain barrier of $n\text{-K}_3$. Generally, the bulky molecules of **MH-12** dye inadequately adsorb on the surface of semiconducting metal oxide leaving behind the larger voids between adsorbed molecules. These created voids would now be covered uniformly by the small molecules of co-sensitizer, providing a larger surface area for light harvesting. Further, the uniform dye adsorption on the TiO_2 surface drastically reduces dye aggregation of **MH-12** as well as back-reaction of the I_3^-/I^- on the TiO_2 surface inside the device.

The enhanced J_{SC} and FF values of $n\text{-K}_3$ may be attributed to its strong intermolecular interactions causing efficient electron injection and charge transport towards the electrodes. Contrarily, the minor reduction in the V_{OC} compared to control can be attributed to the lowering of the TiO_2 Fermi level. Further, the poor device performance in case of $n\text{-K}_2$ as well as $n\text{-K}_4$ is ascribed to reduced electron injection which is because of inhomogeneous dye loading on the TiO_2 surface that is caused by the folding of long bisdodecyloxy chains. Also, in $n\text{-K}_4$, alkoxy chains failed to orient perpendicularly onto the TiO_2 surface in the voids created by **MH-12**, and thereby providing a reduced surface coverage on the TiO_2 surface.

The incident monochromatic photon-to-current conversion efficiencies (*IPCE*, 0-100%) of the fabricated DSSCs using $n\text{-K}_{1-4}$ dyes as co-sensitizers along with reference dye **MH-12** are shown in **Figure 4.2b**. The results obtained from *IPCE* spectra are in agreement with current-voltage measurements. The spectrum of the device with $n\text{-K}_3$ +**MH-12** shows the most intense external quantum efficiency in a broad spectrum of 300-800 nm with a maximum value of 55.4 % at 421 nm when compared to the reference dye **MH-12** (46 % at 442 nm). Similarly, the *IPCE* maximum of $n\text{-K}_1$ is 47 % at 428 nm, $n\text{-K}_2$ is 36 % at 419 nm and $n\text{-K}_4$ is 51 % at 420 nm. Among the dyes, $n\text{-K}_2$ exhibits the least *IPCE* and *PCE* values. The possible reasons for this are an increased spatial separation of dye LUMO level occupied in the excited state from the TiO_2 surface as well as the poor orientation of $n\text{-K}_2$ in between bulky **MH-12** dye molecules adsorbed onto the TiO_2 surface. Interestingly, $n\text{-K}_3$ with mono dodecyloxy chain has superior anchoring onto the TiO_2 surface compared to **MH-12**, which may be due to the greater flexibility in binding orientation. Such kind of reorientation effect caused by $n\text{-K}_3$ and wrapping the Ru-centre of **MH-12** with aliphatic long-chain could account for the enhancement in the irradiative process as well as retardation of recombination reaction.

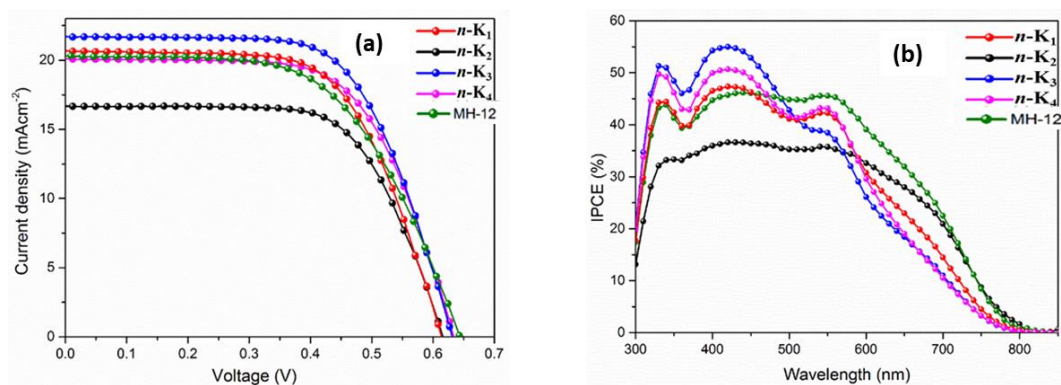


Figure 4.2 (a) Current density-voltage plots; (b) *IPCE* spectra of DSSCs fabricated using $n\text{-K}_{5-11}$ as co-sensitizers along with a Ruthenium-based dye **HD-2** under illumination of simulated solar light (AM 1.5G, 100 mW/cm²)

4.1.4.1.2 Photovoltaic performance of **Series-2** sensitizers/co-sensitizers ($n\text{-K}_{5-11}$)

DSSCs sensitized with $n\text{-K}_{5-11}$

In order to establish the structure-performance relationship for synthesized dyes ($n\text{-K}_{5-11}$), DSSCs using them as sensitizers were fabricated as per the standard protocol mentioned above. In the experiment, dye solutions were prepared in a

particular concentration and directly used for device fabrication studies. **Figure 4.3a** shows J - V curves of sensitizer's n -**K**_{5,11} based DSSCs under AM 1.5G simulated sunlight with a light intensity of 100mW/cm². The observed photovoltaic parameters, viz. open-circuit photovoltage (V_{OC}), short-circuit photocurrent density (J_{SC}), fill factor (FF), and overall solar light to electricity conversion efficiency (η) are summarized in **Table 4.1**. The results indicate that the DSSC devices fabricated with the sensitizers n -**K**_{5,6} show the maximum PCE with the highest J_{SC} and V_{OC} values compared to the dyes n -**K**_{7,11}. The higher PCE of n -**K**_{5,6} can be assigned to significant electron extraction from electron-rich donor moiety followed by electron injection into CB of TiO₂ by a strong cyanoacetic acid and rhodanine acetic acid anchoring groups. Besides, the presence of long alkoxy chains significantly reduces the extent of hydration on the TiO₂ surface. Remarkably, the dye n -**K**₅ shows the highest J_{SC} among all, which can be attributed to the enhanced charge collection at the adjacent contacts and the favorable negative free energy of electron injection (ΔG_{inj}) from the sensitizer to the CB edge of TiO₂ as explained earlier (**Table 3.2**). The lower J_{SC} of n -**K**_{7,11} may be ascribed to poor adsorption of dyes on the TiO₂ surface, causing the low light-harvesting capacity of the cell. The enhanced V_{OC} of n -**K**₅ is mostly due to the relative minimization of interfacial electron recombination losses.

Figure 4.3b shows the % $IPCE$ as a function of the excited wavelength of the dyes coated on the mesoporous TiO₂. From the results, it is clear that the dye n -**K**₅ exhibits the highest $IPCE$ value, which may be due to the good adsorption capacity of the dye onto the TiO₂ surface through strong cyanoacetic acid as acceptor units, which in turn directly influences the electron injection. Also, the increased $IPCE$ nature of n -**K**₅ is correlated to its better current density value. Similarly, the $IPCE$ maxima of n -**K**_{6,11} are relatively less, which can be attributed to the insufficient adsorption of the dye on the TiO₂ surface due to its weak anchoring nature of acceptor groups. Among all dyes, the effective increase in π -conjugation, as well as a strong electron anchoring nature in n -**K**₅ has caused the broadening of visible absorption spectrum, thereby leading to enhanced device performance.

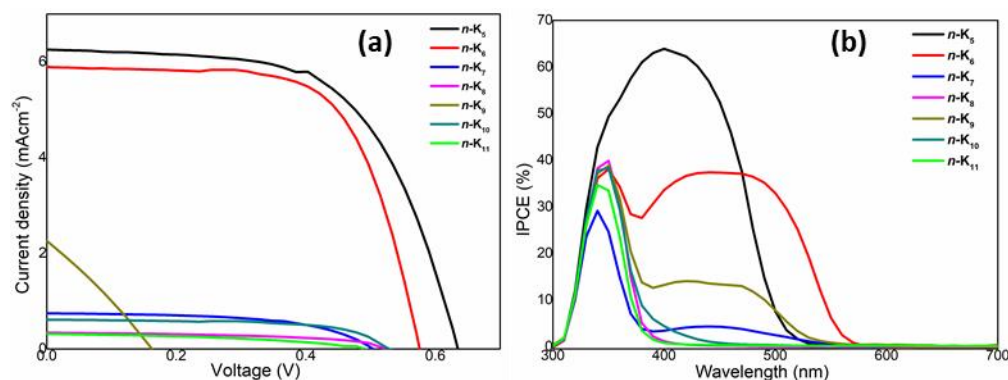


Figure 4.3 (a) Current density-voltage plots; (b) IPCE spectra of DSSCs sensitized with dyes $n\text{-K}_{5-11}$ under illumination of simulated solar light (AM 1.5G, 100 mW/cm^2)

DSSCs co-sensitized using $n\text{-K}_{5-11}$ along with Ru-based HD-2 dye

The photocurrent-voltage curves of DSSCs fabricated using $n\text{-K}_{5-11}$ dyes as co-sensitizers along with a Ruthenium-based dye **HD-2** are manifested in **Figure 4.4a** and the corresponding photovoltaic parameters are listed in **Table 4.2**. Interestingly, the co-sensitizer $n\text{-K}_6$ (i.e. $n\text{-K}_6\text{+HD-2}$) shows a higher PCE of 8.81% ($J_{SC} = 20.72 \text{ mA}\cdot\text{cm}^{-2}$, $V_{OC} = 0.66 \text{ V}$, and $FF = 63.92 \%$) than all other dyes including ruthenium-based **HD-2**. This may be attributed to the fact that the recombination of photo injected electrons is significantly hindered by the strong electron-withdrawing rhodanine acetic acid acceptor unit. Generally, the bulky molecules of **HD-2** dye inadequately adsorb on the surface of semiconducting metal oxide leaving behind the larger voids between adsorbed molecules. These created voids would now be covered uniformly by the small molecules of co-sensitizer, providing a larger surface area for light-harvesting. Further, the uniform dye adsorption on the TiO_2 surface drastically reduces dye aggregation of **HD-2** as well as back-reaction of the I_3^-/I^- on the TiO_2 surface inside the device. The enhanced J_{SC} values of $n\text{-K}_6$, $n\text{-K}_{10}$, and $n\text{-K}_{11}$ may be attributed to its strong intermolecular interactions causing efficient electron injection and charge transport towards the electrodes. Contrarily, the minor reduction in the V_{OC} compared to control can be attributed to the lowering of TiO_2 Fermi level. Further, the poor device performance in case of other dyes is ascribed to reduced electron injection which is because of inhomogeneous dye loading on the TiO_2 surface caused by the poor anchoring nature of acceptor units.

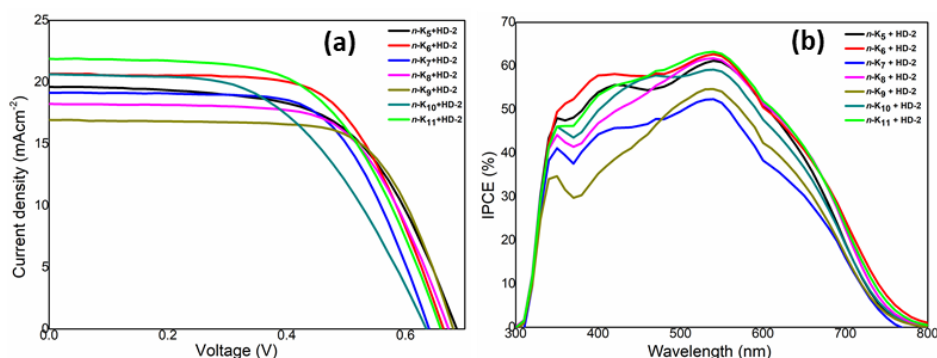


Figure 4.4 (a) Current density-voltage plots; (b) *IPCE* spectra of DSSCs fabricated using $n\text{-K}_{5-11}$ as co-sensitizers along with a Ruthenium-based dye **HD-2** under illumination of simulated solar light (AM 1.5G, 100 mW/cm^2)

The *IPCE* of the fabricated DSSCs using $n\text{-K}_{5-11}$ dyes as co-sensitizers along with reference dye **HD-2** are shown in **Figure 4.4b**. The results obtained from *IPCE* spectra are in agreement with current-voltage measurements. The spectrum of the device with $n\text{-K}_6$ along with **HD-2** shows the most intense external quantum efficiency in a broad spectrum of 300-800 nm compared to the other dyes. The possible reasons for the low *IPCE* value of other dyes could be increased spatial separation of dye LUMO level occupied in the excited state from TiO_2 surface as well as the poor orientation of dyes in between bulky **HD-2** dye molecules adsorbed onto the TiO_2 surface. Interestingly, $n\text{-K}_6+\text{HD-2}$ have superior anchoring onto the TiO_2 surface compared to **HD-2** alone, which may be due to the greater anchoring nature of the acceptor unit. Such kind of effect caused by $n\text{-K}_6$ and wrapping the Ru-centre of **HD-2** with aliphatic long-chain could account for the enhancement in irradiative process as well as retardation of recombination reaction.

4.1.4.1.3 Photovoltaic performance of **Series-3** sensitizers/co-sensitizers ($n\text{-K}_{12-18}$)

DSSCs sensitized with $n\text{-K}_{12-18}$

The current-voltage (*J-V*) curves of DSSCs sensitized with dyes $n\text{-K}_{12-18}$ are depicted in **Figure 4.5a** and the corresponding device parameters are summarized in **Table 4.1**. The *J-V* plots were obtained by using Keithley 2400 source meter under the illumination of AM 1.5G solar light. From the data, it is clear that the DSSC devices fabricated with the sensitizer $n\text{-K}_{12-13}$ show the superior *PCE* of 1.91 % and 1.03 %, respectively, with the highest J_{SC} and V_{OC} values compared to the other dyes $n\text{-K}_{14-18}$. The reason can be ascribed to the enhanced electron extraction from

electron-rich donor moiety followed by electron injection into the CB of TiO₂ by strong anchoring groups such as cyanoacetic acid and rhodanine-3-acetic acid. Surprisingly, the dye ***n-K*₁₂** shows the highest J_{SC} among all, which can be attributed to the enhanced charge collection at the adjacent contacts and the increased electron injection to the surface of TiO₂. The lower J_{SC} of ***n-K*₁₃₋₁₈** may be ascribed to poor adsorption of dyes on the TiO₂ surface, causing the low light-harvesting capacity of the cell. The enhanced V_{OC} of ***n-K*₁₂** can be attributed to the relative minimization of interfacial electron recombination losses. **Figure 4.5b** shows the % *IPCE* as a function of the exciting wavelength of the dyes coated on the mesoporous TiO₂. Among all the dyes, the dye ***n-K*₁₂** displays the highest *IPCE* value, which may be due to the enhanced adsorption capacity of the dye on the semiconductor surface through strong cyanoacetic acid acceptor units, which in turn directly influences the electron injection. Similarly, the *IPCE* maxima of ***n-K*₁₃₋₁₈** are relatively less, which may be due to the presence of weak anchoring groups, ultimately causing insufficient adsorption of the dye on the TiO₂ surface. Among all dyes, the effective increase in π -conjugation as well as, strong electron anchoring nature in ***n-K*₁₂** has caused the broadening of the visible absorption spectrum, thereby leading to significant light harvesting as well as, superior device performance.

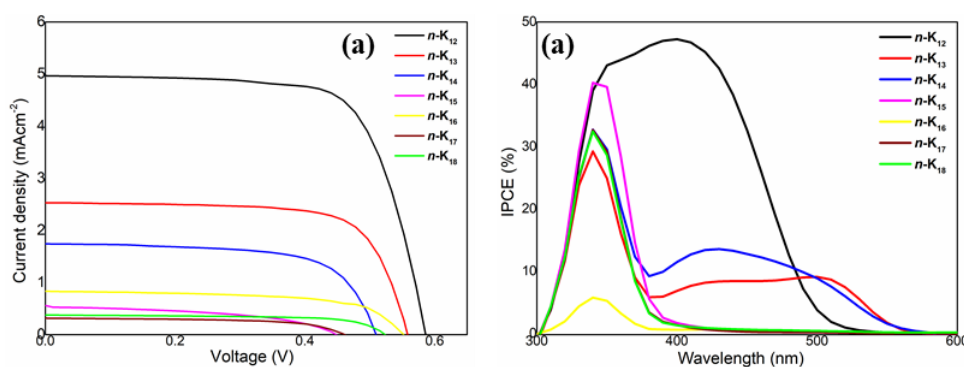


Figure 4.5 (a) Current density-voltage plots; (b) *IPCE* spectra of DSSCs sensitized with dyes ***n-K*₁₂₋₁₈** under illumination of simulated solar light (AM 1.5G, 100 mW/cm²)

*DSSCs co-sensitized using ***n-K*₁₂₋₁₈** along with Ru-based **HD-2** dye*

Figure 4.6a shows the photocurrent-voltage curves of DSSCs fabricated using ***n-K*₁₂₋₁₈** dyes as co-sensitizers along with a Ruthenium-based dye **HD-2** and the

corresponding photovoltaic parameters are listed in **Table 4.2**. Among the devices fabricated, the device based on co-sensitizer $n\text{-K}_{13}$ (i.e. $n\text{-K}_{13}+\text{HD-2}$) shows a higher *PCE* of 8.71 % ($J_{SC} = 20.42 \text{ mA}\cdot\text{cm}^{-2}$, $V_{OC} = 0.66 \text{ V}$, and $FF = 63.95 \%$) than all other dyes including ruthenium-based **HD-2**. Generally, the voids created by bulky Ru-based dye (**HD-2**) while adsorbing on the TiO_2 surface will be uniformly covered by the small molecules of co-sensitizer, providing a larger surface area for light-harvesting. Thus, it drastically suppresses the dye aggregation of **HD-2** as well as, back-reaction of the I_3^-/I^- on the TiO_2 surface inside the device. Further, the enhanced J_{SC} values of $n\text{-K}_{13}$, $n\text{-K}_{17}$, and $n\text{-K}_{18}$ may be attributed to their strong intermolecular interactions causing efficient electron injection and charge transport towards the electrodes. Contrarily, the minor reduction in the V_{OC} compared to control can be attributed to the lowering of the TiO_2 Fermi level. Further, the poor device performances in case of other dyes are ascribed to reduced electron injection which is because of inhomogeneous dye loading on the TiO_2 surface caused by the poor anchoring nature of acceptor units.

The *IPCE* characteristics of the fabricated DSSCs using $n\text{-K}_{12-18}$ dyes as co-sensitizers along with reference dye **HD-2** are shown in **Figure 4.6b**. The spectrum of the device with $n\text{-K}_{13}$ along with **HD-2** shows the most intense external quantum efficiency in a broad spectrum of 300-800 nm compared to the other dyes. The possible reasons for the low *IPCE* values of the other dyes could be the poor orientation of dyes in between bulky Ru-based **HD-2** dye molecules adsorbed onto the TiO_2 surface. Interestingly, $n\text{-K}_{13}+\text{HD-2}$ displays superior *IPCE* when compared to **HD-2** alone, which may be ascribed to the greater anchoring nature of acceptor unit.

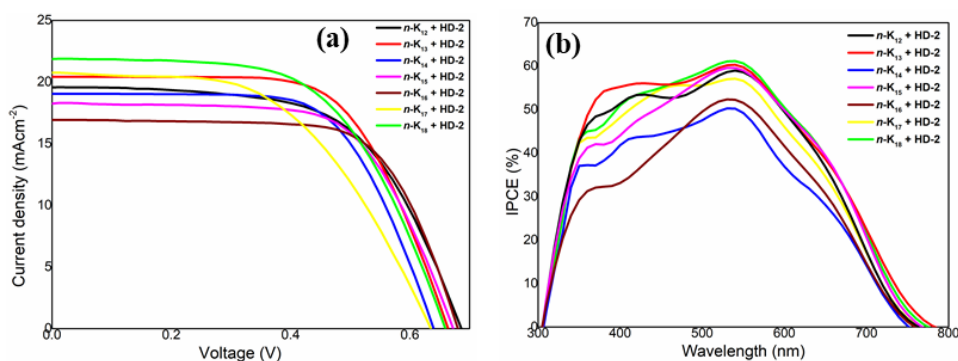


Figure 4.6 (a) Current density-voltage plots; (b) *IPCE* spectra of DSSCs fabricated using $n\text{-K}_{12-18}$ dyes as co-sensitizers along with a Ruthenium-based dye **HD-2** under illumination of simulated solar light (AM 1.5G, $100 \text{ mW}/\text{cm}^2$)

Table 4.1 Photovoltaic performance data of devices sensitized with *n*-type dyes (*n*-**K**₁₋₁₈)

Series	Sensitizer	J_{SC} (mA·cm ⁻²)	V_{oc} (V)	FF (%)	PCE (%)
1	<i>n</i> - K ₁	2.26	0.47	50.09	0.54
	<i>n</i> - K ₂	3.64	0.51	64.49	1.19
	<i>n</i> - K ₃	0.64	0.45	74.33	0.22
	<i>n</i> - K ₄	0.66	0.48	74.63	0.24
2	<i>n</i> - K ₅	6.47	0.64	58.69	2.44
	<i>n</i> - K ₆	5.92	0.57	66.08	2.26
	<i>n</i> - K ₇	1.17	0.49	55.49	0.32
	<i>n</i> - K ₈	0.33	0.53	55.01	0.09
	<i>n</i> - K ₉	2.50	0.16	28.47	0.11
	<i>n</i> - K ₁₀	0.60	0.53	63.19	0.20
	<i>n</i> - K ₁₁	0.32	0.50	45.37	0.07
3	<i>n</i> - K ₁₂	4.97	0.58	65.92	1.91
	<i>n</i> - K ₁₃	2.56	0.56	72.10	1.03
	<i>n</i> - K ₁₄	1.75	0.51	66.29	0.59
	<i>n</i> - K ₁₅	0.53	0.44	47.23	0.11
	<i>n</i> - K ₁₆	0.83	0.55	62.89	0.29
	<i>n</i> - K ₁₇	0.31	0.46	60.95	0.09
	<i>n</i> - K ₁₈	0.38	0.52	67.68	0.13

Table 4.2 Photovoltaic performance data of devices co-sensitized with *n*-type dyes (*n*-**K**₁₋₁₈)

Sensitizer		CDCA (mM)	J_{SC} (mA·cm ⁻²)	V_{oc} (V)	FF (%)	PCE (%)
0.2 mM Ru (II) sensitizer	0.2mM Organic co- sensitizer					
MH-12	--	20	20.26	0.64	59.10	8.19
MH-12	<i>n</i> - K ₁	20	20.64	0.61	63.21	8.01
	<i>n</i> - K ₂	20	16.67	0.62	66.21	6.80
	<i>n</i> - K ₃	20	21.68	0.63	64.27	8.79
	<i>n</i> - K ₄	20	20.07	0.63	64.25	8.17
HD-2	--	20	19.03	0.65	60.49	7.49
	<i>n</i> - K ₅	20	19.43	0.69	60.73	8.15
	<i>n</i> - K ₆	20	20.72	0.66	63.92	8.81
	<i>n</i> - K ₇	20	19.05	0.64	64.67	7.90
	<i>n</i> - K ₈	20	18.33	0.67	64.87	8.01

HD-2	<i>n</i> - K ₉	20	17.00	0.68	68.84	8.01
	<i>n</i> - K ₁₀	20	20.64	0.63	52.94	6.96
	<i>n</i> - K ₁₁	20	21.92	0.66	58.35	8.52
	<i>n</i> - K ₁₂	20	19.58	0.68	60.03	8.07
	<i>n</i> - K ₁₃	20	20.42	0.66	63.95	8.71
	<i>n</i> - K ₁₄	20	19.05	0.64	64.42	7.87
	<i>n</i> - K ₁₅	20	18.30	0.67	64.66	7.97
	<i>n</i> - K ₁₆	20	16.92	0.68	68.99	7.98
	<i>n</i> - K ₁₇	20	20.75	0.64	50.31	6.73
	<i>n</i> - K ₁₈	20	21.89	0.65	58.74	8.47

4.1.4.2 Photovoltaic performance of devices sensitized with *p*-type dyes (*p*-**K**₃₅₋₄₂)

4.1.4.2.1 Photovoltaic performance of **Series-9** sensitizers (*p*-**K**₃₅₋₄₀)

The experimentally obtained *J-V* curves of the DSSCs sensitized with dyes *p*-**K**₃₅₋₄₀ along with the benchmark reference dye 4-(bis-{4-[5-(2,2-dicyanovinyl)-thiophene-2-yl]-phenyl}amino)benzoic acid, **P1** are depicted in **Figures 4.7a-g** and the corresponding photovoltaic parameters are summarized in **Table 4.3**. Amongst the tested dyes, the photovoltaic performance was found to be in the decreasing order of **P1** > *p*-**K**₃₆ > *p*-**K**₃₅ > *p*-**K**₄₀ > *p*-**K**₃₇ > *p*-**K**₃₉ > *p*-**K**₃₈. The difference in the photovoltaic performance of *p*-**K**₃₅₋₄₀ is mainly due to the electron-accepting nature of the six different acceptor units used in the dyes as these acceptor units control the strength of the charge transfer band in the excited state. From the results, we can notice that the device fabricated with *p*-**K**₃₆ shows a maximum *PCE* of 0.031 % (*J*_{SC}: 0.89 mA·cm⁻², *V*_{OC}: 101 mV, and *FF*: 35 %), when compared to the other dyes and display better *FF* values than that of reference dye **P1**. But *J*_{SC} of dye *p*-**K**₃₆ is found to be lower when compared to the device fabricated using dye *p*-**K**₄₀. Interestingly, the device made up of dye *p*-**K**₃₆ exhibits the highest *V*_{OC} when compared to the other members of the series. Besides, the dark current is found to be lower in *p*-**K**₃₆ than other dyes, indicating suppressed interfacial charge recombination with the electrolyte. The reduced interfacial charge recombination causes better shielding of dye on the surface of NiO, which is most probably due to a denser packing on the surface. **Figure 4.8** portrays the *IPCE* spectra of DSSCs fabricated with *p*-**K**₃₅₋₄₀ and reference **P1**. All the dyes display *IPCE* spectra in the broad range of 450-650 nm. In general, the broadening of the *IPCE* spectra is desired for a larger photocurrent which

describes the differences in *PCE* of fabricated dyes. Here, the dye ***p*-K₄₀** along with the benchmark reference dye **P1** displays an improved *IPCE* spectrum, owing to its higher short circuit photocurrent density. The lower *IPCE* of other dyes can be attributed to the poor injection efficiency in the devices.

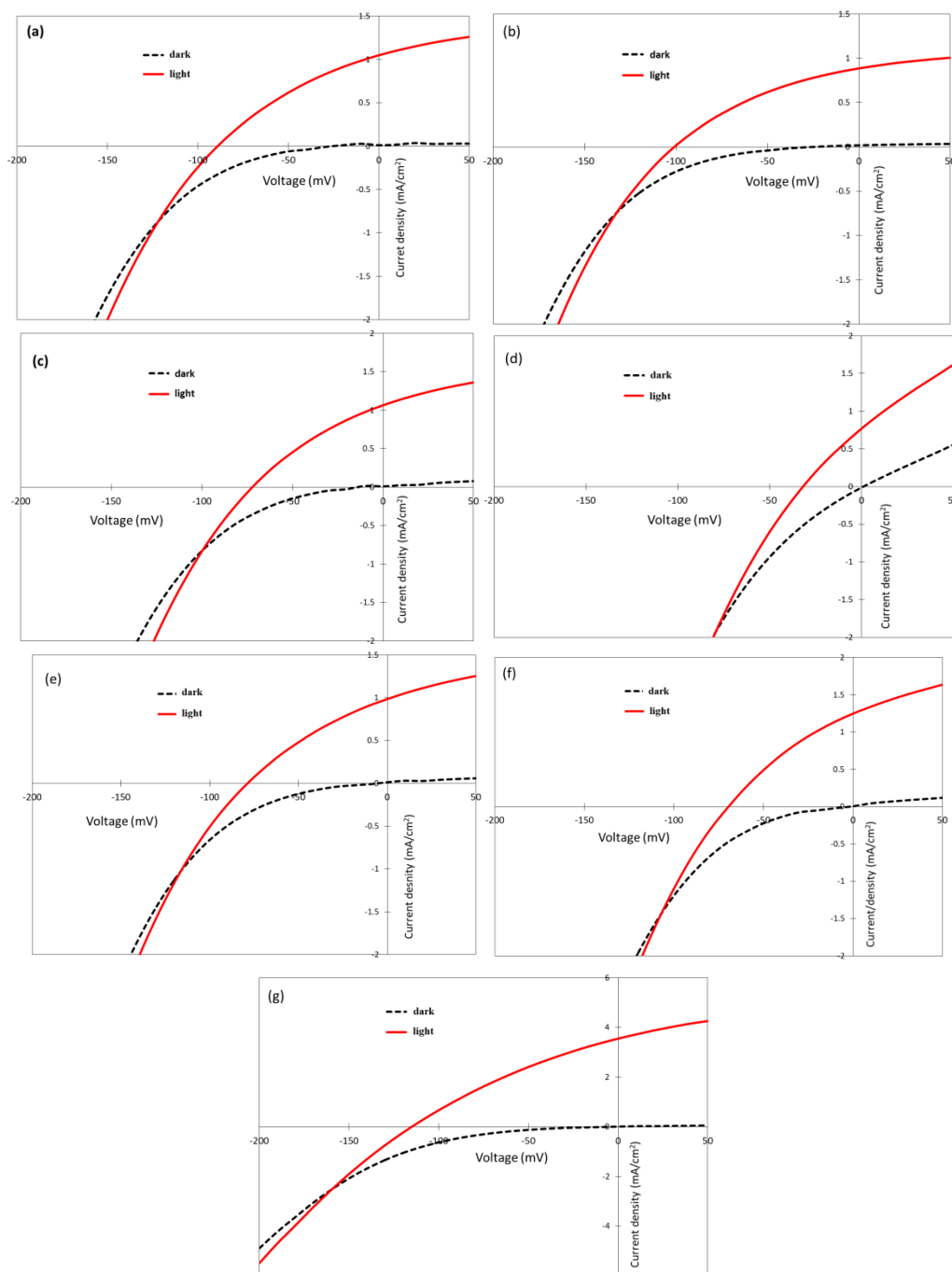


Figure 4.7 Current density-voltage plots of DSSCs sensitized with (a) *p*-K₃₅, (b) *p*-K₃₆, (c) *p*-K₃₇, (d) *p*-K₃₈, (e) *p*-K₃₉, (f) *p*-K₄₀, and (g) P1 dyes

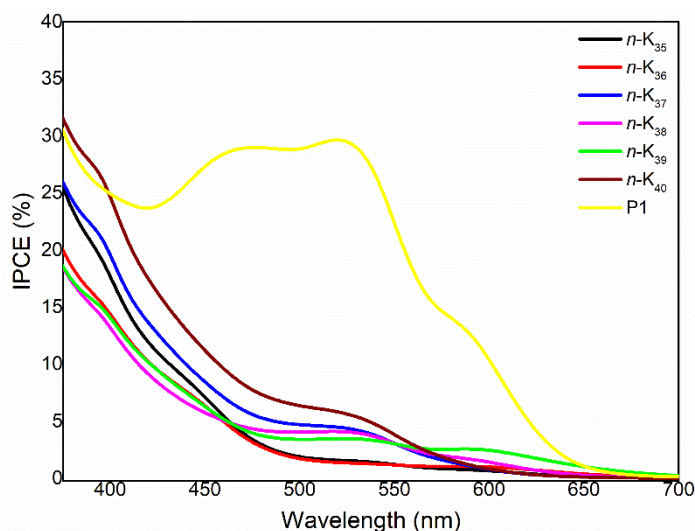


Figure 4.8 IPCE spectra of DSSCs sensitized with dyes **p-K₃₅₋₄₀** under illumination of simulated solar light (AM 1.5G, 100 mW/cm²)

4.1.4.2.2 Photovoltaic performance of **Series-10** sensitizers (**p-K₄₁₋₄₂**)

Figure 4.9 shows the *J-V* characteristics of the DSSCs sensitized with dyes **p-K₄₁₋₄₂** along with the benchmark reference dye **P1** and their corresponding photovoltaic parameters are tabulated in **Table 4.3**. From the results, it is confirmed that the dye **p-K₄₁** carrying malononitrile as electron-withdrawing unit displays better photovoltaic performance (*PCE*: 0.027 %, *J_{SC}*: 0.92 mA·cm⁻², *V_{OC}*: 87 mV, and *FF*: 34 %) than the dye **p-K₄₂** bearing barbituric acid as an electron acceptor (*PCE*: 0.018 %, *J_{SC}*: 0.92 mA·cm⁻², *V_{OC}*: 68 mV, and *FF*: 30 %). Interestingly, both the dyes display similar short-circuit current values, with the major difference in their *V_{OC}* and *FF* values. This can be attributed to the lower interfacial charge recombination dynamics in devices made up of dye **p-K₄₁** and hence results in superior performance. **Figure 4.10** portrays the *IPCE* spectra of DSSCs fabricated with **p-K₄₁₋₄₂** and reference **P1**. Both the dyes display a lower *IPCE* band than that of the reference dye **P1**. The lower *IPCE* may be attributed to the poor charge injection efficiency in the devices. The behavior of *IPCE* spectra is in agreement with the experimental results obtained from *J-V* studies.

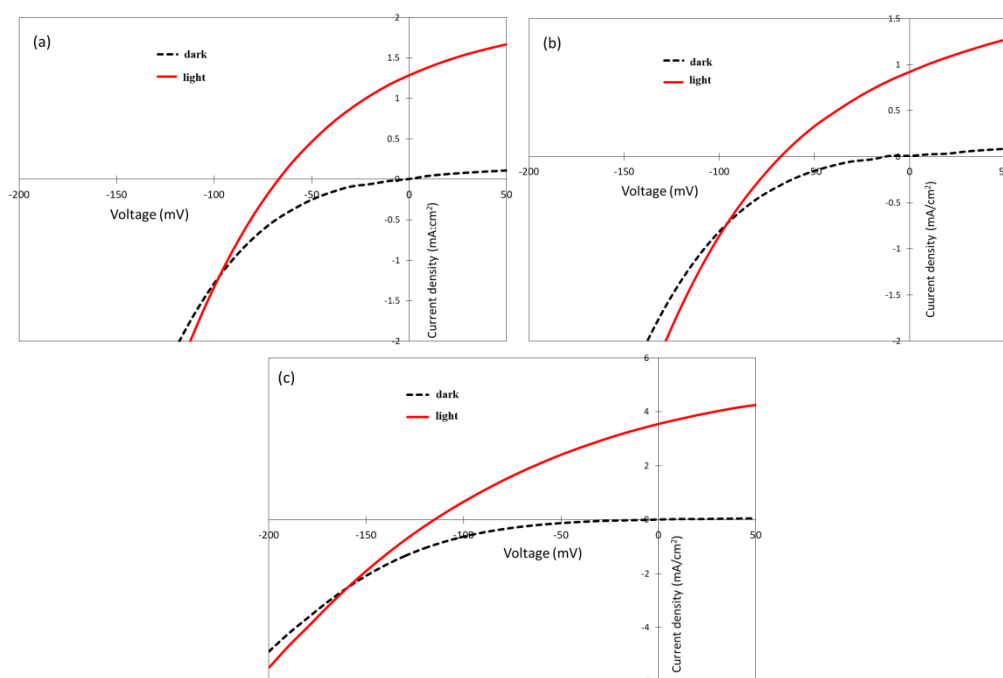


Figure 4.9 Current density-voltage plots of DSSCs sensitized with (a) p - K_{41} , (b) p - K_{42} , and (c) P1 dyes

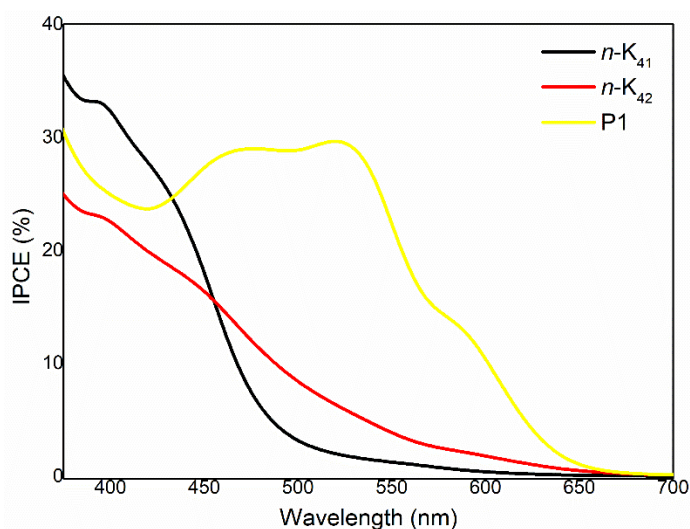


Figure 4.10 IPCE spectra of DSSCs sensitized with dyes p - K_{41-42} under illumination of simulated solar light (AM 1.5G, 100 mW/cm^2)

Table 4.3 Photovoltaic performance data of devices sensitized with p -type dyes (p - K_{35-42})

Series	Sensitizer	J_{SC} ($\text{mA}\cdot\text{cm}^{-2}$)	V_{OC} (mV)	FF (%)	PCE (%)
	P1	3.55	115	31	0.126
	p - K_{35}	1.05	89	33	0.030
	p - K_{36}	0.89	101	35	0.031
	p - K_{37}	1.06	79	32	0.026

9	<i>p</i> - K₃₈	0.77	32	25	0.006
	<i>p</i> - K₃₉	0.98	79	31	0.024
	<i>p</i> - K₄₀	1.25	72	32	0.027
10	<i>p</i> - K₄₁	0.92	87	34	0.027
	<i>p</i> - K₄₂	0.92	68	30	0.018

4.1.4.3 Photovoltaic performance of hole-transporting materials (*h*-**K₄₃₋₄₄**)

In order to evaluate the photoelectrochemical properties of *h*-**K₄₃₋₄₄**, and to correlate their structure-property relationships, new PSCs were fabricated using them as HTMs adopting the well-established procedure. Also, the device based on the state-of-the-art HTM, Spiro-OMeTAD was constructed for accurate and reliable comparisons under similar conditions. **Figure 4.11a** shows the schematic representation of the fabricated device architecture. The current density-voltage (*J*-*V*) characteristic curves of the devices with *h*-**K₄₃₋₄₄** and reference Spiro-OMeTAD under one sun illumination (AM 1.5 full sunlight, 100 mW·cm⁻²) are presented in **Figures 4.11b-d** and the relevant device performance data are listed in **Table 4.4**. It is apparent that the device fabricated using HTM *h*-**K₄₃** displays the uppermost *PCE* of 2.55 % (*J_{SC}*: 7.85 mA·cm⁻², *V_{OC}*: 0.79 V, and *FF*: 40 %) compared to that of *h*-**K₄₄** (*PCE*: 1.71 %, *J_{SC}*: 8.15 mA·cm⁻², *V_{OC}*: 0.4 V, *FF*: 49 %), and is well comparable with reference Spiro-OMeTAD (*PCE*: 4.76%, *J_{SC}*: 12.27 mA·cm⁻², *V_{OC}*: 0.84 V, *FF*: 45%).

The higher *PCE* of *h*-**K₄₃** can be assigned to its significant hole extraction from the donor molecule due to its improved light-harvesting nature as confirmed by its optical studies and hence it can be considered as a better HTM. Besides, *h*-**K₄₃** has a stronger electron-donating capability compared to that of *h*-**K₄₄**, which may be due to the presence of an additional methoxy pendent group on the donor moiety. Indeed, the presence of long branched alkoxy chains on the donor molecule can significantly retard the recombination rate, and thus provides improved *V_{OC}* value. Remarkably, the compound *h*-**K₄₃** shows the highest *V_{OC}* compared to that of *h*-**K₄₄**. The enhanced *V_{OC}* of *h*-**K₄₃** is mostly due to the relative minimization of interfacial electron recombination losses. From the results, it is evident that all the PSCs exhibit *FF* in the range of 40-50 %. The substantial reduction of *FF* in the case of *h*-**K₄₃** and Spiro-OMeTAD could be attributed to the minor interfacial charge recombination, which

may be resulted from the relatively higher series and lower shunt resistance. Thus, we can conclude that the device based on ***h-K*₄₃** as HTM has performed much better than that of ***h-K*₄₄**. Convincingly, the introduction of carbazole moiety with an additional number of pendent groups is an effective strategy in designing new HTMs for perovskite solar cell application.

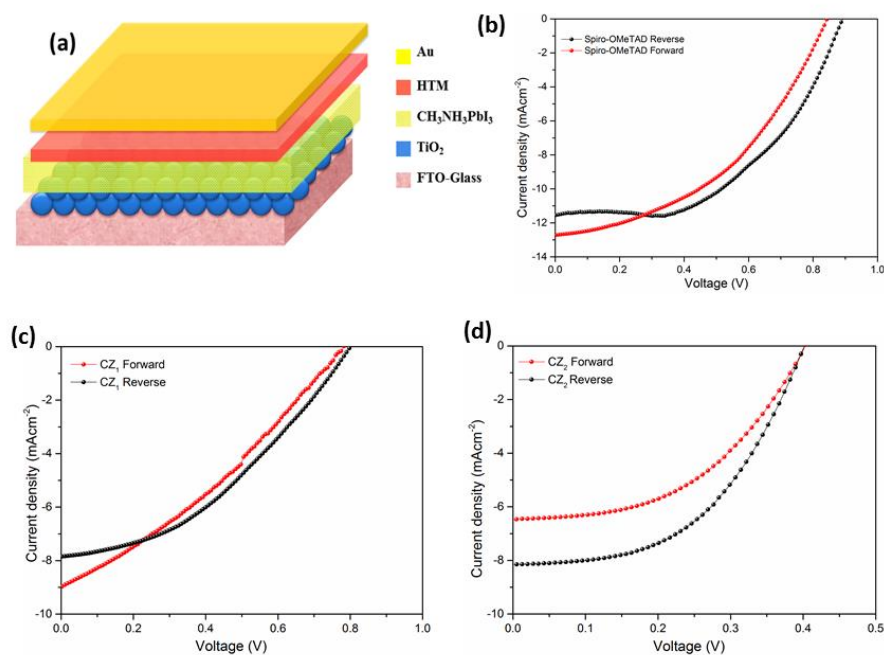


Figure 4.11 (a) Schematic representation of device architecture and *J-V* characteristics of (b) Spiro-OMeTAD, (c) ***h-K*₄₃**, and (d) ***h-K*₄₄**

In general, the photovoltaic parameters of the fabricated devices majorly depend on the interfacial carrier transport and charge recombination kinetics, electron lifetime, and *IPCE* of the cells. The *IPCE* spectra of the devices fabricated using synthesized HTMs ***h-K*₄₃₋₄₄** and the reference Spiro-OMeTAD are depicted in **Figure 4.12**. From the figure, it is clear that the *IPCE* maximum of HTM ***h-K*₄₃** is 30 %, ***h-K*₄₄** is 26 %, and that of Spiro-OMeTAD is 35 % in the entire wavelength range of 300-800 nm. Also, the increased *IPCE* nature of ***h-K*₄₃** when compared to that of ***h-K*₄₄** in a longer wavelength region is correlated to its enhanced charge-transport ability. Along with this, we infer that the hydrophobic branched 2-ethylhexyl chains of synthesized molecules are capable of furnishing enhanced spatial separation between electrons and holes, resulting in retardation of electron recombination kinetics and thereby increasing the device performance.

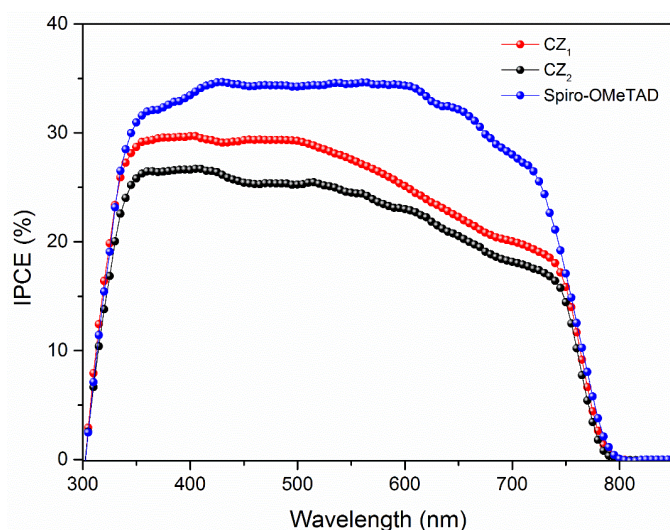


Figure 4.12 IPCE spectra of $h\text{-K}_{43-44}$ along with reference Spiro-OMeTAD under illumination of simulated solar light (AM 1.5G, 100 mW/cm^2)

Table 4.4 Photovoltaic performances of synthesized HTMs ($h\text{-K}_{43-44}$) along with reference Spiro-OMeTAD

Series	Sensitizer	J_{SC} ($\text{mA}\cdot\text{cm}^{-2}$)	V_{OC} (V)	FF (%)	PCE (%)
11	$p\text{-K}_{43}$	7.85	0.79	40	2.55
	$p\text{-K}_{44}$	8.15	0.4	49	1.71
	Spiro-OMeTAD	12.27	0.84	45	4.67

4.2 CONCLUSIONS

The selected three series (**Series 1-3**) of newly synthesized n -type organic dyes ($n\text{-K}_{1-18}$) were subjected to DSSC fabrication studies as sensitizers. The study reveals that the devices sensitized with $n\text{-K}_2$ (D- π -A), $n\text{-K}_5$ (D-A)₂, and $n\text{-K}_{12}$ (D-A)₂ dyes showcase superior photovoltaic performance due to the presence of strong cyanoacetic acid as acceptor/anchoring unit. In addition, eighteen new n -type organic dyes ($n\text{-K}_{1-18}$) were successfully employed as co-sensitizers in DSSCs sensitized with the standard Ru (II) sensitizers (**MH-12/HD-2**). The co-sensitization studies reveal that the devices co-sensitized using dyes $n\text{-K}_3$, $n\text{-K}_6$, and $n\text{-K}_{13}$ along with 0.2 mM of Ru-based **MH-12/HD-2** sensitizer display an improved PCE of 8.89 %, 8.81 %, and 8.71 %, respectively. Further, the eight newly synthesized p -type organic dyes ($p\text{-K}_{35-42}$) were employed in the fabrication of p -type DSSCs as sensitizers and their photovoltaic results disclose that $p\text{-K}_{36}$ sensitized DSSC showcases PCE of 0.031 %, and

which is higher when compared to the other dyes and is comparable with that of benchmark reference **P1**. Finally, among the synthesized HTMs, the ***h-K*₄₃** as HTM displays a better *PCE* of 2.55 % which is comparable with that of standard reference Sipro-OMeTAD in PSCs. To sum up, by further optimizing the molecular structure of dyes/HTMs, it is possible to further ameliorate the photovoltaic performance of DSSCs/PSCs. In the next chapter, detailed studies on carbon-based perovskite solar cells have been discussed.

CHAPTER-5
STUDIES ON CARBON-BASED PRINTABLE
PEROVSKITE SOLAR CELLS

STUDIES ON CARBON-BASED PRINTABLE PEROVSKITE SOLAR CELLS

Abstract

This chapter deals with a detailed investigation on the selection of appropriate solvent for a single-step deposition of mixed-cation perovskites for highly reproducible carbon-based PSCs using the Lewis acid-base adduct approach. Also, it highlights the preparation of new perovskite films using various solvents, and their structural as well as optical characterizations including their device performance studies. Further, it involves the development of highly efficient and stable carbon-based perovskite solar cells (C-PSCs) using CsBr modified mp-TiO₂ beads as a superior electron transport material, with high PCE and a larger area.

5.1 MIXED-CATION HYBRID LEAD HALIDE PEROVSKITE SOLAR CELLS: SOLVENT SELECTION VIA ADDUCT APPROACH

5.1.1 Introduction

The major challenge observed in the fabrication of printable carbon-based mixed-cation hybrid lead halide PSCs is the infiltration of the perovskite solution through triple-layered TiO₂/ZrO₂/C architecture done by the drop-casting method, where the solvent has to penetrate through multilayers, especially with the carbon layer of thickness of 10-12 micron (**Chapter 1**, section 1.6.4 and 1.10.4). Therefore, there is a need for a detailed investigation of infiltration challenges with the mixed-cation hybrid lead halide perovskite (Cs_{0.1}FA_{0.9}PbI₃) precursors involving various solvents following a one-step perovskite deposition method to fabricate carbon-based whole mesostructured PSCs. In the present study, the two-cation (Cs, FA) perovskite has been chosen as the state-of-the-art perovskite, which has been less explored now in terms of stability. Also, the literature survey clearly reveals that no research has been carried out in the area of appropriate solvent selection for single-step-processed two cations based Cs_{0.1}FA_{0.9}PbI₃ mixed cation perovskite deposition on C-PSCs in order to promote their scalable production.

In the present systematic investigation, a detailed study was carried out on the fabrication of high-efficiency mesostructured devices using industrially acceptable eco-friendly solvent DMSO *via* adduct of PbI_2 with sulphur-donor Lewis base. Interestingly, the use of only a single solvent, DMSO, for the perovskite infiltration resulted in high and reproducible device performance over other solvents/mixed solvents. To highlight the positive impact of DMSO solvent, infrared spectral analysis was carried out, which confirms the stronger interaction between DMSO and FA cation. The stronger interaction between DMSO and FA facilitates the formation of stable $\text{FAI}\cdot\text{PbI}_2\cdot\text{DMSO}$ adduct. The surface morphology of the carbon composition, as well as device fabricated using different solvents, are also presented in support of the use of the DMSO solvent. Additionally, the crystal phase composition and light absorption of the $\text{Cs}_{0.1}\text{FA}_{0.9}\text{PbI}_3$ perovskite film were comprehensively examined by x-ray diffraction (XRD), UV/Vis absorption spectra, and photoluminescence (PL) spectra. The reproducibility of the high device performance with DMSO and other solvents is examined by analyzing the photovoltaic parameters of 62 fabricated devices.

5.1.2 Experimental section

5.1.2.1 Preparation of materials

$\text{PbI}_2\cdot\text{DMSO}$ adduct: PbI_2 (461mg, TCI) was dissolved in 2-3 mL of dimethylsulfoxide (DMSO, 99.5%, Sigma-Aldrich). Further, anhydrous absolute ethanol was added to the solution of PbI_2 in DMSO. The pale yellow precipitate formed was filtered and dried in a vacuum oven, which was used for IR spectroscopy measurement.

$\text{CsFAPbI}_3\cdot\text{DMSO}$ adduct: PbI_2 (461mg, TCI), FAI (154.32), and CsI (25.98) were dissolved in a 1 mL solution of DMSO (1M). Diethyl ether was added to the fully-dissolved solution in order to form the precipitate of the corresponding adduct. The precipitate was collected and dried in a vacuum oven, which was used for IR spectroscopy measurement.

5.1.2.2 Solar cell fabrication

All the devices were prepared in an ambient condition (temperature 25-30 °C, 60-70% RH), in which relative humidity was not controlled except for perovskite solution making and device infiltration, which was done in an inert glovebox environment. Fluorine doped tin oxide substrates with a sheet resistance ~14 ohm per square and thicknesses around 2.2 mm were first etched with 1064 nm YAG laser to form the desired pattern followed by sequential cleaning. The cleaning processes consisting of ultrasonication in a soap solution, followed by deionized water (DI water), and finally using ethanol. Each sonication step was repeated twice and held at 40 °C for 30 minutes. The substrates were then submerged in a 50 mM TiCl₄ solution (Wako Pure Chemical Industries, Ltd) for 30 minutes in an oven at 70 °C, followed by rinsing with DI water and finally heated at 500 °C for 30 minutes in order to form the seed layer of TiO₂. Using a screen printer (MicroTec MT320TV) a compact TiO₂ layer was printed using Dyesol BL-1 TiO₂ paste and then annealed at 500 °C for 30 minutes. In order to fill up the defective ‘pinholes’, these substrates were immersed in 100 mM of TiCl₄ solution for 30 minutes at 70 °C followed by rinsing with DI water. Finally, these substrates are subjected to heat treatment at 500 °C which completes the formation of the blocking layer.

A mesoporous TiO₂ layer was printed using a TiO₂ paste (Dyesol 30 NR-D, diluted with terpineol (Sigma, FG) in weight ratio 1:1:4). The layer was annealed at 500 °C for 30 minutes to improve the crystallinity. The thickness of the m-TiO₂ layer was measured using a surface profilometer and was found to be 500 nm. An insulating layer of ZrO₂ with a thickness of 1.2 µm was printed (Solaronix, Zr-Nanoxide ZT/SP) and sequentially annealed at 500 °C for 30 minutes. Finally, a carbon paste was printed on top of the ZrO₂ layer to form the counter electrode, which completes the triple-layer device stack. The carbon paste was supplied by DYESOL, Australia. The substrates were heated at 395 °C for 30 minutes and the thickness was found to be 10-15 µm. The perovskite deposition on top of carbon was done by the drop-casting (infiltration) method inside the glove box.

As the perovskite composition under investigation ($\text{Cs}_{0.1}\text{FA}_{0.9}\text{PbI}_3$) involves one of the precursor ‘CsI’ which has good solubility in DMSO, and limited solubility in GBL and DMF, a mixed solvent approach of GBL:DMSO (1:1), DMF:DMSO (1:1) are considered for the comparison study. For $\text{Cs}_x\text{FA}_{1-x}\text{PbI}_3$, corresponding amount of CsI (Aldrich, 99.9%) was added (25.98 mg of CsI for $x = 0.10$) to replace appropriate amount of FAI. The justification for the appropriate amount of Cs (0.1) content in the perovskite composition is given as follows. When precursor solution was prepared with 0% CsI, it forms a complete non-perovskite yellow phase of FAPbI_3 . When Cs concentration increased, colour of the film gradually changed from the non-perovskite yellow phase to the dark brown perovskite phase. The highest proportion of black phase was formed when Cs concentration is 0.1.

The perovskite solution was prepared by dissolving 1 mmol of PbI_2 (461 mg, Tokyo Chemical Industry), FAI (172 mg) in 1 mL total volume of various combinations of solvents like DMSO (Sigma-Aldrich, >99.9%), DMF (Sigma, >99.9%), DMSO:DMF (Sigma, >99.9%), GBL:DMSO (Sigma, >99.9%). DMSO has a higher viscosity than DMF and GBL at room temperature (25°C), which may hinder the easy infiltration of perovskite solution into the mesoporous scaffold. Reducing the viscosity facilitates the flowability with better infiltration, which is achieved with the heating of the precursor solution at 70 °C for 90 minutes (viscosity of DMSO = 0.91 cP at 70 °C) and carried hot casting of perovskite solution on carbon devices at 70 °C and further annealed at 100 °C (viscosity of DMSO = 0.6 cP) for 5 minutes and continued annealing at 150 °C for 30 minutes as shown in **Figure 5.1**. During the thermal annealing process, $\text{Cs}_{0.1}\text{FA}_{0.9}\text{PbI}_3$ undergoes phase transition inside the mesoporous scaffold as DMSO and FAI have similar size, they can undergo easy exchange inside the precursor (Hou et al., 2019). The adduct of $\text{Cs}_{0.1}\text{FA}_{0.9}\text{PbI}_3$ perovskite in different solvents is formed and during annealing, the phase transition from adduct to perovskite phase (black) *via* hexagonal non-perovskite (yellow) phase is pictorially shown in **Figure 5.1**. The active areas of carbon devices were 0.09 cm² and 0.7 cm². The fabrication process completes by painting silver contacts to ensure good contact, followed by device testing using the solar simulator.

5.1.2.3 Characterization

The current density-voltage curve (I - V characteristics) was measured using a Keithley 2612A source meter under one sun illumination (AM 1.5G, 100 mWcm^{-2}), which was simulated by a solar simulator (San-EI Electric, XEC-301S) equipped with a 450 W xenon lamp. The power of the simulated light was calibrated with the help of a Si reference cell (Fraunhofer) and monitored using a power meter throughout the testing. The black mask with an active area of 0.7 cm^2 was applied on the top of the device. The x-ray diffraction pattern was measured by Bruker AXZ (D8) Advance diffractometer using Cu $K\alpha$ radiation at a scan rate of 4° min^{-1} . External quantum efficiency (EQE) was measured by a specially designed EQE system PV 300 (Bentham), with a dual Xenon/quartz halogen light source, measured in DC mode with no bias light. All the measurements were performed in the air (25°C , 60-70% RH). The thickness of each layer in the device was measured by a surface profiler (NanoMap-5000LS, AEP technology). The adduct-assisted crystallization is further confirmed by FTIR. The morphology and cross-section images of the devices were obtained using FE-SEM (Jeol JSM-7600F Field Emission Scanning Electron Microscope). For Photoluminescence (PL), the micro-PL set-up was used, which is based on a fiber-coupled microscope system, employing a VIS-NIR microscope objective (10x, NA= 0.65). The samples were excited at 405 nm (Picoquant P-C-405B) with a 5-MHz-repetition-rate using picosecond-pulse light-emitting diode and the beam spot size was $\sim 10 \text{ mm}$. EIS measurements were conducted under 1 sun illumination using Autolab instrument (PGSTAT302N, Software version- NOVA 1.11) under frequency range from 1MHz to 1Hz at different applied biases (0.1V-1V)

5.1.3 Results and discussion

The solvents GBL, DMF, and DMSO are extensively used either in a single form or as mixtures of them in the PSCs fabrication. There is a need to justify which solvent is to be used with a scientific understanding. The present study considers the adduct formation in the precursor solution of hybrid perovskite composition when PbI_2 is

dissolved in various solvents such as GBL, DMF, and DMSO. With the study on the adduct formation and thereby perovskite crystallization, the origin of the best *PCE* is to be understood, highlighting the DMSO use. The adduct formation can be understood in Lewis acid-base concept; acid generally accepts an electron-pair, whereas base donates an electron-pair to the chemical species, including all the main group compounds and metal ions. The Lewis acid-base reactions mainly undergo either redox reaction (oxidation or reduction) or adduct formation reaction, where the latter formed is linked by a dative bond to form a coordinate compound. Some examples, such as Pb(II) halides, are considered to be Lewis acids, as they accept iodide anions in order to form iodoplumbate anions. The organic cation such as formamidinium (FA) in FAPbI₃ contains two –NH₂ functional groups that act as Lewis bases.

In the perovskite precursor solution (formamidinium iodide, CsI, and PbI₂ dissolved in a solvent) the polar groups of solvent (Lewis base) and formamidinium iodide (Lewis base) coordinate with PbI₂ (Lewis acid) to form the intermediate adduct phase ‘Cs_xFA_{1-x}PbI₃·Solvent’ (here solvent refers to DMSO, DMF, GBL and its combinations). The solvent DMSO acts as a stronger Lewis base than DMF and GBL due to the presence of higher electron cloud density on S=O of DMSO as compared to the C=O of DMF, and GBL. Hence, DMSO forms a relatively stronger adduct of ‘Cs_xFA_{1-x}PbI₃·Solvent’ (**Figure 5.1a**) as its polar groups can strongly bind with the PbI₂. The order of coordination ability of three different solvents with PbI₂ is DMSO>DMF>GBL and hence expected to have a similar trend in the formation of adducts.

To get highly crystalline and uniform perovskite films, the formation of intermediate adduct plays a vital role as its slow transformation during annealing yields the morphology of perovskite. Apparently, a clear difference in morphology of perovskite using various solvents under consideration is shown in **Figure 5.1b**. The poor morphology of perovskite in the fabricated devices using GBL and DMF is likely to be caused by the difference in crystal growth rate between low solubility of CsI, PbI₂ in the solvent, while DMF and GBL are rapidly evaporating and hence affecting the required slow transformation rate of ‘Cs_xFA_{1-x}PbI₃·Solvent’ adduct. With this adduct approach,

only DMSO shows uniform film formation compared with other solvent combinations, as shown in **Figure 5.1b**. To obtain more insights further analysis is carried out to support the theory and the apparent observations.

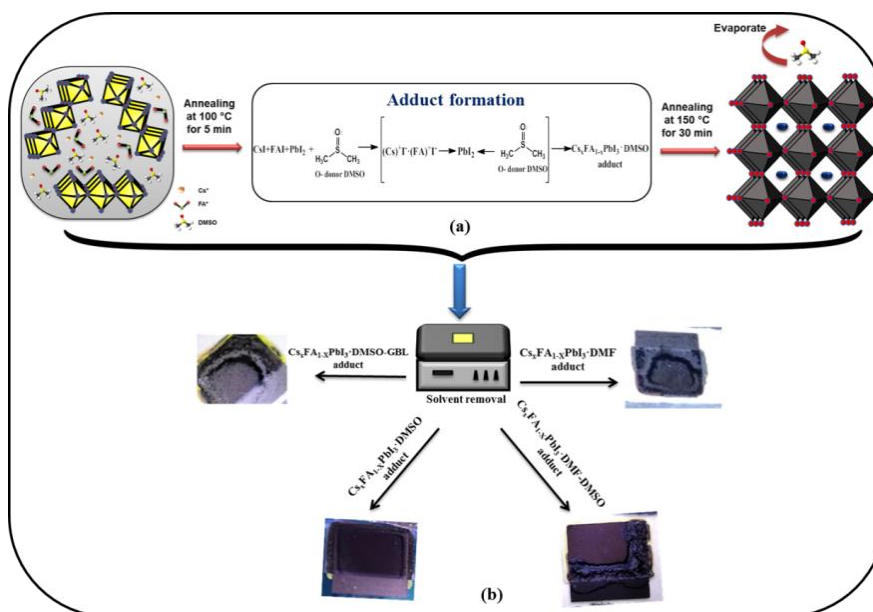


Figure 5.1 (a) Schematic representation of precursor, adduct formation, and the perovskite crystallization process in one of the solvents DMSO; (b) Photographic images of fabricated devices in various solvents *via* adduct approach

5.1.3.1 Structural and optical characterization of perovskite films

The crystalline nature of annealed (150 °C) perovskite, $\text{Cs}_{0.1}\text{FA}_{0.9}\text{PbI}_3$ films using various solvents were characterized by X-ray diffraction (XRD) studies, as shown in **Figure 5.2**. The diffraction peaks at 14.00°, 19.98°, 24.58°, 28.54°, 31.67°, 40.48° and 43.24° confirm the perovskite planes of (110), (112), (202), (220), (310), (224), and (314), respectively (Huang et al., 2017). No impurity phase of PbI_2 was observed. Since the ‘Cs’ was incorporated in the perovskite lattice, the undesired hexagonal non-perovskite δ -phase was also absent. The perovskite layers fabricated using GBL-DMSO, DMF, and DMF-DMSO combinations result in low-intensity XRD patterns which reveal the low crystalline content in the films. The XRD pattern of the perovskite film fabricated using pure DMSO shows a large amount of crystalline material at two different planes (110) and (220), respectively. The high crystallinity is attributed to the strong

coordination of DMSO, forming the CsI-FAI-PbI₂-DMSO complex, which can ultimately retard the rate of crystallization in perovskite structures, and lead to high-quality films (Jeon et al., 2014, Wu et al., 2014). Overall, full-width half-maximum (FWHM) and intensity of peaks originating from black phase Cs_{0.1}FA_{0.9}PbI₃ are highly enhanced for the films prepared using DMSO solvent, which is correlated to significantly increased grain size of Cs_{0.1}FA_{0.9}PbI₃. The crystallite size has been significantly increased for the perovskite film formed using DMSO as a solvent. The average crystal size calculated from XRD measurement using the Scherrer equation was found to be 35.5 nm for DMSO-based film, 25.4 nm for DMF:DMSO film, 34.2 nm for DMF film, and 31.8 for GBL:DMSO film.

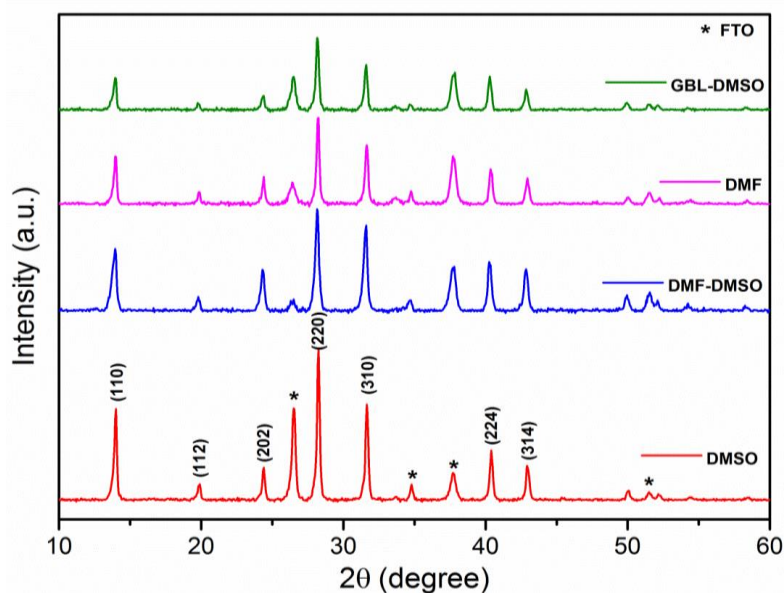


Figure 5.2 X-ray diffraction spectra of Cs_{0.1}FA_{0.9}PbI₃ thin-films fabricated using various solvents

Fourier transform infrared (FTIR) spectroscopy was used to investigate the adduct bonding nature of the compounds. **Figure 5.3** shows the FTIR spectra of the pure DMSO and corresponding adducts PbI₂·DMSO and Cs_{0.1}FA_{0.9}PbI₃·DMSO (the detailed synthesis part of materials has been given in the experimental section). The Lewis acid PbI₂ will react with Lewis bases containing heteroatoms such as nitrogen, oxygen, and sulfur to

form an adduct, where Lewis acid Pb^{2+} in PbI_2 accepts lone pair of electrons of oxygen in DMSO (Gram et al., 1976). Other solvents such as DMF can also form a low-intensity adduct with PbI_2 , but more stable adduct formation is expected from DMSO due to the high polarity of DMSO (relative polarity of DMSO, which is found to be 0.444, whereas 0.386 for DMF. Iodide (I^-) in FAI can also form an adduct with PbI_2 as it is a strong donor in nature. Also, it has been reported that the solubility of PbI_2 in DMSO is relatively faster in the presence of FAI than the solubility of PbI_2 alone, which indicates that the interaction of I^- is stronger with PbI_2 . The stretching vibration peak of $\text{S}=\text{O}$ for the bare DMSO which appears at 1045 cm^{-1} , is shifted to 1025 cm^{-1} for $\text{PbI}_2\cdot\text{DMSO}$ adduct, and 1017 cm^{-1} for $\text{Cs}_{0.1}\text{FA}_{0.9}\text{PbI}_3\cdot\text{DMSO}$ (Figure 5.3).

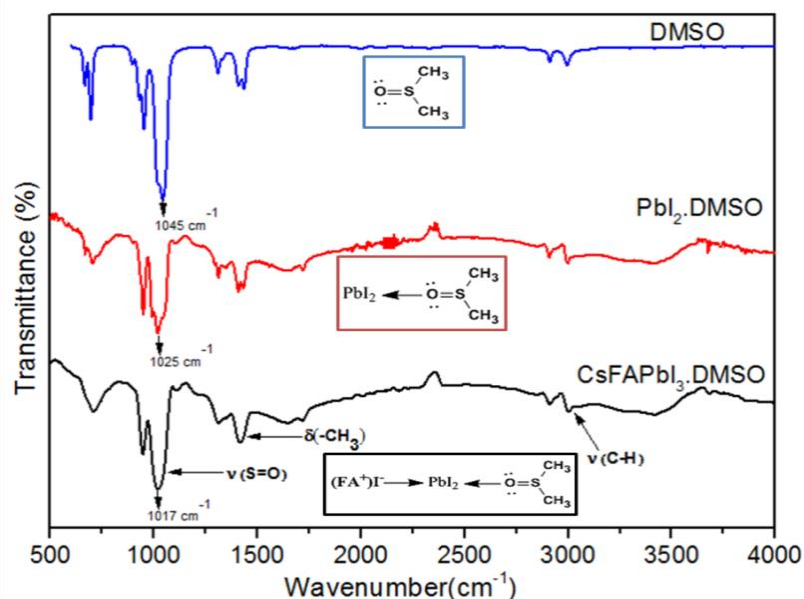


Figure 5.3 FTIR spectra of DMSO (solvent), $\text{PbI}_2\cdot\text{DMSO}$ (powder, adduct), and $\text{FAI}\cdot\text{PbI}_2\cdot\text{DMSO}$ (powder, adduct)

According to the theory of harmonic motion for the diatomic model, vibrational frequency is directly proportional to the square root of the force constant (Kim et al., 2012). Thus, a decrease in force constant indicates the decrease in $\text{S}=\text{O}$ stretching frequency, which is mainly due to the gradual decrease in bond strength between sulfur and oxygen as a consequence of adduct formation with DMSO. It is observed that $\text{S}=\text{O}$

stretching wavenumber for $\text{Cs}_{0.1}\text{FA}_{0.9}\text{PbI}_3\cdot\text{DMSO}$ is lower than that of $\text{PbI}_2\cdot\text{DMSO}$, which is lower than the bare DMSO. As more the number of Lewis acids interact with DMSO, the strength of the S=O bond is expected to be decreased. Based on these observations, we propose that DMSO forms a relatively stable and stronger coordinate bond with FAI and PbI_2 than other solvents such as DMF.

The schematic representation of the solar cell device architecture and the fabrication processing steps are shown in **Figure 5.4a-b**. In brief, the device architecture includes a triple-layer structure of mesoscopic TiO_2 nano-crystallites (around 450 nm), ZrO_2 as an insulating layer (around 1.2-1.4 μm) and mesoscopic carbon layer (10-12 micron), which is screen printed on a compact titanium dioxide deposited on a patterned FTO glass. Perovskite solution was infiltrated through the printed porous stack of different layers of carbon, ZrO_2 , and TiO_2 by manually dripping the solution using a micropipette. The various layers of the screen-printed mesoscopic solar cell were infiltrated with $\text{Cs}_{0.1}\text{FA}_{0.9}\text{PbI}_3$ perovskite and are clearly distinguishable from the cross-section SEM images as shown in **Figure 5.4c**. From the microstructural analysis of perovskite films formed using various solvents, it can be concluded that the best infiltration was observed in only DMSO-based devices. It may be due to the formation of the stable intermediate adduct, that results in uniform and controlled crystallization of the perovskite layer. However, devices based on DMF:DMSO, DMF, and GBL:DMSO show less solvent-perovskite interaction, which results in poor infiltration patterns. Here, it has been observed that only a few parts of the devices got infiltrated, and it can be considered as one of the primary reasons for poor efficiency. One can guess the imperfect contact of FA-DMF, FA-GBL:DMSO, FA-DMF:DMSO layers to poor wettability of the perovskite solution. The different natures of the intermediate phases resulting from the coordinative bond result in the change in the morphology of the $\text{Cs}_{0.1}\text{FA}_{0.9}\text{PbI}_3$ film, as it affects both the nucleation and growth of the film.

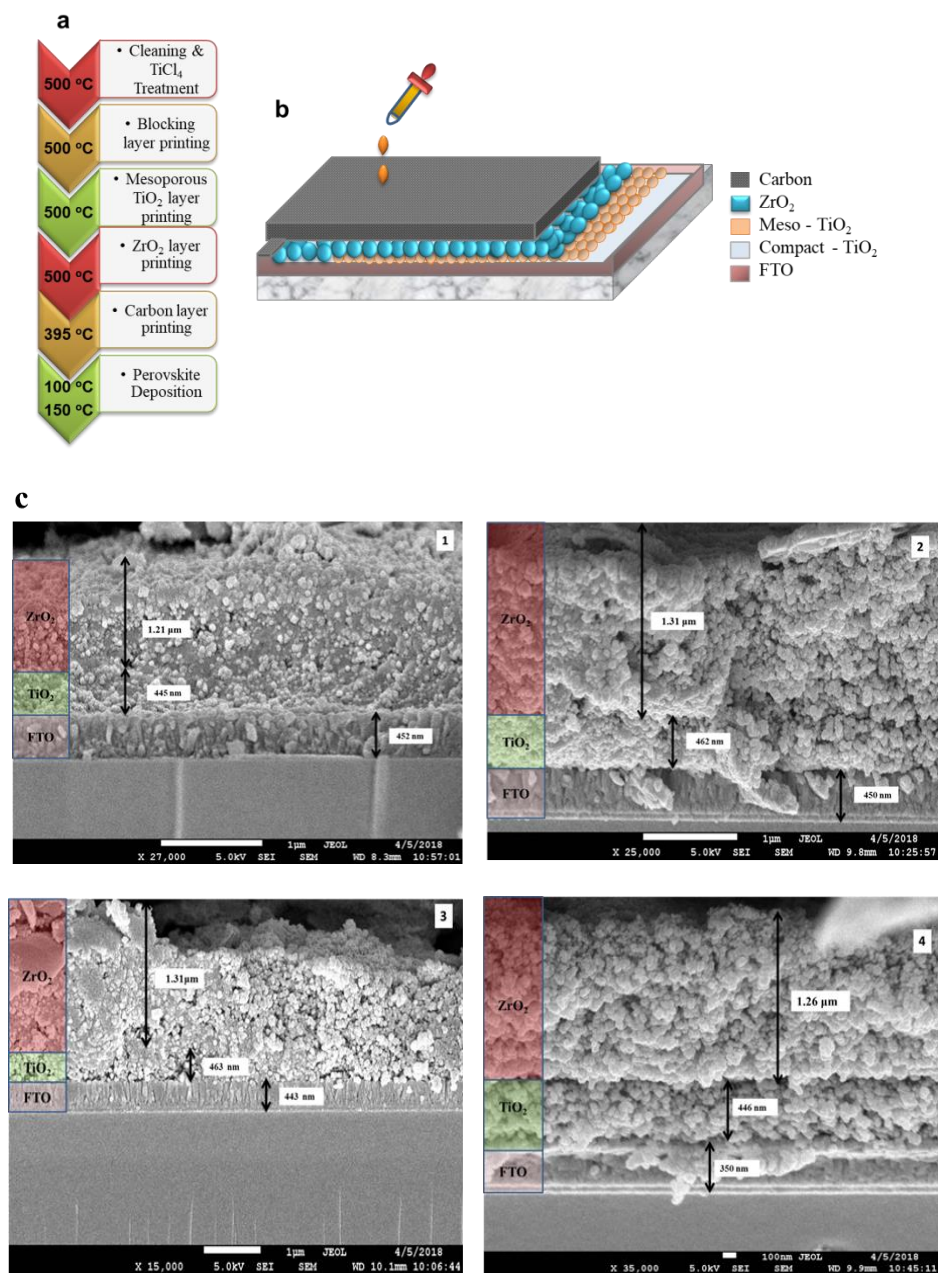


Figure 5.4 a) Device fabrication procedure; b) Schematic representation of the device architecture; c) Cross-section SEM images of the perovskite/carbon solar cells fabricated from 1) DMSO, 2) DMF-DMSO, 3) DMF, and 4) GBL-DMSO

Electrochemical impedance spectroscopy (EIS) is one of the major techniques to characterize the interfacial charge-transfer process across the semiconducting interfaces and is extensively used to study carrier transport and recombination mechanism in PSCs.

Impedance spectra of the CsFAPbI₃ cells were measured in dark conditions (**Figure 5.5**). In carbon-based devices, charge-transfer processes occur at the cathode (TiO₂/perovskite interface), and at the anode (carbon/perovskite interface) and recombination happens within the active area. From the Nyquist plot, a single distinct loop has been obtained which corresponds to the single RC element due to the charge-transfer at the interface between carbon and perovskite (hole injection or extraction). The better interface contact with a significantly large contact area between TiO₂ and perovskite leads to the low charge transfer resistance and hence the fast electron injection (Bashir et al., 2019; Duan et al., 2017; Mhaisalkar et al., 2017).

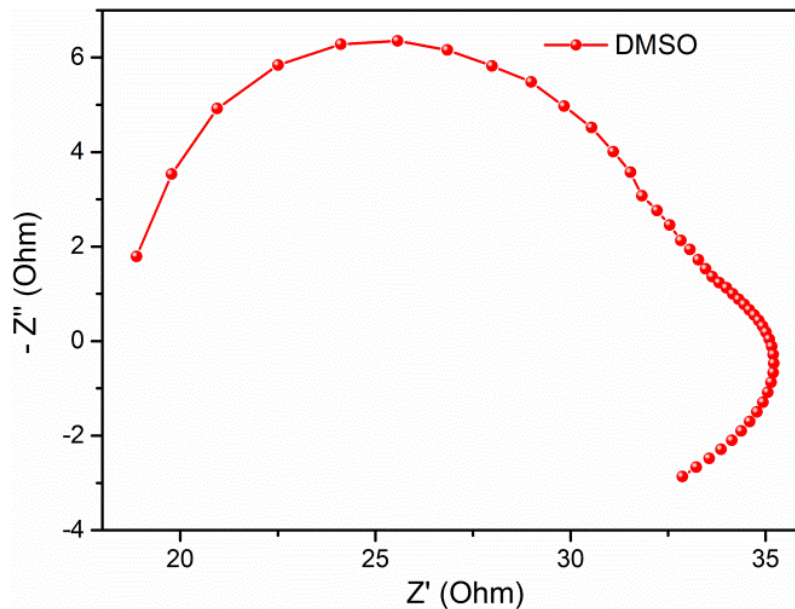


Figure 5.5 Electronic impedance spectroscopy characteristics in the form of the Nyquist plot of the device fabricated using DMSO as a solvent under dark

Figure 5.6a-b indicates the UV-Vis absorption spectra and steady-state normalized photoluminescence (PL) spectra of Cs_{0.1}FA_{0.9}PbI₃ films prepared from CsI·FAI·PbI₂·Solvent (DMSO/DMF:DMSO/DMF/GBL:DMSO) adducts. Over the entire wavelength region, the films prepared using DMSO was found to be highly intensified. The increased crystal size of perovskite enhances the absorption capacity, which leads to higher light-harvesting efficiency, as previously reported in the literature. A slight blue-

shifted absorption onset was observed in the presence of different solvents. Normalized PL peaks show a 10 nm blue shift starting from GBL:DMSO to DMSO. The low absorption of the perovskite films fabricated using DMF/DMF-DMSO is mainly ascribed to the low crystallinity in the film. The reason behind the lower absorption of film fabricated using GBL:DMSO is attributed to the relatively lower solubility of CsI in the solvent. The relatively improved absorbance of the $\text{Cs}_{0.1}\text{FA}_{0.9}\text{PbI}_3$ layers fabricated using DMSO solvent are higher than that of films fabricated from other solvents due to the uniform film coverage and higher volume fraction (also observed from XRD peak intensity as discussed) of crystalline perovskite film.

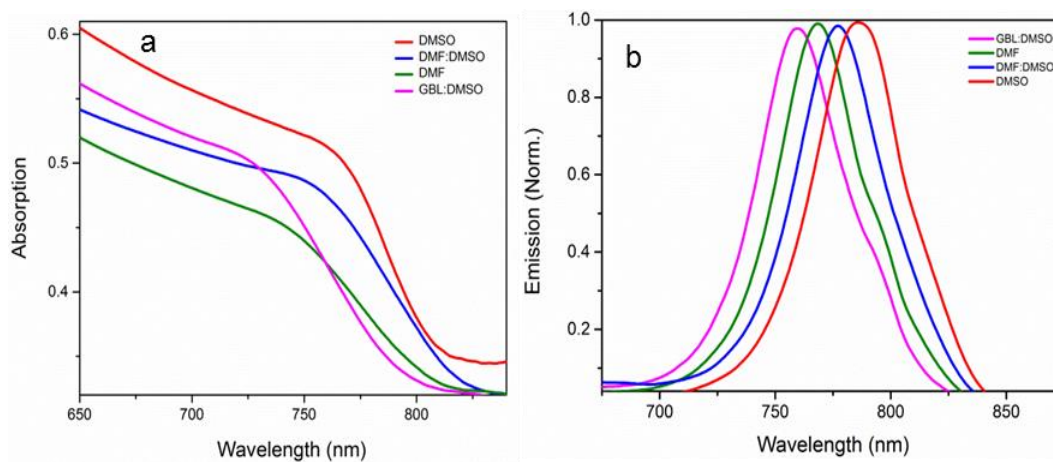


Figure 5.6 Photovoltaic properties. a) UV-Vis absorption spectra, b) steady-state PL spectra of $\text{Cs}_{0.1}\text{FA}_{0.9}\text{PbI}_3$ devices fabricated using various solvents

5.1.3.2 Device performance studies

Current-voltage (I - V) characterizations of the PSCs were performed to evaluate the performance of $\text{Cs}_{0.1}\text{FA}_{0.9}\text{PbI}_3$ based devices in different solvent combinations using the abovementioned architecture. All the devices were fabricated by keeping the $\text{TiO}_2/\text{ZrO}_2/\text{Carbon}$ film at a constant thickness ($\text{TiO}_2 \sim 460$ nm, $\text{ZrO}_2 \sim 1.2$ μm , and carbon ~ 10 μm). **Figure 5.7** shows the current density-voltage (J - V) curves of $\text{Cs}_{0.1}\text{FA}_{0.9}\text{PbI}_3$ devices using different solvents such as DMSO, DMSO:DMF, DMF, and GBL:DMSO and were measured under AM 1.5G simulated solar irradiation (100

$\text{mW}\cdot\text{cm}^{-2}$). The experiment was conducted under relative humidity $>60\%$ and the corresponding photovoltaic parameters are summarized in **Table 5.1**.

Table 5.1 Photovoltaic parameters of the $\text{Cs}_{0.1}\text{FA}_{0.9}\text{PbI}_3$ PSCs fabricated using the different combinations of solvents for a device with an active area of 0.09 cm^2

Solvent	J_{SC} ($\text{mA}\cdot\text{cm}^{-2}$)	V_{OC} (V)	FF (%)	PCE (%)
DMSO	21.08	0.83	71.08	12.33
DMSO:DMF	20.80	0.81	59.12	10.06
DMF	19.41	0.75	55.79	8.07
DMSO:GBL	13.91	0.73	45.19	4.62

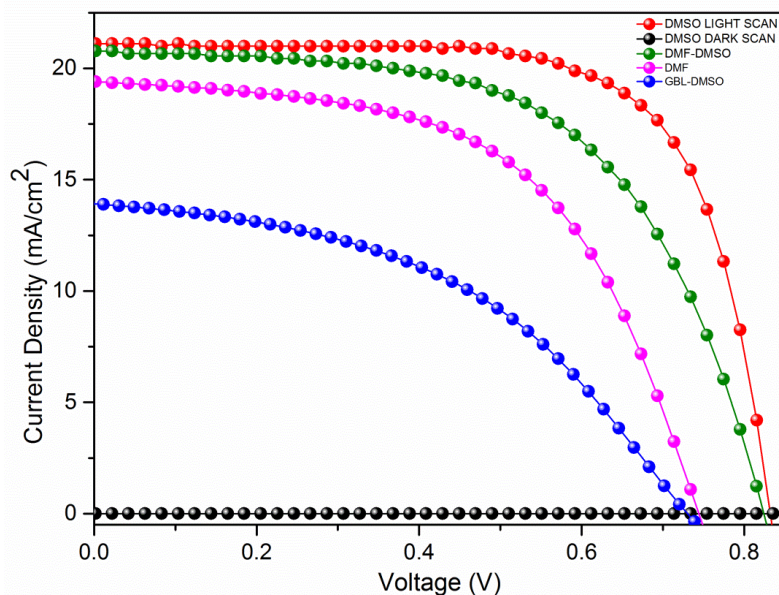


Figure 5.7 J - V characteristics of the PSCs fabricated using different solvents under standard AM 1.5 G illumination at $100\text{ mW}\cdot\text{cm}^{-2}$ and in dark

The steady-state PCE of the supreme device with DMSO as a precursor solution was found to be 12.33 % (J_{SC} : $21.1\text{ mA}\cdot\text{cm}^{-2}$, V_{OC} : 0.82 V and FF : 0.71). Similarly, the PCE of a device made of DMF:DMSO is 10.06% (J_{SC} : $20.8\text{ mA}\cdot\text{cm}^{-2}$, V_{OC} : 0.81 V and FF : 0.59), DMF is 8.07% (J_{SC} : $19.40\text{ mA}\cdot\text{cm}^{-2}$, V_{OC} : 0.75 V and FF : 0.55), and finally GBL:DMSO is 4.62 % (J_{SC} : $13.91\text{ mA}\cdot\text{cm}^{-2}$, V_{OC} : 0.73 V and FF : 0.45). In addition, C-PSC device with an optimized large area (0.7 cm^2) having perovskite composition

$\text{Cs}_{0.1}\text{FA}_{0.9}\text{PbI}_3$ using DMSO also reaches a considerable *PCE* of 10.1 % under ambient air conditions.

As can be seen in **Figure 5.8a-d**, the adduct-induced $\text{Cs}_{0.1}\text{FA}_{0.9}\text{PbI}_3$ in DMSO displays the photovoltaic parameters with minor standard deviation, results in average short-circuit photocurrent density (J_{SC}) of $21.1 \pm 0.2 \text{ mA}\cdot\text{cm}^{-2}$, open-circuit voltage (V_{OC}) of $0.85 \pm 0.02 \text{ V}$, fill factor (*FF*) of 0.65 ± 0.11 , and *PCE* of $10.5 \pm 1.93\%$. The observed rapid charge transport in the devices made of DMSO solvent enhances the overall J_{SC} of devices which could be due to higher crystallinity of $\text{Cs}_{0.1}\text{FA}_{0.9}\text{PbI}_3$ perovskite in DMSO. Similarly, the increased V_{OC} of the device may be attributed to the reduced electron recombination.

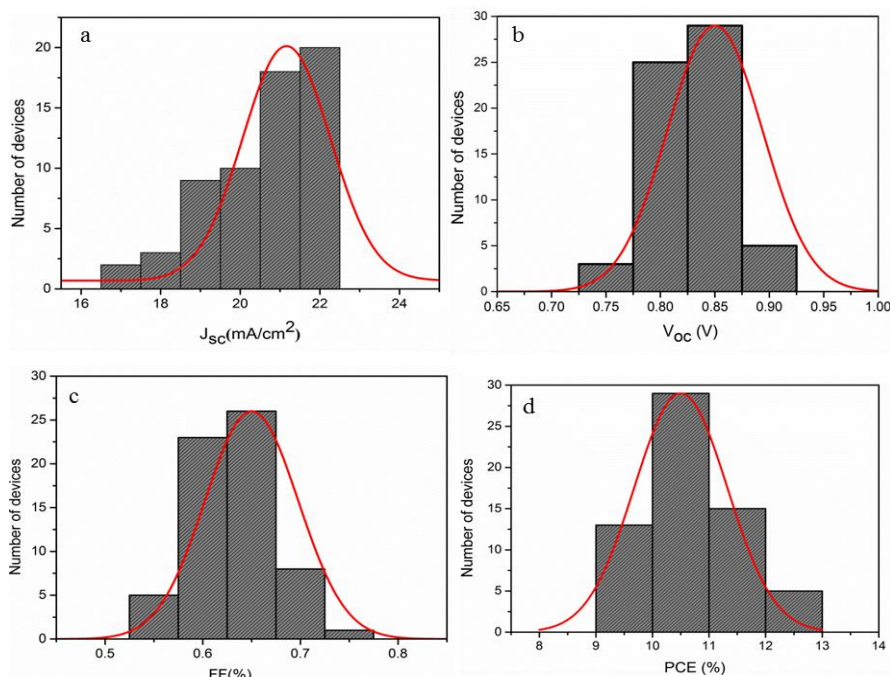


Figure 5.8 Reproducible and efficient $\text{Cs}_{0.1}\text{FA}_{0.9}\text{PbI}_3$ PSCs fabricated using DMSO as a solvent. Histograms of a) short-circuit current density (J_{SC}), b) open-circuit voltage (V_{OC}), c) fill factor (*FF*), and d) power conversion efficiency (*PCE*)

The origin of the change in photocurrent density (J_{SC}) was investigated by external quantum efficiency (EQE) spectra as shown in **Figure 5.9**. The measured J_{SC} values of all devices are well consistent with the integrated current density values

estimated from *IPCE* spectra indicating that the emission of our solar simulator is in coordinate with the spectrum of standard air mass 1.5. The onset of the *IPCE* spectra for the $\text{Cs}_{0.1}\text{FA}_{0.9}\text{PbI}_3$ device is at 840 nm (DMSO), 830 nm (DMF:DMSO), 820 nm (DMF), and 800 nm (GBL:DMSO) are in accordance with the UV-Vis spectra. The higher *IPCE* value (above 80%) for the $\text{Cs}_{0.1}\text{FA}_{0.9}\text{PbI}_3$ in DMSO has been observed as compared to other devices. The compositional inhomogeneity could be the reason for the observed discrepancies in *IPCE* on-set.

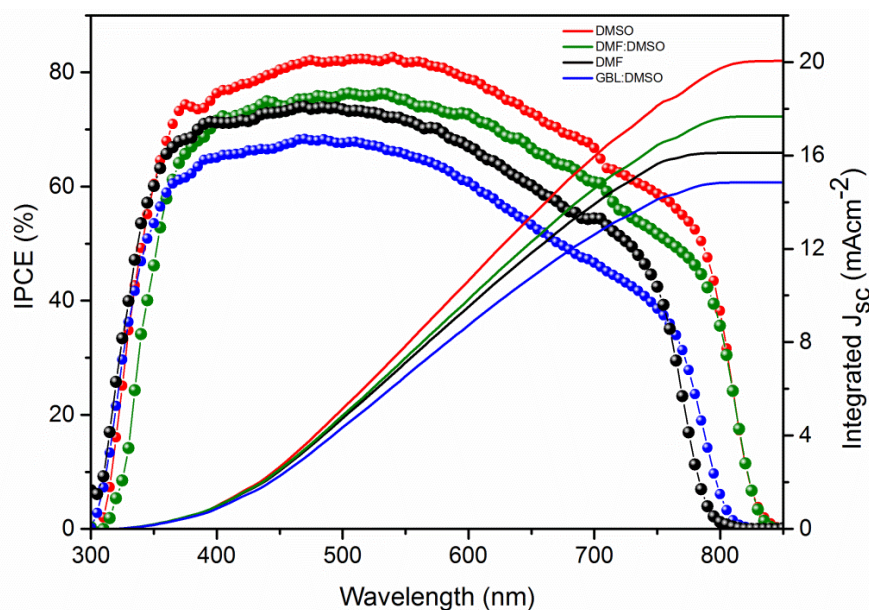


Figure 5.9 *IPCE* spectra of the $\text{Cs}_{0.1}\text{FA}_{0.9}\text{PbI}_3$ perovskite solar cells fabricated using various solvents and their integrated currents

5.1.3.3 Stability and reproducibility studies of the devices

To confirm the long-term stability of perovskite solar cells, the devices made from various solvent combinations were measured under ambient atmospheric conditions, as shown in **Figure 5.10**. As explained earlier, carbon not only acts as an HTM but also provides good encapsulation for perovskite solar cells and ultimately helps in improving device stability by reducing degradation caused by environmental humidity. Generally, the selection of solvent can majorly affect the stability of PSCs. The overall *PCE* deterioration is observed to be negligible in case of devices prepared using DMSO

solvent as compared to DMSO:DMF, DMF, and GBL:DMSO based devices due to the superior quality of crystalline perovskite with DMSO. In the case of DMSO, there is less vulnerability to ambient moisture. The devices with GBL:DMSO solvent combination is not much stable in ambient air for a longer time, causing a drastic decrease in the overall efficiency of the devices. The main cause for the remarkable decrease in PCE of cells made up of DMF:DMSO, DMF, and GBL:DMSO is attributed to a relatively poor crystallization and high degradation on exposure to moisture, thus leads a decrease in J_{SC} and FF , with minor V_{OC} reduction.

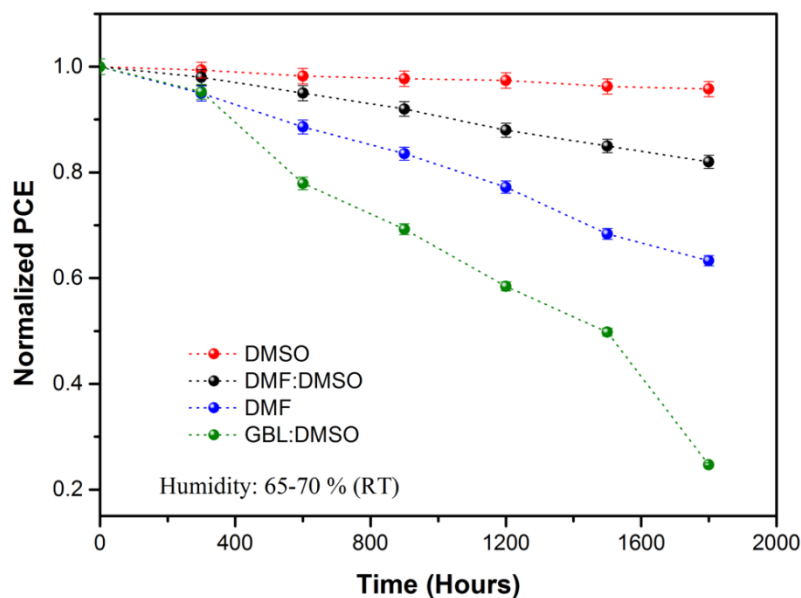


Figure 5.10 The normalized PCE decay of the devices fabricated using different solvent combinations of solvents under ambient environmental conditions and under standard AM 1.5 sun illuminations

Out of all solvents, devices made up of DMSO were found to be much superior in terms of stability and reproducibility. The devices fabricated using other solvents show relatively lower reproducibility as compared to cells prepared using DMSO, which is mainly due to the fact that $\text{Cs}_{0.1}\text{FA}_{0.9}\text{PbI}_3$ perovskite quality is significantly dependent on the nature of the solvent, dripping amount, wettability of surface, infiltration, and annealing time which are observed to be superior in case of pure DMSO. **Figure 5.11a-d** depicts the reproducibility data of devices fabricated in four different solvents such as

DMSO, DMSO:DMF, DMF, and GBL:DMSO suggesting only DMSO can be considered as a potential solvent for the printable carbon-based whole mesostructured PSCs.

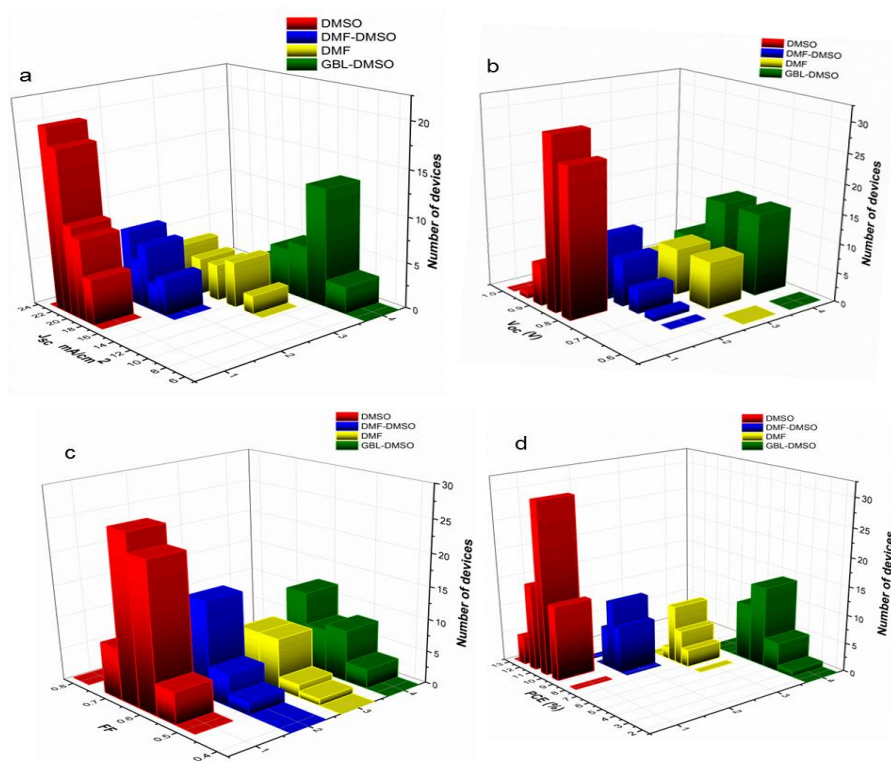


Figure 5.11 Reproducibility data of $\text{Cs}_{0.1}\text{FA}_{0.9}\text{PbI}_3$ perovskite in various solvents. The statistical distribution of photovoltaic parameters, a) J_{sc} , b) V_{oc} , c) FF , and d) PCE across 62 devices

5.1.3.4 Scaling up

From a commercialization point of view, it is essential to produce bulk-scale, highly stable, and efficient carbon-based PSCs modules. By using a two-step perovskite deposition method, it is quite hard to get uniform and high-purity films of perovskite on large substrates in the lab. This scaling-up problem of the two-step deposition method remarkably limits the PCE of highly stable C-PSCs modules. Another major problem is the selection of appropriate solvents in order to obtain a high-quality perovskite layer at a bulk scale. Out of all the solvents mentioned above, DMSO is considered to be a greener and safer solvent, as DMF is more carcinogenic, and extra safety measurements need to be taken while handling bulk scale in industries. The present research on solvent selection

for single-step deposition of mixed cation perovskites gives a better idea for the development of bulk scale perovskite deposition methods for the commercialization of C-PSCs.

5.1.4 CONCLUSIONS

In summary, a detailed investigation has been carried out on the selection of appropriate solvent for a single-step deposition of mixed-cation perovskite for highly reproducible carbon-based PSCs using the Lewis acid-base adduct approach. From the results, it has been concluded that *PCE* values are highly dependent on the crystalline quality, as well as infiltration of the perovskite layer. The results were found to be quite encouraging in the case of devices made up of solvent DMSO, yielding the highest *PCE* (12.33 %). This work may provide a methodological basis to further enhance the commercialization prospect of the carbon-based perovskite solar cells using mixed cation composition, as DMSO is an industrially acceptable potential solvent.

5.2 LARGE-AREA MAPbI₃ PEROVSKITE SOLAR CELLS (70 CM²): IMPROVING THE PERFORMANCE BY INCORPORATING CESIUM HALIDE IN MESOPOROUS TiO₂

5.2.1 Introduction

The introduction of Cs or related compounds in TiO₂ mesoporous and compact layers has gained much interest for the performance enhancement of planar devices (Seo et al., 2018). Cesium introduction into the TiO₂ compact layer helps in enhancing the conduction band maximum and reducing interfacial resistance. By introducing CsX (X= Br, I) modification (coating) to mesoporous TiO₂, it is possible to induce a shift of titanium (Ti) and oxygen (O) to lower energy and to reduce the areal density of pin-holes, which further implements the suppression of oxygen vacancies operating as an electron trap (Yang et al., 2020). In addition, the size of the TiO₂ nanoparticles in the mesoporous layers plays an important role in enhancing the efficiency of planar PSCs. From a detailed introduction and comprehensive literature survey on TiO₂ modification in planar

architecture (**Chapter 1**, section 1.6.4 and 1.10.4), it is evident that the mesoporous layer of TiO₂ with CsX as an active interface modifier has been used in the fabrication of carbon-based perovskite solar cells (C-PSCs) with an active area of 0.7 cm². Further, large areas of 70 cm² monolithic perovskite solar modules were fabricated for further tuning them to the industrial needs. The detailed solar cell fabrication and characterization procedures have been given in section 5.1.2. In the proposed PSCs, the composition of MAPbI₃-AVAI crystal phase and light absorption properties were comprehensively investigated by powdered X-ray diffraction (XRD) and UV/Visible absorption spectra. The steady-state photoluminescence (PL) and time-resolved photoluminescence (TRPL) decay experiments were also conducted to reveal the effect of cesium halide modified TiO₂ on charge extraction and carrier lifetime, respectively. The quantum efficiency measurements were performed for various CsX-modified TiO₂ based C-PSCs to obtain their incident photon to current conversion efficiency (*IPCE*) spectra. Finally, the improved stability aspects were presented by evaluating the current-voltage curves on C-PSCs exposed to ambient and high temperatures conditions for an extended period.

5.2.2 Results and discussion

5.2.2.1 Structural and optical characterization of perovskite films

The sample codes of different mesoporous TiO₂ (mp-TiO₂) layers used are noted as i) mp-TiO₂ made of nanoparticles of size 30 nm represents standard (30NR-D), ii) mp-TiO₂ made of porous nanobeads of size 40 nm represents standard (40NR-D), iii) mp-TiO₂ made of CsX (X= Cl, Br and I) modified porous nanobeads of 40 nm size correspond to CsCl@TiO₂, CsBr@TiO₂, and CsI@TiO₂, respectively. The respective mp-TiO₂ of different formulations was deposited on FTO/c-TiO₂ and subsequently, ZrO₂, and carbon layers were formed on top of mp-TiO₂. Finally, the perovskite (methylammonium lead iodide, MAPbI₃-AVAI) solution was infiltrated from the top.

The effect of various mp-TiO₂ on the crystallization of perovskite was investigated by conducting X-ray diffraction (XRD) studies and the corresponding

diffraction patterns are shown in **Figure 5.12**. From the figure, it can be concluded that there is no apparent difference among the perovskites deposited on different types of mp-TiO₂. The peak positions in the observed diffraction patterns are consistent with that of the perovskite phase. The diffraction peaks at 14.10°, 21.10°, 23.57°, 24.51°, 28.39°, 31.87°, 40.56°, and 43.24° confirm the perovskite planes of (110), (112), (211), (202), (220), (310), (224), and (314), respectively. Here, the absence of residual PbI₂ peaks in the traces clearly demonstrates the purity of the perovskite phase in all the samples irrespective of the type of mp-TiO₂ layer used. Further, the observed full width at half-maximum (FWHM) of the (110) peak and intensity of all other peaks originating from MAPbI₃ indicate the insignificant difference between unmodified and modified TiO₂ based samples. Furthermore, the average perovskite crystal size was calculated from XRD measurements using the Scherrer equation and it was found to be about 22-23 nm for all the substrates with modified or unmodified mp-TiO₂. Thus, these results evidently imply that the CsX modified mp-TiO₂ does not influence much on the crystal growth of the perovskite films.

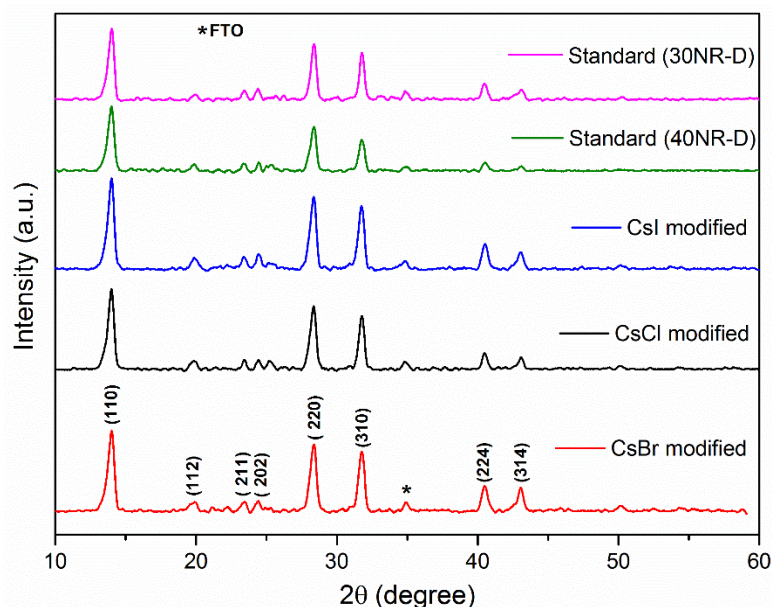


Figure 5.12 X-ray diffraction pattern of MAPbI₃ perovskite films deposited on ‘FTO/c-TiO₂/mp-TiO₂ (with and without CsX)’ substrates annealed at 60 °C for 1 h

Figure 5.13a depicts the schematic representation of the carbon-based device architecture and fabrication procedure. In the present study, for all the devices we followed the similar fabrication procedure as given in section 5.1.2.2, and the only exception being the use of different types of modification in mp-TiO₂. **Figure 5.13b** displays the cross-sectional SEM images showing the multi-layered device with FTO, compact TiO₂, CsBr modified and unmodified mp-TiO₂ (~450 nm), mp-ZrO₂ (~1.2-1.4 μm) and mp-Carbon (~10-12 μm). The SEM image confirms the proper infiltrated MAPbI₃-AVAI perovskite into the mesoporous layers without leaving any unfilled regions in the mesoporous TiO₂ and ZrO₂.

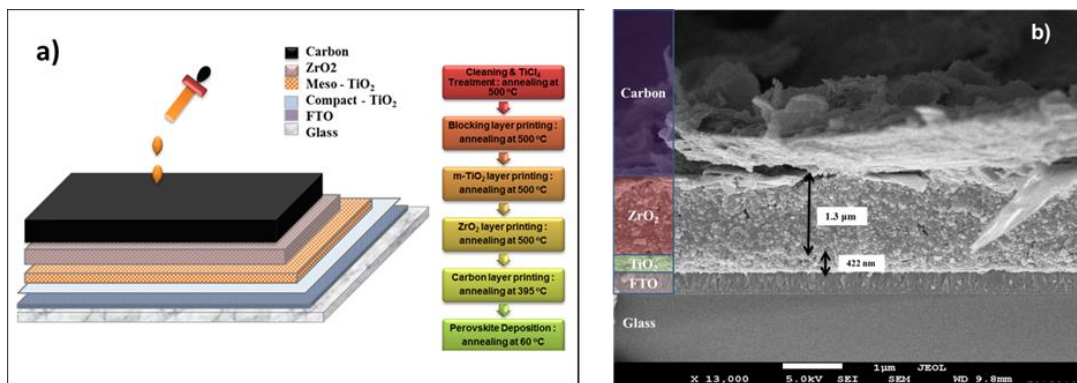


Figure 5.13 (a) Schematic illustration of the device architecture with a flow chart showing the fabrication procedure, (b) Cross-sectional SEM image of the CsBr modified C-PSCs

The kinetics of charge transfer between electron selective layers (ESLs) and perovskite absorber can be efficiently studied using steady-state photoluminescence (PL) and time-resolved photoluminescence (TRPL) spectroscopic studies. **Figure 5.14a** displays steady-state PL quenching of the MAPbI₃ films deposited on ‘glass/c-TiO₂/mp-TiO₂ (with and without CsX)’. As seen, the MAPbI₃ perovskite layer shows a characteristic PL emission with an emission peak at 766 nm, which corresponds to its bandgap. Also, the observed PL emission peak is rather broad, which spans in the range of 700-825 nm; this broad emission is attributed to the nanocrystalline nature of perovskite in the mesoporous structure. When the perovskite gets deposited on the electron transport layer (ETL), the photoelectrons in the conduction band of perovskite

would transfer to the conduction band of mp-TiO₂ or modified mp-TiO₂. The extent of electron transfer from perovskite to mp-TiO₂ reduces the radiative recombination in perovskite and, hence, causes the reduction in PL intensity, which is termed as PL quenching. From **Figure 5.14a**, it is clear that the PL quenching for the CsX@TiO₂ samples is higher than that of unmodified mp-TiO₂. This observed high PL quenching clearly indicates the faster electron extraction at the CsX modified mp-TiO₂/perovskite interface. Among the three halides, the electron extraction at the ‘CsBr modified mp-TiO₂/perovskite’ is expected to be superior.

To investigate the interfacial carrier dynamics and electron injection process from perovskite to m-TiO₂, the time-resolved TRPL measurements were conducted for the same films that were used in the PL quenching studies. **Figure 5.14b** represents TRPL decay plots of the MAPbI₃ films deposited on various mp-TiO₂. The PL decay time was estimated by a double exponential decay function to obtain relaxation lifetimes. The PL decay time was estimated by double exponential decay function to obtain relaxation lifetimes and the obtained results are summarized in **Table 5.2**.

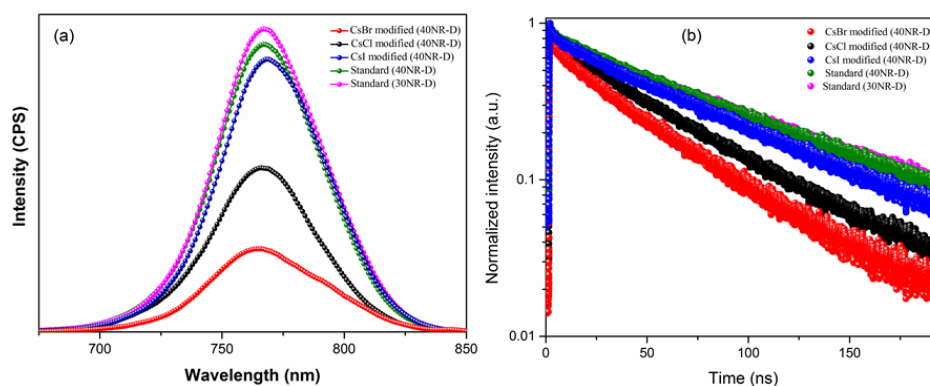


Figure 5.14 (a) Steady-state photoluminescence (PL) spectra and (b) Normalized time-resolved photoluminescence (TRPL) decay plots of the MAPbI₃ perovskite thin films deposited on glass/c-TiO₂/mp-TiO₂ layer

In TRPL, the fast decay component (τ_1) should attribute to the injection of free carriers in the perovskite crystals to the charges collection materials, while the longer part (τ_2) should be the recombination of free carriers in the radiative channel. **Table 5.2** reports the τ_1 and τ_2 components with their relative weights. In all cases, it has been

observed that the average lifetimes decrease with the Cs modifications. Comparing standard 40 NRD and CsI modified, it has been noticed that the τ_2 component becomes shorter while the τ_1 slightly increases but the relative weight decreases. As a result, the average lifetime is always shorter confirming the more efficient charge extraction when the passivation is applied. Further, an average PL decay time (τ_{avg}) estimated for the perovskite deposited on CsBr@TiO₂ ($\tau_{\text{avg}} = 22$ ns) was found to be less than that of the perovskite deposited on 30 NR-D mp-TiO₂ ($\tau_{\text{avg}} = 65$ ns). These results confirm that the CsX modification on mp-TiO₂ has a positive effect on the charge extraction, especially, the CsBr modified mp-TiO₂ is expected to extract the photoelectrons efficiently from the perovskite.

Table 5.2 Fitting parameters for the time-resolved PL measurements

Samples	A1	τ_1 (ns)	A2	τ_2 (ns)	τ_{avg} (ns)
Standard 30NRD	0.27	4.28	0.73	87.76	64.50
Standard 40NRD	0.25	3.96	0.75	81.31	61.83
CsI modified	0.17	6.39	0.73	72.95	61.43
CsCl modified	0.21	6.9	0.72	53.12	43.35
CsBr modified	0.53	1.801	0.47	44.13	21.78

Where τ_1/τ_2 represents the decay time of fast/slow decay; A1/A2 represents the amplitude of the fast-decay/slow-decay component. The PL decay can be fitted by a biexponential function: $y = A1 \exp(-x/\tau_1) + A2 \exp(-x/\tau_2) + y_0$

5.2.2.2 Device performance studies

With the purpose of exploring the influence of CsX modification on the mp-TiO₂ beads, we fabricated different carbon-based PSCs with the aforementioned device architecture and recorded their characteristic current density *versus* voltage (*J-V*) plots. These curves were obtained under the sun (AM 1.5G, 100 mW.cm⁻²) illumination as well as in dark conditions, with both forward and backward scans as shown in **Figures 5.15**. All the experiments were conducted in an ambient atmosphere with relative humidity 60-70% and the corresponding cell performance parameters are tabulated in **Table 5.3**. The comparative analysis of the results was done in two ways, firstly the improvement in PCE

of C-PSCs with mp-TiO₂ of 40 nm particle size (standard 40NR-D) over that of 30 nm particle size (standard 30NR-D), secondly, the PCE enhancement using the CsX modified mp-TiO₂ of 40 nm particle size (CsX@TiO₂).

To study the effect of particle size on the cell-performance, the *J-V* plots of C-PSCs containing different sized mp-TiO₂ (30NR-D, 40NR-D) were recorded. These plots are shown in **Figure 5.15** and the corresponding data are summarized in **Table 5.3**. From the data, it was observed that 40 NR-D mp-TiO₂ accommodates more perovskite infiltration into the mesostructure than that of the 30NR-D mp-TiO₂, because of the fact that the former has enhanced surface area with large pore volume. Therefore, the photocurrent density of standard 40NR-D (20.89 mA·cm⁻²) was found to be higher than that of standard 30NR-D (19.91 mA·cm⁻²). Also, a small increment in the *FF* was observed when the dimension of particles was increased from 30 nm to 40 nm, which might be due to the reduction in the electron transport resistance and improved filling of perovskite in the mesoporous structure of TiO₂. Conclusively, the results confirm that the 40NR-D mp-TiO₂ shows relatively better *PCE* (11.45 %) than that of conventional 30NR-D (10.99 %) in carbon-based PSCs, with an advantage of enhanced short circuit current density (*J*_{SC}).

To further enhance the device performance, the structure of 40NR-D TiO₂ was modified with CsX (X= Cl, Br, and I) and the modified beads were employed in C-PSC fabrications. For preliminary understanding, small area C-PSCs (active area = 0.7 cm²) were fabricated using CsX@TiO₂. Their performance data were compared with that of standard 40NR-D as shown in **Table 5.3**. Evidently, the overall *PCE* of the former (CsX modified) devices are relatively higher than the latter (unmodified 40NR-D) PSCs, demonstrating enhancement in their *J*_{SC}, open-circuit voltage (*V*_{OC}), and fill factor (*FF*). Further, among the CsX doped C-PSCs, CsBr modified devices exhibit the highest *PCE* of 12.59 %, which is significantly revamped when compared to the other devices, with enhanced *J*_{SC} and *FF*, by keeping *V*_{OC} is almost constant. The significant *PCE* improvement can be ascribed to their higher *J*_{SC} compared to the CsCl and CsI modified devices. This observation is logical, as the perovskite coated on CsBr@TiO₂ shows the

highest PL quenching with the lowest carrier decay time among all, facilitating the fast photoelectron transfer from perovskite to ETL. This fast electron transfer is expected to increase the photocurrent (J_{SC}), as observed in CsBr modified C-PSCs. Further, the *PCE* improvements are clearly distinguishable from their *J-V* curves, as shown in **Figure 5.15**.

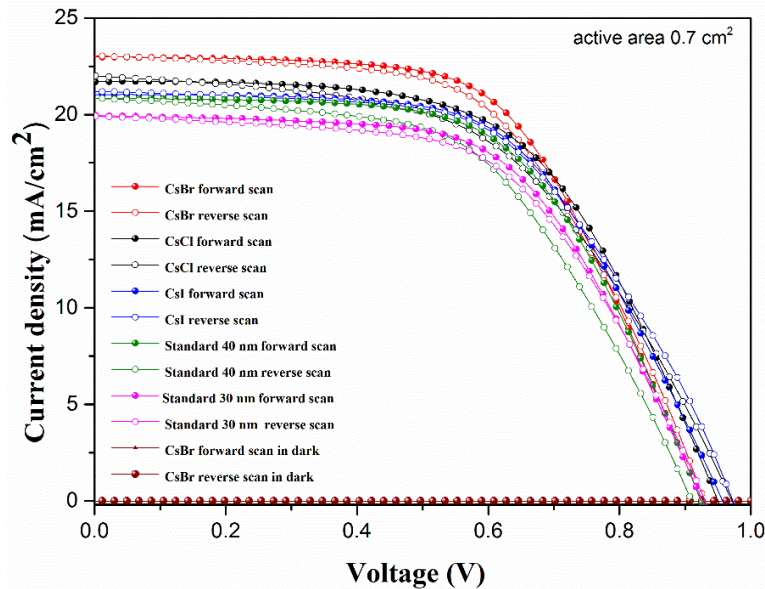


Figure 5.15 *J-V* curves of MAPbI₃ C-PSCs fabricated with and without CsX modification, recorded under standard AM 1.5 G illumination at 100 mW·cm⁻² irradiance and in the dark

Table 5.3 Photovoltaic parameters of modified and unmodified C-PSCs with an active area of 0.7 cm² in both forward (F) as well as reverse (R) scan

ETL type	J_{SC} (mA·cm ⁻²)		V_{OC} (V)		FF (%)		PCE (%)	
	R	F	R	F	R	F	R	F
CsBr-TiO ₂	23.04	23.01	0.93	0.92	56.95	59.49	12.20	12.59
CsCl-TiO ₂	22.19	21.96	0.94	0.92	53.84	58.93	11.26	12.01
CsI-TiO ₂	21.38	21.52	0.95	0.93	56.57	58.58	11.66	11.78
Standard 40NR-D	20.89	20.82	0.90	0.92	55.28	59.12	10.46	11.45
Standard 30NR-D	19.91	19.93	0.92	0.92	57.35	59.10	10.61	10.99

The external quantum efficiency (EQE)/incident photon to current conversion efficiency (*IPCE*) spectra of all types of C-PSCs containing 30NR-D, 40NR-D, and CsX@TiO₂ ETL were recorded and their results are displayed in **Figure 5.16**. As seen from the spectra, the measured changes in photocurrent response in the range 300-800 nm are consistent with the integrated current density values, highlighting the emission of our solar simulator is in great agreement with the spectrum of standard AM 1.5G.

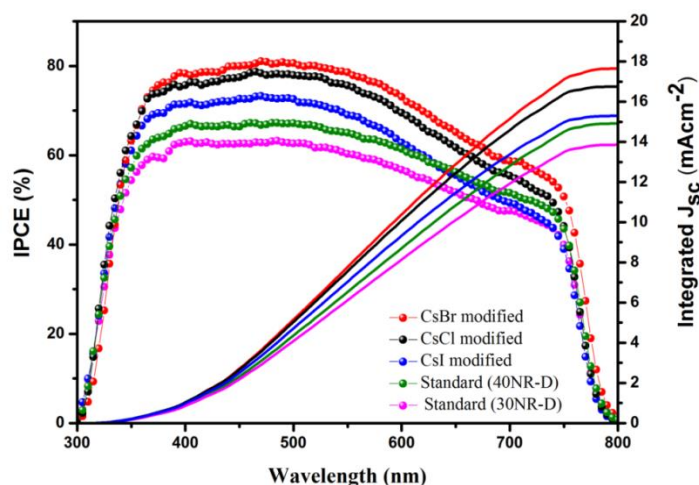


Figure 5.16 *IPCE* spectra of the C-PSCs containing various types of mp-TiO₂ and their integrated currents

On illumination, among all, the standard 30NR-D shows the lowest *IPCE* response in the entire wavelength range of 300-800 nm. Relatively higher *IPCE* was observed for the standard 40NR-D (67.4 %) than that of standard 30NR-D (63.5 %), which might be due to the high surface area of 40NR-D mp-TiO₂ that accommodates relatively greater amounts of perovskite in its mesostructure. Also, the high surface area of 40NR-D extracts the better photoelectrons from the infiltrated perovskite, resulting in improved photocurrent. On comparing, CsX@TiO₂-based C-PSCs display further improved *IPCE* when compared to that of 40NR-D devices. Among CsX@TiO₂-based C-PSCs, CsBr modified devices yield enhanced *IPCE* up to 81.4 % when compared to that of CsCl (78.3 %) and CsI (73.7 %). These results are in agreement with earlier observations of PL quenching and TRPL decay studies (**Figure 5.14**). Finally, it can be concluded that the CsBr modified C-PSCs display the highest *IPCE* compared to CsCl

and CsI modified devices, as they show the enhanced PL quenching and the lowest carrier decay time, thereby causing the highest photocurrent in the whole absorption range of 300-800 nm of illumination.

5.2.2.3 Scaling up

Indeed, for the commercialization of C-PSCs, it is necessary to develop large-scale modules with enhanced efficiency and stability. The majority of the efforts concern the PSC's stability at the perovskite/HTM interface. But it is also important to look for other long-term degradation mechanisms as in case of UV-induced perovskites degradation at the TiO₂/perovskite interface. A thorough literature review clearly indicates that there are no reports available on the modification of ETL by introducing CsX as an interface modifier for the fabrication of stable and efficient large-area C-PSCs. In order to develop the CsX modification in carbon-based large-area modules, the attention has been focused on fabricating highly stable large-area monolithic perovskite modules on a 100 cm² glass substrate (active area 70 cm²) with the knowledge of low dimension CsBr modified C-PSCs and it was successful in achieving it using semi-automated screen-printing technology, which can be directly adopted at an industrial scale. The acquired *J-V* plots of the printed 70 cm² modules of unmodified and CsX modified mp-TiO₂ are portrayed in **Figure 5.17a**. Further, **Figure 5.17b** displays the photographic image of one of the printed 70 cm² active-area C-PSCs, and **Table 5.4** shows the performance data of CsBr modified and unmodified (30NR-D) modules. Here, all the measurements were recorded at standard reporting conditions (AM 1.5G, 60-70% RH). From **Table 5.4**, it is clear that the device parameters qualitatively follow a similar trend as seen for small area C-PSCs. On scaling up, standard 40NR-D (9.79 %) yields improved performance in comparison with the conventional standard 30NR-D devices (8.39 %). As noticed, the CsBr modified module delivers the highest *PCE* of 11.55 % with enhanced *J_{SC}* of 22.62 mA·cm⁻² and *FF* of 56.02 % when compared to CsCl (11.10 %) and CsI (10.91 %) modified modules. Convincingly, these champion devices show the least performance-deviation among all the samples, showing superior *PCE* of 12.59 % on 0.7 cm² and 11.55 % on 70 cm².

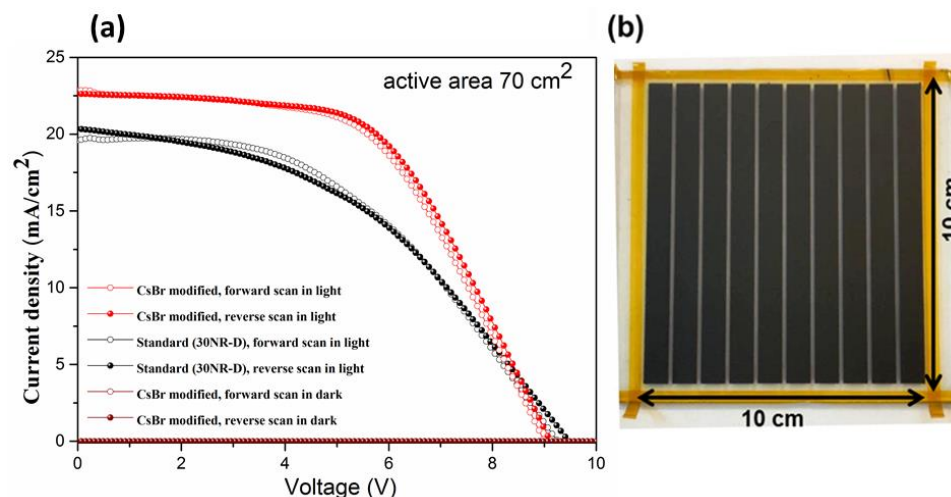


Figure 5.17 (a) J - V traces of unmodified and CsX mod. 40NR-D large area (70 cm^2) C-PSCs, recorded under one sun ($100 \text{ mW}\cdot\text{cm}^{-2}$) light irradiance and in the dark and (b) Photograph of printed CsX mod 40NR-D C-PSC module

Table 5.4 Solar cell parameters of the CsX modified and unmodified C-PSCs with an active area of 70 cm^2

Samples	J_{SC} ($\text{mA}\cdot\text{cm}^{-2}$)		V_{OC} (V)		FF (%)		PCE (%)	
	R	F	R	F	R	F	R	F
CsBr-TiO ₂	22.62	22.86	9.12	9.01	56.02	54.58	11.55	11.24
CsCl-TiO ₂	22.05	21.98	9.12	9.15	55.29	54.77	11.10	11.02
CsI-TiO ₂	21.20	21.47	9.64	9.09	53.37	54.88	10.91	10.72
Standard 40 NR-D	22.09	22.23	9.26	8.94	47.89	49.51	9.79	9.85
Standard 30 NR-D	20.65	19.32	9.25	9.19	43.58	47.35	8.39	8.47

In general, PSCs often exhibit the phenomenon of hysteresis where the forward scan does not trace back to the backward scan in their current-voltage (J - V) curves. This arises due to the presence of mobile ions in perovskite and the electronic traps at the charge collection layers. The C-PSCs normally exhibit low hysteresis as the ionic motion

in perovskite is hindered by the entire mesoscopic structure. Further, for the reduction of hysteresis, it is necessary to mitigate the trap density that minimizes interfacial recombination. Since the CsX surface modification on TiO₂ nanoparticles is expected to reduce the surface traps, the fabricated devices were tested for hysteresis. To evaluate the hysteresis quantitatively, a hysteresis index (HI) is defined using equation (5.1).

$$HI = \frac{J_{RS}(0.5V_{OC}) - J_{FS}(0.5V_{OC})}{J_{RS}(0.5V_{OC})} \quad (5.1)$$

where $J_{RS}(0.5V_{OC})$ and $J_{FS}(0.5V_{OC})$ represent the photocurrent density at 50% of V_{OC} for the reverse (RS) and forward (FS) scan directions, respectively; normally HI takes values between ‘zero to one.’ The value ‘zero’ indicates no hysteresis giving the meaning that there is no difference in voltage-dependent photocurrent in forward or reverse scan. The value ‘one’ indicates the high hysteresis, underlining a significant difference in voltage-dependent photocurrent (a magnitude of J_{RS}) in forward and reverse scans. The HI values were determined for C-PSCs made of unmodified and CsX modified mp TiO₂. As anticipated, CsX modified C-PSCs display relatively lower HI than that of standard 40NR-D (0.0367) and standard 30NR-D (0.0205). Further, among all CsX modified devices, the CsBr modified C-PSCs show the least HI value of ‘0.0065’, producing the best performance among all.

5.2.2.4 Stability and reproducibility studies of the devices

The overall C-PSC-performance stability depends mainly on the stability of infiltrated perovskite, indeed the rest of the device layers like mesoporous oxides and mesoporous carbon materials are chemically stable. The three key factors that influence perovskite stability are humidity, temperature, and light. It can be easily evaluated by testing and recording the *PCE* of the devices by exposing them to ambient air at room temperature and at high temperature.

The aging analysis on all the performance parameters (J_{SC} , V_{OC} , FF , and PCE) is presented in **Figure 5.18**. All the measurements have been recorded at 27°C, 65-70 % RH as a function of time (hours) on the modified as well as unmodified mp-TiO₂ without

encapsulation. During the experimentation, the devices were stored in dark under similar conditions in-between measurements. As seen from the results, the standard 40NR-D unencapsulated devices show relatively better stability than that standard 30NR-D. The reason behind it is that the titania layer offers a high surface area, making the perovskite better infiltrate into the mesostructure, thereby leaving no empty spaces. So, the moisture penetration into the 40NR-D based C-PSCs might be effectively blocked, resulting in the least degradation. Further, as the aging time progresses, the CsX modified C-PSCs show relatively less degradation than the pristine 40NR-D and 30NR-D devices. Out of three halides, the CsBr modified devices exhibit superior stability over 2700 h under an ambient atmosphere. This proves the enhanced stability of CsBr modification for carbon-based PSCs when compared to that CsBr modification in planar architecture. Besides, the long-term stability in C-PSCs could be also due to the inhibition of the photocatalytic activity of CsX@TiO₂. This argument is supported by a UV-stability study of CsX@TiO₂ devices.

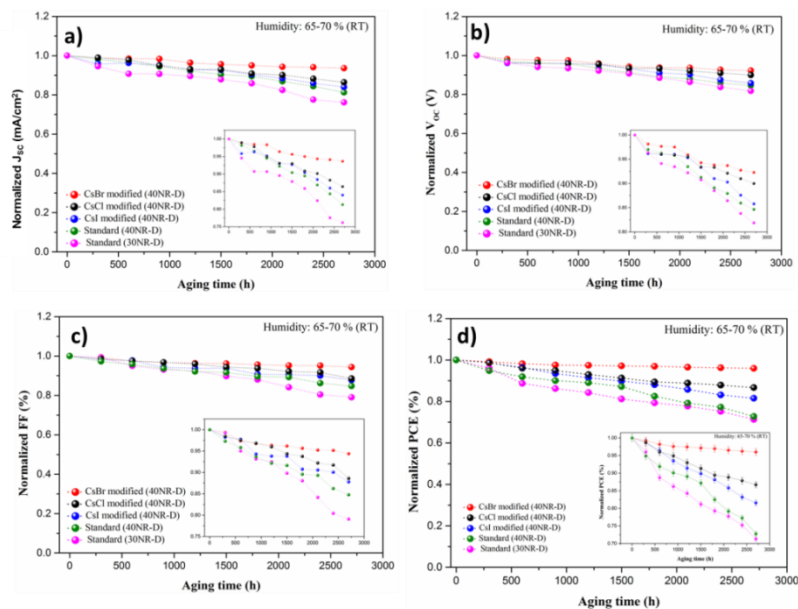


Figure 5.18 Aging analysis with respect to device performance parameters: (a) J_{SC} , (b) V_{OC} , (c) FF , (d) PCE as a function of time

To evaluate the UV-assisted perovskite degradation, studies were carried out for the films deposited on FTO/mp-TiO₂ (30NR-D and CsBr@TiO₂) substrates and were

exposed to the UV irradiation ($\lambda = 365$ nm) with an intensity of $523 \text{ mW}\cdot\text{cm}^{-2}$ in the air for 90 min. X-ray diffractograms were obtained on these two samples which are shown in **Figure 5.19**. The results reveal that the perovskite deposited on standard 30NR-D degrades partially to PbI_2 ($2\theta = 12.45^\circ$ corresponds to (001) diffraction peak), whereas the perovskite deposited on $\text{CsBr}@TiO_2$ does not show any degradation. This means that the CsBr modification on mp- TiO_2 reduces the underlying defects in ETL and effectively retards the perovskite degradation under UV light exposure.

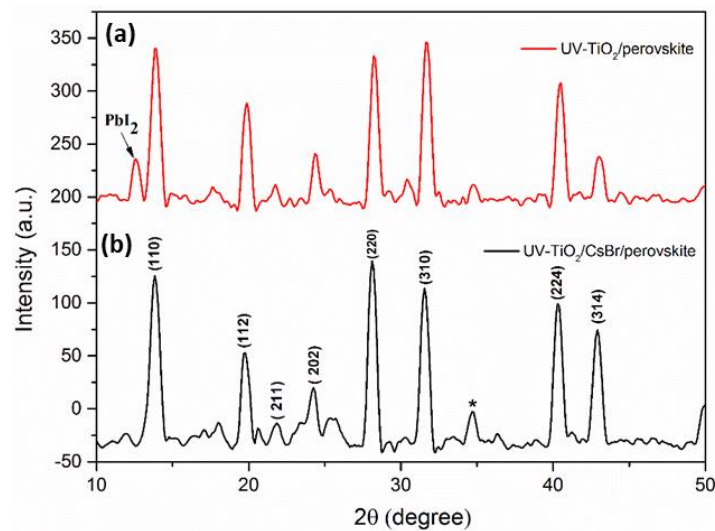


Figure 5.19 XRD patterns with Cu $K\alpha$ radiation ($\lambda = 1.54056 \text{ \AA}$) of MAPbI_3 perovskite film: (a) unmodified m- TiO_2 after UV aging for 90 min, (b) CsBr modified m- TiO_2 after UV aging for 90 min

Finally, the thermal stability test was conducted by exposing the unencapsulated C-PSCs ($\text{CsBr}@TiO_2$ and standard 30NR-D) to continuous heating at a temperature, 85°C in an oven. The *PCE* was recorded on these devices after cooling down to room temperature at regular intervals. **Figure 5.20** shows the normalized *PCE* decay rate at 85°C under ambient air for unencapsulated C-PSCs. From the results, it has been noted that CsBr modified device shows improved thermal stability exhibiting only $\sim 10\%$ *PCE* degradation when compared to $\sim 30\%$ *PCE* decay of 30NR-D device, proving the effectiveness of CsBr modification to mp- TiO_2 layer in C-PSCs.

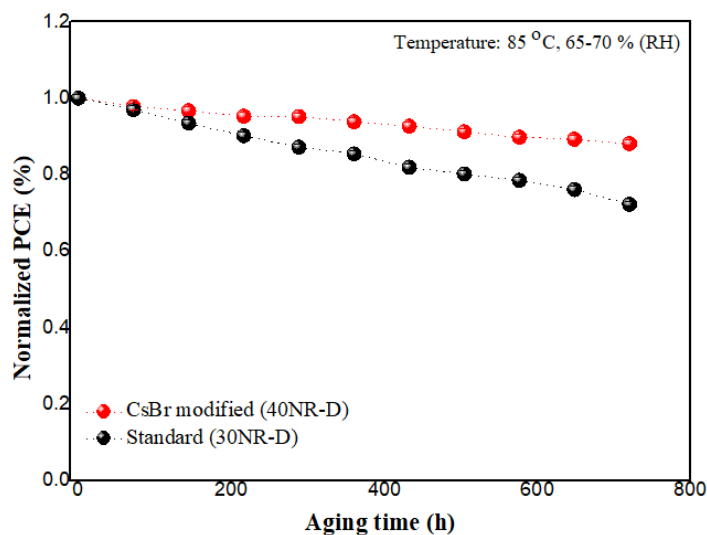


Figure 5.20 Stability studies of C-PSCs with and without CsBr modification, the normalized PCE decay rate at 85 °C under ambient air for unencapsulated C-PSCs

Despite the enormous amount of research that continues to achieve impressive photovoltaic performance in PSCs, the problem of long-term stability and reproducibility factor still prevails, thereby failing by far the market requirements. Therefore, it is very important to study the reproducibility of the fabricated devices. A set of 15 devices were fabricated using the same procedure as mentioned earlier and for each layer, the thickness remained constant. **Figure 5.21a-d** displays the reproducibility data of C-PSCs using CsX modified and unmodified mp-TiO₂. The results clearly indicate that among all the devices, CsBr modified m-TiO₂ devices show excellent reproducibility. Therefore, convincingly, the present investigation delivers good contributions to the development of large-scale perovskite deposition methods for the commercialization of C-PSCs in terms of performance, stability, and reproducibility.

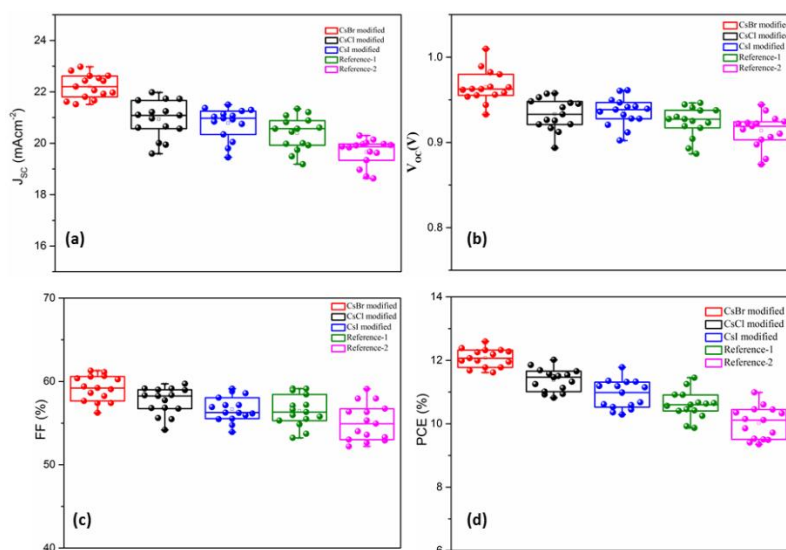


Figure 5.21 Reproducibility data of C-PSCs using CsX modified and unmodified mp-TiO₂. The statistical distribution of photovoltaic parameters: **(a)** J_{SC} , **(b)** V_{OC} , **(c)** FF , **(d)** PCE

5.2.3 CONCLUSIONS

In summary, highly efficient and stable carbon-based perovskite solar cells (C-PSCs) have been developed using CsBr modified mp-TiO₂ beads of 40 nm size as a superior electron transport material, with PCE 12.59% (active area 0.7 cm²) and 11.55 % (active area 70 cm²). In the device, the use of high surface area 40NR-D mp-TiO₂ beads allows effective infiltration of perovskite into the ETL mesostructure. The observed high PL quenching and fast TRPL lifetime decay of perovskite suggest the faster electron extraction for CsX@TiO₂ that results in improved photogenerated electron collection, and hence the enhanced J_{SC} value. Further, the perceived least hysteresis of C-PSCs made of CsBr@TiO₂ infers the reduced electronic traps between ETL and perovskite interface. This argument has been further supported by their UV stability test. As a result of effective perovskite infiltration, reduced electronic traps, improved charge collection, and the least hysteresis, the CsBr modified C-PSCs show good environmental stability. Convincingly, this exploration is expected to provide deeper insights for the further scaling-up of C-PSCs with improved efficiency and stability for their future commercial applications.

CHAPTER-6
SUMMARY AND CONCLUSIONS

SUMMARY AND CONCLUSIONS

Abstract

This chapter contains a summary of the entire research carried out and the important conclusions drawn from the present research work. It also includes a brief account of the scope for further work.

6.1 SUMMARY

Solar energy is considered one of the most abundant renewable energy sources to fulfill the global energy demand. Over the past three decades, the quest for cost-effective and eco-friendly energy generation has led to enhanced attention towards research on third-generation solar cells. In this field, dye-sensitized solar cells (DSSCs) and perovskite solar cells (PSCs) are considered as most promising candidates. So far, quite a lot of research has been carried out to improve the photovoltaic performance as well as stability of the DSSCs/PSCs. Still, there is a lot of scope for further optimization and development of new functional materials for their applications in these solar cells. In this context, the present research work has mainly focused on the three areas of solar cell research, viz. (A) Organic dyes for DSSCs, (B) Organic HTMs for PSCs, and (C) Studies on carbon-based PSCs.

A) Organic dyes for DSSCs

Based on the detailed literature survey, eight new series of *n*-type organic dyes containing thiophene (**Series-1**), carbazole (**Series 2-6**), and phenoxazine core (**Series 7-8**) as a donor with various electron-accepting/anchoring units, were designed for DSSC applications. The new design includes D- π -A (**Series-1**), double D-A (**Series-2** and series-3), double D- π -A (**Series-4** and **Series-5**), A-D- π -D-A (**Series-6**), and A- π -D- π -A (**Series-7** and **Series-8**) architectures. Also, two new series of *p*-type organic dyes carrying phenoxazine (**Series-9**) and carbazole (**Series-10**) with different accepting/anchoring groups have been designed. The newly designed organic dyes were synthesized following standard synthetic protocols starting from simple organic molecules. Their reaction conditions as well as purification techniques were optimized to get the maximum yield. The structural characterization of newly synthesized dyes and their intermediates was performed using various spectral techniques including elemental analysis. Further, the photophysical, electrochemical,

and theoretical studies of newly synthesized *n*-/*p*-type dyes were carried out to evaluate their suitability for their applications in DSSCs as sensitizers/co-sensitizers. Furthermore, DSSCs were fabricated using selected three series of *n*-type organic dyes (**n-K₁₋₁₈**) as sensitizers/co-sensitizers and their photovoltaic parameters were evaluated. In addition, *p*-type DSSCs were fabricated using **p-K₃₅₋₄₂** as sensitizers and obtained results were compared with that of standard benchmark dye **P₁**. Finally, their structure-photovoltaic performance relationship has been studied.

B) Organic HTMs for PSCs

The two new organic HTMs carrying carbazole as a donor (**Series-11**) with different pendent groups have been successfully designed for PSC applications. The newly designed HTMs were synthesized and well-characterized using different spectroscopic techniques. Further, their photophysical, electrochemical, and theoretical studies have been carried out. Finally, the newly synthesized HTMs were employed for the fabrication of PSCs and their various photovoltaic parameters have been measured for studying their structure-property relationships.

C) Studies on carbon-based PSCs

Two different perovskite precursors such as cesium-formamidinium lead halide ($\text{Cs}_{0.1}\text{FA}_{0.9}\text{PbI}_3$) and methylammonium lead halide ($\text{CH}_3\text{NH}_3\text{PbI}_3/\text{MAPbI}_3$) were successfully synthesized and well-characterized. Their composition of perovskite crystal phase, surface morphology, and photophysical studies have been carried out. In order to aim for higher efficiency along with long-term stability, mesoporous triple-layered $\text{TiO}_2/\text{ZrO}_2/\text{C}$ device architecture has been chosen as a state-of-art for the fabrication of fully printable carbon-based perovskite solar cells (C-PSCs). Further, a detailed study has been carried out on the infiltration challenges as well as a selection of appropriate solvents for the one-step deposition of new mixed-cation perovskite ($\text{Cs}_{0.1}\text{FA}_{0.9}\text{PbI}_3$) *via* Lewis acid-base adduct approach for printable C-PSCs. Also, a detailed investigation on electron transport layer (ETL) modification was performed using various CsX modified mesoporous TiO_2 particles for carbon-based MAPbI_3 PSCs. Finally, the C-PSCs were fabricated and their performance parameters were measured.

6.2 CONCLUSIONS

On the basis of experimental results, the following significant conclusions have been drawn from the present research work.

A) Organic dyes for DSSCs

- Total thirty-four push-pull type metal-free organic dyes (***n*-K₁₋₃₄**) as possible *n*-type sensitizers and eight new organic dyes (***p*-K₃₅₋₄₂**) as potential *p*-type sensitizers were successfully designed, synthesized, and well-characterized.
- From their photophysical, electrochemical and molecular modeling studies, it is clear that the synthesized molecules (***n*-K₁₋₃₄** and ***p*-K₃₅₋₄₂**) possess all the prerequisites to act as potential sensitizers.
- From the photophysical characterization, it is evident that all the molecules display strong absorption and emission in the range of 350-580 nm and 457-660 nm, respectively. In addition, the calculated bandgaps are within 2.03-2.90 eV, whereas Stoke shifts are in the range of 1965-8690 cm⁻¹.
- Their electrochemical studies confirm the feasibility of electron injection, regeneration, and recombination in all the synthesized molecules and thus, they can be used as potential *n*-/*p*-type sensitizers for DSSCs.
- Amongst the devices, the DSSC fabricated with ***n*-K₅** displayed the optimum *PCE* of 2.44 %. From the co-sensitization results, it is clear that the DSSC co-sensitized using ***n*-K₆** dye with 0.2 mM of **HD-2** sensitizer showcased an improved *PCE* of 8.81 % compared to other *n*-type dyes.
- The *p*-type organic dyes were sensitized on NiO and their photovoltaic results disclose that ***p*-K₃₆** sensitized DSSC showed *PCE* of 0.031 %, which is comparable with that of benchmark reference **P1**.
- It has been observed that the chemical structure and position of acceptor/anchoring groups play a vital role in determining the overall *PCE* of the DSSCs.

B) Organic HTMs for PSCs

- Two two new push-pull type carbazole-based organic HTMs (***h*-K₄₃₋₄₄**) with D-A-D-A-D architecture were successfully designed, synthesized, and well-characterized.

- The simplicity of their synthesis from the available commercial materials and easy purification steps offer a cost-effective and scalable route.
- Their optical results revealed that ***h-K***₄₃₋₄₄ display λ_{abs} and λ_{emi} in the order of 410-430 nm and 530-560 nm, respectively, with a bandgap in the range of 2.5-2.6 eV. From their photophysical and electrochemical studies, it is clear that the synthesized molecules fulfill all the requirements to function as potential HTMs.
- The quantum chemical simulations have provided a deeper insight into the predictions of their structural, molecular, electronic, and optical parameters.
- Among the synthesized HTMs, the ***h-K***₄₃ as HTM displayed an improved *PCE* of 2.55 % which is comparable with that of standard reference SipromOTAD (4.76%) in PSCs.
- To sum up, by further optimizing the molecular structure of HTMs, it is possible to further ameliorate the photovoltaic performance of HTM-based PSCs.

C) Studies on carbon-based PSCs

- A detailed study has been carried out on the selection of appropriate solvents for the one-step deposition of mixed-cation perovskite in fully printable mesoporous carbon-based perovskite solar cells (C-PSCs).
- Highly reproducible mixed-cation (Cs_{0.1}FA_{0.9}PbI₃) C-PSCs were fabricated using various solvents.
- The *PCE* values were found to be highly dependent on the crystalline quality and infiltration of the perovskite layer, which are superior in the case of devices made up of solvent DMSO.
- The best cell fabricated with the above approach achieved a *PCE* of 12.33 % (the active area is 0.09 cm²) and the average *PCE* for 62 PSCs was found to be 10.5 % under an AM 1.5G illumination. Also, the devices are quite stable with only a change of less than 1 % of the initial days *PCE* for 1800 h under ambient conditions in the dark.
- In continuation, a highly efficient and stable C-PSCs using CsBr modified mp-TiO₂ beads of 40 nm size as a potential ETL has been developed.

- Out of the three cesium halide modifications, devices containing CsBr modified TiO₂ showed the highest short-circuit current density yielding a *PCE* of 12.59 % over the device with 0.7 cm² active area and 11.55 % for a large-area module (70 cm²).
- These devices are stable in an ambient atmosphere (25 °C, 65-70 % RH) over 2700 h as well as at high-temperature (85 °C) over 750 h with virtually no hysteresis.
- This exploration is expected to provide deeper insights for the further scaling-up of C-PSCs with improved efficiency and stability for their future commercial applications.

6.3 SCOPE FOR FUTURE WORK

As concluded, in DSSCs, the sensitizer *n-K₅* and co-sensitizer *n-K₆* with double D-A architecture have displayed the highest photovoltaic performance and their efficiency can be further improved by modifying the structure of the sensitizer as well as optimizing the other components such as semiconductor, electrolyte, and counter electrolyte of the device. Also, for the first time, phenoxazine-based dyes with push-pull architecture have been explored as potential *p*-type sensitizers and their photovoltaic performances are quite encouraging. So, adequate structural modification in *p-K₃₅* and *p-K₃₆* may lead to improvement in photovoltaic performance. The combination of the aforesaid *n*-type and *p*-type dyes with suitable semiconductors can be explored as effective photoactive anode and cathode, for the best performing tandem cells.

In case of mixed-cation C-PSCs, the devices (active area 0.09 and 0.7 cm²) made up of solvent DMSO were found to be much superior in terms of stability as well as reproducibility. The results give a better idea for further development and optimization of fabrication techniques in large-area C-PSCs (> 70 cm²). In addition, the present work also highlights the importance of ETL modification using CsBr modified mp-TiO₂ in the fabrication of highly efficient and stable large-area carbon-based MAPbI₃ perovskite solar modules (70 cm²) for the first time. So, by tuning other parameters such as crystal formation, additives, surface morphology, and

interface engineering, the performance of large-area C-PSCs can be further improved in order to accelerate their commercialization.

Abdellah, I.M. and El-shafei, A. (2020). "Efficiency enhancement of ruthenium-based DSSCs employing A- π -D- π -A organic co-sensitizers." *RSC Adv.*, 10(47), 27940-27953.

Afroz, M.A., Ghimire, N., Reza, K.M., Bahrami, B., Bobba, R.S., Gurung, A., Chowdhury, A.H., Iyer, P.K. and Qiao, Q. (2020). "Thermal stability and performance enhancement of perovskite solar cells through oxalic acid induced perovskite formation." *ACS Appl. Energy Mater.*, 3, 2432-2439.

Althagafi, I. and El-Metwaly, N. (2020). "Enhancement of dye-sensitized solar cell efficiency through co-sensitization of thiophene-based organic compounds and metal-based N719." *Arab. J. Chem.*, 14, 103080.

Ameline, D., Diring, S., Farre, Y., Pellegrin, Y., Naponiello, G., Blart, E., Charrier, B., Dini, D., Jacquemin, D. and Odobel, F. (2015). "Isoindigo derivatives for application in *p*-type dye-sensitized solar cells." *RSC Adv.*, 5(104), 85530-85539.

Babu, D. D., Elsherbiny, D., Cheema, H., El-shafei, A. and Vasudeva, A. (2016). "Dyes and Pigments Highly efficient panchromatic dye-sensitized solar cells: Synergistic interaction of ruthenium sensitizer with novel co-sensitizers carrying different acceptor units." *Dyes Pigm.*, 132, 316-328.

Babu, D.D., Su, R., El-Shafei, A. and Adhikari, A.V. (2016). "From molecular design to co-sensitization; High performance indole-based photosensitizers for dye-sensitized solar cells." *Electrochim. Acta*, 198, 10-21.

Bae, J.H., Lim, S.J., Lee, W. and Kim, J.P. (2018). "Effects of introducing functional groups on the performance of phenoxazine-based dye-sensitized solar cells." *Dyes Pigm.*, 162, 905-915.

Bao, L.Q., Thuy, C.T.T., Lee, J.W., Kim, J.H. and Thogiti, S. (2017). "Synthesis and investigation of triphenylamine-based double branched organic dyes for *p*-type dye-sensitized solar cells." *Mol. Cryst. Liq. Cryst.*, 633, 109-117.

Bashir, A., Shukla, S., Lew, J.H., Bruno, A., Akhter, Z., Priyadarshi, A., Marhews, N. and Mhaisalkar, S.G. (2018). "Spinal Co₃O₄ nanomaterials for efficient and stable large area carbon based printed perovskite solar cells." *Nanoscale*, 10 (5), 2341-2350.

Bashir, A., Jia, L., Shukla, S., Gupta, D., Baikie, T., Bruno, A., Mhaisalkar, S. and Akhter, Z. (2019). "Cu-doped nickel oxide interface layer with nanoscale thickness for

efficient and highly stable printable carbon-based perovskite solar cell." *Sol. Energy*, 182, 225–236.

Borgström, M., Blart, E., Boschloo, G., Mukhtar, E., Hagfeldt, A., Hammarström, L. and Odobel, F. (2005). "Sensitized Hole Injection of Phosphorus Porphyrin into NiO: Toward New Photovoltaic Devices." *J. Phys. Chem. B*, 109 (48), 22928-22934

Bogachuk, D., Zouhair, S., Lim, J., Pettersson, H., Hagfeldt, A. and Hinsch, A. (2020). "Low temperature carbon-based electrodes in perovskite solar cells." *Energy Environ. Sci.*, 13, 3880.

Cheema, H., Islam, A., Han, L. and El-Shafei, A. (2014a). "Influence of number of benzodioxan-stilbazole-based ancillary ligands on dye packing, photovoltage and photocurrent in dye-sensitized solar cells." *ACS Appl. Mater. Interfaces*, 6(14), 11617-24.

Cheema, H., Islam, A., Younts, R., Gautam, B., Bedja, I., Gupta, R.K., Han, L., Gundogdu, K. and El-Shafei, A. (2014b). "More stable and more efficient alternatives of Z-907: carbazole-based amphiphilic Ru(II) sensitizers for dye-sensitized solar cells." *Phys. Chem. Chem. Phys.*, 16 (48), 27078-27087.

Cui, J., Lu, J., Xu, X., Cao, K., Wang, Z., Alemu, G., Yuang, H., Shen, Y., Xu, J., Cheng, Y. and Wang, M. (2014). "Organic Sensitizers with Pyridine Ring Anchoring Group for *p*-Type Dye-Sensitized Solar Cells." *J. Phys. Chem. C*, 118 (30), 16433-16440.

Duan, M., Rong, Y., Mei, A., Hu, Y., Sheng, Y. and Guan, Y. (2017). "Efficient hole-conductor-free fully printable mesoscopic perovskite solar cells with carbon electrode based on ultrathin graphite." 120, 71–76.

El-Shafei, A., Hussain, M., Atiq, A., Islam, A. and Han, L. (2012). "A novel carbazole-based dye outperformed the benchmark dye N719 for high efficiency dye-sensitized solar cells (DSSCs)." *J. Mater. Chem.*, 22(45), 24048.

Farré, Y., Raissi, M., Fihey, A., Pellegrin, Y., Blart, E., Jacquemin, D. and Odobel, F. (2017). "A Blue diketopyrrolopyrrole sensitizer with high efficiency in nickel-oxide-based dye-sensitized solar cells." *ChemSusChem*, 10 (12), 2618-2625.

Farré, Y., Zhang, L., Pellegrin, Y., Planchat, A., Blart, E., Boujtita, M., Hammarström, L., Jacquemin, D. and Odobel, F. (2016). "Second generation of diketopyrrolopyrrole dyes for NiO-based dye-sensitized solar cells." *J. Phys. Chem. C*, 120 (15), 7923-7940.

Fernandes, S.M., Castro, C.R., Mendes, A. and Raposo, M.M. (2017). "Synthesis and

characterization of novel thieno[3,2-b]thiophene based metal-free organic dyes with different heteroaromatic donor moieties as sensitizers for dye-sensitized solar cells.” *Dyes Pigm.*, 136, 46-53.

Fernandes, S.M., Belsley, M., Pereira, A.I., Mendes, A. and Raposo, M.M. (2018). “Push-pull *N,N*-diphenylhydrazones bearing bithiophene or thienothiophene spacers as nonlinear optical second harmonic generators and as photosensitizers for nanocrystalline TiO₂ dye-sensitized solar Cell.” *ACS omega*, 3, 12893-12904.

Fuse, S., Takahashi, R., Maitani, M.M., Kaiho, T., Tanaka, H. and Takahashi, T. (2015). “Synthesis and evaluation of thiophene-based organic dyes containing a rigid and nonplanar donor with secondary electron donors for use in dye-sensitized solar cells.” *Eur. J. Org. Chem.* 508–517.

Gao, L., Zhang, F., Chen, X., Xiao, C., Zhu, K. and Sellinger, A. (2020). “Carbazole-based hole-transport materials for high-efficiency and stable perovskite solar cells.” *ACS Appl. Energy Mater.*, 3, 4492-4498.

Gibson, E.A., Smeigh, A.L., Le Pleux, L., Fortage, J., Boschloo, G., Blart, E., Pellegrin, Y., Odobel, F., Hagfeldt, A. and Hammarström, L. (2009). "A *p*-type NiO-based dye-sensitized solar cell with an open-circuit voltage of 0.35 V." *Angewandte Chemie International Edition*, 48 (24), 4402-4405.

Grätzel, M. (2001). "Photoelectrochemical cells." *Nature*, 414 (6861), 338-344.

Grätzel, M. (2005). "Solar Energy Conversion by dye-sensitized photovoltaic cells." *Inorg. Chem.*, 44 (20), 6841-6851.

Gram, T., Ad, S.T. and Gramstad, T. (1976). “Synthesis and vibrational spectra of some lead (II) halide adducts.” *Can. J. Chem.*, 54, 3430.

Gratia, P., Magomedov, A., Abate, A., Gratzel, M. and Nazeruddin, M.K. (2015). “A methoxydiphenylamine-substituted carbazole twin derivative: An efficient hole-transporting material for perovskite solar cells.” *Angew. Chem.*, 54, 11409 -11413.

Gupta, K. S. V, Suresh, T., Singh, S. P., Islam, A., Han, L., and Chandrasekharam, M. (2014). “Carbazole based A- π -D- π -A dyes with double electron acceptor for dye-sensitized solar cell.” *Org. Electron. physics, Mater. Appl.*, 15(1), 266-275.

Hagfeldt, A., Boschloo, G., Sun, L., Kloo, L. and Pettersson, H. (2010). “Dye-sensitized solar cells.” *Chem. Rev.*, 110, 6595-6663.

- Huang, P., Wang, Y., Ke, J. and Huang, C. (2017). "The effect of solvents on the performance of $\text{CH}_3\text{NH}_3\text{PbI}_3$ perovskite solar cells." *energies*, 10, 599.
- He, S., Qui, L., Liu, Z., Ono, L., Stecker, C. and Qi, Y. (2019). "Carbon-based electrode engineering boosts the efficiency of all low-temperature processed perovskite solar cells." *ACS energy Lett.*, 4, 2032-2039.
- He, J., Lindström, H., Hagfeldt, A. and Lindquist, S.E. (1999). "Dye-Sensitized Nanostructured *p*-Type Nickel Oxide Film as a Photocathode for a Solar Cell." *J. Phys. Chem. B.*, 103, 8940-8943.
- Ito, S., Zakeeruddin, S.M., Humphry-Baker, R., Liska, P., Charvet, R., Comte, P., Nazeeruddin, M.K., Péchy, P., Takata, M., Miura, H., Uchida, S. and Grätzel, M. (2006). "High-efficiency organic dye-sensitized solar cells controlled by nanocrystalline- TiO_2 electrode thickness." *Adv. Mater.*, 18 (9), 1202-1205.
- Jeon, N.J., Noh, J.H., Kim, Y.C., Yang, W.S., Ryu, S. and Seok, S.I. (2014). "Solvent engineering for high performance Inorganic-Organic Hybrid Perovskite Solar Cells." *Nat. Mater.*, 13, 897-903.
- Ji, Z., Natu, G., Huang, Z. and Wu, Y. (2011). "Linker effect in organic donor-acceptor dyes for *p*-type NiO dye sensitized solar cells." *Energy Environ. Sci.*, 4(8), 2818.
- Kapoor, V., Bashir, A., Haur, L.J., Shukla, S., Bruno, A., Mathews, N. and Mhaisalkar, S. (2017). "Effect of excess PbI_2 in fully printable carbon-based perovskite solar cells." *Energy Tech*, 5 (10), 1880-1886.
- Karlsson, K.M., Jiang, X., Eriksson, S.K., Hagfeldt, A. and Sun, L. (2011). "Phenoxazine dyes for dye-sensitized solar cells: relationship between molecular structure and electron lifetime." *Chem. Eur. J.* 17, 6415-6424.
- Kim, H., Lee, C., Im, J., Lee, K., Moehl, T., Marchioro, A., Moon, S., Humphry-baker, R., Yum, J., Moser, J.E. and Gratzel, M. (2012). "Lead iodide perovskite sensitized all-solid-state submicron thin film mesoscopic solar cell with efficiency exceeding 9%." *Sci. Rep.*, 2, 591.
- Kojima, A., Teshima, K., Shirai, Y. and Miyasaka, T. (2009). "Organometal halide perovskites as visible-light sensitizers for photovoltaic cells." *J. Am. Chem. Soc.*, 131, 6050-6051.
- Koops, S.E., O'Regan, B.C., Barnes, P.R.F. and Durrant, J.R. (2009). "Parameters influencing the efficiency of electron injection in dye-sensitized solar cells." *J. Am.*

Chem. Soc., 131 (13), 4808-4818.

Li, L., Gibson, E.A., Qin, P., Boschloo, G., Gorlov, M., Hagfeldt, A. and Sun, L. (2010). "Double-layered NiO photocathodes for *p*-type DSSCs with record IPCE." *Adv. Mater.*, 22 (15), 1759–1762.

Li, J., Yang, X., Cheng, M. and Sun, L. (2015). "Phenoxazine-based panchromatic organic sensitizers for dye-sensitized solar cells." *Dyes Pigm.*, 116, 58-64.

Li, X., Tschumi, M., Babkair, S.S., Zaakiruddin, S.M. and Gratzel, M. (2015). "Outdoor performance and stability under elevated temperatures and long-term light soaking of triple-layer mesoporous perovskite photovoltaics." *Energy Technol.* 3, 551-555.

Lin, R. Y.-Y., Wu, F.-L., Chang, C.-H., Chou, H.-H., Chuang, T.-M., Chu, T.-C., Hsu, C.-Y., Chen, P.-W., Ho, K.-C., Lo, Y.-H. and Lin, J. T. (2014). "Y-shaped metal-free D- π -(A)₂ sensitizers for high-performance dye-sensitized solar cells." *J. Mater. Chem. A*, 2(9), 3092-3101.

Lim, D.S., Park, K.W., Wiles, A.A. and Hong, J. (2019). "Metal-free organic chromophores featuring an ethynyl-thienothiophene linker with an *n*-hexyl chain for translucent dye-sensitized solar cells." *Materials*, 12, 1741-1750.

Lokhande, P.K.M., Sonigara, K., Jadhav, M.M., Patil, D. and Sekar, N. (2019). "Multi-dentate carbazole based Schiff-base dyes with chlorovinylene group in spacer for dye-sensitized solar cells: A Combined Theoretical and Experimental Study." *Chem. Select*, 4, 4044 –4056.

Luo, J., Wan, Z., Jia, C., Wang, Y. and Wu, X. (2016a). "A co-sensitized approach to efficiently fill the absorption valley, avoid dye aggregation and reduce the charge recombination." *Electrochim. Acta*, 215, 506-514.

Luo, J., Wan, Z., Jia, C., Wang, Y., Wu, X. and Yao, X. (2016b). "Co-sensitization of dithiafulvenyl-phenothiazine based organic dyes with N719 for efficient dye-sensitized solar cells." *Electrochim. Acta*, 211, 364-374.

Mei, A., Li, X., Liu, L., Ku, Z., Liu, T., Rong, Y. and Han, H. (2014). "A hole-conductor free fully printable mesoscopic perovskite solar cells with high stability." *Science*, 345, 295-297.

Meng, F.S., Yao, Q.H., Shen, J.G., Li, F.L., Huang, C.H., Chen, K.C. and Tian, H. (2003). "Novel Cyanine Dyes with Multi-carboxyl Groups and their Sensitization on

- Nanocrystalline TiO₂ Electrode." *Synthetic Metals*, 137 (1-3), 1543-1544.
- Murali, M. G., Wang, X., Wang, Q. and Valiyaveetil, S. (2016). "New banana shaped A-D- π -D-A type organic dyes containing two anchoring groups for high performance dye-sensitized solar cells." *Dye. Pigment.*, 134, 375-381.
- Morandeira, A., Fortage, J., Edvinsson, T., Le Pleux, L., Blart, E., Boschloo, G., Hagfeldt, A., Hammarström, L. and Odobel, F. (2008). "Improved photon-to-current conversion efficiency with a nanoporous *p*-Type NiO electrode by the use of a sensitizer-acceptor dyad." *J. Phys. Chem. C*, 112 (5), 1721-1728.
- Naik, P., Elmorsy, M., Su, R., El-Shafei, A. and Adhikari, A.V. (2018). "Enhancing photovoltaic performance of DSSCs sensitized with Ru-II complexes by D- π -A configured carbazole based co-sensitizers." *New J. Chem.*, 42, 9443-9448.
- Naik, P., Elmorsy, M., El-Shafei, A. and Adhikari, A.V. (2018). "New carbazole based dyes as effective co-sensitizers for DSSCs sensitized with ruthenium (II) complex (NCSU-10)." *J. Energy Chem.*, 27, (2), 351-360.
- Nazeeruddin, M.K., Kay, A., Rodicio, I., Humphry-Baker, R., Mueller, E., Liska, P., Vlachopoulos, N. and Graetzel, M. (1993). "Conversion of light to electricity by cis-bis(2,2'-bipyridyl-4,4'-dicarboxylate)ruthenium(II) charge-transfer sensitizers (X = Cl-, Br-, I-, CN-, and SCN-) on nanocrystalline titanium dioxide electrodes." *J. Am. Chem. Soc.*, 115 (14), 6382-6390.
- Neshelei, F.G., Hosseinzadeh, B. and Hosseinzadeh, R. (2020). "Design, synthesis and photophysical analysis of new unsymmetrical carbazole based dyes for dye-sensitized solar cells." *J. Photochem. Photobiol. A*, 397, 112521.
- Odobel, F., Le Pleux, L., Pellegrin, Y. and Blart, E. (2010). "New Photovoltaic Devices Based on the Sensitization of *p*-type Semiconductors: Challenges and Opportunities." *Acc. Chem. Res.*, 43 (8), 1063-1071.
- Odobel, F., Pellegrin, Y., Gibson, E.A., Hagfeldt, A., Smeigh, A.L. and Hammarström, L. (2012). "Recent advances and future directions to optimize the performances of *p*-type dye-sensitized solar cells." *Coordination Chemistry Reviews*, 256 (21), 2414-2423.
- O'Regan, B. and Gratzel, M. (1991). "A low-cost, high-efficiency solar cell based on dye-sensitized colloidal TiO₂ films." *Nature*, 353, 737-740.

- Priyadarshi, A., Haur, L. J., Murray, P., Fu, D., Kulkarni, S., Xing, G., Sum, T.C., Mathews, N. and Mhaisalkar, S.G. (2016). "A Large Area (70 cm²) Monolithic Perovskite Solar Module with a High Efficiency and Stability." *Energy Environ. Sci.*, 9, 3687-3692.
- Qin, P., Linder, M., Brinck, T., Boschloo, G., Hagfeldt, A. and Sun, L. (2009). "High Incident Photon-to-Current Conversion Efficiency of *p*-Type Dye-Sensitized Solar Cells Based on NiO and Organic Chromophores." *Adv. Mater.*, 21 (29), 2993-2996.
- Qin, P., Wiberg, J., Gibson, E.A., Linder, M., Li, L., Brinck, T., Hagfeldt, A., Albinsson, B. and Sun, L. (2010). "Synthesis and Mechanistic Studies of Organic Chromophores with Different Energy Levels for *p*-Type Dye-Sensitized Solar Cells." *J. Phys. Chem. C*, 114 (10), 4738-4748.
- Qin, P., Zhu, H., Edvinsson, T., Boschloo, G., Hagfeldt, A. and Sun, L. (2008). "Design of an Organic Chromophore for *p*-type Dye-Sensitized Solar Cells." *J. Am. Chem. Soc.*, 130 (27), 8570-8571.
- Pleux, L.L., Smeigh, A.L., Gibson, E., Pellegrin, Y., Blart, E., Boschloo, G., Hagfeldt, A., Hammarström, L. and Odobel, F. (2011). "Synthesis, photophysical and photovoltaic investigations of acceptor-functionalized perylenemonoimide dyes for nickel oxide *p*-type dye-sensitized solar cells." *Energy Environ. Sci.*, 4 (6), 2075-2084.
- Ramkumar, S. and Anandan, S. (2013). "Synthesis of bianchored metal free organic dyes for dye sensitized solar cells." *Dye. Pigment.*, 97(3), 397-404.
- Ramkumar, S., Manoharan, S. and Anandan, S. (2012). "Synthesis of D-(π -A)₂ organic chromophores for dye-sensitized solar cells." *Dye. Pigment.*, 94(3), 503-511.
- Robertson, N., Santos, J.M., Tanaka, E. and Wiles, A.A. (2021). "Donor free oligothiophene based dyes with the di-anchor architecture for dye-sensitized solar cells." *Mol. Syst. Des. Eng.*, 6, 381-389.
- Sahiner, F., Ali, A.K., Kandemir, Z. and Erten-Ela, S. (2020). "Naphthalene imides as novel *p*-type sensitizers for NiO-based *p*-type dye-sensitized solar cells." *New J. Chem.*, 44, 15526-15537.
- Saritha, G., Mangalaraja, R.V. and Anandan, S. (2017). "High-efficiency dye-sensitized solar cells fabricated using D-D- π -A (donor-donor/ π -spacer-acceptor) architecture." *Solar Energy*, 146, 150-160.

- Seo, K. D., Song, H. M., Lee, M. J., Pastore, M., Anselmi, C., Angelis, F. De, Nazeeruddin, M. K., Grätzel, M. and Kim, H. K. (2011). "Coumarin dyes containing low-band-gap chromophores for dye-sensitized solar cells." *Dye. Pigment.*, 90(3), 304-310.
- Seo, J., Uchida, R., Kim, H., Saygili, Y., Luo, J., Moore, C., Kerrod, J., Wagstaff, A., Eklund, M., Mcintyre, R., Pellet, N., Zakeeruddin, S. M., Hagfeldt, A. and Grätzel, M. (2018). "Boosting the Efficiency of Perovskite Solar Cells with CsBr-Modified Mesoporous TiO₂ Beads as Electron-Selective Contact." *Adv. Funct. Mater.*, 28 (15), 1705763.
- Shen, P., Liu, X., Jiang, S., Huang, Y., Yi, L., Zhao, B. and Tan, S. (2011). "Effects of aromatic π -conjugated bridges on optical and photovoltaic properties of N,N-diphenylhydrazone-based metal-free organic dyes." *Org. Electron.*, 12(12), 1992- 2002.
- Tang, J., Hua, J., Wu, W., Li, J., Jin, Z., Long, Y. and Tian, H. (2010). "New starburst sensitizer with carbazole antennas for efficient and stable dye-sensitized solar cells." *Energy Environ. Sci.*, 3(11), 1736.
- Thomas, S., Deepak, T.G., Anjusree, G.S., Arun, T.A., Nair, S.V. and Nair, A.S. (2014). "A review on counter electrode materials in dye-sensitized solar cells." *J. Mater. Chem. A*, 2(13), 4474-4490.
- Tian, H., Yang, X., Chen, R., Pan, Y., Li, L., Hagfeldt, A. and Sun, L. (2007). "Phenothiazine derivatives for efficient organic dye-sensitized solar cells." *Chem. Commun.*, (36), 3741-3743.
- Wang, G., Wu, Y., Ding, W., Yu, G., Hu, Z., Wang, H., Liu, S., Zou, Y. and Pan, C. (2015). "Photovoltaic performance of long-chain poly(triphenylamine-phenothiazine) dyes with a tunable π -bridge for dye-sensitized solar cells." *J. Mater. Chem. A*, 3(27), 14217-14227.
- Wang, P., Zakeeruddin, S. M., Moser, J. E., Nazeeruddin, M. K., Sekiguchi, T. and Grätzel, M. (2003). "A stable quasi-solid-state dye-sensitized solar cell with an amphiphilic ruthenium sensitizer and polymer gel electrolyte." *Nat. Mater.*, 2(6), 402-407.
- Wang, Y., Wan, Z., Jia, C. and Yao, X. (2016). "Indole-based organic dyes with different electron donors for dye-sensitized solar cells." *Synth. Met.*, 211, 40-48.
- Wang, S., Shen, W., Chu, Y., Zhang, W., Hong, L., Mei, A., Tang, Y., Hu, Y. and Han, H. (2020). "Mesoporous carbon-based fully-printable all-inorganic monoclinic CsPbBr₃

- perovskite solar cells with ultrastability under high temperature and high humidity.” *J. Phys. Chem. Lett.*, 11, 9689–9695.
- Wang, L., Guo, Y., Zhang, W., Li, Y., Liu, P. and Sun, L. (2019). “Impact of linking topology on the properties of carbazole-based hole-transport materials and their application in solid-state mesoscopic solar cells.” *Sol. RRL*, 3, 1900196.
- Warnan, J., Pellegrin, Y., Blart, E., Zhang, L., Brown, A., Hammarström, L., Jacquemin, D. and Odobel, F. (2014). “Acetylacetonate anchoring group for NiO-based dye-sensitized solar cell.” *Dye. Pigment.*, 105, 174-179.
- Wei, Z., Yan, K., Chen, H., Yi, Y., Zhang, T. and Yang, S. (2014). “Cost-efficient clamping solar cells using candle soot for hole extraction from ambipolar perovskites.” *Energy Environ. Sci.*, 7 (10), 3326-3333.
- Wonneberger, H., Pschirer, N., Bruder, I., Bauerle, P. and Mullen, K. (2011). “Double donor-thiophene dendron-perylene monoimide: efficient light-harvesting metal-free chromophore for solid-state dye-sensitized solar cells.” 6 (7), 1744-1747.
- Wu, Y. and Zhu, W. (2013). "Organic sensitizers from D- π -A to D-A- π -A: effect of the internal electron-withdrawing units on molecular absorption, energy levels and photovoltaic performances." *Chem. Soc. Rev.*, 42 (5), 2039-2058.
- Wu, F., Zhu, L., Zhao, S., Song, Q. and Yang, C. (2016). “Engineering of organic dyes for highly efficient *p*-type dye-sensitized solar cells.” *Dyes Pigm.*, 124, 93-100.
- Wu, Y., Islam, A., Yang, X., Qin, C., Liu, J., Zhang, K., Peng, W. and Han, L. (2014). “Retarding the crystallization of PbI₂ for highly Reproducible Planar-Structured Perovskite Solar cells via sequential deposition.” *Energy Environ. Sci.*, 7, 2934–2938.
- Xie, Y., Gao, J. and Wu, L. (2018). “Novel indeno[2,1-b]carbazole donor-based organic dyes for dye-sensitized solar cells.” *Photochem. Photobiol. Sci.*, 17, 423-431.
- Xu, B., Liu, P., Zhang, J., Tian, H., Kloo, L., Hagfeldt, A. and Sun, L. (2014). “carbazole-based hole-transport materials for efficient solid-state dye-sensitized solar cells and perovskite solar cells.” *Adv. Mater.*, 26, 6629-6634.
- Xu, B., Wrede, S., Curtze, A., Tian, L., Kloo, L., Wu, Y. and Tian, H. (2019). “An Indacenodithieno [3,2-b]thiophene-based organic dye for solid-state *p*-type dye-sensitized solar cells.” *ChemSusChem*, 12, 3243-3248.

- Yang, S., Wang, L., Gao, L., Cao, J. and Han, Q. (2020). "Excellent Moisture Stability and Efficiency of Inverted All-Inorganic CsPbIBr₂ Perovskite Solar Cells through Molecule Interface Engineering." *ACS Appl. Mater. Interfaces*, 12, 13931-13940.
- Yen, Y.S., Chou, H.H., Chen, Y.C., Hsu, C.Y. and Lin, J.T. (2012). "Recent developments in molecule-based organic materials for dye-sensitized solar cells." *J. Mater. Chem.*, 22 (18), 8734-8747.
- Yen, Y.S. and Indumathi, V. (2021). "Effect of π -conjugated spacer in *N*-alkylphenoxazine-based sensitizers containing double anchors for dye-sensitized solar cells." *Polymers*, 13 (8), 1304.
- Zhang, L. and Cole, J. M. (2015). "Anchoring Groups for Dye-Sensitized Solar Cells." *ACS Appl. Mater. Interfaces*, 7, 3427-3455.
- Zhang, L.P., Jiang, K.J., Li, G., Zhang, Q.Q. and Yang, L.M. (2014). "Pyrazino[2,3-*g*]quinoxaline dyes for solar cell applications." *J. Mater. Chem. A*, 2 (36), 14852-14857.
- Zhang, Q.Q., Jiang, K.J., Huang, J.H., Zhao, C.W., Zhang, L.P., Cui, X.P., Su, M.J., Yang, L.M., Song, Y.L. and Zhou, X.Q. (2015). "A push-pull thienoquinoidal chromophore for highly efficient *p*-type dye-sensitized solar cells." *J. Mater. Chem. A*, 3, 7695-7698.
- Zhang, S., Islam, A., Yang, X., Qin, C., Zhang, K., Numata, Y., Chen, H. and Han, L. (2013). "Improvement of spectral response by co-sensitizers for high efficiency dye-sensitized solar cells." *J. Mater. Chem. A*, 1(15), 4812.
- Zhao, Z., Sun, W., Li, Y., Ye, S., Rao, H., Gu, F., Bian, Z. and Huang, C. (2017). "Simplification of device structures for low-cost, high-efficiency perovskite solar cells." *J. Mater. Chem. A*, 5, 4756-4773.
- Zhou, H., Chen Q., Li, G., Luo, S., Hong, Z. and You, J. (2014). "Interface engineering of highly efficient perovskite solar cells." *Science*, 345, 542-546.
- Zhou, L., Zuo, Y., Mallick, T.K. and Sundaram, S. (2019). "Enhanced efficiency of carbon-based mesoscopic perovskite solar cells through a tungsten oxide nanoparticle additive in the carbon electrode." *Sci. Rep.*, 9(1), 8778.
- Zhu, W., Zhang, Z., Chai, W., Chen, D., Xi, H., Zhang, J., Zhang, C. and Hao, Y. (2019). "Benign pinholes in CsPbIBr₂ absorber film enable efficient carbon-based, all inorganic perovskite solar cells." *ACS Appl. Energy Mater.*, 2, 5254-5262.

LIST OF PUBLICATIONS

PAPERS PUBLISHED IN INTERNATIONAL JOURNALS

1. **Kavya S. Keremane**, Sateesh Prathapani, Lew Jia Haur, Annalisa Bruno, Anish Priyadarshi, Airody Vasudeva Adhikari, Subodh G Mhaisalkar, (2021). “Improving the performance of carbon-based perovskite solar modules (70 cm²) by incorporating cesium halide in mesoporous TiO₂.” *ACS Applied Energy Materials*, 4(1), 249-258. DOI: <https://doi.org/10.1021/acsaem.0c02213>
2. **Kavya S. Keremane**, and Airody Vasudeva Adhikari, (2021). “Simple carbazole derivatives with mono/dimethoxyphenylacrylonitrile substituents as hole-transporting materials: performance studies in hybrid perovskite solar cells.” *Wiley-Electrochemical Science Advances*, 1(3), e2000036. DOI: <https://doi.org/10.1002/elsa.202000036>
3. **Kavya S. Keremane**, Islam M. Abdellah, Praveen Naik, Ahmed El-Shafei, and Airody Vasudeva Adhikari, (2020). “Simple thiophene-bridged D- π -A type chromophores for DSSCs: A comprehensive study on their sensitization and co-sensitization properties.” *RSC-Physical Chemistry Chemical Physics*, 22, 23169-23184. DOI: [10.1039/D0CP02781B](https://doi.org/10.1039/D0CP02781B)
4. **Kavya S. Keremane**, Rathnamala Rao, and Airody Vasudeva Adhikari, (2020). “Simple 3,6-disubstituted carbazoles as potential hole-transport materials: Photophysical, electrochemical and theoretical studies.” *Wiley-Photochemistry and Photobiology*, 97, 289-300. DOI: [10.1111/php.13337](https://doi.org/10.1111/php.13337)
5. **Kavya S. Keremane**, Sateesh Prathapani, Lew Jia Haur, D. Bahulayan, Anish Priyadarshi, Airody Vasudeva Adhikari, and Subodh G Mhaisalkar, “Solvent selection for highly reproducible carbon-based mixed-cation hybrid lead halide perovskite solar cells via adducts approach.” *Elsevier-Solar Energy*, 2020, 199, 761–771. DOI: [10.1016/j.solener.2020.02.063](https://doi.org/10.1016/j.solener.2020.02.063)
6. **Kavya S. Keremane**, Praveen Naik, and Airody Vasudeva Adhikari, (2020). “Simple thiophene-based organic dyes as active photosensitizers for DSSC application: from molecular design to structure property relationship.” *SSU-*

Journal of Nano- and Electronic Physics, 12, 02039. DOI: [10.21272/jnep.12\(2\).02039](https://doi.org/10.21272/jnep.12(2).02039)

7. **Kavya S. Keremane** and Airody Vasudeva Adhikari, (2021). “Simple phenylene-bridged D- π -A type photosensitizers for DSSC application: Synthesis, optical, electrochemical and theoretical studies.” *J. of. Org. Chem. Synthesis. and Proc. Develop.* 1, 24-32.

RESEARCH PAPERS PRESENTED IN NATIONAL/INTERNATIONAL CONFERENCES

1. **Kavya S. Keremane**, Subodh G. Mhaisalkar, and Airody Vasudeva Adhikari, “Carbon Based Mixed-Cation Hybrid Lead Halide Perovskite Solar Cells: Towards Commercialization”, 1st International Conference on Thin Films & Nanotechnology: Knowledge, Leadership, & Commercialization (ICTN-KLC), organized by Thin Film Lab, Department of Physics, Indian Institute of Technology, Delhi, India, August 24-26, 2021 (**Best Poster Presentation Award**).
2. **Kavya S. Keremane** and Airody Vasudeva Adhikari, “Simple thiophene-bridged D- π -A type chromophores for DSSCs: A comprehensive study on their sensitization and co-sensitization properties”, Engineering & Material Science session, National Symposium on Future of STI: Impacts on Education, Skills, and Work, organized by Yenepoya University, Mangalore, India, February 27, 2021 (**Best Oral Presentation Award**).
3. **Kavya S. Keremane** and Airody Vasudeva Adhikari, “Structurally simple D- π -A type organic sensitizers/co-sensitizers for dye-sensitized solar cells: Effect of anchoring moieties on the photovoltaic performance”, Virtual International conference on Sustainable energy and environmental technologies (V-ICSEET-2020), organized by Department of Chemistry, REVA University, Bangalore, India, November 02-04, 2020.
4. **Kavya S. Keremane** and Airody Vasudeva Adhikari, “Design, synthesis and photovoltaic investigation of new thiophene-based metal-free organic sensitizers

- for DSSC application”, International Virtual Conference on Creative Research in Chemical Science and Allied Applications (CRCSA-2020) organized by P.G. Department of Chemistry, SDM College, Ujire, India, August 18-19, 2020.
5. **Kavya S. Keremane** and Airody Vasudeva Adhikari, “Synthesis and performance studies of new carbazole-based organic hole-transporting materials for hybrid perovskite solar cells”, 1st international Conference on Accelerating Innovations in Material Science (AIMS-2020), organized by Department of Chemistry, BMS Institute of Technology & Management, Bengaluru, India, August 04-07, 2020.
 6. **Kavya S. Keremane**, Praveen Naik, Airody Vasudeva Adhikari, “A simple thiophene based organic dyes as active photosensitizers for DSSC application: From molecular design to structure property relationship”, International Conference on Smart Materials and Nanotechnology (ICSMN-2020), organized by Department of Engineering Physics and Chemistry, SKN Sinhgad College of Engineering, Maharashtra, India, January 02-04, 2020 (*Outstanding Women Research award*).
 7. **Kavya S. Keremane**, Islam M. Abdellah, Ahmed El- Shafei, and Airody Vasudeva Adhikari, “Synergistic interaction of ruthenium sensitizer with novel co-sensitizers carrying different acceptor units in dye-sensitized solar cells”, 3rd International conference on Recent Advances in Material Chemistry (ICRAMC 2019), organized by SRM Institute of Science and Technology, Chennai, India, February 13-15, 2019.
 8. **Kavya S. Keremane**, Islam M. Abdellah, Ahmed El- Shafei, and Airody Vasudeva Adhikari, “Effect of alkyl chain length on the sensitizing action of simple thiophene-based molecules for *n*-type dye-sensitized solar cells”, 37th National Annual Conference Indian Council of Chemists (ICC-2018), organized by National Institute of Technology Karnataka, Surathkal, India, December 12-14, 2018.

9. **Kavya S. Keremane** and Airody Vasudeva Adhikari, “Molecular Engineering of carbazole based conjugated molecules as potential hole-transporting material for perovskite solar cells”, International Conference on Recent Trends in Material Science and Technology (ICMST-2018), organized by Indian Institute of Space Science and Technology, Thiruvananthapuram, Kerala, India, October 10-13, 2018.
10. **Kavya S. Keremane** and Airody Vasudeva Adhikari, “Synthesis, characterization and performance studies of a new metal-free organic sensitizer for DSSC application”, International NUS-ACS Research Symposium (NUS-ACS, 2018), organized by National University of Singapore (NUS), Singapore, February 21, 2018
11. **Kavya S. Keremane** and Airody Vasudeva Adhikari, “Design and synthesis of new metal-free organic chromophore for dye sensitized solar cell application” National Conference on Science and Technology: Reaching the Unreached (NCST-RU-2017), Mangalore university, Mangalore, Karnataka, India, September 08-09, 2017 (*Best Oral Presentation Award*).

* * * * *

CURRICULUM VITAE

KAVYASHREE S. KEREMANE

PRESENT ADDRESS

Department of Chemistry
National Institute of Technology Karnataka
Surathkal, Mangalore-575025
Karnataka, India

PERMANENT ADDRESS

#1756/B, "Balusmruti",
Puralakki bena, Near K.E.B
Post-Vandige, Ankola-581314
Karnataka, India

CONTACT DETAILS

Email: kavyakeremane@gmail.com

Mobile: +918050143688

EDUCATION

Doctor of Philosophy (Ph.D.) Chemistry, National Institute of Technology- Karnataka, (NITK) Surathkal, India	July 2016 - present
Masters of Science (M.Sc.) Organic Chemistry, Mangalore University, Karnataka, India	2014 First Class with Distinction (75 %)
Bachelor of Science (B.Sc) Physics, Chemistry, Mathematics (PCM) Karnataka University Dharwad, Karnataka, India	2012 First Class with Distinction (93 %)
Pre-University Education (10+2) Department of Pre-University Education, Karnataka, India	2009 First Class with Distinction (90 %)
Higher Secondary Education (10th) Karnataka Secondary Education Examination Board	2007 First Class with Distinction (94 %)

RESEARCH EXPERIENCE

05/2013 - 07/2013 (Supervisor: Dr. Sathya Shanker P.)	Syngene International Ltd., Bangalore	Summer Internship Fellow	Organic Synthesis
06/2014 - 02/2015 (Supervisor: Dr. Chandu C. Malakar)	SignalChem Life Sciences Corporation, Bangalore	Junior Scientist	Drug Discovery
03/2015 - 05/2016 (Supervisor: Prof. P. S. Mukherjee)	Indian Institute of Science (IISc), Bangalore	Research Assistant	Catalysis
01/2018 - 07/2018 (Supervisor: Prof. Subodh G. Mhaisalkar)	Nanyang Technological University (NTU), Singapore	Research Intern	Perovskite solar cells (PSCs)

07/2016- ongoing (Supervisor: Prof. A. V. Adhikari)	National Institute of Technology-Karnataka, (NITK)- Surathkal	Doctoral Student	Dye-sensitized solar cells & PSCs
--	---	---------------------	---

ACHIEVEMENTS

- **Best Poster presentation award** in International Conference on Thin Films & Nanotechnology: Knowledge, Leadership, & Commercialization (ICTN-KLC), organized by Thin Film Lab, Department of Physics, Indian Institute of Technology, Delhi, August 24-26, 2021
- **Best Oral presentation award** in the “Engineering & Material Science” session of National Symposium on “Future of STI: Impacts on Education, Skills, and Work” organized by Yenepoya University, Mangalore, India, February 27, 2021.
- **Outstanding Women Research Award** in International Conference on Smart Materials and Nanotechnology (ICSMN-2020), organized by Department of Engineering Physics and Chemistry, SKN Sinhgad College of Engineering, Maharashtra, India, January 02-04, 2020
- **Excellent Performance Award** in NTU-India Connect Research Internship Programme-2018, Nanyang Technological University (NTU), Singapore.
- **Best Poster Presentation Award** in University Grants Commission (UGC) Sponsored National level Seminar on “New Vistas in Sustainable Development-2014”, Sri Bhuvanendra College, Karkala, Mangalore.
- Mentored four M.Sc and two B.Tech. students during Ph.D. studies.
- **Karnataka Science and Technology scholarship** during M.Sc study, 2012-2014
- Secured 2nd rank with distinction in Master of Science (Organic Chemistry) at Mangalore University, India.
- Secured 7th rank in Bachelor of Science to Karnatak University, Dharwad, India.
- **Sir C. V. Raman fellowship** during B.Sc study, 2009-2012.

RESEARCH PUBLICATIONS

Papers published in international journals	: 07 (first author)
Papers Presented in National/International Conferences	: 11
Workshops attended	: 18

PERSONAL INFORMATION

Nationality:	Indian
Languages:	English, Hindi, Kannada, German (Elementary)
